Development of bifunctional small molecules to induce acetylation by CBP/p300



Oliver J. Stratton

St Hugh's College,

University of Oxford

A thesis submitted in partial fulfilment for the degree of

Doctor of Philosophy

Trinity 2024

Under the supervision of:
Prof. Stuart J. Conway,
Prof. Ester M. Hammond

Abstract

Lysine acetylation is a common, reversible, highly dynamic post-translational modification which occurs at thousands of sites in the human proteome. Lysine acetyltransferases (KATs) catalyse the transfer of an acetyl group onto lysine, while lysine deacetylases (KDACs) catalyse the removal of the modification.

Heat shock protein 90 (Hsp90α and Hsp90β) are ATP-dependent molecular chaperones that maintain active conformations of client proteins. Previous studies involving the knockdown or chemical inhibition of KDACs (particularly HDAC6) have shown hyper-acetylation on Hsp90α attenuates chaperone function, while Hsp90α K/Q mutants (acetyl-lysine mimetic) have unique interaction profiles with co-chaperones and client proteins.

Induced proximity between an effector enzyme and a target protein with a bifunctional molecule promotes post-translational modification on the target. This concept is the basis of target protein degradation and has recently been shown to be applicable to lysine acetylation.

The aim of this thesis was to develop a bifunctional molecule, termed Acetylation Directing Chimera (AcDC), that recruits the acetyl transferases CBP/p300 towards Hsp90 and induces an increase in lysine acetylation on that specific target protein. Starting with the CBP/p300 bromodomain inhibitor, inobrodib, and Hsp90 N-terminal domain inhibitor, BIIB021, we designed and synthesised AcDCs comprising varied linkers (AcDC-**1**–**4**). We demonstrated specific AcDC-induced proximity with recombinant proteins in an AlphaScreen based assay and validated a co-operative binding model with isothermal calorimetry (ITC). NanoBRET based assays demonstrated target engagement and induced proximity with full-length proteins in a cellular system. Co-immunoprecipitation of endogenous Hsp90 from showed AcDC-2 forms a stable complex with CBP (but not necessarily p300). We studied whether this induced proximity results in a significant change in lysine acetylation on Hsp90, and determined the observed phenotypic effects were predominantly driven by inhibition of the proteins' binding domains.

Acknowledgements

I am indebted to my supervisors for their ongoing support and for helping me accomplish this thesis. It is hard to put into words how grateful I am for everything they have taught me. I want to thank Prof. Stuart Conway for giving me the opportunity to initiate this project and for his continued faith in me as I worked through its trials and challenges. I also want to thank Prof. Ester Hammond for always having an open door and allowing me to explore the world of biology under her benevolent supervision. I could always count on them to provide support and inspiration. I have learned so much under their mentorship, and I am grateful for their wisdom and advice in my doctoral studies and beyond. I would also like to extend my gratitude to my industrial mentors, Dr Sam Dalton and Dr Mark Rackham, and to MSD (UK) for their support of this project.

I have had the pleasure of working in two amazing research groups during my DPhil, resulting in a long list of names to whom I owe gratitude in this regrettably short section of the thesis.

I would like to thank Dr Marta Serafini, Dr Pascal Heitel, Dr Antoine Wallabregue, and Dr Glen Brodie for their inspiring dedication as chemists and for being great fun to work with in the lab. I am grateful for their advice, words of encouragement, and for reassuring me in moments of uncertainty.

My special thanks go to Dr Chumin Zhou, Dr Hala Estephan, and Dr Lina Hacker for all that they have taught me in biology. I have learned so much from all of them, as they have not only taught me a huge number of new techniques and skills but also showed me the joys of biological research.

I consider myself privileged to have shared the entirety of my DPhil journey with Harriet Haysom, Alistair Boyd, Michael Platt, and Sophie Twigger. I couldn’t have hoped for better people to embark on a DPhil with, especially in the middle of a pandemic! They have been like my anchors in the storm, and I am grateful to each of them for their companionship

along the way. I am also especially grateful to Ceri Foster and Jenny Carter, my desk neighbours, with whom I shared many laughs and fantastic conversations.

I would like to thank Bernie, Çağla, Tiff, Patrick, Darius, and Adam, as the wise former DPhil students in the Conway and Hammond groups. They provided invaluable advice and wisdom, for which I am extremely grateful. I am also grateful that my time in the groups overlapped with Kat, Ed, Louise, and Keefe, and I wish them the best of luck with their own DPhils. I also extend my best wishes to the amazing Part II students I have had the pleasure of helping along the way: Hannah, Jonny, and Romi. All these people have made this DPhil an incredible experience and given me such great memories. I thank them all for making the lab such a positive working environment.

I am indebted to Dr Kilian Huber for allowing me to visit his lab and for providing invaluable advice. I am especially grateful to Ludwig Bauer, from whom I have learned a lot in chemical biology, but also for being a great friend.

My heartfelt thanks go to Pearse, for his constant support during this DPhil. I am excited for our future and look forward to life's next adventure.

My deepest gratitude goes to my family for their unwavering love and support. I feel incredibly fortunate to have been raised by parents who encouraged me unconditionally in all my pursuits. To my dad, though time has not allowed you to see this accomplishment, I know you would be proud.

Contents

Abstract ..... **i**

Acknowledgements ..... **ii**

Contents ..... **iv**

List of Figures ..... **viii**

List of Tables ..... **xiii**

List of Abbreviations ..... **xv**

1 Introduction **1**

1.1 Lysine acetylation **1**
1.1.1 Post-translational modifications 1
1.1.2 Chemistry 2
1.1.3 Dynamic regulation of KAc: writers, readers and erasers 2
1.1.4 Functions of KAc: Epigenetics 3
1.1.5 Functions of KAc on non-histone proteins 4
1.1.6 Lysine acetyltransferases (KATs) 5
1.1.7 Non-enzymatic acetylation 8
1.1.8 Lysine deacetylases (KDACs) 8
1.1.9 Bromodomains (BRDs) 10

1.2 CREBBP and EP300 ..... **12**
1.2.1 Structure 12
1.2.2 Functions, activity and regulation 14
1.2.3 Small molecule inhibitors for the BRD 15

1.3 Heat shock protein 90 (Hsp90) **17**
1.3.1 Heat shock proteins and HSP90 family members 17
1.3.2 Structure 18
1.3.3 Functions and disease 19
1.3.4 Small molecule Inhibitors of the *N*-terminal domain 20
1.3.5 Lysine acetylation on Hsp90 22

1.4 Proximity induction in drug discovery **24**
1.4.1 Molecular Glues and Bifunctionals 24
1.4.2 Proteolysis targeting chimeras (PROTACs) 26
1.4.3 Bifunctionals beyond PROTACs 28
1.4.4 Current works relevant to this thesis 30

1.5 Thesis aims **33**

2 Synthesis of Acetylation Directing Chimeras (AcDCs) and derivatives . 35

2.1 Design of AcDCs **35**
2.1.1 Selection of Inobrodib as a ligand to recruit p300/CBP 35
2.1.2 Selection of BIIB021 as a ligand to target Hsp90 39
2.1.3 Overall design of Hsp90 AcDCs 41

2.2 Synthesis of AcDC-1–4 and its containing ligands **42**
2.2.1 Synthesis of inobrodib 42

2.2.2 Synthesis of a piperidine-inobrodib analogue (pip-obrodib) 44
2.2.3 Synthesis of BIIB021 and Iodo-BIIB021 47
2.2.4 Synthesis of chemical linkers 48
2.2.5 Assembly of AcDC compounds 49
2.3 Synthesis of tools to investigate CBP^{BRD} engagement in cells. 52
2.3.1 Synthesis of an inobrodib-BODIPY tracer 52
2.4 Summary 56
3 Biophysical characterisation of AcDCs 57
3.1 Validation of chemical linker extension from inobrodib scaffold 57
3.2 AcDC-Induced proximity between recombinant p300^{BRD} and Hsp90α^{NTD} ... 59
3.2.1 Production of recombinant GST-Hsp90α^{NTD} 59
3.2.2 Development of an AlphaScreen based assay to show AcDC induced proximity 63
3.3 Validation of specific binding in ternary complex formation 69
3.4 Measurement of cooperative binding between in induced ternary complexes 71
3.5 Conclusions 74
4 Biological characterisation of AcDCs in cell-based assays 75
4.1 NanoBRET based experiments 75
4.1.1 NanoBRET target engagement assay with CBP^{BRD} 75
4.1.2 NanoBRET protein-protein interaction assay with CBP 78
4.1.3 NanoBRET protein-protein interaction assay with p300 82
4.2 Co-immunoprecipitation to measure complex formation in an endogenous system 85
4.3 Biological consequences of induced proximity between CBP/p300 and Hsp90 88
4.3.1 AcDC-1–4 do not induce target protein degradation 88
4.3.2 AcDC-1–4 reduced JJN-3 cell viability 93
4.3.3 Apparent AcDC-2 induced increase in Hsp90α(K294Ac) 95
4.3.4 Further investigation into AcDC-2 induced increase in Hsp90α(K294Ac) by dose-dependent treatment at 6 h 98
4.3.5 Competition between AcDC-2 with inobrodib and BIIB021, or inhibition with A-485 shows no effect on Hsp90α(K294Ac) 101
4.3.6 AcDC-2 treatment shows consistent phenotypes in A549 and MCF-7 cell lines, and in a hypoxia-induced stress response 104
4.3.7 CBP/p300 and Hsp90 show distinct subcellular compartmentalisations and AcDC-2 treatment does not induce translocation 107
4.4 Further investigation of consequences to Hsp90 from induced proximity with CBP/p300 in cells 109
4.4.1 Initial studies of lysine acetylation beyond K294 109
4.4.2 Validation of antibodies used in detection of acetylated Hsp90 110
4.4.3 Investigation of lysine acetylation on nuclear Hsp90 112
4.4.4 Investigation of the stability of acetylated Hsp90α in IP procedures 113
4.5 Summary 116
5 Discussion 118

5.1 Summary and conclusions 118
5.2 Discussion and future work 120
6 Materials and Methods 123
6.1 Biology Materials 123
6.1.1 Primary Antibodies 123
6.1.2 Secondary Antibodies 124
6.1.3 Mammalian cell culture reagents 124
6.1.4 Bacterial culture reagents 124
6.1.5 Commercially available drugs 125
6.1.6 Buffer formulations 125
6.1.7 Mammalian cell lines 126
6.1.8 Primers 126
6.1.9 Plasmid constructs, vectors, and bacterial cell lines 127
6.2 Biology Methods 128
6.2.1 Molecular cloning 128
6.2.2 Recombinant protein expression in *E. coli* 133
6.2.3 Recombinant protein purification 135
6.2.4 Recombinant protein concentration measurement 137
6.2.5 AlphaScreen 137
6.2.6 Isothermal titration calorimetry 138
6.2.7 Routine Tissue Culture 139
6.2.8 Compound treatments of cells 141
6.2.9 Hypoxia treatments 141
6.2.10 Western Blotting 141
6.2.11 Cell fractionation 142
6.2.12 Immunoprecipitation (IP) 143
6.2.13 Chemical Acetylation of recombinant protein 146
6.2.14 NanoBRET 146
6.2.15 Statistical analyses 147
6.3 Chemistry Experimental 149
6.3.1 Chemicals 149
6.3.2 Anhydrous solvents 149
6.3.3 NMR Spectroscopy 149
6.3.4 ^{1}H NMR 149
6.3.5 ^{13}C NMR 150
6.3.6 ^{19}F NMR 150
6.3.7 Chromatography and mass spectrometry 150
6.3.8 TLC 151
6.3.9 Normal phase silica gel flash column chromatography 151
6.3.10 Preparative liquid chromatography 151
6.3.11 Reverse phase HPLC 151
6.3.12 Low resolution electrospray ionisation (ESI) MS 152
6.3.13 High resolution MS 152
6.3.14 FT-IR Spectroscopy 152
6.3.15 Specific optical rotations 153
6.3.16 Melting points 153
6.3.17 Synthetic Procedures 154
References 209
Appendices i

Appendix A Supplementary notes and figures to chapters..... i
A.i Figures.....i
A.ii Comparison of 6×His-CBP^{BRD} and 6×His-p300^{BRD} sequences iii
A.iii Controls to ensure measured K294Ac levels are genuine iii
Appendix B Annotated maps of plasmid clones created in this thesis..... v
Appendix C SDS-PAGE and LC-MS of purified recombinant proteins viii
Appendix D ITC Traces..... xii
Appendix E NMR spectra of novel compounds..... xxvii
Appendix F HPLC chromatograms of novel compounds used in biology ... lxxxi

List of Figures

Figure 1.1: Acetylated lysine is formed by the transfer of an acetyl group from Ac-CoA onto the ε-amino group of lysine. 2
Figure 1.2: Lysine acetylation is a dynamic post-translational modification. 3
Figure 1.3: DNA is associated with histone proteins and organised into chromatin. 4
Figure 1.4: Domain architectures of canonical lysine acetyl transferases (KATs). 7
Figure 1.5: Proposed mechanisms for GNAT/MYST and CBP/p300 family KATs. 8
Figure 1.6: Co-crystal structure of the CBP BRD in complex with KAc as a representation of the canonical BRD structure 11
Figure 1.7: Structural homology of CBP and p300. 12
Figure 1.8: Chemical structures of a selection of reported inhibitors for the CBP/p300 bromodomain. 16
Figure 1.9: Domain architecture of HSP90 family members. 18
Figure 1.10: Comparison of the protein sequences of Hsp90α and Hsp90β. 19
Figure 1.11 Chemical structures of a selection of reported inhibitors for the Hsp90 N-terminal domain. 21
Figure 1.12: Positions of identified KAc residues on Hsp90α and Hsp90β. Orange lines mark the positions of lysine residues. 23
Figure 1.13: Representations of canonical molecular glues and bifunctional molecules as chemicals that induce proximity. 24
Figure 1.14: Illustration of the dose-dependent hook effect encountered with bifunctional molecules. 25
Figure 1.15: Mode of action of bifunctional molecules is demonstrated by the mechanism of PROTAC induced degradation of a protein of interest (POI). 26
Figure 1.16: Approaches to design of bifunctionals to increase binding cooperativity and create molecular glue-like molecules. 28
Figure 1.17: Graphic summary of current works on bifunctional molecules that recruit CBP/p300 as an effector. 30
Figure 2.1: X-ray co-crystal structure of inobrodib (pink) in complex with CBP^{BRD} (green) (PDB: 7XH6[176]) demonstrates that the methoxycyclohexyl group is solvent-exposed and is a suitable point for extension of the chemical linker (dark orange arrow). 36
Figure 2.2: The methoxycyclohexyl group on inobrodib was substituted with a piperidine group to generate the compound pip-obrodib which can be amide coupled to chemical linkers. 37

Figure 2.3: The substitution of the methoxycyclohexyl group in inobrodib for a piperidine is also demonstrated in recent works on the discovery of p300/CBP PROTACs (QC182,[177] XYD190,[178] and XYD198).[178] 37
Figure 2.4: SGC-CBP30 shows a similar conformation to inobrodib in co-crystal structures with CBP^{BRD} and is derivatised into heterobifunctional compounds. 38
Figure 2.5: Chemical structures of the Hsp90 inhibitors BIIB021,[183] EC144[180] and the Hsp90 PROTAC BP3.[181] 39
Figure 2.6: X-ray co-crystal structure of BIIB021 (pale orange) in complex with $Hsp90\alpha^{NTD}$ (blue) (PDB: 3QDD) shows that the purine *N*-7 position is solvent-exposed and a suitable vector for extension of a chemical linker (dark orange arrow). 40
Figure 2.7: The 6-chloroguanine on BIIB021 was substituted for 6-chloro-7-iodo-deazaguanine to generate the compound iodo-BIIB021 which could be cross-coupled to chemical linkers using a Sonagashira coupling. 41
Figure 2.8: Overall design of Hsp90 AcDC molecules constructed by amide coupling pip-obrodib and Sonagashira cross-coupling iodo-BIIB021 to PEG or alkyl containing chemical linkers functionalised with propargyl alcohol and acetate groups. 41
Figure 2.9: Formation of a mixed anhydride with **6** and *iso*-butyl chloroformate was converted to carbamate **18** rather than the desired amide coupling product (**12**). 46
Figure 2.10: Chemical structure of **inobrodib-BODIPY**, a novel fluorescent tracer compound that binds to the p300/CBP bromodomain. 52
Figure 3.1: The protein construct 6×His-$p300^{BRD}$ comprises the $p300^{BRD}$ with an *N*-terminal 6×His tag. 57
Figure 3.2: The protein construct GST-$Hsp90\alpha^{NTD}$ comprises the *N*-terminal domain of Hsp90α (residues 9–236) fussed to an *N*-terminal GST tag (grey box). 59
Figure 3.3: SDS-PAGE analysis of lysate soluble component in expression trials of GST-$Hsp90^{NTD}$ in Rosetta 2 (DE3) *E. coli*. 60
Figure 3.4: SDS-PAGE analysis of GSTrap purification of GST-$Hsp90\alpha^{NTD}$ shows good capture and release of desired recombinant protein at *c.* 50 kDa. 61
Figure 3.5: SDS-PAGE and chromatogram analysis of SEC purification of GST-$Hsp90\alpha^{NTD}$ shows multiple distinct forms of recombinant protein from GSTrap. 62
Figure 3.6: Principle of AlphaScreen based assay for ternary complex formation. 64
Figure 3.7: 6×His-GST was used as a technical positive control to optimise the AlphaScreen based assay for induced proximity. 65
Figure 3.8: Optimisation of AlphaScreen based assay for AcDC-induced proximity with protein concentration of 30 nM. 66
Figure 3.9: AcDCs induce proximity between recombinant $p300^{BRD}$ and $Hsp90^{NTD}$ by AlphaScreen assay. 67

Figure 3.10: Principle of AlphaScreen based competition assay to show specific binding in AcDC induced proximity. 69
Figure 3.11: AlphaScreen-based competition assay shows that titration of BIIB021 or inobrodib causes antagonistic loss of signal, confirming that AcDCs induce proximity by specifically binding to the bromodomain and *N*-terminal domains. 70
Figure 3.12: Principle of ITC based assay to measure co-operativity (**α**) of AcDC binding as ternary complex. 72
Figure 4.1: Principle of NanoBRET target engagement assay to show compound interaction with the NL-CBP^{BRD} fusion in a cellular context. 76
Figure 4.2: NanoBRET target engagement assay shows antagonistic loss of BRET signal upon titration of inobrodib and AcDC-**1**–**4**. 77
Figure 4.3: Principle of NanoBRET protein-protein interaction assay to show induced proximity between NL-CBP and HT-Hsp90 constructs in cells. 79
Figure 4.4: NanoBRET protein-protein interaction assay with NL-CBP^{BRD} and HT-Hsp90α shows gain of signal upon titration of AcDC-**1**–**4** but not inobrodib. 80
Figure 4.5: NanoBRET protein-protein interaction assay with NL-CBP^{FL} and HT-Hsp90 shows gain of signal upon titration of AcDC-**1**–**4** but not inobrodib or BIIB021. 82
Figure 4.6: NanoBRET protein-protein interaction assay to compare the AcDC-**2** induced interaction between CBP^{FL}-NL and p300^{FL}-NL with HT-Hsp90α and HT-Hsp90β could not produce a significant trend due to technical issues from weak signal. 84
Figure 4.7: Co-immunoprecipitation of Hsp90α/β and immunoblotting for CBP and p300 shows AcDC-**2** induces a stable interaction between Hsp90 and CBP but not p300. 86
Figure 4.8: Western blots show treatment of JJN-3 cells with AcDC-**1**–**4** after 24 h did not cause dose-dependent degradation of p300 and CBP; however decreased cMyc, and increased Hsp70 and Hsp90. 91
Figure 4.9: Western blot quantification for images shown in **Figure 4.8** for each detected protein. 92
Figure 4.10: MTT assays show AcDC-**1**–**4** and BIIB021 significantly reduced viability of JJN-3 cells after treatment for 24 h, while inobrodib had a less pronounced effect. 94
Figure 4.11: Western blot analysis of JJN-3 cells treated with AcDC-1–4 or combination of BIIB021 and inobrodib, each at 0.5 μM for 1, 3, 6, 16 and 24 h. 96
Figure 4.12: Western blot quantification for images shown in **Figure 4.11** for Hsp90α(K294Ac) at each measured time point. 97
Figure 4.13: Western blots show treatment of JJN-3 cells with AcDC-**2** after 6 h did not cause dose-dependent change in Hsp90α(K294Ac), Hsp90α/β, or HDAC6; however decreased CDK4 at high concentrations. 99
Figure 4.14: Western blot quantification for blots presented in **Figure 4.13**. 100

Figure 4.15: Western blots show treatment of JJN-3 cells with combination of BIIB021 and Inobordib, A-485, AcDC-**2** or panobinostat after 6 h did not cause significant change in Hsp90α(K294Ac) but did change H3(K18Ac) as expected. 102
Figure 4.16: Western blot quantification for blots presented in **Figure 4.15** for H3(K18Ac) and Hsp90α(K294Ac). 103
Figure 4.17: Western blots show treatment of **A** A549 and **B** MCF-7 cells with AcDC-**2** or combination of BIIB021 and inobrodib for 6 h did not cause dose-dependent change in Hsp90α(K294Ac), Hsp90α/β, or HDAC6; however, both sets of conditions decreased CDK4 at high concentrations. 105
Figure 4.18: Western blots show treatment of HEK293 cells with AcDC-**2** or combination of BIIB021 and inobrodib in either normoxia (21% O_2) or hypoxia (0.1% O_2) for 6 h and 24 h. 106
Figure 4.19: Cell fractionation analysed by immunoblotting shows treatment of HEK293 cells with AcDC-**2** or combination of BIIB021 and inobrodib for 6 h and 24 h does not cause translocation of CBP or p300 to the cytosol (C), or Hsp90 to the nucleus (N). 108
Figure 4.20: Comparison of the protein sequences of Hsp90α and Hsp90β with the position of lysine residues highlighted (orange lines). 109
Figure 4.21: Immunoprecipitation of Hsp90α/β and immunoblotting for pan-KAc shows no hyperacetylation on Hsp90α/β following treatment of HEK293 cells with combination of BIIB021 and inobrodib or AcDC-**2**, or panobinostat for 6 h. 110
Figure 4.22: Western blot analysis shows recombinant Hsp90α (r-Hsp90α) is chemically acetylated and recognised by pan-KAc and Hsp90α(K294Ac) antibodies, but r-Hsp90α is not recognised by Hsp90α/β (sc-13119) in all its forms. 112
Figure 4.23: Immunoprecipitation of Hsp90α from nuclear extracts and immunoblotting for pan-KAc shows no hyperacetylation on Hsp90α following treatment of HEK293 cells with combination of inobrodib and BIIB021 or AcDC-**2** for 6 h, or panobinostat treatment for 24 h before harvest. 113
Figure 4.24: Spike-and-recover experiment shows chemically acetylated recombinant Hsp90α (r-Ac-Hsp90α) is detected within the matrix of HEK293 whole cell lysate following the immunoprecipitation and immunoblotting procedure. 115
Figure 4.25: Denaturing immunoprecipitation of Hsp90α from HEK293 cells and immunoblotting for pan-KAc shows no hyperacetylation on Hsp90α following treatment of HEK293 cells with combination of inobrodib and BIIB021 or AcDC-**2** at 1 and 10 μM for 6 h, or panobinostat treatment for 24 h before harvest. 116
Figure A.1: Principle of ITC for measuring compound-protein dissociation constant (K_D)...i
Figure A.2: Summary of molecular cloning methods used in this thesis. ii

Figure A.3: Comparison of the aligned sequences of 6×His-TEV-p300^{BRD} and 6×His-TEV-CBP^{BRD}. iii

Figure A.4 Formation of carbamates at lysine residues on proteins in urea containing buffers by decomposition of urea into isocyanate and ammonia. iii

Figure A.5: Immunoblot analysis of HEK293 whole cell lysate prepared in a range of different lysis buffers shows consistent Hsp90α(K294Ac) signal levels in urea containing buffer (UTB) and non-urea containing buffers. iv

List of Tables

Table 1.1 Summary of the ten highest frequency post-translational modification types and the residues on which they occur. 1

Table 1.2: Human lysine acetyltransferases explored in drug discovery efforts, their classification into families, subcellular localisations and domains that have been targeted by small-molecule ligands.[23] 6

Table 1.3: Human lysine deacetylases, their classification into five families, and their subcellular localisations. 9

Table 1.4: Members of the HSP90 family of proteins in humans and their subcellular localisations. 18

Table 1.5 Changes in binding interactions of Hsp90α lysine-to-glutamine mutants compared to wt with co-chaperones (CHIP, p23, Hsp70), ATP and client protein (RAF-1) reported by Yang *et al.*[124] 23

Table 1.6: Overview of recent bifunctional molecules beyond PROTACs, the biological effectors they recruit and the intended function. 28

Table 2.1: Attempted reaction conditions for amide coupling between *o*-aryldiamine (**11**) and (*S*)-6-oxopiperidine-2-carboxylic acid (**6**) to form the intermediate **12** [**Scheme 2**, Step (iii)]. 45

Table 2.2: Summary of measured conversions for the solvent screen performed in **Scheme 8**. 51

Table 2.3: Summary of measured conversions for the lipase screen performed on 25 μmol scale for the reaction shown in **Scheme 9**, step (vi). 54

Table 3.1 Summary of binding affinities of AcDCs with the 6×His-p300^{BRD} protein construct. 58

Table 3.2: Mean EC_{50} values from experimental repeats of AlphaScreen based assay for induced proximity. 68

Table 3.4: Mean IC_{50} values from experimental repeats of AlphaScreen based competition assay for loss of induced proximity. 70

Table 3.5: Summary of dissociation constants (K_d) and cooperativity (α) values for 6×His-p300^{BRD} with AcDC-**1**–**4** and AcDC-**1**–**4** in complex with GST-Hsp90α^{NTD}. 73

Table 4.1: Summary of IC_{50} values from the NanoBRET target engagement assays. 77

Table 4.2 Summary of CC_{50} values from the combined data produced by three independent MTT assays. 95

Table 6.1: Names and specifications of primary antibodies used in this study. 123

Table 6.2: Names and specifications of secondary antibodies used in this study. 124

Table 6.3: Names and specifications of routine tissue culture reagents used in this study. 124
Table 6.4: Names and specifications of bacterial culture reagents used in this study. ... 124
Table 6.5 Names and formulations of bacterial culture media. 124
Table 6.6: Specifications of 1000× antibiotic stock solution preparations used in this study. 124
Table 6.7: Names and specifications of commercially available drugs used in this study. 125
Table 6.8: Names and formulations of commonly referenced buffers. 125
Table 6.9: Cell lines and their specifications, as used in this study. 126
Table 6.10: Details of primers used in this study. 126
Table 6.11: Details of plasmid constructs, vectors and the transformed cell lines used in this study. 127
Table 6.12 Names and specifications of chemically competent *E. coli* used in this study. 127
Table 6.13: Thermocycling conditions for PCR of long products (>6 kb) 130
Table 6.14: Details of conditions used in induction of recombinant protein expression used in this study. 134
Table 6.15 Names and molar extinction coefficients of recombinant proteins used in this study 137

List of Abbreviations

Ac	Acetyl
AcDC	Acetylation directing chimera
AceTAC	Acetylation targeting chimera
AceTAG	Acetylation tagging system
AIL	Autoinhibitory loop
Ala	Alanine
Aq.	Aqueous
Ar	Argon
Arg	Arginine
Asn	Asparagine
Asp	Aspartic acid
ATAT1	α-Tubulin acetyltransferase 1
ATCC	American type culture collection
ATP	Adenosine triphosphate
ATTEC	Autophagy-tethering compounds
AU	Absorbance units
AUTAC	Autophagy targeting chimera
BCL6	B-Cell lymphoma 6 protein
BCP	Bromodomain containing protein
BET	Bromodomain and extra-terminal domain
BiP	Binding immunoglobulin protein
Boc	*tert*-butyloxycarbonyl
BODIPY	4,4-difluoro-4-bora-3a,4a-diaza-*s*-indacene
Bpin	Pinacol boronate
BRD	Bromodomain
BRD4	Bromodomain containing protein 4
BRET	Bioluminescence Resonance Energy Transfer
BSA	Bovine serum albumin
Bu	Butyl
C	Cysteine
cAMP	Cyclic adenosine mono-phosphate
CBP	CREB binding protein
Cbz	Benzyloxycarbonyl
CDK	Cyclin-dependent kinase
CEL	Chan-Evans-Lam
CHAPS	3-[(3-cholamidopropyl)dimethylammonio]-1-propanesulfonate
CHIP	Carboxyl terminus of Hsc70-interacting protein
Chromo	Chromodomain
CIDE	Chemical inducers of degradation
CK1a	Casein kinase 1α
CLOCK	Circadian locomotor output cycles kaput protein
CoA	Coenzyme A
COSY	Homonuclear correlation spectroscopy
CRBN	Cereblon
CRE	cAMP response element
CREB	CRE binding protein

CREBBP	CREB binding protein
CTD	C-terminal domain
Da	Dalton
DAD	Diode array detector
DCC	*N,N′*-Dicyclohexylcarbodiimide
DCE	1,2-Dichloroethane
DEPC	Diethyl pyrocarbonate
DIPEA	*N,N*-Diisopropylethylamine
DMAP	4-Dimethylaminopyridine
DMEM	Dulbecco's modified Eagle's medium
DMF	Dimethylformamide
DMSO	Dimethyl sulfoxide
DNA	Deoxyribonucleic acid
DUBTAC	Deubiquitinase-targeting chimeras
E1A	Adenovirus early region 1A
EBI	European Bioinformatics Institute
EC_{50}	Concentration for half-maximal effective response
EDTA	Ethylenediaminetetraacetic acid
EI	Electron ionisation
EM	Election microscopy
EMBL	European Molecular Biology Laboratory
EP300	E1A-associated protein 300
eq.	Equivalent(s)
ESI	Electron spray ionisation
Et	Ethyl
F	Phenylalanine
FBS	Fetal Bovine Serum
FBXL17	F-Box And Leucine Rich Repeat Protein 17
FKBP12	FK506-Binding Protein 1A
FL	Full length
FPLC	Fast protein liquid chromatography
FT-IR	Fourier transform infrared
GHKL	Gyrase, Hsp90, His kinase and MutL
GIST	Gastrointestinal stromal tumour
Gly	Glycine
GNAT	Gcn5-related *N*-acetyltransferase
Grp94	Glucose-regulated protein 94
GST	Glutathione *S*-transferase
h	Hour(s)
HAT	Histone acetyltransferase
HATU	Hexafluorophosphate azabenzotriazole tetramethyl uronium
HbF	Foetal haemoglobin
HDAC	Histone deacetylase
HEMTAC	Heat shock protein 90 (Hsp90)-mediated targeting chimera
HEPES	4-(2-Hydroxyethyl)-1-piperazineethanesulfonic acid
HER2	Receptor tyrosine-protein kinase ErbB-2
HIF-1α	Hypoxia-inducible factor 1α
His	Histidine

HMBC	Heteronuclear Multiple Bond Correlation
HPLC	High performance liquid chromatography
HRMS	High resolution mass spectroscopy
HSP	Heat shock protein
HSQC	Heteronuclear single quantum coherence spectroscopy
HSR	Heat shock response
HT	HaloTag
HTS	High-throughput screening
HyT	Hydrophobic tag
IBiD	Interferon binding domain
IC_{50}	Concentration for half-maximal inhibitory response
IKZF	IKAROS Family Zinc Finger
IMAC	Immobilized metal affinity chromatography
IMiD	Immunomodulatory drug
IP	Immunoprecipitation
IPTG	Isopropyl β-d-1-thiogalactopyranoside
ITC	Isothermal titration calorimetry
K	Lysine
KAP	Kidney androgen-regulated protein
KAT	lysine acetyltransferase
K_d	Dissociation constant
KDAC	lysine deacetylase
KID	Kinase-inducible domain
KIX	KID interacting domain
LB	Lysogeny broth
LC	Liquid chromatography
Leu	Leucine
LP	Low pass
LRMS	Low resolution mass spectrometry
Lys	Lysine
LYTAC	Lysosome targeting chimera
m.p.	Melting point
MALDI	Matrix-assisted laser desorption ionisation
MAPK	Mitogen-Activated Protein Kinase
MD	Middle domain
Me	Methyl
MEM	Minimum essential medium
MES	2-Morpholinoethanesulphonic acid
Met	Methionine
min	Minute(s)
MOF	Males absent on the first protein
mol	Moles
mol.	Molecular
MORF	MOZ-related factor
MOZ	Monocytic leukaemia zinc finger protein
MS	Mass spectrometry
MSD (UK)	Merck Sharp & Dohme (United Kingdom)
mTORC1	Mechanistic/mammalian target of rapamycin complex 1

MTT	3-(4, 5-dimethylthiazol-2-yl)-2,5-diphenyltetrazolium bromide
MW	Microwave
MWCO	Molecular weight cut-off
MYST	MOZ, YBF2, Sas2p, TIP
NAD	Nicotinamide adenine dinucleotide
NCBD	Nuclear co-activator binding domain
NEB	New England BioLabs
NICE	Nuclear import and control of expression
NL	NanoLuciferase
NMI	*N*-Methylimidazole
NMR	Nuclear magnetic resonance
NOESY	Nuclear overhauser effect spectroscopy
NTA	Nitrilotriacetic acid
NTD	*N*-Terminal domain
OGTAC	*O*-GlcNAcylation TArgeting Chimeras
p300	EP300
PAGE	Polyacrylamide gel electrophoresis
PBS	Phosphate buffered salien
PCAF	p300/CBP association factor
PCNA	Proliferating cell nuclear antigen
PCR	Polymerase chain reaction
PDB	Protein data bank
PEG	Polyethylene glycol
PET	Positron emission tomography
PHD	Plant homeodomain
Phe	Phenylalanine
PHICS	Phosphorylation-Inducing Chimeric Small Molecules
PhoRC	Phosphatase recruiting chimeras
PhosTAC	Phosphorylation targeting chimeras
PIFA	Phenyliodine bis(trifluoroacetate)
PMSF	Phenylmethylsulfonyl fluoride
POI	Protein of interest
PPI	Protein-protein interaction
ppm	Parts per million
Pr	Propyl
PROTAC	Proteolysis targeting chimera
PTFE	Polytetrafluoroethylene
PTM	Post-translational modification
Py	Pyridine
Q	Glutamine
RAF	Rapidly Accelerated Fibrosarcoma
RE	Restriction endonuclease
R_f	Retention factor
RIBOTAC	Ribonuclease targeting chimeras
RING	Really interesting new gene domain
RIPA	Radioimmunoprecipitation
RNA	Ribonucleic acid
RP	Reversed Phase

rpm	Rotations per minute
RPMI	Roswell Park Memorial Institute
rt	Room temperature/ambient temperature
s	Second(s)
s.d.	Standard deviation
s.e.m.	Standard error of mean
SAR	Structure activity relationship
SDS	Sodium dodecyl sulphate
SEC	Size exclusion chromatography
SGC	Structural genomics consortium
SIRT	Sirtuin
SMAD7	Mothers Against Decapentaplegic Homolog 7
S_NAR	Nucleophilic aromatic substitution
SPR	Surface-plasmon resonance
TAE	Tris acetate EDTA
TAF1	TATA-Box Binding Protein Associated Factor 1
Tat	Tyrosine Aminotransferase
TAZ	Transcription adaptor zinc finger domain
TBAB	Tetrabutylammonium bromide
TBS	Tris-buffered saline
TBST	Tris-buffered saline tween 20
TCEP	Tris(2-carboxyethyl)phosphine
TCFH	*N*'-tetramethylformamidinium hexafluorophosphate
TCIP	Transcriptional/Epigenetic chemical inducer of proximity
TEMPO	(2,2,6,6-Tetramethylpiperidin-1-yl)oxyl
TEV	Tobacco Etch Virus
TFA	Trifluoroacetic acid
THF	Tetrahydrofuran
TLC	Thin-layer chromatography
TNF	Tumour necrosis factor
TOF	Time of flight
TR-FRET	Time-resolved fluorescence energy transfer
TRAP	TNF receptor associated protein
Tris	Tris(hydroxymethyl)aminomethane
TSA	Trichostatin A
Tyr	Tyrosine
UCL	University College London
UPS	Ubiquitin-proteasome system
UTB	Urea tris buffer
UV	Ultraviolet
V	Valine
WB	Western blot
WIZ	Widely-interspaced zinc finger-containing protein
Y	Tyrosine
ZnF	Zinc Finger
ZZ	ZZ-type zinc finger domain
γ-H2AX	Phosphorylated H2A histone family member X

1 Introduction

1.1 Lysine acetylation

1.1.1 Post-translational modifications

Once synthesised, proteins can be altered by modification to their molecular structure, referred to as a post-translational modification, or PTM. Whilst there are 20 naturally occurring amino acids, post-translational modification expands the repertoire of protein building blocks and alters their chemistries. These changes allow diversification of the proteome as proteins carry unique patterns of PTMs which can augment their activity, function, stability and molecular interactions.[1] A key biological advantage of PTMs is that they can be dynamically regulated, and at a much faster rate and lower energy cost than protein turnover. PTMs can also arise from environmental factors, such as redox changes, and allow the initiation of a molecular response to changing conditions.[2]

Distinct PTM types are restricted to specific residues, even though it may be chemically feasible for these to occur on a wider range of amino acids. The number of different types of PTM is on the order of hundreds;[3] however, only a selection of these have been well characterised at the proteome level. A selection of the most common and well-studied PTMs is presented in **Table 1.1**.[3, 4]

Table 1.1 Summary of the ten highest frequency post-translational modification types and the residues on which they occur. Frequency refers to the abundances the PTM is experimentally reported in the SwissProt database.[3]

Entry	Post-translation modification	Residues	Frequency
1	Phosphorylation	Serine, threonine	57,191
2	Acetylation	Lysine	6,656
3	*N*-linked glycosylation	Asparagine	5,343
4	Amidation	*C*-term.	2,830
5	Hydroxylation	Proline, lysine	1608
6	Methylation	Lysine, arginine	1497
7	*O*-linked Glycosylation	Serine, threonine	1104
8	Ubiquitylation	Lysine, cysteine, serine, threonine, *N*-term.	843
9	Pyrrolidone Carboxylic acid	Glutamic acid, glutamine	810
10	Sulfation	Tyrosine	495

1.1.2 Chemistry

Lysine acetylation is an evolutionarily conserved PTM, occurring in both prokaryotes and eukaryotes.[5] The post-translation modification occurs on lysine residues (K) where an acetyl group (Ac) is transferred from acetyl coenzyme A (CoA) onto the ε-amino group to form acetylated lysine (KAc) (**Figure 1.1**). This modification results in the neutralisation of the ammonium positive charge in physiological conditions, resulting in a change in protein structure and function.

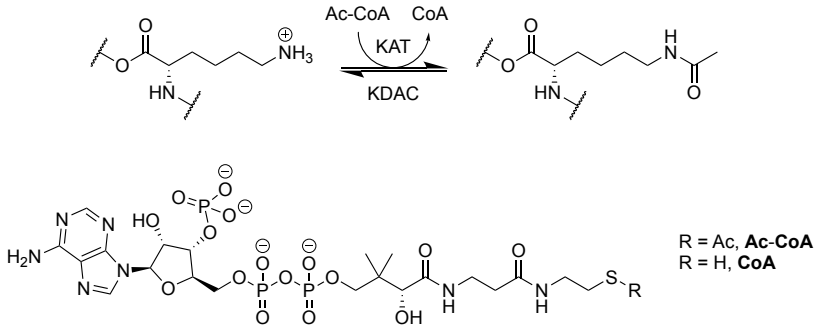


Figure 1.1: Acetylated lysine is formed by the transfer of an acetyl group from Ac-CoA onto the ε-amino group of lysine. The modification results in the neutralisation of an otherwise positive ammonium. The reaction is catalysed by a lysine acetyltransferase (KAT) and reversed by a lysine deacetylase (KDAC).

Another PTM often conflated with lysine acetylation is *N*-terminal acetylation, where proteins are acetylated on the α-amino group at the *N*-terminus.[6] This modification is both co-translational and post-translational, is irreversible and is found on 80–90% of human proteins.[7] However, it is functionally distinct from lysine acetylation and catalysed by a separate family of enzymes referred to as *N*-terminal acetyltransferases (NATs).[8]

1.1.3 Dynamic regulation of KAc: writers, readers and erasers

Lysine acetylation is a reversible and dynamic post-translational modification. It is regulated by two classes of enzymes: lysine acetyl transferases (KATs) and lysine deacetylases (KDACs). KATs 'write' the PTM onto proteins as they catalyse the formation of KAc, and KDACs 'erase' the PTM as they catalyse the reverse reaction and remove the acetyl group from lysine (**Figure 1.1**). These enzyme classes are also referred to as histone acetyl transferases (HATs) and histone deacetylases (HDACs), respectively due to their discovery in modifying lysine acetylation on histone proteins and regulating gene transcription. The

modification, however, is not limited to histones and is identified across the proteome. It is implicated in diverse cellular processes and human diseases. In addition to writers and erasers, bromodomains (BRDs) are a class of non-enzymatic protein domain which are able to 'read' acetylated lysine residues. BRDs bind to KAc and recruit the bromodomain containing protein (BCP) to the site of the PTM (**Figure 1.2**).

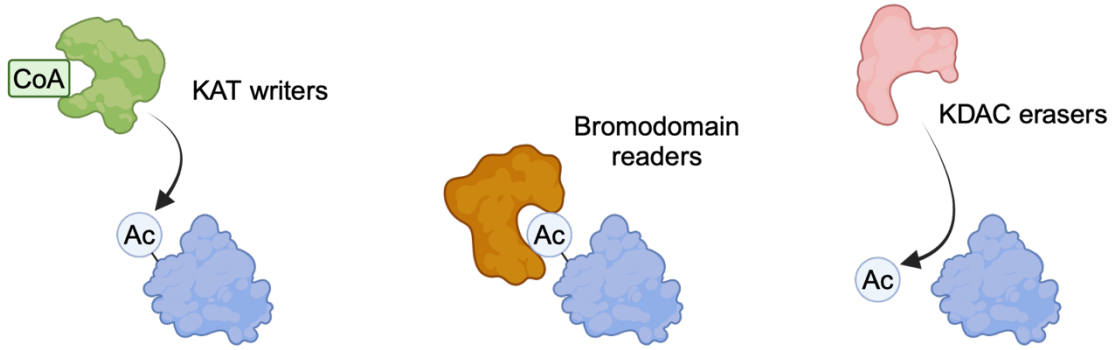


Figure 1.2: Lysine acetylation is a dynamic post-translational modification. The PTM is 'written' by KATs which catalyse the acetylation of lysine residues. Bromodomains can 'read' the PTM, as they selectively bind to KAc. The PTM is 'erased' by KDACs which catalyse the hydrolysis of KAc. Figure generated with BioRender.com

1.1.4 Functions of KAc: Epigenetics

In Eukaryotic cells, chromosomal DNA is packed into chromatin, which is composed of repeating units called nucleosomes. Each nucleosome contains approximately 146 base pairs of DNA wrapped around an octamer of 'core' proteins called histones (formed of an H3-H4 tetramer and two H2A, H2B dimers), and these are linked by approximately 20 base pairs of DNA and an additional histone (H1) (**Figure 1.3**). Histones are small basic proteins consisting of a globular domain and a more flexible lysine-rich 'tail' that protrudes from the nucleosome.[9]

The hierarchical structures that condense chromatin (referred to as heterochromatin) create a repressive environment that inhibits the activities of enzymes that require direct access to DNA. Acetylation of the lysine residues on the histone tails, among other post-translational modifications such as methylation and ubiquitylation, changes the structure of chromatin, allowing control of processes such as transcription, DNA repair, replication and recombination. It was initially suggested that KAc on histone tails reduce the electrostatic

interactions between the otherwise positively charged ammonium groups and negatively charged phosphate groups in DNA.[9] The reduction in electrostatic interactions gives rise to a less tightly packed form of chromatin referred to as euchromatin which is associated with increased gene transcription. However, this interpretation of the PTM function is an oversimplification, as BCPs also bind to KAc sites on histones and initiate the assembly of multi-component protein complexes involved in transcription. The PTMs associated with histone proteins impart a signalling role on chromatin, as a defined pattern of PTMs or 'marks' gives rise to defined downstream phenotypes. This is known as the 'histone code' concept.[10]

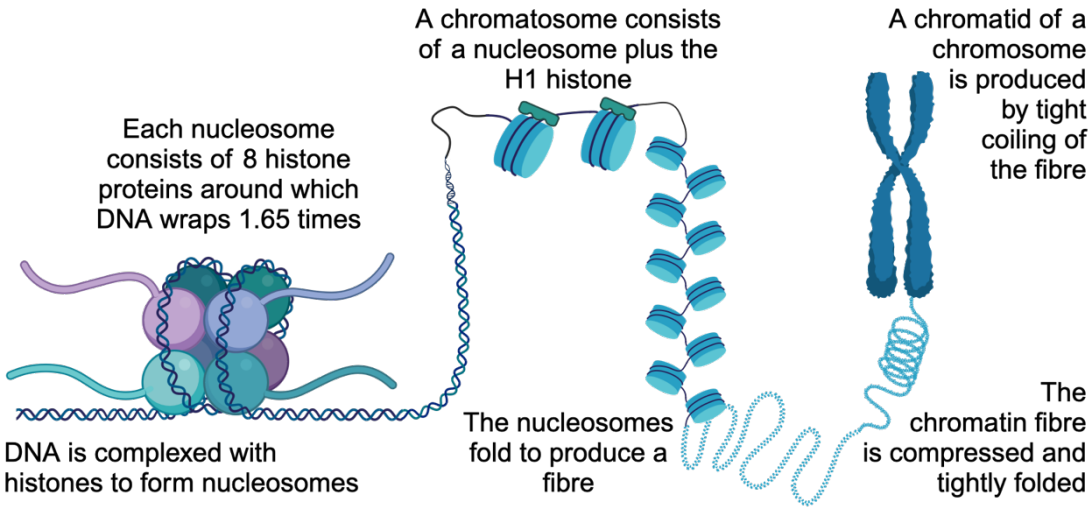


Figure 1.3: DNA is associated with histone proteins and organised into chromatin. Figure generated with BioRender.com

1.1.5 Functions of KAc on non-histone proteins

Owing to the technical challenges in identifying KAc sites,[11] it was more than 20 years following the discovery of histone acetylation before the first non-histone protein, tubulin, was found to contain KAc marks.[12] Following this, another 10 years passed before additional non-histone proteins, p53[13] and Tat,[14, 15] were also found to be regulated by KAc marks.[12] It was not until proteomics studies reported in the early 21st century revealed that KAc occurs across the proteome in diverse cellular compartments and was shown to have a prevalence comparable to protein phosphorylation.[11, 16]

The modification is implicated in several cellular processes and human diseases; examples include cellular signalling, protein folding, cytoskeleton organisation, protein aggregation, RNA processing and stability, autophagy, and subcellular translocalisation.[16]

Lysine residues frequently participate in protein-protein interactions, enzymatic activities, and protein degradation pathways. The acetylation of these residues can positively or negatively modulate these functions.[16] An example is the cell cycle-regulating kinases CDK1, CDK2 and CDK5 which can be acetylated at a conserved lysine that is directly involved in ATP binding; consequently, acetylation prevents ATP binding and inhibits kinase activity.[17] Conversely, autoacetylation enhances the activity of several KATs including CBP/p300, PCAF and MOF by relieving an autoinhibition mechanism.[18, 19] Protein stabilisation can occur when a lysine residue is acetylated instead of polyubiquitinated (which would otherwise result in proteasome-dependent degradation, see **§1.4.2**) Here, the acetyl group is acting as a protecting group, an example this is observed in the p300-mediated acetylation of SMAD7.[20] However, lysine acetylation can also lead to protein degradation as demonstrated by the p300-mediated acetylation of PRMT1 in triggering its degradation through FBXL17-mediated ubiquitination.[21] In summary, the effects of KAc on non-histone proteins are diverse and specific to the particular substrate and site of the modification.

1.1.6 Lysine acetyltransferases (KATs)

The human proteome contains several proteins with reported KAT activity, although there doesn't appear to be a literature consensus on the exact number. The most well characterised (canonical) KATs can be placed into three major families based on homology, and biochemical features (**Table 1.2**). These families include 'GCN5-related *N*-acetyltransferases' (GNAT); 'CBP/p300'; and 'MOZ, Ybf2, Sas2, and Tip60' (MYST). There is little homology between these families, and there are a significant number of established KATs that do not fit within this classification, such as ATAT1, TAF1 and CLOCK.[22]

Table 1.2: Human lysine acetyltransferases explored in drug discovery efforts, their classification into families, subcellular localisations and domains that have been targeted by small-molecule ligands.[23]

Entry	Family	Gene	Aliases	Localisation	Domains targeted by small-molecule ligands
1	GNAT	HAT1	KAT1	Nuclear, cytoplasmic	HAT[24]
2		KAT2A	GCN5	Nuclear	BRD[25]
3		KAT2B	PCAF	Nuclear	BRD[25]
4	CBP/p300	CREBBP	CBP, KAT3A	Nuclear, cytoplasmic	HAT,[26] BRD[27]
5		EP300	P300, KAT3B	Nuclear, cytoplasmic	HAT,[26] BRD[27]
6	MYST	KAT5	TIP60	Nuclear, cytoplasmic	HAT[28]
7		KAT6A	MOZ, MYST3	Nuclear	HAT[29, 30]
8		KAT6B	MORF, MOZ2, MYST4	Nuclear	HAT[29, 30]
9		KAT7	HBO1, MYST2	Nuclear	HAT[31]
10		KAT8	MOF, MYST1	Nuclear, mitochondrial	HAT[32]
11	Other	TAF1	KAT4, TAFII-250	Nuclear	BRD[33, 34]

Structurally, the KATs contain a catalytic domain responsible for their enzymatic activity but also harbour non-catalytic binding domains that enable them to interact with distinct substrates and interaction partners (**Figure 1.4**). The GNAT family (except for HAT1), CBP/p300, and TAF1 all contain at least one BRD module. Conversely, the MYST family contain chromodomains, plant homeodomain finger domains (PHDs) or zinc-finger (ZnF) domains.

The molecular basis for the substrate specificity of the KAT catalytic domains remains elusive and consensus substrate recognition sequences have not been identified.[35] The neighbouring non-catalytic domains are suggested to define substrate specificity, as they dictate the subcellular localisation, interacting proteins and the accessibility of lysine residues in the substrate proteins.[16, 35] Except for ATAT1, all identified KATs are primarily localised in the nucleus, although they have populations in the cytoplasm where they exhibit activities.[36]

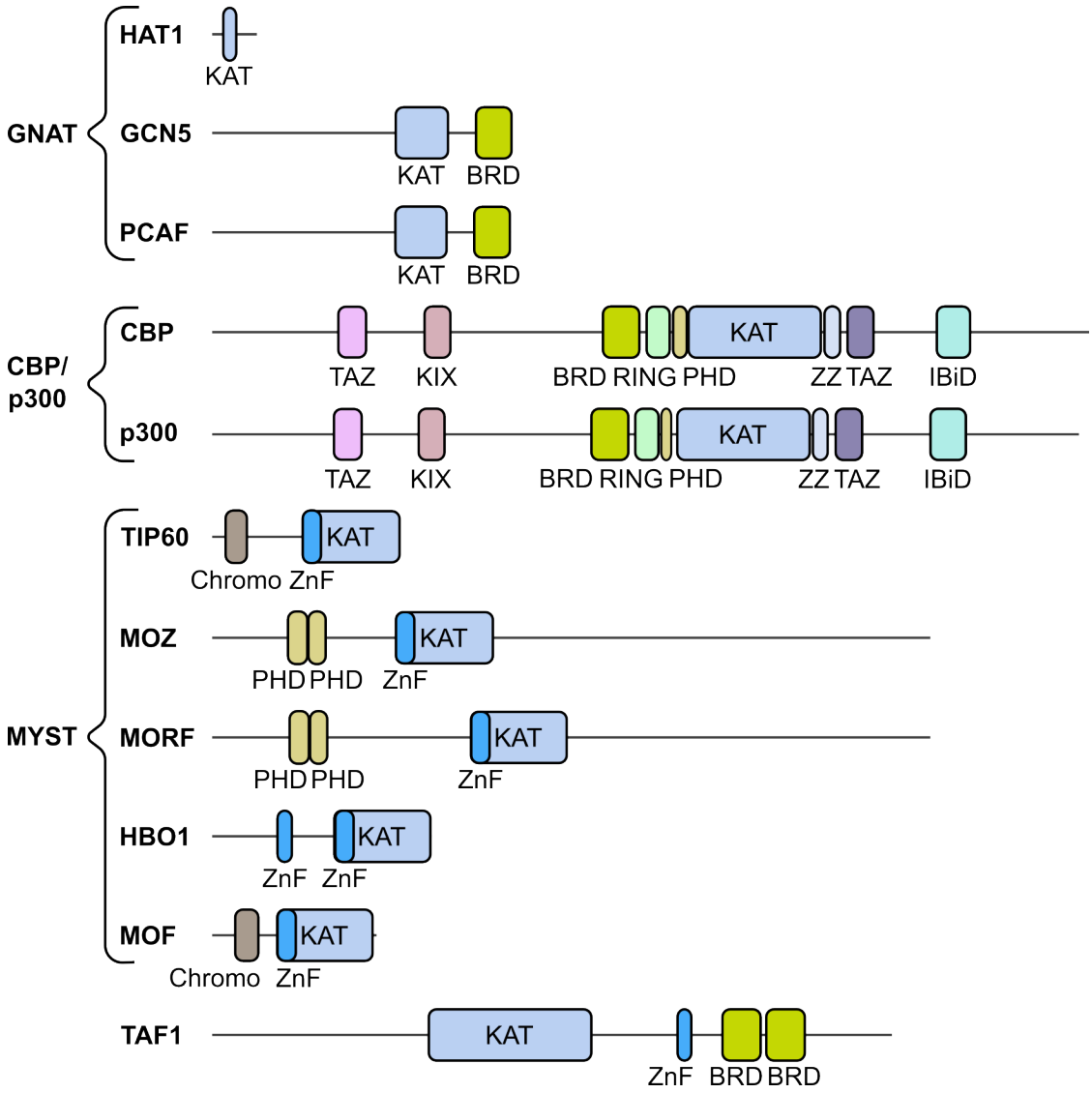


Figure 1.4: Domain architectures of canonical lysine acetyl transferases (KATs). Protein primary sequences represented by lines proportional to their length. Structurally defined domains represented by colourful boxes: KAT (pale blue), BRD (green), transcription adaptor zinc finger domain (TAZ, pink/purple), kinase-inducible domain (KID) interacting domain (KIX, peach), really interesting new gene domain (RING, turquoise), plant homeodomain (PHD, beige), ZZ-type zinc finger domain (ZZ, grey), interferon binding domain (IBiD, sky blue), chromodomain (brown). Domains and sequence length information was obtained from InterPro tool by EMBL-EBI.[37]

Mechanistically, CBP/p300 differ from the GNAT and MYST families in the transfer of the Ac group onto lysine (**Figure 1.5**).[22] CBP/p300 follow a Theorell-Chance mechanism also referred to as a hit-and-run mechanism where there is no stable ternary complex between the substrate and enzyme active site. Here, the substrate associates very transiently with the enzyme in a shallow catalytic pocket which is already complexed with Ac-CoA and then leaves as soon as the reaction is complete. CoA then departs from the enzyme complex

more slowly.[38] This mechanism may partially explain the relative substrate promiscuity observed for CBP/p300.[38, 39]

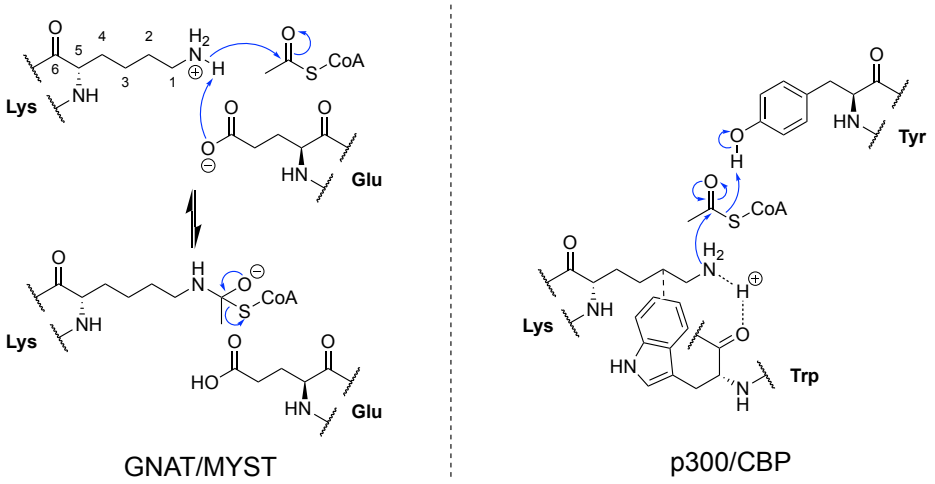


Figure 1.5: Proposed mechanisms for GNAT/MYST and CBP/p300 family KATs. The GNAT/MYST family KATs contain a glutamate residue (Glu) in the active site which initially deprotonates the lysine (Lys) ε-amine, which enables nucleophilic attack of the Ac-CoA carbonyl, followed by formation of a transient tetrahedral intermediate and its subsequent collapse into KAc and CoA. The CBP/p300 family KATs follow a 'hit and run' (Theorell-Chance) mechanism, as they contain a tryptophan residue (Trp) in the active site which steers the lysine sidechain and lowers its pK_a to allow nucleophilic attack of Ac-CoA. A tyrosine residue (Tyr) acts as an acid to protonate the sulfhydryl of CoA and facilitate the formation of KAc and CoA.

1.1.7 Non-enzymatic acetylation

In addition to enzymatic regulation, lysine acetylation can also occur non-enzymatically.[16] KAc is found to be increased in cells that are metabolically active but growth arrested,[40] and is dependent on the availability of Ac-CoA.[40] The site of non-enzymatic acetylation is preferred by proximal positively charged residues[41] and a higher pH environment (such as in the mitochondrial matrix).[42] This mechanism may significantly contribute to the abundance of KAc on mitochondrial proteins, where Ac-CoA is more available.[43] Additionally, proximal cysteine residues can also facilitate non-enzymatic acetylation by thiol exchange with Ac-CoA followed by intramolecular *S*-to-*N* transfer.[44]

1.1.8 Lysine deacetylases (KDACs)

The human proteome contains 19 KDACs that can be grouped into two major families: the Zn^{2+}-dependent HDACs and the NAD^{+}-dependent sirtuins. The Zn^{2+}-dependent HDACs can be further characterised into four classes based on sequence similarities: classes I, IIa, IIb and IV; while the sirtuins are referred to as class III KDACs (**Table 1.3**).[8]

KDACs are localised in both the nucleus and cytoplasm however only the sirtuins (class III) are additionally found in the mitochondria. Compared to the KATs, there are more instances of KDACs localised in the cytoplasm, however not all KDACs display activity here, as cytoplasmic shuttling is attributed as a regulatory mechanism to reduce their activity in the nucleus.[36] The most extensively studied cytoplasmic KDAC is the class IIb enzyme HDAC6, which has several cytoplasmic substrates including tubulin,[45] cortactin,[46] Hsp90,[47] β-catenin,[48] and peroxiredoxin.[49] Interestingly, all Class I, II, and IV HDACs predate the evolution of histone proteins, suggesting that the primary substrates for this HDAC family may be non-histones.[50]

Table 1.3: Human lysine deacetylases, their classification into five families, and their subcellular localisations.

Entry	Class	Gene	Subcellular localisation
1	I	HDAC1	Nuclear (primarily)
2		HDAC2	Nuclear
3		HDAC3	Nuclear (primarily)
4		HDAC8	Nuclear, cytoplasmic
5	IIa	HDAC4	Nuclear, cytoplasmic
6		HDAC5	Nuclear, cytoplasmic
7		HDAC7	Nuclear, cytoplasmic
8		HDAC9	Nuclear, cytoplasmic
9	IIb	HDAC6	Cytoplasmic (primarily)
10		HDAC10	Cytoplasmic (primarily)
11	III (Sirtuins)	SIRT1	Nuclear
12		SIRT2	Cytoplasmic
13		SIRT3	Mitochondrial
14		SIRT4	Mitochondrial
15		SIRT5	Mitochondrial
16		SIRT6	Nuclear
17		SIRT7	Nucleolar
18	IV	HDAC11	Nuclear (primarily)

In contrast to KATs, all members of the metal-dependent KDAC family exhibit a highly conserved catalytic domain structure.[51] The proposed catalytic mechanism is identical for all Zn^{2+}-dependent KDACs, involving activation of the acetate for hydrolysis by a zinc ion and general acid/base catalysis by a histidine residue.[51] The sirtuins also share a conserved catalytic core which is distinct from the other KDAC classes.[22]

Similarly to KATs, the KDACs also function in large macromolecular complexes that dictate the substrate specificity and activity. The Class I, II and IV KDACs present very low deacetylase activity when purified to homogeneity.[50]

From a clinical perspective, the development of Zn^{2+}-dependent KDAC inhibitors has been successful with the approval of pan-KDAC inhibitors vorinostat, panobinostat, belinostat and romidepsin, predominantly for the treatment of T-cell lymphoma.[52] These chemical tools are also used in the discovery of KAc on proteins, by inhibiting its removal, this causes an increase in global KAc.[53]

1.1.9 Bromodomains (BRDs)

Bromodomains are evolutionarily conserved protein-protein interaction (PPI) domains which mediate the recognition of KAc residues. Within the human proteome, no fewer than 61 BRDs have been identified which are found across 46 proteins containing bromodomains (BCPs). These can be classified into eight families based on sequence homologies.[54]

Bromodomains are a well-conserved structure despite large sequence variations, they comprise approximately 110 amino acid residues arranged into four α-helices (α_Z, α_A, α_B, α_C) joined by three loops (ZA, AB, BC; respectively) (**Figure 1.6**). The KAc binding site is located between the ZA and BC loops, with the residues on these loops showing the highest variability, determining the substrate specificity by forming key interactions with residues neighbouring the KAc.[55] The KAc binding site of canonical bromodomains contains an asparagine and five water molecules that form the base of the pocket, despite being predominantly hydrophobic in character. The carbonyl oxygen on the KAc accepts a hydrogen bond from the conserved asparagine, in addition to forming water mediated hydrogen bonds with other residues including a tyrosine residue.[54]

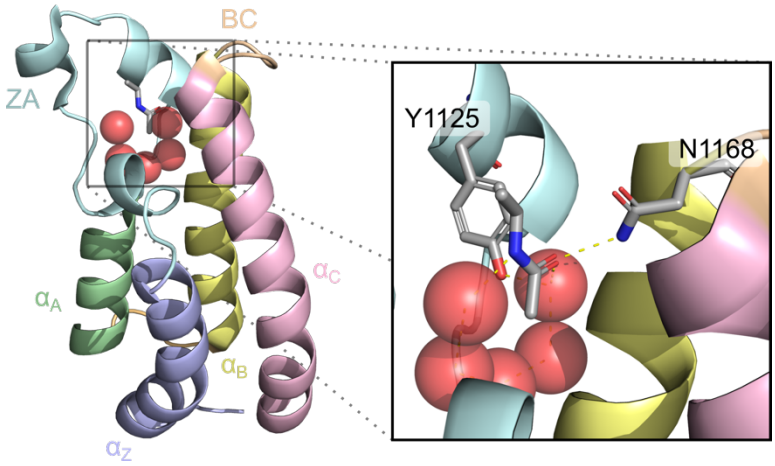


Figure 1.6: Co-crystal structure of the CBP BRD in complex with KAc as a representation of the canonical BRD structure The BRD comprises four α-helices (α_Z (purple), α_A (green), α_B (yellow), α_C (pink)) joined by three loops (ZA (light blue), AB (light orange), BC (wheat). The base of the binding pocket is lined by five conserved water molecules (red spheres). A direct hydrogen bond (yellow dashed line) forms between the KAc (grey) acetyl carbonyl and an asparagine residue, and a water mediated hydrogen bonds forms with a tyrosine residue. PDB: 3P1C.[54] Figure generated with PyMol.

1.2 CREBBP and EP300

1.2.1 Structure

CREBBP and EP300 are paralogous genes which encode for the expression of CREB binding protein (CBP) and E1A-associated protein p300 (p300), respectively. CBP was discovered and cloned in 1993 as a binding partner to CREB, a transcription factor that binds cAMP (cyclic adenosine mono-phosphate) response elements (CREs). p300 was first cloned in 1994 and found to be a binding partner of E1A, an adenovirus oncogenic transcription factor. p300 is also approximately 300 kDa in size, giving it its name.

The two proteins present a high degree of structural homology and are collectively referred to as CBP/p300. The paralogues are composed of multiple domains including an acetyltransferase domain (KAT) that confers enzymatic activity, but also several non-enzymatic domains that primarily function to govern the proteins' substrates, interaction partners, and modulate its activity (**Figure 1.7**).

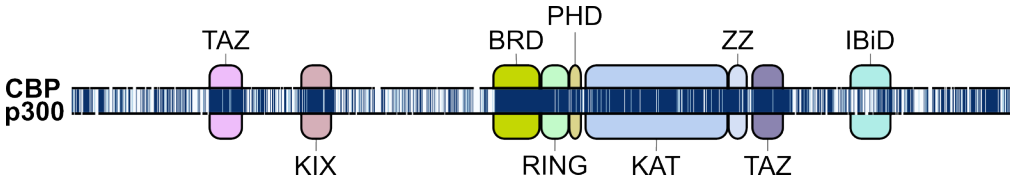


Figure 1.7: Structural homology of CBP and p300. The central horizontal bar shows shared sequence identity (dark blue) and similarity (light blue) between the proteins' primary structures, truncations are shown by a break in the labelled horizontal lines (as determined using the EMBL-EBI EMBOSS matcher tool,[56] and plotted using the Matplotlib python package). The underlaid boxes show the shared domain architecture along the protein sequences: transcription adaptor zinc finger domain (TAZ), kinase-inducible domain (KID) interacting domain (KIX), bromodomain (BRD), really interesting new gene domain (RING), plant homeodomain (PHD), lysine acetyltransferase domain (KAT), ZZ-type zinc finger domain (ZZ), interferon binding domain (IBiD). Drawn to scale with each residue represented by 0.05 mm in the horizontal direction.

The highest sequence similarity is found in the structurally defined domains, particularly within a central 'catalytic cassette' comprising the bromodomain (BRD), really interesting new gene (RING), plant homeodomain (PHD), KAT, and ZZ-type zinc finger domain (ZZ). KAT activity is regulated by a long, lysine-rich and intrinsically disordered loop contained within the KAT domain, termed the autoinhibitory loop (AIL).[18] In the hypoacetylated form, the AIL impedes KAT activity,[18] with its deacetylation mediated by Sirt2.[57] Seminal work by Delvechio *et al*. showed the RING domain also has a regulatory role on KAT activity, as it

works synergistically with the AIL to sterically occlude the KAT substrate pocket.[58] This inhibition is released upon auto-hyperacetylation of the AIL, leading to a more open conformation where the KAT pocket is more accessible to substrate binding.[58]

The RING and PHD domains have non-canonical structures and do not display the expected functions of interacting with ubiquitin[59] or trimethylated lysine,[60] respectively. However, the PHD is implicated in working synergistically with the BRD to modulate KAT substrate specificity: p300 mutants containing a deletion of the PHD displayed increased autoacetylation but impaired histone acetylation activity compared to the wildtype, although p53 acetylation activity was not affected.[60]

As previously introduced, the BRD acts to bind to KAc residues,[61] and in the context of CBP/p300 this occurs on both histone[62] and non-histone proteins.[63] While the BRD has been shown to be essential for p300 to bind to chromatin *in vitro,*[62] chemical inhibition of the bromodomain has been shown *not* to disrupt the localisation of CBP/p300 onto chromatin, but does reduce acetylation at specific sites such as H3K27Ac.[64] The ZZ domain is another chromatin binding domain that modulates the activity of the HAT domain. It has been shown to promote selective acetylation of H3K27 and H3K18 by p300, but not necessarily CBP.[65]

This catalytic cassette is flanked by long stretches of intrinsically disordered residues (IDRs) which exhibit reduced sequence similarity and could confer a degree of substrate specificity between the two paralogues.[66] The IDRs have also been hypothesised to drive liquid-liquid phase separation, and could potentially contribute to the regulation of the proteins' activity.[67-69]

The transcription adaptor zinc finger (TAZ) domains and the kinase-inducible domain interacting domain (KIX) mediate interactions with transcription factors to promote target gene expression. In addition, the interferon binding domain (IBiD), also known as the nuclear co-activator binding domain (NCBD), interacts with several non-homologous transcription factors including IRF3 and STAT1. Together, these domains have been shown

to be essential for CBP/p300 to bind to chromatin through multivalent interactions with transcription factors.

There is no clear literature consensus on the extent to which BRD serves to recruit CBP/p300 onto its substrates. A recent study by Ferrie *et al.* showed the isolated catalytic cassette from p300 had essentially no ability to bind to chromatin in live cells, and a construct containing a deletion of the catalytic cassette (ΔBRD–ZZ) showed enhanced binding to chromatin compared to the wild type protein.[70] There is, however, significant biochemical data that shows the BRD binds to KAc sites to direct the KAT domain to additional specific sites, including cryo-EM structures of the interaction between p300 and acetylated histone tails on nucleosomes.[65, 67, 71, 72] A common hypothesis is that the BRD orientates the KAT domain, while the overall proteins' localisation and substrate binding is dictated by the *N* and *C*-terminal binding domains.[71] This is supported by the observation that the BRD exhibits micromolar affinity for acetylated peptides *in vitro*,[54] while TAZ have nanomolar affinity for transcription factor peptides.[70, 73, 74]

1.2.2 Functions, activity and regulation

CBP/p300 were originally identified as transcriptional co-activators due to their KAT activity towards histones and their ability to bind transcription factors, bridging them to the transcription machinery. However, more recent works show that the proteins' KAT activity extends to non-histone proteins in the regulation of diverse cellular processes including autophagy,[75] DNA damage repair,[76] and stress response pathways.[77] Over 100 proteins have been implicated as CBP/p300 acetylation substrates, and more than 400 proteins serve as binding partners.[39]

CREBBP and EP300 are essential genes for normal development in mammals and double knockouts or double heterozygosity ($CREBBP^{+/-}$/ $EP300^{+/-}$) show embryonic lethality.[78, 79] While CBP/p300 have overlapping functions, the paralogues are not functionally redundant as they have been identified to have distinct roles.[80]

The proteins are ubiquitously expressed in human tissues, with temporal and spatial control, and their subcellular localisation can be distinct and regulated in several cell types during development.[81, 82] Both paralogues show subcellular localisation to the nucleus; however, they also show significant activity in the cytoplasm, and recent work has shown that p300 shows cytoplasm-to-nucleus shuttling,[83] which can be regulated by nutrient availability and in turn contributes to the activation of mTORC1.[84]

The activity of CBP/p300 can be regulated by PTMs, such as the autoacetylation of the AIL. Interactions with binding partners also govern the proteins' activity.[39] The two mechanisms can also be synergistic as work by Ortega *et al.* showed that kinase-activated transcription factor dimerisation enables p300 autoacetylation on the AIL.[85] In addition, site-specific phosphorylation can also positively or negatively regulate KAT activity.[39]

1.2.3 Small molecule inhibitors for the BRD

Great effort has been put into the development of small molecule inhibitors targeting the CBP/p300 BRDs (**Figure 1.8**). Indeed, they are the second most frequent BRD targets after the BET family.[86] Due to the high sequence identity within the BRD (97%), no paralogue selective ligands have been reported.

The first sub-micromolar affinity ligands were published in 2014 by the Conway and Brennan laboratories at the University of Oxford, namely (*R*)-2 (CBP K_d = 390 nM)[87] and SGC-CBP30 (CBP K_d = 21 nM, p300 K_d = 32 nM)[27] respectively. Notably, the compounds possess distinct KAc mimetic chemotypes. In (*R*)-2, this is a lactam on the dihydroquinoxalinone which establishes crucial hydrogen bonds at the base of the binding pocket, whereas this function is fulfilled by an isoxazole in SGC-CBP30. Since the discovery of these ligands, a number of other inhibitors have been reported containing other KAc mimics, as examples: benzodiazepinone ((–)-OXFBD05,[88] CPI-637)**;** benzoxazepine (I-CBP112**)**; and pyrazolopiperidine derivatives (GNE-272,[89] GNE-207,[90] GNE-781).[91]

The most significant challenge in the development of these molecules has been achieving selectivity for the CBP/p300 BRD against the other 59 BRDs in the human proteome, with

the most common off targets being BET family BRDs. The first published compounds to overcome this barrier originated from Constellation Pharmaceuticals and Genentech, with CPI-637 (CBP K_d = 0.03 μM, >360-fold selectivity over BRD4(1))[92] and GNE-272 (CBP IC_{50} = 0.02 μM, >650-fold selectivity over BRD4(1)), the latter: suitable for use as a probe *in vivo*.[89] Genentech has since developed two additional optimised orally-bioavailable inhibitors with improved pharmacokinetic profiles: GNE-207 (CBP IC_{50} = 1 nM, >2500-fold selectivity against BRD4(1))[90] and GNE-781 (CBP IC_{50} = 0.94 nM, >5400-fold selectivity against BRD4(1)).

The only CBP/p300 BRD inhibitor to progress to clinical trials is inobrodib (also known as CCS1477) from CellCentric, for the treatment of haematological malignancies and advanced tumours. Its structure is reminiscent of SGC-CBP30 with slight modifications providing a boost in affinity (CBP K_d = 1.7 nM, p300 K_d = 1.3 nM, >130-selectivity over BRD4(1)).[93]

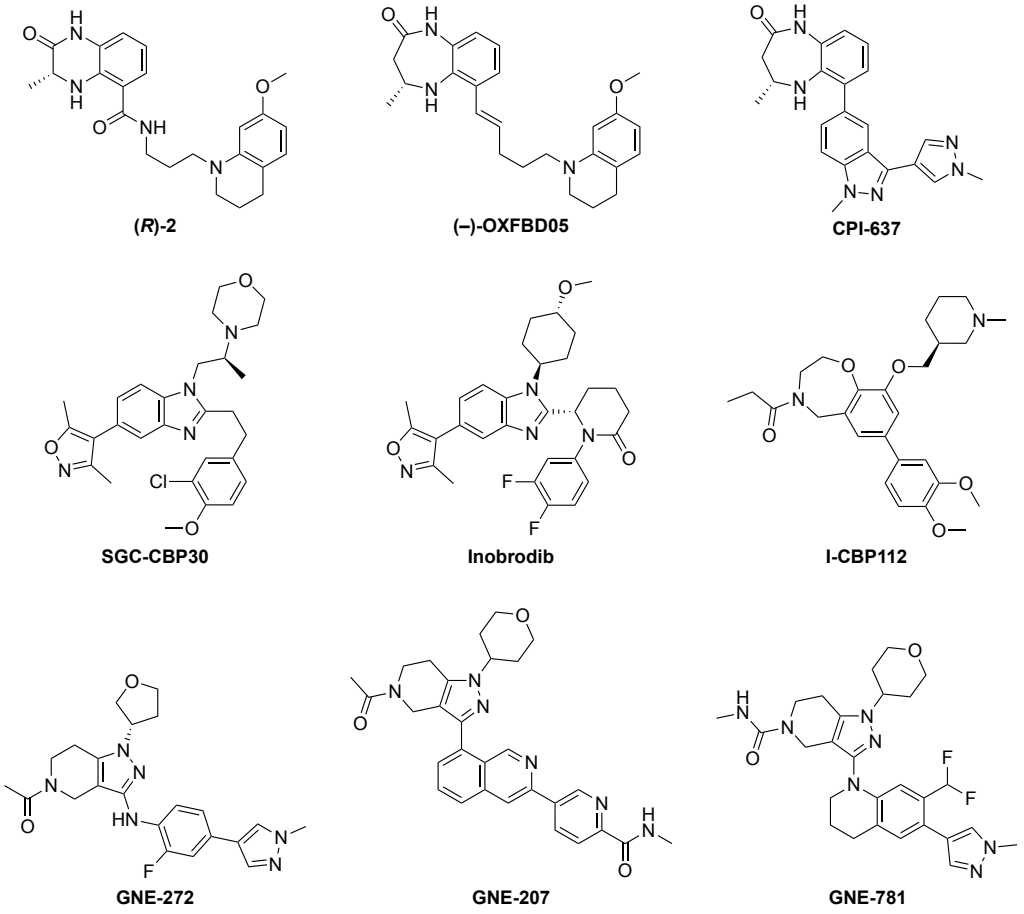


Figure 1.8: Chemical structures of a selection of reported inhibitors for the CBP/p300 bromodomain.

1.3 Heat shock protein 90 (Hsp90)

1.3.1 Heat shock proteins and HSP90 family members

The term “heat shock proteins” (HSPs) originates from the pioneering work of Ritossa who serendipitously observed characteristic puffing of the chromosomes from *Drosophilia* which had unintentionally been incubated at elevated temperatures.[94, 95] This phenomenon, termed the heat shock response (HSR) was attributed to increased gene expression of specific proteins, subsequently identified as HSPs. The HSR is a universal response to an extensive array of stresses, such as hyperthermia, anoxia, hypoxia, heavy metals, or other chemical agents that may induce proteotoxic stress. It is characterised by an increase in HSP expression mediated by inducible transcription factors termed heat shock factors (HSFs).[96]

HSPs are referred to as molecular chaperones: they inhibit inappropriate associations and facilitate the correct folding and maturation of other cellular proteins, collectively termed clients. Chaperones rarely function alone but participate in large multicomponent machines that contain other chaperones (co-chaperones), modulators of ATP activity, and other accessory proteins. Importantly, they usually do not contribute to the final mature structures that their clients form.[97]

The protein class is categorised into families based on molecular weights with the majority belonging to the groups HSP27, HSP40, HSP60, HSP70, HSP90 and large HSPs. The proteins are predominantly ATP-dependent except for a few small HSPs.[96]

In humans, the heat shock protein 90 family comprises of 4 homologues, approximately 90 kDa in size (**Table 1.4**). These are categorised into three sub-types: HSP90A (conventionally and henceforth referred to as Hsp90) comprises the closely related Hsp90α and Hsp90β; HSP90B comprises glucose regulated protein 94 (Grp94); and tumour necrosis factor (TNF) receptor-associated protein 1 (TRAP1). In normal cells, Hsp90 is predominantly cytosolic with a small nuclear pool, while Grp94 is localised to the endoplasmic reticulum and TRAP is localised to mitochondria.[98]

Table 1.4: Members of the HSP90 family of proteins in humans and their subcellular localisations.

Entry	Sub-family	Gene	Alias	Subcellular localisation
1	HSP90A	HSP90AA1	Hsp90α	Cytosolic
2		HSP90AB1	Hsp90β	Cytosolic
3	HSP90B	HSP90B1	Grp94	Endoplasmic reticulum
4	TRAP	TRAP1	TRAP	Mitochondrial

Despite their name, HSPs are ubiquitously expressed under normal conditions. Hsp90 comprises 1–2% of total cellular protein content,[99] and this amount only increases 2-fold under stress.[100] Hsp90 is evolutionarily well-conserved from bacteria to humans, with a sequence homology of 53% between *E. coli* and humans, indicating the protein's essential nature throughout evolutionary history.[97]

1.3.2 Structure

Functional HSP90 family proteins in solution consist of a homodimer of two protomers. These protomers comprise three structurally defined domains (**Figure 1.10**): an *N*-terminal domain (NTD) which binds ATP as well as co-chaperones; a middle domain (MD) that mediates interactions with client proteins and co-chaperones, together with the NTD forms a split ATPase; and a *C*-terminal domain (CTD) that contains the dimerization motif and interaction sites for additional co-chaperones.[101] The NTD and MD are separated by an intrinsically disordered region which contains several charged residues which also mediate the proteins' activity.[102] Hsp90 is related to other 'split ATPases' such as DNA gyrase, and is a member of the gyrase, Hsp90, His kinase and MutL (GHKL) superfamily.[103]

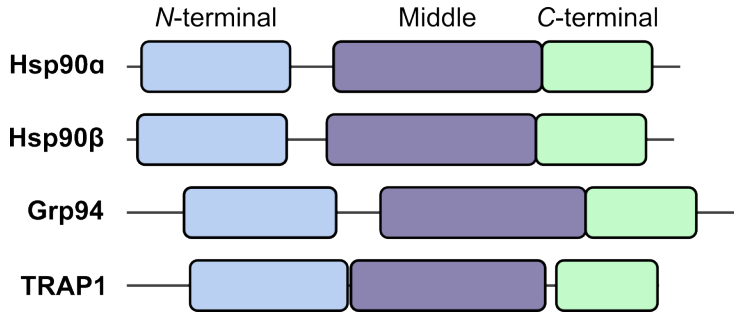


Figure 1.9: Domain architecture of HSP90 family members. Protein primary sequences represented by lines proportional to their length. Structurally defined domains represented by colourful boxes.

Comparing the HSP90 family members, cytosolic Hsp90 paralogs contain a longer charged linker between the *N*-terminal and middle domains, while Grp94 and TRAP contain *N*-

terminal leader sequences. In humans, there is no evidence for heterodimer formation between HSP90 family members.[104]

Hsp90α and Hsp90β present a high degree of structural homology with 85% sequence identity and 93% sequence similarity across the proteins' lengths. The largest structural difference is located at the *N*-terminus where Hsp90α contains an extended sequence compared to Hsp90β, but smaller differences along the proteins' length contribute to their slightly different functions.



Figure 1.10: Comparison of the protein sequences of Hsp90α and Hsp90β.The central horizontal bar shows shared sequence identity (dark blue) and similarity (light blue) between the proteins' primary structures, truncations are shown by a break in the labelled horizontal lines (as determined using the EMBL-EBI EMBOSS matcher tool,[56] and plotted using the Matplotlib python package). The underlaid boxes show the shared domain architecture along the protein sequences. Plotted to scale.

1.3.3 Functions and disease

In normal cells, Hsp90 is a vital regulator of the cell cycle, proliferation, signal transduction and transcriptional regulation. However, under stress conditions, Hsp90 induction is increased to compensate for misfolding and overexpression of clients. The basal expression of Hsp90α and Hsp90β varies depending on cell-type; however, Hsp90α is highly inducible, while Hsp90β is thought to be constitutive.[104] There are hundreds of reported Hsp90 client proteins which have been summarised in a Hsp90 molecular chaperone complex database curated by the Picard laboratory.[105]

Hsp90 undergoes dynamic conformational changes upon ATP binding which facilitate its chaperoning activity. It is able to bind its client proteins in different conformations through multiple contact points predominantly in the MD, rather than distinct recognition motifs.[97]

In addition to promoting protein folding, Hsp90 is also involved in the degradation of misfolded proteins as it interacts directly with multiple E3 ligases to accelerate their degradation.[97]

The upregulation of Hsp90 promotes the survival of cancer cells in harsh tumour microenvironments, but also protects an array of mutated and overexpressed oncoproteins

from misfolding and degradation.[100] Consequently, Hsp90 has been identified as a potential therapeutic target for cancer treatment, and the subsequent section presents the development of inhibitors.

1.3.4 Small molecule Inhibitors of the *N*-terminal domain

The first identified Hsp90 inhibitor was the natural product geldanamycin, which was found to compete with ATP in binding to the *N*-terminal domain. Since its discovery, Hsp90 has been the target of many campaigns in medicinal chemistry. A range of additional Hsp90 NTD inhibitors have been developed which can be categorised into 4 classes based on shared scaffolds (**Figure 1.11**): ansamycin-based, resorcinol-based, purine-based and benzamide-based.

The ansamysin-based compounds include, but are not limited to, geldanamycin (IC_{50} = 5 nM), 17-AAG (IC_{50} = 31 nM) and 17-DMAG (IC_{50} = 24 nM), which were sequentially developed to give improved solubility and biological activities.[106] The compounds have not progressed in clinical trials, predominantly due to challenges with hepatotoxicity.[107]

The resorcinol-based compounds are derived from the natural product, radicicol (IC_{50} = 30 nM); however, the compound is rapidly metabolised in serum. Co-crystallisation revealed the resorcinol pharmacophore and enabled the use of HTS and fragment-based approaches to derive STA-9090 (IC_{50} = 6 nM)[108] and AUY922 (IC_{50} = 8 nM)[109], among other inhibitors.

The purine-based compounds were the first fully synthetic inhibitors of Hsp90, based on the co-crystal structure of ATP bound to the *N*-terminal domain. PU-3 was the first reported purine-based inhibitor and was further developed into BIIB021 (K_i = 1.7 nM)[110] as the first-in-class to enter clinical trials but did not advance past phase II.[107] The most recent purine-based inhibitor to conclude clinical trials in 2014 is PU-H71. It showed promising results but has not yet advanced past phase I,[111] with current research focusing using ^{124}I-labelled analogues as PET tracers.[112]

The benzamide-based compounds were the latest class to be discovered with the first-in-class inhibitor SNX-2112 (K_d = 16 nM)[113] which was derived into the prodrug SNX-5422 and entered clinical trials in 2007.

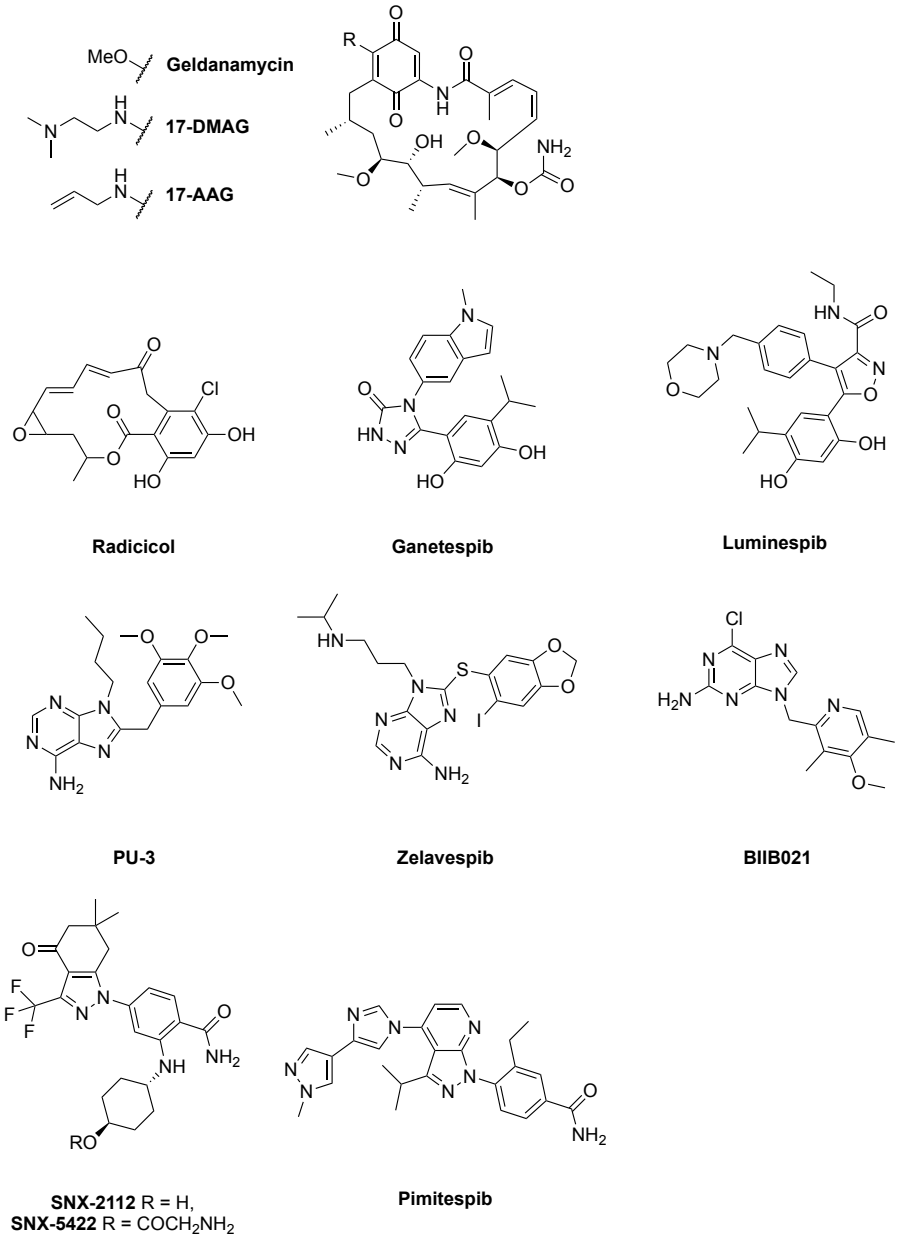


Figure 1.11 Chemical structures of a selection of reported inhibitors for the Hsp90 N-terminal domain. Compounds can be categorised into four families based on shared scaffolds: ansamycin-based (geldanamycin, 17-DMAG, 17-AAG), resorcinol-based (radicicol, ganetespib, luminespib), purine-based (PU-3, zelavespib, BIIB021) and benzamide-based (SNX-2112, SNX-5422, pimitespib).

The compounds discussed thus far exhibit comparable inhibitory effects on all HSP90 family homologues, which is believed to prevent their advancement through clinical trials.[114] However, more recent efforts have been made into the development of homologue-

selective compounds, with approaches either incorporating organelle-targeting groups or exploiting structural differences in the proteins' NTDs. Notably, pimitespib is a cytosolic Hsp90 selective inhibitor (Hsp90β K_i = 21.3 nM, Hsp90α K_i = 34.7 nM; >1400-fold selective against Grp94 and TRAP)[115] and was the first Hsp90 inhibitor to successfully breakthrough into clinic use in Japan for the treatment of gastrointestinal stromal tumors (GIST).[116, 117]

1.3.5 Lysine acetylation on Hsp90

Hsp90 function is modulated by numerous PTMs which include phosphorylation, acetylation, methylation, SUMOylation, and *S*-nitrosylation.[118] Yu *et al.* were first to report lysine acetylation on Hsp90 as a consequence of pan-KDAC inhibition and showed this resulted in loss-of-function as hyperacetylated Hsp90 failed to chaperone client proteins including HER2, RAF-1 and mutant p53.[119] Later works have also demonstrated the hyperacetylation on Hsp90 upon KDAC inhibition, and this is thought to be one of the mechanisms in which KDACs elicit an antiproliferative effect.[47, 120-122]

The putative KAT for Hsp90 is p300, although this has only been demonstrated using isolated proteins *in vitro.*[123, 124] Other KATs may also acetylate Hsp90 as Zhang *et al.* reported that MOF overexpression results in hyperacetylation on Hsp90 and MOF knockdown resulted in decreased acetylated.[125] A systematic or unbiased analysis of possible KATs has not been reported. The reported KDAC for Hsp90 is HDAC6. This has been demonstrated by gene ablation and RNA interference studies;[47, 122] however, other KDACs may also possess the capability to deacetylate Hsp90. HDAC1 and HDAC10 have been reported to exhibit such activity.[126, 127] It is possible that different KATs and KDACs affect the acetylation status at specific sites on Hsp90 with different downstream effects, similar to the histone-code hypothesis.[128]

Sites of KAc on Hsp90 were initially investigated in work by Scroggins *et al.* where Edman degradation was used to identify multiple sites that were mapped to the lysine-rich charged region located between the NTD and MD. Further analysis by MALDI-TOF identified Hsp90α(K294Ac)/β(K286Ac) located in the MD. It is not conserved in Grp94 and TRAP1

where it is substituted for a glutamine. Mutagenesis studies were used to investigate the effect of the modification by creating lysine-to-glutamine (K/Q, KAc mimic) or lysine-to-arginine (K/R, non-Ac K mimic) mutants of Hsp90α. K294Q-mutants had decreased binding to client proteins and certain co-chaperones.[129] Further work by Yang *et al.* identified seven additional KAc sites in Hsp90 and mutagenesis studies found different K/Q mutants had unique interaction profiles, suggesting different phenotypes may arise depending on the site of KAc.[124] Additionally, they reported hyperacetylation on Hsp90α stimulates its extracellular export and found K69Q, K100Q and K558Q mutations promoted the export and extracellular location of Hsp90α.

Table 1.5 Changes in binding interactions of Hsp90α lysine-to-glutamine mutants compared to wt with co-chaperones (CHIP, p23, Hsp70), ATP and client protein (RAF-1) reported by Yang *et al.*[124] Loss in detectable interaction is represented by two red arrows (↓↓), decrease in interaction is represented by a red arrow (↓), increase in interaction is represented by a green arrow (↑), and no change is represented by a dash (-)

Entry	Hsp90α mutant	Change in binding interaction compared to wt Hsp90α				
		CHIP	P23	Hsp70	ATP	RAF-1
1	K69Q	-	-	-	-	-
2	K100Q	↓↓	↓	-	-	-
3	K292Q	-	↓	↓	↑	↓
4	K327Q	↓↓	↓	↑	↓	↑
5	K478Q	↓↓	↓	-	-	↓
6	K546Q	↓↓	↓	-	↓	↓
7	K558Q	↓↓	↓	-	↓	↓

In addition to these works, high throughput acetylomics experiments have identified other KAc sites on Hsp90, following perturbations to KAT and KDAC activity. However, these KAc sites have not been experimentally validated and their phenotypic effect has not been determined. A summary of all the identified KAc sites is presented in **Figure 1.12**.

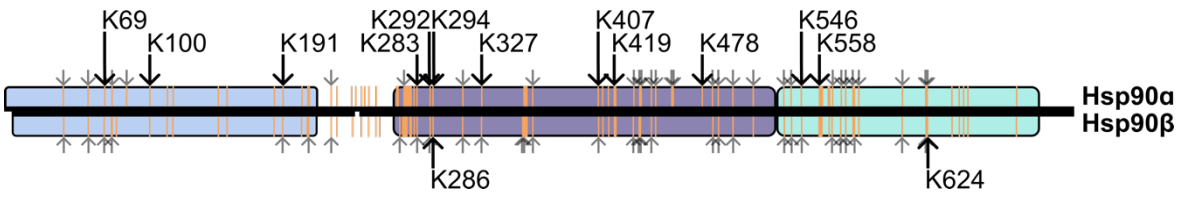


Figure 1.12: Positions of identified KAc residues on Hsp90α and Hsp90β. Orange lines mark the positions of lysine residues. Solid arrows (black) mark the positions of experimentally determined KAc residues, shaded arrows (grey) mark the positions of KAc residues identified in high-throughput proteomics experiments, but are not necessarily validated. The underlaid boxes show the shared domain architecture along the protein sequences. Data obtained from PhosphoSitePlus.[130]

1.4 Proximity induction in drug discovery

1.4.1 Molecular Glues and Bifunctionals

Elementary kinetics informs us that the rate an enzymatic reaction is greatly enhanced with respect to a substrate if its effective concentration is increased. On a molecular basis this higher effective concentration is interpreted as an increase in the probability density that the substrate exists within the sphere of the enzyme or vice versa, but put more simply, they are in proximity. This concept describes one of the most common biological regulatory mechanisms which underpins post-translational modifications.

The first chemical small-molecules shown to induce molecular proximity in biology were identified in the 1990s, in investigations on the mechanism of natural products FK506,[131] rapamycin[132] and cyclosporin.[133] These molecules, referred to as molecular glues, bind to a protein, creating a neo-protein or neo-substrate with an enhanced affinity for binding another protein/element.[134] The binding is referred to as cooperative, as the affinity between any two constituents is weaker than the overall binding between the complex of two of the constituents with the third.

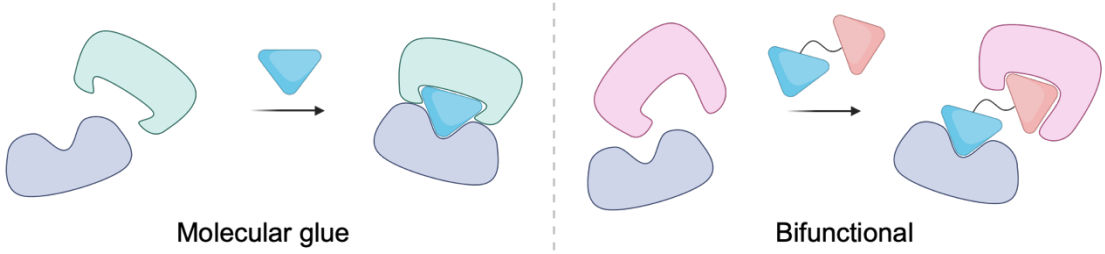


Figure 1.13: Representations of canonical molecular glues and bifunctional molecules as chemicals that induce proximity.[135] A molecular glue (blue triangle) causes the two proteins (green and grey) to form a stable complex due to an induced fit with a high degree of cooperativity, while a bifunctional (linked blue and red triangles) binds independently to the two proteins (pink and grey) to induce proximity. Figure created with Biorender.com.

Famous examples of molecular glues are the immunomodulatory drugs (IMiDs) such as thalidomide and lenalidomide, which stabilise the interaction of the cereblon (CRBN) E3 ligase and neo-substrates (*e.g.* IKZF1, IKZF3 and CK1α) leading to ubiquitination and degradation of the neo-substrates.[136, 137] These molecules saw use in the clinic well before their known targets or mechanisms of action were elucidated, resulting in catastrophic repercussions.[138] However, modern approaches to the development of molecular glues for

therapeutic intervention show a promising future. A recent example is the development of dWIZ-1, a lenalidomide-based compound, which selectively targets WIZ, a transcriptional repressor of foetal haemoglobin (HbF). Treatment with dWIZ-1 induces WIZ degradation and subsequent re-expression of HbF, offering a potential therapeutic for sickle cell disease.[139] These examples show the power of chemically induced proximity as a drug modality, but also highlight the requirement of target selectivity, and understanding their mechanisms of action.

Shortly after the discovery of molecular glues, bifunctional compounds were conceived in the 1990s as chemical inducers of proximity.[135, 140] They are typically chimeric molecules, comprising of a pharmacophore that binds one protein connected by a chemical linker to a second element that binds a second protein (**Figure 1.13**). Unlike molecular glues, a simpler rational approach can be taken in the design of bifunctional molecules to selectively induce proximity between targeted proteins. However, a significant shortcoming is the weaker degree of cooperativity in binding when compared to molecular glues.[134] As the binding of each head of the chimera is independent, this can result in a hook effect: increasing compound concentrations favour a one-to-one (binary) binding model, and this outcompetes with the formation of ternary complexes (**Figure 1.14**).

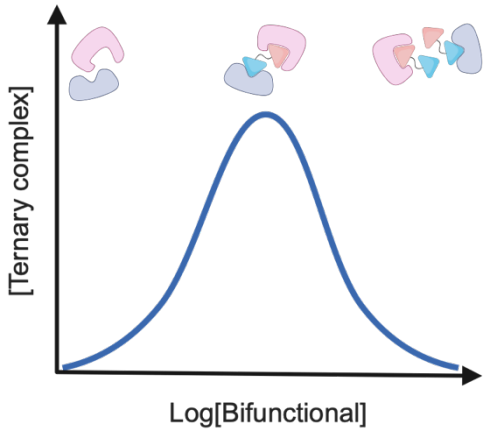


Figure 1.14: Illustration of the dose-dependent hook effect encountered with bifunctional molecules. Increasing concentration of bifunctional compound favours a one-to-one binding model and results in a reduced concentration of formed ternary complexes. Figure created with Biorender.com.

1.4.2 Proteolysis targeting chimeras (PROTACs)

Proteolysis targeting chimeras (PROTACs) were first reported in 2001, but the first all-small-molecule compounds were not reported until 2008.[141] PROTACs are an example of a bifunctional compound that specifically engages an E3 ligase.

The ternary complex formed between an E3 ligase, PROTAC and protein of interest (POI) results in the polyubiquitination of the POI as the induced proximity redirects the enzymatic activity of the E3 towards the POI. Polyubiquitination marks the POI for degradation by the 26S proteasome as a downstream process, part of the ubiquitin-proteasome system (UPS). The mechanism of action, summarised in **Figure 1.15**, is catalytic as one drug molecule can potentially mediate multiple rounds of POI ubiquitination, allowing sub-stoichiometric compound efficacy.

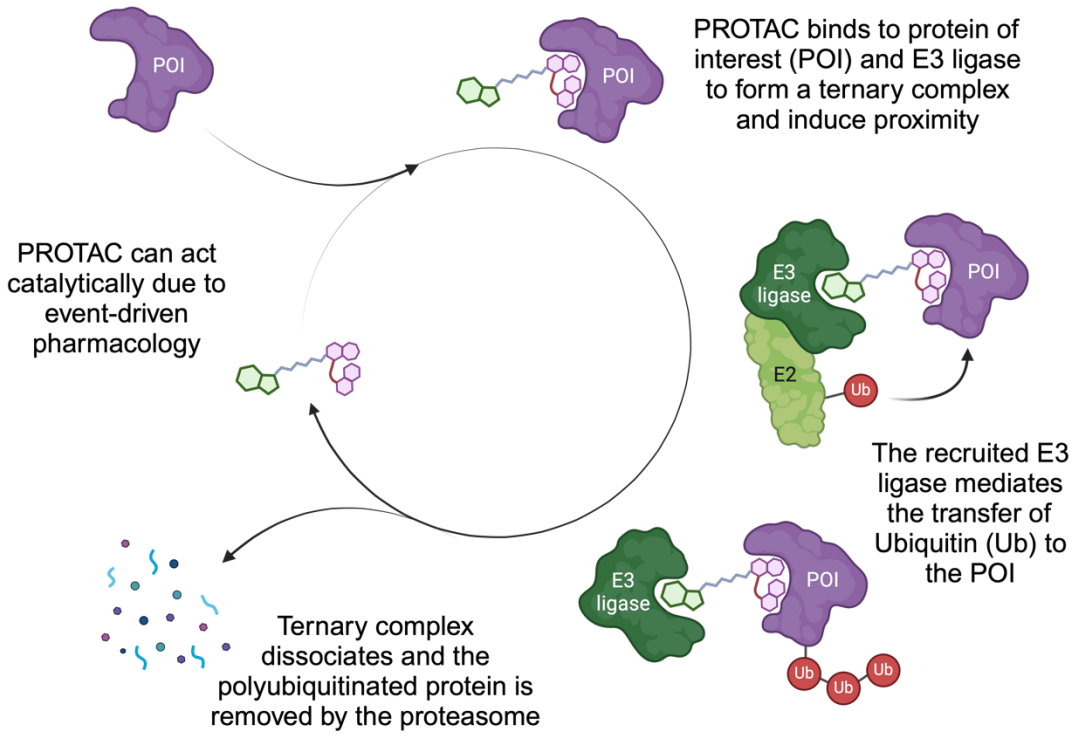


Figure 1.15: Mode of action of bifunctional molecules is demonstrated by the mechanism of PROTAC induced degradation of a protein of interest (POI). Figure created with Biorender.com.

PROTACs have been widely explored within medicinal chemistry with an explosion starting around 2015. They are the leading proximity-based modality in drug discovery.[142] Because

of these huge efforts within medicinal chemistry, many of the nuisances of bifunctional based drug modalities are best exemplified by PROTACs.

Evidence has shown that the activities of PROTACs do not directly correlate the binding affinity of the constituent ligands, but are instead driven by the stability, and in some cases, structural differences in the ternary complex formed.[143] This is clearly demonstrated in works using promiscuous or non-selective ligands in PROTACs that show selective degradation profiles. For example, fortenib, a kinase inhibitor that binds over 130 kinases at 10 μM, when incorporated into a PROTAC only degrades a subset of its binders, with distinct and non-overlapping degradation profiles observed depending on the recruited E3 ligase.[144] Further work on the fortenib-based PROTACs showed degradation selectivity could be achieved between p38 MAPK family members by tuning the linker length and orientation of the E3 ligase to bias the degradation outcome, despite the PROTACs demonstrating similar binding affinities to all family members, and forming ternary complexes.[145]

Additionally, the reported PROTAC, 'MC-1', binds to both CBP and p300 HAT domains, but shows paralogue-selective degradation of p300. This could not be predicted by target engagement or formation of a ternary complex but can be rationalised by differential predicted interactions at the protein-protein interface, and non-conserved lysine residues in the EP300 HAT domain.[146]

These examples highlight that the canonical model of bifunctional-induced proximity between proteins as involving two independent binding events to form a ternary complex, is insufficient in determining activity. The use of linkerology–the exploration of chemical linkers of varied length, polarity and rigidity–plays a significant role in the development of functional PROTACs and blurs the distinction between bifunctional and molecular glue (**Figure 1.16**). In these instances, a model emerges that induced proximity only results in activity if a constructive stable ternary complex is formed.

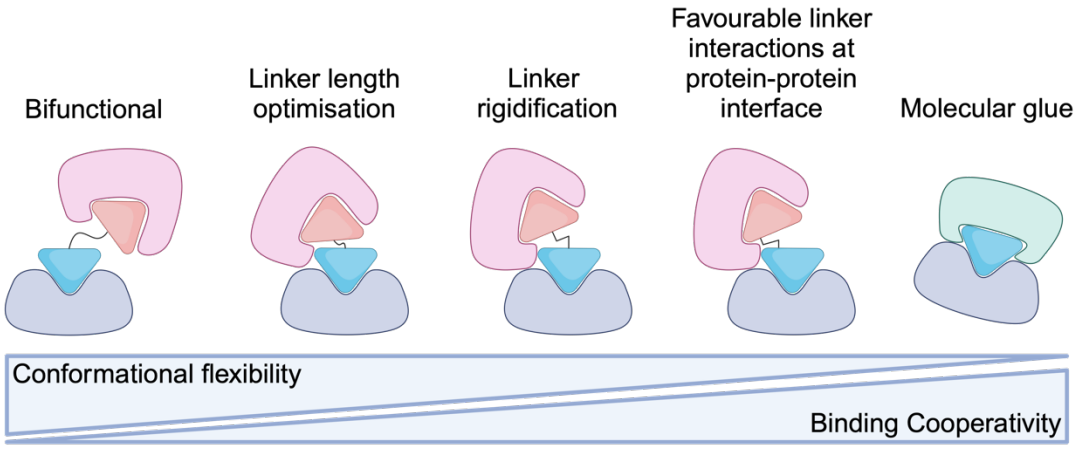


Figure 1.16: Approaches to design of bifunctionals to increase binding cooperativity and create molecular glue-like molecules. Figure created with Biorender.com.

1.4.3 Bifunctionals beyond PROTACs

Following the success of PROTACs, more diverse proximity-based modalities have emerged in the last 5 years. These include molecules that induce target protein degradation by mechanisms other than the UPS, such as lysosomal degradation,[147] or autophagy.[148, 149] However, several bifunctionals have been developed that do not aim to degrade targets, but elicit other downstream effects such as transcriptional upregulation,[150, 151] protein stabilisation[152] or impact post-translational modifications including phosphorylation,[153, 154] acetylation[155, 156] and glycosylation.[157] A broad selection of example bifunctional molecules beyond PROTACs is presented in **Table 1.6**.

Table 1.6: Overview of recent bifunctional molecules beyond PROTACs, the biological effectors they recruit and the intended function.

Entry	Target Function	Biological effector	Molecule
1	Post-translational modification	Dephosphorylase	PhoRC,[153] PhosTAC[154]
2		Kinase	PHICS[158]
3		Lysine acetyltransferase	AceTAG,[155] AceTAC[156]
4		*O*-GlcNAcylation transferase	OGTAC[157]
5	Protein stabilisation	Deubiquitinase	DUBTAC[152]
6	Degradation	26S proteasome	CIDE[159]
7		Autophagosome	AUTAC,[148] ATTEC[149]
8		Lysosome	LYTAC[147]
9		Chaperones	HyT[160]
10		Ribonuclease	RIBOTAC[161]
11	Transcriptional reprogramming	BRD4, CDKs	TCIP[150, 151]
12	Subcellular translocation	BRD4	NICE[162]
13		Shuttle proteins: NMNAT1, nuclear hormone receptors	TRAM[163]

Examining the mechanism of action of these compounds, two modalities begin to emerge: (i) compounds that recruit an enzyme onto a target protein as a substrate (*e.g.* **Table 1.6**, **entries 1–5**), and (ii) compounds that induce the proximal interaction between the target and effector without direct modification of the target by the other member of the ternary complex (*e.g.* **Table 1.6, entries 11–13**).

An interesting facet demonstrated in the later modality is that it may not be necessary to form a constructive stable ternary complex to elicit effects, but a bifunctional-induced increase in general proximity can be sufficient. This is demonstrated by CDK-TCIP molecules which recruit CDK9 to BCL6-bound loci on chromatin by directly binding to BCL6 (a transcriptional repressor of proapoptotic genes) and the catalytic domain of CDK9 (kinase subunit of pTEFb).[150] The compounds cause increased BCL6-target proapoptotic gene expression by direct phosphorylation of RNA Pol II, causing release from transcriptional pausing.[164] Most interestingly, it was shown that the catalytic activity of recruited CDK9 was essential for the observed effect, despite its inhibition upon bifunctional molecule binding. A "capture-and-release" mechanism was proposed where dissociation of CDK9 from the bifunctional-BCL6 complex was necessary to rationalise the increase in activity at BCL6-bound loci.

This modality is also demonstrated by DUBTACs which comprise a non-covalent inhibitor for the USP7 deubiquitinase.[165] These molecules recruit USP7 towards targets such as CFTR and AMPK, but crucially do not irreversibly inhibit its deubiquitinase activity, resulting in stabilisation of the target proteins.

These examples highlight the complexities of bifunctional-based approaches to drive downstream effects beyond degradation. While the formation of a tight ternary complex is highly correlated with degradation efficiency; in systems where the target protein is not removed, too tight of a complex can result in an effective inhibition of the effector protein and reduce the activity, as the turnover frequency of the bifunctional molecule is reduced.

1.4.4 Current works relevant to this thesis

Current works have shown that ligands for the CBP/p300 bromodomain can be incorporated into bifunctional molecules to recruit the paralogues in a manner similar to that observed in the natural cellular environment.

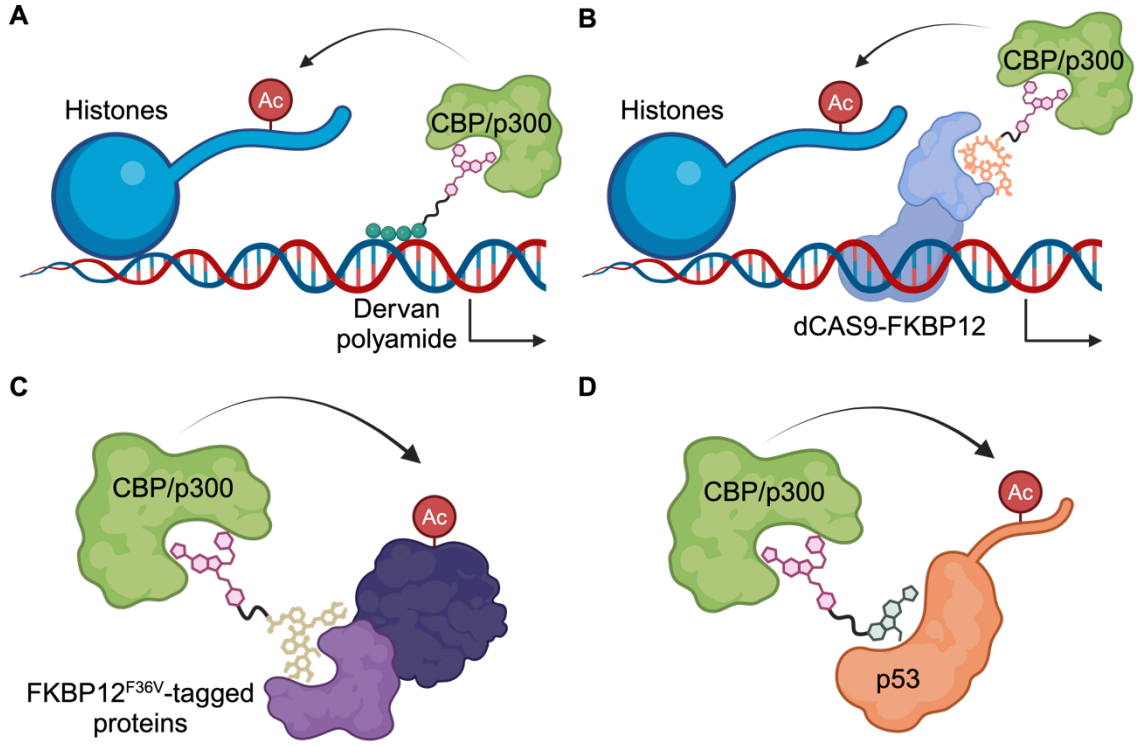


Figure 1.17: Graphic summary of current works on bifunctional molecules that recruit CBP/p300 as an effector. **A** Taniguchi *et al.* show Dervan polyamides conjugated to the ligand SGC-CBP30 can recruit CBP/p300 onto chromatin; **B** Chiarella *et al.* show FK506 conjugated to SGC-CBP30 can recruit CBP/p300 to specific gene loci using a catalytically inactive Cas9 fused to FKBP12; **C** Wang *et al.* show AP1867 conjugated to SGC-CBP30 can recruit CBP/p300 to $FKBP12^{F36V}$-tagged proteins exogenously expressed in cells; **D** Kabir *et al.* show bifunctional molecules comprising the ligand PK9328 conjugated to SGC-CBP30 can increase acetylation on endogenous mutant-$p53^{Y220C}$ in cells. Figure created with BioRender.com.

In work by Taniguchi *et al.,* Dervan polyamides (which bind in the minor groove of DNA in a sequence-specific manner)[166] were conjugated to the bromodomain inhibitor, SGC-CBP30, and shown to recruit the proteins to chromatin. This was demonstrated by an increase in acetylation on nucleosomes *in vitro*, and altered chromatin acetylation in cells, resulting in changes in gene expression (**Figure 1.17A**).[167]

Work by Chiarella *et al.* applied a similar concept and used catalytically inactive CAS9 (dCAS9) fused with an FKBP12 tag, in combination with bifunctional molecules comprising a FK506 ligand linked to SGC-CBP30. Here, the dCAS9 fusion binds to gene loci to provide

an anchoring point for the bifunctional as FK506 binds to the FKBP12 tag. The work showed the induced change in gene expression was both dose-dependent and specific to the binding mode of the bifunctional (**Figure 1.17B**).[168]

Since the inception of this thesis, more recent works have shown that bifunctional molecules can recruit CBP/p300 onto proteins as substrates for lysine acetylation. These bifunctional molecules also incorporate scaffolds based on SGC-CBP into their design and bind to the CBP/p300 bromodomain. This concept was first demonstrated in work by Wang *et al.* where $FKBP12^{F36V}$-tagged proteins were exogenously expressed in cells and targeted using bifunctional molecules termed AceTAGs (**Figure 1.17C**).[155] In a similar approach to the dTAG system used in target protein degradation;[169] AceTAGs incorporate an AP1867 ligand which selectively binds to the $FKBP12^{F36V}$-tag as a bump-and-hole pair.[170] AceTAG treatment increased KAc on fusion proteins of H3.3, p53, and p65 (RelA), all of which are otherwise endogenous CBP/p300 substrates. The magnitude of the increase varied between substrates as AceTAG treatment (0.625 μM for 2 h) approximately caused a maximum 12-fold increase in H3K18Ac, while p65(K310Ac) showed a maximum 3-fold increase. KAc sites were found to be increased in intrinsically disordered regions, but the targeted proteins were not hyperacetylated at all lysine residues, as AceTAG treatment did not increase H3K9Ac, H3K14Ac, or H3K79Ac. However, besides increasing H3K18Ac and H3K27Ac (known substrates of CBP/p300),[171] AceTAG treatment also increased H3K23Ac, which previous research has shown not to be a substrate of CBP/p300 using chemical inhibition and genetic ablation.[26, 171, 172]

Work by Kabir *et al.* showed that endogenous mutant-$p53^{Y220C}$ could be targeted with bifunctionals termed AceTACs that recruit CBP/p300 in cells (**Figure 1.17D**).[156] Their lead compound, MS78, comprised the ligand, PK9328,[173] which binds to a cavity formed in mutant-$p53^{Y220C}$ and stabilises the protein. NCI-H1299 cells treated with MS78 (10 μM for 24 h) showed an approximate 4-fold increase in $p53^{Y220C}$(K382Ac), compared to the vehicle control. p53(K382Ac) is a known substrate of CBP/p300 however other KAc sites were not explored in this work. The phenotypic effect of MS78 was shown to be distinct from the

parent inhibitors as it exhibited a superior antiproliferative effect and upregulated unique signalling pathways.

Most recently, work by Chen *et al.* has also shown that PCAF/GCN5 can be recruited as a KAT using the bromodomain ligand, L-Moses,[25] incorporated into AceTAG bifunctionals which target $FKBP12^{F36V}$-p53.[174]

1.5 Thesis aims

The principle aim of this thesis was to develop a bifunctional molecule that recruits the acetyl transferases CBP/p300 towards Hsp90 and induce an increase in lysine acetylation on that specific target protein to modulate its activity and interaction profile with co-chaperones and client proteins.

As discussed, previous studies have explored the effect of both hyperacetylation and site specific KAc on Hsp90 by either inhibiting the activity of KDAC enzymes, or through mutagenesis to introduce KAc mimetic residues, respectively. Those studies have established biological consequences of KAc on Hsp90, however the methods used were limited. KDAC inhibition causes a global increase in KAc across the proteome, giving rise to the possibility that off-target activities could drive the phenotypic effect observed. Mutagenesis studies rely on exogenous gene expression which lacks temporal control and can introduce artificial expression levels. We decided it was therefore paramount that an all-chemical approach towards the development of bifunctional molecules was taken, rather than a chemo-genetic system, to allow the exploration of induced acetylation within an endogenous cellular system.

In addition, bifunctional molecules can derive selective activities from promiscuous inhibitors, and present other unique properties that give them pharmacological value. We envisaged a therapeutic value in targeting Hsp90, if the induced increase in acetylation occurred at a lysine residue not conserved in its other family members, such as Hsp90α(K294Ac)/β(K286Ac).

In the context of current works that recruit CBP/p300 with bifunctional molecules, these have predominantly focused on targets involved in transcription or related to gene expression. Unlike Hsp90, chromatin and the transcription factors are well established binding partners of CBP/p300 with interaction domains identified in the protein structure. This thesis therefore presents novelty in exploring the scope of substrates that can be targeted with CBP/p300 recruiting bifunctionals and explores the consequence of an induced non-endogenous interaction between CBP/p300 and Hsp90.

In summary, the aims of this thesis can be summarised as three points, which form the basis of each chapter:

- Rational design and synthesis of a series of heterobifunctional molecules based on inhibitors for the CBP/p300 bromodomain and Hsp90 *N*-terminal domain. These bifunctionals, which we term acetylation directing chimeras (AcDCs), comprise varied linker lengths to explore the effect this plays in simultaneously engaging CBP/p300 and Hsp90.
- Demonstrate that AcDCs maintain interactions with the proteins' binding domains and form a ternary complex with CBP^{BRD}/$p300^{BRD}$ and $Hsp90^{NTD}$ recombinant proteins *in vitro*.
- Evaluate AcDC activities in cells by confirming induced proximity between endogenous CBP/p300 and Hsp90 and explore the biological consequence of this interaction including induced acetylation on Hsp90.

2 Synthesis of Acetylation Directing Chimeras (AcDCs) and derivatives

2.1 Design of AcDCs

2.1.1 Selection of Inobrodib as a ligand to recruit CBP/p300

In Chapter 1, the reported inhibitors of the CBP/p300 bromodomain are introduced. In this work the compound Inobrodib (CSS1477) was selected as a ligand to bind the CBP/p300 bromodomain for its high binding affinity [$p300^{BRD}$ K_d = 1.3 nM, CBP^{BRD} K_d = 1.7 nM (SPR)][175] and selectivity against BRD4 [>130-fold selective, K_d = 222 nM (SPR)][175]. While other CBP/p300 bromodomain inhibitors also demonstrate high binding affinities and selectivity, such as GNE-781 [CBP IC_{50} = 0.94 nM (TR-FRET)],[91] the synthesis of Inobrodib appeared more tractable. An additional benefit of Inobrodib was its development for use in clinical trials, suggesting its binding affinity, selectivity, and physicochemical characteristics are optimised for target engagement in physiologically relevant and cellular systems.

Examination of the co-crystal structure of inobrodib in complex with CBP^{BRD} (PDB: 7XH6)[176] was used to inform the selection of points on the scaffold for linker extension (**Figure 2.1**). The 3,5-dimethylisoxazole group forms key hydrogen-bond interactions with Asp-1168 and water-mediated hydrogen bonding with Tyr-1125 at the base of the KAc binding pocket. Additionally, the carbonyl of the lactam moiety in inobrodib forms a hydrogen bond with Arg-1173, which contributes to an induced-fit pocket where the difluorophenyl group sits and forms cation-π interactions with Arg-1173.[176] The top of the pocket around the methoxycyclohexyl group mostly comprises lipophilic residues (Leu-1119, Leu-1120, and Leu-1109), allowing for possible hydrophobic interactions with the ligand. The methoxycyclohexyl group itself appeared solvent-exposed and projects out of the pocket into the ZA channel, making it an attractive site for modification and linker extension.

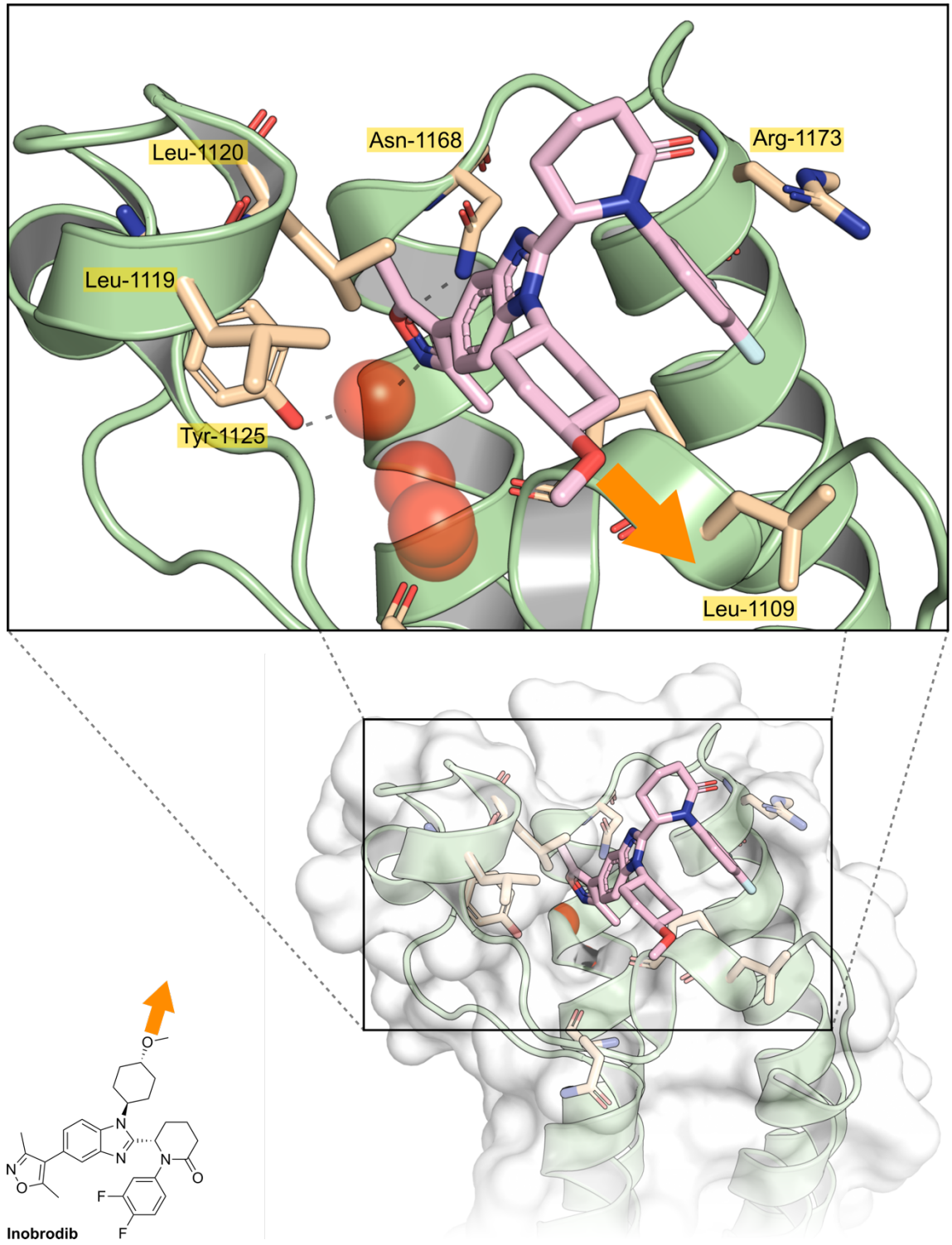


Figure 2.1: X-ray co-crystal structure of inobrodib (pink) in complex with CBP^{BRD} (green) (PDB: 7XH6[176]) demonstrates that the methoxycyclohexyl group is solvent-exposed and is a suitable point for extension of the chemical linker (dark orange arrow). Key residues (carbon = yellow) forming interactions with inobrodib (Asn-1168, Tyr-1125, Arg-1173), residues at the surface of the KAc binding pocket (Leu-1119, Leu-1120, Leu-1109, Gln-1113) (yellow), and structural water molecules (red spheres) are shown. The skeletal formula of inobrodib is shown for reference**.** Images were generated using PyMOL and arranged using Inkscape.

Functionalisation of inobrodib with a reactive group at the position of the methoxycyclohexyl group was sought, to enable attachment to a range of linkers and facilitate derivatisation into a library of heterobifunctional compounds. Substitution of the methoxycyclohexyl group for a piperidine moiety was chosen to generate the compound pip-obrodib, which could be amide coupled to chemical linkers functionalised with a terminal carboxyl group (**Figure 2.2**).

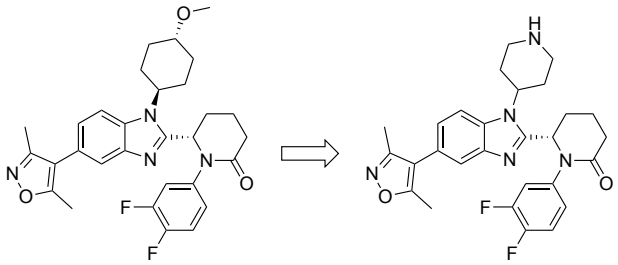


Figure 2.2: The methoxycyclohexyl group on inobrodib was substituted with a piperidine group to generate the compound pip-obrodib which can be amide coupled to chemical linkers.

In further support of our choice of exit vector in inobrodib, more recent works have shown the compound can be developed into PROTACs by the extension of a chemical linker from the methoxycyclohexyl group (**Figure 2.3**).[177, 178]

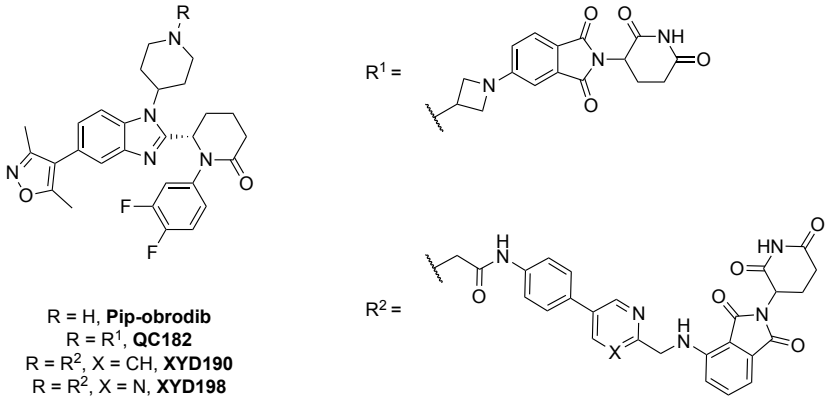


Figure 2.3: The substitution of the methoxycyclohexyl group in inobrodib for a piperidine is also demonstrated in recent works on the discovery of CBP/p300 PROTACs (QC182,[177] XYD190,[178] and XYD198).[178]

Recent studies have developed bifunctional molecules recruiting CBP/p300, and have employed a ligand based on the inhibitor SGC-CBP30,[27, 179] using an exit vector extending from the phenyl group (**Figure 2.4**).[155, 156] Inobrodib and SGC-CBP30 are structurally similar and the compounds adopt similar binding conformations with CBP^{BRD} in the co-crystal

structures (PDB: 4NR7)[27] (**Figure 2.4A**). However, linker extension from the difluorophenyl group in inobrodib appeared less attractive due to the greater conformational constrain in the scaffold generated by the lactam moiety, which forces the difluorophenyl group into the induced-fit pocket with Arg-1173.[176] In the development of SGC-CBP30, early analogues with the ethyl phenyl group adopted an alternative conformation in the co-crystal structure with CBP^{BRD} where the phenyl group fails to form the induced-fit pocket and forms hydrophobic interactions with Leu-1120, reflecting a degree of flexibility in the scaffold.[27]

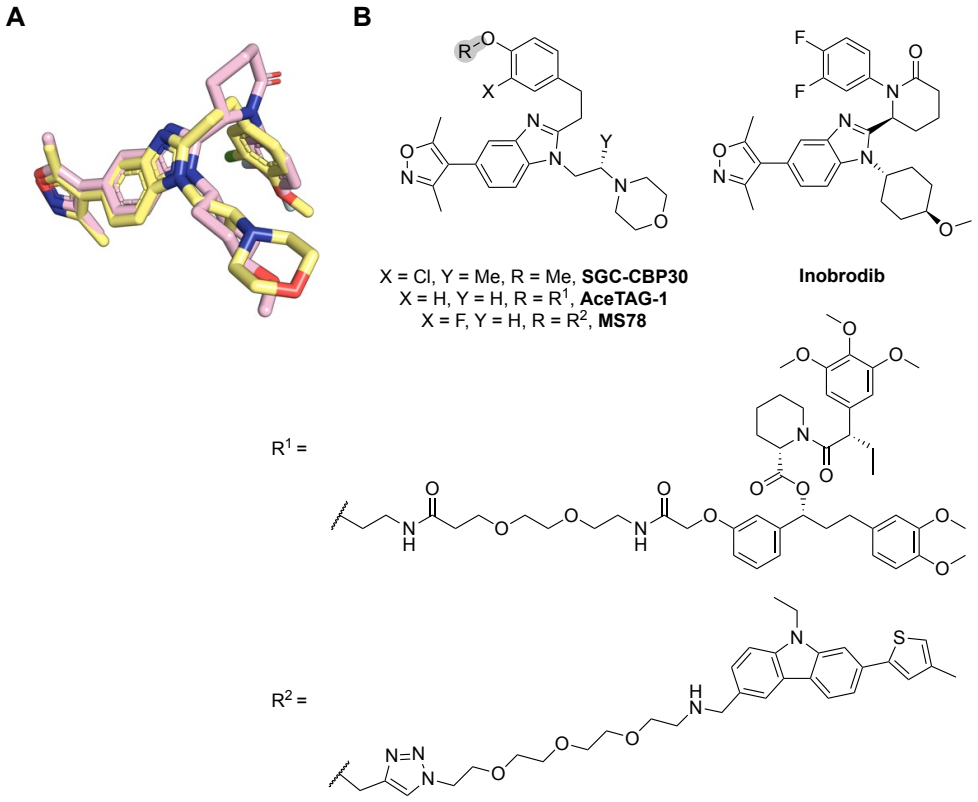


Figure 2.4: SGC-CBP30 shows a similar conformation to inobrodib in co-crystal structures with CBP^{BRD} and is derivatised into heterobifunctional compounds. **A**) Overlay of inobrodib (carbon = pink, PDB: 7XH6) and SGC-CBP30 (carbon = yellow, PDB: 4NR7) in the binding conformations extracted from the co-crystal structure with CBP^{BRD}. **B**) Acetylation Targeting Chimera (AceTAG-1 and MS78) used a scaffold based on SGC-CBP30**,** extending a chemical linker from the phenyl group.

2.1.2 Selection of BIIB021 as a ligand to target Hsp90

BIIB021 was selected as the Hsp90 binding ligand because it is a fully synthetic, potent (IC_{50} = 5.1 nM),[180] and low-molecular-weight inhibitor of the *N*-terminal nucleotide-binding pocket. Additionally, BIIB021 has previously been developed into a second-generation inhibitor, EC144,[180] and heterobifunctional molecules such as BP3 (**Figure 2.5**).[181, 182]

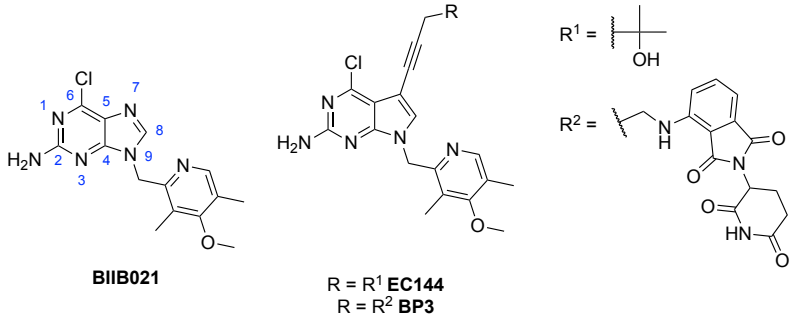


Figure 2.5: Chemical structures of the Hsp90 inhibitors BIIB021,[183] EC144[180] and the Hsp90 PROTAC BP3.[181]

Examination of the co-crystal structure of BIIB021 in complex with Hsp90α^{NTD} (PDB: 3QDD)[180] aids the rationalisation of the chosen extension vector (**Figure 2.6**). We considered extending a chemical linker from the *C*-6 position by S_NAr on the chloro-group which would not have required modification of the scaffold, however the 6-chloroguanine *N*-7 position appeared a more attractive point. The BIIB021 co-crystal structure showed a clear vector from the *N*-7 position into solvent, while the *C*-6 position appeared more hindered. We considered the three water molecules that sit at the top of the pocket, forming hydrogen bonds with Lys-58, Asp-102, and the backbone carbonyl of Gly-97. The displacement of either of these water molecules can be compensated by the introduction of a hydrogen bonding atom in the chemical linker at this position. This was observed when comparing the binding affinities of BIIB021 (IC_{50} = 5.1 nM) with EC144 (IC_{50} = 1.1 nM), as the alcohol on EC144 displaces these water molecules.[180]

Additionally, we also deemed the *N*-7 position a lower risk option, given EC144 and BP3 demonstrated linker extension along this vector maintained binding affinity.

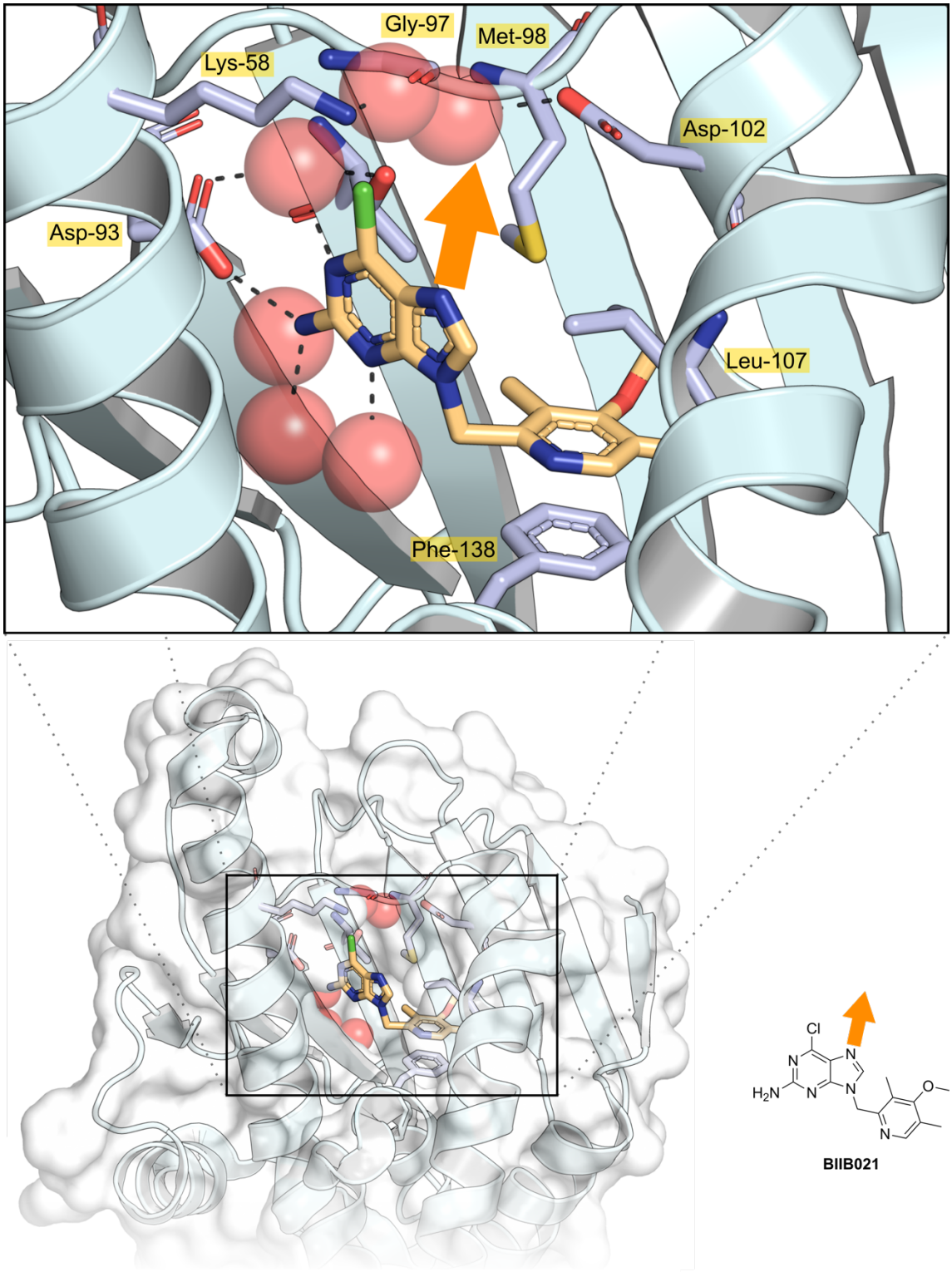


Figure 2.6: X-ray co-crystal structure of BIIB021 (pale orange) in complex with Hsp90α^{NTD} (blue) (PDB: 3QDD) shows that the purine *N*-7 position is solvent-exposed and a suitable vector for extension of a chemical linker (dark orange arrow). Key residues are shown in mauve. The skeletal formula of BIIB021 is shown as a reference. The 6-chloroguanine amine forms a direct hydrogen bond with Asp-93 as well as hydrogen bonding with water molecules located at the bottom of the pocket. The pyridine group sits in a hydrophobic pocket between Leu-107 and Phe-138, forming π–π interactions. Water molecules (red spheres) and residues at the top of the pocket (Lys-58, Gly-97, and Asp-102) are shown. Images were generated using PyMOL.

We adopted the substitution of the 6-chloro-guanine for 6-chloro-7-deazaguanine (**Figure 2.7**) which was iodinated and cross-coupled to chemical linkers, as previously described.[180-182]

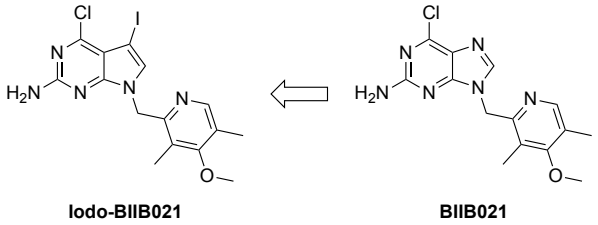


Figure 2.7: The 6-chloroguanine on BIIB021 was substituted for 6-chloro-7-iodo-deazaguanine to generate the compound iodo-BIIB021 which could be cross-coupled to chemical linkers using a Sonagashira coupling.

2.1.3 Overall design of Hsp90 AcDCs

With the selected ligands, an initial set of AcDC compounds were designed with linkers comprising polyethylene glycol (PEG) chains functionalised with terminal acetate and propargyl groups, to enable amide coupling and Sonagashira cross-coupling to pip-obrodib and iodo-BIIB021, respectively (**Figure 2.8**). PEG linkers were chosen as they are flexible: we wanted to prioritise exploring the effect of linker length in the first generation of AcDC, rather than conformational effects of more complex linker designs.

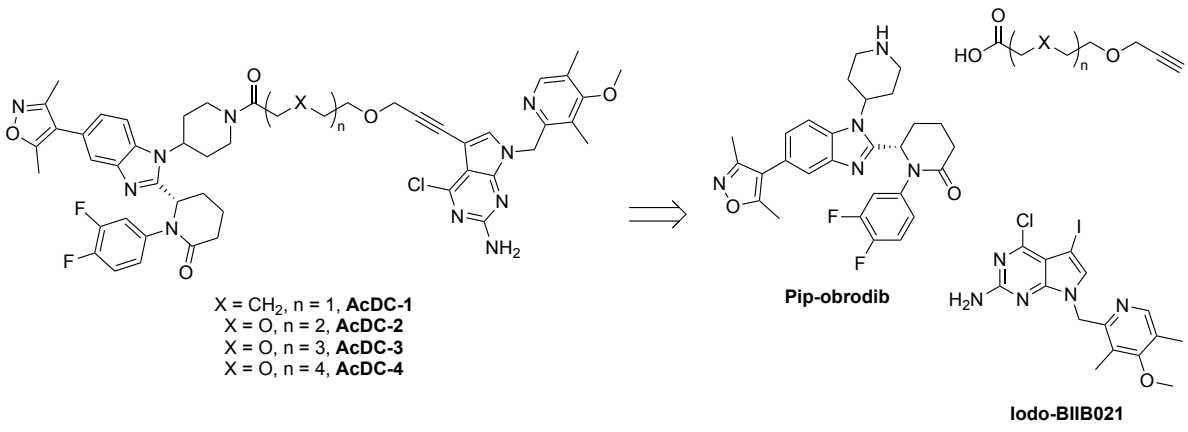


Figure 2.8: Overall design of Hsp90 AcDC molecules constructed by amide coupling pip-obrodib and Sonagashira cross-coupling iodo-BIIB021 to PEG or alkyl containing chemical linkers functionalised with propargyl alcohol and acetate groups.

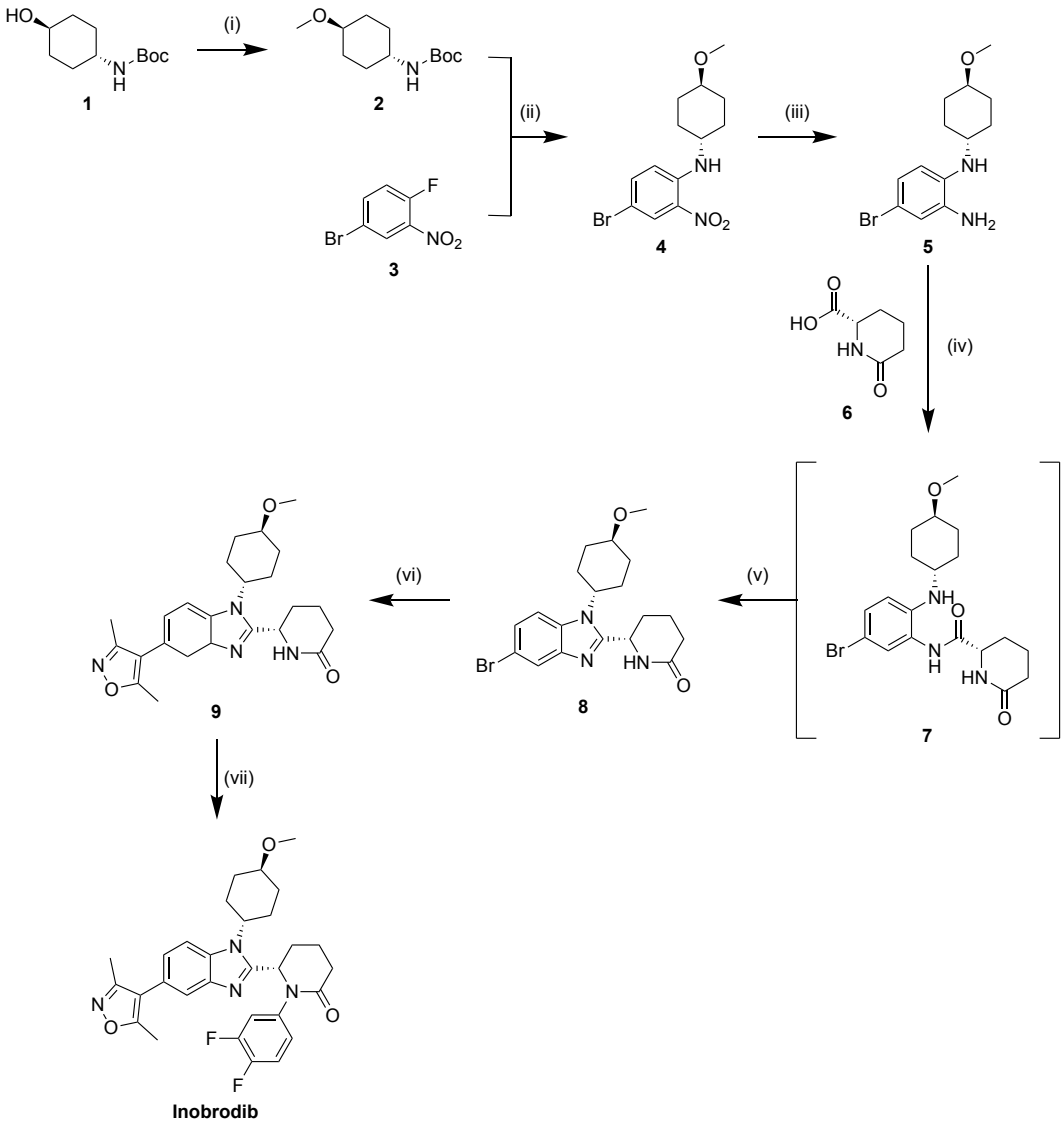
For the shortest chemical linker, a methylene group was introduced instead of an oxygen atom. It was rationalised that an alkyl linker could provide more conformational flexibility than an ethylene glycol equivalent, and the resultant change in physicochemical properties from a single atom substitution would be tolerated once incorporated in the final AcDC.

2.2 Synthesis of AcDC-1–4 and its containing ligands

2.2.1 Synthesis of inobrodib

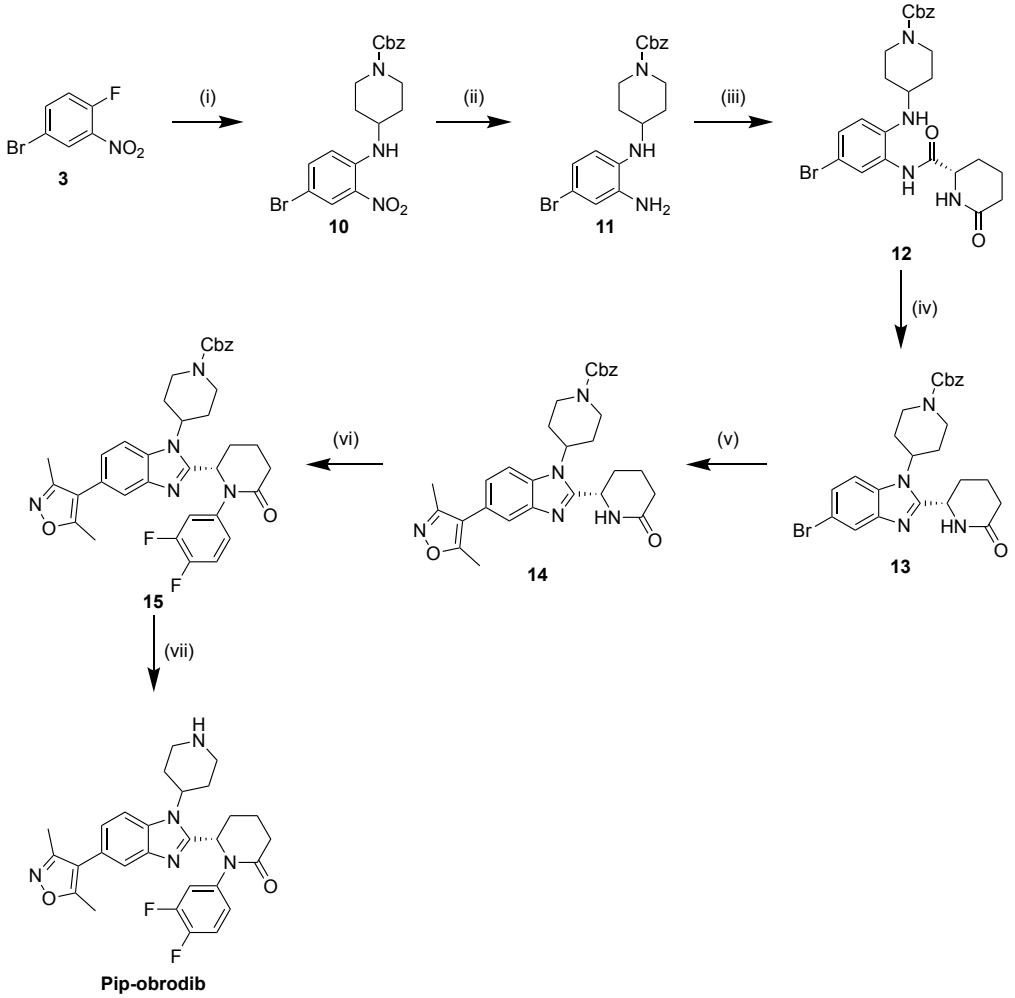
As a starting point, inobrodib was synthesised to provide material that could be used as a positive control of CBP/p300 bromodomain inhibition in future assays. At the point this project was undertaken, there were two published synthetic routes towards inobrodib: the first from the compound's discovery[184] and the second from its preparation on large scale (kilogram quantity).[185] The routes most notably differed in whether a Suzuki cross-coupling reaction was performed in the first or penultimate step to install the 3,5-dimethylisoxazole moiety. The route chosen in this work followed the latter procedure (large scale synthesis), for its reported higher overall yield (**Scheme 1**), and is described below.

Initially, *trans*-4-(Boc-amino)-cyclohexanol (**1**) was *O*-methylated to afford **2** in 55% yield, with *N*-methylation as the major side product. One-pot Boc-deprotection of **2**, followed by an S_NAr reaction of the resulting amine on **3** installed the methoxy-cyclohexane group and afforded **4** in 90% yield. This was followed by reduction of the nitro- group with sodium dithionite to afford **5** in 73% yield. The benzimidazole core (**8**) was then formed by amide coupling between the *o*-aryldiamine (**5**) and (*S*)-6-oxopiperidine-2-carboxylic acid (**6**) to form intermediate **7**, which was not isolated but subjected to acid-catalysed condensation. Intermediate **9** was obtained in 39% yield, with the main side-product found to be 2-methyl-benzimidazole. We suspected that this was formed by incomplete amide coupling, followed by acetylation with the solvent, followed by condensation. The 3,5-dimethylisoxazole group was then coupled to the benzimidazole (**8**) using a Suzuki cross-coupling to afford the intermediate **9** in 30% yield. Finally, a Chan-Evans-Lam (CEL) coupling was used to install the 3,4-difluorophenyl group in 66% yield to give inobrodib**.**



Scheme 1: Synthesis of inobrodib. *Reagents and conditions:* (i) NaH, anhydrous THF, 0 ºC, 20 min, then dimethyl sulphate, 0 ºC – rt, 20 h, 55%; (ii) HCl (4 M in dioxane), dioxane, 0 ºC – rt, 30 min, then **3,** K_2CO_3, MeCN, 70 ºC, 16 h, 90%; (iii) $Na_2S_2O_4$, NH_4OH (aq. 1.65 M), H_2O:THF (1:1), rt, 4 h, 73%; (iv) **6**, T_3P, DIPEA, CH_2Cl_2, 0 ºC, 30 min, then **5** 0 ºC – rt, 4 h; (v) AcOH, 50 ºC, 5 days, 39% over two steps; (vi) 3,5-dimethyl-4-(4,4,5,5-tetramethyl-1,3,2-dioxaborolan-2-yl)isoxazole, $Pd(PPh_3)_4$, K_2CO_3, dioxane, H_2O, 90 ºC, 18 h, 30%; (vi) (3,4-Difluorophenyl)boronic acid, $Cu(OAc)_2$, Py, CH_2Cl_2, 3 Å mol. sieves, rt, 18 h, 66%.

2.2.2 Synthesis of a piperidine-inobrodib analogue (pip-obrodib)



Scheme 2: Synthesis of pip-obrodib. *Reagents and conditions:* (i) 4-Amino-1-*N*-Cbz-piperidine**,** K_2CO_3, MeCN, 70 ºC, 16 h, >99%; (ii) $Na_2S_2O_4$, NH_4OH (aq. 1.3 M), H_2O:THF (1:1), 75 ºC, 4 h, 54%; (iii) **6,** *N*,*N*,*N*',*N*'-Tetramethylchloroformamidinium hexafluorophosphate, *N*-Methylimidazole, MeCN, rt, 16 h, >99%; (iv) AcOH, 80 ºC, 16 h, 97%; (v) 3,5-dimethyl-4-(4,4,5,5-tetramethyl-1,3,2-dioxaborolan-2-yl)isoxazole, $Pd(PPh_3)_4$, K_2CO_3 (aq. 5 M), Dioxane:H_2O 5:1, 90 ºC, 18 h, 77%; (vi) (3,4-Difluorophenyl)boronic acid, $Cu(OAc)_2.H_2O$, Py, CH_2Cl_2, rt, 18h, 94%; (vii) Pd/C, H_2, MeOH, rt, 5 h, 71%.

An analogous route was used for the synthesis of pip-obrodib (**Scheme 2**). Protection of the piperidine was considered necessary throughout the synthesis to prevent undesired reactivity in the amide coupling, condensation, and CEL coupling steps of the synthesis. Acknowledging the synthetic route also involved both acid and base-mediated reactions, Cbz protection was rationalised as a suitable protecting group that could be removed in a late stage hydrogenolysis.

An initial S_NAr reaction installed a commercially available Cbz protected piperidine moiety to afford **10**. This compound was then subjected to reduction using similar conditions as for

the **inobrodib** synthesis, to afford **11** in 54% yield. For the subsequent amide coupling, different conditions to those previously used were explored on test-scale to ensure good conversion to intermediate **12** (**Table 2.1**).

Table 2.1: Attempted reaction conditions for amide coupling between *o*-aryldiamine (**11**) and (*S*)-6-oxopiperidine-2-carboxylic acid (**6**) to form the intermediate **12** [**Scheme 2**, Step (iii)]. Conversion was determined by LC-MS analysis and isolated yields are presented where available.

Entry	Reagents and conditions	Results
1	PyBOP, DIPEA, DMF, rt, 6 h	42% conversion to **12;** tris(pyrrolidino)phosphine oxide by-product presented purification challenges
2	**6**, i*so*-Butyl chlorofomate (1.10 eq.), NEt_3, (1.0 eq.) CH_2Cl_2, 0 ºC 30 min, then **12**, 0 ºC – rt, 6 h.	90% conversion to *iso*-butyl carbamate (**18**)
3	$SOCl_2$, DMF (cat.), DIPEA, CH_2Cl_2 0 ºC, 30 min; then **12**, CH_2Cl_2, 0 ºC – rt, 18h	Isolated yield: 79%
4	TCFH, NMI, MeCN, rt, 6 h	Isolated yield: 99%

We suspected amide coupling by formation of a mixed anhydride intermediate (**17**) with *iso*-butyl chloroformate led to formation of an *iso*-butyl carbamate (**18**) in high conversion as determined by LC-MS (**Table 2.1**, Entry 2). This result highlighted the steric hinderance around the carboxylic acid, due to preferential nucleophilic attack on the less hindered side of the anhydride (**Figure 2.9**). Amide coupling *via* formation of an acid chloride gave the desired product (**12**) in 79% yield, while *in situ* formation of an acyl imidazolium with *N*,*N*,*N*',*N*'-Tetramethylchloroformamidinium hexafluorophosphate (TCFH) and *N*-methylimidazole (NMI) gave the product in 99% yield, and were selected as the conditions employed in the synthesis of **12.**[186]

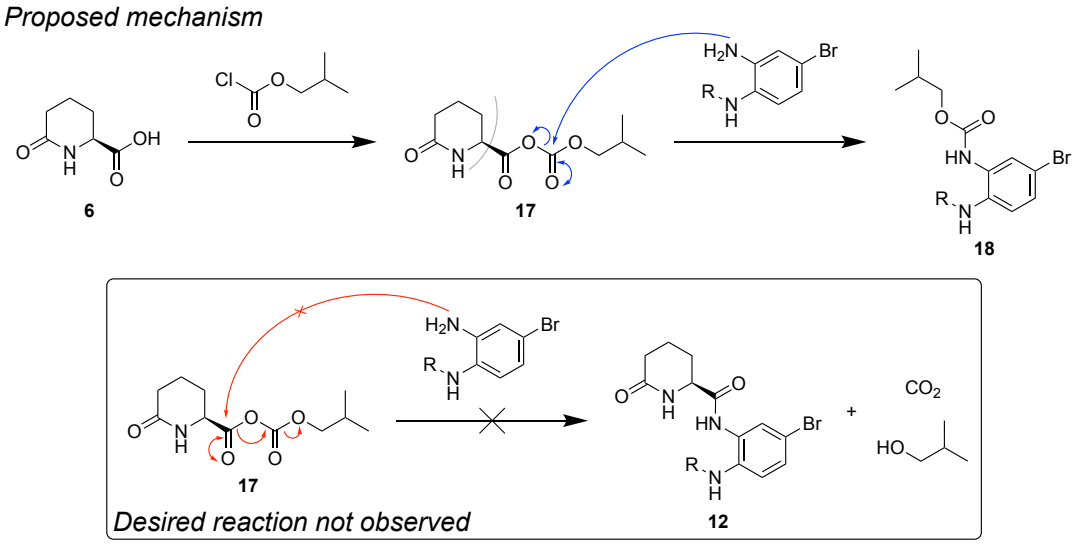


Figure 2.9: Formation of a mixed anhydride with **6** and *iso*-butyl chloroformate was converted to carbamate **18** rather than the desired amide coupling product (**12**). The mechanism is shown for the expected reaction (red) and the observed reaction (blue). Steric hindrance to nucleophilic attack is indicated in grey.

The benzimidazole core was formed by acid-catalysed condensation to afford **13** in 97% yield, which was then subjected to Suzuki cross-coupling to afford **14** in 77% yield. The increased yield achieved in this reaction, compared to Suzuki cross-coupling in **Scheme 1**, could be rationalised by differences in experimental procedures. For the initial attempt, addition of K_2CO_3 as a solid to the reaction mixture followed by solvents was suspected to have altered rate of hydrolysis of the boron pinacol ester (BPin) to boronic acid, and create a mismatch between the rate of *trans*-metalation versus protodeboronation;[187] compared to addition of K_2CO_3 as a 5 M aqueous solution to the reaction mixture which encouraged phase separation from dioxane.

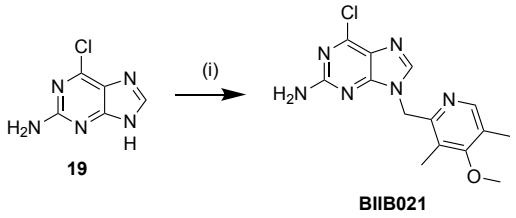
The CEL reaction was then performed to afford **15** in 94% yield. Again, the yield achieved here reflected an improvement on that achieved in **Scheme 1**. An initial test reaction was performed with stoichiometric copper(II) acetate monohydrate rather than the anhydrous salt, and without the addition of molecular sieves to the reaction mixture. The CEL coupling is widely reported as requiring anhydrous conditions, but the addition of an excess of molecular sieves to the reaction mixture can quench the reaction,[188] and the presence of water can improve reaction yields.[189]

The final step of the synthesis involved the deprotection of the Cbz group by hydrogenolysis which afforded pip-obrodib in 71% yield. A higher conversion was expected in this reaction, but the formation of side-products from over-reduction of the substrate was observed, as determined by LC-MS analysis. Previous reports have used similar conditions for the reduction of isoxazoles by hydrogenic fission of the labile N–O bond,[190] which could account for this observation.

During the project, additional pip-obrodib material was provided as a TFA salt (1:2) by MSD (UK).

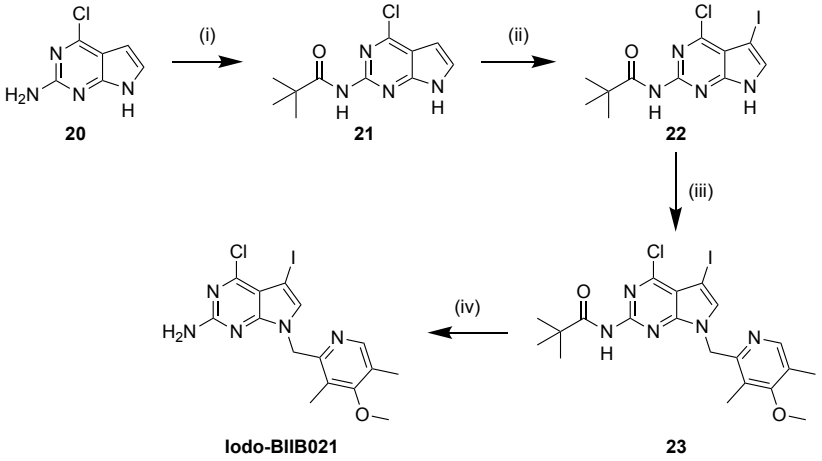
2.2.3 Synthesis of BIIB021 and Iodo-BIIB021

BIIB021 was readily obtained in one step from commercially available materials (**Scheme 3**). The purine **19** was alkylated with 2-(chloromethyl)-4-methoxy-3,5-dimethylpyridine and purified by crystallisation from the reaction mixture in 56% yield.



Scheme 3: Synthesis of BIIB021. *Reagents and conditions:* (i) 2-(Chloromethyl)-4-methoxy-3,5-dimethylpyridine, K_2CO_3, NaI, DMF, 40 ºC, 6 h, 56%.

To obtain iodo-BIIB021, the purine **19** was substituted for an analogous 6-chloro-7-deazaguanine (**20**), to allow iodination at the 7-position and Sonagashira cross-coupling to alkyne containing linkers. This was achieved following the procedure of Shi *et al.*[180]

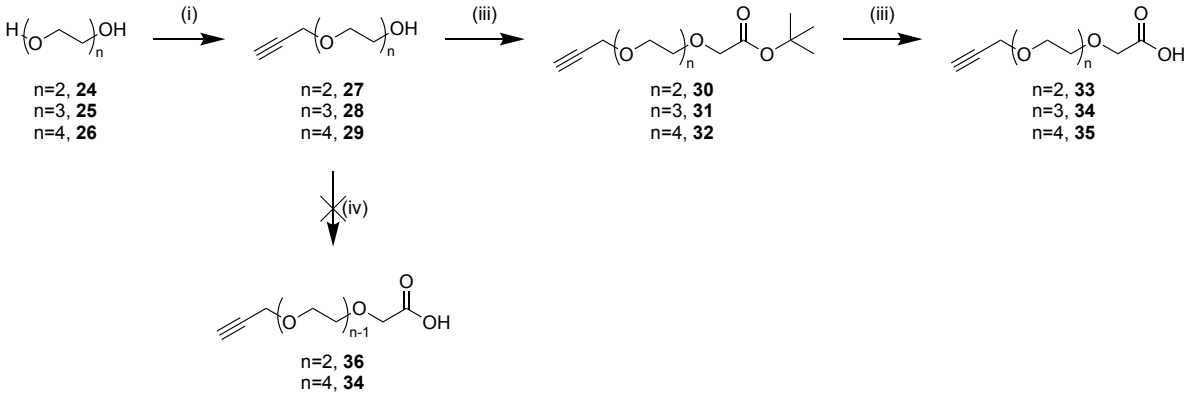


Scheme 4: Synthesis of iodo-BIIB021. *Reagents and conditions*: (i) Pivaloyl chloride, pyridine, rt, 2 h, 79%; (ii) *N*-Iodosuccinimide, THF, rt, 30 min, 62%; (iii) 2-(Chloromethyl)-4-methoxy-3,5-dimethylpyridine, K_2CO_3, NaI, DMF, rt, 18 h, 91%; (iv) $ZnCl_2$, EtOH:H_2O 20:1, 85 ºC, 24 h, 69%.

6-Chloro-7-deazaguanine **(20)** was first protected with a pivaloyl group to afford **21** in 79% yield, which was then subjected to iodination to give **22** in 62% yield. Compound **22** was then alkylated as described in the synthesis of BIIB021 to obtain **23** in 91% yield. The pivaloyl group was removed by $ZnCl_2$ catalysed hydrolysis to afford iodo-BIIB021 in 69% yield.

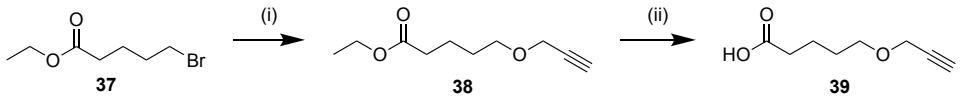
2.2.4 Synthesis of chemical linkers

Chemical linkers functionalised with terminal alkyne and carboxylic acid groups were prepared as outlined in **Scheme 5**.



Scheme 5: Preparation of alkyne-PEG-acetic acid functionalised chemical linkers. *Reagents and Conditions:* (i) **24–26** (2 eq.), ^{t}BuOK, propargyl bromide (1 eq.), THF 0 ºC–rt, 80% (**27**), 62% (**28**), 59% (**29**); (ii) *tert*-Butyl bromoacetate, TBAB, NaOH (35% *w/v* aq.), H_2O:CH_2Cl_2 1:1, 0 ºC–rt 81% **(30**), 51% (**31**), 45% (**32**); (iii) HCl, dioxane, 0 ºC – rt, 18–24 h, >99% (**33–35**); (iv) trichloroisocyanuric acid (2 eq.), NaBr (20 mol%), TEMPO (2 mol%), $NaHCO_3$ (sat. aq.), H_2O:acetone 1:4, 0 ºC–rt, 5 h.

Polyethylene glycols (PEGs, **24**–**26**) were mono-alkylated with propargyl bromide to afford the intermediates **27**–**29** in 59–80% yield. To obtain the carboxylic acid functionality, oxidation of the second terminal hydroxyl group was attempted using TEMPO-mediated oxidation with trichloroisocyanuric acid. While feasible on a reactivity basis, this approach proved impractical due the high aqueous solubility of the product which precluded conventional work-up procedures and created challenges in isolating the product from the reaction mixture. The carboxylic acid moiety was thus installed by a second alkylation with *tert*-butyl bromoacetate, under Schotten-Baumann conditions, to afford intermediates **30**–**32** in 81–45% yield. *tert*-Butyl (^{t}Bu) esters (**30**–**32**) were readily purified using flash column chromatography, and deprotected by acid mediated elimination of the ^{t}Bu-group in organic solvent which negated the need for aqueous work-up, and allowed linkers **33**–**35** to be obtained in quantitative yield.

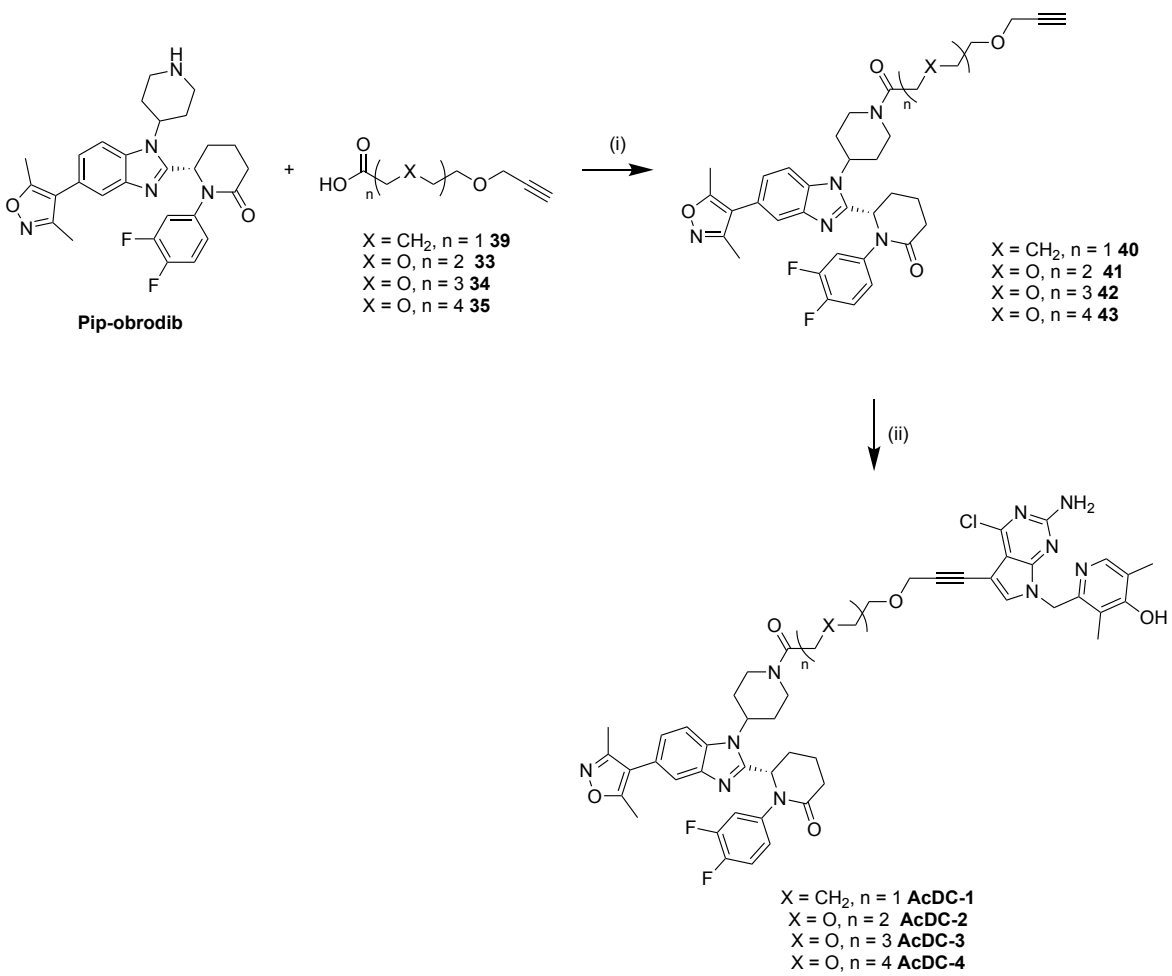


Scheme 6: Preparation of alkyne-alkyl-carboxylic acid functionalised linker. *Reagents and Conditions:* (i) Propargyl alcohol, NaH, DMF, 3 h, 56%; (ii) NaOH (aq. 2 M), H_2O:EtOH (1:4), 40 ºC, 1 h, 93%.

For the shortest chemical linker, a methylene group was introduced instead of an oxygen atom. This chemical linker was obtained in two steps (**Scheme 6**) by alkylation of propargyl alcohol with ethyl 5-bromovalerate to obtain the ester **38** (which was then hydrolysed to give **39** in 93% yield.

2.2.5 Assembly of AcDC compounds

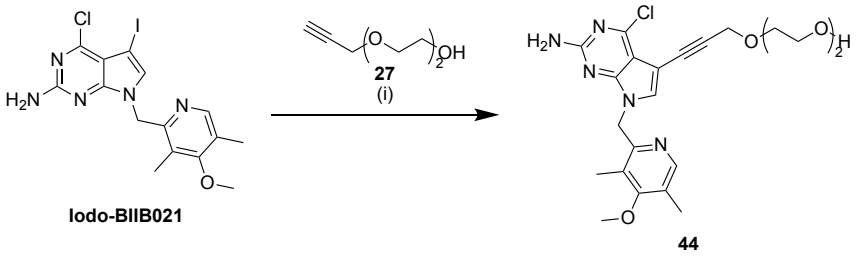
The assembly of AcDC molecules was accomplished by sequential amide coupling between pip-obrodib and functionalised chemical linkers (**33**–**35**, **39**), followed by Sonagashira cross-coupling to iodo-BIIB021**,** as outlined in **Scheme 7**. While the cross-coupling as a final step is recognised as not ideal due to its potential for transition-metal contamination of compounds used in biological assays, the potential for amide coupling between the acid and the amine group in iodo-BIIB021 rendered the amide coupling as the final coupling step unfavourable.



Scheme 7: Synthesis of AcDC-**1**–**4**. *Reagents and conditions:* (i) $SOCl_2$, DMF (cat.), NEt_3, CH_2Cl_2 0 ºC, 30 min; then **17**, CH_2Cl_2, 0 ºC–rt, 2 h, 90% (**44**), 1 h, 62% (**45**), 2 h, 62% (**46**) 2 h, 41% (**47**); (ii) $Pd(PPh_3)_2Cl_2$, CuI, NEt_3, MeCN, 70 ºC, 3 h, 46% (AcDC-**1**), 3 h, 44% (AcDC-**2**), MW hv 1 h, 21% (AcDC-**3**), 4 h, 52% (AcDC-**4**).

The amide coupling between pip-obrodib and alkyl linker **39** was first attempted using DCC and DMAP as coupling reagents, which afforded the intermediate **40** in 55% yield, while sequential generation of the acid chloride with oxalyl chloride followed by reaction with pip-obrodib afforded **40** in 90% yield and produced fewer by-products in the reaction mixture which facilitated purification. With this result in hand, amide couplings for **33**–**35** were also performed by formation of an acid chloride intermediate to afford **41, 42** and **43** in 62%, 62%, and 41% yields, respectively. An initial attempt at the final Sonagashira cross-coupling was performed on intermediate **40** with Iodo-BIIB021 to afford AcDC-**1** in a disappointing yield of 5% [using the reagents and conditions: $Pd(PPh_3)_2Cl_2$, CuI, NEt_3, CH_2Cl_2, 40 ºC (sealed vial), 18 h]. iodo-BIIB021 was observed to exhibit poor solubility in most organic solvents, consequently attempts were made to optimise the Sonagashira reaction

conditions by performing a solvent screen using **27** as a surrogate for the compounds **40–43** (**Scheme 8**) and the results are summarised in **Table 2.2**. Higher boiling point solvents were employed, and the reaction temperature increased to 70 ºC to increase solubility and it was hypothesised more forcing conditions were required to overcome steric hinderance presented by the chlorine atom present in iodo-BIIB021 and allow oxidative addition.



Scheme 8: Optimisation of Sonagashira cross-coupling conditions by solvent screening. *Reagents and conditions:* (i) **27**, $Pd(PPh_3)_2Cl_2$, CuI, NEt_3, DMF/MeCN/EtOH, 70 ºC, 6 h.

Table 2.2: Summary of measured conversions for the solvent screen performed in **Scheme 8**. Conversions were determined by quantitative ^{1}H NMR using trimethoxybenzene as an internal standard.

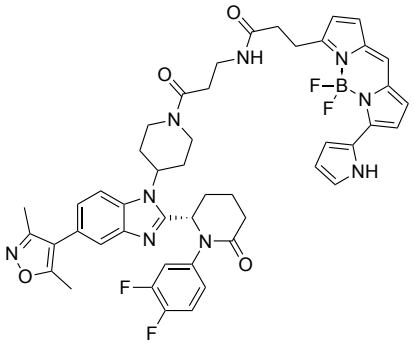
Entry	Solvent	Solvent properties	Conversion
1	EtOH	Polar protic	53%
2	DMF	Polar aprotic	63%
3	MeCN	Polar aprotic	84% (Isolated yield: 80%)

Good conversion was observed in all the conditions tested but MeCN gave the highest yield and was used as the solvent to the synthesis of AcDC-**1** and AcDC-**2** (**Scheme 7**, (ii)) in yields of 46% and 44%, respectively. To further increase the yield, the synthesis of AcDC-**3** was attempted by heating with microwave irradiation (MW hν) but a yield of only 21% was obtained, with full consumption of **42** judged by LC-MS analysis. Ultimately, AcDC-**4** was synthesised in yield 52% under the same conditions as AcDC-**1**–**2**. Further optimisation of the reaction conditions was considered unnecessary given the availability of AcDC-**1**–**4**.

2.3 Synthesis of tools to investigate CBP^{BRD} engagement in cells.

2.3.1 Synthesis of an inobrodib-BODIPY tracer

Previous work has established the extension of the chemical linker from the BIIB021 scaffold along the chosen vector maintains in-cell target engagement with Hsp90.[181] However, it remained unknown as to whether this held true for pip-obrodib. To address this question, a NanoBRET target engagement assay as envisaged. In Chapter 4, a more comprehensive discussion of the NanoBRET target engagement assay is provided. This can be briefly described as a competitive binding assay in which a fluorescent tracer molecule binds to the protein of interest and its displacement by the test compound is measured. Towards the development of the assay, a novel fluorescent tracer compound (inobrodib-BODIPY, **Figure 2.10**) was designed and synthesised, and assay optimisation was carried out by Ludwig Bauer (PhD Student, under the supervision of Dr Kilian Huber).

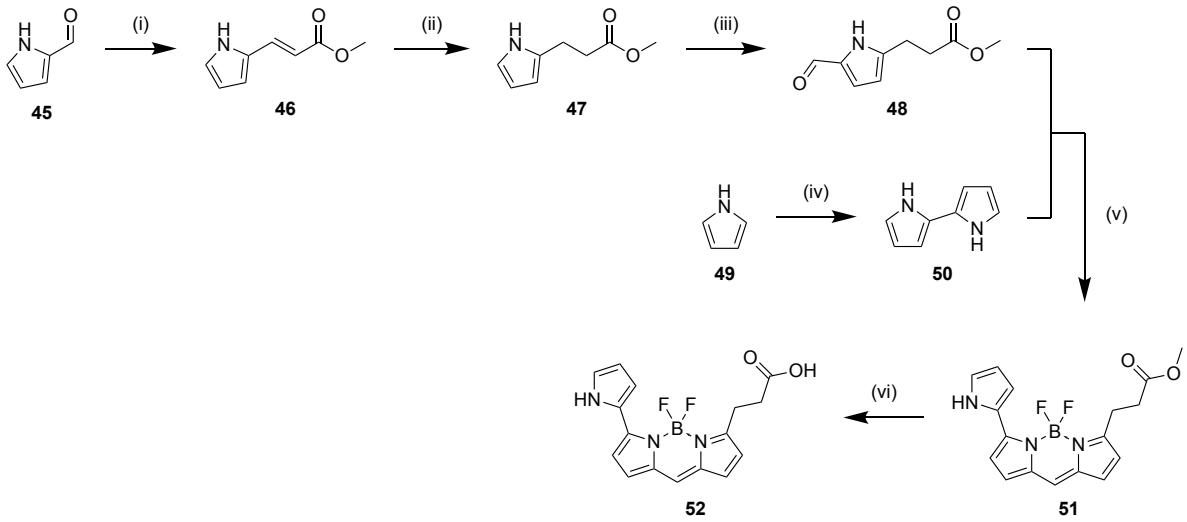


Inobrodib-BODIPY

Figure 2.10: Chemical structure of **inobrodib-BODIPY**, a novel fluorescent tracer compound that binds to the CBP/p300 bromodomain. The compound comprises **pip-obrodib** conjugated by a short alkyl linker to the fluorophore BODIPY 576/589.

The methyl ester derivative of BODIPY 576/589 (**51**) was synthesised in five steps, following the procedure described by Kim *et al.*[191] (**Scheme 9**). A short alkyl linker was attached to pyrrole-2-carboxaldehyde using the Horner-Wadsworth-Emmons reaction, to afford **46**, which was then subjected to hydrogenation to reduce the alkene to afford **47** in 80% yield. Compound **47** was then formylated in a Vilsmeier-Haack reaction to produce **48** in 85% yield. 2,2'-Bipyrrole **50** was obtained in 70% yield from the oxidation of pyrrole **49**

in one step, and was condensed with **48** and subsequently complexed with boron-trifluoride to afford BODIPY **51** in 21% yield.



Scheme 9: Synthesis of BODIPY 576/589 carboxylic acid (**52**). *Reagents and conditions:* (i) NaH, THF, 0 ºC – rt, 18 h, >99%; (ii) H_2, Pd/C, MeOH, rt, 18 h, 80%; (iii) $POCl_3$, DMF, DCE, 0 ºC – rt, 30 min, then **50**, DCE, 0 ºC – 85 ºC, 30 min, then NaOAc (aq. 1 M), H_2O, DCE, rt – 100 ºC, 45 min, 86%; (iv) PIFA, TMSBr, anhydrous CH_2Cl_2, –78 ºC, 1 h, 70%; (v) $POCl_3$, anhydrous CH_2Cl_2, 0 ºC, 3 h, then anhydrous DIPEA, $BF_3.OEt_2$, anhydrous CH_2Cl_2, 0 ºC, 30 min, 21%; (vi) Amano Lipase PS, Dulbecco's phosphate buffered saline solution (aq.), MeOH:hexane:H_2O 1:10:50, 18 h, 40 ºC, 40%.

Initial attempts to hydrolyse the methyl ester (**51**) using phosphoric acid-catalysis led to compound degradation and loss of fluorescence, likely due to the acid-catalysed polymerisation of pyrrole. Base-catalysed hydrolysis was also attempted but led to the substitution of fluorine atoms on boron, as determined by ^{19}F NMR. Enzyme-mediated hydrolysis was envisaged as a mild method for hydrolysing methyl esters without the need for acid/base catalysis. The reaction, which is biphasic, involves the addition of a lipase enzyme to the buffered aqueous component, the ester (**51**) is dissolved in the organic component, and the lipase operates at the interface. Here, hexane was used as the organic phase, with MeOH used to dissolve **51** and create a mixture.

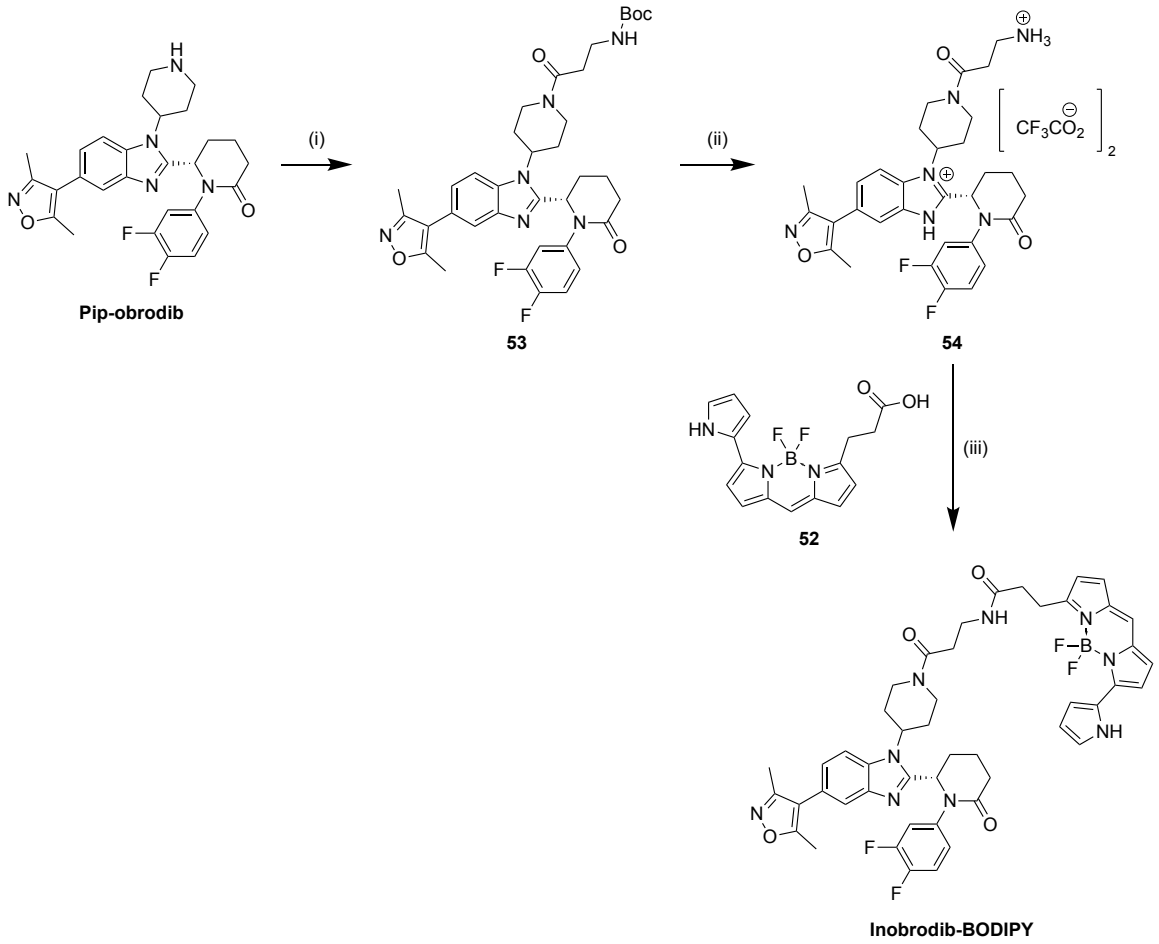
The reactivity of any lipase can be difficult to predict, with varying efficiencies depending on the substrate. Thus, a chemical screen was initiated with a selection of lipases at hand, a stock solution of **51** was prepared and 25 µmol was added to reactions performed in parallel, all lipases were prepared as 5 mg mL^{-1} solutions in PBS. The reactions were

stopped after 24 h, diluted with EtOAc, acidified with HCl and the organic supernatant was analysed using HPLC. The results are summarised in **Table 2.3**.

Table 2.3: Summary of measured conversions for the lipase screen performed on 25 μmol scale for the reaction shown in **Scheme 9**, step (vi). Reactions were stopped after 24 h, diluted with EtOAc and acidified with 1 M HCl aq. Conversions were determined using HPLC analysis of the of the organic supernatant using a single point calibration.

Entry	Lipase	Conversion after 24 h
1	from *Candida rugosa*	0%
2	From Porcine pancreas	63%
3	Lipozyme TL IM	10%
4	Amano PS	83%

Amano Lipase PS gave the highest conversion and was used in the final synthesis. The carboxylic acid derivative of BODIPY 576/589 (**52**) was obtained in 40% yield, with 52% starting material (**51**) recovered. It was disappointing that a higher yield was not achieved when the reaction was scaled up, which is attributed to the insolubility of the substrate (**51**) under the reaction conditions. Improvement in yield could be achieved by a more thorough screening of solvents employed in the reaction. Regardless, the yield obtained was sufficient to continue the synthesis of inobrodib-BODIPY**.**



Scheme 10: Synthesis of the inobrodib-BODIPY tracer. *Reagents and conditions:* (i) Boc-β-Ala-OH, *iso*-butyl chloroformate, NEt_3, anhydrous CH_2Cl_2, 0 ºC, 10 min, then pip-obrodib, 0 ºC – rt, 30 min, 85%; (ii) TFA:CH_2Cl_2 1:1, rt, 30 min, 77%; (iii) **52,** HATU, DIPEA, DMF, rt, 5 h, 30%.

With BODIPY (**52**) in hand, the synthesis of the inobrodib based tracer was performed as outlined in **Scheme 10**. A short chemical linker was introduced between the pip-obrodib and BODIPY scaffolds to ensure that BODIPY is solvent-exposed and free from the bromodomain once the compound is in complex with the protein. Amide coupling between pip-obrodib and Boc-β-Ala-OH was performed using *iso*-butyl chloroformate to afford intermediate **53** in 85% yield. The Boc-group was then removed to afford the primary amine **54** as a TFA salt in 77% yield. Finally, amide coupling between **54** and **52** was performed using HATU as a coupling reagent to afford inobrodib-BODIPY in 30% yield. The intermediate (**54**) was then also coupled to carboxyl functionalised beads to be used as an affinity pulldown probe in a collaborative research project with Ludwig Bauer (PhD student, under the supervision of Dr Kilian Huber).

2.4 Summary

Here the design and synthesis of heterobifunctional compounds termed AcDC-**1**–**4** has been described. The compounds incorporated scaffolds based on the inhibitors inobrodib and BIIB021 as binding ligands to the CBP/p300 bromodomain and Hsp90 *N*-terminal binding domains, respectively. AcDC-**1**–**4** differed in composition of chemical linker, with a focus given to exploring the effect of linker length on the formation of a ternary complex with the binding domains.

Inspection of the co-crystal structures of inobrodib with CBP^{BRD} and BIIB021 with $Hsp90^{NTD}$ informed the rational design of AcDC-**1**–**4**. At the point the project was started, inobrodib had not previously been incorporated into heterobifunctional compounds, so a vector for extension of a chemical linker from the scaffold was identified. pip-obrodib was synthesised as a novel analogue of inobrodib, to allow derivatisation of the CBP/p300 bromodomain ligand by amide coupling.

Previously reported procedures methods were used for the incorporation of the BIIB021 scaffold into heterobifunctional molecules, with rational of its binding to Hsp90 used to inform the design of chemical linkers employed in AcDC-**1**–**4**

Lastly, a novel fluorescent tracer compound (inobrodib-BODIPY) was also developed, to be used in NanoBRET assays for measuring target engagement with the CBP/p300 bromodomain.

3 Biophysical characterisation of AcDCs

3.1 Validation of chemical linker extension from inobrodib scaffold

The modification and linker extension on the inobrodib scaffold to afford AcDC-**1**–**4** was designed to maintain binding affinity with CBP/p300 bromodomain. To establish this experimentally, isothermal titration calorimetry (ITC) was used to measure the binding between AcDC-**1**–**4** and the p300^{BRD} as the protein construct 6×His-p300^{BRD} (**Figure 3.1**).

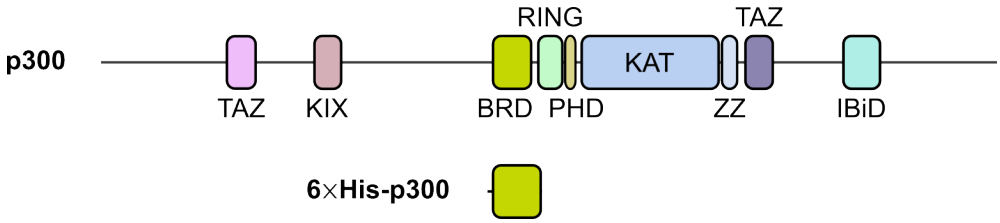


Figure 3.1: The protein construct 6×His-p300^{BRD} comprises the p300^{BRD} with an *N*-terminal 6×His tag. Domain structure of full length human CBP/p300 is shown as reference. KAT (pale blue), BRD (green), transcription adaptor zinc finger domain (TAZ, pink/purple), kinase-inducible domain (KID) interacting domain (KIX, peach), really interesting new gene domain (RING, turquoise), plant homeodomain (PHD, beige), ZZ-type zinc finger domain (ZZ, grey), interferon binding domain (IBiD, sky blue). Domain positions and sequence length information was obtained from InterPro tool by EMBL-EBI.[37]

The selection of the p300^{BRD} over the CBP^{BRD} was arbitrary, given that they share 95% sequence identity and 99% sequence similarity. A comparison of their sequences is presented in **Appendix Figure A.3**

Binding affinity can be determined through ITC by titrating a protein or ligand against its binding partner (at known concentrations) and measurement of the power generated upon binding. At the equivalence point, a transition is observed as the binding partner becomes saturated and no further heat is generated by addition of titrant. By integration of the power generated, the heat of binding (ΔH) is determined and plotted against the molar ratio (n) of titrant to binding partner. The dissociation constant is determined by the inverse of the gradient of transition at the equivalence point in this curve (**Appendix Figure A.1**).

To carry out this assay, expression and purification of recombinant 6×His-p300 (**Figure 3.1**) was performed as previously described.[192] In brief, the recombinant protein was purified using immobilised metal affinity chromatography (IMAC) on Ni-NTA resin, followed by two

rounds of size exclusion chromatography (SEC). This 6×His tag was not cleaved at the TEV site during purification to allow the use of the fusion construct in later AlphaScreen assays.

ITC experiments were performed with inobrodib as a positive control and were used to optimise protein and compound concentrations. Recombinant protein was used as the titrant and added to compounds. The analysis of ITC data from two independent experiments is summarised in **Table 3.1** and traces are provided in **Appendix D.**

Table 3.1 Summary of binding affinities of AcDCs with the 6×His-p300^{BRD} protein construct. K_d values were determined by ITC and represent the mean of two independent experiments. Error bars represent the standard error of mean. The literature reported K_d value for inobrodib for the p300 bromodomain is 1.3 nM (SPR).[175]

Entry	Compound	K_d (nM)
1	AcDC-1	655 ± 29.5
2	AcDC-2	247 ± 47.5
3	AcDC-3	282 ± 38.5
4	AcDC-4	162 ± 1.00
5	Inobrodib	62.3 ± 22.6

The measured K_d value for inobrodib (62.3 ± 22.6 nM) was above the literature reported value of 1.3 nM for the p300 bromodomain (determined by surface plasmon resonance (SPR)).[175] However, such a tight binding value can be difficult to obtain by ITC, due to a sharp transition in the titration, causing fewer data points to be measured near the equivalence point, leading to inaccuracy. Additionally, it is known that artifacts in SPR, such as mass transport, nonspecific binding, and avidity effects, can cause an artificially high binding affinity.[193] The K_d value for inobrodib has been determined as 26.4 nM for the structurally similar CBP bromodomain,[176] and our measured value was determined to be within range of this reported value.

We observed a decreased binding affinity for all AcDC compounds compared to inobrodib, with a trend of shorter linker lengths bearing the largest penalty; all compounds displayed sub-micromolar K_d values and were judged to have sufficient binding affinity to carry forward into additional assays. We concluded that chemical linker extension from pip-obrodib is tolerated in binding to the p300 bromodomain and could be used to develop chemical probes or additional heterobifunctional compounds.

3.2 AcDC-Induced proximity between recombinant p300^{BRD} and Hsp90α^{NTD}

3.2.1 Production of recombinant GST-Hsp90α^{NTD}

The binding of AcDC-**1**–**4** to Hsp90 in a ternary complex with 6×His-p300^{BRD} was subsequently measured using an AlphaScreen based proximity assay. The section below provides a detailed discussion of the AlphaScreen-based proximity assay; to carry out this assay, a suitable protein construct was required that contained the Hsp90 *N*-terminal domain (at the very least) and an orthogonal tag that would enable selective binding of the protein construct to donor/acceptor beads, in contrast to the 6×His tag used on 6×His-p300^{BRD}. The fusion construct GST-Hsp90α^{NTD} was selected, and available as a plasmid construct from Addgene (plasmid #22481), circumventing the need for molecular cloning.

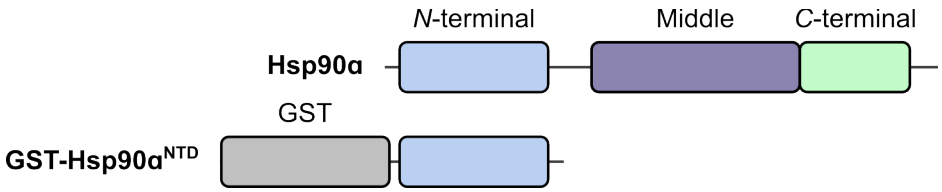


Figure 3.2: The protein construct GST-Hsp90α^{NTD} comprises the *N*-terminal domain of Hsp90α (residues 9–236) fussed to an *N*-terminal GST tag (grey box). Domain architecture of full-length Hsp90 is shown as reference: NTD (blue box), MD (purple box) and CTD (light green box). Domain positions and sequence length information was obtained from InterPro tool by EMBL-EBI.[37]

The expression of GST-Hsp90α^{NTD} was first attempted using similar conditions to those employed in the expression of 6×His-p300^{BRD}: induction with IPTG at 0.1 mM at 18 ºC for 20 h. These expression conditions produced no detectable recombinant protein in the initial steps of purification, and gel electrophoresis analysis of the lysate showed no significant levels of induced protein expression compared to an un-induced control.

Given that assay development can require large amounts of purified soluble protein, efficient expression of GST-Hsp90α^{NTD} was sought. To explore the effect of temperature and concentration of IPTG on expression levels, small scale expression trials were conducted. A starter culture was grown until early log-growth phase, split and induced with varying concentrations of IPTG, and incubated at either 16 ºC or 25 ºC for 20 h.

Cultures were split into duplicate samples, collected by centrifugation and lysed in either a non-denaturing or denaturing lysis buffer. The samples in non-denaturing lysis buffer were cleared of debris and the supernatant containing the soluble protein fraction was first analysed by SDS-PAGE (**Figure 3.3**). Induction with 0.5 mM IPTG and incubation at 25 ºC caused a significant band to appear at 50 kDa corresponding to the expression of soluble GST-Hsp90^{NTD}.

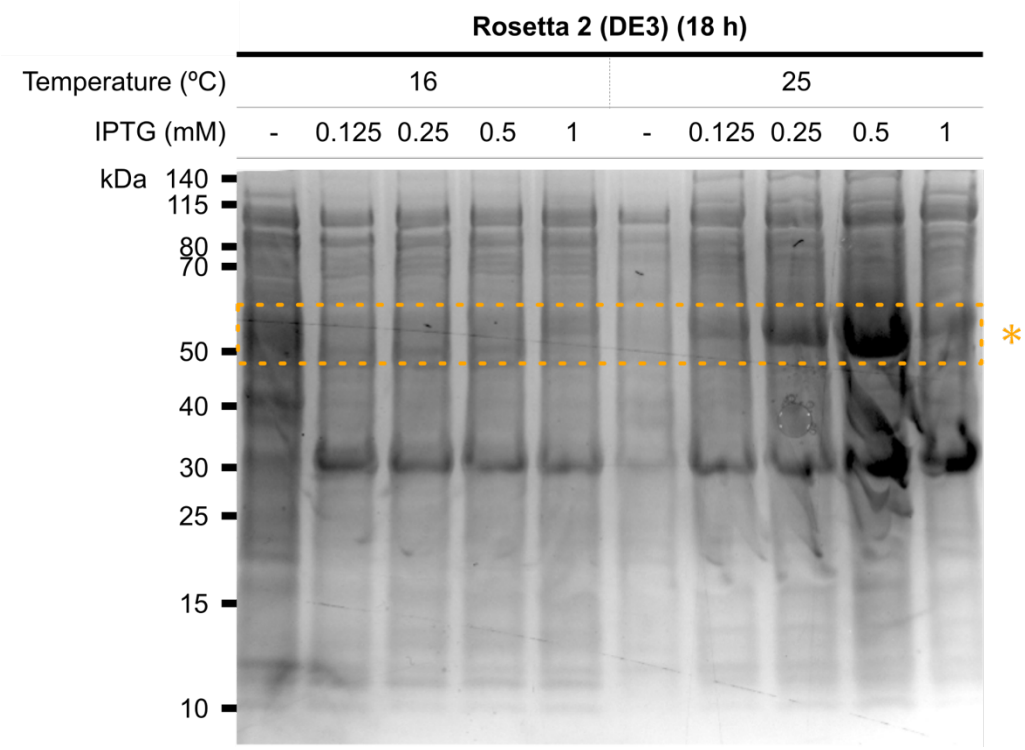


Figure 3.3: SDS-PAGE analysis of lysate soluble component in expression trials of GST-Hsp90^{NTD} in Rosetta 2 (DE3) *E. coli*. Dashed orange square marked with an asterisk (∗) highlights expected region of overexpressed GST-Hsp90^{NTD}. SDS-PAGE was run on a 4–12% Bis-Tris gel run in MES buffer with PageRuler™ pre-stained protein ladder as a reference of annotated molecular weights.

Using these conditions, expression and purification of the recombinant protein was performed on batch scale by FPLC. The recombinant protein was first purified by affinity chromatography on glutathione resin in flow using a GSTrap. SDS-PAGE analysis of the bacterial lysate (input), flow-through, and eluate showed good capture and release of the target recombinant protein (**Figure 3.4**), but substantial amounts remained in the flow-through component, which was attributed to binding saturation of the GSTrap.

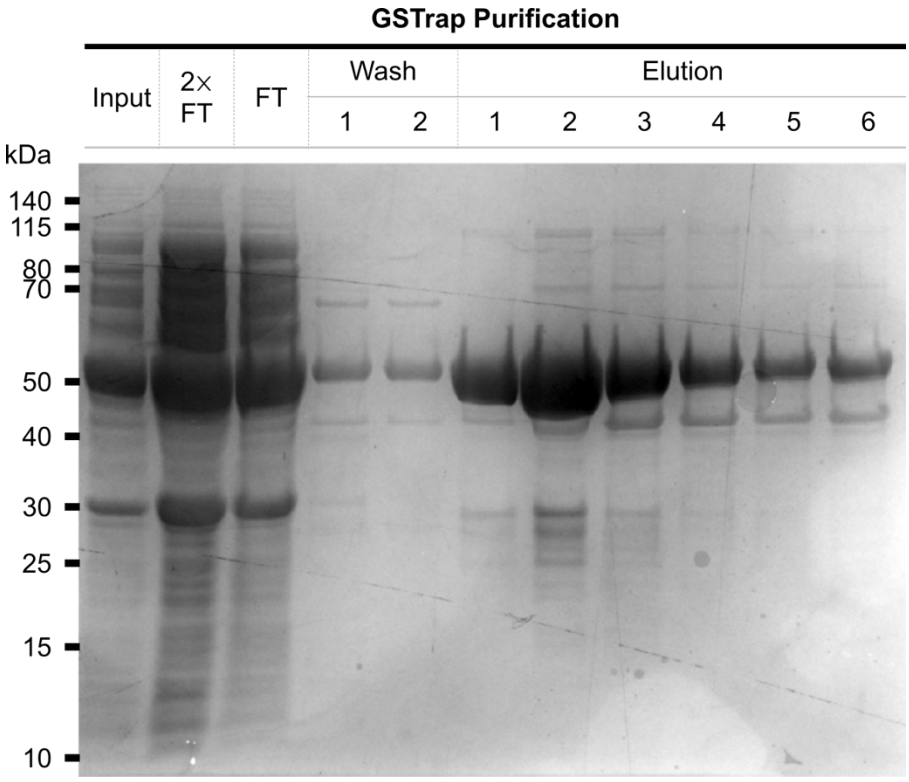


Figure 3.4: SDS-PAGE analysis of GSTrap purification of GST-Hsp90α^{NTD} shows good capture and release of desired recombinant protein at *c.* 50 kDa. Input refers to a sample of the bacterial lysate used in purification. 2× FT refers to the flow-through component of the GSTrap with twice the amount loaded compared to the input, while FT is an equal amount of flow-through loaded compared to Input. Wash 1,2 refer to the first two fractions obtained from washing the GSTrap with binding buffer. Elution 1–6 refer to the fraction obtained from washing the GSTrap with elution buffer.

Re-subjection of the flow-through component to affinity chromatography yielded additional recombinant protein in the eluate. Affinity chromatography limited the yield of purified recombinant protein, but this was seen as a pleasing problem to have, and two rounds of affinity chromatography captured 70 mg of protein that was deemed sufficient to proceed. Size exclusion chromatography was then performed on the combined GSTrap eluate. The chromatogram showed three peaks (**Figure 3.5A**) which contained protein which migrated at 50 kDa when analysed by SDS-PAGE (**Figure 3.5B**). The initial peaks were suspected to correspond to protein aggregates or un-folded forms of the protein, with the main third peak corresponding to the desired protein form. To rule out the possibility of a dimer/multimer species, the fractions corresponding to the third peak were collected, concentrated and re-subjected to size exclusion chromatography (**Figure 3.5C**). Here, we observed a single peak which eluted at the same retention time as before, confirming the

protein species to be a distinct form from those corresponding to the other peaks in the first round of SEC.

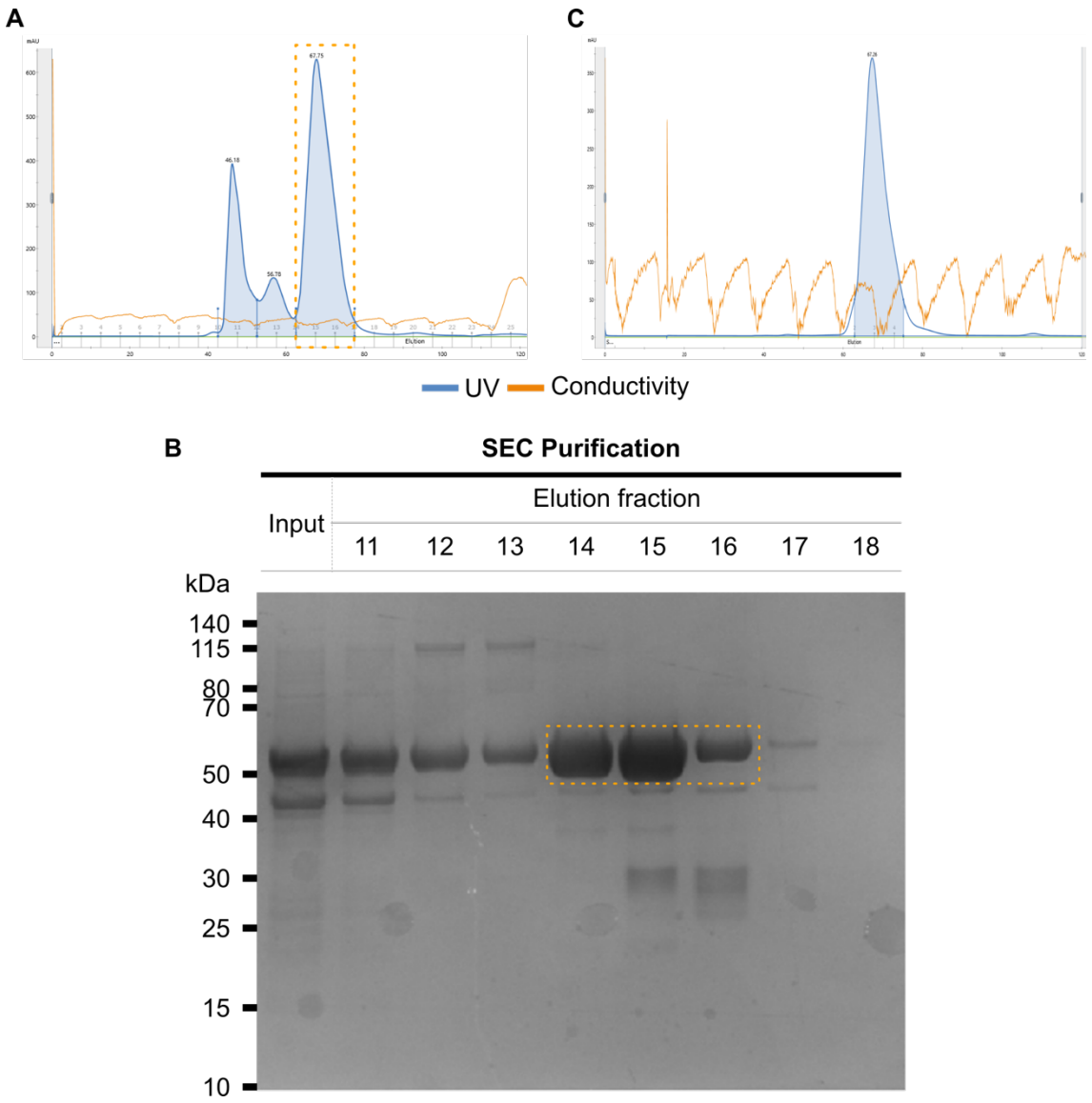


Figure 3.5: SDS-PAGE and chromatogram analysis of SEC purification of GST-Hsp90α^{NTD} shows multiple distinct forms of recombinant protein from GSTrap. **(A)** Chromatogram of initial SEC purification shows three distinct peaks over elution fractions 10–17 shaded in blue. Dashed orange square highlights fractions containing the expected desired recombinant protein in correctly folded form. **(B)** SDS-PAGE analysis of initial SEC fractions. Dashed orange square highlights fractions corresponding to those highlighted in (A). Input refers to a sample of combined GSTrap eluate passed into SEC purification. **(C)** Chromatogram of highlighted fractions in (A) once combined concentrated and resubjected to SEC shows a single peak of identical retention time.

SDS-PAGE analysis of fractions eluted in the second round of SEC was used to determine protein purity, and the cleanest fraction was concentrated to afford recombinant protein that could be used in assays. SDS-PAGE analysis and LC-MS verification of this recombinant protein are available in **Appendix C.**

3.2.2 Development of an AlphaScreen based assay to show AcDC induced proximity

As previously mentioned, an AlphaScreen based proximity assay was envisaged to measure the binding of AcDCs with recombinant Hsp90α^{NTD} and p300^{BRD} in a ternary complex. AlphaScreen based assays have previously been used to characterise ternary complex formation in the development of PROTACs[194-198] and other heterobifunctionals.[155, 158] Alpha based assays comprise one binding partner attached to a donor bead and another binding partner attached to an acceptor bead. The donor beads are photosensitised to convert ambient oxygen into singlet oxygen ($^1O_2$) when excited with 680 nm light, while the acceptor beads convert energy from $^1O_2$ into luminescence and emit light at 520–620 nm. $^1O_2$ has a short half-life (4 μs) and can only diffuse *c.* 200 nm in solution, so the signal is amplified when the donor and acceptor beads are held in proximity.[198]

GST-Hsp90^{NTD} was conjugated to glutathione donor beads and 6×His-p300^{BRD} was conjugated to nickel chelate acceptor beads. For AcDCs capable of forming ternary complexes, we expected a titration of the compounds to produce a bell-shaped distribution when plotting luminescence signal against concentration of AcDC (**Figure 3.6**). An initial increase in AcDC concentration leads to ternary complex formation with GST-Hsp90^{NTD} and 6×His-p300^{BRD} and hence, donor and acceptor beads are held into proximity and an increased signal is observed. However, at higher AcDC concentrations, the concentration of available unbound protein becomes limiting, and a hook effect is observed resulting in a gradual decrease in signal. The maximal luminescence signal is proportional to the relative population of ternary complexes, allowing AcDCs to be ranked by their ability to form ternary complexes.

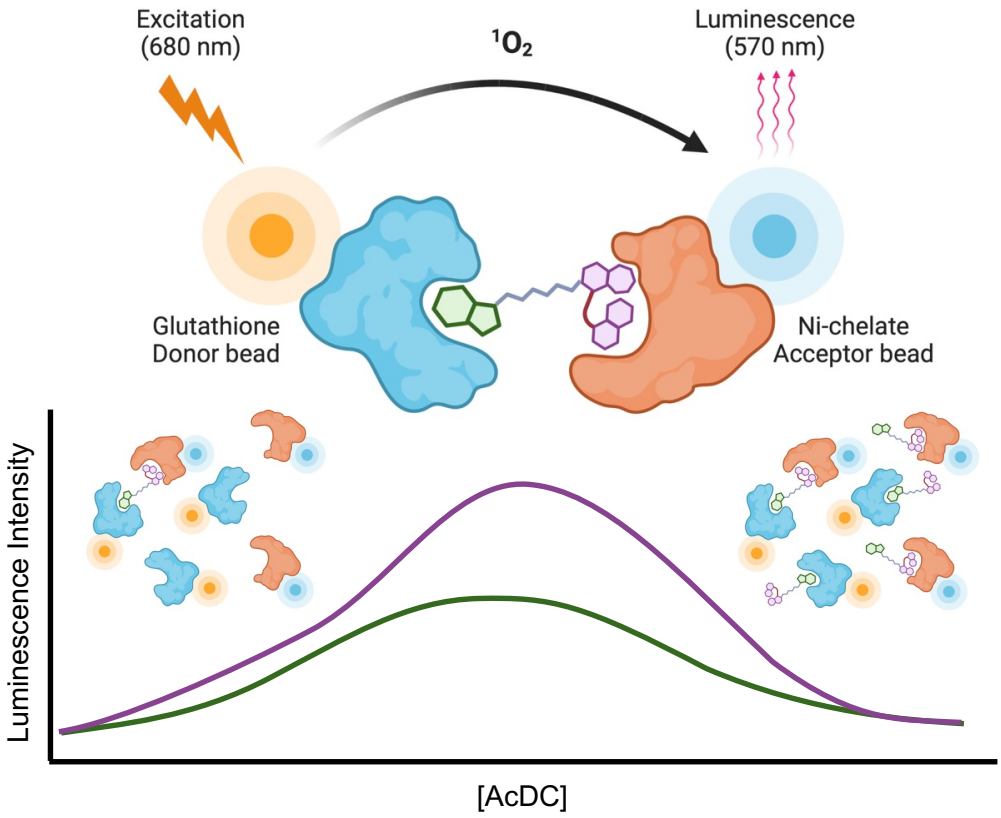


Figure 3.6: Principle of AlphaScreen based assay for ternary complex formation. Proteins (binding partners) are conjugated to donor and acceptor beads. Excitation of donor bead causes conversion of $^1O_2$ followed by energy transfer to acceptor bead in proximity and observed luminescence signal. Titration of hetero-bifunctional molecules capable of forming ternary complexes between binding partners produces a bell-shaped distribution from an initial positive signal-response, followed by a hook effect at higher concentrations.

Initial attempts in performing the assay failed to produce any significant signal in all test conditions, so a technical positive control was sought to enable optimisation of reagents and microplate reader parameters. The recombinant protein construct 6×His-GST was titrated in place of **AcDC-1–4**, Hsp90^{NTD} and 6×His-p300^{BRD} to ensure a signal can be produced by the donor and acceptor beads and measured (**Figure 3.7**). It was pleasing to see a bell-shaped signal-response curve was produced upon optimisation of plate reader parameters, with EC_{50} values of 12 nM and 55 nM for the left and right sides of the curve, respectively. The bell-shaped curve originated from a hook effect of protein binding to the beads and suggested the optimum concentration of binding partners to be within the range of the EC_{50} values.

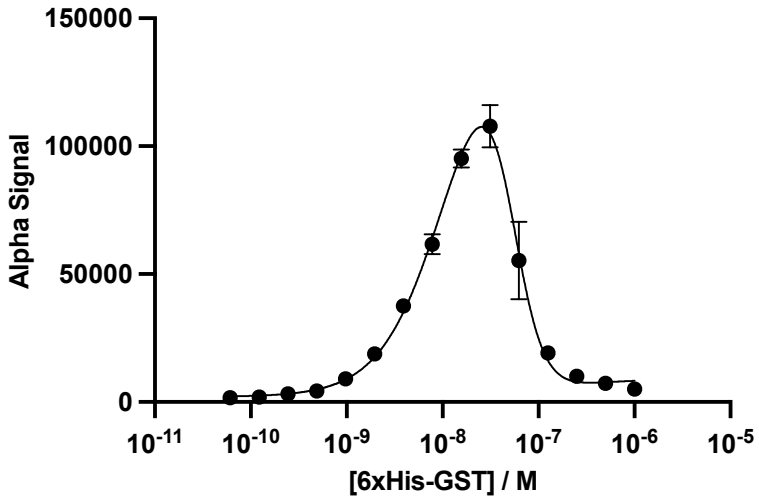


Figure 3.7: 6×His-GST was used as a technical positive control to optimise the AlphaScreen based assay for induced proximity. A bell-shaped signal response was observed from 6×His-GST titrated in a 1:2 concentration series from 1 μM against glutathione donor and nickel chelate acceptor beads at 10 μg mL^{-1}.

The assay was repeated with Hsp90α^{NTD} and 6×His-p300^{BRD} each at 30 nM and AcDC-**1**–**4** titrated with 1:2 serial dilutions from 5 μM to 10 nM in 10 assay points (in triplicate). Using these optimised conditions, a signal was observed for AcDC-**1**–**4**, while the negative control, combination of the ligands (BIIB021 + inobrodib), failed to show concentration dependent change in signal (**Figure 3.8A**). However, within the selected concentration range, a loss of signal was predominantly observed, rather than a bell-shaped curve as originally expected.

With an additional five datapoints to give a concentration range of 5000–0.3 nM (15 × 1:2 serial dilutions), and 6×His-GST included as a technical positive control, we then observed a bell-shaped curve indicative of ternary complex formation (**Figure 3.8B)**. However, AcDC-**1**–**4** appeared to give similar profiles, with similar maximal signals, preventing ranking of the relative populations of ternary complex produced. The datapoints within each compound series also appeared 'flat' near the signal maxima and it was proposed the signal was reaching the detection limit and a lower bead or protein concentration was required. It was also interesting to note that 6×His-GST had a much lower maximal signal compared to the AcDC-**1**–**4**, which we rationalised as reduced binding to the Alpha beads compared to the 6×His-p300^{BRD} and GST-Hsp90^{NTD}. Alternatively, the reduced signal could be due to

conformational effects or rigidity in the 6×His-GST Alpha bead complex, contrasted to a more flexible complex with a similar radius of gyration, where the beads may come into closer proximity over the course of the measurement.

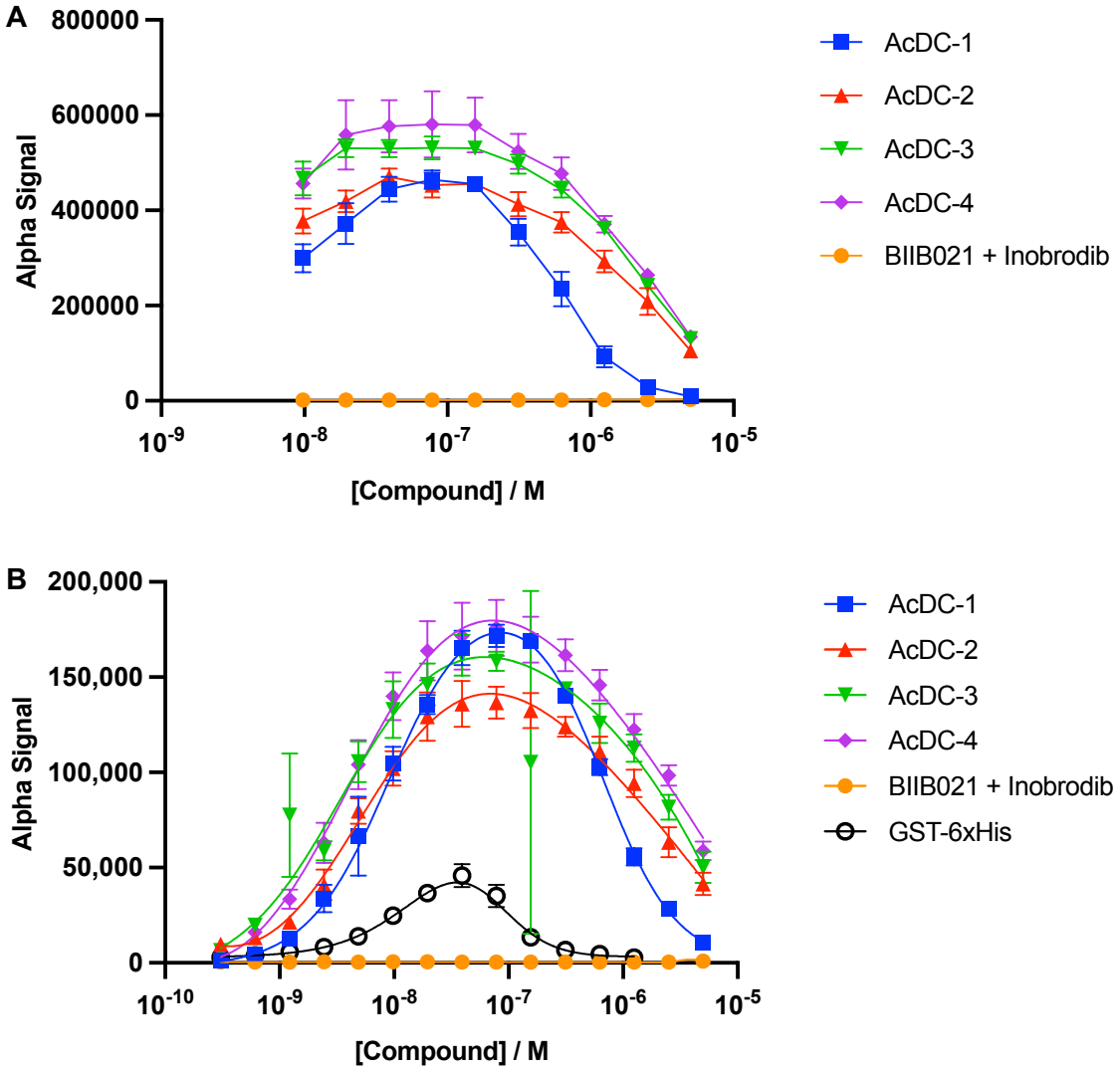


Figure 3.8: Optimisation of AlphaScreen based assay for AcDC-induced proximity with protein concentration of 30 nM. **A** Data from initial assay optimisation shows significant signal at the lowest concentration of AcDCs tested in the assay. **B** A wider concentration range of AcDCs gives a characteristic bell-shaped curve allowing a non-linear regression model to be fitted, but likely reached detection saturation as evidenced by the flat appearance of datapoints around the maxima.

The assay was then repeated using a lower protein concentration of 10 nM and we observed tighter bell-shaped curves which had a clearer maximal intensity than previous attempts (**Figure 3.9A**). It was interesting to see a clear difference in the binding profiles of AcDC-**1** compared to the analogues AcDC-**2**–**4**, which appeared to have increased maximal signal intensity correlating with linker length. Additionally, AcDC-**1** has a higher initial EC_{50}_1

value (the concentration of compound that gives a half-maximal Alpha signal on the upward slope of the bell curve) and lower second EC_{50}_2 value (the EC_{50} on the downward slope of the bell curve) compared to the other compounds, suggesting the formation of a weaker ternary complex. To ensure reproducibility, the assay was performed an additional two times, the calculated best-fit values were plotted (**Figure 3.9B,C**), and their mean values were determined (**Table 3.2**).

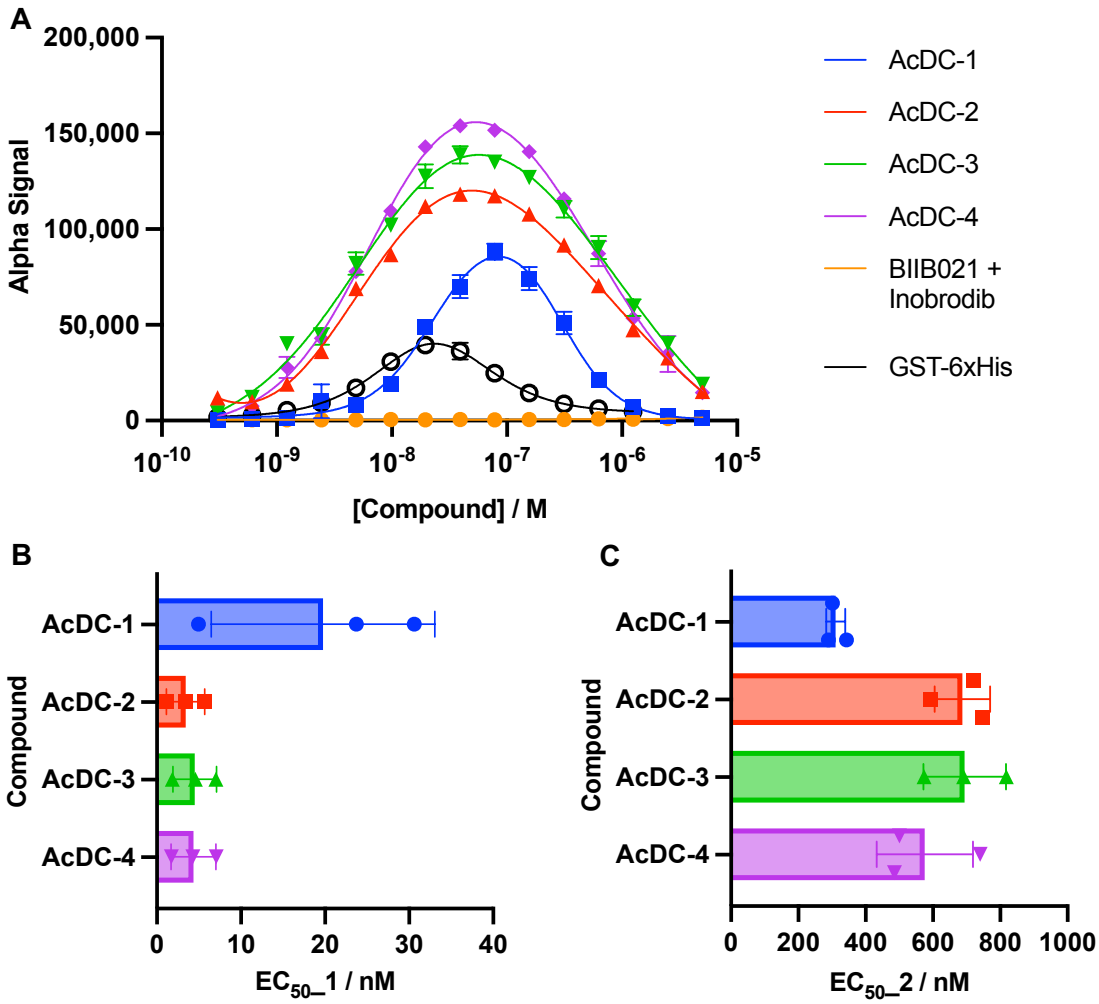


Figure 3.9: AcDCs induce proximity between recombinant $p300^{BRD}$ and $Hsp90^{NTD}$ by AlphaScreen assay. AcDC-**1** (blue) appears to form weaker ternary complexes than AcDC-**2**–**4**. (**A**) Titrations of AcDCs produced clear bell-shaped curves in AlphaScreen, indicative of ternary complex formation (protein concentration of 10 nM). Data representative of three biological repeats. (**B**) Plotted EC_{50}_1 values (on upward slope of bell curve) from all experimental repeats, error bars represent s.d. (**C**) Plotted EC_{50}_2 values (on downward slope of bell curve) from all experimental repeats, error bars represent s.d.

Table 3.2: Mean EC_{50} values from experimental repeats of AlphaScreen based assay for induced proximity. EC_{50}_1 represents the concentration of compound (nM) that gives a half-maximal Alpha signal on the upward slope of the bell curve, while EC_{50}_2 represents the concentration of compound that gives a half-maximal Alpha signal on the downward slope of the bell curve.

Entry	Compound	Mean EC_{50}_1 ± s.d / nM	Mean EC_{50}_2 ± s.d. / nM
1	AcDC-1	19.8 ± 13.3	311 ± 28.2
2	AcDC-2	3.41 ± 2.28	688 ± 82.4
3	AcDC-3	4.49 ± 2.59	694 ± 123
4	AcDC-4	4.34 ± 2.67	576 ± 143

Experimental repeats confirmed the initial observations, and it could be concluded that AcDC-**1** forms a weaker ternary complex between 6×His-$p300^{BRD}$ and GST-$Hsp90^{NTD}$ than AcDC-**2**–**4**, as the compound consistently gave a lower maximal intensity. AcDC-**1** also gave narrower bell-shaped curves compared to other compounds, suggesting ternary complex formation requires higher concentrations of compound and a hook effect begins to operate at lower concentrations compared to AcDC-**2**–**4**.

3.3 Validation of specific binding in ternary complex formation

To validate these conclusions and confirm that induced ternary complex formation is due to specific binding between AcDCs, the bromodomain of 6×His-p300^{BRD} and the ATP pocket of GST-Hsp90α^{NTD}; a modification of the AlphaScreen proximity assay was devised. A competition based assay was developed where the inhibitors BIIB021 or inobrodib were titrated against AcDC-**1**–**4** (20 nM) in complex with 6×His-p300^{BRD} and GST-Hsp90^{NTD} at their optimal concentrations, as established in the previous assay. We expected to see inhibition binding curves with an IC_{50} value corresponding to the concentration of BIIB021 or inobrodib required to compete with the AcDC and disrupt the ternary complex (**Figure 3.10**).

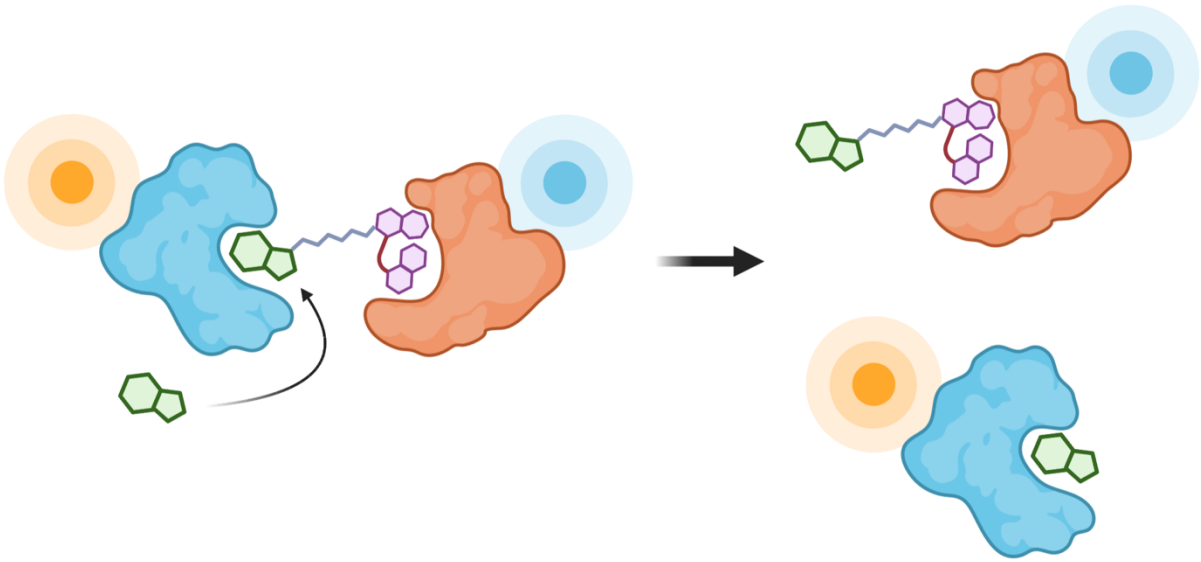


Figure 3.10: Principle of AlphaScreen based competition assay to show specific binding in AcDC induced proximity. BIIB021 or inobrodib were titrated into a system comprising AcDC-**1**–**4** at 20 nM, GST-Hsp90α^{NTD}, and 6×His-p300^{BRD} (10 nM each). The inhibitors compete with AcDC and cause loss of induced proximity and result in antagonistic loss of Alpha signal.

We observed inhibition curves as expected (**Figure 3.11A,B**), and noted that competition between AcDC-**1** and either inobrodib or BIIB021 gave a significantly lower mean IC_{50} than AcDC-**2**–**4** (**Figure 3.11C, Table 3.3)**, while all other AcDCs had comparable IC_{50} values. From this we could confidently conclude that ternary complexes are formed by specific binding of AcDC-**1**–**4** to the protein constructs (opposed to random lipophilic or artefactual

binding). Second, the ternary complex formed with AcDC-**1** to 6×His-p300^{BRD} and GST-Hsp90α^{NTD} is weaker than those formed with AcDC-**2**–**4**.

Table 3.3: Mean IC_{50} values from experimental repeats of AlphaScreen based competition assay for loss of induced proximity. IC_{50} represents the concentration of competitor (nM) that gives a half-maximal Alpha signal when titrated against the ternary complex formed with AcDC-**1**–**4** at 20 nM and Hsp90^{NTD} & p300^{BRD} at 10 nM each.

Entry	Compound	BIIB021 Mean IC_{50} ± s.d. / nM	Inobrodib Mean IC_{50} ± s.d. / nM
1	AcDC-1	4.14 ± 0.91	4.84 ± 1.74
2	AcDC-2	14.6 ± 2.00	17.9 ± 4.82
3	AcDC-3	15.9 ± 3.94	15.3 ± 5.14
4	AcDC-4	14.7 ± 4.00	13.1 ± 3.35

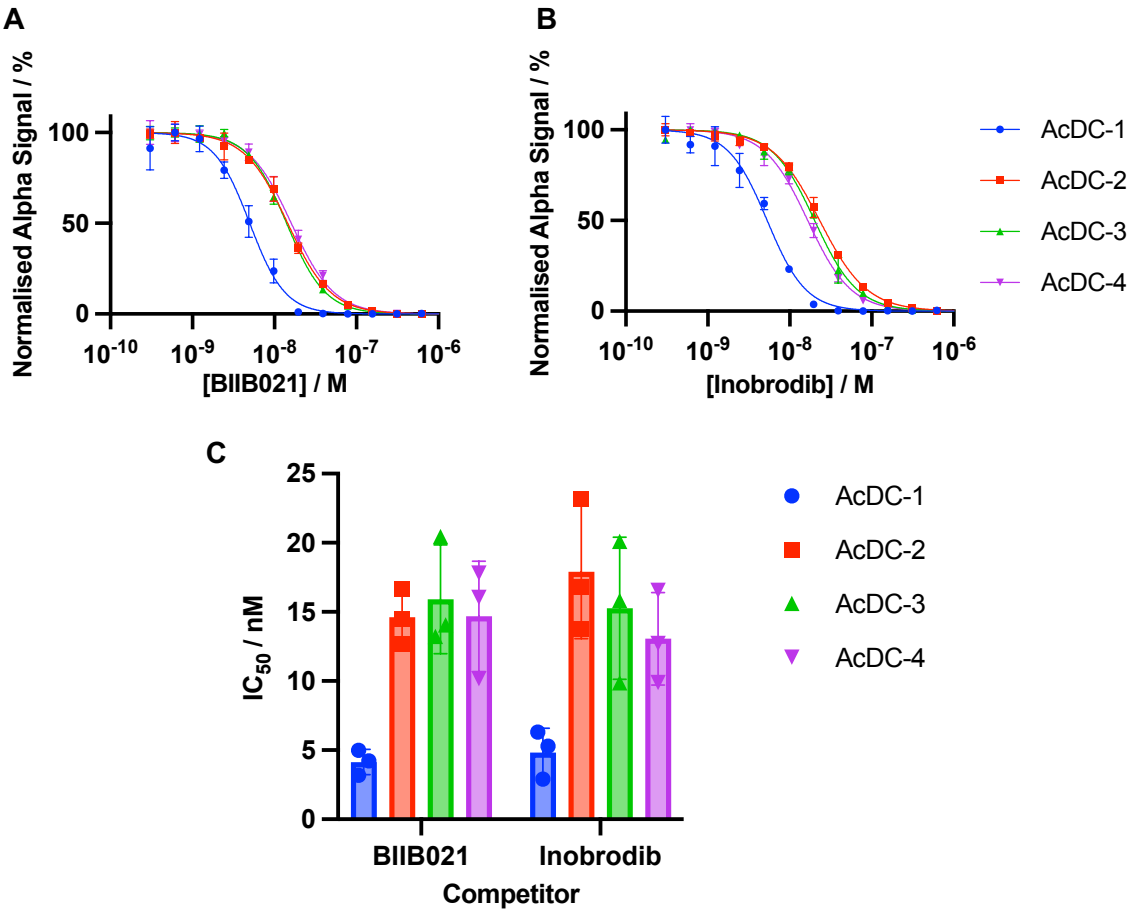


Figure 3.11: AlphaScreen-based competition assay shows that titration of BIIB021 or inobrodib causes antagonistic loss of signal, confirming that AcDCs induce proximity by specifically binding to the bromodomain and *N*-terminal domains. AcDC-**1** (blue) is outcompeted at lower concentrations of inhibitors than AcDC-**2**–**4**. Representative binding curves from three biological repeats show competition with (**A**) BIIB021 and (**B**) inobrodib. (**C**) Plotted IC_{50} values from all biological replicates; error bars represent s.d.

3.4 Measurement of cooperative binding between in induced ternary complexes

The AlphaScreen ternary complex formation assay revealed an interesting observation, as the measured EC_{50}_1 values were significantly lower than the K_d values measured between AcDC-**1**–**4** and 6×His-p300^{BRD} by ITC. To further investigate the binding properties of AcDC-**1**–**4** with the protein binding domains in a ternary complex, ITC was used to explore the extent of cooperativity, and further support compound induced proximity. Cooperativity (**α**) refers to the ratio between the dissociation constant of a binary complex and that of the corresponding binding step in the ternary complex (**Equation 1**).[199] Positive cooperativity (**α** > 1) results from higher ternary complex binding affinity compared to corresponding binary complex. Conversely, negative cooperativity (**α** < 1) is a potential consequence of unfavourable protein-protein interactions (PPIs). Isoform-specific positive cooperativity in PROTAC induced proximity has been shown to lead to selectivity in the degradation profile of PROTACs capable of binding multiple isoforms in binary.[196]

Equation 1: Cooperativity factor (**α**) is determined as the ratio between the dissociation constant (K_d) of a binary complex and that of the corresponding binding step in the ternary complex. The equation below describes the system A + B + C where B is a bifunctional compound capable of binding A (AB in complex) and C (BC in complex) to form a ternary complex (ABC).

$$ABC \leftrightarrows A + BC \leftrightarrows A + B + C \rightleftharpoons AB + C \rightleftharpoons ABC$$

$$\alpha = \frac{K_D(A + BC)}{K_D(A + B)} = \frac{K_D(AB + C)}{K_D(B + C)}$$

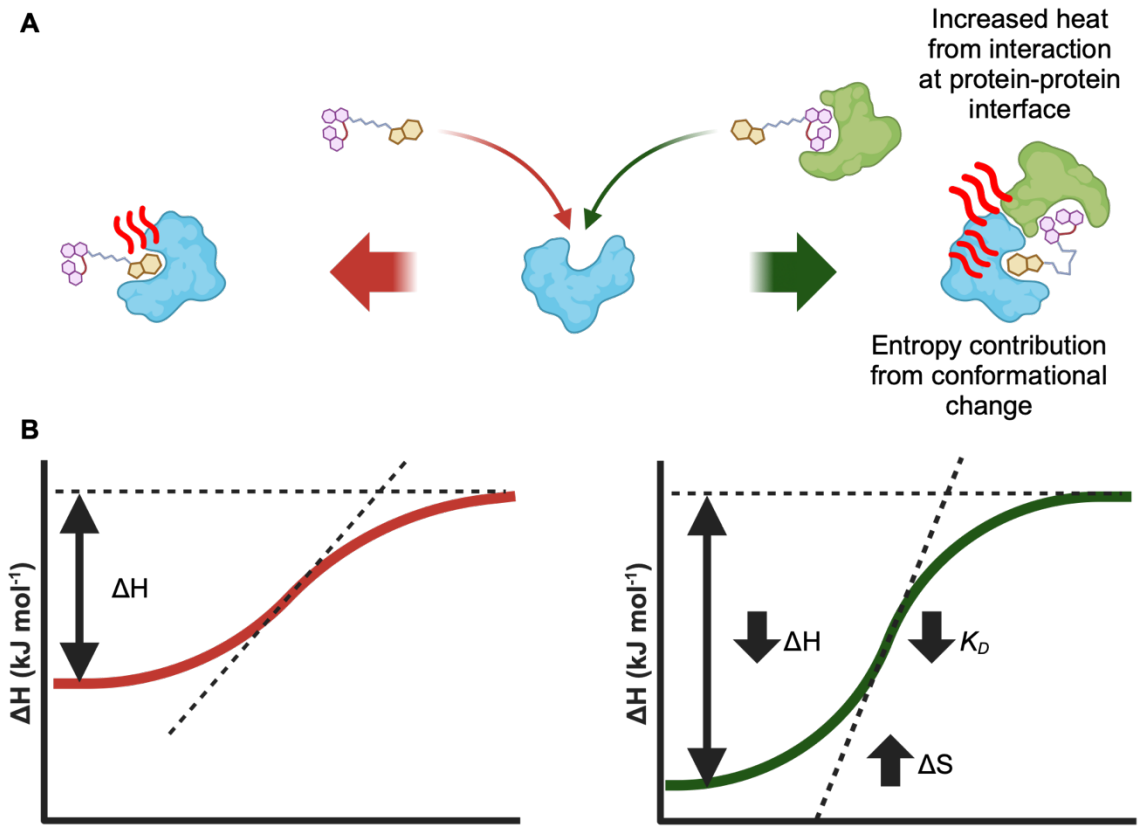


Figure 3.12: Principle of ITC based assay to measure co-operativity (α) of AcDC binding as ternary complex. (**A**) ITC is performed with titration of 6×His-p300^{BRD} into AcDC (shown by red arrow) or into AcDC in complex with GST-Hsp90α^{NTD} (shown by dark green arrow). (**B**) A change in K_d is observed when AcDCs bind in a ternary complex (compared to binding in binary) due to a larger enthalpy of binding originating from favourable interactions at the protein-protein interface and changes in the conformation of the system that contribute an entropic component to binding.

In this experiment, K_d values were determined by titration of 6×His-p300^{BRD} against the AcDC (binary interaction) and compared to the K_d value obtained when titrated against AcDC pre-complexed with GST-Hsp90^{NTD} (ternary interaction). The reverse titration (addition of protein to compound) was performed to avoid a hook effect observed with increasing concentrations of heterobifunctional. We expected to observe a decrease in K_d when the AcDC is pre-complexed with GST-Hsp90^{NTD}, corresponding to a positive cooperativity due an enthalpic contribution from favourable PPIs at the interface, an entropic contribution from conformational changes in the system, or a combination of these factors (**Figure 3.12**). The analysis of ITC data from two independent experiments is summarised in **Table 3.4**.

Table 3.4: Summary of dissociation constants (K_d) and cooperativity (α) values for 6×His-p300^{BRD} with AcDC-**1**–**4** and AcDC-**1**–**4** in complex with GST-Hsp90α^{NTD}. α was determined according to **Equation 1**. The dissociation constant was also measured for 6×His-CBP^{BRD} with AcDC-**1**–**4** in complex with GST-Hsp90α^{NTD}, K_d values were determined by ITC and represent the mean of two independent experiments. Error bars represent the standard error of mean.

Entry	Compound	6×His-p300^{BRD}-Compound K_d (nM)	6×His-p300^{BRD}-Compound+ GST-Hsp90^{NTD} K_d (nM)	α	6×His-CBP^{BRD}-Compound+ GST-Hsp90^{NTD} K_d (nM)
1	AcDC-1	655 ± 29.5	390 ± 162	1.68 ± 0.70	662 ± 32.5
2	AcDC-2	247 ± 47.5	49.4 ± 17.9	4.99 ± 2.05	95.9 ± 2.85
3	AcDC-3	282 ± 38.5	119 ± 82.9	2.36 ± 1.67	138 ± 30.5
4	AcDC-4	162 ± 1.00	81.9 ± 40.1	1.98 ± 0.97	159 ± 16.0

All AcDC compounds demonstrated some degree of positive cooperativity with AcDC-**2** having the highest α value of 4.99 ± 2.05. Inspection of the binding curve shows an increase in ΔH compared to the binary binding interaction with 6×His-p300^{BRD}, suggestive of beneficial PPIs at the protein surface and that the linker employed in AcDC-**2** is likely the optimum distance to maintain engagement with the two proteins binding domains.

To compare the interaction of the structurally similar CBP bromodomain, the K_d was determined for the protein construct 6×His-CBP^{BRD} against AcDC-**1**–**4** pre-complexed with GST-Hsp90^{NTD} and shown in **Table 3.4**. Two-way ANOVA analysis of the K_d values showed no significant effect ($p = 0.31$) between the two protein constructs.

3.5 Conclusions

Here was shown that AcDC-**1**–**4** induce proximity between the CBP/p300 bromodomain and Hsp90 *N*-terminal binding domains in an *in vitro* system.

Extension of a chemical linker from the inobrodib scaffold along our chosen exit vector was shown to sustain interaction with the p300 bromodomain, as evidenced by the measured dissociation constants for AcDC-**1**–**4** with 6×His-p300^{BRD}. This suggests amide coupling from pip-obrodib is a viable method to develop additional chemical probes for the CBP/p300 bromodomain.

AlphaScreen based assays were optimised with the recombinant proteins 6×His-p300^{BRD} and GST-Hsp90^{NTD} and demonstrated that AcDC-**1**–**4** can induce proximity between the binding domains in a ternary complex. The induced proximity was also shown to be specific to AcDCs interacting with the binding domains, by antagonistic competition with the inhibitors inobrodib and BIIB021. AcDC-**1** was shown to form the weakest ternary complex, as it was more readily competed by the inhibitors at lower concentrations, while AcDC-**2**–**4** had comparable activities.

The thermodynamic properties of the ternary complex formation were explored, and AcDC-**1**–**4** binding interactions were shown to have positive cooperativity. AcDC-**2** demonstrated the highest degree cooperativity, driven by beneficial PPIs at the protein surface. From this we concluded the linker employed in AcDC-**2** is the optimum length to maintain engagement with the two proteins binding domains.

4 Biological characterisation of AcDCs in cell-based assays

4.1 NanoBRET based experiments

In the previous chapter, we showed that AcDC-**1**–**4** were capable of forming ternary complexes with the binding domains of the proteins of interest; however, it is important to recognise the significant limitations of the *in vitro* assays presented - addition of compounds to the isolated exogenous protein constructs at artificial concentrations in a plastic-tube may not be representative of the native cellular *milieu intérieur*. Thus, it was yet to be determined whether the desired compound interactions could occur with full-length proteins within the complex intracellular microenvironment.

To address this unknown, NanoBRET (Nano-bioluminescence resonance energy transfer) assays were developed to demonstrate that AcDC-**1**–**4** could maintain interactions with CBP/p300 and Hsp90 in live cells. NanoBRET based assays have previously been used to characterise ternary complex formation with PROTACs.[200, 201] The NanoBRET assay relies on the principle of energy transfer between a bioluminescent protein (the donor) and a fluorescent small molecule (the acceptor), which only occurs when they are in close proximity. This is measured by using the signal at 618 nm (the fluorophore emission wavelength) and normalising it relative to the signal at 460 nm (the bioluminescence wavelength). The bioluminescent protein is exogenously expressed in cells by transient transfection of a construct comprising the protein of interest with an *N*-terminal or *C*-terminal fusion to a NanoLuc® (NL) luciferase, which allows for the assay to be carried out in live cells at the point of measurement. [202]

4.1.1 NanoBRET target engagement assay with CBP^{BRD}

The NanoBRET target engagement assay uses a small-molecule fluorescent tracer capable of binding the protein of interest, the CBP^{BRD}. Cells transfected to express the bioluminescent protein construct and treated with the fluorescent tracer molecule produce a BRET signal.[203] However, if the cells are co-treated with an inhibitor for the protein binding

domain, the BRET signal is lost, as the inhibitor competes with the fluorescent tracer (**Figure 4.1**). For CBP/p300, inobrodib-BODIPY was designed and synthesised as the fluorescent tracer, as described in chapter 2. Commercially available plasmid constructs comprising the fusion of NanoLuc luciferase (NL) *N*-terminal of the CBP bromodomain (NL-CBP^{BRD}) or the fusion of NL *C*-terminal of full-length CBP protein (CBP^{FL}-NL) were used.

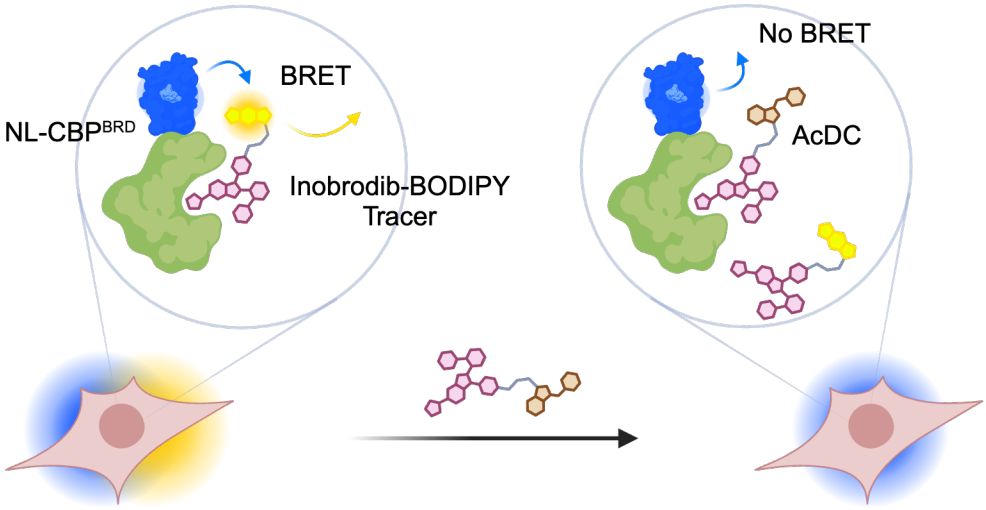


Figure 4.1: Principle of NanoBRET target engagement assay to show compound interaction with the NL-CBP^{BRD} fusion in a cellular context. HEK293 cells are transfected to transiently express a NL-CBP^{BRD} fusion protein comprising the CBP^{BRD} (green) and NanoLuc luciferase (blue). Cells are treated with a inobrodib-BODIPY tracer which gives a signal (yellow) when bound to the CBP^{BRD}. Competition with compounds causes loss of BRET signal as the inobrodib-BODIPY tracer is displaced. Created with BioRender.com

Optimisation of the NanoBRET target engagement assay, including titrations of inobrodib-BODIPY against NL-CBP^{BRD} and CBP^{FL}-NL was performed by Ludwig Bauer (a DPhil student under the supervision of Dr Kilian Huber). A strong BRET signal was observed for cells transfected with NL-CBP^{BRD}, which was dose-dependent with respect to inobrodib-BODIPY treatment. Co-treatment with inobrodib caused an antagonistic loss of this BRET signal. The full-length CBP protein fusion (CBP^{FL}-NL) showed a substantially weaker BRET signal than NL-CBP^{BRD}, and it was decided an assay could not be established with CBP^{FL}-NL as the window between baseline and maximum BRET signal would be too narrow. The weaker signal was likely due to the larger distance between the NL energy donor (at the protein *C*-terminus) and the fluorophore acceptor bound to the bromodomain located at the centre of the protein domain architecture.

The NanoBRET target engagement assay was performed with NL-CBP^{BRD} and inobrodib-BODIPY at 0.5 µM and a titration of AcDC-**1**–**4** or inobrodib. Increased concentrations of AcDC-**1**–**4** were expected to outcompete inobrodib-BODIPY and an antagonistic loss of signal would be observed, as was demonstrated for the positive control (inobrodib) from assay optimisation. Pleasingly, all compounds tested in the assay gave the expected result, as demonstrated in **Figure 4.2** and IC_{50} values are summarised in **Table 4.1**.

Table 4.1: Summary of IC_{50} values from the NanoBRET target engagement assays. IC_{50} values describe the concentration of compound necessary to displace the inobrodib-BODIPY compound such that the BRET signal relative to the untreated DMSO vehicle control was reduced by 50%. Values represent the mean of two independent experiments. Error bars represent the standard error of mean.

Entry	Compound	IC_{50} (µM)
1	AcDC-1	0.241 ± 0.122
2	AcDC-2	0.0617 ± 0.0248
3	AcDC-3	0.109 ± 0.0150
4	AcDC-4	0.104 ± 0.0288
5	Inobrodib	0.0203 ± 0.00702

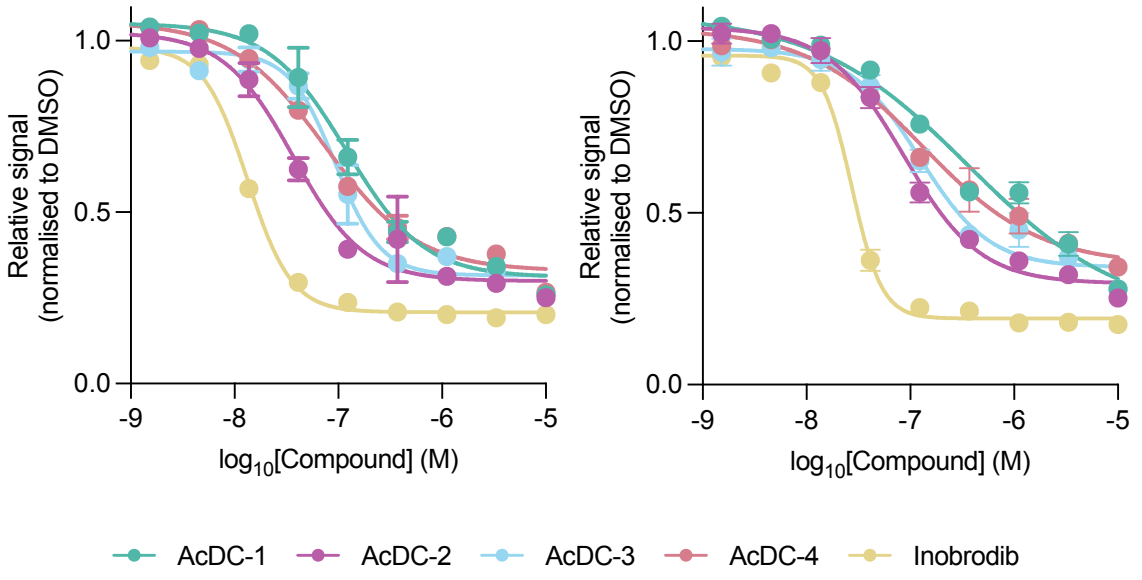


Figure 4.2: NanoBRET target engagement assay shows antagonistic loss of BRET signal upon titration of inobrodib and AcDC-**1**–**4**. Inobrodib shows the lowest IC_{50} value, followed by AcDC-**2** while AcDC-**1,3,4** have comparable values. Graphs show the results from two independent biological repeats. Data points represent the mean value from technical repeat measurements in triplicate and error bars represent the s.d.

The observed competition demonstrates that the compounds are cell permeable, engage with the NL-CBP^{BRD} and exhibit some degree of stability in the cellular *milieu intérieur*.

Inspection of the IC_{50} values shows that all the compounds tested outcompete inobrodib-BODIPY below the assay concentration of 0.5 μM, with inobrodib demonstrating the strongest competition. When comparing the competition activity within AcDC-**1**–**4**, it was interesting to note that a consistent trend was observed in the cooperativity ITC experiments in chapter 3: AcDC-**1** gave the largest IC_{50} and K_d values, and AcDC-**2** gave the lowest IC_{50} and K_d values (when in complex with Hsp90). If a ternary complex was not formed, we might expect AcDC-**4** to demonstrate the lowest IC_{50} value, as it was shown to have the lowest K_d with 6xHis-$p300^{BRD}$ in a binary binding model. However, the trend observed in the NanoBRET target engagement assay is only partly driven by binding affinity as compound permeability also contributes to the observed IC_{50}. While it was encouraging to see that AcDC-**2** gave the lowest IC_{50} value, it may be attributable to a higher permeability than AcDC-**3**–**4**, which would be expected due to the increased size and molecular weight of AcDC-**3**–**4**.

4.1.2 NanoBRET protein-protein interaction assay with CBP

To investigate whether AcDC-**1**–**4** were capable of forming ternary complexes with CBP/p300 and Hsp90 in cells, a NanoBRET protein-protein interaction (PPI) assay was developed.[202] In the NanoBRET PPI assay, cells are co-transfected with a HaloTag (HT) Hsp90 fusion construct in addition to the NL fusion construct. Cells are then treated with a small-molecule fluorescent tracer with a chloro-alkyl group which irreversibly binds to the HT with a high selectivity, making the Hsp90 fusion protein a suitable energy acceptor for BRET. When cells are co-treated with AcDC-**1**–**4**, we expect the NL and the fluorophore to come into proximity and a BRET signal to be observed (**Figure 4.3**).

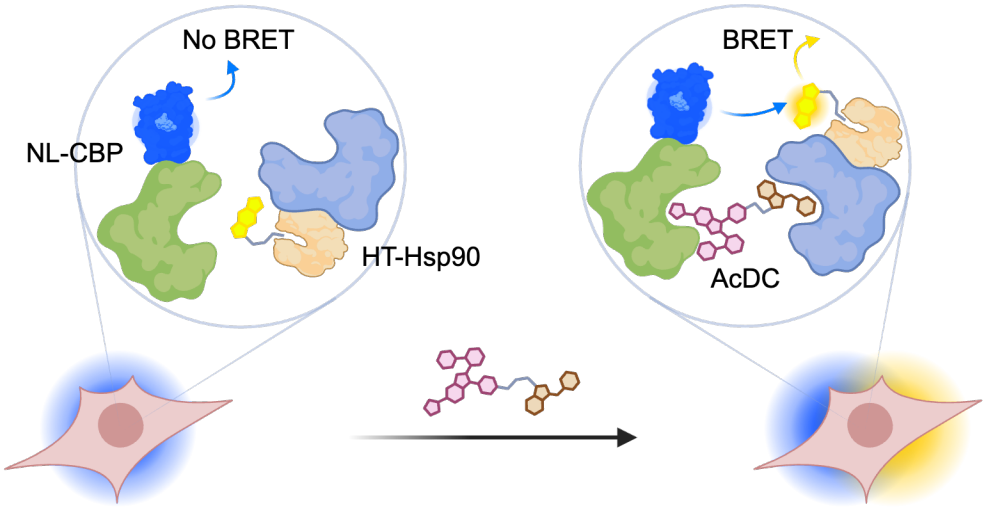


Figure 4.3: Principle of NanoBRET protein-protein interaction assay to show induced proximity between NL-CBP and HT-Hsp90 constructs in cells. HEK293 cells are transfected to transiently express NL-CBP and HT-Hsp90 fusion proteins comprising CBP^{BRD} or CBP^{FL} (green), NanoLuc luciferase (blue), Hsp90 (indigo) and HaloTag (straw). Cells are treated with a chloroalkyl fluorescent ligand that selectively binds to the HaloTag. Treatment with compounds that induce proximity between NL-CBP and HT-Hsp90 gives rise to an observed BRET signal (yellow). Created with BioRender.com

As a corollary of the Alpha based assays presented in chapter 3, an initial NanoBRET PPI assay employed co-transfection with NL-CBP^{BRD} and HT-Hsp90α. The Alpha based assay established that induced proximity could be measured between 6xHis-$p300^{BRD}$ and GST-$Hsp90α^{NTD}$ by conjugation of donor and acceptor species to the tags located at the *N*-terminus of the binding domains. By maintaining the NL and HT tags at the *N*-termini of the protein binding domains, the focus of the initial NanoBRET PPI assay was therefore exploring the consequences of measuring the induced proximity in a cellular context.

Here, it was expected that a similar trend as the Alpha based assay for ternary complex formation would be observed: treatment of cells with increasing concentrations of AcDC-**1**–**4** would initially lead to an increase in BRET signal, until a hook effect dominates, and signal would begin to decrease. As shown in **Figure 4.4**, we mostly observed a gain of signal for AcDC-**1**–**4** but not inobrodib which served as a negative control. The EC_{50} values for the increase of signal were determined using a constrained non-linear regression model where the bottom of the curve is set to 1.0. A slight hook effect was observed for AcDC-**1**–**2** at the highest concentrations, although this is less pronounced for AcDC-**3**–**4**. All compounds showed a weaker hook effect than the Alpha based assay, which could be

attributed to the different stoichiometries of the binding proteins between the two assays and attenuation of high intracellular compound concentrations due to limited permeability.

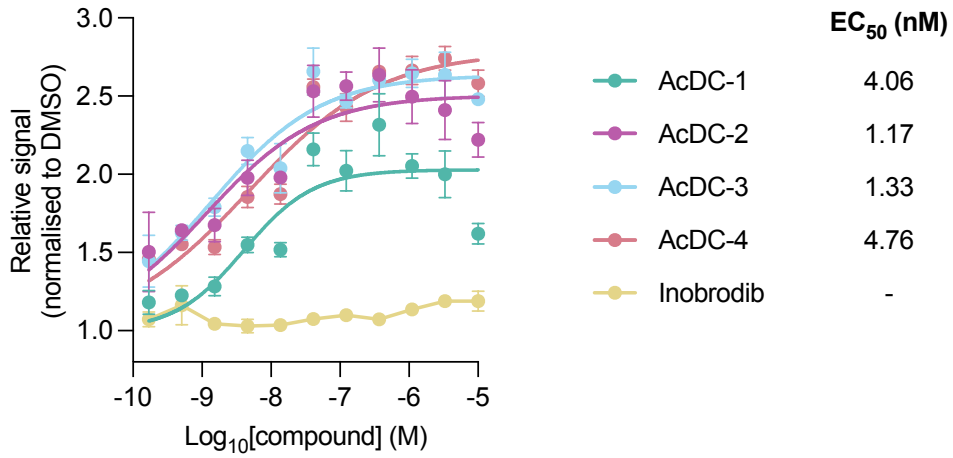


Figure 4.4: NanoBRET protein-protein interaction assay with NL-CBP^{BRD} and HT-Hsp90α shows gain of signal upon titration of AcDC-**1**–**4** but not inobrodib. EC_{50} values for the increase of signal were determined using a constrained non-linear regression model where the bottom of the curve is set to 1.0. Data points represent the mean value from technical repeat measurements in triplicate and error bars represent the s.d.

From the encouraging results of this preliminary experiment, the NanoBRET PPI assay was then performed with CBP^{FL}-NL to determine if the induced proximity is sustained with the full-length CBP protein. While a functional NanoBRET target engagement assay could not be developed for CBP^{FL}-NL, the PPI assay involved a different fluorophore positioned away from the bromodomain which may have sufficient proximity with the energy donor to allow an observable BRET signal once a ternary complex was formed.

Cells were co-transfected with CBP^{FL}-NL and HT-Hsp90α and treated with AcDC-**1**–**4** or inobrodib as a negative control and the BRET signal was measured. The results shown in **Figure 4.5A** were consistent with those obtained with NL-CBP^{BRD}: Treatment with increasing concentrations led to an increase in BRET signal; however, a more pronounced hook effect was observed with CBP^{FL}-NL. Fitting of the data by a non-linear regression model was not possible due to insufficient datapoints at the top and bottom of the signal range.

A repeat of the assay was performed with a higher concentration range to enhance the hook effect and to allow a bell-distribution model to be fitted (**Figure 4.5B**). However, an

unexpected result was observed at the highest concentrations (above 10 μM), with an apparent inflection and increase of BRET signal. This was attributed to assay interference consistent with the observation that the test compounds were insufficiently soluble in the assay medium at such concentrations.

To investigate potential differences in ternary complex formation between Hsp90α and Hsp90β with CBP, the NanoBRET PPI assay was performed with co-transfection of HT-Hsp90β and CBP^{FL}-NL, and treatment with AcDC-**1**–**4**, inobrodib or BIIB021. The results shown in **Figure 4.5C** demonstrate a similar trend to the experiments performed with Hsp90α, although a weaker hook effect was observed at the highest concentrations of AcDC-**1**–**4**. This could be attributed to different stoichiometries of HT-Hsp90 isoforms between experiments being dependent on the transfection efficiency of each plasmid construct.

Further attempts at the assay were made, but the assay exhibited significant variability. This inconsistency can be attributed to a week donor signal which adversely affected the measurement of the acceptor signal, thereby giving a large error in the result. Poor transfection efficiency of the NL and HT plasmid constructs was suspected of causing the variability between experimental repeats.

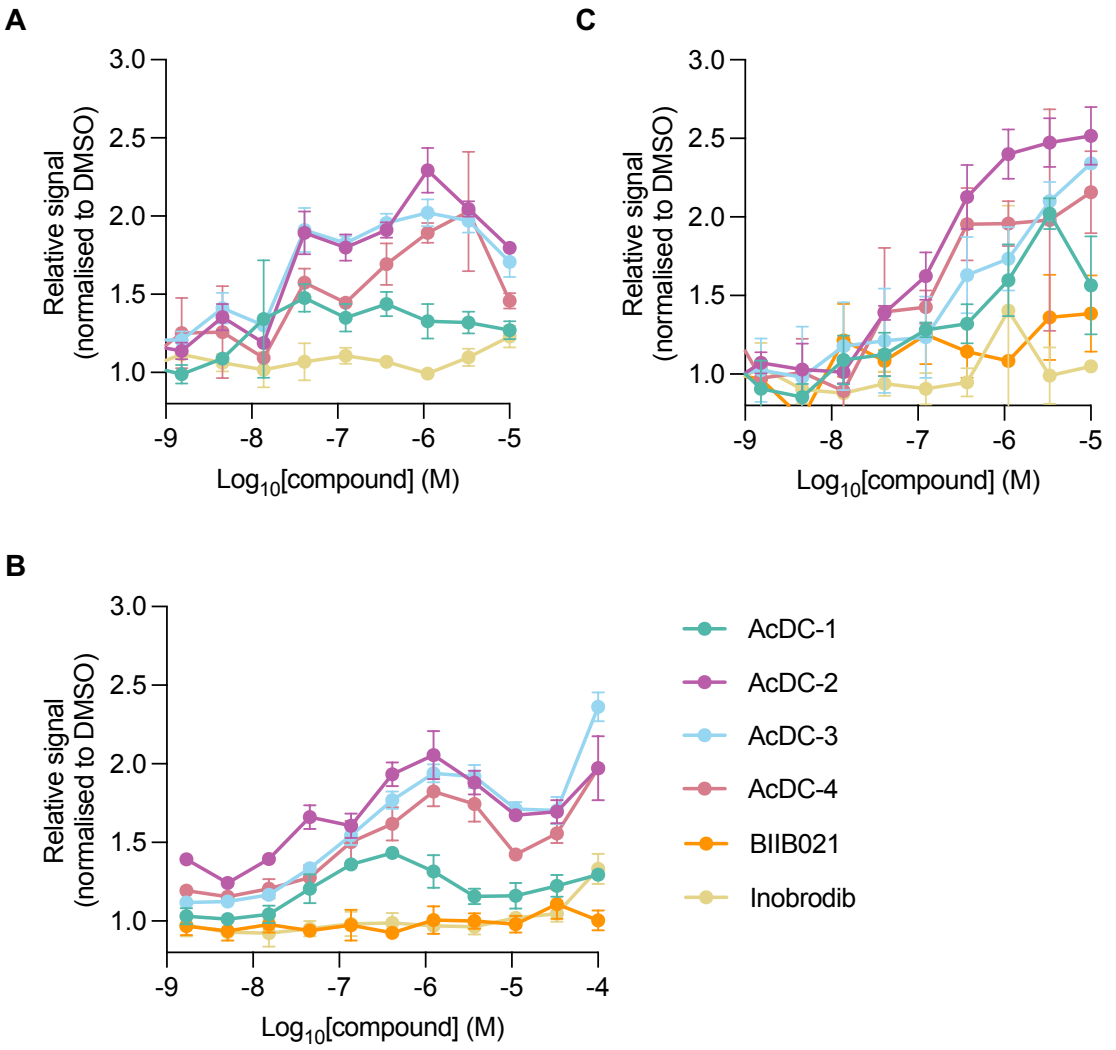


Figure 4.5: NanoBRET protein-protein interaction assay with NL-CBP^{FL} and HT-Hsp90 shows gain of signal upon titration of AcDC-**1**–**4** but not inobrodib or BIIB021. All graphs have been plotted on the same axis to allow comparison and represent independent experimental repeats. **A** and **B** show the interaction between HT-Hsp90α and NL-CBP^{FL} where **B** has been performed at a higher concentration range. **C** shows the interaction between HT-Hsp90β and NL-CBP^{FL}. Data points represent the mean value from technical repeat measurements in triplicate and error bars represent the s.d.

4.1.3 NanoBRET protein-protein interaction assay with p300

In the previous chapter, it was shown by ITC that the CBP and p300 bromodomains had similar binding affinities for AcDC-**1**–**4** in complex with the Hsp90α^{NTD} domain. This was rationalised by the high sequence homology of the two protein constructs. However, the full-length proteins have less sequence homology than the bromodomains alone, particularly in the region adjacent to the bromodomain, posing the question of whether structural differences in the full-length proteins could alter the ability of p300 and CBP to

form a ternary complex with Hsp90. To investigate this possibility, we attempted to use the NanoBRET PPI assay with full length p300 and treatment of AcDC-**2** to allow a comparison. While NL containing plasmid constructs for CBP were commercially available, molecular cloning was required to create the equivalent constructs for p300. Two plasmid constructs were generated and annotated maps are provided in **Appendix B.**

The first (p300^{FL}-NL) comprised the EP300 gene with a *C*-terminal NL fusion, which served as an equivalent to the CBP^{FL}-NL construct and enabled a direct comparison of the two proteins. The second (NL-p300^{FL}) featured an *N*-terminal NL fusion to the EP300 gene, with the intention of examining whether changing the position of the NL would result in an improved BRET signal. The large length of the EP300 gene (7.2 kB) prohibited the use of *de novo* gene synthesis, so a plasmid construct containing the EP300 gene (1245 pCMVb EP300) was obtained and used as a template for molecule cloning methods, which are outlined in **Appdenix Figure A.2**

To enable a comparison between CBP and p300, and their respective abilities to form ternary complex with Hsp90α and Hsp90β, four different co-transfectants were prepared for analysis in the same experiment, each expressing one of the various combinations of CBP^{FL}-NL or p300^{FL}-NL with HT-Hsp90α or HT-Hsp90β. A titration of AcDC-**2** was used in all combinations. The co-transfection with CBP^{FL}-NL and HT-Hsp90α was to serve as a positive control based on previously obtained results. The data from two independent experiments is shown in **Figure 4.6**; however, no meaningful trend was observed as the positive control failed to show the expected result. The high degree of variability in the data was attributed to the previously mentioned issues encountered with poor donor signal impacting the measurement of BRET.

The inconsistency between experimental repeats of the NanoBRET PPI interaction assay hindered the ability to obtain reliable and reproducible results, thereby impacting the overall efficacy of the assay. We focused efforts on exploring whether the induced proximity could be observed in an endogenous context, using an orthogonal technique to validate the results.

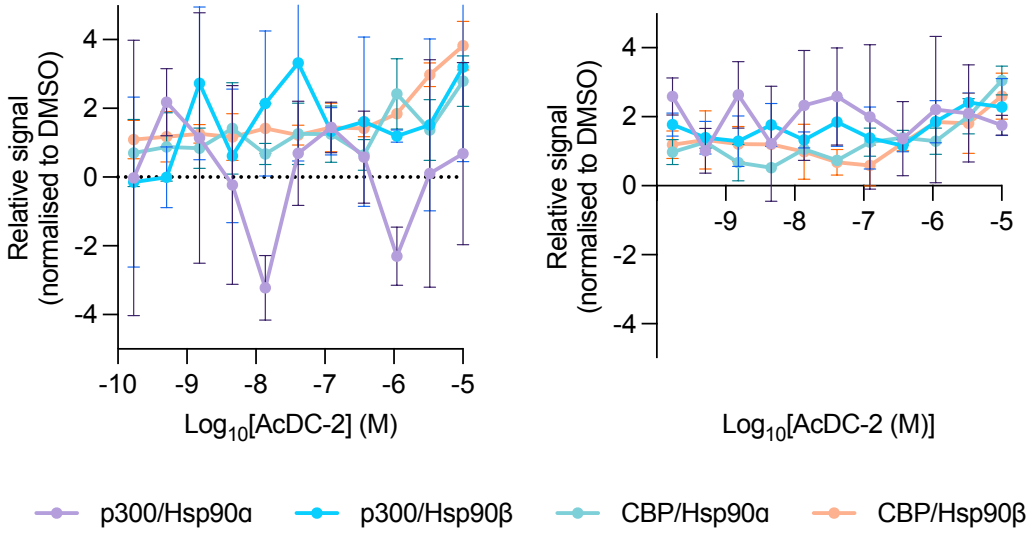


Figure 4.6: NanoBRET protein-protein interaction assay to compare the AcDC-**2** induced interaction between CBP^{FL}-NL and $p300^{FL}$-NL with HT-Hsp90α and HT-Hsp90β could not produce a significant trend due to technical issues from weak signal. Graphs show the results from two independent biological repeats. Data points represent the mean value from technical repeat measurements in triplicate and error bars represent the s.d.

4.2 Co-immunoprecipitation to measure complex formation in an endogenous system

Towards our goal of determining whether AcDCs were capable of inducing proximity between CBP/p300 and Hsp90 in a cellular context, a co-immunoprecipitation (co-IP) experiment was developed. In this experiment, cells were treated with AcDC-**1**–**4**, following which they were lysed in a mild, non-denaturing lysis buffer to maintain intermolecular interactions between proteins. The protein of interest (Hsp90) was enriched from the lysate mixture using an antibody immobilised on a bead to enable solid-phase extraction. Hsp90 acted as a bait for interacting proteins that form a complex which were also enriched, these proteins were then detected by immunoblotting. The enrichment process involved repeated washing of the beads, meaning that only proteins forming a stable complex with the bait were co-immunoprecipitated, while proteins forming weaker interactions were washed away. Comparing co-IP with the NanoBRET PPI assay, the latter determines whether the exogenous protein constructs are in proximity in live-cells at the point of measurement; however, the result is not indicative of whether the proteins are in a stable complex as the induced proximity could be transient in nature.

Practically, the co-IP procedure was less amenable to miniaturisation than the NanoBRET assay and could not be performed in a high-throughput format, thereby limiting the number of test conditions explored. Accordingly, the results of the NanoBRET PPI assay informed the decision to use a single treatment concentration in the co-IP experiments.

Wildtype (wt) HEK293 cells were treated with AcDC-**1**–**4** at 0.5 μM for 6 h before immunoprecipitation of Hsp90 using an antibody reported as non-specific to its isoforms (Hsp90α/β, Santa Cruz, sc-13119), and CBP and p300 were probed by immunoblotting. The Hsp90 antibody was chosen as its epitope is mapped to the *C*-terminal tail of Hsp90, to prevent occlusion of the interaction between Hsp90 and CBP/p300 which is occurring at the *N*-terminal domain. As shown in **Figure 4.7**, we observed successful co-IP of CBP with treatment of AcDC-**2** and this result was reproduced in three biological repeats of the experiment.

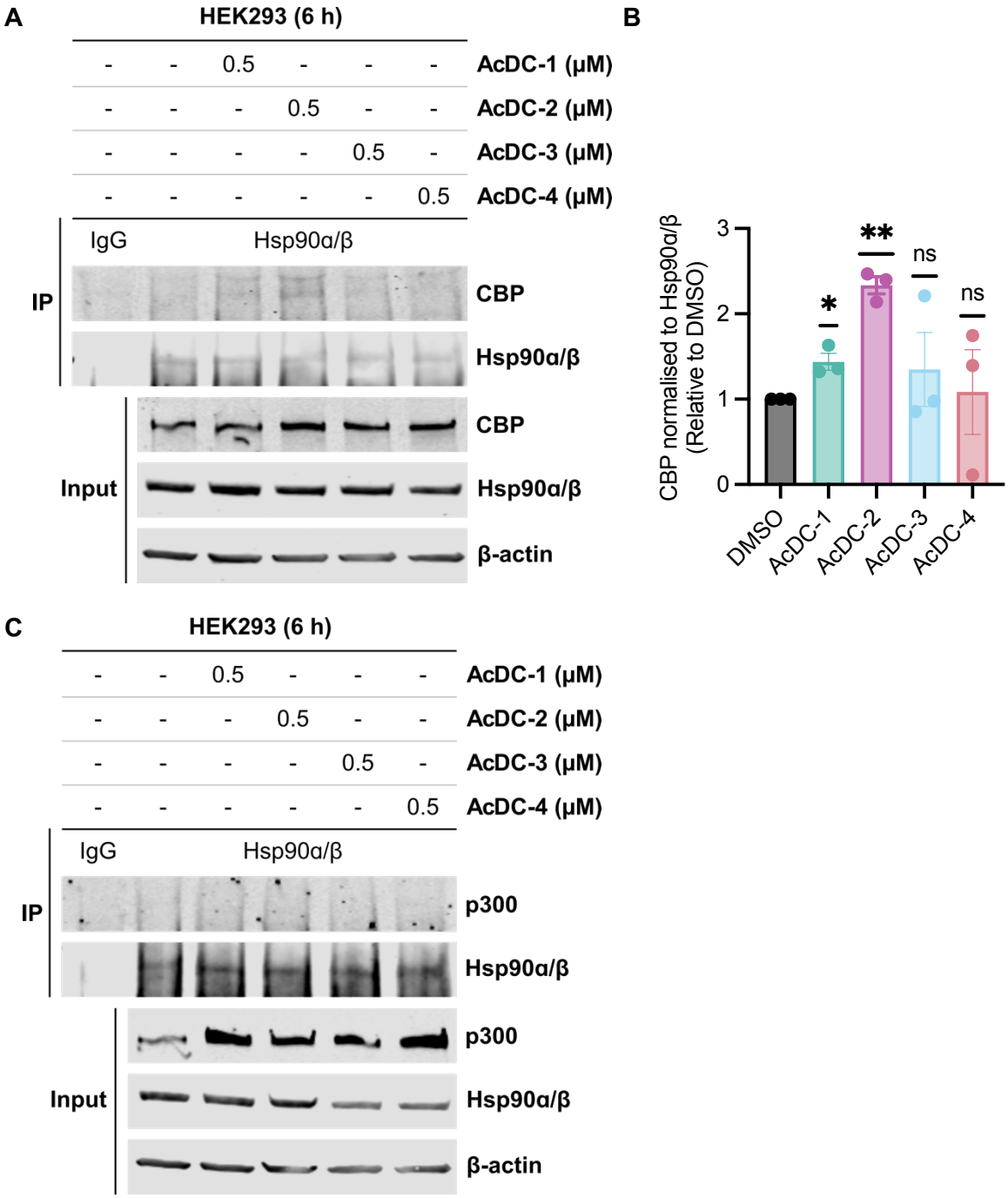


Figure 4.7: Co-immunoprecipitation of Hsp90α/β and immunoblotting for CBP and p300 shows AcDC-**2** induces a stable interaction between Hsp90 and CBP but not p300. HEK293 cells were treated with AcDC-**1**–**4** at 0.5 μM for 6 h or an equal volume of DMSO was added to cells not treated with compounds, as a vehicle control. Samples labelled with IgG show the fraction of DMSO-treated cells that were immunoprecipitated using a non-specific antibody with the same isotype as α-Hsp90α/β. Samples labelled with input show analysis of an aliquot the lysate used in the immunoprecipitation procedure. Images are representative of three biological repeats. **A** Immunoblot analysis of co-immunoprecipitation of CBP and Hsp90. **B** Quantification of the immunoblot signal of CBP co-immunoprecipitated with Hsp90. Error bars represent the s.e.m. and statistical significance was determined using an unpaired two-tailed student's *t*-test against DMSO. *$p < 0.05$; **$p < 0.01$. **C** Immunoblot analysis of co-immunoprecipitation of p300 and Hsp90.

Co-IP of p300 was not detected, but this may have been due the amount of co-immunoprecipitated protein being lower than the limit of detection in immunoblotting, rather than no interaction occurring. Due to the two paralogues having a similar molecular weight and migration in SDS-PAGE, samples used in Western Blotting were analysed in duplicate and transferred onto two separate membranes probed either for CBP or for p300. Comparison of the signal in the input controls showed a stronger signal for CBP than p300 despite performing concerted electro-transfer, handling of membranes and imaging. Expression of the two paralogues in HEK293 cells is reported to be equivalent,[204] suggesting a difference in the detection affinity of the antibodies used in this study. At the point this study was incepted, no treatment was known to induce the interaction between p300 and Hsp90 in wt HEK293 cells and without this positive control for the co-IP assay, it was not possible to conclude whether the interaction between p300 and Hsp90 was *not* increased by AcDC-**2** treatment.

4.3 Biological consequences of induced proximity between CBP/p300 and Hsp90

4.3.1 AcDC-1–4 do not induce target protein degradation

Confident that AcDC-**1**–**4** engaged with the protein targets in a cellular system, and that AcDC-**2** induced a stable interaction between CBP and Hsp90, our attention turned to exploring the phenotypic effect of this chemically induced non-endogenous interaction.

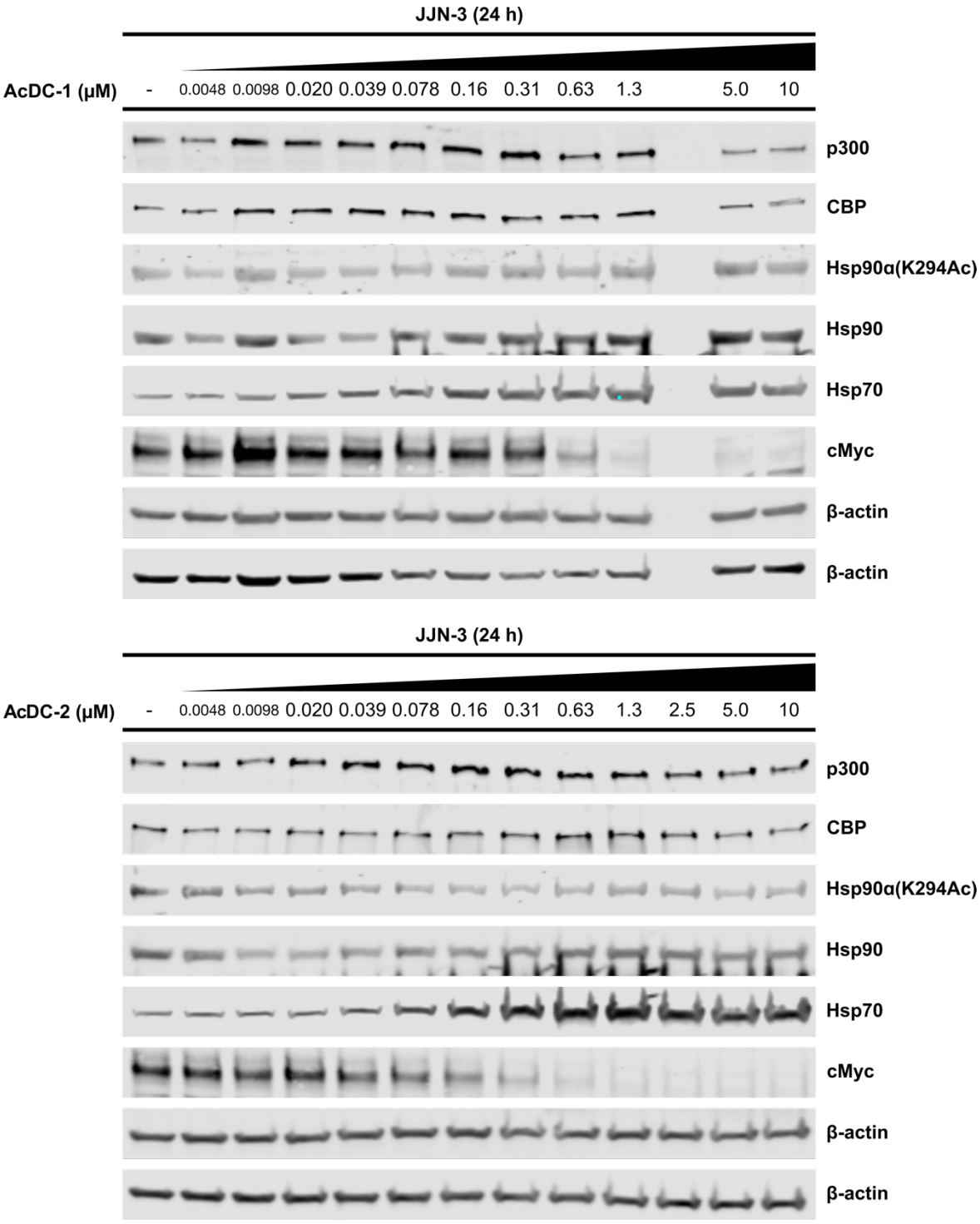
Since the inception of this thesis, work by Li *et al.* suggested that chemically induced proximity between Hsp90 and CDK4/6 by heterobifunctional molecules termed HEMTACs (heat shock protein 90 mediated targeting chimeras) can decrease CDK4/6 levels by a targeted protein degradation mechanism.[205] While Hsp90 is not an E3 ligase, it endogenously interacts with multiple E3 ligases, assisting in the degradation of misfolded proteins.[206, 207] However, inhibition of the Hsp90 *N*-terminal domain prevents its molecular chaperone function and causes the degradation of misfolded client proteins such as CDK4/6.[110, 208] HEMTACs intrinsically inhibit the Hsp90 *N*-terminal domain as the BIIB021 scaffold is incorporated as a structural motif to recruit Hsp90. This thesis condones the term *targeted* protein degradation when considering the effect of HEMTACs, however we deemed it necessary to explore whether AcDC-**1**–**4** would cause protein degradation of CBP/p300, given that the compounds share the BIIB021 scaffold within their structure.

If one of AcDC-**1**–**4** behaved like a HEMTAC, we expected to see CBP/p300 levels decrease to below that of the vehicle control (DMSO) upon compound treatment and potentially return to this baseline level at the highest treatment concentrations, if there was a hook effect. Dose-dependent treatment of JJN-3 cells over 24 h was performed and the levels of CBP/p300 were analysed by western blotting (**Figure 4.8**). Change in p300 or CBP levels upon compound treatment was not observed and quantification of this over three independent experiments revealed no significant trends (**Figure 4.9**).

To ensure that the compounds demonstrated the effects of inhibition, levels of Hsp70, Hsp90 and c-Myc were also measured as respective downstream markers of Hsp90 and CBP/p300 bromodomain inhibition.[110, 209, 210] We observed an increase in Hsp70 and Hsp90

levels upon treatment with increasing compound concentrations, consistent with the initiation of the heat shock response due to inhibition of Hsp90. We also observed a decrease in cMyc with increasing compound treatment concentration, which may be indicative of CBP/p300 bromodomain inhibition. However, this conclusion is caveated with the possibility that the phenotype could also be driven by inhibition of Hsp90, as c-Myc has been reported as a client of Hsp90,[211] or the decrease could be a result of BRD4 inhibition, which is known off-target of the inobrodib pharmacophore at higher compound concentrations.

As a corollary of AcDC-**1**–**4** induced proximity between CBP/p300 and Hsp90, lysine acetylation levels on Hsp90 were expected to increase, although the extent or site of this modification was yet to be established. We were able to measure levels at K294 on Hsp90α with a commercially available antibody and observed no significant change upon dose-dependent treatment of AcDC-**1**–**4** over 24 h. This analysis was complicated by the increasing level of total Hsp90, the level of Hsp90α(K294Ac) may have appeared to increase relative to the loading control (β-actin), but this was controlled in quantification of the modification by measuring the normalised signal relative to total Hsp90.


JJN-3 (24 h)
AcDC-1 (μM)
-
0.0048
0.0098
0.020
0.039
0.078
0.16
0.31
0.63
1.3
5.0
10
p300
CBP
Hsp90α(K294Ac)
Hsp90
Hsp70
cMyc
β-actin
β-actin
JJN-3 (24 h)
AcDC-2 (μM)
-
0.0048
0.0098
0.020
0.039
0.078
0.16
0.31
0.63
1.3
2.5
5.0
10
p300
CBP
Hsp90α(K294Ac)
Hsp90
Hsp70
cMyc
β-actin
β-actin

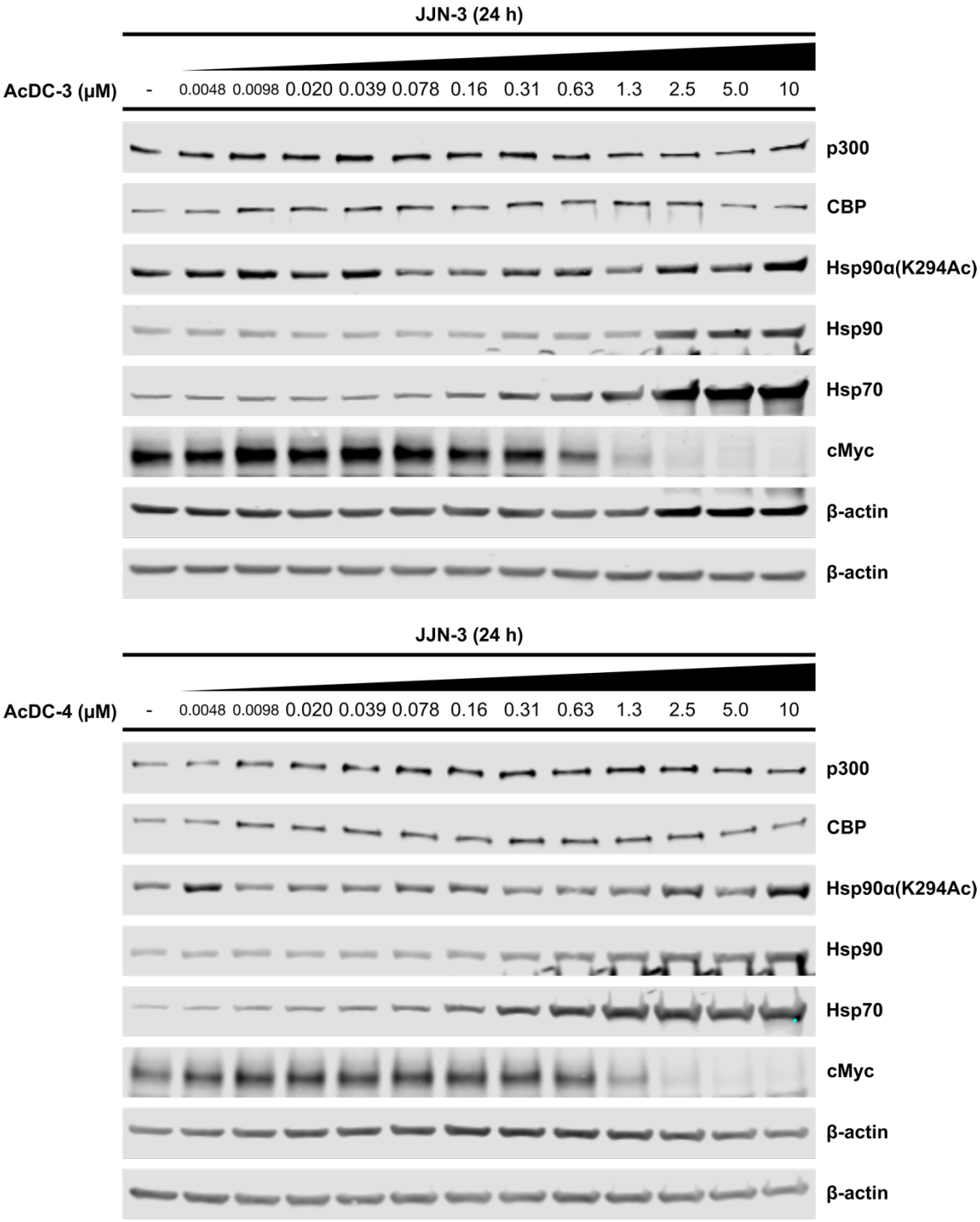


Figure 4.8: Western blots show treatment of JJN-3 cells with AcDC-**1**–**4** after 24 h did not cause dose-dependent degradation of p300 and CBP; however decreased cMyc, and increased Hsp70 and Hsp90. DMSO was added to cells not treated with AcDC-**1**–**4**, as a vehicle control. β-actin (top row) is shown as a loading control for p300, Hsp90α(K294Ac), Hsp90 and Hsp70; β-actin (bottom row) is shown as loading control for CBP and cMyc. Images are representative of three biological repeats.

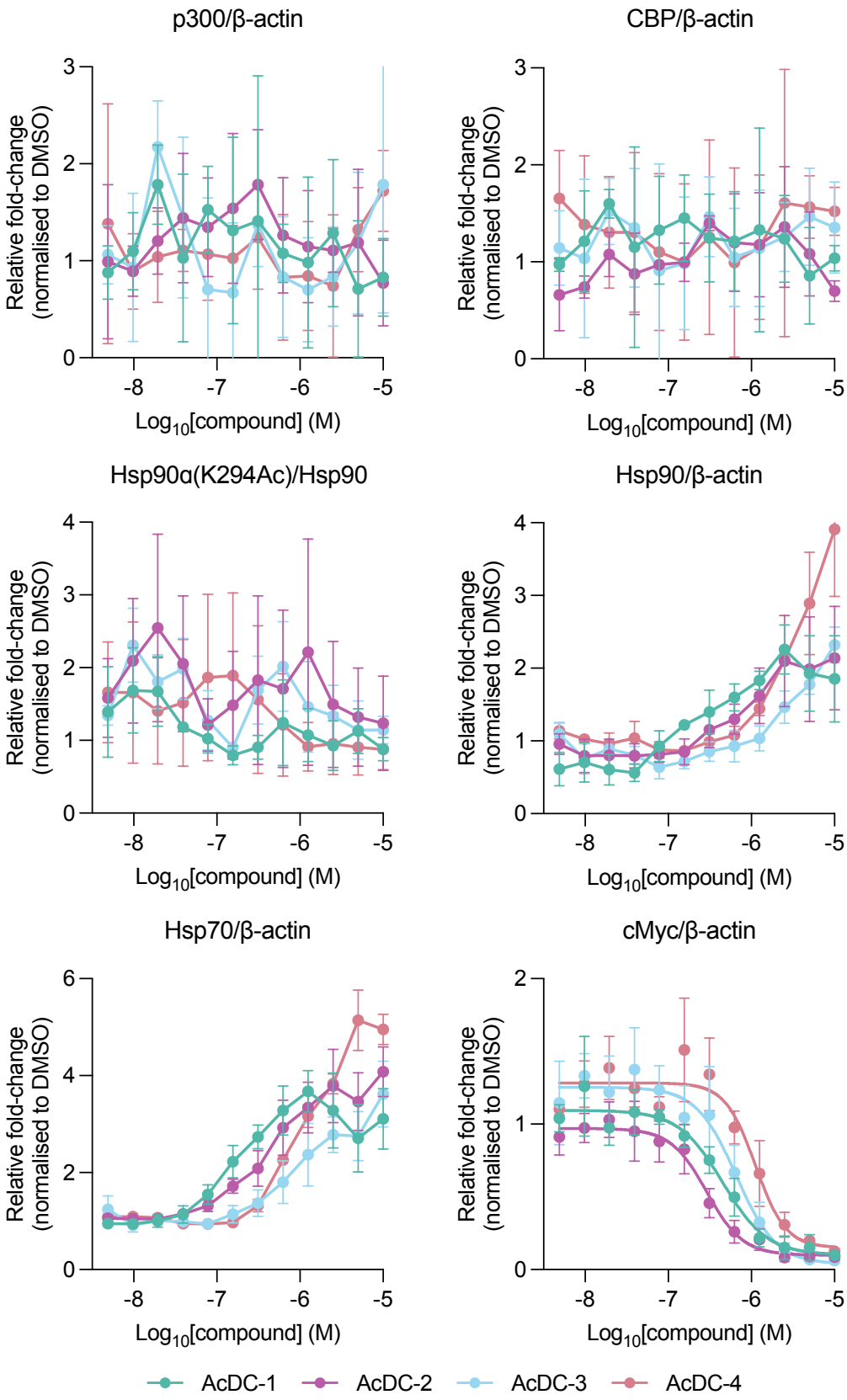


Figure 4.9: Western blot quantification for images shown in **Figure 4.8** for each detected protein. Measured signals are corrected for loading by normalising against the β-actin signal, and relative fold change compared to the vehicle control (DMSO) is calculated. Values represent the mean of three biological repeats. Error bars represent the s.e.m.

4.3.2 AcDC-1–4 reduced JJN-3 cell viability

In the previously presented experiment, it was anecdotally observed that AcDC-**1**–**4** treatment impacted the viability of JJN-3 cells, so we sought to measure this more thoroughly by means of a MTT assay. We postulated that if an AcDC were operating by an event-driven pharmacology, rather than by inhibition alone, then this might become apparent in other phenotypic effects such as cellular viability. We expected to see AcDC treatment have a more pronounced effect than inhibition with the parent inhibitors (BIIB021 or inobrodib), or the potency to far surpass that of the inhibitors, which would highlight the transiently induced proximity between CBP/p300 and Hsp90 as causing a significant biological consequence distinct from simply binding to the respective proteins. As evidenced in **Figure 4.10**, treatment with all compounds over 24 h reduced viability of JJN-3 cells. A non-linear regression model was fitted to all treatments and the calculated EC_{50} values are summarised in **Table 4.2** except for AcDC-**2** where a lower plateau could not be established at the highest concentration used in this assay.

BIIB021 presented a degree of cytotoxicity which is consistent with its reported antiproliferative activity in other cancer cell lines. The CC_{50} value obtained in JJN-3 cells was also comparable to the reported value for MCF-7 (CC_{50} = 0.31 μM).[110] Additionally, treatment with inobrodib appeared to have a less pronounced impact on cell viability than BIIB021, with a lower CC_{50} value of 0.018 μM, which is consistent with previously reported values for other hematologic cell lines.[209] The cytotoxicity profile of AcDC-**1,3** and **4** appeared to be comparable to that of BIIB021, albeit at increased CC_{50} values, suggesting that the BIIB021 pharmacophore in AcDCs is driving the observed phenotype due to occupancy-driven inhibition of Hsp90. However, while AcDC-**2** appeared to decrease the cell viability of JJN-3 cells beyond that of BIIB021 or inobrodib at the highest concentrations tested, the effect was small and could not be shown to be statistically significant. From this, we concluded that the AcDC-induced proximity between CBP/p300 and Hsp90 likely does not illicit a distinct biological response in JJN-3 cells that is distinct from the proteins' loss of function due to inhibition.

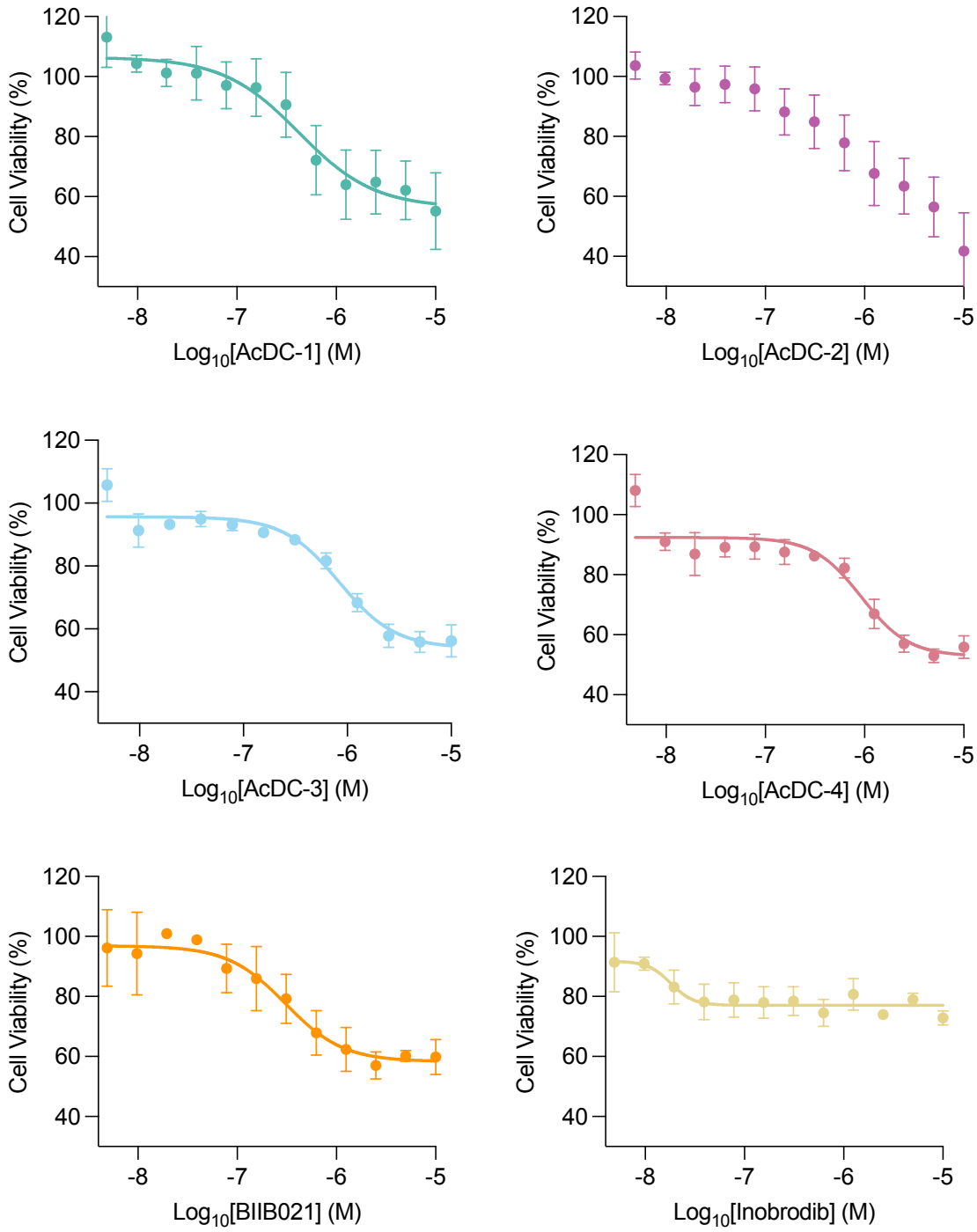


Figure 4.10: MTT assays show AcDC-**1**–**4** and BIIB021 significantly reduced viability of JJN-3 cells after treatment for 24 h, while inobrodib had a less pronounced effect. Cell viability is normalised against the vehicle control (DMSO) = 100%. Curves show the fitting of a non-linear regression model (variable slope). Data points represent the mean value from three independent biological experiments, each performed in triplicate, error bars represent s.e.m.

Table 4.2 Summary of CC_{50} values from the combined data produced by three independent MTT assays. CC_{50} values describe the concentration of compound necessary to reduce cell viability to 50% that of the maximum effect.

Entry	Compound	CC_{50} (μM)
1	AcDC-1	0.42
2	AcDC-2	N/A
3	AcDC-3	0.84
4	AcDC-4	0.93
5	BIIB021	0.31
6	Inobrodib	0.018

4.3.3 Apparent AcDC-2 induced increase in Hsp90α(K294Ac)

Although we had not observed a dose-dependent AcDC induced change in Hsp90α(K294Ac) at 24 h, we considered that lysine acetylation is a dynamically regulated PTM, and cellular homeostasis may have recovered the change over the chosen time-course. This idea was further supported by work published since the inception of this thesis by the Parker and Jin laboratories, where heterobifunctional induced proximity between CBP/p300 and $FKBP12^{F36V}$ fusion constructs, or p53 showed increase acetylation on those target proteins over shorter time-courses (less than 8 h), but the phenotype was reduced beyond this.[155, 156]

We therefore studied the effect of the time-depended treatment of AcDC-**1**–**4** at a fixed concentration of 0.5 μM. This concentration was chosen based on the previously presented experiments with a 24 h time-course, so that it was sufficient to engage with the proteins and illicit an inhibitory effect, but not such that a hook effect dominates. The results shown in **Figure 4.11** demonstrate that treatment with AcDC-**2** caused an apparent increase in Hsp90α(K294Ac) at 6 h; however, this effect was lost over longer treatment time-courses where an increase in the underlying level of total Hsp90 is observed. Co-treatment with the inhibitors BIIB021 and inobrodib was included in this experiment to ensure the observed effects were not a consequence of inhibition alone. At 6 h we did not observe the increase in Hsp90α(K294Ac) comparable to treatment with AcDC-**2**.

Quantification of Hsp90α(K294Ac) normalised to total Hsp90 levels also confirms that a significant increase occurred upon treatment of AcDC-**2** over 6 h (**Figure 4.12**).

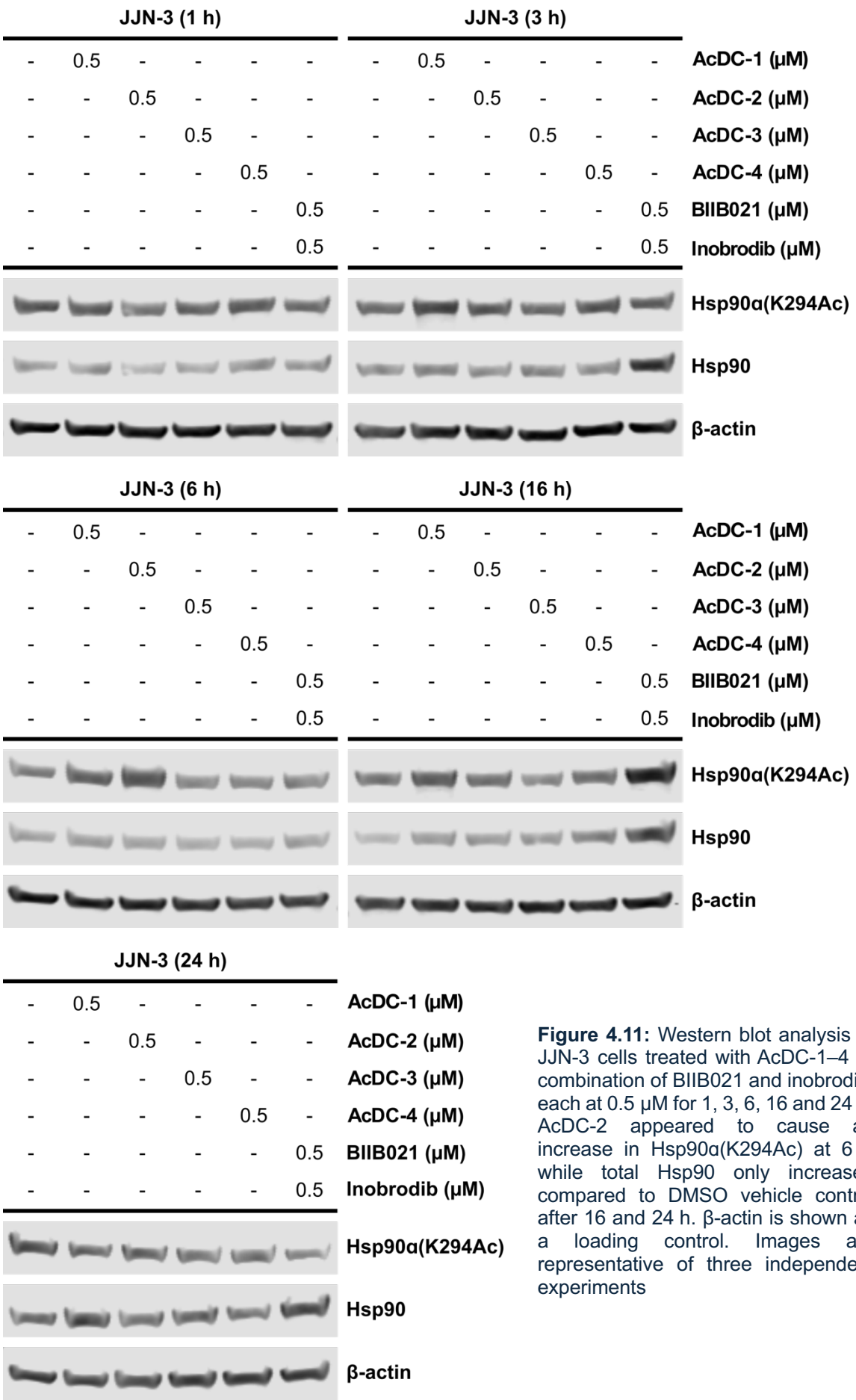


Figure 4.11: Western blot analysis of JJN-3 cells treated with AcDC-1–4 or combination of BIIB021 and inobrodib, each at 0.5 μM for 1, 3, 6, 16 and 24 h. AcDC-2 appeared to cause an increase in Hsp90α(K294Ac) at 6 h, while total Hsp90 only increased compared to DMSO vehicle control after 16 and 24 h. β-actin is shown as a loading control. Images are representative of three independent experiments

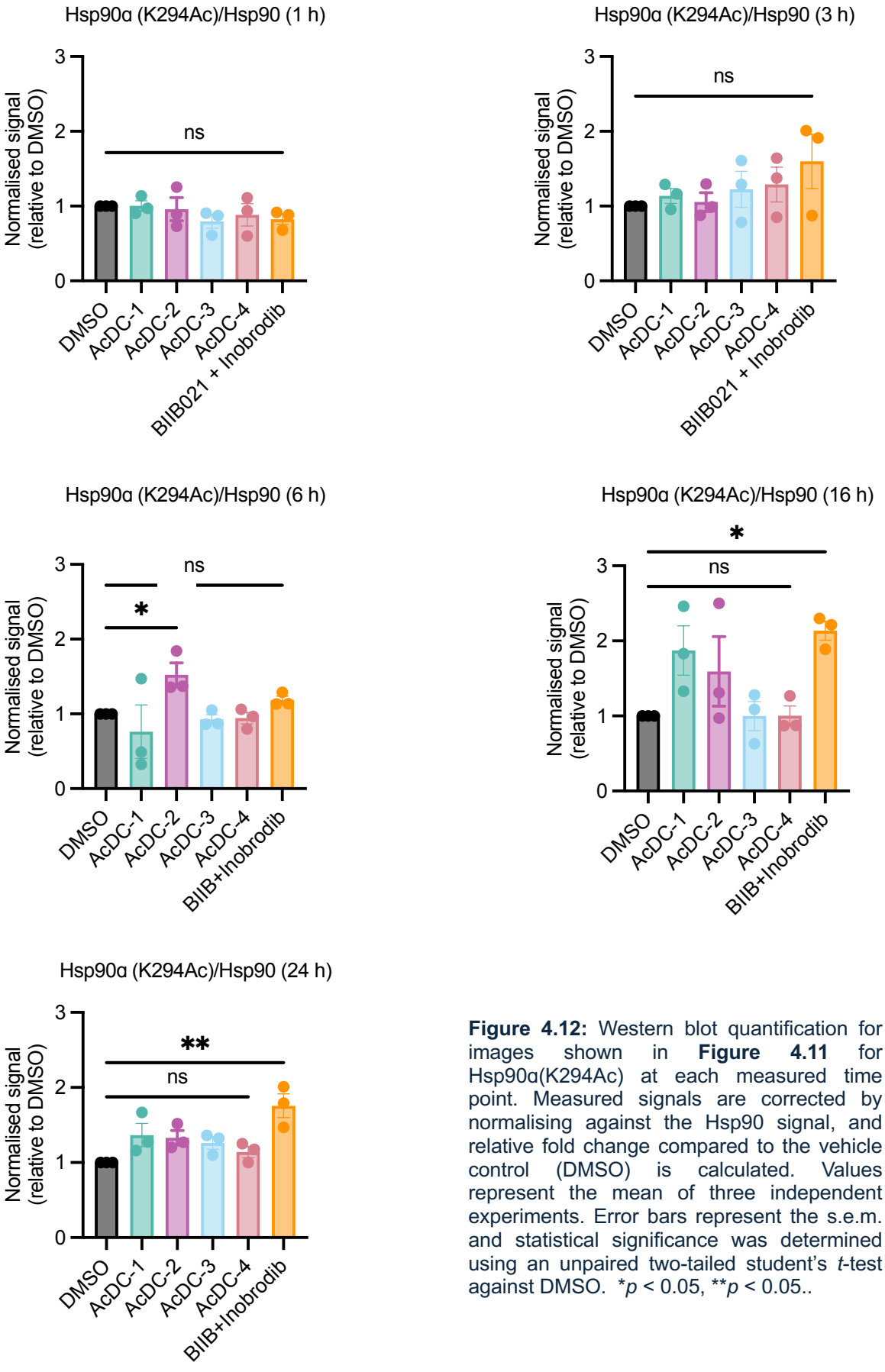


Figure 4.12: Western blot quantification for images shown in **Figure 4.11** for Hsp90α(K294Ac) at each measured time point. Measured signals are corrected by normalising against the Hsp90 signal, and relative fold change compared to the vehicle control (DMSO) is calculated. Values represent the mean of three independent experiments. Error bars represent the s.e.m. and statistical significance was determined using an unpaired two-tailed student's *t*-test against DMSO. $*p < 0.05$, $**p < 0.05$..

4.3.4 Further investigation into AcDC-2 induced increase in Hsp90α(K294Ac) by dose-dependent treatment at 6 h

While the results of the time-course experiment were encouraging, it was surprising that AcDC-**2** induced an increase in Hsp90α(K294Ac) only at 6 h and that there did not appear to be an effect at 3 or 16 h. To probe this further, dose-dependency of AcDC-**2** was restudied using the shorter time point of 6 h. The results in **Figure 4.13** show no apparent change in Hsp90α(K294Ac) with respect to dose-dependent treatment with AcDC-**2** and quantification of this over three independent biological repeats showed no significant difference compared to the vehicle control.

We also inspected levels of HDAC6, the reported KDAC that acts on Hsp90,[47] to ensure that its levels remained unchanged in response to treatment with AcDC-**2**. We thought it possible that HDAC6 levels could change in response to AcDC-**2** treatment as it is also an identified client protein of Hsp90, so inhibition of Hsp90 could create a positive feedback system that eventually results in its hyperacetylation.[212] Conversely, we also envisaged a situation where an increase in HDAC6 levels would counteract AcDC activity in order to maintain homeostasis. However, we found HDAC6 levels broadly remained constant over the time-course, and assuming its activity remained constant, we could rule-out the described feedback systems as driving acetylation on Hsp90.

CDK4 levels were also measured. As an established client of Hsp90, the protein also has a short half-life and is rapidly degraded following inhibition of Hsp90 chaperone activity.[110] We expected to see this decrease in response to AcDC-**2** treatment due to the compound's inhibitory effects, but also hypothesised that acetylation occurring at another site on Hsp90 could control the interaction between Hsp90 and E3 ligases. Previous mutagenesis studies have described that Hsp90 K/Q mutants that mimic KAc have reduced interaction with CHIP,[124] and thus acetylation could disrupt the pathway by which misfolded client proteins are degraded. However, we saw a significant decrease in CDK4 at concentrations above 0.50 μM. This is consistent with the occupancy-driven inhibition of Hsp90.

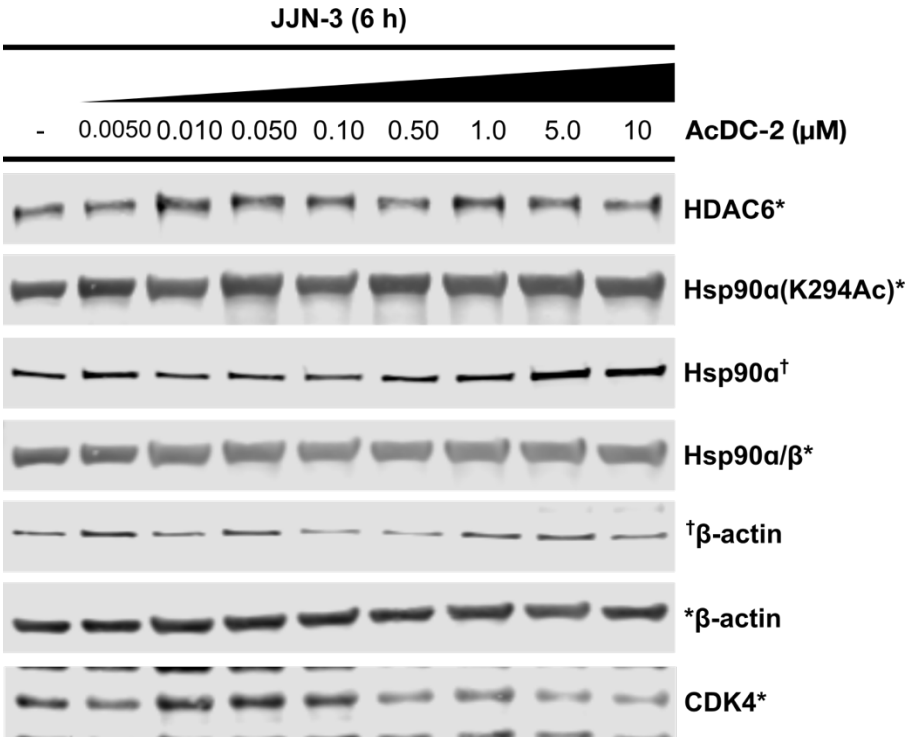


Figure 4.13: Western blots show treatment of JJN-3 cells with AcDC-**2** after 6 h did not cause dose-dependent change in Hsp90α(K294Ac), Hsp90α/β, or HDAC6; however decreased CDK4 at high concentrations. DMSO was added to cells not treated with AcDC-**2**, as a vehicle control. †β-actin (top row) is shown as a loading control for Hsp90α; *β-actin (bottom row) is shown as loading control for HDAC6, Hsp90α(K294Ac), Hsp90α/β, CDK4. Images are representative of three independent experiments.

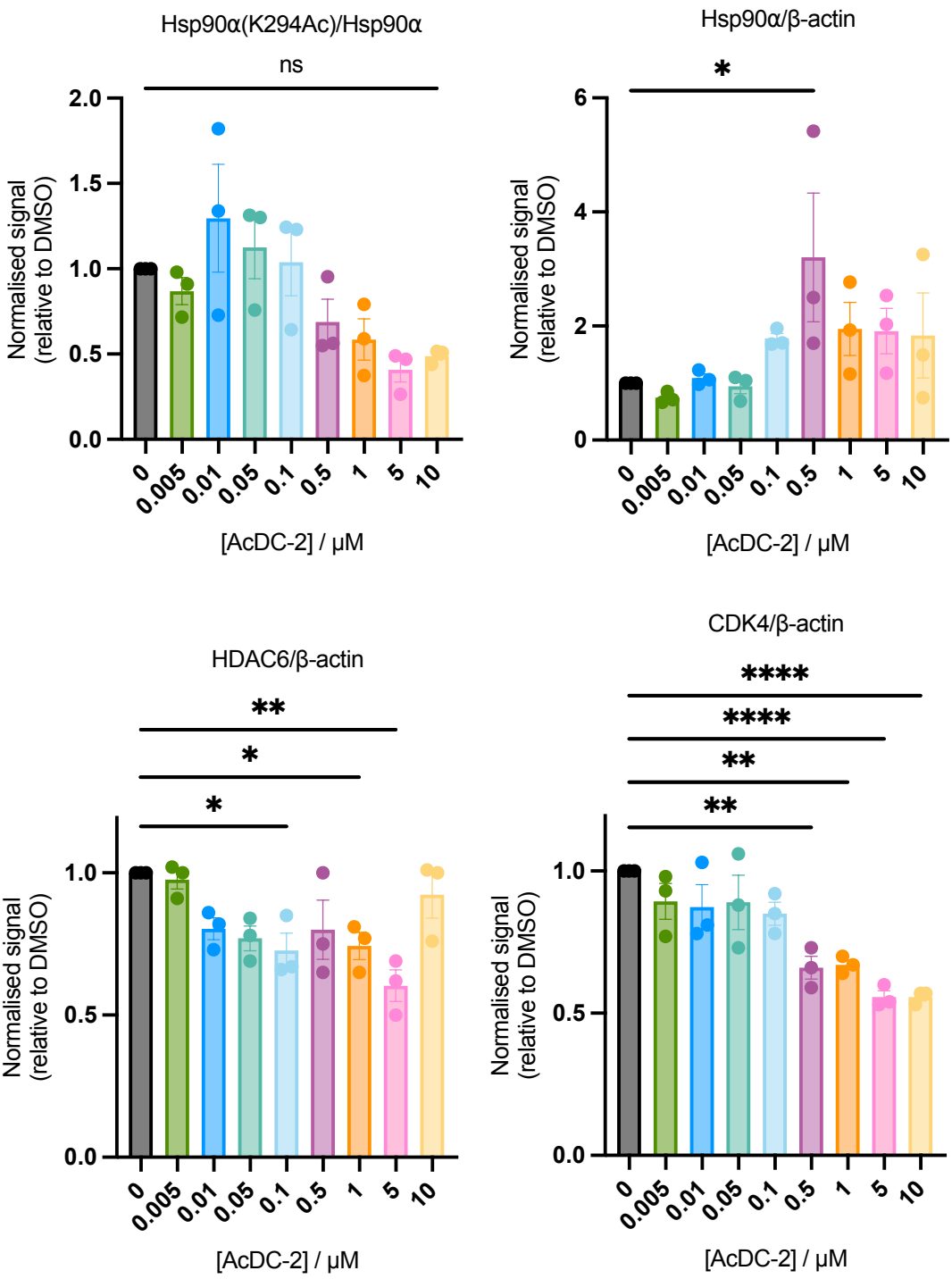


Figure 4.14: Western blot quantification for blots presented in **Figure 4.13**. Measured signals are corrected for loading by normalising against the total protein level or β-actin, and relative fold change compared to the vehicle control (DMSO) is calculated. Values represent the mean of three biological repeats. Error bars represent the s.e.m. and statistical significance was determined using an unpaired two-tailed student's *t*-test against DMSO. **p* < 0.05, ***p* < 0.01, *****p* < 0.0001.

4.3.5 Competition between AcDC-2 with inobrodib and BIIB021, or inhibition with A-485 shows no effect on Hsp90α(K294Ac)

A second experiment to probe whether the previously observed changes in Hsp90α(K294Ac) were induced by treatment with AcDC-**2** was envisaged, wherein we expected to rescue the phenotype by co-treatment with either the CBP/p300 KAT inhibitor, A-485,[213] or competition with the inhibitors BIIB021 or inobrodib. JJN-3 cells were treated with either a combination of the inhibitors BIIB021 and inobrodib, or A-485, without co-treatment with AcDC-**2** to ensure that the observed effects are not due to combination effects or inhibition. Treatment with panobinostat was also included as a positive control. As the drug is a broad-spectrum KDAC inhibitor, we expected to see an increase in global KAc, including on Hsp90,[120] the extent of which would be dependent on the activity of the endogenous KAT that writes this modification onto Hsp90.

As shown in **Figure 4.15**, we failed to see a significant change in Hsp90α(K294Ac) in all the conditions employed in this experiment. These surprising results led us to question the stability of compound stocks, but analysis of these by HPLC showed no apparent degradation or impurities, and consistent results were obtained in an independent experimental repeat employing freshly prepared compound stock solutions.

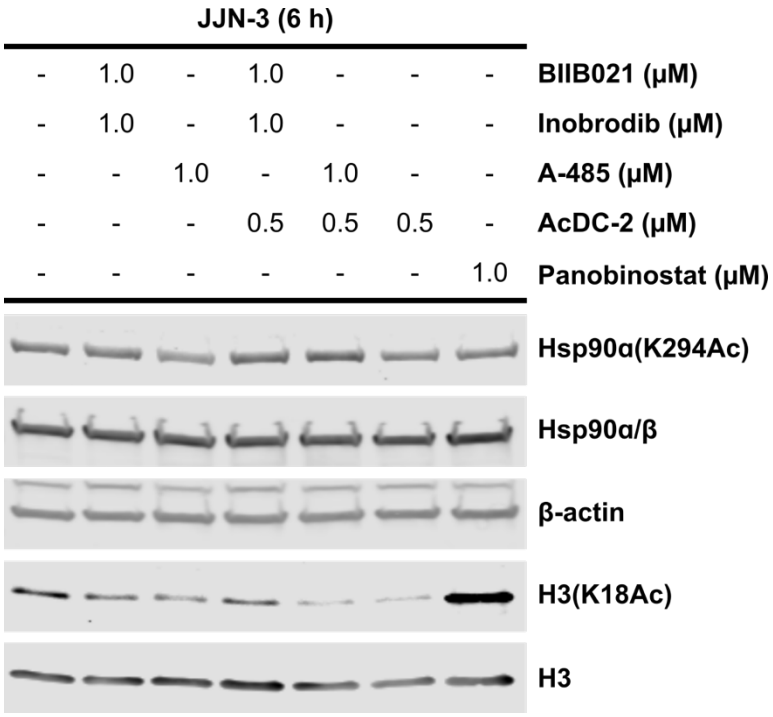


Figure 4.15: Western blots show treatment of JJN-3 cells with combination of BIIB021 and Inobordib, A-485, AcDC-**2** or panobinostat after 6 h did not cause significant change in Hsp90α(K294Ac) but did change H3(K18Ac) as expected. DMSO was added to cells not treated with compounds, as a vehicle control. β-actin and H3 are shown as a loading controls. Images are representative of three independent experiments.

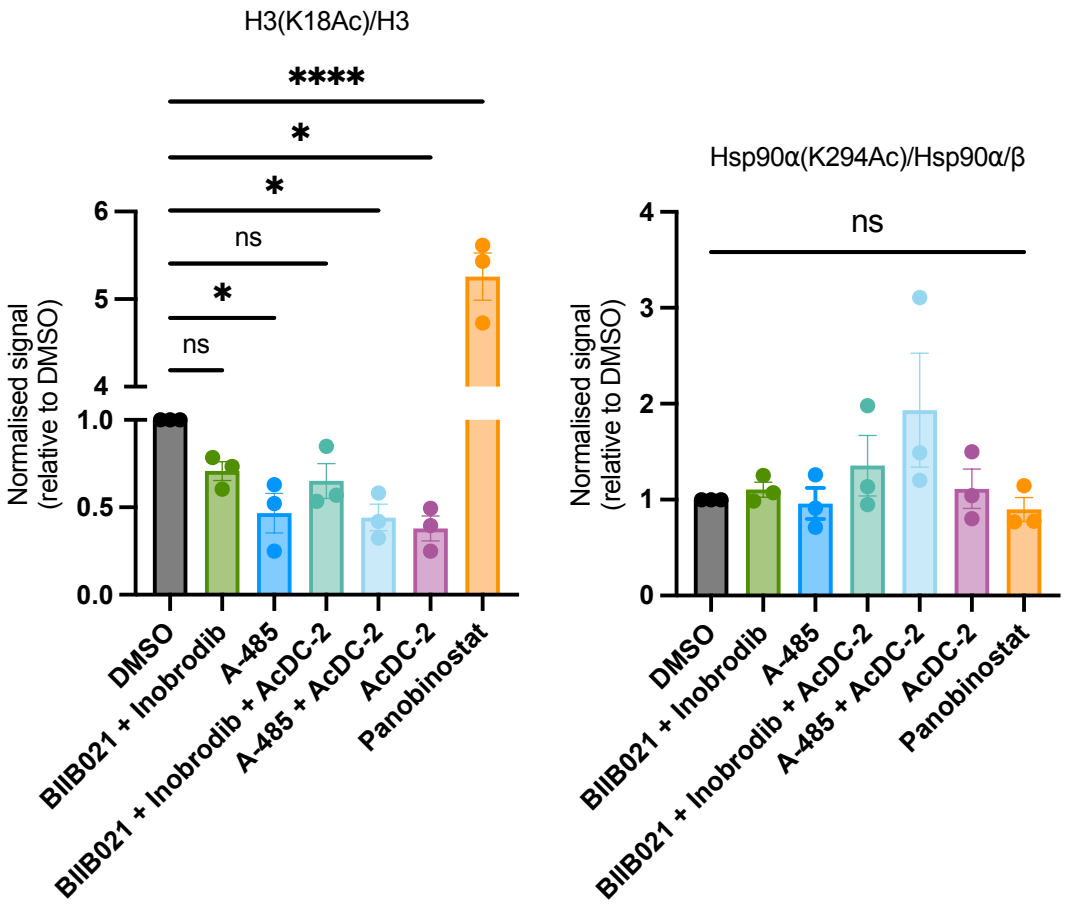


Figure 4.16: Western blot quantification for blots presented in **Figure 4.15** for H3(K18Ac) and Hsp90α(K294Ac). Measured signals are corrected for loading by normalising against the total protein level, and relative fold change compared to the vehicle control (DMSO) is calculated. Values represent the mean of three biological repeats. Error bars represent the s.e.m. and statistical significance was determined using an unpaired two-tailed student's *t*-test against DMSO. *$p < 0.05$. ****$p < 0.0001$.

Analysis of H3(K18Ac) was used to determine whether KAc had been perturbed on a *bona fide* substrate of CBP/p300. Here, we expected H3(K18Ac) to increase with panobinostat treatment as KDAC activity is inhibited, and H3(K18Ac) to decrease upon A485 treatment as KAT activity is inhibited,[213] which was consistent with the observed result in **Figure 4.15**. We did not expect H3(K18Ac) to change with treatment of BIIB021 and inobrodib, as previous work has shown that H3(K18Ac) is a CBP/p300 substrate that is not dependent on bromodomain activity.[64] We did however observe a slight decrease in H3(K18Ac) upon treatment with AcDC-**2** and postulated this was a consequence of complex formation between CBP/p300 and Hsp90 which could lead to steric occlusion of the KAT domain despite the compound engaging with the BRD.

The analysis of H3(K18) demonstrated the compounds' activity as we expected, so we could not rationalise the lack of change in Hsp90α(K294Ac), as previous reports have shown that panobinostat treatment results in hyperacetylation on Hsp90. However, there are literature accounts detailing difficulty in reproducing this phenotype.[214, 215] Additionally, investigation of datasets from acetylomics experiments carried out in the laboratory of Chunaram Choudhary show that treatment of mouse embryonic fibroblasts with CBP/p300 KAT inhibitors did not result in any significant fold-change in measured KAc sites on Hsp90.[172]

We also considered whether protein synthesis and turnover affected the abundance of Hsp90α(K294Ac), as we knew that AcDC-**2** treatment initiated a heat shock response and resulted in significantly increased levels of total Hsp90 over time-courses exceeding 6 h. Co-treatment with cycloheximide, a protein synthesis inhibitor, over 6, 18 and 24 h was explored. The experiments presented extremely inconsistent results between independent repeats, and no conclusions could be drawn.

4.3.6 AcDC-2 treatment shows consistent phenotypes in A549 and MCF-7 cell lines, and in a hypoxia-induced stress response

We next investigated whether AcDC-**2** induced proximity between CBP/p300 could result in a different phenotype in other cell lines, as slightly different basal expression levels of CBP/p300 or Hsp90 may influence the activity of AcDC-**2**. We therefore treated both MCF-7 and A549 cells with either AcDC-**2** or a combination of BIIB021 and inobrodib at a range of concentrations, and measured induced change in levels of HDAC6, Hsp90α(K294Ac), Hsp90 and CDK4 (**Figure 4.17**). We observed changes consistent to the treatment of JJN-3 cells, suggesting that the observed affects were not an artefact of one cell line but were consistent in a selection of different cancer types.

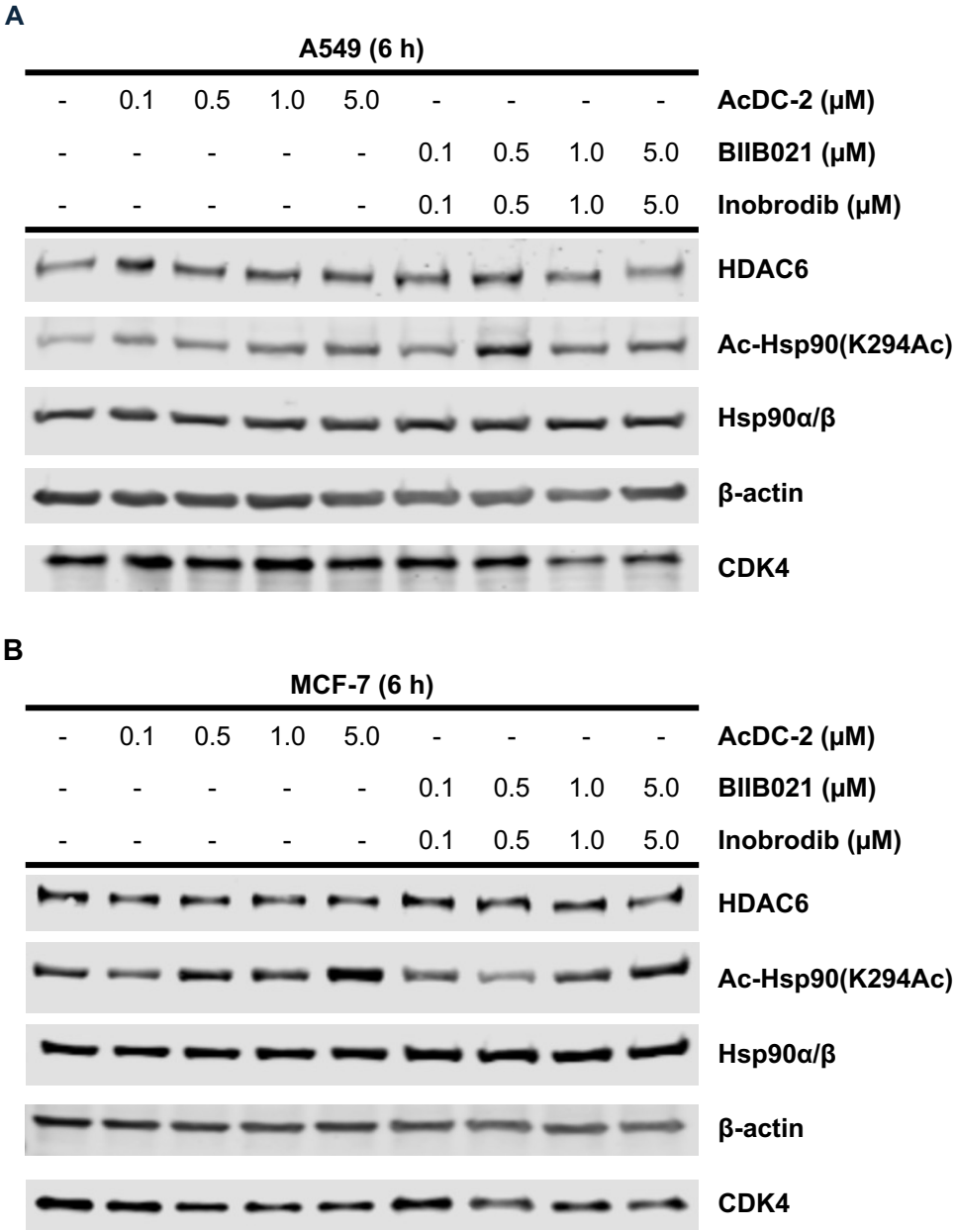


Figure 4.17: Western blots show treatment of **A** A549 and **B** MCF-7 cells with AcDC-**2** or combination of BIIB021 and inobrodib for 6 h did not cause dose-dependent change in Hsp90α(K294Ac), Hsp90α/β, or HDAC6; however, both sets of conditions decreased CDK4 at high concentrations. DMSO was added to cells not treated with compounds, as a vehicle control. β-actin is shown as a loading control. Images are representative of three independent experiments

Following this, we also investigated whether treatment with AcDC-**2** would illicit different effects in the context of a stress-response induced by hypoxia treatment. Cancer cells can become addicted to heat shock proteins as their microenvironments become increasingly toxic and they require higher levels of heat shock proteins like Hsp90 to maintain proteostasis.[216] We hypothesised the AcDC-induced interaction between CBP/p300 and pEHsp90 could have distinct effects within the context of a stress-response that were not

observed in normoxia. We focused on measurement of downstream markers of canonical stress responses including the DNA damage response (as demonstrated by increased levels of γH2AX and pKAP-1),[217, 218] and the unfolded protein response (demonstrated by increased levels of Grp78/BiP).[219] However, as demonstrated in **Figure 4.18**, we did not observe any significant difference between the drug treatment conditions for cells treated in hypoxia or normoxia. In summary, the biological consequence of treatment of AcDC-**2** appeared in the context of hypoxia-induced stress appeared insignificant.

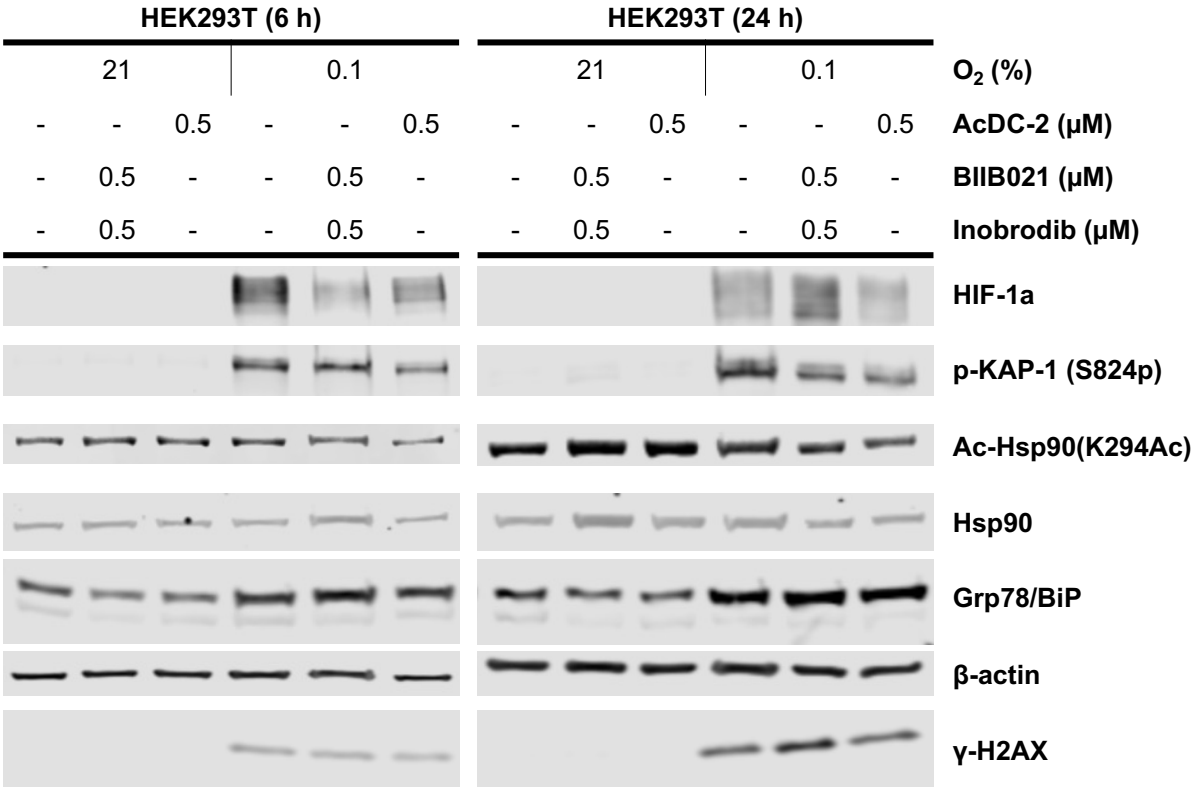


Figure 4.18: Western blots show treatment of HEK293 cells with AcDC-**2** or combination of BIIB021 and inobrodib in either normoxia (21% O_2) or hypoxia (0.1% O_2) for 6 h and 24 h. Compound treatment did not have a significant effect on markers of DNA damage (γH2AX and p-KAP-1) or the unfolded protein response (Grp78/BiP) in the context of hypoxia, nor did Ac-Hsp90α(K294Ac) change to a different extent upon AcDC-**2** treatment in normoxia or hypoxia. DMSO was added to cells not treated with compounds, as a vehicle control. β-actin is shown as a loading control. Images are representative of two independent experiments.

4.3.7 CBP/p300 and Hsp90 show distinct subcellular compartmentalisations and AcDC-2 treatment does not induce translocation

As mentioned in Chapter 1, it is known that CBP/p300 are predominantly localised to the nucleus, while Hsp90α/β isoforms are predominantly localised to the cytosol; however, it is important to recognise that both families of proteins have a distribution in each compartment. Additionally, it has been demonstrated that the localisation of these proteins is regulated and distinct stimuli can cause their translocation to elicit cell-signalling responses. For example, p300 can translocate to the cytosol upon nutrient addition to starved cells.[84] Hsp90 has also been shown to shuttle from the cytoplasm to nucleus in complex with immature steroid receptor substrates, upon steroid activation before client dissociation.[220]

Given that we have previously demonstrated that AcDC compounds induce proximity between the proteins, we questioned the subcellular localisation in which this occurs and whether a stable complex between CBP/p300 and Hsp90 could influence the proteins' subcellular compartmentalisations by translocation. This concept has been demonstrated more recently in work by Gibson *et al.* where treatment with a heterobifunctional compound targeting BRD4 (a nuclear protein) and $FKBP^{F36V}$-tagged proteins could induce the translocation of the tagged proteins to the nucleus.[162]

HEK293 cells were treated with AcDC-**2** for 6 h prior to sub-cellular fractionation to analyse the distribution of proteins in the nuclear and cytoplasmic components. We thought an AcDC-**2**-mediated stable complex formed between the proteins could increase the level of cytoplasmic CBP/p300 or nuclear Hsp90; however, as shown in **Figure 4.19**, this was not observed. Combination treatment of BIIB021 and inobrodib was included as a negative control to ensure any observed translocation was not a consequence of inhibition, but this also was not observed. We also probed levels of Hsp90α(K294Ac) to see if this mark was increased in a particular subcellular compartment; however, we saw a signal that was

consistent with the total level of Hsp90 in each compartment. Further discussion on the intensity of the Hsp90α(K294Ac) signal is presented in **Appendix A.iii.**

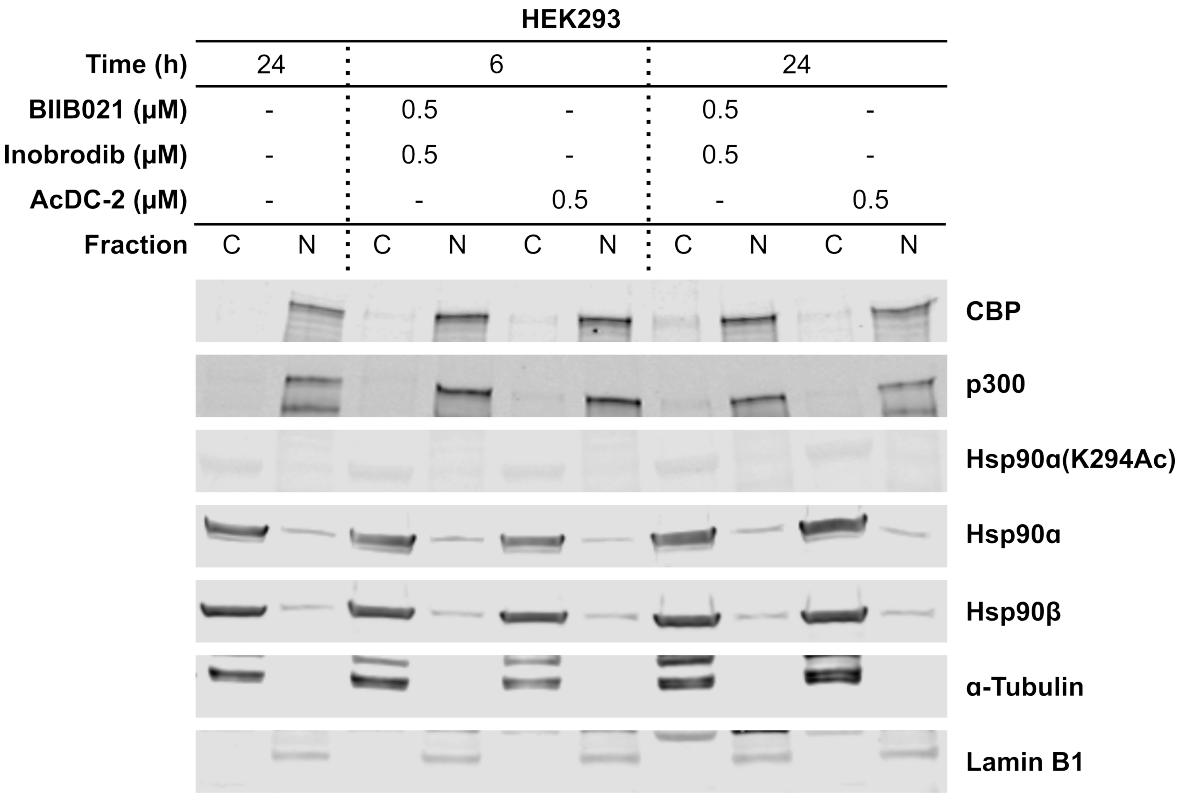


Figure 4.19: Cell fractionation analysed by immunoblotting shows treatment of HEK293 cells with AcDC-**2** or combination of BIIB021 and inobrodib for 6 h and 24 h does not cause translocation of CBP or p300 to the cytosol (C), or Hsp90 to the nucleus (N). DMSO was added to cells not treated with compounds, as a vehicle control. α-Tubulin is shown as a cytosolic loading control. Lamin B1 is shown as a nuclear loading control. Images are representative of two independent experiments

4.4 Further investigation of consequences to Hsp90 from induced proximity with CBP/p300 in cells

4.4.1 Initial studies of lysine acetylation beyond K294

Up to this stage in the project, our examination of the potential of AcDC-**2** to trigger lysine acetylation on Hsp90 has been limited to analysis at a single lysine residue, specifically K294. This has been driven by the lack of tools available to measure KAc specifically on Hsp90. However, **Figure 4.20** illustrates the distribution of lysine residues within the Hsp90 sequence. Although not all of these residues will be exposed to solvent, and some may be sterically hindered, a number of these other sites could be modified by CBP/p300 in an induced complex with AcDC-**2**.



Figure 4.20: Comparison of the protein sequences of Hsp90α and Hsp90β with the position of lysine residues highlighted (orange lines). The central horizontal bar shows shared sequence identity (dark blue) and similarity (light blue) between the proteins' primary structures, truncations are shown by a break in the labelled horizontal lines (as determined using the EMBL-EBI EMBOSS matcher tool,[56] and plotted using the Matplotlib python package). The underlaid boxes show the shared domain architecture along the protein sequences. Plotted to scale.

We therefore sought to investigate the total acetylation level on Hsp90 by enrichment through immunoprecipitation followed by probing KAc in immunoblotting with a non-specific antibody against pan-KAc. This approach has been reported to show hyperacetylation on Hsp90α following treatment with HDAC inhibitor, panobinostat, over 24 h, so this treatment was included as a positive control in all experiments.[47, 120, 124] HEK293 cells were treated with either BIIB021 and inobrodib as a negative control of inhibition, AcDC-**2**, or panobinostat. KAc was expected to increase across the proteome upon panobinostat treatment, which we would see on immunoprecipitated Hsp90 and in the input control. We expected AcDC treatment to only increase acetylation on Hsp90, and co-treatment with BIIB021 and inobrodib to have little effect. However, as shown in **Figure 4.21**, we failed to see any induced change on acetylation on Hsp90 in all conditions.

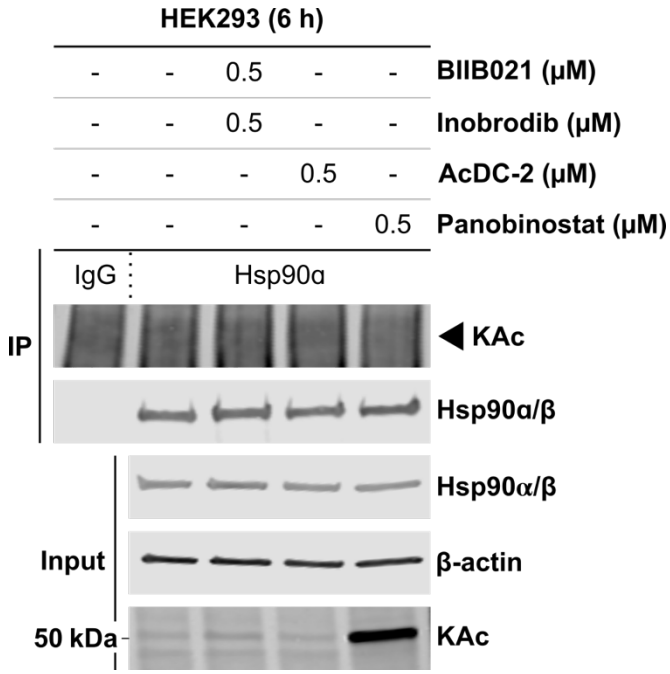


Figure 4.21: Immunoprecipitation of Hsp90α/β and immunoblotting for pan-KAc shows no hyperacetylation on Hsp90α/β following treatment of HEK293 cells with combination of BIIB021 and inobrodib or AcDC-**2**, or panobinostat for 6 h. An equal volume of DMSO was added to cells not treated with compounds, as a vehicle control. Samples labelled with IgG show the fraction of DMSO-treated cells that were immunoprecipitated using a non-specific antibody with the same isotype as α-Hsp90α. Samples labelled with input show analysis of an aliquot the lysate used in the immunoprecipitation procedure. A section of the input control samples at in the region of 50 kDa is shown to demonstrate the observed hyperacetylation upon panobinostat treatment. Images are representative of two independent experiments.

This result suggested a technical error in the experimental methodology as the positive control (panobinostat treatment) failed to replicate the anticipated result (increased KAc on Hsp90) reported in the literature. Inspection of KAc in the input control showed a global increase upon panobinostat treatment, particularly at distinct bands around 50 kDa and 15 kDa, likely corresponding to p53 and histones respectively. This observed increase in KAc in the input control suggested that the immunoprecipitation protocol required optimisation, rather than the lack of observed KAc in the immunoprecipitated being a biological phenomenon.

4.4.2 Validation of antibodies used in detection of acetylated Hsp90

One possibility for the lack of observed KAc on Hsp90 was that the acetylation of lysine residues at the epitope caused the protein to no longer be recognised by the capture antibody used in immunoprecipitation. To check this, we used recombinant Hsp90α (r-Hsp90α) that was chemically acetylated with acetic anhydride *in vitro* at a range of

concentrations (to give varied extents of lysine acetylation) before analysing the protein by immunoblotting. If acetylation of lysine residues at the epitope did abrogate the binding of the antibody to the protein, then we would see a loss of signal between r-Hsp90α and the chemically acetylated form (r-Ac-Hsp90). The result of this experiment is shown in **Figure 4.22**. It was pleasing that both the pan-KAc and Hsp90α(K294Ac) antibodies showed a signal for (r-Ac-Hsp90) that was dependent on the concentration of acetic anhydride used, and no signal was seen for r-Hsp90α. This result validates these antibodies as detecting the acetylated forms of the protein. However, to our surprise we were unable to detect all forms of the recombinant protein with the antibody used in immunoprecipitation (Hsp90α/β, sc-13119). Closer inspection showed that the antibody was raised against a C-terminal fragment of the Hsp90β where there is a low degree of sequence similarity between the two isoforms. Despite the manufacturer's description as non-specific to both isoforms of Hsp90, and its cited use in 723 publications at the point of writing, we concluded this antibody is likely only selective to Hsp90β.

We also observed that the highest concentrations of acetic anhydride used in the chemical acetylation caused a loss of all signals at the expected molecular weight range (**Figure 4.22**). Imaging of the SDS-PAGE gel prior to electro-transfer showed diffuse bands at a wide range of higher-than-expected molecular weights for r-Hsp90α. This was rationalised as an artefact of protein aggregation or insolubility in the assay due the reduction in pH upon acetic anhydride treatment, rather than a detection phenomenon.

Moving forward, we used an antibody specific to Hsp90α for immunoprecipitation, as this exact antibody was used in the reported literature which showed the protein to be hyperacetylated upon inhibition of KDACs.[47, 120, 124]

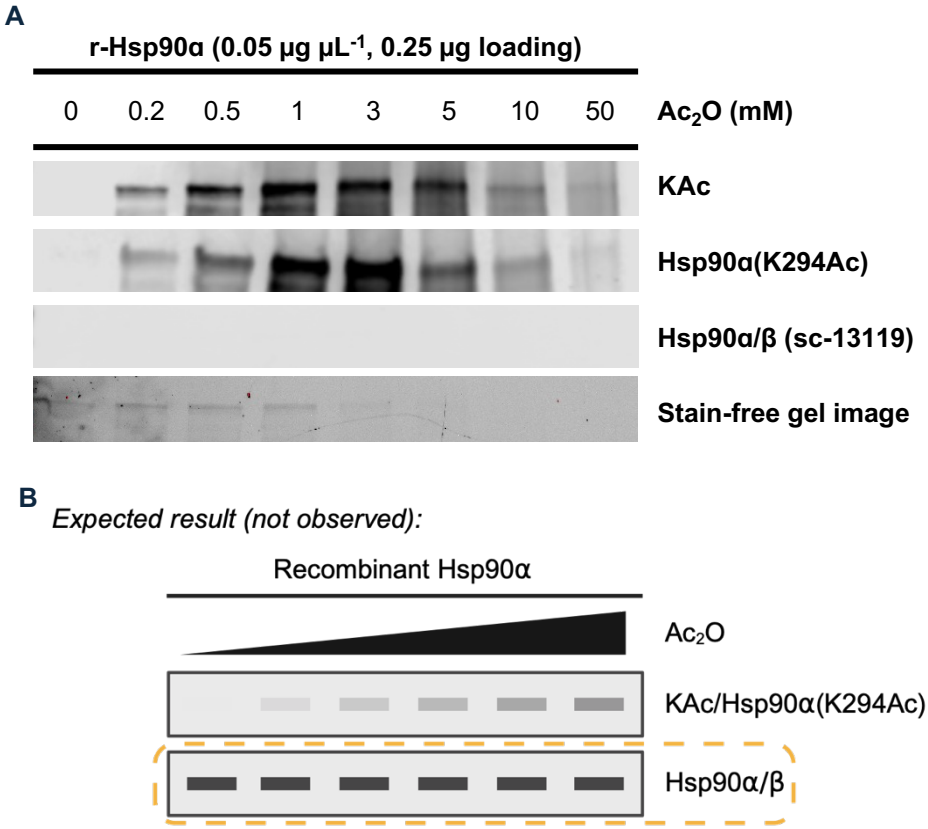


Figure 4.22: Western blot analysis shows recombinant Hsp90α (r-Hsp90α) is chemically acetylated and recognised by pan-KAc and Hsp90α(K294Ac) antibodies, but r-Hsp90α is not recognised by Hsp90α/β (sc-13119) in all its forms. (**A)** Experimental images representative of two independent experiments. Protein loading is showed by stain-free gel image prior to electro transfer. (**B**) Graphic highlighting the expected result of Hsp90α recognition by Hsp90α/β (sc-13119).

4.4.3 Investigation of lysine acetylation on nuclear Hsp90

Given the nuclear localisation of CBP/p300 and the results presented in § 4.3.7, we postulated that the population of Hsp90 in the nucleus would be more likely to be acetylated by CBP/p300 than the cytosolic fraction, as the stoichiometric ratio of the acetyltransferase:substrate is higher. Towards our goal of measuring AcDC-**2** induced acetylation on Hsp90, we therefore incorporated a nuclear extraction step prior to immunoprecipitation of Hsp90α, anticipating that we would be more likely to observe any slight change in KAc induced by AcDC-**2** treatment. Additionally, the duration of panobinostat treatment was lengthened to 24 hours using a staggered start of treatment, as previous works used treatment time-courses in the range of 16 to 24 hours.[47, 120, 124]

Additional steps were also taken to improve the immunoprecipitation procedure. RIPA buffer was used for lysis and wash procedures, rather than IP buffer as the SDS content prevented

non-specific protein-protein interactions with Hsp90, and therefore reduced background noise. Chemical cross-linking of antibodies to beads was also performed to reduce background noise caused by IgG, despite orthogonal species of antibodies used for immunoprecipitation and immunoblotting. Together these steps improved the signal for KAc at the position of Hsp90α, as shown in **Figure 4.23**; however, we could not observe the hyperacetylation phenotype on Hsp90α upon panobinostat treatment.

A possible explanation is that nuclear Hsp90α is intrinsically hyperacetylated due to the higher abundance of KAT enzymes in the nucleus. This would explain why HDAC inhibition has little effect compared with the vehicle control, although this conclusion cannot be drawn without comparing immunoprecipitated Hsp90α from other subcellular compartments.

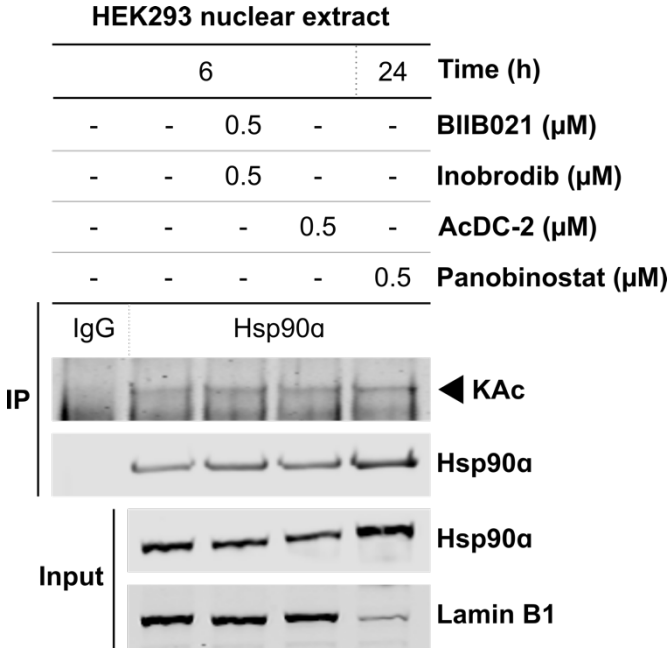


Figure 4.23: Immunoprecipitation of Hsp90α from nuclear extracts and immunoblotting for pan-KAc shows no hyperacetylation on Hsp90α following treatment of HEK293 cells with combination of inobrodib and BIIB021 or AcDC-**2** for 6 h, or panobinostat treatment for 24 h before harvest. An equal volume of DMSO was added to cells not treated with compounds, as a vehicle control. Samples labelled with IgG show the fraction of DMSO-treated cells that were immunoprecipitated using a non-specific antibody with the same isotype as α-Hsp90α. Samples labelled with input show analysis of an aliquot the lysate used in the immunoprecipitation procedure. Representative image form three independent biological repeats.

4.4.4 Investigation of the stability of acetylated Hsp90α in IP procedures

We repeatedly speculated that our inability to detect hyperacetylated Hsp90 might be due to the loss of this modification during the immunoprecipitation process. This loss could potentially be attributed to KDAC enzyme activity occurring after cell lysis, despite

supplementing all lysis and wash buffers with Trichostatin A (10 μM) and Nicotinamide (20 mM) as broad-spectrum KDAC and sirtuin inhibitors, respectively. To test our hypothesis, we devised an experiment akin to a spike-and-recovery test where we spiked r-Ac-Hsp90 into freshly prepared whole cell lysate from the same population of HEK293 cells. We also spiked a sample of lysate with r-Hsp90 as a negative control and included the input controls of adding buffer to whole cell lysate and adding the recombinant proteins to lysis buffer. If the KAc mark is lost in the immunoprecipitation procedure, then we would observe the whole cell lysate spiked with r-Ac-Hsp90 and r-Hsp90 to have the same KAc signal following immunoprecipitation. Input samples were also analysed to compare the amount of spiked r-(Ac)-Hsp90 to endogenous Hsp90 in whole cell lysate.

As shown in **Figure 4.24**, a minor but notable increase in the KAc signal was observed in the Hsp90α immunoprecipitated from whole cell lysate that had been supplemented with r-Ac-Hsp90, compared to the sample spiked with r-Hsp90. Comparing the Hsp90α signal for the input control of r-Hsp90 and r-Ac-Hsp90α shows that both forms are equally detected by the Hsp90α antibody in immunoblotting, confirming lysine acetylation does not mask the epitope. The input control Hsp90α signal also demonstrates the small ratio of r-Hsp90α to endogenous Hsp90α in whole cell lysate samples. This rationalises why the increased KAc signal in the spiked immunoprecipitate is small, if the Hsp90 captured in immunoprecipitation represents an unbiased sample of the total population. In summary, we can deduce that the KAc mark remains present on Hsp90 throughout the immunoprecipitation process and is not lost by action of KDACs post-lysis.

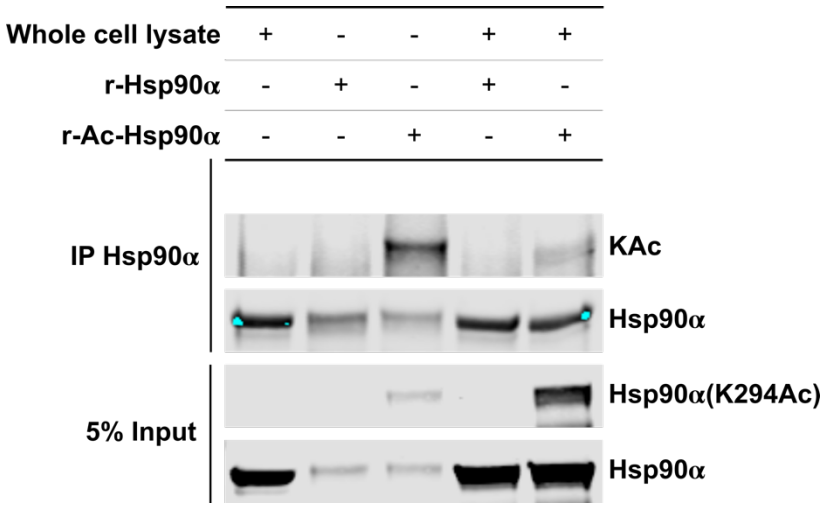


Figure 4.24: Spike-and-recover experiment shows chemically acetylated recombinant Hsp90α (r-Ac-Hsp90α) is detected within the matrix of HEK293 whole cell lysate following the immunoprecipitation and immunoblotting procedure.

An anomalous result was seen in the input control Hsp90α(K294Ac) signal as the whole cell lysate spiked with r-Ac-Hsp90 gave a significantly brighter signal than the buffer spiked with r-Ac-Hsp90. The source of this observation remains unconfirmed but may be linked to potential chemical *O*- and *S*-acetylation occurring on adjacent residues, which subsequently transfers to unmodified lysine residues on native Hsp90α after spiking. Alternatively, the acetylated form of Hsp90α could be less soluble or more prone to aggregation than the non-modified form, and its addition to whole cell lysate stabilises it to some extent. This would be further supported by data presented in § 4.4.2, where chemical acetylation at high concentrations of acetic anhydride caused loss of protein due the apparent formation of aggregates.

We investigated whether our inability to detect hyperacetylated Hsp90 was due to its insolubility by conducting a denaturing-immunoprecipitation experiment. This method utilised a lysis buffer with high SDS concentration to denature, linearise, and solubilise proteins. Subsequently, the SDS concentration was reduced by dilution with IP lysis buffer to facilitate immunoprecipitation. This method both inactivated any enzymatic activity post-lysis and solubilised proteins such that an insoluble debris pellet was not observed. The results of this experiment shown in **Figure 4.25** demonstrate that in our hands, we could

not detect hyperacetylated Hsp90α upon treatment of HEK293 cells with the KDAC inhibitor panobinostat, nor did AcDC-**2** treatment result in in a detectable increase in KAc on Hsp90α.

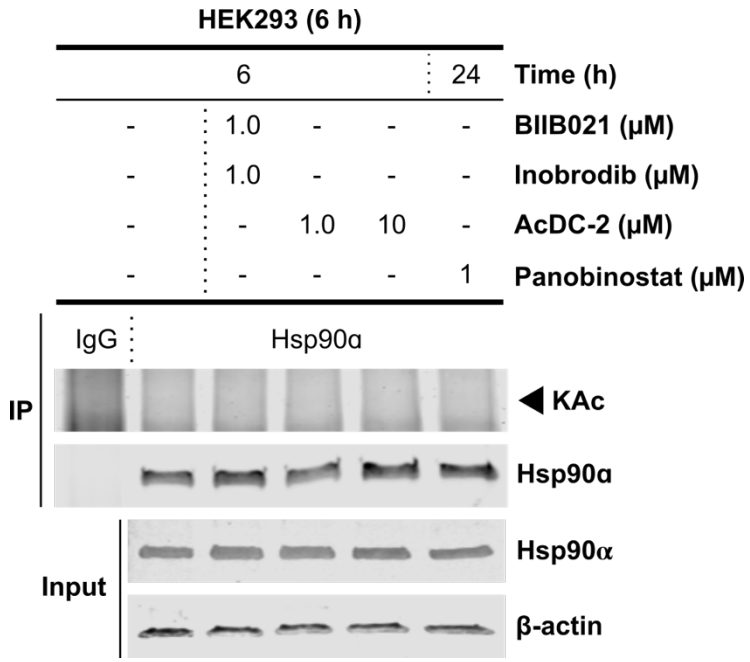


Figure 4.25: Denaturing immunoprecipitation of Hsp90α from HEK293 cells and immunoblotting for pan-KAc shows no hyperacetylation on Hsp90α following treatment of HEK293 cells with combination of inobrodib and BIIB021 or AcDC-**2** at 1 and 10 μM for 6 h, or panobinostat treatment for 24 h before harvest. An equal volume of DMSO was added to cells not treated with compounds, as a vehicle control. Samples labelled with IgG show the fraction of DMSO-treated cells that were immunoprecipitated using a non-specific antibody with the same isotype as α-Hsp90α. Samples labelled with input show analysis of an aliquot the lysate used in the immunoprecipitation procedure. Representative image form two independent biological repeats.

4.5 Summary

We have shown that AcDC compounds demonstrate cellular permeability and engage with the bromodomain of CBP in a cellular system, by a NanoBRET target engagement assay. AcDC-**2** demonstrated the lowest IC_{50} value in this assay, consistent with its cooperative binding between the structurally similar $p300^{BRD}$ and $Hsp90^{N\text{-term}}$.

We showed that AcDC compounds induce proximity between the full length CBP protein and Hsp90 isoforms in a dose-dependent manner, by a NanoBRET protein-protein interaction assay. To validate these results, co-immunoprecipitation experiments were performed with wild type HEK293 cells which demonstrated that AcDC-**2** forms a stable complex between endogenous Hsp90 and CBP, but not necessarily p300.

Encouraged by the results of the induced proximity between these proteins, we sought to explore the biological implication of this and used western blotting to demonstrate that AcDCs do not lead to target protein degradation of CBP/p300. Due to the availability of commercial antibodies, we focused on whether AcDC treatment increased the acetylation on Hsp90 at residue K294. When we examined this on a time-course treatment, we identified 6 h as a point where AcDC-**2** treatment appeared to increase Hsp90α(K294Ac) without a significant increase in the underlying total Hsp90 level. However, this was disproven by further control experiments where we tried to demonstrate dose-dependence and loss of phenotype from competitive inhibition or inhibition of the CBP/p300 KAT domain. We explored whether treatment with AcDC-**2** elicited different effects in the context of stress-response induced by hypoxia, but we observed no significant differences between co-treatments in hypoxia and the respective co-treatment in normoxia. We therefore rationalised the limited activity of AcDC compounds was due to CBP/p300 and Hsp90 showing distinct subcellular compartmentalisations without an observed translocation of either protein upon AcDC treatment.

Towards our goal of showing the induced proximity between CBP/p300 and Hsp90 results in increased KAc on Hsp90, we attempted to immunoprecipitate hyperacetylated Hsp90 followed by immunoblotting with a pan-KAc antibody. Treatment of cells with KDAC inhibitors was used a positive control; however, we were unable to establish this assay to demonstrate hyperacetylated Hsp90 as previously described in the literature.

5 Discussion

5.1 Summary and conclusions

At the outset of this thesis, our initial hypothesis was that a heterobifunctional molecule could recruit CBP/p300 towards Hsp90 as a target protein to induce a specific increase in lysine acetylation within an endogenous cellular system. The main aims were thus to design and synthesise such a compound, validate that it can engage with both proteins to form a ternary complex, and to evaluate the biological consequences of this induced proximity within cellular systems and identify an increase in KAc on Hsp90.

Chapter 2 summarised the rational design and synthesis of bifunctional compounds based on the inhibitors inobrodib and BIIB021 as binding ligands for the CBP/p300 bromodomain and Hsp90 *N*-terminal binding domains, respectively. We prepared four bifunctional molecules termed 'acetylation directing chimeras' (AcDC-**1**–**4**) which had different chemical linkers. This was done to focus on exploring the effect of linker length on the formation of a ternary complex with the binding domains. At the point this project was conceived, incorporation of inobrodib into heterobifunctional compounds had not yet been reported, so a vector for extension of a chemical linker from the scaffold was identified. A piperidine-containing analogue, pip-obrodib, was synthesised as a novel analogue of inobrodib to allow derivatisation of the CBP/p300 bromodomain ligand by amide coupling. Previously reported procedures were used for the incorporation of the BIIB021 scaffold into AcDCs, with rationalisation of its binding to Hsp90 used to inform the design of chemical linkers. Additionally, a novel fluorescent tracer compound (inobrodib-BODIPY) was developed and used in NanoBRET assays for measuring target engagement with the CBP/p300 bromodomain in a cellular system.

In chapter 3, we demonstrated that extension of a chemical linker from the inobrodib scaffold along our chosen exit vector sustained interaction with the p300 bromodomain as evidenced by the measured dissociation constants for AcDC-**1**–**4** with 6×His-p300^{BRD}. AlphaScreen based assays were optimised with the recombinant proteins 6×His-p300^{BRD}

and GST-Hsp90^{NTD} and demonstrated that AcDC-**1**–**4** can induce proximity between the binding domains in a ternary complex. The induced proximity was also shown to be specific to AcDCs interacting with the binding domains by antagonistic competition with the inhibitors inobrodib and BIIB021. AcDC-**1** was shown to form the weakest ternary complex as it was more readily outcompeted by the inhibitors at lower concentrations, while AcDC-**2**–**4** had comparable activities to inhibitors. The thermodynamic properties of the ternary complex formation were explored and AcDC-**1**–**4** binding interactions were shown to have positive cooperativity. AcDC-**2** demonstrated the highest degree of cooperativity driven by beneficial PPIs at the protein surface. From this we concluded that the linker employed in AcDC-**2** is the optimum length to maintain engagement with the two proteins' binding domains.

Chapter 4 demonstrated that AcDC compounds are cell-permeable and engage with the bromodomain of CBP in a cellular system by using a NanoBRET target engagement assay. AcDC-**2** demonstrated the lowest IC_{50} value in this assay, consistent with its cooperative binding between the structurally similar p300^{BRD} and Hsp90^{NTD}. We showed that AcDC compounds induce proximity between the full length CBP protein and Hsp90 isoforms in a dose-dependent manner by using a NanoBRET protein-protein interaction assay. To validate these results, co-immunoprecipitation experiments were performed with wild type HEK293 cells which demonstrated that AcDC-**2** forms a stable complex between endogenous Hsp90 and CBP, but not necessarily p300. Encouraged by these results, we sought to explore the biological implication of this induced proximity and used western blotting to demonstrate that AcDCs do not lead to target protein degradation of CBP/p300. Due to the availability of commercial antibodies, we focused on whether AcDC treatment increased the acetylation on Hsp90α at residue K294; however, we were unable to detect a robust change in this mark upon AcDC-**2** treatment. We explored whether treatment with AcDC-**2** elicited a unique phenotype in the context of stress-response induced by hypoxia, but observed no significant differences and rationalised the limited activity of AcDC compounds was due to CBP/p300 and Hsp90 showing distinct subcellular

compartmentalisations without an observed translocation of either protein upon AcDC treatment. Towards our goal of showing that the induced proximity between CBP/p300 and Hsp90 results in increased KAc on Hsp90, we attempted to immunoprecipitate hyperacetylated Hsp90 followed by immunoblotting with a pan-KAc antibody. Treatment of cells with KDAC inhibitors was used as a positive control; however, we were unable to establish this assay as a means to demonstrate hyperacetylated Hsp90 as previously described in the literature.

In summary, we have developed bifunctional molecules that bind and induce proximity between Hsp90 and CBP/p300 in an endogenous cellular system. We explored the effect of varied linker length in the design of AcDCs and identified a lead compound, AcDC-**2**, which formed a stable complex between Hsp90 and CBP (but not necessarily p300) in cells. We have not been able to establish whether this induced proximity results in a significant change in lysine acetylation on Hsp90, nor have we observed a significant phenotypic effect beyond that demonstrated by engaging with the proteins' binding domains.

5.2 Discussion and future work

To rationalise our observation that AcDC-induced proximity did not increase KAc on Hsp90, we formed two hypotheses: (i) while AcDC-**2** treatment did not result in a measured hyperacetylation on Hsp90, the induced proximity may have increased KAc at a specific site that we have not been able to measure with our methods; (ii) the complex formed by AcDC-**2** adopted a conformation where lysine residues on Hsp90 were close but just out of reach of the CBP/p300 KAT domain.

In support of our first hypothesis, works published since the outset of this thesis from the Parker laboratory demonstrated that the recruitment of KATs CBP/p300 and PCAF/GCN5 using AceTAG molecules did not cause an increase in KAc at all possible sites on target proteins, but that the KATs continue to show substrate specificity and distinct acetylation profiles on the target proteins.[155, 174] Methods to study site-specific KAc on target proteins (including Hsp90) in cells are limited as commercially available antibodies for site-specific

marks are lacking, and pan-KAc antibodies have limited coverage.[221] This may explain why we failed to observe hyperacetylated Hsp90 upon KDAC inhibition as previously described. A non-biased method to study the KAc sites would be to use a MS-based proteomics approach by enrichment of the target protein. The stoichiometry of KAc could also be quantified using chemical modification of unmodified lysine residues with acetyl groups bearing heavy isotopes to generate peptide-isotopologues that differentiate endogenous acetylation.[222] These approaches; however, are non-trivial and may require prior-confidence that the induced CBP/p300-mediated acetylation of Hsp90 is feasible in cells.

Additionally, we have focused on the cytosolic isoforms of Hsp90 in this work, but BIIB021 is not a selective inhibitor. It shows affinity towards the other HSP90 family members as well as potential off targets, such as other ATPases. To allow investigation of possible AcDC-induced acetylation on these proteins, a chemical probe could be developed incorporating the BIIB021 pharmacophore to allow for a chemo-affinity pulldown. If induced increase in KAc on proteins does not change their affinity for BIIB021, then this approach would allow for a less biased profiling of KAc on the proteins that we expect to bind to AcDCs.

To address our second hypothesis, computational approaches could be used to model the ternary complex formed by AcDC-**2**. This would provide insight into the orientation of the protein domains with respect to one another. Such approaches have been applied to rationalise PROTAC activities with variable accuracy;[223] however, our system differs as there is greater information on the site of KAT activity compared to polyubiquitination by an E3-E2 complex.

Both the CBP and p300 catalytic cassettes have been structurally characterised by X-ray crystallography and cryo-electron microscopy,[58, 71, 85] as have the domains of Hsp90.[97] Modelling the allowed-conformations formed by Hsp90 and CBP/p300 by protein-protein docking constrained by distance between $Hsp90^{NTD}$ and $CBP/p300^{BRD}$ would provide insight on possible K residues that would be accessible to the KAT domain. This approach is limited; however, as it cannot account for structural flexibility in the proteins and large

sections of CBP/p300 are not structurally defined, nor is the lysine rich charged linker region in Hsp90.

The main aim of this thesis was to develop a bifunctional molecule that recruits the acetyl transferases CBP/p300 towards Hsp90 as a target and which induces an increase in lysine acetylation on that specific protein. The compounds and assays developed in this thesis provide a foundation for future work which could focus on developing a second-generation of bifunctional molecules with a more extensive exploration of linkerology. Additionally, a significant challenge in assessing the activities of AcDCs in cellular systems has been distinguishing the effects of induced-proximity from occupancy-driven inhibition of Hsp90. This could be addressed by new AcDCs incorporating an allosteric Hsp90-targetting ligand which engages with one of the other domains on Hsp90. Ligands for the Hsp90 C-terminal domain have been reported but with no reported co-crystal structures. This stymies SAR analysis and additional biochemical investigation is required into the compounds' mode of action.[224] Finally, given lessons learned from the development of PROTACs, different E3 ligases demonstrate greater activities towards specific substrates,[144] and the same principles may apply to the development of AcDCs such that greater KAT activities could be achieved by targeting a different substrate protein or recruiting a different acetyltransferase.

6 Materials and Methods

6.1 Biology Materials

6.1.1 Primary Antibodies

Table 6.1: Names and specifications of primary antibodies used in this study.

Name	Species	Dilution	Supplier	Catalogue Number	Application
CBP	rabbit	WB 1:1000	Cell Signalling Technologies	7389	WB/IP
P300	rabbit	WB 1:1000	Cell Signalling Technologies	86377	WB/IP
β-actin	mouse	WB: 1:2000	Santa Cruz	sc-69879	WB
Hsp90α	mouse	WB: 1:2000	Enzo Life Science	ADI-SPA-840	WB/IP
Hsp90α(K294Ac)	rabbit	WB: 1:1000	Rockland	600-401-981	WB
Hsp90α/β	mouse	WB: 1:5000	Santa Cruz	sc-13119	WB/IP
Hsp90	mouse	WB: 1:1000	Abcam	ab13492	WB
Hsp70	mouse	WB 1:2000	Santa Cruz	sc-24	WB
cMyc	rabbit	WB 1:2000	Cell Signalling Technologies	5605	WB
Lamin-B1	rabbit	WB: 1:1000	Invitrogen	MA1-06103	WB
H3	mouse	WB 1:1000	Cell Signalling Technologies	3638	WB
H3(K18Ac)	rabbit	WB: 1:1000	Cell Signalling Technologies	9675	WB
Ac-α-Tubulin	rabbit	WB 1:1000	Cell Signalling Technologies	5335	WB
α-Tubulin	mouse	WB 1:1000	Santa Cruz	sc-5286	WB
CDK4	rabbit	WB 1:2000	Proteintech	11026-1-AP	WB
HDAC6	rabbit	WB 1:2000	Proteintech	12834-1-AP	WB
KAc	rabbit	WB 1:1000	Cell Signalling Technologies	9441	WB/IP
KAc	mouse	WB 1:1000	Cell Signalling Technologies	9681	WB
γ-H2AX	rabbit	WB 1:1000	Merck Millipore	07-627	WB
p-KAP-1	Rabbit	WB 1:1000	Bethyl Laboratories	A300-767A	WB
HIF-1α	mouse	WB: 1:500	BD Biosciences	610959	WB
Grp78/BiP	Mouse	WB: 1:2000	BD Biosciences	610978	WB

6.1.2 Secondary Antibodies

Table 6.2: Names and specifications of secondary antibodies used in this study.

Name	Species	Dilution	Supplier	Catalogue Number	Application
IRDye® 800CW Goat anti-Rabbit IgG	Goat	1:10,000	LI-COR	925-32211	WB
IRDye® 680RD Goat anti-Mouse IgG	Goat	1:10,000	LI-COR	926-68070	WB
IRDye® 800CW Goat anti-Mouse IgG	Goat	1:10,000	LI-COR	926-32210	WB
IRDye® 680RD Goat anti-Mouse IgG	Goat	1:10,000	LI-COR	926-68070	WB

6.1.3 Mammalian cell culture reagents

Table 6.3: Names and specifications of routine tissue culture reagents used in this study.

Name	Supplier	Catalogue Number
Dulbecco's modified Eagle's medium (DMEM)	Life Technologies Ltd	41965062
RPMI-1640 medium	Sigma-Aldrich	R8758
Fetal Bovine Serum (FBS)	Sigma-Aldrich	F7524
Penicillin-Streptomycin (10,000 U/mL)	Life Technologies Ltd	15140122
Trypsin-EDTA solution	Sigma-Aldrich	T3924
Trypan Blue solution	Sigma-Aldrich	T8154
DMSO	Sigma-Aldrich	D2650

6.1.4 Bacterial culture reagents

Table 6.4: Names and specifications of bacterial culture reagents used in this study.

Name	Supplier	Catalogue Number
LB broth (Lennox) powder	Sigma-Aldrich	L3022
LB broth with agar (Lennox) powder	Sigma-Aldrich	L2897
SOC medium	Sigma-Aldrich	S1797
Tryptone	Fisher Scientific	10525943
Yeast extract	Fisher Scientific	11385992
NaCl	Sigma-Aldrich	S7653
Ampicillin	Apollo Scientific	BIA0104
Kanamycin sulphate	Fisher Scientific	10031553
Chloramphenicol	Sigma-Aldrich	C0378
Isopropyl-1-thio-β-D-galactopyranoside (IPTG)	Fluorochem	M02726
Glycerol	Sigma-Aldrich	G5516

Table 6.5 Names and formulations of bacterial culture media. All media were reconstituted with deionised water before autoclave sterilisation and stored at ambient temperature. Antibiotics were supplemented from 1000× stock solutions as outlined in **Table 6.6**.

Name	Formulation
Lysogeny broth (LB) medium	20 g L^{-1} LB broth (Lennox) powder, or 10 g L^{-1} Tryptone, 5 g L^{-1} yeast extract 5 g L^{-1} NaCl
LB Agar	35 g L^{-1} LB broth with agar (Lennox) powder

Table 6.6: Specifications of 1000× antibiotic stock solution preparations used in this study.

Antibiotic	Stock Concentration	Solvent
Ampicillin	100 mg mL^{-1}	Water
Kanamycin	50 mg mL^{-1}	Water
Chloramphenicol	25 mg mL^{-1}	Ethanol

6.1.5 Commercially available drugs

Table 6.7: Names and specifications of commercially available drugs used in this study.

Name	Supplier	Catalogue Number
Panobinostat	Sigma Aldrich	SML3060
A-485	BLD Pharmatech GmbH	BD00789375
TSA	Stratech Scientific Ltd	A8183-APE-1mg
SW-100	MedChemExpress	HY-115475
Cycloheximide	Sigma Aldrich	C7698
Inobrodib (CCS1477)	This study	N/A
BIIB021	This study	N/A

6.1.6 Buffer formulations

Table 6.8: Names and formulations of commonly referenced buffers. All solutions were prepared in deionised water and stored at ambient temperature, unless otherwise specified.

Name	Formulation
TBS	25 mM Tris (adjusted to pH 7.6 with HCl), 150 mM NaCl; prepared as a 10× solution and autoclave sterilised
TBST	0.1% (v/w) Tween 20, TBS buffer
PBS	10 tab. L^{-1} Oxoid phosphate buffered saline tablets; autoclave sterilised
Urea Lysis buffer (UTB)	8 M Urea, 50 mM Tris (adjusted to pH 7.6 with HCl), 15 mM 2-mercaptoethanol (supplemented immediately prior to use)
IP Lysis buffer	25 mM Tris (adjusted to pH 7.6 with HCl), 150 mM NaCl, 1% Triton X-100; supplemented with cOmplete protease inhibitor (Roche) and 1 mM PMSF immediately prior to use.
RIPA buffer	50 mM Tris (adjusted to pH 8.0 with HCl), 150 mM NaCl, 10 mM NaCl, 5 mM EDTA, 1 mM EGTA, 1% Triton X-100, 0.1% SDS, 0.5% sodium deoxycholate, 20 mM nicotinamide; prepared as a 2× solution and supplemented with cOmplete protease inhibitor (Roche) 10μM TSA, and 1 mM PMSF immediately prior to use
Cytoplasmic lysis buffer	10 mM HEPES (adjusted to pH 7.5 with NaOH), 10 mM KCl, 340 mM sucrose, 10% (v/v) glycerol, 20 mM nicotinamide; prepared as a 2× solution and supplemented with cOmplete protease inhibitor (Roche), 1 mM PMSF, and 10 μM TSA immediately prior to use.
Nuclear lysis buffer	10 mM HEPES (pH adjusted to 7.5 with NaOH), 5 mM EDTA, 1 mM EGTA, 20 mM nicotinamide; prepared as a 2× solution and supplemented with cOmplete protease inhibitor (Roche), 1 mM PMSF, and 10 μM TSA immediately prior to use.
Laemmli buffer 2×	120 mM Tris (adjusted to pH 6.8 with HCl), 4% SDS (*w/v*), 20% glycerol (v/v), 0.02% *w/v* bromophenol blue, 5% v/v 2-mercaptoethanol (supplemented immediately prior to use)
Tris-glycine running buffer	25 mM Tris, 192 mM glycine, 0.1% SDS, pH 8.2 following dilution; prepared as a 10× solution
Transfer buffer	20% turbo transfer buffer (propriety, BioRad), 20% Methanol
Blocking buffer	5% *w/w* non-fat milk powder, TBST buffer
Cross-linking reaction buffer	100 mM triethanolamine hydrochloride (adjusted to pH 8.2 with NaOH)
Cross-linking quenching buffer	100 mM ethanolamine (adjusted to pH 8.2 with HCl)
Cross-linking elution buffer	100 mM glycine (adjusted to pH 2 with HCl)
Cross-linked antibody-bead storage buffer	0.1% (v/w) Tween 20, 0.02% (*w/w*) sodium azide, PBS buffer

6.1.7 Mammalian cell lines

Table 6.9: Cell lines and their specifications, as used in this study. Details of exact media compositions are available from the commercial suppliers as outlined in **Table 6.3**.

Cell Line	Cell type	Culture Medium	Source of cells
HEK293	Embryonic kidney epithelial-like	DMEM	ATCC
A549	Lung carcinoma epithelial	DMEM	ATCC
MCF7	Breast adenocarcinoma epithelial	DMEM	ATCC
JJN-3	Plasma cell leukemia	RPMI-1640	Prof. Claire Edwards*

*University of Oxford; UCL, University of London.

6.1.8 Primers

Table 6.10: Details of primers used in this study. Primers were purchased from Life Technologies Ltd or Sigma Aldrich, synthesised on 0.025 µmol scale, and purified by desalting; unless otherwise specified.

Name	Forward	Reverse	Notes
attB1-EP300 fragment for N-terminal tagged fusion	ggggacaagtttgtacaaaaaagcaggcttaATGGCCGAGAATGTGGTGGA	ggggaccactttgtacaagaaagctgggttCTAGTGTATGTCTAGTGTACTCTGTGAGAGGTT	Hybridisation sequence for EP300 (uppercase) in-frame with attB1 sequence (lowercase)
PvuI-EP300-XhoI fragment for C-terminal tagged fusion	tgtcgatcgccATGGCCGAGAATGT	tcactcgagccgagagaaacGTGTATGTCTAGTGTACT	Hybridisation sequence for EP300 (uppercase) in frame with restriction sites and 3-bp leader sequence (lowercase)
PvuI-EP300-XhoI_Short	TGTCGATCGCCATGGC	ACACTCGAGCCGAGAGAAA	For PCR amplification of PvuI-EP300-XhoI fragment
EP300(729–2129)	GATATTACTCAGGATCTTCG	TTTACAGTCTTCCACTTTAG	For colony PCR and detection of EP300 gene
EP300(2152–3412)	CCTGGATTAGGTTTGATAAA	GATCCTGAGTAATATCTTCG	For colony PCR and detection of EP300 gene
T7	TAATACGACTCACTATAGGG		Sanger Sequencing
T7term		CTAGTTATTGCTCAGCGGT	Sanger Sequencing
M13uni-21	TGTAAAACGACGGCCAGT		Sanger Sequencing
M13rev-29		CAGGAAACAGCTATGACC	Sanger Sequencing
p300-FOR-1558	TGGAGGAATGCCCAACATGG		Sanger Sequencing
p300-FOR-2653	TGCAGGCATGGTTCCAGTTTC		Sanger Sequencing
p300-REV-3058		CATTTGTGCTTGAGACACTGGAG	Sanger Sequencing
p300-FOR-3761	AGTACTTCAGCTACCCAGTC		Sanger Sequencing
p300-REV-4168		TCTGCCACAACAGTATCCAAGG	Sanger Sequencing
p300-FOR-4860	ACCTCGATAGTGTTCATTTCTTCC		Sanger Sequencing

p300-REV-5308		TTTGCTGTCTCCCT TGGTCACATC	Sanger Sequencing
p300-FOR-5964	TGCAGCATACCAAG GGTTGCAAAC		Sanger Sequencing
p300-REV-6482		TCTCCGCTGCTCTC TGAATC	Sanger Sequencing

6.1.9 Plasmid constructs, vectors, and bacterial cell lines

Table 6.11: Details of plasmid constructs, vectors and the transformed cell lines used in this study.

Name	Vector	Transformed cell lines	Source
6xHis-TEV-CREBBP^{BRD}	pNIC28-Bsa4	Mach1, BL21(DE3)	This was a gift from Nicola Burgess-Brown (Addgene plasmid # 38977)
6xHis-TEV-EP300^{BRD}	pNIC28-Bsa4	Mach1, BL21(DE3)	This was a gift from Nicola Burgess-Brown (Addgene plasmid # 39018)
1245 pCMVb EP300	pCMVβ	DH5α	This was a gift from William Sellers (Addgene plasmid # 10717))
GST-Hsp90^{NTD}	pGEX-4T3	DH5α	This was a gift from William Sessa (Addgene plasmid # 22481)
6xHis-HSP90AA1	pT7C	DH5α	This was a gift from Jeff Kuret (Addgene plasmid # 177658)
6xHis-HSP90AB1	pT7C	DH5α, Rosetta 2(DE3)	This was a gift from Jeff Kuret (Addgene plasmid # 177659)
HT-HSP90AA1	pFN21A	DH5α	Promega (Cat. # FHC25301)
HT-HSP90AB1	pFN21A	DH5α	Promega (Cat. # FHC01815)
CREBBP^{BRD}-NL	pFC32K	DH5α	Promega (non-catalogue item)
CREBBP^{FL}-NL	pFC32K	DH5α	Promega (non-catalogue item)
EP300^{FL}-NL	pFC32K	DH5α	This work
pDONR221	pDONR221	-	Life Technologies (Cat. # 12536017)
pENTR_EP300	pENTR221	DH5α	This work
pDEST_NL	pDEST_NL	-	Prof. Kilian Huber*
pEXP_NL-EP300	pEXP_NL	DH5α, Stbl3	This work

*University of Oxford

Table 6.12 Names and specifications of chemically competent *E. coli* used in this study.

Name	Uses	Supplier	Catalogue Number
Mach1	Plasmid amplification	Invitrogen (Life Technologies)	C862003
DH5α	Plasmid amplification	NEB	C2987H
BL21(DE3)	Protein expression	Agilent Technologies	230132
Rosetta 2(DE3)	Protein expression	Novagen (Sigma Aldrich)	71400-3
Stbl3	Plasmid amplification	Invitrogen (Life Technologies)	C737303

6.2 Biology Methods

6.2.1 Molecular cloning

6.2.1.1 Transformation of *E. coli*

Chemically competent *E. coli* were thawed on ice for at least 30 min before the addition of plasmid (1–100 ng). The tube was mixed by gently flicking and then incubated on ice for 30 min. Competent bacteria were heat shocked by placing the tube in a 42 ºC water bath for 30 s and then placed back on ice for 5 min before the addition of ambient temperature SOC media (250 µL). Transformed *E. coli* were outgrown by incubating at 37 ºC in a shaking incubator at 225 rpm to develop antibiotic resistance and then 50 µL and 150 µL portions were spread onto 10 cm LB agar plates in duplicate containing the appropriate antibiotic. The plates were inverted and incubated at 37 ºC overnight before visible colonies formed and were stored at 4 ºC.

6.2.1.2 Plasmid amplification and purification

Clones received as an agar stab were streaked onto 10 cm LB agar plates in duplicate containing appropriate antibiotics. Transformation colonies were selected and isolated from LB agar plates with a sterile pipette tip and used to inoculate LB medium (5 mL) supplemented with antibiotics. The culture was incubated at 37 ºC in a shaking incubator overnight at 225 rpm before harvesting by centrifugation (5,000 *g*, 5 min, 4 ºC). For plasmid DNA purification, all buffers and materials were from QIAGEN Plasmid Mini Kit (QIAGEN) or GeneJET Plasmid Miniprep Kit (Thermo Scientific). Briefly, the bacterial cell pellet was resuspended in a buffer supplemented with RNAse A (250 µL) followed by addition of a lysis buffer (250 µL). The lysate was gently mixed by inverting (5 times) and incubated at room temperature for 3 min. A neutralisation buffer (350 µL) was then added, and the lysate was mixed by inversion (5 times). The mixture was then centrifuged (17,000 *g*, 15 min, 4 ºC) to clear insoluble debris and the supernatant (800 µL) was passed through a spin column by centrifugation (17,000 *g*, 1 min). The spin column was then washed with buffer PB (500 µL, QIAGEN Plasmid Mini Kit only) and buffer PE (750 µL), each followed by

centrifugation (17,000 *g*, 1 min). The spin column was then centrifuged again (17,000 *g*, 1 min) before it was transferred to a clean micro-centrifuge tube and DEPC-treated water (50 µL) was added to elute DNA. The spin column was then left to equilibrate for 1 min, before centrifugation (17,000 *g*, 1 min) to collect eluted DNA which is then stored at –20 ºC.

6.2.1.3 Preparation of glycerol stocks and cryopreservation of bacterial cell lines

Glycerol stocks of transformed *E. coli* were prepared from an aliquot of confluent culture in LB medium (0.5 mL), which was mixed with sterile 50% (*v/v*) glycerol solution (0.5 mL) and transferred to a 1.5 mL cryovial before freezing and storing at –80 ºC.

6.2.1.4 Gel electrophoresis

DNA samples were analysed by gel electrophoresis on 0.6–1% agarose gels. Gels were prepared by addition of agarose to TAE buffer (prepared from a 50× stock solution) and heated by microwave irradiation until a homogenous mixture was achieved. The molten gel was allowed to cool to *c.* 50 ºC before addition of ethidium bromide (0.5 µg mL^{-1} final concentration) and then cast in a suitable gel tray with comb in place. Samples were prepared by addition of 6× gel loading dye (NEB) and loaded into the gel with Quick-load® 1 kb Plus DNA Ladder (NEB) as reference. Gels were run in TAE buffer at 150 – 200 V until sufficient separation of the DNA fragments had been achieved. Gels were visualised on a transilluminator imaging system (BioRad ChemiDoc XRS+).

6.2.1.5 Polymerase Chain Reaction (PCR)

Q5 High-Fidelity Master-mix (NEB) was used according to the manufacturer's protocol. Briefly, reactions (50 µL) comprised: Q5 High-fidelity Master Mix (25 µL), forward and reverse primers (2 × 2.5 µL, 10 µM), template DNA (1.0 µL, 1 ng $µL^{-1}$), DEPC-treated water (19 µL). All reaction components were added to 0.2 mL PCR tubes on ice, before transferred quickly to a thermocycler preheated to the denaturation temperature (98 ºC). The thermocycler method is outlined in **Table 6.13**.

Table 6.13: Thermocycling conditions for PCR of long products (>6 kb)

Step	Temperature	Time
Initial Denaturation	98 ºC	30 s
30 cycles	98 ºC	10 s
	PCR annealing temperature as determined using the NEB Tm calculator tool	15 s
	72 ºC	20 s kb^{-1}
Final extension	72 ºC	2 min
Hold	4 ºC	-

6.2.1.6 Gateway® cloning

PCR was used to generate suitable DNA fragments for a Gateway® BP recombination reaction. Primers were designed to append *att*B1 sites onto 5' and 3' ends of the EP300 gene, and their sequences are outlined in **Table 6.10**.

PCR products were purified by addition of TE buffer (150 µL) and 30% PEG 8000 / 30 mM $MgCl_2$ (100 µL). The mixture was mixed by vortex and immediately centrifuged (10,000 *g*, 15 min, rt) before the supernatant was aspirated and the pellet resuspended in TE buffer (10 µL). The *att*B-PCR product was confirmed by gel electrophoresis. An entry clone was generated using Gateway® BP Clonase™ II Enzyme Mix (Invitrogen) for the recombination reaction according to the manufacturer's protocol. Briefly, reactions (10 µL) comprised: *att*B-PCR product (7 µL 30 ng μL^{-1}), pDONR221 vector (1 µL, 150 ng μL^{-1}), and BP Clonase™ II enzyme mix (2 µL). Reactions were mixed by vortex (2 × 2 s) and then incubated at ambient temperature for 2 h. The reactions were quenched by addition of Proteinase K solution (1 µL), mixed by vortex, and then incubated at 37 ºC for 10 min. The BP recombination reaction product (1 µL) was used to transform DH5α chemically competent *E. coli* as previously described. Clones were selected and the plasmid amplified and purified as previously described. Clones were identified as containing the EP300 gene by restriction mapping as described below and validated by sequencing as described below. To generate an expression plasmid construct, the Gateway® LR recombination reaction was performed using Gateway® LR Clonase™ II Enzyme Mix (Invitrogen) according to the manufacturer's protocol. Briefly, reactions (10 µL) comprised: pENTR_EP300 (1 µL 150 ng μL^{-1}), pDEST_NL vector (2 µL, 75 ng μL^{-1}), and LR Clonase™ II enzyme mix (1 µL).

Reactions solutions were mixed by vortex (2 × 2 s) and then incubated at ambient temperature for 2 h. The reactions were quenched by addition of Proteinase K solution (1 µL), mixed by vortex, and then incubated at 37 ºC for 10 min. The LR recombination reaction product (1 µL) was used to transform DH5α chemically competent *E. coli* as previously described.

6.2.1.7 Restriction enzyme cloning

PCR was used generate suitable DNA fragments with compatible restriction sites for insertion into a destination vector. Primers were designed to append PvuI and XhoI restriction sites onto 5' and 3' ends of the EP300 gene respectively, and their sequences are outlined in **Table 6.10**. To increase yield of the PCR product, a second round of PCR was performed on the initial crude PCR product, using truncated primers (**Table 6.10**: PvuI-EP300-XhoI_Short) with a more favourable annealing temperature.

PCR products were purified using the Monarch® PCR & DNA Clean-up Kit (NEB; Cat. # T1030S) according to the manufacturer's instructions. Briefly, the reaction mixture (50 µL) was diluted with Binding Buffer (2:1, 100 µL) and loaded onto a spin column and centrifuged (16,000 *g*, 1 min). The column was then washed twice with Wash buffer (2 × 200 µL) with centrifugation (16,000 *g*, 1 min) between additions. The spin column was then centrifuged again (16,000 *g*, 1 min) before it was transferred to a clean micro-centrifuge tube and DEPC-treated water (10 µL) was added to elute DNA. The spin column was then left to equilibrate for 1 min, before centrifugation (16,000 *g*, 1 min) to collect eluted DNA.

The purified PCR product and pFC32K_CREBBP^{FL}-NL plasmid construct were subjected to double digestion with PvuI-HF and XhoI restriction endonucleases. DNA (2 µg) was mixed with 10× rCutSmart buffer (5 µL, NEB), diluted with DEPC-treated water to 48 µL, before addition of restriction endonucleases (each: 20 units, 1 µL). The reaction solution was briefly mixed by vortex and then incubated at 37 ºC for 1 h. The DNA fragments were purified by gel electrophoresis as previously described, using a predicted digestion pattern to identify the relevant bands, followed by band excision and extraction using the Monarch®

DNA Gel Extraction Kit according to the manufacturer's instructions. Briefly, the agarose gel was visualised on a transilluminator, and bands excised with a scalpel and transferred to a pre-weighed microcentrifuge tube. Gel was dissolved in gel dissolving buffer (4 µL per 1 mg of agarose gel slice) at 50 ºC until the gel was completely dissolved (*c.* 10 min). The mixture was loaded onto a spin column and centrifuged (16,000 *g*, 1 min). The column was then washed twice with wash buffer (2 × 200 µL) with centrifugation (16,000 *g*, 1 min) between additions. The spin column was then centrifuged again (16,000 *g*, 1 min) before it was transferred to a clean micro-centrifuge tube and DEPC-treated water (10 µL) was added to elute DNA. The spin column was then left to equilibrate for 1 min, before centrifugation (16,000 *g*, 1 min) to collect eluted DNA. The purified DNA fragments were ligated using T4 DNA ligase (NEB; M0202S) according to the manufacturer's protocol. Briefly, in a microcentrifuge tube, plasmid vector (50 ng) and DNA insert (1:3 molar ratio) were mixed with T4 DNA Ligase Buffer (2 µL), T4 DNA Ligase (1 µL) and diluted with DEPC-treated to a final volume of 20 µL. The reaction was incubated at ambient temperature for 1 h before heat inactivated at 65 ºC for 10 min. The ligation reaction product (1 µL) was used to transform DH5α chemically competent *E. coli* as previously described. Clones were selected and identified as containing the EP300 gene by colony PCR as described below before plasmid amplification, purification, and validation by sequencing, as described below.

6.2.1.8 Colony PCR

To determine incorporation of the DNA insert, transformation colonies were selected and isolated from LB agar plates with a sterile pipette tip and mixed with sterile DEPC-treated water (20 µL). PCR was then performed as previously described, with insert specific primers and slight modification to the protocol: colony cell suspensions (1 µL) were used in place of template DNA, and quantities of all components were halved to give a final reaction volume of 25 µL. Additionally, PCR was performed on the vector without insert and the original plasmid containing the cloned insert, as negative and positive controls respectively.

The PCR products were analysed by gel electrophoresis with the presence of a band indicating presence of the insert DNA.

6.2.1.9 Restriction mapping

Purified plasmids from recombination reactions were subject to restriction digest and analysed using gel electrophoresis to confirm the inclusion of the EP300 gene. Briefly, DNA samples (<1 µg) were mixed with 10× rCutSmart Buffer (1 µL) and NcoI-HF (0.2 µL) and diluted to a final reaction volume of 10 µL with DEPC treated water. Reactions were then incubated at 37 ºC for 15 – 30 min before addition of 6× gel loading dye (NEB) and analysed using gel electrophoresis, as previously described.

6.2.1.10 Sequencing

Sanger sequencing of plasmids was performed by Eurofins Genomics using the primers outlined in **Table 6.10**. Oxford Nanopore sequencing of plasmids was performed by Source BioScience. Plasmid samples were prepared at 30 ng μL^{-1} by approximating the DNA concentration from gel electrophoresis and measuring the supercoiled band intensity against to the reference standard amounts in the ladder.

6.2.2 Recombinant protein expression in *E. coli*

6.2.2.1 Induced expression trials

Single transformation colonies were selected and isolated from LB agar plates with a sterile pipette tip and used to inoculate LB medium (25 mL) supplemented with an appropriate antibiotic. The culture was incubated at 37 ºC in a shaking incubator overnight at 200 rpm before sub-culturing (1:100) into LB medium (250 mL) supplemented with an appropriate antibiotic and further cultured at 37 ºC, 200 rpm until mid-log phase of growth, as determined by a measured OD_{600} value of 0.6. At this point, the culture was split into 10 mL aliquots and transferred into duplicate 50 mL centrifuge tubes pre-dispensed with IPTG to afford a final concentration of 0, 1, 0.5, 0.25, or 0.125 mM. The duplicate cultures were then divided into groups and placed in a shaker incubator at 180 rpm, equilibrated at 25 or 16 ºC. The cultures were harvested after 18 h by centrifugation (5000 *g*, 15 min, 4 ºC), the

supernatant was aspirated and pellets were resuspended in lysis buffer (500 µL; 50 mM HEPES pH 7.6, 500 mM NaCl, 10% glycerol, supplemented with SigmaFAST™ protease inhibitor cocktail tablet EDTA free (Sigma Aldrich) and 10 mM 2-mercaptoethanol immediately prior), snap frozen and stored at –80 ºC until analysis.

Lysates were thawed on ice and lysis was completed by sonication (microtip probe, 10% amplitude, 5 s burst/10 s pause on ice, for 3 cycles) before lysates were cleared by centrifugation (14,000 *g*, 30 min, 4 ºC). The soluble component was then analysed using SDS-PAGE followed by staining with Coomassie protein stain (InstantBlue, AbCam).

6.2.2.2 Batch-scale induced expression

A general procedure was followed with specific conditions for each expressed fusion protein outlined in **Table 6.14**. Single transformation colonies were selected and isolated from LB agar plates with a sterile pipette tip and used to inoculate LB medium (100 mL) supplemented with an appropriate antibiotic. The culture was incubated at 37 ºC in a shaking incubator overnight at 200 rpm before sub-culturing (1:100) into LB medium (*n* × 1,000 mL in Tunair baffled shake flasks). The culture was incubated at 37 ºC in a shaking incubator at 180 rpm until the culture entered the mid-log phase of growth as determined by the measured OD_{600} value. Only then was the incubation temperature reduced and protein expression induced by addition of isopropyl-1-thio-β-D-galactopyranoside (IPTG) from a 1000× stock solution. After induction, the culture was incubated in a shaking incubator at 180 rpm overnight before harvesting by centrifugation (5000 *g*, 15 min, 4 ºC). Cell pellets were transferred to 50 mL falcon tubes (*c.* 20 g per tube) and stored at –80 ºC.

Table 6.14: Details of conditions used in induction of recombinant protein expression used in this study.

Fusion protein	Strain of *E. coli*	Antibiotic	OD_{600} at induction	Final [IPTG] (mM)	Expression temperature (ºC)
6xHis-TEV-EP300^{BRD}	BL21(DE3)	Kanamycin (50 µg mL^{-1})	0.5	0.1	16
6xHis-TEV-CREBBP^{BRD*}	BL21(DE3)	Kanamycin (50 µg mL^{-1})	0.5	0.1	16
GST-Hsp90α^{NTD}	Rosetta 2 (DE3)	Ampicillin (100 µg mL^{-1}) Chloramphenicol (25 µg mL^{-1})	0.7	0.5	25

*Expression of 6xHis-TEV-CREBBP^{BRD} was performed in collaboration with Alistair Boyd and Katrina Andrews.

6.2.3 Recombinant protein purification

All buffers were filtered (0.2 µm porosity) under vacuum before use. Gel filtration buffers were thoroughly de-gassed by stirring under a vacuum for approximately 30 min before use. Buffers were stored at 4 ºC.

The purified recombinant protein was characterised by intact mass spectrometry using a Waters Xevo G2-S QTof mass spectrometer and purity was evaluated using SDS-PAGE.

6.2.3.1 Purification of human 6xHis-p300^{BRD} and 6xHis-CREBBP^{BRD} fusion proteins:

The procedure was performed as previously described.[192] The bacteria pellet was re-suspended in lysis buffer (50 mM HEPES pH 7.6, 500 mM NaCl, 10% glycerol, supplemented with SigmaFAST™ protease inhibitor cocktail tablet EDTA free (Sigma Aldrich) and 10 mM 2-mercaptoethanol immediately prior to use) at a ratio of 100 mL per 20 g cell pellet. Cell lysis was completed by sonication on ice (35% amplitude, 5 s burst/10 s pause cycle for 15 min), and the DNA was removed by addition of polyethyleneimine [0.15% (*v/v*) final concentration] and incubated on ice for 30 min to allow precipitation. Lysate were cleared by centrifugation (30,000 *g*, 30 min, 4 ºC) and filtered (0.45 µm porosity) before it was applied to a Nickel affinity column (HisTrap™ HP 5 mL (Cytiva)) equilibrated with binding buffer (50 mM HEPES pH 7.6, 500 mM NaCl, 10% glycerol, 10 mM 2-mercaptoethanol) on an ÄKTA fast protein liquid chromatography (ÄKTA FPLC) system (GE Healthcare) at 4 ºC. The column was washed with 30 mL of binding buffer then 20 mL of binding buffer containing 30 mM imidazole. Proteins were eluted into 5 mL fractions using a 20 mL step elution method with imidazole in binding buffer (50, 100, 150, 250 mM, 500 mM imidazole). All fractions were collected and monitored by SDS-PAGE (Invitrogen NuPage Precast Gels, 4%–12% Bis-Tris in MES buffer). The desired eluted protein was concentrated using Spin-X® centrifugal concentrators (Corning) employing 5 kDa cut-offs (5 MWCO) and further purified by size exclusion chromatography (SEC) on a HiLoad 16/600 Superdex 75 pg gel filtration column (GE Healthcare) equilibrated with gel filtration

buffer (50 mM HEPES pH 7.6, 500 mM NaCl, 20 mM sodium citrate) on an ÄKTA FPLC at 4 ºC. Purified protein was concentrated to 10 mg/mL as before, using Spin-X® centrifugal concentrators, and aliquoted (100 µL) before flash frozen in liquid nitrogen and stored at −80 ºC.

6.2.3.2 Purification of human GST-Hsp90α$^{N(9–236}$ fusion protein:

The bacteria pellet was re-suspended in lysis buffer (50 mM HEPES pH 7.5, 500 mM NaCl, 10% glycerol, supplemented with SigmaFAST™ protease inhibitor cocktail tablet EDTA free (Sigma Aldrich) and 10 mM 2-mercaptoethanol immediately prior to use) at a ratio of 100 mL per 20 g cell pellet. Cell lysis was completed by sonication on ice (35% amplitude, 5 s burst/10 s pause cycle for 15 min), and the DNA was removed by addition of polyethyleneimine [0.15% (*v/v*) final concentration] and incubated on ice for 30 min to allow precipitation. Lysate were cleared by centrifugation (50,000 *g*, 30 min, 4 ºC) and filtered (0.45 µm porosity) before it was applied to a glutathione sepharose column (GSTrapTM HP 5 mL (Cytiva)) at 1 mL min^{-1}, pre-equilibrated with binding buffer (50 mM HEPES pH 7.5, 500 mM NaCl, 10% glycerol, 10 mM 2-mercaptoethanol) on an ÄKTA fast protein liquid chromatography (ÄKTA FPLC) system (GE Healthcare) at 4 ºC. The flow-through was retained and the column was washed with 30 mL of binding buffer then eluted in 5 mL fractions with 50 mL of binding buffer containing 10 mM reduced glutathione at 5 mL min^{-1}. All fractions were collected and monitored by SDS-PAGE (Invitrogen NuPage Precast Gels, 4%–12% Bis-Tris in MES buffer). Analysis of input and flow-through revealed binding saturation of the GSTrap so the flow-through was resubjected to a second round of affinity chromatography performed as before. The desired eluted protein was concentrated using Pierce™ centrifugal concentrators (Life Technologies) employing 30 kDa cut-offs (30 MWCO) and further purified by size exclusion chromatography (SEC) on a HiLoad 16/600 Superdex 200 pg gel filtration column (GE Healthcare) equilibrated with gel filtration buffer (10 mM HEPES pH 7.5, 250 mM NaCl, 10 mM TCEP) on an ÄKTA FPLC at 4 ºC. Purified protein was concentrated to 15 mg/mL as before, using Pierce™ centrifugal

concentrators, and aliquoted (100 µL) before flash frozen in liquid nitrogen and stored at −80 ºC.

6.2.4 Recombinant protein concentration measurement

The concentration of recombinant protein solutions was determined by measurement of the absorbance of the mixture at a wavelength of 280 nm using a Thermo Scientific Nanodrop, with the Protein A280 Program. From this measurement, the approximate concentration of protein samples was determined following the Beer-Lambert Law:

$$c = \frac{A}{\varepsilon l}$$

Where c is the concentration of the protein (M), A is the measured absorbance (AU), l is the path length (set to 1.0 cm), and ε is the molar extinction coefficient of the protein (M^{-1} cm^{-1}). Each measurement of absorbance was taken a minimum of three times, from which the average is used. Molar extinction coefficients for proteins used in this study are outlined in **Table 6.15**, and were estimated from the protein primary sequence, using the Expasy ProtParam tool from the Swiss Institute of Bioinformatics.[225]

Table 6.15 Names and molar extinction coefficients of recombinant proteins used in this study

Name	**Extinction coefficient (M^{-1} cm^{-1})**
6xHis-CBP^{BRD}	26930
6xHis-$p300^{BRD}$	28420
GST-$Hsp90^{NTD}$	58790

6.2.5 AlphaScreen

Assay buffer (25 mM HEPES pH 7.5, 100 mM NaCl, 0.05% CHAPS, and 1 mg mL^{-1} BSA.) was freshly prepared on the day of experiment by dilution from a 5× stock solution, supplemented with BSA, pH adjusted, filter sterilised (0.22 µm porosity), and stored at 4 ºC until use. Assays were performed at room temperature and plates sealed with transparent film between addition of reagents to prevent well contamination and evaporation. Initially, a concentration series of compounds was prepared in a 384-well plate by dilution from a 1 mM stock into assay buffer supplemented with 1% DMSO, and then serially diluted 1:2 (30 µL per well). From this plate, compounds solutions were transferred in triplicate (3 × 7 µL per well) to an OptiPlate-384 well microplate (PerkinElmer) containing recombinant

GST-Hsp90^{NTD} and 6xHis-p300^{BRD} (6 µL per well) to give a final assay protein concentration of 10 nM. The assay plate was incubated on an orbital plate shaker at 300 rpm for 1 h, before addition of glutathione Alpha donor beads and nickel chelate AlphaScreen acceptor beads (7 µL per well, 10 µg mL-1 final assay concentration). Plates were covered with aluminium foil and incubated in the dark for 60 min. Plates were read on a BMG Labtech PHERAstar FS microplate reader with an excitation wavelength of 680 nm and emission wavelength of 570 nm. Within each read there was a settling time of 0.1 s, an excitation time of 0.3 s, integration start at 0.34 s, and an integration time of 0.6 s. Intensity values were plotted using Graphpad Prism. For competition experiments, AcDCs were kept constant at a final concentration of 20 nM and either inobrodib or BIIB021 were serially diluted 1:2 (30 µL per well) into assay buffer supplemented with 1% DMSO before transferring in triplicate (3 × 7 µL per well) as before.

6.2.6 Isothermal titration calorimetry

Assay buffer (50 mM HEPES pH 7.4, 150 mM NaCl and 0.5% *v/w* DMSO) was prepared, filtered (0.2 µm porosity), de-gassed by stirring under vacuum for 15 min, and stored at 4 ºC. Recombinant proteins were dialysed against the assay buffer (400 mL) using a Slide-A-Lyzer® MINI Dialysis Device (2000 MWCO; Life Technologies Ltd.) for a minimum of 6 h at 4 ºC, followed by a second round for 18 h at 4 ºC. The dialysed protein was then transferred to a microcentrifuge tube, allowed to warm to ambient temperature and centrifuged to remove aggregates (3 min, 17,000 *g*, 20 ºC). Protein concentrations were then measured and adjusted with assay buffer, as necessary. Small molecule ligands were dissolved in DMSO to give stock solutions (10 mM) and diluted appropriately using dialysis buffer and DMSO, as necessary. All calorimetry experiments were performed on a MicroCal PEAQ-ITC (Malvern) and analysed with MicroCal PEAQ-ITC Analysis Software (Malvern), using a single binding site model. The solution in the cell was stirred at 750 rpm, reference power at 5 µcal s^{-1} and temperature set to 25 ºC. After an initial delay of 60 s, 20 × 2 µL injections (first injection of 0.4 µL) were performed, with 150 s intervals between injections.

Heat of dilutions were measured under the same conditions and subtracted for analysis. Small molecule solutions in the calorimeter cell (300 µL, 20 µM) were titrated with the protein solutions in the syringe (70 µL, 160 µM).

6.2.7 Routine Tissue Culture

6.2.7.1 Cell culture conditions

All cell lines were maintained in a 5% CO_2 humidified incubator at 37 ºC. Aseptic technique was used to handle cultures, with use of a laminar flow cabinet to prevent contamination. Cell lines were cultured in DMEM or RPMI-1640 media as outlined in **Table 6.9**, supplemented with 10% FBS and 100 U/mL penicillin-streptomycin, hence referred to as complete media. For adherent cell lines, cells were passaged when confluency reached approximately 80 – 90%: the culture medium was aspirated, and the cell monolayer was washed with PBS, before cells were dissociated with trypsin-EDTA solution. The action of trypsin-EDTA solution was quenched by addition of twice the volume of pre-warmed complete media and cells were thoroughly resuspended before sub-culturing. For suspension cell lines, cells were passaged routinely with confluency assessed by culture turbidity and regular counting: cells were collected by centrifugation (300 *g*, 3 min), before the culture medium was aspirated, and the cell pellet resuspended in pre-warmed complete media. Cell density and viability were determined by dilution of an aliquot of cell suspension with an equal volume of Trypan Blue solution, and manually counted with a haemocytometer.

6.2.7.2 Mycoplasma testing

Cell cultures were routinely tested for mycoplasma contamination using either the MycoAlert® Mycoplasma Detection Kit (Lonza) or MycoStrip™ Mycoplasma Detection Kit (InvivoGen). Cells were cultured in media without supplementation with penicillin-streptomycin for at least 48 h before an aliquot (2 mL) of culture media was sampled. The procedures were performed according to the manufacturer's instructions, and briefly outlined below.

For the MycoAlert® Mycoplasma Detection Kit: culture media was centrifuged (5 min, 200 *g*) and 100 µL of the supernatant was transferred to 96-well plate. The MycoAlert® reagent and substrate were reconstituted in assay buffer, aliquoted and frozen upon arrival, and allowed to equilibrate to ambient temperature at the point of performing the assay. The MycoAlert® reagent (100 µL) was added to the sample and the luminescence was measured after 5 min on a BMG POLARstar Omega plate-reader. The MycoAlert® substrate (100 µL) was then added to the sample and the luminescence was re-measured. The presence of mycoplasma contamination was indicated by a ratio of the luminescence measurements of >1.2, while a negative result had a ratio of <0.9, and samples with a measurement between these values were retested after a further 24 h incubation.

For the MycoStrip™ Mycoplasma Detection Kit: culture media was centrifuged (5 min, 13,000 *g*) and the supernatant discarded, while ensuring less than 50 µL of supernatant remained. The pellet was resuspended with 500 µL of sterile PBS. In a microcentrifuge tube, 5 µL of reaction buffer, 15 µL of reaction mix and 5 µL of prepared sample (or sterile PBS as a negative control) were combined and incubated at 65 ºC for 40 min. Migration buffer (200 µL) was added to stop the reaction and 100 µL of the processed sample was loaded onto a lateral flow device. The presence of mycoplasma contamination was indicated by the presence of two colorimetric bands, while a negative result was indicated by a single control band.

6.2.7.3 Cryopreservation of cell lines

Cells were grown to 70% confluency before dissociating with Trypsin-EDTA solution as previously described. The cell suspension was collected by centrifugation (300 *g*, 5 min) and resuspended in 1 mL of freezing media comprising FBS supplemented with 10% *v/v* DMSO. The cell suspension was transferred to a 1.5 mL cryovial and placed in a Mr. Frosty™ freezing container (Nalgene) and this was placed in a –80 ºC freezer overnight. Once frozen, the cells were transferred to a liquid nitrogen storage tank for long-term cryopreservation.

When required, cells were removed from liquid nitrogen, transported on dry ice, and rapidly thawed in a 37 ºC water bath. The cell suspension was transferred to 10 mL of pre-warmed complete media and collected by centrifugation (300 *g*, 5 min). The supernatant was then removed, and the cell pellet was resuspended in fresh complete media. The cell suspension was transferred to a culture flask and incubated under normal conditions.

6.2.8 Compound treatments of cells

Cells were treated with the indicated compounds at the indicated concentrations by dilution of the compound in media from a stock solution dissolved in DMSO, such that the final overall DMSO concentration did not exceed 1% *v/v*. Treatment with DMSO alone was included in all experiments as a negative vehicle control. For adherent cultures, the media was aspirated and replaced with fresh complete media containing the test compound or DMSO alone. For suspension cultures, the medium was collected by tilting each dish and the drug was added directly from a 100× stock solution in DMSO, followed by mixing by swirling the dish.

6.2.9 Hypoxia treatments

Hypoxia treatment was carried out using a Bactron II anaerobic chamber (Shel Lab®), or a Bactron EZ anaerobic chamber (Shel Lab®). These chambers are under a positive pressure of an anaerobic nitrogen gas mixture. No oxygen is supplied to this chamber; however, it is not possible to guarantee 0% oxygen due to potential leaks. It is estimated that the oxygen concentration at a given time is no higher than 0.1%. Therefore, the oxygen tension for experiments carried out in these chambers will be referred to as <0.1% O_2 throughout the text. For experiments performed in the anaerobic chambers, glass dishes were used for plating cells.

6.2.10 Western Blotting

Cells were washed twice with PBS, scrapped in PBS and pelleted by centrifugation (300 *g,* 3 min, 4 ºC) before the supernatant was discarded and the cell pellet was resuspended in UTB lysis buffer (approximately 10 times the volume of the packed cell pellet). Lysis was

completed by one freeze-thaw cycle before sonication for 20 s twice with 10 s on ice in between. Insoluble debris was cleared by centrifugation (17,000 *g*, 10 min, 4 ºC) and the protein concentration of the supernatant was either determined by Bradford DC assay or approximated by measuring the absorbance at 280 nm using a Thermo Scientific Nanodrop. Samples were prepared by mixing 10 – 100 ug of protein with 2× Laemmli buffer and heated at 100 ºC for 5 min. For SDS-PAGE, 3 µL of protein ladder (BioRad, Precision Plus Protein Standards) was loaded for indication of molecular weight of the bands. Samples were electrophoresed in tris-glycine running buffer on 4-20% pre-cast gels (BioRad, Mini-PROTEAN TGX^{TM}) at 150 V for approximately 60 min, until sufficient separation of the protein ladder had been achieved. Gels were electro-transferred onto a nitrocellulose membrane using a Transblot-Turbo machine (BioRad) for 7–10 min in transfer buffer. The membranes were placed in blocking buffer for 1 h before washing with TBST. Membranes were probed with primary antibody (diluted in TBST) with constant agitation overnight at 4 ºC or up to 4 h at ambient temperature. Primary antibodies used are listed in **Table 6.1**. Membranes were washed 3 times with TBST for 10 min each time before probing with secondary antibodies (diluted to 1:10,000 in TBST) for 1 h at room temperature with constant agitation. Secondary antibodies used are listed in **Table 6.2**. The membranes were then washed three times with TBST buffer for 10 min each time before the blots were developed using the Odyssey Infrared imaging system.

6.2.11 Cell fractionation

Cells were seeded at 2×10^6 per 10 cm dish and allowed to settle overnight before treatment. At the point of harvest, cells were washed twice with PBS, scrapped in PBS, transferred to a microcentrifuge tube, and pelleted by centrifugation (300 *g,* 3 min, 4 ºC). All steps going forward were performed on ice. The supernatant was discarded, and the cell pellet was resuspended in cytoplasmic lysis buffer (approximately two times the packed cell pellet volume). The cell suspension was then lysed by addition of 1% (*v/v*) Triton X-100 solution (1:100 cell suspension volume) to afford a final Triton X-100 concentration of 0.01%

and mixed carefully by tapping the microcentrifuge tube. The mixture was incubated on ice for 5 min before the nuclei were collected by centrifugation (500 *g*, 3 min, 4 ºC) and the supernatant was transferred to a separate microcentrifuge tube, as the cytoplasmic fraction. The nuclei were washed two times by resuspending in cytoplasmic lysis buffer without detergent (approximately two times the original packed cell volume), collection by centrifugation (500 *g*, 3 min, 4 ºC), and discarding the supernatant. The nuclei were finally resuspended in hypotonic nuclear lysis buffer (approximately an equal volume of the packed nuclear pellet volume) and incubated in ice for 10 min. Lysis was completed by sonication for 20 s twice with 10 s intervals on ice. All lysate fractions were further cleared of insoluble debris by centrifugation (17000 *g*, 10 min, 4 ºC) before analysis.

6.2.12 Immunoprecipitation (IP)

6.2.12.1 Co-IP between Hsp90α/β and CBP

Cells were seeded 1×10^7 per 15 cm dish and allowed to settle overnight, the following day, media was replaced and supplemented with test compounds (0.5 μM) or DMSO (0.5% *w/v*) as vehicle control. Cells were placed in an incubator for 6 h before culture medium was aspirated and cells were washed with ice-cold PBS (2 × 5 mL per dish), scraped in ice-cold PBS (2 mL) and pelleted by centrifugation (500 *g*, 3 min, 4 ºC). Cell pellets were re-suspended in IP lysis buffer (approximately 10× packed cell pellet volume) Lysis was completed by sonication before cell debris was removed by centrifugation (17,000 *g*, 10 min, 4 ºC) to yield the soluble lysate supernatant which was transferred to a new microcentrifuge tube. Lysate protein concentration was determined by DC Bradford assay and normalised to 4 mg mL^{-1}. To 2 mg aliquots (500 μL) were taken 5% (25 μL) which was prepared for Western blotting as previously described and retained as input control samples, while to the remaining aliquoted samples were added 5 μg of primary antibody or 5 μg of IgG isotype control and the mixtures were incubated on an end-over-end rotator at 4 ºC for 2 h. Dynabeads™ Protein A beads (50 μL per sample) were washed with IP lysis buffer (2 × 500 μL) by dispensing into a microcentrifuge tube which was placed against a

magnet to separate the beads from the supernatant. Following incubation of the antibody-sample mixtures, the lysis buffer was removed from the beads and the samples were transferred to the tubes containing the beads. The bead-antibody-sample mixtures were returned to the end-over-end rotator and incubated at 4 ºC overnight. Samples were placed on a magnetic rack and the supernatant was aspirated, the beads were washed with cold lysis buffer (2 × 100 µL), by gently pipetting the beads in lysis buffer and reapplying to the magnetic rack. For the final wash, the beads were transferred to a clean microcentrifuge tube, the wash lysis buffer was aspirated, and the beads were resuspended in 2× Laemmli buffer (40 µL) and boiled for 5 min at 100 ºC with agitation. The sample is finally placed against a magnetic rack and the supernatant was analysed by Western Blotting as previously described.

6.2.12.2 Cross-linking of antibodies to beads

Dynabeads™ Protein G beads (10 µL per sample) were washed with PBS (2 × 500 µL) by dispensing into a microcentrifuge tube which was placed against a magnet to separate the beads from the supernatant. The beads were finally resuspended in PBS and primary antibody was added (1 µg per sample) to give a final volume of 500 µL. The mixture was incubated at ambient temperature for 1 h on an end-over-end rotator to allow the antibody-bead conjugate to form. The beads were then washed with cross-linking reaction buffer (2 × 500 µL) and resuspended in cross-linking reaction buffer (400 µL) followed by addition of a freshly prepared 25 mM dimethyl pimelimidate dihydrochloride solution in cross-linking reaction buffer (100 µL, to give a final concentration 5 mM). The cross-linking reaction was then mixed on an end-over-end rotator at ambient temperature for 1 h before the reaction was quenched by washing the bead-antibody conjugates with cross-linking quenching buffer (500 µL) and then incubating in quenching buffer (500 µL) on an end-over-end rotator at ambient temperature for 1 h. To remove non-crosslinked antibody, the antibody-bead conjugates were washed with elution buffer (500 µL) and then incubated in elution buffer (500 µL) on an end-over-end rotator at ambient temperature for 30 min. Finally, the beads

were washed with cross-linked antibody-bead storage buffer (3 × 500 µL). The beads were either then used directly or stored at 4 ºC storage buffer (10 µL per sample) until use.

6.2.12.3 IP of Hsp90α for probing KAc

Cells were seeded at 2×10^6 per 10 cm dish and allowed to settle overnight. The following day, media was replaced and supplemented with test compounds or DMSO (0.5% *w/v*) as vehicle control. Cells were placed in an incubator before culture medium was aspirated and cells were washed with PBS (1 mL), scraped in PBS (1 mL), collected in a microcentrifuge tube and pelleted by centrifugation (500 *g*, 3 min, 4 ºC). The lysate was then prepared by cellular fractionation (as previously described), or as whole cell lysate by resuspending in RIPA buffer (approximately 10× packed cell pellet volume) or denaturing IP buffer (100 µL; 25 mM Tris pH 7.5, 150 mM NaCl, 2% SDS). For denaturing-IP, samples were immediately boiled at 95 ºC for 5 min and then diluted in immunoprecipitation lysis buffer (900 µL) to quench excess SDS. The lysate viscosity was reduced by sonication and cleared of debris by centrifugation (17,000 *g*, 10 min, 4 ºC) and the supernatant transferred to a clean microcentrifuge tube. Lysate protein concentration was determined by DC Bradford assay and normalised to 1 mg mL^{-1} with lysis buffer. To 500 µg aliquots (500 µL) were taken 5% (25 µL) which was prepared for Western blotting as previously described and retained as input control samples, while to the remaining aliquoted samples were added 1 µg of primary antibody or 1 µg of IgG isotype control pre-conjugated to Dynabeads™ Protein G beads. The mixtures were incubated on an end-over-end rotator at 4 ºC for 1 h, before the beads were washed with IP lysis buffer supplemented with TSA (10 µM) and Nicotinamide (20 mM) (3 × 100 µL), by gently pipetting the beads in lysis buffer and reapplying to the magnetic rack. For the final wash, the beads were transferred to a clean microcentrifuge tube, and the beads were resuspended in 2× Laemmli buffer (40 µL) and boiled for 5 min at 95 ºC with agitation. The sample is finally placed against a magnetic rack and the supernatant was analysed by Western blotting as previously described.

6.2.13 Chemical Acetylation of recombinant protein

Recombinant Hsp90α (abcam, ab48801) (2 µL, 1 µg µL^{-1}) was diluted with PBS (16 µL) in a microcentrifuge tube, followed by addition of freshly prepared acetic anhydride in MeOH (2 µL, 0–500 mM) to give a final reaction volume of 20 µL and protein concentration of 0.1 mg mL^{-1}. The reaction was mixed by vortex and incubated at 37 ºC for 1 h. The reaction was quenched by addition of 1 M ethanolamine solution (adjusted to pH 8.2 with HCl) (20 µL), mixed by vortex and incubated at 37 ºC for 1 h. The chemically acetylated recombinant protein was then analysed by Western blotting as previously described or used to spike immunoprecipitation samples as a standard.

6.2.14 NanoBRET

6.2.14.1 Transient transfection for NanoBRET experiments

Cells were seeded at 8×10^5 per well in 2 mL of media without antibiotic supplementation on a 6-well plate and allowed to settle for 4–6 h. For each well, DNA transfection mixture was prepared in a microcentrifuge tube by dilution of HaloTag acceptor (2 µg) and NanoLuc donor (0.02 µg) plasmid constructs in Opti-MEM®, no phenol red (100 µL) followed by addition of FuGENE® transfection reagent (Promega) (6 µL) and mixed by inverting the tube 10 times. The transfection mixture was incubated at ambient temperature for 30 min before it was dispensed onto cells by dropwise addition in a circular pattern across the well. The cells were incubated overnight (18 h) to allow protein expression to occur.

6.2.14.2 NanoBRET experiments for dose response of test compounds

Culture medium was aspirated and cells were detached with trypsin (0.5 mL per well) and resuspended in the assay media (Opti-MEM®, no phenol red, supplemented with 4% FBS) (2 mL per well). The cell density was measured and adjusted to 2×10^5 cells mL^{-1} by dilution in assay media before cells were divided into two pools, either treated with HaloTag® NanoBRET™ 618 ligand (100 nM final concentration), or DMSO control (0.1% final concentration). Cells were then plated in 384-well format (40 µL per well) with 22 wells containing cells treated with DMSO control, and all others treated with HaloTag®

NanoBRET™ 618 ligand. Plates were centrifuged (100 *g,* 5 s) before and after addition of test compounds or DMSO vehicle control (10 µL per well) from a 5× stock solution prepared in assay media supplemented with 4.5% DMSO, to afford a final assay DMSO concentration of 1%. Cells were incubated for 6 h before addition of NanoBRET™ Nano-Glo® substrate as a 6x stock solution in OptiMEM® (no phenol red) (10 µL). Within 10 min of addition, plates were centrifuged (100 *g,* 5 s), mixed and BRET was determined by measurement of donor [610 nm/low pass (LP)] and acceptor [460 nm/bandpass (BP) 80 nm] emission on a PheraSTAR FSX microplate reader. The milli-BRET (mBRET) ratio was determined according to the equation below, where $Acceptor_{Em}$ and $Donor_{Em}$ and the measured signal intensities from the 610 nm/low pass (LP) and 460 nm/bandpass (BP) 80 nm channels respectively.

$$\frac{Acceptor_{Em}}{Donor_{Em}} \times 1000 = Raw\ mBRET\ Ratio\ [mBU]$$

The measured mBRET was corrected by subtraction of the mBRET ratio from wells containing cells not treated with HaloTag® NanoBRET™ 618 ligand, according to equation below.

$$Raw\ mBRET\ Ratio - Mean\ mBRET\ Ratio\ (no\ ligand) = Corrected\ mBRET\ Ratio$$

To normalise signal between compounds and experiments, the mBRET ratio was divided by the mean value from wells containing cells treated with HaloTag® NanoBRET™ 618 ligand and then DMSO as compound vehicle control, according to the equation below.

$$\frac{Corrected\ mBRET\ Ratio_{Compound}}{Mean\ Corrected\ mBRET\ Ratio_{DMSO}} = Relative\ signal\ (normalised\ to\ DMSO)$$

6.2.15 Statistical analyses

Statistical analyses were carried out using Graphpad Prism or Microsoft Excel softwares. The standard error of mean ($s.e.m.$) was calculated using the following formula:

$$s.e.m. = \frac{S.D.}{\sqrt{n}}$$

Wherein $s.d.$ is the standard deviation, and n is the number of samples. Statistical significance was determined using unpaired two-tailed Student's *t* tests: *$p < 0.05$; **$p < 0.01$; ***$p < 0.001$; ****$p < 0.0001$.

6.3 Chemistry Experimental

6.3.1 Chemicals

All chemicals were purchased from the following list of suppliers: Alfa Aesar, Sigma Aldrich UK, Fluorochem, Chem Cruz, Thermo scientific, Fluka UK, Merck Millipore and Fisher Chemical. All small molecule compounds were of ≥95% purity, solvents were of at least reagent grade when performing reactions, HPLC grade or higher purity solvents were utilised for semi-preparative LC, HPLC and LC-MS. All reactions with non-aqueous solvents were performed in a flask under an argon atmosphere unless otherwise stated.

6.3.2 Anhydrous solvents

These include DMF, THF, Et_2O, CH_2Cl_2, MeCN, toluene and NEt_3; were dried by passing through a column of activated basic alumina according to Grubbs' procedure. These solvents were then left overnight on activated molecular sieves (3 Å) under an argon atmosphere. In the case of anhydrous DMSO, and MeOH, these were purchased from Sigma Aldrich UK in SureSeal^{TM} bottles and were used without further purification. Some solvents (particularly for cross coupling reactions) were degassed by sparging with argon for 15 min prior to use, or by three freeze-pump-thaw cycles, as indiciated.

6.3.3 NMR Spectroscopy

All solvents used for NMR spectroscopy were ≥99.8% deuterated and were purchased from Eurisotop or Sigma Aldrich UK. NMR data were processed using MestReNova 14.3.0 or Bruker Topspin 4.1.4 software.

6.3.4 ^{1}H NMR

Spectra were recorded using a Bruker AVIIIHD 400 nanobay (400 MHz) spectrometer, Bruker AVII500 (500 MHz) spectrometer with dual $^{13}C(^1H)$ cryoprobe, Bruker AVIIHD 500 (500MHz) spectrometer in the stated solvents as a reference for the internal deuterium lock or Bruker NEO 600 (600 MHz) spectrometer with broadband helium cryoprobe. The chemical shift for each signal is given as δ_H in units of parts per million (ppm) relative to tetramethylsilane (δ_c = 0.00 ppm) and the spectra were calibrated using the solvent peak(s)

and the known chemical shifts.[226] The coupling constants are determined by analysis using picked peaks on MestReNova version 14.3.0 software. ^{1}H NMR spectra are reported as follows: chemical shift (number of protons, multiplicity (s (singlet); br (broad singlet); d (doublet); t (triplet); q (quartet); m (multiplet) or combinations thereof), coupling constants *J* (to the nearest 0.1 Hz), assignment). The ^{1}H were assigned using COSY, HSQC, HMBC and NOESY experiments as appropriate.

6.3.5 ^{13}C NMR

Spectra were recorded using a Bruker AVIIIHD 400 nanobay (101 MHz) spectrometer, Bruker AVII500 (500 MHz) spectrometer with dual ^{13}C(^{1}H) cryoprobe in the stated solvent with broadband proton decoupling and an internal deuterium lock, or Bruker NEO 600 (151 MHz) spectrometer with broadband proton decoupling. Chemical shifts for each signal are given as δ_c in units of parts per million (ppm) relative to tetramethylsilane (δ_c = 0.00 ppm) and the spectra were calibrated using the solvent peak(s) and the known chemical shifts. Peaks were picked using the MestReNova 14.3.0 software. The carbon nuclei were assigned using HSQC and HMBC experiments, as appropriate.

6.3.6 ^{19}F NMR

Spectra were recorded using a Bruker AVIIHD 400 nanobay (376 MHz) spectrometer using a deuterium internal lock. The chemical shift for each signal is given as δ_F in units of parts per million (ppm). The multiplicity of each signal is indicated by: s (singlet); d (doublet); t (triplet); q (quartet) or m (multiplet). Coupling constants (*J*) are quoted in Hz and reported to the nearest 0.1 Hz. The coupling constants are determined by analysis using picked peaks on MestReNova version 14.3.0 software.

6.3.7 Chromatography and mass spectrometry

Below are the methods carried out for chromatographic and mass spectrometry analysis. HPLC and-preparative LC were analysed using Agilent OpenLab Chemstation software While LC-MS and low resolution MS were analysed using MestReNova 14.3.0 software.

6.3.8 TLC

TLC was carried out on normal phase Merck Silica gel 60 F_{254} aluminium-supported chromatographic sheets. Visualisation was by: UV light absorption (λ_{max} 254 or 365 nm) using a UVItec lamp inside of a black box or by chemical staining using iodine vapour, or thermal development after dipping into ethanolic ninhydrin or aqueous potassium permanganate.

6.3.9 Normal phase silica gel flash column chromatography

This technique was performed either by manual column chromatography using Geduran® (Merck Millipore) silica gel 60 (40-63 μM) or on a Biotage SP1 automated column chromatography system using KP-Sil® SNAP Flash silica cartridges.

6.3.10 Preparative liquid chromatography

Compounds that were purified using preparative liquid chromatography (Preparative HPLC) were dissolved in the minimum amount of MeCN with some samples containing water or DMSO, as necessary to obtain a homogenous solution. The solution was then filtered through a Fisherbrand PTFE syringe filter (30 mm, 0.2 μM) into an Agilent 5 mL vial with a pre-slit cap. Then the samples were purified using an Agilent 1260 Infinity II Semi Prep system with an Agilent prep C_{18} [5 μM, 50 × 21.2 mm] column, the flow rate was kept constant at 25 mL min^{-1} and the column was at room temperature. The mobile phases used unless otherwise stated were deionised water (mobile phase A) and HPLC grade MeCN (mobile phase B). After purification the fractions were collected and lyophilised. The injection volume was varied between purifications ranging from 50-1000 μL depending upon the level of resolution of the chromatograms.

6.3.11 Reverse phase HPLC

Compounds that were analysed for purity by HPLC were first dissolved in 1 mL of MeCN and were then filtered through either a Gilson PTFE syringe filter (13 mm, 0.22 μM) or Fisherbrand PTFE filter (13 mm, 0.2 μM) into a pre-slit Restek 1.5 mL vial. Compounds were analysed for purity on an Agilent 1260 Infinity II system with a quaternary LC pump,

DAD and Agilent Infinity Fraction Collector. An Agilent InfinityLab Poroshell 120 EC-C18 [4 μm, 4.6 mm × 150 mm] column heated to 40 ºC was used along with constant flow rate of 1 mL min^{-1} and UV detection at indicated wavelengths. The mobile phases used unless otherwise stated were distilled water containing 0.1% *v/v* formic acid (mobile phase A) and HPLC grade MeCN containing 0.1% *v/v* formic acid. The gradients utilised were as follows: 0-1 min hold at 5% mobile phase B, 1-11 min 5-100% mobile phase B, then a 5 min hold at 100% mobile phase B. The purities of compounds are calculated based upon percentage peak area of the chromatogram at a wavelength of 254 nm with a 100 nm bandwidth.

6.3.12 Low resolution electrospray ionisation (ESI) MS

Direst injection of a sample dissolved in MeCN at ~1 mg mL^{-1} into an Agilent 6120 quadrupole spectrometer was used in either positive or negative mode (as specified) to give low resolution mass spectra.

6.3.13 High resolution MS

Either of the following instruments was used for high resolution MS: Bruker microToF (high resolution), or Waters BioAccord LC-MS (high resolution) spectrometer using ESI or electron ionisation (EI). Samples were dissolved in 1 mL of MeCN, filtered through a Gilson PTFE syringe filter (13 mm, 0.22 μM) or Fisherbrand PTFE filter (13mm, 0.2μM) and were then diluted to the appropriate concentration. *m/z* values are reported in Daltons and followed by their percentage abundance in parentheses.

6.3.14 FT-IR Spectroscopy

Were obtained from either neat samples (liquid or solid) or a concentrated solution in a low boiling point solvent which was then evaporated to give a thin film. The spectra were recorded using a Bruker Tensor 27 spectrometer. Absorption maxima are reported in wavenumbers (cm^{-1}) and are reported as s (strong), m (medium), w (weak) or br (broad). Only the main relevant peaks are reported for each compound.

6.3.15 Specific optical rotations

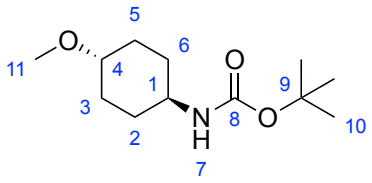
Were determined using a Schmidt Haensch Unipol polarimeter, using a sodium lamp at 589 nm and a path length of 1.0 dm. The concentration (*c*) is expressed in g/100 mL (equivalent to g/0.1 dm^3). Specific rotations are quoted as an average of 10 measurements. They are denoted $[\alpha]_D^T$ and are given in implied units of $10^{-1} \circ cm^2\ g^{-1}$ (where T = ambient temperature in).

6.3.16 Melting points

Were determined using a Griffin capillary tube melting point apparatus and are uncorrected. The melting point range is given from first apparent phase change to fully melted. The crystallisation solvent is given in parentheses.

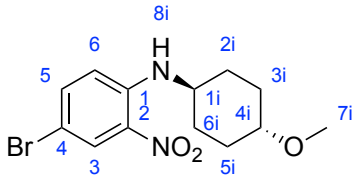
6.3.17 Synthetic Procedures

tert-Butyl _N_-[(1_r_,4_r_)-4-methoxycyclohexyl]carbamate (2)



To a solution of *trans*-4-boc-amino-cyclohexanol (**1**) (5.00 g, 23.2 mmol, 1.00 eq.) in anhydrous THF (100 mL) at 0 ºC was added sodium hydride (60% *w/w* in mineral oil, 1.39 g, 34.8 mmol, 1.50 eq.) portion wise over 5 min. The reaction mixture was stirred for 20 min before addition of dimethyl sulphate (2.20 mL, 23.2 mmol, 1.00 eq.) dropwise over 5 min at 0 ºC. The reaction mixture was then allowed to warm to ambient temperature and stirred for 20 h. The reaction was quenched by addition of water (100 mL) and extracted with EtOAc (3 × 100 mL), the combined organic extracts were washed with brine (100 mL), dried ($MgSO_4$), filtered, and concentrated *in vacuo*. The crude material was purified using flash column chromatography on silica gel (10–15% EtOAc/petroleum ether) and further purified by recrystallisation from boiling hexane to afford the title compound as a colourless needles (2.94 g, 12.8 mmol, 55%). $\boldsymbol{R_f}$ 0.35 (25% EtOAc/petroleum ether); **m.p.** 79–80 ºC (hexane); **^{1}H NMR** (400 MHz, $CDCl_3$): 4.36 (1H, s, H-7), 3.43 (1H, s, H-1), 3.33 (3H, s, H-11), 3.10 (1H, tt, *J* 10.4, 3.7, H-4), 2.08–1.96 (4H, m, H-2,6), 1.43 (9H, s, H-10), 1.37–1.23 (2H, m, H-3',5'), 1.19–1.06 (2H, m, H-3'',5''); **LRMS** *m/z* (ESI^+) 252 ($[M+Na]^+$, 100%), 481 ($[2M+Na]^+$, 62%) 459 ($[2M+H]^+$, 55%). These data are in good agreement with the literature values.[227]

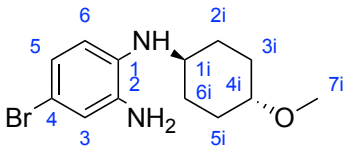
4-Bromo-_N_-((1_r_,4_r_)-4-methoxycyclohexyl)-2-nitroaniline (4)



Step 1: To a solution of *tert*-butyl *N*-[(1r,4r)-4-methoxycyclohexyl]carbamate (**2**) (2.20 g, 9.60 mmol, 1.05 eq.) in dioxane (10 mL) was added hydrogen chloride solution in dioxane

(4 M, 10 mL) at 0 ºC. The reaction mixture was allowed to warm to ambient temperature and stirred for 30 min and formation of a colourless precipitate was observed. The reaction mixture was concentrated *in vacuo* to remove excess hydrogen chloride solution in dioxane. *Step 2:* The residue was redissolved in MeCN (30 mL) followed by addition of K_2CO_3 (3.16 g, 22.9 mmol, 2.50 eq.) and 4-bromo-1-fluoro-2-nitrobenzene (**3**) (2.01 g, 9.14 mmol, 1.00 eq.). The reaction mixture was heated to 70 ºC and stirred for 16 h before TLC analysis indicated complete consumption of the limiting reagent. The reaction mixture was diluted with H_2O (100 mL) and extracted with EtOAc (3 × 75 mL). The combined organic extracts were washed with brine (50 mL), dried ($MgSO_4$), filtered, and concentrated *in vacuo*. The crude material was purified using recrystallisation from boiling hexane/EtOAc to afford the title compound as orange needles (2.71 g, 8.23 mmol, 90%). R_f 0.27 (20% EtOAc/hexane); **m.p.** 106–108 ºC (hexane/EtOAc); **^{1}H NMR** (400 MHz, $CDCl_3$): 8.31 (1H, d, *J* 2.3, H-3), 8.05 (1H, d, *J* 7.5, H-8i), 7.47 (1H, dd, *J* 9.2, 2.4, H-5), 6.78 (1H, d, *J* 9.3, H-6), 3.31–3.19 (1H, m H-4i), 2.20–2.06 (4H, m, H-2i,6i), 1.49–1.34 (4H, m, H-3i,5i); **LRMS** *m/z* (ESI$^+$) 331 ([M+H]$^+$, 100%), 329 ([M+H]$^+$, 97%); **HRMS** *m/z* (ESI$^+$) [found: [M+H]$^+$ 329.0493, $C_{13}H_{18}BrN_2O_3^+$ requires 329.0495]. These data are in good agreement with the literature values.[228]

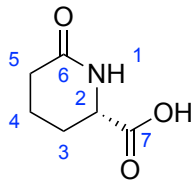
4-Bromo-1-*N*-((1*r*,4*r*)-4-methoxycyclohexyl)benzene-1,2-diamine (5)



To a solution of 4-bromo-*N*-((1*r*,4*r*)-4-methoxycyclohexyl)-2-nitroaniline (**4**) (2.71 g, 8.21 mmol, 1.00 eq.) in THF (80 mL) was added an aqueous solution of NH_4OH (1.65 M, 80 mL, 132 mmol, 16.0 eq.) and $Na_2S_2O_4$ (14.3 g, 82.1 mmol, 10.0 eq.). The bi-phasic reaction mixture was stirred vigorously at ambient temperature for 4 h before the reaction was judged to be complete by TLC analysis. The reaction mixture was partitioned and the aqueous phase was further extracted with EtOAc (2 × 50 mL). The combined organic components were washed with brine (100 mL), dried (Na_2SO_4), filtered and concentrated *in*

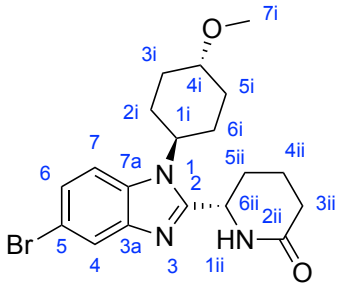
vacuo. The crude residue was passed through a short silica plug eluting with EtOAc to afford the title compound as a brown oil (1.81 g, 6.04 mmol, 73%). R_f 0.30 (50% EtOAc/petroleum ether); **^{1}H NMR** (400 MHz, $CDCl_3$): 6.88 (1H, dd, *J* 8.4, 2.3, H-5), 6.83 (1H, d, *J* 2.2, H-3), 6.51 (1H, d, *J* 8.4, H-6), 3.36 (3H, s, H-7i), 3.34–3.24 (1H, m H-8i), 3.19 (1H, tt, *J* 10.2, 3.7, H-4i), 2.16–2.05 (4H, m, H-2i,6i), 1.42–1.12 (4H, m, H-3i,5i); **LRMS** *m/z* (ESI^+) 299 ([M(^{79}Br)+H]$^+$, 100%), 301 ([M(^{81}Br)+H]$^+$, 100%); **HRMS** *m/z* (ESI^+) [found: $[M+H]^+$ 299.0747, $C_{13}H_{20}BrN_2O^+$ requires 229.0754]. These data are in good agreement with the literature values.[228]

(*S*)-6-Oxopiperidine-2-carboxylic acid (6)



L-2-Aminoadipic acid (1.00 g, 6.21 mmol, 1.00 eq.) was dissolved in glacial acetic acid (10 mL) and heated to reflux at 130 ºC for 4 h before the reaction was judged to be complete by LC-MS analysis. The reaction was cooled to ambient temperature and concentrated *in vacuo*. The crude material was further concentrated *in vacuo* by formation of an azeotropic mixture with toluene (20 mL). The crude residue was washed with diethyl ether (25 mL) and recrystallised in boiling water to afford an off-white crystalline solid which was collected by vacuum filtration. The collected crystals were further dried on a Schlenk line to afford the title compound as an off-white crystalline solid (880 mg, 6.15 mmol, 99%). R_f 0.35 (15% H_2O + 15% AcOH/^{n}BuOH); **m.p.** 102–104 ºC (water) [lit.[229] 101–104 ºC (water)]; $[\alpha]_D^{25}$ = 15.6 (c. 2.0 H_2O) [lit.[229] 13.7 c. 2.0 H_2O]; **^{1}H NMR** (400 MHz, $CDCl_3$): 8.99 (1H, s, H-1), 4.06 (1H, dd, *J* 11.4, 4.1, H-2), 2.49–2.23 (3H, m, H-3'',5), 2.07–1.94 (1H, m, 3'), 1.87–1.58 (2H, m, H-4); **LRMS** *m/z* (ESI^+) 287 ($[2M+H]^+$, 100%). These data are in good agreement with the literature values.[229]

(6*S*)-6-(5-Bromo-1-[(1*r*,4*r*)-4-methoxycyclohexyl]-1*H*-1,3-benzodiazol-2-yl)piperidin-2-one (8)

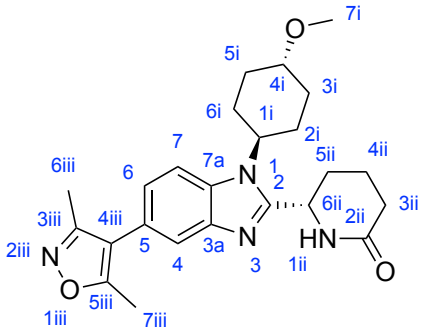


Step 1: To a stirring solution of (*S*)-6-oxopiperidine-2-carboxylic acid (**6**) (754 mg, 5.26 mmol, 1.05 eq.) in CH_2Cl_2 (5 mL) at 0 ºC was added DIPEA (1.05 mL, 6.02 mmol, 1.20 eq.), followed by T_3P solution in EtOAc (50 wt %, 9.6 mL, 15.0 mmol, 3.00 eq.) dropwise over 10 min. The reaction solution was stirred for 30 min at 0 ºC before dropwise addition of a solution of 4-bromo-1-*N*-((1*r*,4*r*)-4-methoxycyclohexyl)benzene-1,2-diamine (**5**) (1.50 g, 5.01 mmol, 1.00 eq.) in CH_2Cl_2 (10 mL). The reaction solution was stirred for a further 20 min at 0 ºC before it was allowed to warm to ambient temperature. After 4 h, the reaction had been judged to be complete by TLC analysis and quenched by addition of sat. aq. $NaHCO_3$ (50 mL) and extracted with CH_2Cl_2 (3 × 50 mL). The combined organic extracts were washed with sat. aq. NH_4Cl solution (50 mL), brine (50 mL), dried (Na_2SO_4), filtered and concentrated *in vacuo*.

Step 2: The crude residue was dissolved in AcOH (50 mL) and the reaction solution was heated to 50 ºC and stirred under nitrogen for 5 days, after which time the reaction was judged to be complete by LC-MS analysis and concentrated *in vacuo*. The crude residue was purified using flash column chromatography on silica gel (0–20% MeOH/EtOAc) to afford the title compound as a pink solid. $\boldsymbol{R_f}$ 0.27 (20% MeOH/EtOAc); **^{1}H NMR** (400 MHz, $CDCl_3$): 7.90 (1H, d, J 1.6, H-4), 7.38–7.31 (2H, m, H-6,7), 6.41 (1H, s, H-1ii), 4.93 (1H, dd, *J* 9.0, 4.3, H-6ii), 4.22 (1H, tt, *J* 12.5, 4.1, H-1i), 3.42 (3H, s, H-7i), 3.34 (1H, tt, *J* 10.9, 3.8, H-4i), 2.62–2.42 (2H, m, H-2i'',6i''), 2.42–2.27 (4H, m, H-3ii,2i',6i'), 2.25–2.18 (1H, m, H-5ii''), 2.14–2.07 (1H, m, H-5ii'), 2.04–1.87 (4H, m, H-3i'',4ii,5i''), 1.50–1.37 (2H, m, H-3i',5i'); **LRMS** *m/z* (ESI$^+$) 408 ([M(^{79}Br)+H]$^+$, 100%), 406 ([M(^{81}Br)+H]$^+$, 95%); **HRMS** *m/z*

(ESI$^+$) [found: $[M+H]^+$ 406.1128, $C_{19}H_{25}BrN_3O_2^+$ requires 406.1125]. These data are in good agreement with the literature values.[228]

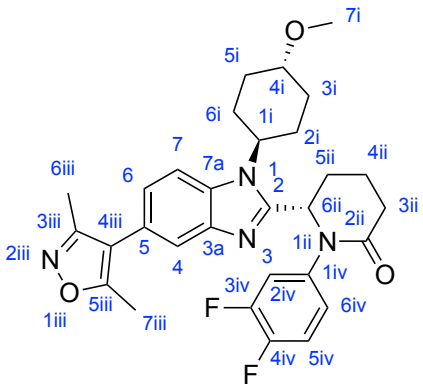
(6*S*)-6-(5-(3,5-Dimethyl-1,2-oxazol-4-yl)-1-((1*r*,4*r*)-4-methoxycyclohexyl)-1*H*-1,3-benzodiazol-2-yl)piperidin-2-one (9)



A vial was charged with (6*S*)-6-(5-bromo-1-[(1*r*,4*r*)-4-methoxycyclohexyl]-1*H*-1,3-benzodiazol-2-yl)piperidin-2-one (**8**) (750 mg, 1.85 mmol, 1.00 eq.), 3,5-dimethyl-4-(4,4,5,5-tetramethyl-1,3,2-dioxaborolan-2-yl)isoxazole (618 mg, 2.77 mmol, 1.50 eq.) and K_2CO_3 (1.02 g, 7.38 mmol, 4.00 eq.), and sealed with a septum. The mixture was suspended in dioxane (5.5 mL) and water (1 mL) and the reaction mixture was degassed by three freeze-pump-thaw cycles with argon. The reaction vial was then charged with tetrakis(triphenylphosphine)palladium(0) (106 mg, 92.3 µmol, 0.05 eq.) and re-sealed with a new septum before the reaction was further degassed by two freeze-pump-thaw cycles with argon. The reaction was then heated to 90 ºC for 18 h after which time the reaction was judged to have stalled by TLC analysis. The reaction mixture was diluted with brine (100 mL) and extracted with CH_2Cl_2 (3 × 100 mL), the combined organic components were dried (Na_2SO_4), filtered, and concentrated *in vacuo*. The crude material was purified using flash column chromatography on silica gel (0–5% MeOH/CH_2Cl_2) and further purified using flash column chromatography on reversed phase silica gel (0–50% MeCN/H_2O) and lyophilised to afford the title compound as a colourless powder (228 mg, 2.63 mmol, 30%). R_f 0.17 (5% MeOH/CH_2Cl_2); **^{1}H NMR** (400 MHz, $CDCl_3$): 7.68 (1H, d, *J* 1.6, H-4), 7.61 (1H, d, *J* 8.6, H-7), 7.19 (1H, dd, *J* 8.5, 1.6, H-6), 7.10 (1H, s, H-1ii), 5.16 (1H, dd, *J* 6.5, 6.5, H-6ii), 4.40 – 4.29 (1H, m, H-1i), 3.42 (3H, s, H-7i), 3.36 (1H, tt, *J* 10.6, 4.2, H-4i), 2.51 (2H,

t, *J* 6.3, H-2i'',6i''), 2.40 (3H, s, H-7iii), 2.46 – 2.19 (5H, m, H-2i',6i'a,5ii''), 2.26 (3H, s, H-6iii), 2.19–1.86 (5H, m, H-3i'',4ii,5i'',5ii'), 1.46 (2H, dd, *J* 14.2, 10.4, H-3i',5i'); **^{13}C NMR** (101 MHz, $CDCl_3$): 172.3 (2ii), 165.6 (5iii), 158.9 (3iii), 153.5 (2), 140.1 (3a), 132.4 (7a), 126.1 (5), 125.0 (6), 119.8 (4), 116.4 (4iii), 113.2 (7), 77.9 (4i), 77.4, 56.5 (1i), 56.3 (7i), 50.7 (6ii), 31.2 (3i/5i), 31.1 (3i/5i), 29.4 (3ii), 29.0 (2i, 6i), 28.5 (5ii), 19.6 (4ii), 11.6 (7iii), 10.9 (6iii); **LRMS** *m/z* (ESI^+) 423 ($[M+H]^+$, 100%); **HRMS** *m/z* (ESI^+) [found: $[M+H]^+$ 423.2405, $C_{24}H_{31}N_4O_3^+$ requires 423.2391] These data are in good agreement with the literature values.[228]

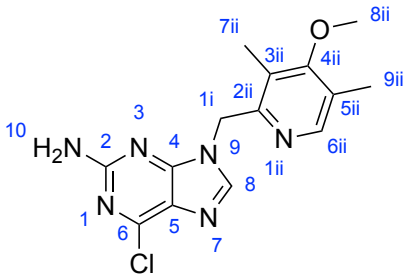
(6*S*)-1-(3,4-difluorophenyl)-6-(5-(3,5-dimethyl-1,2-oxazol-4-yl)-1-[(1*r*,4*r*)-4-methoxycyclohexyl)-1*H*-1,3-benzodiazol-2-yl)piperidin-2-one (Inobrodib)



To a solution of (6*S*)-6-(5-(3,5-dimethyl-1,2-oxazol-4-yl)-1-((1*r*,4*r*)-4-methoxycyclohexyl)-1*H*-1,3-benzodiazol-2-yl)piperidin-2-one (**9**) (50 mg, 0.118 mmol, 1.00 eq.) in anhydrous CH_2Cl_2 (4 mL) at ambient temperature was added copper(II) acetate (24.3 mg, 0.122 mmol, 1.03 eq.), anhydrous pyridine (95 µL, 1.19 mmol, 10.0 eq.) and 3 Å mol. sieves. The reaction solution was stirred for 15 min before addition of 3,4-difluorophenylboronic acid (37.4 mg, 0.237 mmol, 2.00 eq.) and stirred at ambient temperature overnight for 18 h before the reaction was judged to be complete by TLC analysis. The reaction was quenched by addition of H_2O (10 mL), the organic layer separated, and the aqueous component was further extracted with CH_2Cl_2 (2 × 20 mL). The combined organic components were washed with aq. EDTA solution (1 M, 20 mL), aq. hydrochloric acid solution (1 M, 20 mL), aq. $NaHCO_3$ solution (20 mL), brine (20 mL), dried (Na_2SO_4), filtered, and concentrated *in*

vacuo. The crude material was purified using flash column chromatography on silica gel (0–5% MeOH/CH_2Cl_2) and further purified by preparative HPLC and lyophilised to afford the title compound as a colourless powder (42 mg, 78.6 µmol, 66%); ***R*$_f$** 0.63 (10% MeOH/CH_2Cl_2); **m.p.** 125–128 ºC (MeCN/H_2O); **^{1}H NMR** (400 MHz, $CDCl_3$): 7.68 (1H, s, H-4), 7.48 (1H, d, *J* 8.4, H-7), 7.17–6.93 (4H, m, H-2iv,5iv,6,6iv), 5.23 (1H, dd, *J* 4.9, 4.9, H-6ii), 4.09 – 3.98 (1H, m, H-1i), 3.40 (3H, s, H-7i), 3.34–3.24 (1H, m, H-4i), 2.85 (1H, ddd, *J* 18.0, 5.7, 5.7, H-3ii'), 2.72–2.58 (1H, m, H-3ii''), 2.44 (3H, s, H-7iii), 2.31 (3H, s, H-6iii), 2.49 – 2.14 (7H, m, H-2i,3i',5i',5ii',6i), 1.97–1.82 (2H, m, H-4ii'',5ii''), 1.49–1.23 (3H, m, H-3i'',4ii',5i''); **^{19}F NMR** (377 MHz, $CDCl_3$): –135.30 (m), –138.28 (m); **LRMS** *m/z* (ESI^+) 535 ($[M+H]^+$, 100%); **HRMS** *m/z* (ESI^+) [found: $[M+H]^+$ 535.2522, $C_{30}H_{33}F_2N_4O_3^+$ requires 535.2515]. **RP-HPLC** Retention time: 8.742 min (98 %). These data are in good agreement with the literature values.[228]

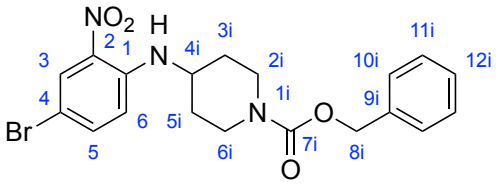
6-Chloro-9-((4-methoxy-3,5-dimethylpyridin-2-yl)methyl)purin-2-amine (BIIB021)



2-Amino-6-chloropurine (271 mg, 1.60 mmol, 1.00 eq.), 2-(chloromethyl)-4-methoxy-3,5-dimethyl pyridine hydrochloride (355 mg, 1.60 mmol, 1.00 eq.), sodium iodide (24.0 mg, 0.16 mmol, 0.10 eq.) and potassium carbonate (663 mg, 4.80 mmol, 3.00 eq.) were suspended in anhydrous DMF (8.0 mL) at ambient temperature. The reaction solution was heated to 40 °C stirred under an argon atmosphere for 6 h until the reaction was judged to be complete by TLC analysis. The reaction solution was quenched by addition of H_2O (25 mL) which caused the product to precipitate. The solid was collected by vacuum filtration, washed with H_2O (10 mL), and the powder was further dried on a Schlenk line to afford the title compound as an off-white (288 mg, 0.903 mmol, 56%). ***R*$_f$** 0.20 (5% MeOH/CH_2Cl_2); **m.p.** 191–194 ºC (DMF/water); **^{1}H NMR** (400 MHz, $CDCl_3$): 8.18 (1H, s, H-

6ii), 7.88 (1H, s, H-8), 5.32 (2H, s, H-1i), 5.12 (2H, s, H-10), 3.75 (3H, s, H-8ii), 2.29 (3H, s, H-9ii), 2.24 (3H, s, H-7ii); **LRMS** *m/z* (ESI^+) 319 ($[M+H]^+$, 100%); **HRMS** *m/z* (ESI^+) [found: $[M+H]^+$ 319.1074, $C_{14}H_{16}ClN_6O^+$ requires 319.1069]. **RP-HPLC** Retention time: 7.975 min (99 %). These data are in good agreement with the literature values.[205]

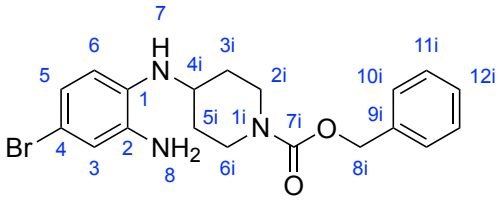
Benzyl 4-((4-bromo-2-nitrophenyl)amino)piperidine-1-carboxylate (10)



A flask fitted with a condenser was charged with benzyl 4-aminopiperidine-1-carboxylate (1.76 g, 7.50 mmol, 1.50 eq.), potassium carbonate (1.73 g, 12.5 mmol, 2.50 eq.) and a solution of 4-bromo-1-fluoro-2-nitrobenzene (616 µL, 5.00 mmol, 1.00 eq.) in acetonitrile (15 mL). The reaction mixture was heated to 80 ºC and stirred for 3 h before the reaction was judged to be complete by TLC analysis. The reaction solution was cooled to ambient temperature, diluted with H_2O (100 mL) and extracted with EtOAc (2 × 100 mL). The combined organics were washed with brine (50 mL), dried (Na_2SO_4), filtered and concentrated *in vacuo*. The crude material was purified using flash column chromatography on silica gel (20-25% EtOAc/pentane) to afford the title compound as an orange crystalline solid (2.25 g, 5.18 mmol, >99%); R_f 0.17 (20% EtOAc/petroleum ether); **m.p.** 120–121 ºC ($CDCl_3$); $\tilde{\nu}_{max}$ (thin film)/cm^{-1} 3364 (N-H, 2° amine), 1702 (C=O), 1616 (N-H), 1565 (C=C), 1504 (N-O), 1430 (C-H) 1232 (N-O), 763 (C-H, aromatic); **^{1}H NMR** (400 MHz, $CDCl_3$): 8.32 (1H, d, *J* 2.4, H-3), 8.05 (1H, d, *J* 7.4, N-H), 7.49 (1H, ddd, *J* 9.2, 2.4, 0.6, H-5), 7.42 – 7.28 (5H, m, H-10i,11i,12i), 6.78 (1H, d, *J* 9.2, H-6), 5.15 (2H, s, H-8i), 4.10 (2H, d, *J* 13.6, H-2i',6i'), 3.67 (1H, tdt, *J* 9.7, 7.4, 3.8, H-4i), 3.14 (2H, t, *J* 12.1, H-2i'', H-6i''), 2.06 (2H, d, *J* 12.9, H-3i,5i), 1.64 – 1.50 (2H, m, H-3i'',5i''); **^{13}C NMR** (101 MHz, $CDCl_3$): 155.3 (C-7i), 143.2 (C-1), 139.1 (C-5), 136.7 (C-9i), 132.6 (C-2), 129.4 (C-3), 128.7 (C-10i), 128.3 (C-12i), 128.1 (C-11i), 115.7 (C-6), 106.8 (C-4), 67.5 (C-8i), 49.4 (C-4i), 42.4 (C-2i,6i); **LRMS** *m/z* (ESI^+) 456 ($[M(^{79}Br)+Na]^+$, 100%), 434 ($[M(^{79}Br)+H]^+$, 86%); **HRMS** *m/z* (ESI^+)

[found: $[M+Na]^+$ 456.0526, $C_{19}H_{20}BrN_3O_4Na^+$ requires 456.0529]; **RP-HPLC** (Method 1) Retention time: 11.627 min (94%).

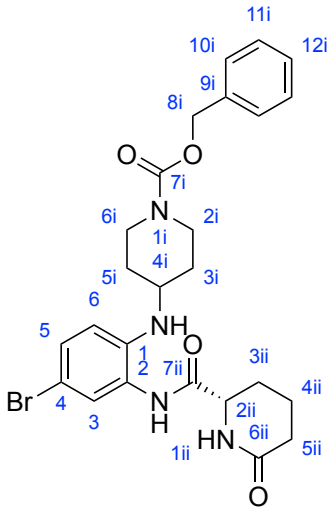
Benzyl 4-((2-amino-4-bromophenyl)amino)piperidine-1-carboxylate (11)



To a flask fitted with a condenser was added Benzyl 4-((4-bromo-2-nitrophenyl)amino)piperidine-1-carboxylate (**10**) (4.10 g, 9.44 mmol, 1.00 eq.) which was dissolved in THF (100 mL), followed by an aqueous solution of NH_4OH (1.32 M, 100 mL, 132 mmol, 14.0 eq.) and $Na_2S_2O_4$ (8.22 g, 47.2 mmol, 5.00 eq.). The bi-phasic reaction mixture was stirred vigorously and heated to 75 ºC for 4 h before the reaction was judged to be complete by TLC analysis and a colour change from orange to colourless was observed. The reaction mixture was cooled to ambient temperature and partitioned before the aqueous phase was further extracted with EtOAc (3 × 50 mL). The combined organic components were washed with brine (50 mL), dried ($MgSO_4$), filtered and concentrated *in vacuo*. The crude residue was passed through a short silica plug eluting with 50% EtOAc/petroleum ether to afford the title compound as a brown crystalline solid (2.06 g, 5.10 mmol, 54%); R_f 0.55 (40% EtOAc/petroleum ether); **m.p.** 105–108 ºC (EtOAc); $\tilde{\nu}_{max}$ (solid)/cm^{-1} 3422 (N-H), 3364 (N-H), 2963 (C-H), 1656 (C=O); **^{1}H NMR** (400 MHz, $CDCl_3$): 7.43 – 7.28 (5H, m, H-10i,11i,12i), 6.87 (1H, dd, *J* 8.4, 2.3, H-5), 6.82 (1H, d, *J* 2.2, H-3), 6.51 (1H, d, *J* 8.4, H-6), 5.16 (2H, s, H-8i), 4.12 (2H, d, *J* 15.4, H-2i', H-6i'), 3.35 (1H, tt, *J* 10.0, 3.9, H-4i), 3.02 (2H, t, *J* 12.4, H-2i",6i"), 2.00 (2H, dd, *J* 12.9, 3.8, H-3i',5i'), 1.37 (2H, td, *J* 11.5, 10.0, H-3i",5i"); **^{13}C NMR** (101 MHz, $CDCl_3$): 155.2 (C-7i), 136.8 (C-2), 136.7 (C-9i), 134.6 (C-1), 128.5 (C-10i), 128.0 (C-12i), 127.8 (C-11i), 122.5 (C-5), 119.1 (C-3), 114.6 (C-6), 110.9 (C-4), 67.1 (C-8i), 49.9 (C-4i), 42.6 (C-2i,6i), 32.1 (C-3i, 5i); **LRMS** *m/z* (ESI^+) 404 ($[M(^{79}Br)+H]^+$, 100%), 406 ($[M(^{81}Br)+H]^+$, 98%); **HRMS** *m/z* (ESI^+)

[found: $[M+H]^+$ 404.0967, $C_{19}H_{23}BrN_3O_2^+$ requires 404.0968]. **RP-HPLC** Retention time: 10.769 min (100%).

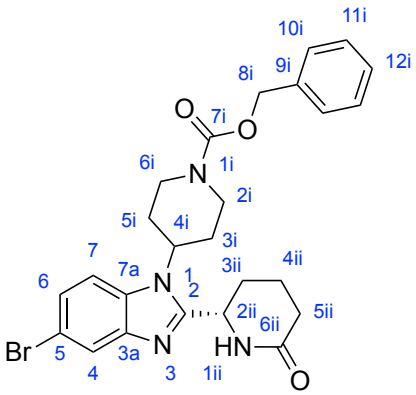
Benzyl 4-((4-bromo-2-((2*S*)-6-oxopiperidine-2-amido)phenyl)amino)piperidine-1-carboxylate (12)



To a solution of benzyl 4-((2-amino-4-bromophenyl)amino)piperidine-1-carboxylate (**11**) (2.06 g, 5.10 mmol, 1.00 eq.) and (*S*)-6-oxo-2-piperidinecarboxylic acid (802 mg, 5.60 mmol, 1.10 eq.) in MeCN (40 mL) was added *N*-methylimidazole (853 µL, 10.7 mmol, 2.10 eq.) and *N*,*N*,*N*′,*N*′-tetramethylchloroformamidinium hexafluorophosphate (1.57 g, 5.60 mmol, 1.10 eq.) at ambient temperature. The reaction solution was stirred at ambient temperature for 16 h before a second addition of (*S*)-6-Oxo-2-piperidinecarboxylic acid (0.10 eq.) and *N*,*N*,*N*′,*N*′-tetramethylchloroformamidinium hexafluorophosphate (0.10 eq.) and allowed to stir at ambient temperature for 1 h before the reaction was judged to be complete by TLC analysis. The volatile components were removed *in vacuo* before the residue was diluted with EtOAc (100 mL) and washed with sat. aq. NH_4Cl (50 mL), sat. aq. $NaHCO_3$ (50 mL), brine (50 mL), dried ($MgSO_4$), filtered and concentrated *in vacuo* to afford the title compound as a red foam (2.70 g, 5.10 mmol >99%); R_f 0.42 (EtOAc); $[\alpha]_D^{25}$ = –105 (c. 1.0 $CHCl_3$); $\tilde{\nu}_{max}$ (thin film)/cm^{-1} 2949 (C-H), 1695 (C=O), 1231, 762 **^{1}H NMR** (500 MHz, DMSO, 353 K) 7.41 – 7.28 (6H, m, H-3,10i,11i,12i), 7.17 (1H, dd, *J* 8.7, 2.4, H-5), 6.74 (1H, d, *J* 8.8, H-6), 5.10 (2H, s, H-8i), 4.12 (1H, ddd, *J* 6.3, 5.6, 2.4, H-2ii),

3.94 (2H, dt, *J* 13.9, 4.1, H-2i',6i'), 3.51 (1H, tt, *J* 9.4, 3.9, H-4i), 3.07 (2H, ddd, *J* 14.1, 11.3, 3.1, H-2i'',6i''), 2.19 (2H, t, *J* 6.6, H-5ii), 2.07 – 1.97 (1H, m, H-3ii''), 1.93 (2H, dd, *J* 13.3, 3.7, H-3i'',5i''), 1.83 (2H, m H-3ii',4ii''), 1.75 – 1.63 (1H, m, H-4ii'), 1.41 – 1.30 (2H, m, H-3i',5i'); **^{13}C NMR** (126 MHz, DMSO, 353 K): 170.9 (6ii), 170.1 (7ii), 154.2 (7i), 140.3 (1), 136.7 (9i), 128.5 (2), 128.0 (5), 128.0 (11i), 127.3 (12i), 127.0 (10i), 125.0 (3), 113.8 (6), 106.1 (4), 65.8 (8i), 55.1 (2ii), 48.6 (4i), 42.0 (2i, 6i), 31.1 (3i, 5i), 30.9 (5ii), 25.6 (3ii), 18.3 (4ii); **LRMS** *m/z* (ESI$^+$) 529 ([M(^{79}Br)+H]$^+$, 100%), 531 ([M(^{81}Br)+H]$^+$, 100%); **HRMS** *m/z* (ESI$^+$) [found: [M+H]$^+$ 529.1433, $C_{25}H_{30}BrN_4O_4^+$ requires 529.1445]. **RP-HPLC** Retention time: 9.366 min (98%).

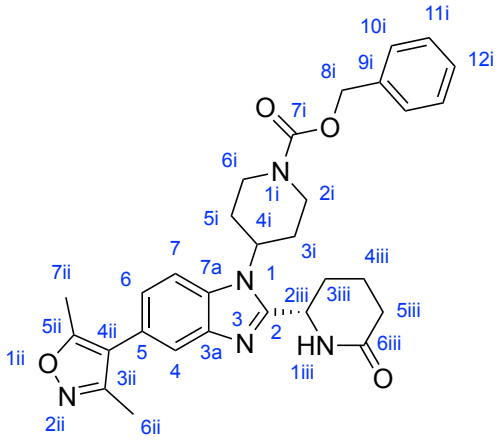
Benzyl 4-(5-bromo-2-[(2*S*)-6-oxopiperidin-2-yl]-1*H*-1,3-benzodiazol-1-yl)piperidine-1-carboxylate (13)



Benzyl 4-((4-bromo-2-((2*S*)-6-oxopiperidine-2-amido)phenyl)amino)piperidine-1-carboxylate (**12**) (500 mg, 0.944 mmol, 1.00 eq.) was dissolved in glacial acetic acid (20 mL) and heated to 80 ºC under a nitrogen atmosphere for 16 h, after which time the reaction was judged to be complete by TLC analysis. The reaction solution was concentrated *in vacuo* and residual acetic acid was removed by addition of toluene (15 mL) to form an azeotropic mixture and concentrated *in vacuo*. The crude residue was dissolved in EtOAc (100 mL) and washed with saturated aqueous $NaHCO_3$ solution (2 × 50 mL), brine (50 mL), dried ($MgSO_4$), filtered, and concentrated *in vacuo*. The crude residue was further purified using flash column chromatography on silica gel (20% MeOH/EtOAc) to afford the title compound as a colourless foam (470 mg, 0.919 mmol, 97%); R_f 0.35 (20%

MeOH/EtOAc); $[\alpha]_D^{25}$ = −5.03 (c. 1.0 $CHCl_3$); $\tilde{\nu}_{max}$ (thin film)/cm^{-1} 1754, 1692 (C=O), 1650 (C=O), 1441 1237; **^{1}H NMR** (500 MHz, DMSO, 353 K) 7.81 (1H, d, *J* 2.0, H-4), 7.53 (1H, d, *J* 8.7, H-7), 7.47 (1 H, d, *J* 1.7, H-1ii), 7.45 – 7.37 (4H, m, 10i, H-11i), 7.37 – 7.32 (1H, m, H-12i), 7.30 (1H, dd, *J* 8.7, 2.0, H-6), 5.16 (2H, s, H-8i), 5.07 (1H, ddd, *J* 7.2, 5.3, 2.2, H-2ii), 4.67 (1H, tt, *J* 12.1, 4.1, H-4i), 4.23 (2H, ddd, *J* 13.3, 4.6, 2.3, H-3i",5i)", 3.15 – 3.00 (2H, m, H-3i',5i'), 2.35 – 2.19 (4H, m, H-2i",5ii,6i"), 2.16 – 2.07 (1H, m, H-3ii"), 1.98 – 1.82 (4H, m, H-2i',3ii',4ii",6i'), 1.82 – 1.71 (1H, m, H-4ii'); **^{13}C NMR** (126 MHz, DMSO, 353 K) 170.0 (6ii), 155.7 (7i), 154.2 (2), 143.9 (3a), 136.7 (9i), 132.4 (7a), 128.0 (11i), 127.4 (12i), 127.2 (10i), 124.2 (6), 121.5 (4), 113.6 (5), 113.4 (7), 66.1 (8i), 52.9 (4i), 48.5 (2ii), 42.9, 42.8 (3i, 5i), 30.9 (5ii), 29.5 (2i, 6i), 29.4, 27.4 (3ii), 18.1 (4ii).; **LRMS** *m/z* (ESI$^+$) 513 ([M(^{81}Br)+H]$^+$, 100%), 511 ([M(^{79}Br)+H]$^+$, 99%), 1023 ([M(^{79}Br)+M(^{81}Br)+H]$^+$, 69%); **HRMS** *m/z* (ESI$^+$) [found: [M+H]$^+$ 511.1348, $C_{25}H_{28}BrN_4O_3^+$ requires 511.1339]. **RP-HPLC** Retention time: 9.310 min (>99%).

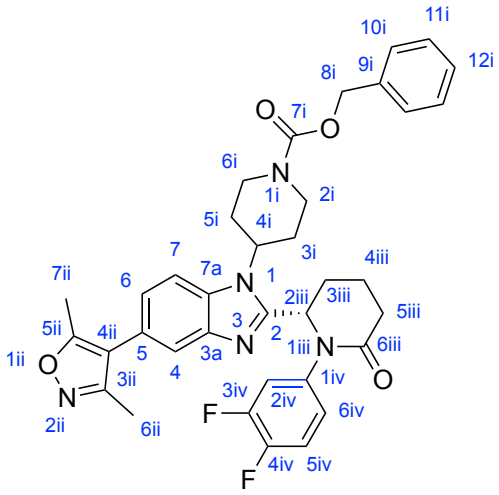
Benzyl 4-[5-(3,5-dimethyl-1,2-oxazol-4-yl)-2-[(2*S*)-6-oxopiperidin-2-yl]-1*H*-1,3-benzodiazol-1-yl]piperidine-1-carboxylate (14)



A vial was charged with benzyl 4-(5-bromo-2-[(2*S*)-6-oxopiperidin-2-yl]-1*H*-1,3-benzodiazol-1-yl)piperidine-1-carboxylate (**13**) (1.74 g, 3.40 mmol, 1.00 eq.), 3,5-dimethyl-4-(4,4,5,5-tetramethyl-1,3,2-dioxaborolan-2-yl)isoxazole (1.14 g, 5.10 mmol, 1.50 eq.), and tetrakis(triphenylphosphine)palladium(0) (197 mg, 170 µmol, 0.05 eq.), and the atmosphere was replaced with argon by three purge/fill cycles. The reagents were

dissolved in dioxane (10 mL) and an aqueous potassium carbonate solution (5 M, 2.04 mL, 10.1 mmol, 3.00 eq.) was added before the reaction mixture was degassed by three freeze-pump-thaw cycles with argon. The reaction mixture was heated to 90 ºC for 18 h, after which time the reaction was judged to be complete by TLC analysis. The reaction mixture was diluted with H_2O (100 mL) and extracted with CH_2Cl_2 (3 × 100 mL), the combined organic components were washed with brine (100 mL), dried (Na_2SO_4), filtered, and concentrated *in vacuo*. The crude material was purified using flash column chromatography on silica gel (0 – 10% MeOH/CH_2Cl_2) to afford the title compound as a colourless foam (1.39 g, 2.63 mmol, 77%); R_f 0.14 (5% MeOH/CH_2Cl_2); $[\alpha]_D^{25}$ = −6.69 (c. 1.0 $CHCl_3$); $\tilde{\nu}_{max}$ (thin film)/cm^{-1} 1694 (C=O), 1655 (C=O), 1437, 1229; **^{1}H NMR** (500 MHz, DMSO, 363 K) 7.63–7.57 (2 H, m, H-4,7), 7.46–7.37 (5H, m, H-1iii,10i,11i), 7.38–7.32 (1H, m, H-12i), 7.14 (1H, dd, *J* 8.4, 1.7, H-6), 5.19 (2H, s, H-8i), 5.10 (1H, ddd, *J* 7.2, 5.3, 2.1, H-2iii), 4.70 (1H, dddd, *J* 12.2, 12.2, 4.2, 4.2, H-4i), 4.30–4.22 (2H, m, H-2i'',6i''), 3.18–3.05 (2H, m, H-2i',6i'), 2.40 (3H, s, H-7ii), 2.39–2.25 (4H, m, H-3i'',5i'',5iii), 2.23 (3H, s, H-6ii), 2.15 (1H, ddd, *J* 13.2, 6.4, 4.2, H-3iii''), 2.04–1.87 (4H, m, H-3i',3iii',4iii'',5i'), 1.85–1.75 (1H, m, H-4iii'); **^{13}C NMR** (126 MHz, DMSO) 170.0 (6iii), 164.2 (5ii), 157.8 (3ii), 155.0 (2), 154.2 (7i), 142.7 (3a), 136.7 (9i), 132.6 (7a), a, 122.8 (5), 122.7 (6), 119.6 (4), 116.0 (4ii), 112.1 (7), 66.0 (8i), 52.8 (4i), 48.5 (2iii), 42.9 (2i, 6i), 30.8 (5iii), 29.6 (3i, 5i), 29.4, 27.4 (3iii), 18.1 (4iii), 10.7 (7ii), 9.8 (6ii).; **LRMS** *m/z* (ESI$^+$) 528 ([M+H]$^+$, 100%); **HRMS** *m/z* (ESI$^+$) [found: [M+H]$^+$ 528.2610, $C_{30}H_{34}N_5O_4^+$ requires 528.2605].

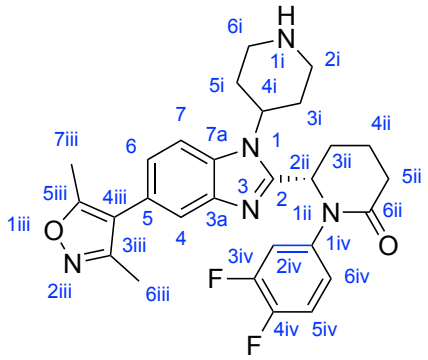
Benzyl 4-(2-((2*S*)-1-(3,4-difluorophenyl)-6-oxopiperidin-2-yl)-5-(3,5-dimethyl-1,2-oxazol-4-yl)-1*H*-1,3-benzodiazol-1-yl)piperidine-1-carboxylate (15)



A flask fitted with a drying tube was charged with benzyl 4-[5-(3,5-dimethyl-1,2-oxazol-4-yl)-2-[(2*S*)-6-oxopiperidin-2-yl]-1*H*-1,3-benzodiazol-1-yl]piperidine-1-carboxylate (**14**) (1.00 g, 1.90 mmol, 1.00 eq.) and copper(II) acetate monohydrate (378 mg, 1.90 mmol, 1.00 eq.), and then suspended with anhydrous CH_2Cl_2 (8 mL) and pyridine (0.8 mL). The reaction solution was allowed to stir at ambient temperature for 10 min before addition of 3,4-difluorophenylboronic acid (599 mg, 3.79 mmol, 2.00 eq.), and then stirred vigorously under dry air for 18 h before the reaction was judged to be complete by TLC analysis. The reaction mixture was diluted with CH_2Cl_2 (50 mL) and washed with aq. hydrochloric acid (0.2 M, 50 mL), the aqueous component was extracted with CH_2Cl_2 (50 mL) and the combined organic components were washed with sat. aq. EDTA solution (pH. 8.0, 2 × 25 mL), sat. aq. $NaHCO_3$ (50 mL), brine (50 mL), dried (Na_2SO_4), filtered and concentrated *in vacuo*. The crude material was purified using flash column chromatography on silica gel (0–10% MeOH/CH_2Cl_2) to afford the title compound as a colourless foam (1.14 g, 1.78 mmol, 94%); R_f 0.34 (10% MeOH/CH_2Cl_2); $[\alpha]_D^{25}$ = −77.16 (c. 1.0 $CHCl_3$); $\tilde{\nu}_{max}$ (thin film)/cm^{-1} 1700 (C=O), 1657 (C=O), 1516 (C-F), 1434, 1226; **^{1}H NMR** (600 MHz, DMSO, 373 K) 7.65 (1H, dd, *J* 1.7, 0.6, H-4), 7.55 (1H, dd, *J* 8.4, 0.7, H-7), 7.44–7.36 (4H, m, H-10i,11i), 7.37–7.31 (1H, m, H-12i), 7.32–7.22 (2H, m, H-2iv,5iv), 7.13 (1H, dd, *J* 8.4, 1.7, H-6), 7.05 (1H, dddd, *J* 8.9, 4.1, 2.5, 1.6, H-6iv), 5.69 (1H, dd, *J* 5.7, 4.2, H-2iii), 5.17

(2H, s, H-8i), 4.59 (1H, dddd, *J* 12.2, 12.1, 4.3, 4.2, H-4i), 4.24 (1H, dddd, *J* 13.4, 4.6, 2.3, 2.2, H-2i'' or H-6i''), 4.17 (1H, dddd, *J* 13.4, 4.6, 2.4, 2.1, H-2i'' or H-6i''), 3.04 (2H, m, H-2i',6i'), 2.64 (1H, dddd, *J* 17.7, 6.1, 5.0, 1.1, H-5iii''), 2.54 (1H, ddd, *J* 17.6, 9.0, 6.6, H-5iii'), 2.47 – 2.41 (1H, m, H-3iii''), 2.40 (3H, s, H-7ii), 2.30 – 2.20 (1H, m, H-3i'' or 5i''), 2.23 (3H, s, H-6ii), 2.18 (1H, dd, *J* 12.4, 4.7, H-3i' or H-5i'), 2.16 – 2.03 (2H, m, H-3iii',4iii''), 1.89 – 1.81 (2H, m, H-4iii',H-5i' or H-3i'), 1.35 (1H, dddd, *J* 12.7, 3.9, 2.3, 1.0, H-3i' or H-5i'); **^{13}C NMR** (151 MHz, DMSO, 373 K) 169.3 (6iii), 164.1 (5ii), 157.6 (3ii), 154.1 (7i), 153.3 (2), 148.3 (dd, *J* 245.9, 13.4, C-3iv), 147.4 (dd, *J* 245.7, 12.4, C-4iv), 142.4 (3a), 138.8 (dd, *J* 8.0, 3.5, C-1iv), 136.6 (9i), 132.2 (7a), 127.8 (11i), 127.3 (12i), 127.0 (10i), 123.8 (dd, *J* 6.6, 3.2, C-6iv), 123.2 (5), 122.9 (6), 119.4 (4), 116.7 (d, *J* 18.1, C-5iv), 116.3 (d, *J* 17.9, 2iv), 115.8 (4ii), 112.1 (7), 66.0 (8i), 56.0 (2iii), 52.6 (4i), 42.8 (2i or 6i), 42.6 (2i or 6i), 31.7 (5iii), 29.5 (3i or 5i), 29.3 (3i or 5i), 28.3 (3iii), 17.0 (4iii), 10.6 (7ii), 9.7 (6ii);**^{19}F NMR** (470 MHz, DMSO, 373 K) –138.0 (1F, m, F-3iv), –140.7 (1F, m, F-4iv); **LRMS** *m/z* (ESI^+) 640 ($[M+H]^+$, 100%); **HRMS** *m/z* (ESI^+) [found: $[M+H]^+$ 640.2746, $C_{36}H_{36}F_2N_5O_4^+$ requires 640.2730].

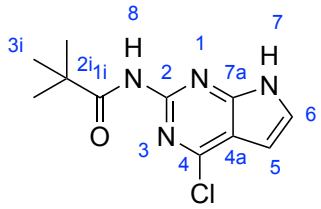
(6*S*)-1-(3,4-Difluorophenyl)-6-(5-(3,5-dimethyl-1,2-oxazol-4-yl)-1-(piperidin-4-yl)-1*H*-1,3-benzodiazol-2-yl)piperidin-2-one (Pip-obrodib)



A solution of benzyl 4-(2-((2*S*)-1-(3,4-difluorophenyl)-6-oxopiperidin-2-yl)-5-(3,5-dimethyl-1,2-oxazol-4-yl)-1*H*-1,3-benzodiazol-1-yl)piperidine-1-carboxylate (**15**) (1.10 g, 1.72 mmol, 1.00 eq.) in MeOH (17 mL) was sparged with argon for 15 min before the addition of Pd/C (10 wt.%, 172 µmol, 183 mg, 0.10 eq.). The atmosphere was then replaced for hydrogen

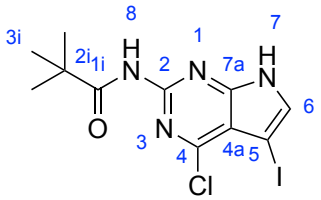
by three purge/fill cycles and the reaction mixture was stirred vigorously under a hydrogen atmosphere for 5 h before the reaction was judged to be complete by TLC analysis. The reaction mixture was sparged with argon for 15 min before it was filtered over Celite® and the filtrate concentrated *in vacuo*. The crude material was purified using flash column chromatography on reversed phase silica (5–50% MeCN/H_2O) and product fractions were combined, volatiles removed *in vacuo* until a precipitate was observed and then the remaining aq. mixture was extracted with CH_2Cl_2 (5 × 50 mL). The combined organic extracts were washed with brine (25 mL), dried (Na_2SO_4), filtered and concentrated *in vacuo* to afford the title compound as a colourless foam (614 mg, 1.21 mmol, 71%); R_f 0.00 (10% MeOH/CH_2Cl_2); $\tilde{\nu}_{max}$ (solid)/cm^{-1} 3651 (N-H), 2980 (C-H), 2889 (C-H), 1652 (C=O), 1623, 1516, 1456, 1383, 1254, 1154; **^{1}H NMR** (500 MHz, DMSO, 353 K) 7.78 (1H, d, *J* 8.5, H-7), 7.66 (1H, d, *J* 1.7, H-4), 7.36 – 7.23 (2H, m, H-2iv,5iv), 7.16 (1H, dd, *J* 8.4, 1.7, H-6), 7.06 7.06 (1 H, dddd, *J* 9.0, 4.0, 2.5, 1.6, H-6iv), 5.69 (1H, dd, *J* 5.5, 3.9, H-2ii), 4.39 (1 H, dddd, *J* 12.2, 12.1, 4.4, 4.2, H-4i), 3.14 – 2.98 (2H, m, H-2i",6i"), 2.72 – 2.53 (3H, m, 2i', 5ii, 6i'), 2.48 – 2.35 (1H, m, H-3ii'), 2.41 (3H, s, H-7iii), 2.24 (3H, s, H-6iii), 2.30 – 2.14 (2H, m, H-3i",5i"), 2.14 – 2.02 (2H, m, H-3ii",4ii'), 1.88 – 1.80 (1H, m, H-4ii"), 1.71 (1H, d, J 12.9, H-3i' or H-5i'), 1.22 (1H, d, *J* 12.2, H-3i' or H-5i').; **^{13}C NMR** (126 MHz, DMSO, 353 K) 169.4 (6ii), 164.2 (5iii), 157.8 (3iii), 153.3 (2), 148.3 (dd, J 245.2, 13.8, 3iv), 147.4 (dd, J 245.8, 13.0, 4iv), 142.7 (3a), 138.9 (dd, J 8.2, 4.0, 1iv), 132.5 (7a), 124.1 (dd, J 6.7, 3.2, 6iv), 123.0 (5), 122.6 (6), 119.5 (4), 116.8 (d, J 18.1, 5iv), 116.4 (d, J 18.0, 2iv), 116.0 (4iii), 112.5 (7), 56.1 (2ii), 53.6 (4i), 45.3 (2i or 6i), 45.2 (2i or 6i), 31.9 (5ii), 31.3 (3i or 5i), 31.1 (3i or 5i), 28.4 (3ii), 17.1 (4ii), 10.8 (7iii), 9.9 (6iii); **^{19}F NMR** (471 MHz, DMSO, 353 K) -137.9– -138.3 (m), -140.7– -141.0 (m); **LRMS** *m/z* (ESI^+) 506 ($[M+H]^+$, 100%); **HRMS** *m/z* (ESI^+) [found: $[M+H]^+$ 506.2369, $C_{28}H_{30}F_2N_5O_2^+$ requires 506.2362]. **RP-HPLC** Retention time: 6.300 min (98%).

_N_-(4-Chloro-7_H_-pyrrolo[2,3-_d_]pyrimidin-2-yl)pivalamide (21)



To a solution of 4-chloro-7*H*-pyrrolo[2,3-*d*]pyrimidin-2-amine (843 mg, 5.00 mmol, 1.00 eq) in anhydrous pyridine (4 mL) was added pivaloyl chloride (769 uL, 6.25 mmol, 1.25 eq) dropwise over 15 min at ambient temperature. The reaction solution was stirred at ambient temperature for 2 h before the reaction was judged to be complete by TLC analysis. The reaction was quenched by addition of H_2O (10 mL) and the resulting precipitate was collected by vacuum filtration. The filter cake was washed with H_2O (10 mL) before further drying *in vacuo,* to afford the title compound as a brown solid (995 mg, 79%): R_f 0.39 (5% MeOH/CH_2Cl_2), 0.48 (50% EtOAc/petroleum ether); **m.p.** 205 – 210 ºC, decomposition [lit.[230] m.p. 212 ºC, decomposition]; **^{1}H NMR** (400 MHz, $CDCl_3$): 12.16 (1H, br, H-7), 8.28 (1H, s, H-8), 7.53 (1H, dd, *J* 3.6, 2.4, H-6), 6.53 (1H, dd, *J* 3.6, 1.9, H-5), 1.39 (9 H, s, H-3i); **^{13}C NMR** (101 MHz, $CDCl_3$) 176.3 (C-1i), 152.6 (C-2), 151.8 (C-7a), 150.7 (C-4), 128.7 (C-6), 114.8 (C-4a), 99.6 (C-5), 40.3 (C-2), 27.6 (C-3i); **LRMS** *m/z* (ESI+) 527 ([2M+Na]+, 100%), 253 ([M+H]$^+$, 64%); **HRMS** *m/z* (ESI$^+$) [found: [M+H]$^+$ 253.0856, $C_{11}H_{14}ClN_4O^+$ requires 253.0851]. These data are in good agreement with the literature values.[180, 182, 230]

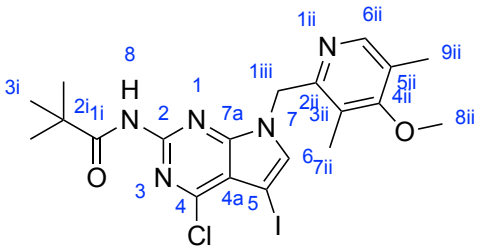
_N_-(4-Chloro-5-iodo-7_H_-pyrrolo[2,3-d]pyrimidin-2-yl)pivalamide (22)



To a solution of *N*-(4-chloro-7*H*-pyrrolo[2,3-*d*]pyrimidin-2-yl)pivalamide (**21**) (995 mg, 3.94 mmol, 1.00 eq.) in THF (20 mL) was added *N*-iodosuccinimide (974 mg, 4.33 mmol, 1. eq.) at ambient temperature. The reaction was stirred at ambient temperature for 30 min

before the reaction was judged to be complete by TLC analysis. The reaction was quenched by addition of aqueous solution of $Na_2S_2O_4$ (0.15 M, 10 mL) before extracting with CH_2Cl_2 (3 × 50 mL). The combined organic extracts were washed with H_2O (50 mL), saturated aqueous solution of $Na_2S_2O_3$ (50 mL) and brine (50 mL), dried (Na_2SO_4), filtered and concentrated *in vacuo*. The crude material was purified by crystallisation from hot EtOH to afford the title compound as a colourless powder (924 mg, 62%); $\boldsymbol{R_f}$ 0.25 (30% EtOAc/petroleum ether); **m.p.** 224–230 ºC (EtOH) [lit.[182] m.p. 182 – 184 ºC, lit.[231] m.p. 240 ºC]; **^{1}H NMR** (400 MHz, $CDCl_3$): 12.20 (1H, s, H-7), 8.24 (1H, s, H-8), 7.61 (1H, d, *J* 1.3, 6), 1.39 (9H, s, H-3i); **^{13}C NMR** (101 MHz, $CDCl_3$): 176.5 (C-1i), 152.7 (C-2), 152.2 (C-7a), 150.7 (C-4), 134.4 (6), 113.9 (C-4a), 51.08 (C-5), 40.4 (C-2i), 27.6 (C-3i); **LRMS** *m/z* (ESI^+) 379 ($[M+H]^+$, 100%); **HRMS** *m/z* (ESI^+) [found: $[M+H]^+$ 378.9814, $C_{11}H_{13}ClIN_4O^+$ requires 378.9817]. These data are in good agreement with the literature values.[180, 182, 231]

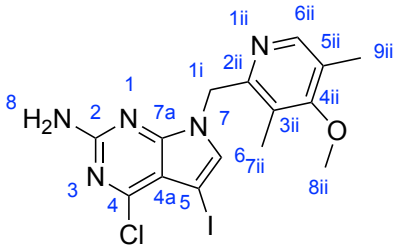
_N_-(4-Chloro-5-iodo-7-((4-methoxy-3,5-dimethylpyridin-2-yl)methyl)-7_H_-pyrrolo[2,3-_d_]pyrimidin-2-yl)pivalamide (23)



To a mixture of *N*-(4-chloro-5-iodo-7*H*-pyrrolo[2,3-d]pyrimidin-2-yl)pivalamide (**22**) (600 mg, 1.58 mmol, 1.00 eq.), K_2CO_3 (657 mg, 4.75 mmol, 3.00 eq.), and sodium iodide (23.8 mg, 0.158 mmol, 0.10 eq.) in anhydrous DMF (8 mL) at ambient temperature was added 2-chloromethyl-4-methoxy-3,5-dimethylpyridine hydrochloride (370 mg, 1.66 mmol, 1.05 eq.). The reaction mixture was stirred at ambient temperature for 16 h before it was diluted with CH_2Cl_2 (100 mL) and washed with H_2O (100 mL), brine (100 mL), dried (Na_2SO_4), filtered and concentrated *in vacuo*. The solid was further dried on a Schlenk line to afford the title compound as a yellow solid (764 mg, 1.45 mmol, 91%); $\boldsymbol{R_f}$ 0.30 (25% EtOAc/petroleum ether); **m.p.** 74–77 ºC (MeOH) [lit.[182] 201 – 203]; **^{1}H NMR** (400 MHz,

$CDCl_3$): 8.20 (1H, s, H-6ii), 8.11 (1H, s, H-8), 7.34 (1H, s, H-6), 5.48 (2H, s, H-1iii), 3.73 (3H, s, H-8ii), 2.28 (3H, s, H-7ii), 2.24 (3H, s, H-9ii), 1.34 (8H, s, H-3i); **^{13}C NMR** (101 MHz, $CDCl_3$): 175.6 (C-1i), 164.5 (C-4ii), 153.1 (C-2ii), 152.7 (C-2), 151.9 (C-7a), 151.4 (C-4), 149.7 (C-6ii), 134.3 (C-6), 126.5 (C-5ii), 125.9 (C-3ii), 113.2 (C-4a), 60.1 (C-8ii), 51.4 (C-5), 47.9 (C-1iii), 40.4 (C-2i), 27.6 (C-3i), 13.5 (C-9ii), 11.2 (C-7ii); **LRMS** *m/z* (ESI^+) 528 ($[M+H]^+$, 100%); **HRMS** *m/z* (ESI^+) [found: $[M+Na]^+$ 550.0489, $C_{20}H_{23}ClIN_5O_2Na^+$ requires 550.0477]. These data are in good agreement with the literature values.[180, 182]

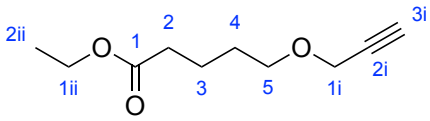
4-Chloro-5-iodo-7-((4-methoxy-3,5-dimethylpyridin-2-yl)methyl)-7*H*-pyrrolo[2,3-*d*]pyrimidin-2-amine (Iodo-BIIB021)



To a suspension of *N*-(4-Chloro-5-iodo-7-((4-methoxy-3,5-dimethylpyridin-2-yl)methyl)-7*H*-pyrrolo[2,3-*d*]pyrimidin-2-yl)pivalamide (**23**) (750 mg, 1.42 mmol, 1.00 eq.) in a mixture of EtOH:H_2O (10:1, 50 mL) was added zinc chloride (968 mg, 7.11 mmol, 5.00 eq.). The reaction mixture was heated to 85 ºC and stirred overnight after which time the reaction was judged to be complete by TLC analysis. The reaction was allowed to cool to ambient temperature and diluted with H_2O (70 mL) causing the product to precipitate. The resultant solid was collected by vacuum filtration and purified by recrystallisation from hot MeOH to afford the title compound as a colourless solid (440 mg, 0.992 mmol, 70%); ***R*$_f$** 0.55 (10% MeOH/CH_2Cl_2); **m.p.** 225–230 ºC, decomposition (MeOH) [lit.[182] 128–130 ºC]; **^{1}H NMR** (400 MHz, $CDCl_3$): 8.24 (1H, s, H-6ii), 7.08 (1H, s, H-6), 5.33 (2H, s, H-1i), 4.97 (2H, s, H-8), 3.76 (3H, s, H-8ii), 2.27 (3H, s, H-7ii), 2.22 (3H, s, H-9ii).; **^{13}C NMR** (151 MHz, $CDCl_3$): 165.0 (C-4ii), 158.3 (C-4), 153.4 (C-2), 153.3 (C-7a), 153.1 (C-2ii), 149.3 (C-6ii), 131.5 (C-6), 126.7 (C-3ii), 125.8 (C-5ii), 110.1 (C-4a), 60.2 (C-8ii), 51.6 (C-5), 47.3 (C-1i), 13.6 (C-9ii), 11.2 (C-7ii); **LRMS** *m/z* (ESI^+) 444 ($[M+H]^+$, 100%); **HRMS** *m/z* (ESI^+) [found:

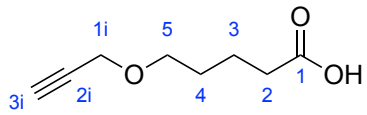
[M+H]$^+$ 444.0070, $C_{15}H_{16}ClIN_5O^+$ requires 444.0083]. These data are in good agreement with the literature values.[180, 182]

Ethyl 5-(prop-2-yn-1-yloxy)pentanoate (38)



To a suspension of NaH (60% *w/w*, 440 mg, 1.00 mmol, 0.10 eq.) in anhydrous DMF (10 mL) at 0 ºC was added propargyl alcohol (1.15 mL 20.0 mmol, 2.00 eq.) dropwise over 5 min. The reaction mixture was allowed to stir for 30 min at 0 ºC before dropwise addition of ethyl bromovalerate (1.37 mL, 10.0 mmol, 1.00 eq.) over 5 min and then allowed to warm to ambient temperature and stirred for 3 h before the reaction was judged to be complete by TLC analysis. The reaction solution was quenched by addition of sat. aq. NH_4Cl solution (25 mL) and extracted with Et_2O (2 × 50 mL). The combined extracts were washed with LiCl aq. solution (0.5 M, 50 mL), HCl aq. solution (1 M, 50 mL), sat. aq. $NaHCO_3$ solution (50 mL), brine (50 mL), dried ($MgSO_4$), filtered, and concentrated *in vacuo*. The crude material was purified using flash column chromatography on normal phase silica gel (5—20% Et_2O/petroleum ether) to afford the title compound as a colourless oil (840 mg, 4.56 mmol, 56%); R_f 0.20 (10% Et_2O/petroleum ether); **^{1}H NMR** (400 MHz, $CDCl_3$): 4.17–4.07 (4H, m, H-1i,1ii), 3.52 (2H, t, *J* 6.2, H-5), 2.41 (1H, t, *J* 2.4, H-3i), 2.32 (2H, t, *J* 7.3 H-2), 1.80 – 1.57 (4H, m, H-3,4), 1.25 (3H, t, *J* 7.1, H-2ii).; **LRMS** *m/z* (ESI$^+$) 185 ([M+H]$^+$, 100%); **HRMS** *m/z* (ESI$^+$) [found: [M+H]$^+$ 185.1171, $C_{10}H_{17}O_3^+$ requires 185.1172]. These data are in good agreement with the literature values.[232]

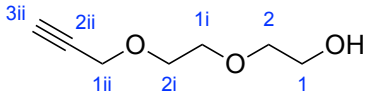
5-(Prop-2-yn-1-yloxy)pentanoic acid (39)



To a solution of ethyl 5-(prop-2-yn-1-yloxy)pentanoate (**38**) (800 mg, 4.34 mmol, 1.00 eq.) in EtOH (25 mL) was added aq. NaOH solution (2 M, 6.51 mL, 13.03 mmol, 5.00 eq.) at ambient temperature. The reaction solution was heated to 40 ºC and stirred for 1 h after

which time the reaction was judged to be complete by TLC analysis. The reaction solution was diluted with water (50 mL) and washed with Et_2O (2 × 25 mL), the aqueous component was acidified with aqueous hydrochloric acid solution (2 M) until a precipitate formed which was then extracted with Et_2O (2 × 50 mL). The combined organic components were washed with brine (50 mL), dried ($MgSO_4$), filtered, and concentrated *in vacuo* to afford the title compound as a colourless oil (630 mg, 4.03 mmol, 93%); $\boldsymbol{R_f}$ 0.35 (5% MeOH/CH_2Cl_2); $\tilde{\nu}_{max}$ (thin film)/cm^{-1} 3294 (C-H), 2946 (O-H), 2874 (C-H), 2117 (C≡C), 1710 (C=O), 1102; **^{1}H NMR** (400 MHz, $CDCl_3$): 4.13 (2H, d, *J* 2.4, H-1i), 3.53 (2H, t, *J* 6.1, H-5), 2.42 (1H, t, *J* 2.4, H-3i), 2.39 (2H, t, *J* 7.2, H-2), 1.79 – 1.59 (4H, m, H-3,4); **^{13}C NMR** (131 MHz, $CDCl_3$): 179.9 (C-1), 79.8 (C-2i), 74.3 (C-3i), 69.5 (C-5), 58.1 (C-1i), 33.7 (C-2), 28.7 (C-4), 21.4 (C-3); **LRMS** *m/z* (ESI$^+$) 139 ([M-OH]$^+$, 100%) 179 ([M+Na]$^+$, 18%); **HRMS** *m/z* (ESI$^-$) [found: [M–H]$^-$ 155.0709, $C_8H_{11}O_3^-$ requires 155.0714].

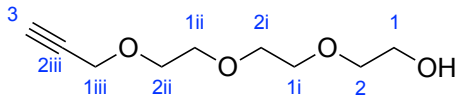
2-(2-(Prop-2-yn-1-yloxy)ethoxy)ethan-1-ol (27)



To a suspension of potassium *tert*-butoxide (5.92 g, 52.8 mmol, 1.00 eq.) in anhydrous THF (150 mL) under an inert atmosphere at 0 ºC was added diethylene glycol (10.0 mL, 106 mmol, 2.00 eq.) dropwise over 15 min. The reaction mixture was stirred at 0 ºC for 30 min before dropwise addition of a propargyl bromide solution (80 wt.% in toluene, 5.88 mL, 52.8 mmol, 1.00 eq.) in anhydrous THF (50 mL) over 60 min. The reaction mixture was allowed to warm to ambient temperature and stirred under an inert atmosphere for 4 days before it was filtered over Celite® and the filtrate concentrated *in vacuo*. The crude residue was purified using flash column chromatography on normal phase silica (60% EtOAc/petroleum ether) to afford the title compound as a pale yellow oil (6.07 g, 42.1 mmol, 80%); $\boldsymbol{R_f}$ 0.24 (60% EtOAc/petroleum ether); **^{1}H NMR** (400 MHz, $CDCl_3$): 4.20 (2H, d, *J* 2.4, H-1ii), 3.79 – 3.64 (2H, m, H-1), 3.72 – 3.67 (4H, m, H-1i, H-2i), 3.64 – 3.56 (2H, m, H-2), 2.44 (1H, t, *J* 2.4, H-3ii), 2.30 (1H, s, O-H); **LRMS** *m/z* (ESI$^+$) 167 ([M+Na]$^+$, 100%) 145

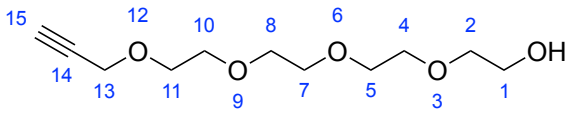
([M+H]$^+$, 28%); **HRMS** *m/z* (ESI$^+$) [found: [M+H]$^+$ 145.0860, $C_7H_{13}O_3^+$ requires 145.0859]. These data are in good agreement with the literature values.[233]

2-(2-(2-(Prop-2-yn-1-yloxy)ethoxy)ethoxy)ethan-1-ol (28)



To a solution of triethylene glycol (5.00 mL, 37.4 mmol, 2.00 eq.) in anhydrous THF (60 mL) under an inert atmosphere at 0 ºC was added potassium *tert*-butoxide portion-wise. The reaction mixture was stirred at 0 ºC for 30 min before dropwise addition of a propargyl bromide solution (80 wt.% in toluene, 2.08 mL, 18.7 mmol, 1.00 eq.) in anhydrous THF (40 mL) over 10 min. The reaction mixture was allowed to warm to ambient temperature and stirred under an inert atmosphere for 20 h before it was filtered over Celite® and the filtrate concentrated *in vacuo*. The crude residue was purified using flash column chromatography on normal phase silica (50–100% Et_2O/petroleum ether) to afford the title compound as a pale yellow oil (2.18 g, 11.6 mmol, 62%); R_f 0.18 (Et_2O); **^{1}H NMR** (400 MHz, $CDCl_3$): 4.19 (2H, d, *J* 2.4, H-1iii), 3.76 – 3.63 (10H, m, H-1,1i,1ii,2i,2ii), 3.61 – 3.56 (2H, m, H-2), 2.46 (1H, s, O-*H*), 2.42 (1H, t, *J* 2.4, H-3iii); **LRMS** *m/z* (ESI$^+$) 211 ([M+Na]$^+$, 100%), 189 ([M+H]$^+$, 34%); **HRMS** *m/z* (ESI$^+$) [found: [M+H]$^+$ 189.1121, $C_9H_{17}O_4^+$ requires 189.1121]. These data are in good agreement with the literature values.[234]

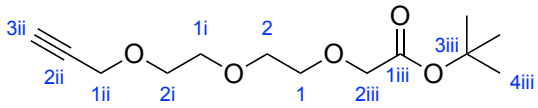
3,6,9,12-Tetraoxapentadec-14-yn-1-ol (29)



To a suspension of potassium *tert*-butoxide (5.61 g, 50.0 mmol, 1.00 eq.) in anhydrous THF (150 mL) under an inert atmosphere at 0 ºC was added tetraethylene glycol (17.3 mL, 100 mmol, 2.00 eq.) dropwise over 15 min. The reaction mixture was stirred at 0 ºC for 60 min before dropwise addition of a propargyl bromide solution (80 wt.% in toluene, 5.88 mL, 52.8 mmol, 1.00 eq.) in anhydrous THF (50 mL) over 60 min. The reaction mixture was allowed to warm to ambient temperature and stirred under an inert atmosphere for 16 h

before it was filtered over Celite® and the filtrate concentrated *in vacuo*. The crude residue was purified using flash column chromatography on normal phase silica (5% MeOH/EtOAc) to afford the title compound as a pale yellow oil (6.86 g, 29.5 mmol, 59%); R_f 0.29 (5% MeOH/EtOAc); **^{1}H NMR** (400 MHz, $CDCl_3$): 4.20 (2H, d, *J* 2.4, H-13), 3.73 – 3.70 (2H, m, H-1), 3.70 – 3.67 (4H, m, H-10,11), 3.67 – 3.63 (8H, m, H-4,5,7,8), 3.62 – 3.58 (2H, m, H-2), 2.42 (1H, t, *J* 2.4, H-15); **LRMS** *m/z* (ESI^+) 255 ($[M+Na]^+$, 100%), 233 ($[M+H]^+$, 54%); **HRMS** *m/z* (ESI^+) [found: $[M+H]^+$ 233.1375, $C_{11}H_{21}O_5^+$ requires 233.1384]. These data are in good agreement with the literature values.[233, 234]

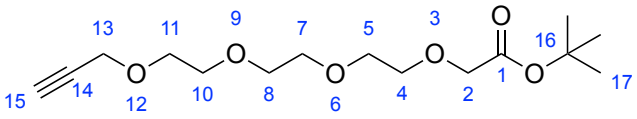
***tert*-Butyl 2-(2-(2-(prop-2-yn-1-yloxy)ethoxy)ethoxy)acetate (30)**



To a solution of 2-(2-(prop-2-yn-1-yloxy)ethoxy)ethan-1-ol (**27**) (500 mg, 3.47 mmol, 1.00 eq.) in CH_2Cl_2 (17 mL) at 0 ºC was added tetrabutylammonium chloride (289 mg, 1.04 mmol, 0.33 eq.), *tert*-butyl bromoacetate (1.54 mL, 10.4 mmol, 3.00 eq.) and an aqueous solution of sodium hydroxide (35% *w/w*, 17 mL). The biphasic reaction was allowed to warm to ambient temperature and stirred vigorously for 6 h before the reaction was judged to be complete by TLC analysis. The reaction mixture was diluted with CH_2Cl_2 (30 mL) and partitioned, the aqueous component was further extracted with CH_2Cl_2 (2 × 50 mL) and the combined organic extracts were washed with water (50 mL), brine (25 mL), dried ($MgSO_4$), filtered and concentrated *in vacuo*. The crude residue was purified using flash column chromatography on normal phase silica gel (10 – 50% Et_2O/petroleum ether) to afford the title compound as a colourless oil (727 mg, 2.81 mmol, 81%); R_f 0.39 (50% Et_2O/petroleum ether); **^{1}H NMR** (400 MHz, $CDCl_3$): 4.19 (2H, d, *J* 2.4, H-1ii), 4.01 (2H, s, H-2iii), 3.75 – 3.64 (8H, m, H-1,1i,2,2i), 2.41 (1H, t, *J* 2.4, H-3ii), 1.46 (9H, s, H-4iii); **^{13}C NMR** (126 MHz, $CDCl_3$): 169.8 (C-1iii), 81.6 (C-3iii), 79.8 (C-2ii), 74.6 (C-3ii), 70.8, 70.7, 70.5, 69.21, 69.17, 58.5 (C-1ii), 28.2 (C-4iii); **LRMS** *m/z* (ESI^+) 281

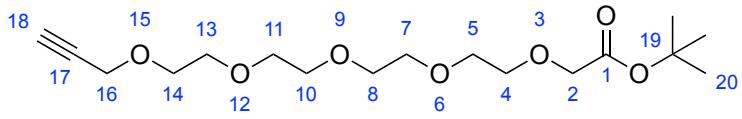
([M+Na]$^+$, 100%); **HRMS** *m/z* (ESI$^+$) [found: [M+Na]$^+$ 281.1351, $C_{13}H_{22}O_5Na^+$ requires 281.1360]. These data are in good agreement with the literature values.[235, 236]

***tert*-Butyl 3,6,9,12-tetraoxapentadec-14-ynoate (31)**



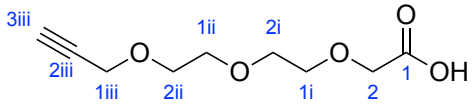
To a solution of 2-(2-(2-(prop-2-yn-1-yloxy)ethoxy)ethoxy)ethan-1-ol (**28**) (2.18 g, 11.6 mmol, 1.00 eq.) in CH_2Cl_2 (60 mL) at 0 ºC was added tetrabutylammonium chloride (1.06 g, 3.82 mmol, 0.33 eq.), *tert*-butyl bromoacetate (5.13 mL, 34.8 mmol, 3.00 eq.) and an aqueous solution of sodium hydroxide (35% *w/w*, 60 mL). The biphasic reaction was allowed to warm to ambient temperature and stirred vigorously for 6 h before the reaction was judged to be complete by TLC analysis. The reaction mixture was partitioned, the aqueous component was further extracted with CH_2Cl_2 (3 × 50 mL) and the combined organic extracts were washed with aqueous HCl solution (1 M, 20 mL), brine (25 mL), dried ($MgSO_4$), filtered and concentrated under a constant stream of nitrogen. The crude residue was triturated with Et_2O (50 mL), filtered, and the filtrate was concentrated onto silica *in vacuo* before purification by flash column chromatography on normal phase silica gel (75% Et_2O/petroleum ether) to afford the title compound as a colourless oil (1.80 g, 5.95 mmol, 51%); R_f 0.34 (75% Et_2O/petroleum ether); **^{1}H NMR** (400 MHz, $CDCl_3$): 4.13 (2H, d, *J* 2.4, H-13), 3.95 (2H, s, H-2), 3.68 – 3.55 (12H, m, H-4–11), 2.38 (1H, t, *J* 2.3, H-15), 1.41 (9H, s, H-17); **LRMS** *m/z* (ESI$^+$) 320 ([M+NH_4]$^+$, 100%), 325 ([M+Na]$^+$, 58%); **HRMS** *m/z* (ESI$^+$) [found: [M+NH_4]$^+$ 320.2059, $C_{15}H_{30}O_6N^+$ requires 320.2068]. These data are in good agreement with the literature values.[236]

***tert*-Butyl 3,6,9,12,15-pentaoxaoctadec-17-ynoate (32)**



To a solution of 3,6,9,12-tetraoxapentadec-14-yn-1-ol (**29**) (500 mg, 2.15 mmol, 1.00 eq.) in CH_2Cl_2 (10 mL) at 0 ºC was added tetrabutylammonium chloride (197 mg, 0.710 mmol, 0.33 eq.), *tert*-butyl bromoacetate (954 µL, 6.46 mmol, 3.00 eq.) and an aqueous solution of sodium hydroxide (35% *w/w*, 10 mL). The biphasic reaction was allowed to warm to ambient temperature and stirred vigorously for 6 h before the reaction was judged to be complete by TLC analysis. The reaction mixture was diluted with CH_2Cl_2 (25 mL) and partitioned, the aqueous component was further extracted with CH_2Cl_2 (2 × 25 mL) and the combined organic extracts were washed with brine (25 mL), dried ($MgSO_4$, filtered and concentrated *in vacuo*. The crude residue was triturated with Et_2O, filtered, and the filtrate was concentrated onto silica *in vacuo* before purification by flash column chromatography on normal phase silica gel (60% EtOAc/petroleum ether) to afford the title compound as a colourless oil (337 mg, 0.972 mmol, 45%); R_f 0.25 (50% EtOAc/petroleum ether); **^{1}H NMR** (400 MHz, $CDCl_3$): 4.19 (2H, d, *J* 2.4, H-16), 4.01 (2H, s, H-2), 3.74–3.61 (16H, m, H-4,5,7,8,10,11,13,14), 2.42 (1H, t, *J* 2.4, H-18), 1.52–1.43 (9H, m, H-20).; **LRMS** *m/z* (ESI^+) 364 ($[M+NH_4]^+$, 100%) 369 ($[M+Na]^+$, 46%); **HRMS** *m/z* (ESI^+) [found: $[M+Na]^+$ 369.1891, $C_{17}H_{30}O_7Na^+$ requires 369.1884]. These data are in good agreement with the literature values.[237]

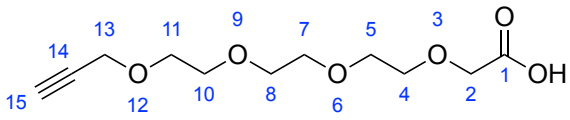
2-(2-(2-(Prop-2-yn-1-yloxy)ethoxy)ethoxy)acetic acid (33)



To a solution of *tert*-butyl 2-(2-(2-(prop-2-yn-1-yloxy)ethoxy)ethoxy)acetate (**30**) (700 mg, 2.71 mmol, 1.00 eq.) in dioxane (6 mL) was added hydrogen chloride solution in dioxane (4 N, 2 mL) at 0 ºC. The reaction solution was allowed to warm to ambient temperature and stirred for 16 h before addition of aqueous hydrochloric acid (12 N, 0.5 mL) and warmed to

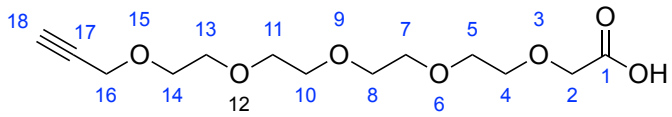
40 ºC for 1 h before the reaction was judged to be complete by TLC analysis. The reaction solution was concentrated *in vacuo* and the residue diluted in CH_2Cl_2 (50 mL), dried ($MgSO_4$), filtered, and concentrated *in vacuo* to afford the title compound as a pale yellow oil (548 mg, 2.71 mmol, >99%); R_f 0.32 (5% MeOH/CH_2Cl_2); **^{1}H NMR** (400 MHz, $CDCl_3$) 6.68 (1H, s, O-H), 4.17 (2H, d, *J* 2.4, H-1iii), 4.14 (2H, s, H-2), 3.75–3.63 (8H, m, H-1i,1ii,2i,2ii), 2.44 (1H, t, *J* 2.4, H-3iii); **^{13}C NMR** (101 MHz, $CDCl_3$) 173.4 (1), 79.5 (2iii), 74.9 (3iii), 71.1 (1i), 70.4, 70.4 (2i,1ii), 69.0 (2ii), 68.6 (2), 58.4 (1iii); **LRMS** *m/z* (ESI^-) 201 ([M-H]$^-$, 100%); **HRMS** *m/z* (ESI^-) [found: $[M-H]^-$ 201.0767, $C_9H_{13}O_5^-$ requires 201.0768]. These data are in good agreement with the literature values.[235]

3,6,9,12-Tetraoxapentadec-14-ynoic acid (34)



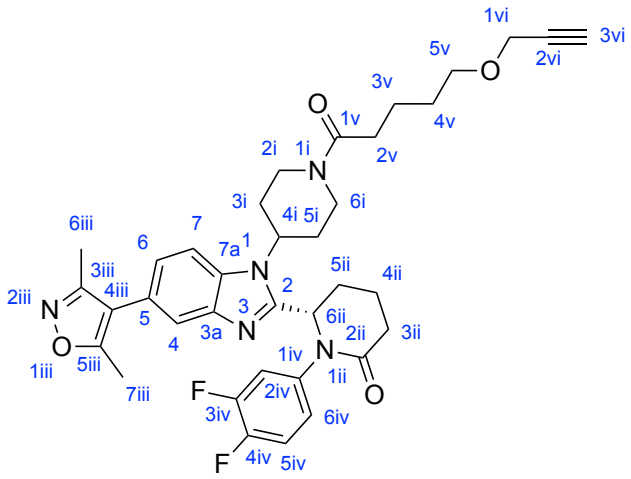
tert-Butyl 3,6,9,12-tetraoxapentadec-14-ynoate (**31**) (1.80 g, 5.95 mmol, 1.00 eq.) was dissolved in hydrogen chloride solution in dioxane (4 N, 5 mL) at 0 ºC. The reaction solution was allowed to warm to ambient temperature and stirred for 20 h before a further portion of hydrogen chloride solution in dioxane (4 N, 5 mL) was added and the reaction was heated to 40 ºC. After 4 h, the reaction was judged to be complete by TLC analysis and concentrated *in vacuo* to afford the title compound as a colourless oil (1.50 g, 6.09 mmol, >99%); R_f 0.26 (5% MeOH/CH_2Cl_2); **^{1}H NMR** (400 MHz, $CDCl_3$): 4.20 (2H, d, *J* 2.4, H-13), 4.16 (2H, s, H-2), 3.78 – 3.62 (12H, m, H-4,5,7,8,10,11), 2.43 (1H, t, *J* 2.3, H-15); **LRMS** *m/z* (ESI^-) 245 ([M-H]$^-$, 100%), 245; **HRMS** *m/z* (ESI^-) [found: $[M-H]^-$ 245.1037, $C_{11}H_{17}O_6^-$ requires 245.1031]. These data are in good agreement with the literature values.[238]

3,6,9,12,15-Pentaoxaoctadec-17-ynoic acid (35)



tert-Butyl 3,6,9,12,15-pentaoxaoctadec-17-ynoate (**32**) (280 mg, 0.080 mmol, 1.00 eq.) was dissolved in hydrogen chloride solution in dioxane (4 N, 5 mL) at 0 ºC. The reaction solution was allowed to warm to ambient temperature and stirred for 20 h before the reaction was judged to be complete by TLC analysis and concentrated *in vacuo* to afford the title compound as a colourless oil (235 mg, 0.080 mmol, >99%); R_f 0.20 (5% MeOH/CH_2Cl_2); **^{1}H NMR** (400 MHz, $CDCl_3$) 9.32 (1 H, s, O-H), 4.17 (2H, d, *J* 2.4, H-16), 4.14 (2H, s, H-2), 3.75–3.59 (16H, m, H-4–14), 2.41 (1H, t, *J* 2.4, H-18); **^{13}C NMR** (101 MHz, $CDCl_3$) 173.0 (1), 79.6 (17), 74.7 (18), 71.3, 70.6, 70.5, 70.4, 70.4 (4–13), 69.0 (14), 68.8 (2), 58.4 (16); **LRMS** *m/z* (ESI^-) 289 ([M–H]$^-$, 100%); **HRMS** *m/z* (ESI^-) [found: [M–H]$^-$ 289.1290, $C_{13}H_{21}O_7^-$ requires 289.1293]. These data are in good agreement with the literature values.[239]

(6*S*)-1-(3,4-Difluorophenyl)-6-(5-(3,5-dimethyl-1,2-oxazol-4-yl)-1-(1-(5-(prop-2-yn-1-yloxy)pentanoyl)piperidin-4-yl)-1*H*-1,3-benzimidazol-2-yl]piperidin-2-one (40)



Method 1:

Step 1: To a solution of 5-(prop-2-yn-1-yloxy)pentanoic acid (**39**) (63.7 mg, 408 µmol, 1.50 eq.) in anhydrous CH_2Cl_2 (5 mL) was added oxalyl chloride (117 uL, 1.36 mmol,

5.00 eq.) dropwise at 0 ºC, followed by dropwise addition of DMF (3 µL, 40.8 µmol, 0.15 eq.). The reaction mixture was then allowed to warm to ambient temperature and stirred for 30 min. Conversion to the acid chloride intermediate was judged to be complete by TLC analysis by diluting an aliquot of the reaction mixture in EtOH to form an ethyl ester derivative. The reaction mixture was then concentrated *in vacuo* to remove excess oxalyl chloride.

Step 2: The crude residue was dissolved in anhydrous CH_2Cl_2 (5 mL) and cooled to 0 ºC, followed by addition of (6*S*)-1-(3,4-difluorophenyl)-6-(5-(3,5-dimethyl-1,2-oxazol-4-yl)-1-(piperidin-4-yl)-1*H*-1,3-benzodiazol-2-yl)piperidin-2-one (**Pip-obrodib**) as a 1:2 TFA salt (200 mg, 272 µmol, 1.00 eq.) and NEt_3 (380 µL, 2.72 mmol, 10.0 eq.) at 0 ºC. The reaction solution was allowed to warm to ambient temperature and stirred for 2 h before the reaction was judged to be complete by TLC analysis. The reaction solution was quenched by addition of MeOH (5 mL) and concentrated *in vacuo*. The crude residue was purified using flash column chromatography on silica gel (0–4% (1% NH_4OH/MeOH)/CH_2Cl_2) to afford the title compound (157 mg, 244 µmol, 90%).

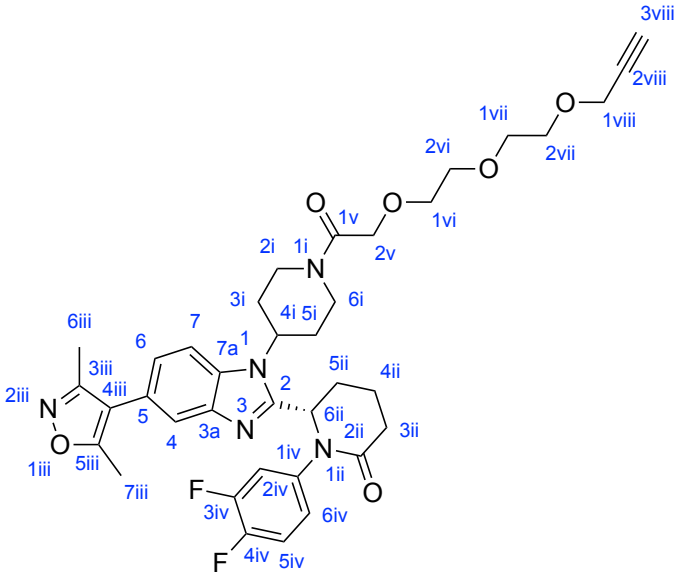
Method 2:

To a solution of 5-(prop-2-yn-1-yloxy)pentanoic acid (**39**) (23.4 mg, 0.150 mmol, 1.10 eq.) in anhydrous CH_2Cl_2 (1 mL) was added *N*,*N*′-dicyclohexylcarbodiimide (30.9 mg, 0.150 mmol, 1.10 eq.), 4-dimethylaminopyridine (1.66 mg, 13.6 µmol, 0.10 eq.), (6*S*)-1-(3,4-difluorophenyl)-6-(5-(3,5-dimethyl-1,2-oxazol-4-yl)-1-(piperidin-4-yl)-1*H*-1,3-benzodiazol-2-yl)piperidin-2-one (**Pip-obrodib**) as a 1:2 TFA salt (100 mg, 0.136 mmol, 1.00 eq.) and NEt_3 (57 µL, 0.408 mmol, 3.00 eq.) at ambient temperature. The reaction solution was stirred at ambient temperature for 20 h before the reaction was judged to be complete by TLC and LC-MS analysis. The reaction mixture was filtered, and the filter cake washed with CH_2Cl_2 (5 mL). The filtrate was diluted with CH_2Cl_2 (20 mL), washed with saturated $NaHCO_3$ aqueous solution (25 mL), dried (Na_2SO_4), filtered, and concentrated *in vacuo*. The crude residue was purified using flash column chromatography on silica gel (0–

4% (1% NH_4OH/MeOH)/CH_2Cl_2) to afford the title product as an off-white solid (48.2 mg, 74.9 μmol, 55%).

***R*$_f$** 0.21 (5% MeOH/CH_2Cl_2); **m.p.** 86–92 ºC (MeCN/H_2O); $[\alpha]_D^{25}$ = –113 (c. 1.0 MeCN); $\tilde{\nu}_{max}$ (thin film)/cm^{-1} 3300 (C-H, alkynyl), 1640 (C=O), 1516 (C=C, aromatic), 1450 (C-H) **^{1}H NMR** (600 MHz, DMSO, 393 K) 7.64 (1H, d, *J* 1.7, H-4), 7.59 (1H, d, *J* 8.4, H-7), 7.32 – 7.20 (2H, m, H-2iv,5iv), 7.14 (1H, dd, *J* 8.4, 1.7, H-6), 7.05 (1H, dddd, *J* 8.6, 4.1, 2.5, 1.5, H-6iv), 5.66 (1H, dd, *J* 5.7, 4.2, H-6ii), 4.60 (1H, tt, *J* 12.1, 4.3, H-4i), 4.46 – 4.21 (2H, m, H-2i'',6i''), 4.12 (2H, d, *J* 2.4, H-1vi), 3.52 (2H, t, *J* 6.1, H-5v), 3.09 (1H, t, *J* 2.3, H-3vi), 2.97 (2H, s, H-2i',6i'), 2.66 (1H, dddd, *J* 17.6, 6.2, 5.1, 1.1, H-5ii''), 2.55 (1H, ddd, *J* 17.4, 8.7, 6.6, H-5ii'), 2.49 – 2.41 (3H, m, 2v, H-3ii''), 2.40 (3H, s, H-7iii), 2.22 (3H, s, H-6iii), 2.29 – 2.07 (4H, m, H-3i'',3ii',4ii'',5i''), 1.92 – 1.83 (2 H, m, H-3i',4ii'), 1.70–1.61 (4 H, m, H-3v,4v), 1.38 (1H, ddt, *J* 12.8, 4.7, 2.5, H-5i'); **^{13}C NMR** (151 MHz, DMSO, 393 K) 170.1 (1v), 169.2 (2ii), 164.0 (5iii), 157.5 (3iii), 153.3 (2), 148.2 (dd, *J* 246.0, 13.4, 3iv), 147.3 (dd, *J* 245.9, 12.5, 4iv), 142.6 (3a), 138.8 (dd, *J* 8.1, 3.6, 1iv), 132.2 (7a), 123.8 (dd, *J* 6.5, 3.3, 6iv), 123.1 (5), 122.7 (6), 119.4 (4), 116.6 (d, *J* 18.4, 5iv), 116.1 (d, *J* 18.0, 2iv), 115.7 (4iii), 111.9 (7), 80.1 (2vi), 75.3 (3vi), 68.6 (5v), 56.8 (1vi), 56.0 (6ii), 52.8 (4i), 41.9 (2i/6i), 40.1 (6i/2i), 31.7 (3ii), 31.4 (2v), 29.8 (3i/5i), 29.6 (5i/3i), 28.3 (5ii), 28.0 (4v), 21.1 (3v), 17.0 (4ii), 10.4 (7iii), 9.5 (6iii); **^{19}F NMR**: (565 MHz, DMSO, 393 K) -138.0 – -138.1 (m), -140.7 – -140.8 (m); **LRMS** *m/z* (ESI$^+$) 644 ([M+H]$^+$, 100%), 666 ([M+Na]$^+$, 30%); **HRMS** *m/z* (ESI$^+$) [found: [M+Na]$^+$ 666.2879, $C_{36}H_{39}F_2N_5O_4Na^+$ requires 666.2862]; **RP-HPLC** Retention time: 8.485 min (96%).

(6*S*)-1-(3,4-Difluorophenyl)-6-(5-(3,5-dimethyl-1,2-oxazol-4-yl)-1-(1-(2-(2-(2-prop-2-ynoxyethoxy)ethoxy)acetyl)piperidin-4-yl)benzimidazol-2-yl)piperidin-2-one (41)



Method 1:

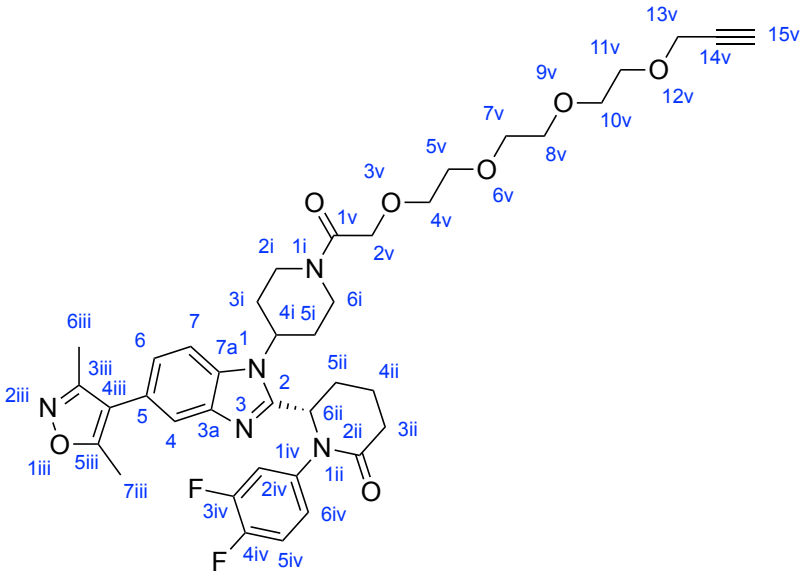
Step 1: To a solution of 2-(2-(2-(prop-2-yn-1-yloxy)ethoxy)ethoxy)acetic acid (**33**) (30 mg, 148 µmol, 1.5 eq.) in anhydrous CH_2Cl_2 (5 mL) was added oxalyl chloride (42 uL, 494 µmol, 5.0 eq.) dropwise at 0 ºC, followed by dropwise addition of DMF (1 µL, 12.9 µmol, 0.14 eq.). The reaction mixture was then allowed to warm to ambient temperature and stirred for 30 min. Conversion to the acid chloride intermediate was judged to be complete by TLC analysis by diluting an aliquot of the reaction mixture in MeOH to form an methyl ester derivative. The reaction mixture was then concentrated *in vacuo* to remove solvent and excess oxalyl chloride.

Step 2: The crude residue was dissolved in anhydrous CH_2Cl_2 (5 mL) and cooled to 0 ºC, followed by addition of (6*S*)-1-(3,4-difluorophenyl)-6-(5-(3,5-dimethyl-1,2-oxazol-4-yl)-1-(piperidin-4-yl)-1*H*-1,3-benzodiazol-2-yl)piperidin-2-one (**Pip-obrodib**) (50 mg, 98.9 µmol, 1.0 eq.) and NEt_3 (138 µL, 0.99 mmol, 10 eq.) at 0 ºC. The reaction solution was allowed to warm to ambient temperature and stirred for 1 h before the reaction was judged to be complete by TLC analysis. The reaction solution was diluted with CH_2Cl_2 (25 mL) and quenched by addition of sat. aq. $NaHCO_3$ solution (25 mL). The mixture was partitioned,

and the aqueous component further extracted with CH_2Cl_2 (2 × 25 mL). The combined organic extracts were washed with brine (25 mL), dried (Na_2SO_4), filtered and concentrated *in vacuo*. The crude residue was purified using flash column chromatography on silica gel (0–7% MeOH/CH_2Cl_2 + 0.1% NH_4OH) to afford the title compound (42.5 mg, 62 µmol, 62%);

$\boldsymbol{R_f}$ 0.19 (5% MeOH/CH_2Cl_2); **m.p.** 75–83 ºC (MeCN/H_2O); $[\boldsymbol{\alpha}]_{\boldsymbol{D}}^{\mathbf{25}}$ = −80.0 (c. 1.0 MeCN); $\tilde{\boldsymbol{\nu}}_{\boldsymbol{max}}$ (thin film)/cm^{-1} 3480 (N-H), 1672 (C=O), 1517 (C=C, aromatic), 1201 (C-F); **^{1}H NMR:** (600 MHz, DMSO, 393 K) 7.64 (1H, d, *J* 1.7, H-4), 7.61 (1H, d, *J* 8.4, H-7), 7.31–7.21 (2H, m, H-2iv,5iv), 7.14 (1H, dd, *J* 8.5, 1.7, 6), 7.05 (1H, dddd, *J* 8.9, 4.0, 2.5, 1.6, H-6iv), 5.66 (1H, dd, *J* 5.7, 4.2, H-6ii), 4.61 (1H, dddd, *J* 12.2, 12.2, 4.3, 4.3, H-4i), 4.39–4.25 (2H, m, H-2i',6i'), 4.23 (2H, s, H-2v), 4.11 (2H, d, *J* 2.4, H-1viii), 3.68 – 3.55 (8H, m, H-1vi,1vii,2vi,2vii), 3.08 (1H, t, *J* 2.5, H-3viii), 3.04–2.93 (2H, m, H-2i'',6i''), 2.66 (1H, dddd, *J* 17.6, 6.2, 5.2, 1.1, H-5ii'), 2.55 (1H, ddd, *J* 17.5, 8.7, 6.9, H-5ii''), 2.50–2.41 (1H, m, H-3ii'), 2.40 (3H, s, H-7iii), 2.35–2.17 (2H, m, H-3i',5i'), 2.22 (3H, s, H-6iii), 2.18–2.07 (2H, m, H-3ii'',4ii''), 1.92–1.83 (2H, m, H-3i'',4ii'), 1.38 (1H, dddd, *J* 15.0, 4.7, 2.5, 2.5, H-5i''); **^{13}C NMR:** (151 MHz, DMSO, 393 K) 169.2 (1v), 166.7 (2ii), 164.0 (5iii), 157.5 (3iii), 153.3 (2), 148.2 (dd, *J* 246.1, 13.5, 3iv), 147.3 (dd, *J* 245.8, 12.3, 4iv), 142.6 (3a), 138.8 (dd, *J* 8.0, 3.6, 1iv), 132.2 (7a), 123.7 (dd, *J* 6.4, 3.4, 6iv), 123.1 (5), 122.7 (6), 119.4 (4), 116.6 (d, *J* 18.1, 5iv), 116.1 (d, *J* 18.0, 2iv), 115.7 (4iii), 112.0 (7), 79.8 (2viii), 75.5 (3viii), 69.5, 69.4, 69.2, 69.0 (2v, 1vi, 2vi, 1vii), 68.2 (2vii), 57.0 (1viii), 56.0 (6ii), 52.7 (4i), 41.8 (2i or 6i), 40.1 (6i or 2i), 31.6 (5ii), 29.7 (3i or 5i), 29.5 (5i or 3i), 28.3 (3ii), 17.0 (4ii), 10.4 (7iii), 9.5 (6iii); **^{19}F NMR:** (565 MHz, DMSO, 393 K) –138.0 – –138.1 (m), –140.7 – –140.9 (m); **LRMS** *m/z* (ESI$^+$) 690 ([M+H]$^+$, 100%), 712 ([M+Na]$^+$, 45%); **HRMS** *m/z* (ESI$^+$) [found: [M+H]$^+$ 690.3118, $C_{37}H_{42}F_2N_5O_6^+$ requires 690.3098]; **RP-HPLC** (Method 1) Retention time: 7.973 min (91%)**.**

(6*S*)-1-(3,4-Difluorophenyl)-6-(5-(3,5-dimethyl-1,2-oxazol-4-yl)-1-(1-(3,6,9,12-tetraoxapentadec-14-ynoyl)piperidin-4-yl)benzimidazol-2-yl)piperidin-2-one (42)



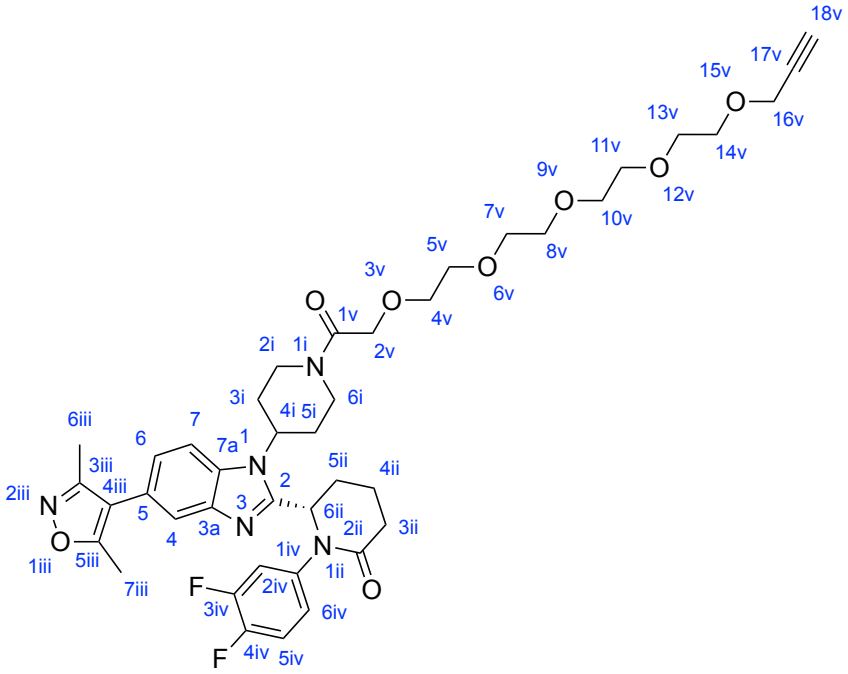
Step 1: To a solution of 3,6,9,12-tetraoxapentadec-14-ynoic acid (**34**) (100 mg, 408 µmol, 1.50 eq.) in anhydrous CH_2Cl_2 (5 mL) was added oxalyl chloride (117 uL, 1.36 mmol, 5.00 eq.) dropwise at 0 ºC, followed by dropwise addition of DMF (3 µL, 40.8 µmol, 0.15 eq.). The reaction mixture was then allowed to warm to ambient temperature and stirred for 30 min. Conversion to the acid chloride intermediate was judged to be complete by TLC analysis by diluting an aliquot of the reaction mixture in MeOH to form an methyl ester derivative. The reaction mixture was then concentrated *in vacuo* to remove solvent and excess oxalyl chloride.

Step 2: The crude residue was dissolved in anhydrous CH_2Cl_2 (5 mL) and cooled to 0 ºC, followed by addition of (6*S*)-1-(3,4-difluorophenyl)-6-(5-(3,5-dimethyl-1,2-oxazol-4-yl)-1-(piperidin-4-yl)-1*H*-1,3-benzodiazol-2-yl)piperidin-2-one (**Pip-obrodib**) as a 1:2 TFA salt (200 mg, 272 µmol, 1.00 eq.) and NEt_3 (380 µL, 2.72 mmol, 10.0 eq.) at 0 ºC. The reaction solution was allowed to warm to ambient temperature and stirred for 2 h before the reaction was judged to be complete by TLC analysis. The reaction solution was diluted with CH_2Cl_2 (25 mL) and quenched by addition of sat. aq. $NaHCO_3$ solution (10 mL). The mixture was partitioned and the aqueous component further extracted with CH_2Cl_2 (2 ×

25 mL). The combined organic extracts were dried (Na_2SO_4), filtered and concentrated *in vacuo*. The crude residue was purified using flash column chromatography on silica gel (5% MeOH/CH_2Cl_2 + 0.1% NH_4OH) to afford the title compound as an off-white solid (124 mg, 169 µmol, 62%);

R_f 0.17 (5% MeOH/CH_2Cl_2); **m.p.** 63–68 ºC (CH_2Cl_2); $[\alpha]_D^{25}$ = –105.52 (c. 1.0 MeCN); $\tilde{\nu}_{max}$ (thin film)/cm^{-1} 3497 (N-H), 1648 (C=O), 1516 (C=C, aromatic), 1215 (C-F); **^{1}H NMR**: (600 MHz, DMSO, 393 K) 7.64 (1H, d, *J* 1.7, H-4), 7.61 (1H, d, *J* 8.4, H-7), 7.32–7.20 (2H, m, H-2iv,5iv), 7.14 (1H, dd, *J* 8.5, 1.7, H-6), 7.05 (1H, dddd, *J* 9.0, 4.1, 2.5, 1.6, H-6iv), 5.66 (1H, dd, *J* 5.7, 4.2, H-6ii), 4.61 (2H, dddd, *J* 12.2, 12.2, 4.3, 4.3, H-4i), 4.38 – 4.25 (2H, m, H-2i',6i'), 4.23 (2H, s, H-2v), 4.12 (2H, d, *J* 2.4, H-13v), 3.68 – 3.50 (12H, m, H-4v,5v,7v,8v,10v,11v), 3.10 (1H, t, *J* 2.4, H-15v), 3.06–2.92 (2H, m, H-2i'',6i''), 2.69–2.62 (1H, m, H-5ii'), 2.55 (1H, ddd, *J* 17.5, 8.7, 6.7, H-5ii''), 2.45 (1H, ddd, *J* 10.0, 7.4, 5.0, H-3ii''), 2.40 (3H, s, H-7iii), 2.35–2.18 (2H, m, H-3i',5i'), 2.22 (3H, s, H-6iii), 2.17 – 2.07 (2H, m, H-3ii',4ii'), 1.92–1.83 (2H, m, H-3i'',4ii''), 1.38 (1H, dddd, *J* 12.8, 4.1, 2.1, 1.0, H-5i''); **^{13}C NMR** (151 MHz, DMSO, 393 K) 169.2 a(1v), 166.7 (2ii), 164.0 (5iii), 157.5 (3iii), 153.3 (2), 148.2 (dd, *J* 246.0, 13.4, 4iv), 147.3 (dd, *J* 245.7, 12.5, 3iv), 142.6 (3a), 138.8 (dd, *J* 8.1, 3.5, 1iv), 132.2 (7a), 123.7 (dd, *J* 6.5, 3.3, 6iv), 123.1 (5), 122.7 (6), 119.4 (4), 116.5 (d, *J* 18.3, 2iv), 116.1 (d, *J* 18.1, 5iv), 115.7 (4iii), 112.0 (7), 79.8 (14v), 75.5 (15v), 69.6, 69.4, 69.3, 69.3, 69.2, 69.0, 68.2 (11v), 57.0 (13v), 56.0 (6ii), 52.7 (4i), 41.8 (2i), 40.1 (6i), 31.6 (5ii), 29.7 (3i), 29.6 (5i), 28.3 (3ii), 17.0 (4ii), 10.4 (7iii), 9.5 (6iii); **^{19}F NMR**: (565 MHz, DMSO, 393 K) -137.9 – -138.1 (m), -140.7 – -140.9 (m); **LRMS** *m/z* (ESI$^+$) 734 ([M+H]$^+$, 100%) 756 ([M+Na]$^+$, 32%); **HRMS** *m/z* (ESI$^+$) [found: [M+H]$^+$ 734.3356, $C_{39}H_{46}F_2N_5O_7^+$ requires 734.3360]; **RP-HPLC** Retention time: 8.406 min (95%)**.**

(6*S*)-1-(3,4-Difluorophenyl)-6-(5-(3,5-dimethyl-1,2-oxazol-4-yl)-1-(1-(3,6,9,12,15-pentaoxaoctadec-17-ynoyl)piperidin-4-yl)benzimidazol-2-yl)piperidin-2-one (43)

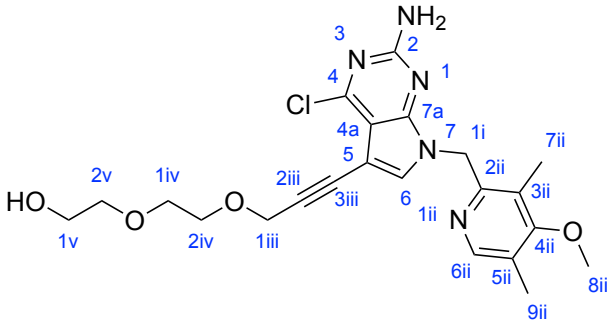


Step 1: To a solution of 3,6,9,12,15-pentaoxaoctadec-17-ynoic acid (**35**) (118 mg, 408 µmol, 1.50 eq.) in anhydrous CH_2Cl_2 (5 mL) was added oxalyl chloride (118 uL, 1.36 mmol, 5.00 eq.) dropwise at 0 ºC, followed by dropwise addition of DMF (3 µL, 40.8 µmol, 0.15 eq.). The reaction mixture was then allowed to warm to ambient temperature and stirred for 30 min. Conversion to the acid chloride intermediate was judged to be complete by TLC analysis by diluting an aliquot of the reaction mixture in MeOH to form an methyl ester derivative. The reaction mixture was then concentrated *in vacuo* to remove solvent and excess oxalyl chloride.

Step 2: The crude residue was dissolved in anhydrous CH_2Cl_2 (5 mL) and cooled to 0 ºC, followed by addition of (6*S*)-1-(3,4-difluorophenyl)-6-(5-(3,5-dimethyl-1,2-oxazol-4-yl)-1-(piperidin-4-yl)-1*H*-1,3-benzodiazol-2-yl)piperidin-2-one (**Pip-obrodib**) as a 1:2 TFA salt (200 mg, 272 µmol, 1.00 eq.) and NEt_3 (380 µL, 2.72 mmol, 10.0 eq.) at 0 ºC. The reaction solution was allowed to warm to ambient temperature and stirred for 2 h before the reaction was judged to be complete by TLC analysis. The reaction solution was quenched by addition of MeOH (5 mL) and concentrated *in vacuo*. The crude residue was purified using

flash column chromatography on silica gel (0–10% MeOH/CH_2Cl_2 + 0.1% NH_4OH) to afford the title compound as an amorphous yellow solid (86.3 mg, 111 μmol, 41%); R_f 0.14 (5% MeOH/CH_2Cl_2); $[\alpha]_D^{25}$ = –81.85 (c. 1.0 MeCN); $\tilde{\nu}_{max}$ (thin film)/cm^{-1} 3428 (N-H), 3259 (C-H), 2926 (C-H), 2868 (C-H), 2114 (C≡C), 1646 (C=O), 1516 (C=C), 1104 (C-F); **^{1}H NMR:** (600 MHz, DMSO, 393 K) 7.64 (1H, d, *J* 1.7, H-4), 7.61 (1H, d, *J* 8.4, H-7), 7.32–7.20 (2H, m, H-2iv,5iv), 7.14 (1H, dd, *J* 8.5, 1.7, H-6), 7.05 (1H, dddd, *J* 8.9, 4.1, 2.5, 0.8, H-6iv), 5.66 (1H, dd, *J* 5.7, 4.2, H-6ii), 4.61 (1H, dddd, *J* 12.2, 12.2, 4.3, 4.3, H-4i), 4.38–4.24 (2H, m, H-2i'',6i''), 4.23 (2H, s, H-2v), 4.12 (2H, d, *J* 2.4, H-16v), 3.68–3.49 (16H, m, H-4v,5v,7v,8v,10v,11v,13v,14v), 3.09 (1H, t, *J* 2.4, H-18v), 2.99 (2H, s, H-2i',6i'), 2.69–2.61 (1H, m, H-5ii''), 2.59–2.51 (1H, m, H-5ii'), 2.49–2.41 (1H, m, H-3ii''), 2.39 (3H, s, H-7iii), 2.35–2.17 (2H, m, H-3i'',5i''), 2.22 (3H, s, H-6iii), 2.17–2.07 (2H, m, H-3ii',4ii''), 1.91–1.82 (2H, m, H-3i',4ii'), 1.37 (1H, dddd, *J* 12.8, 4.1, 2.1, 1.0, H-5i'); **^{13}C NMR**: (151 MHz, DMSO, 393 K) 169.2 (1v), 166.7 (2ii), 164.0 (5iii), 157.5 (3iii), 153.3 (2), 148.2 (dd, *J* 246.0, 13.4, 4iv), 147.3 (dd, *J* 245.8, 12.5, 3iv), 142.6 (3a), 138.8 (dd, *J* 8.1, 3.5, 1iv), 132.2 (7a), 123.7 (dd, *J* 6.5, 3.3, 6iv), 123.1 (5), 122.7 (6), 119.4 (4), 116.5 (d, *J* 18.2, 2iv), 116.1 (d, *J* 18.2, 5iv), 115.7 (4iii), 112.0 (7), 79.8 (17v), 75.5 (18v), 69.6, 69.4, 69.3, 69.3, 69.2, 69.0, 68.2 (14v), 57.0 (16v), 56.0 (6ii), 52.7 (4i), 41.8 (6i), 40.1 (2i), 31.6 (5ii), 29.7 (3i), 29.6 (5i), 28.3 (3ii), 17.0 (4ii), 10.4 (7iii), 9.5 (6iii); **^{19}F NMR:** (565 MHz, DMSO, 393 K) -138.0 (dt, *J* 22.9, 10.8), -140.7 – -140.8 (m); **LRMS** *m/z* (ESI^+) 778 ($[M+H]^+$, 100%) 800 ($[M+Na]^+$, 16%); **HRMS** *m/z* (ESI^+) [found: $[M+H]^+$ 778.3628, $C_{41}H_{50}F_2N_5O_8^+$ requires 778.3622]; **RP-HPLC** (Method 1) Retention time: 8.421 min (95%).

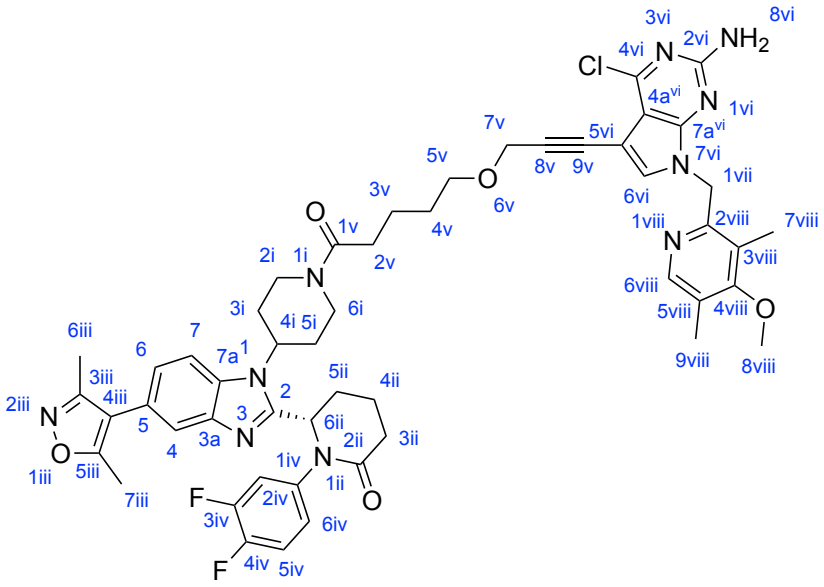
2-(2-(3-(2-Amino-4-chloro-7-((4-methoxy-3,5-dimethylpyridin-2-yl)methyl)pyrrolo[2,3-*d*]pyrimidin-5-yl)prop-2-ynoxy)ethoxy)ethanol (44)



In a GreenHouse parallel synthesiser™, vials were charged with 4-chloro-5-iodo-7-((4-methoxy-3,5-dimethylpyridin-2-yl)methyl)-7*H*-pyrrolo[2,3-*d*]pyrimidin-2-amine (**Iodo-BIIB021**) (22.2 mg, 50.0 µmol, 1.00 eq.), CuI (1.6 mg, 8.5 µmol, 0.17 eq.), $Pd(PPh_3)_2Cl_2$ (3.0 mg, 4.3 µmol, 0.09 eq.), and 2-(2-(prop-2-yn-1-yloxy)ethoxy)ethan-1-ol (**27**) (6.8 µL, 7.2 mg, 50 µmol, 1 eq.). The atmosphere was then purged for argon by three purge/fill cycles. The reaction was then dissolved with MeCN, ethanol, dioxane, or DMF (1 mL) which had been sparged with nitrogen for 15 min. The reaction was then stirred and heated to 70 ºC for 6 h, taking 5 µL aliquots with a micro-syringe at regular intervals. The reaction was cooled to ambient temperature and then concentrated *in vacuo*. The yield of each reaction was determined by quantitative ^{1}H NMR using 1,3,5-trimethoxybenzene as an internal standard. The reaction performed in MeCN was diluted with EtOAc (25 mL) and aq. HCl solution (1 M, 25 mL) and partitioned. The aqueous phase was further washed with EtOAc (25 mL) before the pH was adjusted to 10 with sat. aq. K_2CO_3 solution and then extracted with EtOAc (2 × 25 mL). The combined organic extracts were dried (Na_2SO_4), filtered, and concentrated *in vacuo.* The crude residue was purified using flash column chromatography on silica gel (EtOAc) to afford the title compound as a beige solid (18.0 mg, 41.3 ¨µmol, 83%). R_f 0.25 (EtOAc); $\tilde{\nu}_{max}$ (thin film)/cm^{-1} 3467, 3309, 2232; 1629, 1607, 1558, 1453, 1071; **^{1}H NMR** (600 MHz, DMSO) 8.05 (1H, s, H-6ii), 7.40 (1H, s, H-6), 6.74 (2H, s, NH_2), 5.29 (2H, s, H-1i), 4.57 (1H, t, *J* 5.5, H-3), 4.38 (2H, s, H-1iii), 3.73 (3H, s, H-8ii), 3.64 (2H, dd, *J* 5.9, 3.7, H-2iv), 3.57 (2H, dd, *J* 5.8, 3.7, H-1iv), 3.49 (2H, ddd, *J* 5.7,

5.5, 4.8, H-1v), 3.42 (2H, dd, *J* 5.7, 4.8, H-2v), 2.26 (3 H, s, H-7ii), 2.16 (3 H, s, H-9ii); **^{13}C NMR** (151 MHz, DMSO): 163.8 (4ii), 160.1 (2), 154.0 (7a), 153.8 (2ii), 152.0 (4), 149.3 (6ii), 132.7 (6), 125.5 (5ii), 123.8 (3ii), 107.8 (4a), 94.4 (5), 88.1 (2iii), 79.5 (3iii), 72.8 (2v), 70.0 (1iv), 69.0 (2iv), 60.7 (1v), 60.3 (8ii), 58.8 (1iii), 46.9 (1i), 13.3 (9ii), 10.7 (7ii); **LRMS** *m/z* (ESI^+) 460 ($[M+H]^+$, 100%); **HRMS** *m/z* (ESI^+) [found: $[M+H]^+$ 460.1739, $C_{12}H_{27}ClN_5O_4^-$ requires 460.1746]. **RP-HPLC** Retention time: 6.803 min (>99%).

(6*S*)-6-(1-(1-(5-((3-(2-Amino-4-chloro-7-((4-methoxy-3,5-dimethylpyridin-2-yl)methyl)-7*H*-pyrrolo[2,3-*d*]pyrimidin-5-yl)prop-2-yn-1-yl)oxy)pentanoyl)piperidin-4-yl)-5-(3,5-dimethyl-1,2-oxazol-4-yl)-1*H*-1,3-benzimidazol-2-yl)-1-(3,4-difluorophenyl)piperidin-2-one (AcDC-1)

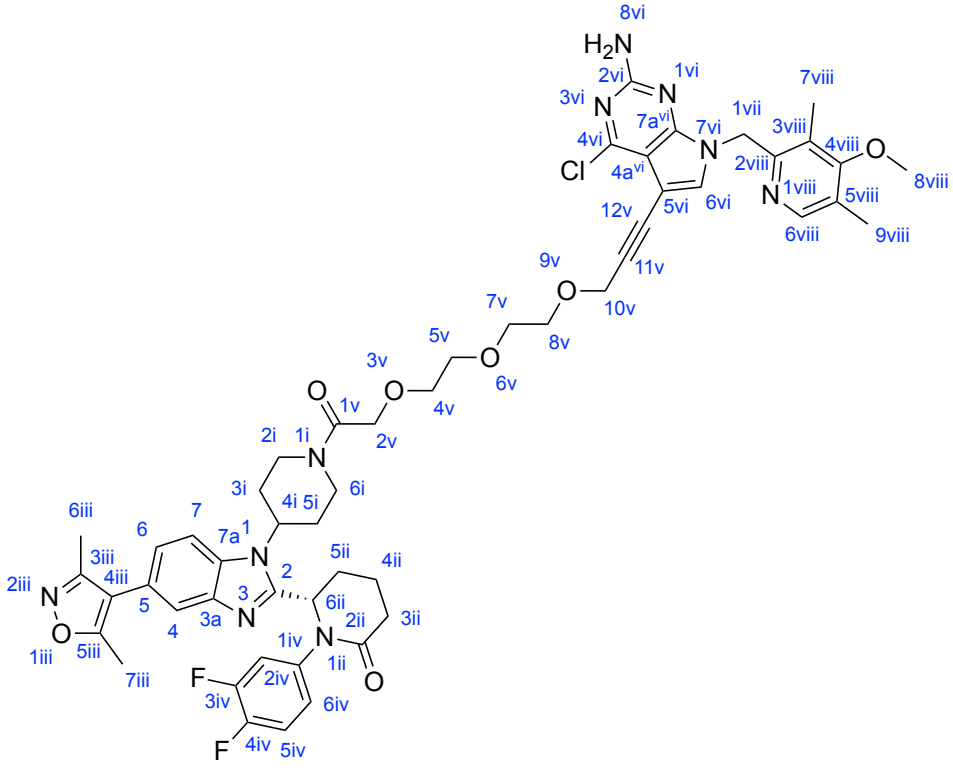


A microwave vial was charged with (6*S*)-1-(3,4-difluorophenyl)-6-(5-(3,5-dimethyl-1,2-oxazol-4-yl)-1-(1-(5-(prop-2-yn-1-yloxy)pentanoyl)piperidin-4-yl)-1*H*-1,3-benzimidazol-2-yl]piperidin-2-one (**40**) (50.0 mg, 77.7 µmol, 1.00 eq.), 4-chloro-5-iodo-7-((4-methoxy-3,5-dimethylpyridin-2-yl)methyl)-7*H*-pyrrolo[2,3-*d*]pyrimidin-2-amine (**Iodo-BIIB021**) (36.2 mg, 109 µmol, 1.40 eq.), $Pd(PPh_3)_2Cl_2$ (2.73 mg, 3.89 µmol, 0.05 eq.), and CuI (1.48 mg, 7.77 µmol, 0.10 eq.), and then suspended in MeCN (5 mL) followed by addition of NEt_3 (54 uL, 388 µmol, 5.00 eq.). The vial was sealed and sparged with argon for 20 min before heating 70 ºC for 3 h, after which time LC-MS analysis showed complete

consumption of the limiting starting material. The reaction mixture was diluted with water (25 mL) and extracted with CH_2Cl_2 (3 × 25 mL). The combined organic components were washed with aqueous EDTA solution (pH 8, 1 M, 25 mL), saturated aqueous $NaHCO_3$ solution (25 mL), brine (25 mL), dried (Na_2SO_4), filtered, and concentrated *in vacuo*. The crude residue was first purified using flash column chromatography on silica gel (1–7% MeOH/CH_2Cl_2) and then further purified by preparative HPLC before lyophilisation to afford the title compound as a yellow powder (34.2 mg, 35.6 µmol, 46%); $\boldsymbol{R_f}$ 0.39 (10% MeOH/CH_2Cl_2); **m.p**. 136 – 140 ºC (MeCN/H_2O); $[\alpha]_D^{25}$ = −73.21 (c. 1.00 MeCN); $\tilde{\nu}_{max}$ (thin film)/cm^{-1} 3459 (N-H), 2981 (C-H), 1610 (C=O), 1450 (C=C); **^{1}H NMR** (600 MHz, $CDCl_3$) 8.19 (1H, s, H-6viii), 7.70 (1H, d, *J* 1.6, 4), 7.45–7.40 (1H, m, H-7), 7.19–7.13 (1H, m, H-5iv), 7.12 (1H, dd, *J* 8.4, 1.6, H-6), 7.11 (1H, s, H-6vi), 7.09–7.02 (1H, m, H-2iv), 7.02–6.97 (1H, m, H-6iv), 5.29 (2H, s, H-1vii), 5.32–5.25 (1H, m, H-6ii), 5.07 (2H, s, H-8vi), 4.97–4.83 (1H, m, H-2i'/6i'), 4.37 (2H, s, H-7v), 4.23 (1H, dddd, *J* 12.4, 12.4, 4.3, 4.3, H-4i), 4.16 – 4.01 (1H, m, H-2i'/6i'), 3.75 (3H, s, H-8viii), 3.65 (2H, t, *J* 6.3, H-5v), 3.20–3.03 (1H, m, H-2i''/6i''), 2.87 (1H, dddd, *J* 18.0, 5.4, 4.7, 2.1, H-3ii'), 2.66 (1H, ddd, *J* 18.0, 8.6, 6.5, H-3ii''), 2.67–2.51 (1H, m, H-6i''), 2.49 – 2.45 (2H, m, H-2v), 2.44 (3H, s, H-7iii), 2.43–2.36 (1H, m, H-5ii'), 2.31 (3H, s, H-6iii), 2.37–2.12 (4H, m, H-3i',3i'',4ii',5ii''), 2.25 (3H, s, H-9viii), 2.22 (3H, s, H-7viii), 1.95–1.90 (1H, m, H-4ii''), 1.88–1.77 (3H, m, 3v, H-5i''), 1.73 (2H, tt, *J* 7.5, 7.3, H-4v), 1.41–1.32 (1H, m, H-5i'); **^{13}C NMR** (151 MHz, $CDCl_3$) 171.6 (1v), 170.9 (2ii), 165.3 (5iii), 164.5 (4viii), 158.95, (4vii), 158.93 (3iii), 153.2 (2viii), 153.2 (2vi), 153.1 (7a^{vi}), 152.4 (2), 150.1 (dd, *J* 154.7, 11.4, 3iv), 149.6 (6viii), 149.5 (dd, *J* 249.7, 12.3, 4iv), 143.4 (3a), 138.6 (d, *J* 17.1, 1iv), 132.8 (7a, α), 132.7 (7a, β), 130.8 (6vi), 126.4 (5viii), 125.4 (3viii), 124.9 (5), 124.4 (6iv), 124.2 (6), 121.1 (4), 118.0 (d, *J* 18.0, 5iv), 117.5 (d, *J* 18.0, 2iv), 116.7 (4iii), 112.4 (7, α), 112.3 (7, β), 109.6 (4a^{vi}), 96.3 (5vi), 87.9 (8v), 78.7 (9v), 69.6 (5v), 60.1 (8viii), 59.1 (7v), 57.9 (6ii, α), 57.8 (6ii, β), 54.6 (4i), 47.4 (1vii), 45.1 (2i/6i, α), 45.0 (2i/6i, β), 41.3 (6i), 33.0 (2v), 32.5 (3ii), 31.3 (3i/5i, α), 31.2 (3i/5i, β), 30.42 (3i/5i α), 30.38 (3i/5i β), 29.8 (5ii), 29.2 (4v), 22.3 (3v), 18.2 (4ii), 13.4 (9viii), 11.7 (7iii), 11.0 (6iii), 11.0 (7viii), N.B. presence of conformers denoted by α/β notation; **^{19}F NMR** (565 MHz,

$CDCl_3$) -135.0 – -135.3 (m), -137.8 – -138.1 (m); **LRMS** *m/z* (ESI^+) 959 ($[M+H]^+$, 100%), 480 ($[M+2H]^{2+}$, 67%); **HRMS** *m/z* (ESI^+) [found: $[M+H]^+$ 959.3952, $C_{51}H_{54}ClF_2N_{10}O_5^+$ requires 959.3930]; **RP-HPLC** (Method 2) Retention time: 9.028 min (>99%).

(6*S*)-6-(1-(1-(2-(2-(2-((3-(2-Amino-4-chloro-7-((4-methoxy-3,5-dimethylpyridin-2-yl)methyl)-7*H*-pyrrolo[2,3-*d*]pyrimidin-5-yl)prop-2-yn-1-yl)oxy)ethoxy)ethoxy)acetyl)piperidin-4-yl)-5-(3,5-dimethyl-1,2-oxazol-4-yl)-1*H*-1,3-benzimidazol-2-yl)-1-(3,4-difluorophenyl)piperidin-2-one (AcDC-2)



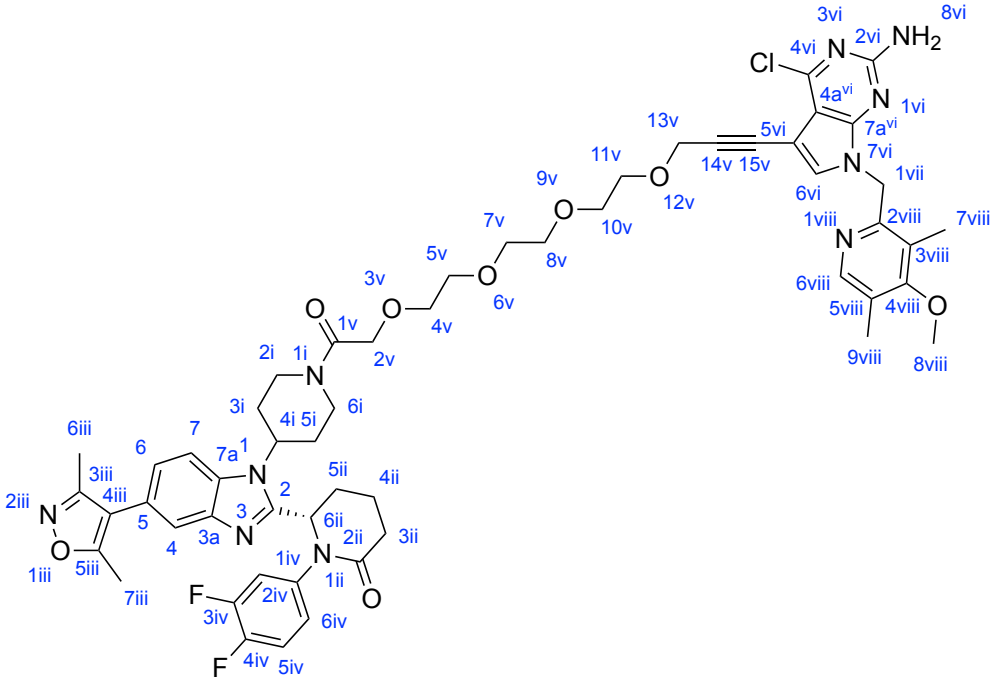
A microwave vial was charged with (6*S*)-1-(3,4-difluorophenyl)-6-(5-(3,5-dimethyl-1,2-oxazol-4-yl)-1-(1-(2-(2-(2-prop-2-ynoxyethoxy)ethoxy)acetyl)piperidin-4-yl)benzimidazol-2-yl)piperidin-2-one (**41**) (50.0 mg, 62.2 µmol, 1.00 eq.), 4-chloro-5-iodo-7-((4-methoxy-3,5-dimethylpyridin-2-yl)methyl)-7*H*-pyrrolo[2,3-*d*]pyrimidin-2-amine (**Iodo-BIIB021**) (21.7 mg, 65.3 µmol, 1.05 eq.), $Pd(PPh_3)_2Cl_2$ (2.18 mg, 3.11 µmol, 0.05 eq.), and CuI (1.18 mg, 6.22 µmol, 0.10 eq.), and then suspended in MeCN (4 mL) followed by addition of

NEt_3 (43 uL, 311 µmol, 5.00 eq.). The vial was sealed and sparged with argon for 20 min before heating 70 ºC for 3 h, after which time LC-MS analysis showed complete consumption of the limiting starting material. The reaction mixture was diluted with water (25 mL) and extracted with CH_2Cl_2 (3 × 25 mL). The combined organic components were washed with aqueous EDTA solution (pH 8, 1 M, 25 mL), saturated aqueous $NaHCO_3$ solution (25 mL), brine (25 mL), dried (Na_2SO_4), filtered, and concentrated *in vacuo*. The crude residue was first purified using flash column chromatography on silica gel (1–7% MeOH/CH_2Cl_2) and then further purified by preparative HPLC before lyophilisation to afford the title compound as a yellow powder (27.3 mg, 27.1 µmol, 44%);

R_f 0.25 (5% MeOH/CH_2Cl_2); **m.p.** 131–135 ºC (from MeCH/H_2O); $[\alpha]_D^{25}$ = −73.08 (c. 0.5 MeCN); $\tilde{\nu}_{max}$ (thin film)/cm^{-1} 3470, 2944, 1641, 1612, 1452, 1090; **^{1}H NMR** (600 MHz, DMSO, 393 K) 8.09 (1H, s, H-6viii), 7.64 (1H, d, *J* 1.7, H-4), 7.61 (1H, d, *J* 8.4, H-7), 7.31–7.20 (3H, m, H-2iv,5iv,6vi), 7.14 (1H, dd, *J* 8.4, 1.7, H-6), 7.05 (1H, dddd, *J* 9.0, 4.0, 2.5, 1.5, H-6iv), 6.23 (2H, s, H-8vi), 5.67 (1H, dd, *J* 5.7, 4.2, H-6ii), 5.29 (2H, s, H-1vii), 4.62 (1 H, dddd, *J* 12.1, 12.1, 4.3, 4.3, H-4i), 4.35 (2H, s, H-10v), 4.33 – 4.24 (2H, m, H-2i'',6i''), 4.23 (2H, s, H-2v), 3.77 (3H, s, H-8viii), 3.69–3.59 (8H, m, H-4v,5v,7v,8v), 3.07–2.93 (2H, m, H-2i',6i'), 2.65 (1H, ddd, *J* 17.4, 5.7, 5.7, H-5ii''), 2.59–2.52 (1H, m, H-5ii'), 2.49–2.41 (1H, m, H-3ii''), 2.39 (3H, s, H-7iii), 2.28 (3H, s, H-9viii), 2.35 – 2.17 (2H, m, H-3i'',5i''), 2.22 (3H, s, H-6iii), 2.19 (3H, s, H-7viii), 2.17–2.05 (2H, m, H-3ii',4ii'), 1.91–1.82 (2H, m, H-3i',4ii''), 1.41–1.35 (1H, m, H-5i'); **^{13}C NMR** (151 MHz, DMSO, 393 K): 169.2 (1v), 166.8 (2ii), 164.0 (5iii), 163.1 (4viii), 159.0 (4vi), 157.5 (3iii), 153.3 (2), 153.0 (2vi), 152.6 (7a^{vi}), 151.2 (2viii), 148.4 (6viii), 148.2 (dd, *J* 246.0, 13.4, 3iv), 147.3 (dd, *J* 246.1, 12.7, 4iv), 142.6 (3a), 138.8 (dd, *J* 8.2, 3.5, 1iv), 132.2 (7a), 130.9 (6vi), 124.3 (3viii), 123.7 (dd, *J* 6.4, 3.4, 6iv), 123.1 (5viii), 123.1 (5), 122.7 (6), 119.4 (4), 116.6 (d, *J* 18.4, 5iv), 116.1 (d, *J* 17.8, 2iv), 115.7 (4iii), 112.0 (7), 107.2 (4a^{vi}), 94.0 (5vi), 87.1 (11v), 78.4 (12v), 69.5, 69.4, 69.2, 69.1 (2v,1vi,2vi,1vii), 68.1 (8v), 59.1 (8viii), 57.9 (10v), 56.0 (6ii), 52.7 (4i), 46.0 (1vii), 41.7 (2i), 40.1 (6i), 31.7 (5ii), 29.7 (3i), 29.6 (5i), 28.3 (3ii), 17.0 (4ii), 12.0 (9viii), 10.4 (7iii), 9.7 (7viii), 9.5 (6iii); **^{19}F NMR** (565 MHz, DMSO, 363 K) -138.0 (m), -140.7 (m); **LRMS** *m/z* (ESI$^+$) 1005

([M+H]$^+$, 100%), 503 ([M+2H]$^{2+}$, 68%), 1027 ([M+Na]$^+$, 31%); **HRMS** *m/z* (ESI$^+$) [found: [M+H]$^+$ 1005.3993, $C_{52}H_{56}ClF_2N_{10}O_7^+$ requires 1005.3985]; **RP-HPLC** (Method 2) Retention time: 8.465 min (98%).

(6*S*)-6-(1-(1-(15-(2-Amino-4-chloro-7-((4-methoxy-3,5-dimethylpyridin-2-yl)methyl)-7*H*-pyrrolo[2,3-*d*]pyrimidin-5-yl)-3,6,9,12-tetraoxapentadec-14-ynoyl)piperidin-4-yl)-5-(3,5-dimethyl-1,2-oxazol-4-yl)-1*H*-1,3-benzodiazol-2-yl)-1-(3,4-difluorophenyl)piperidin-2-one (AcDC-3)

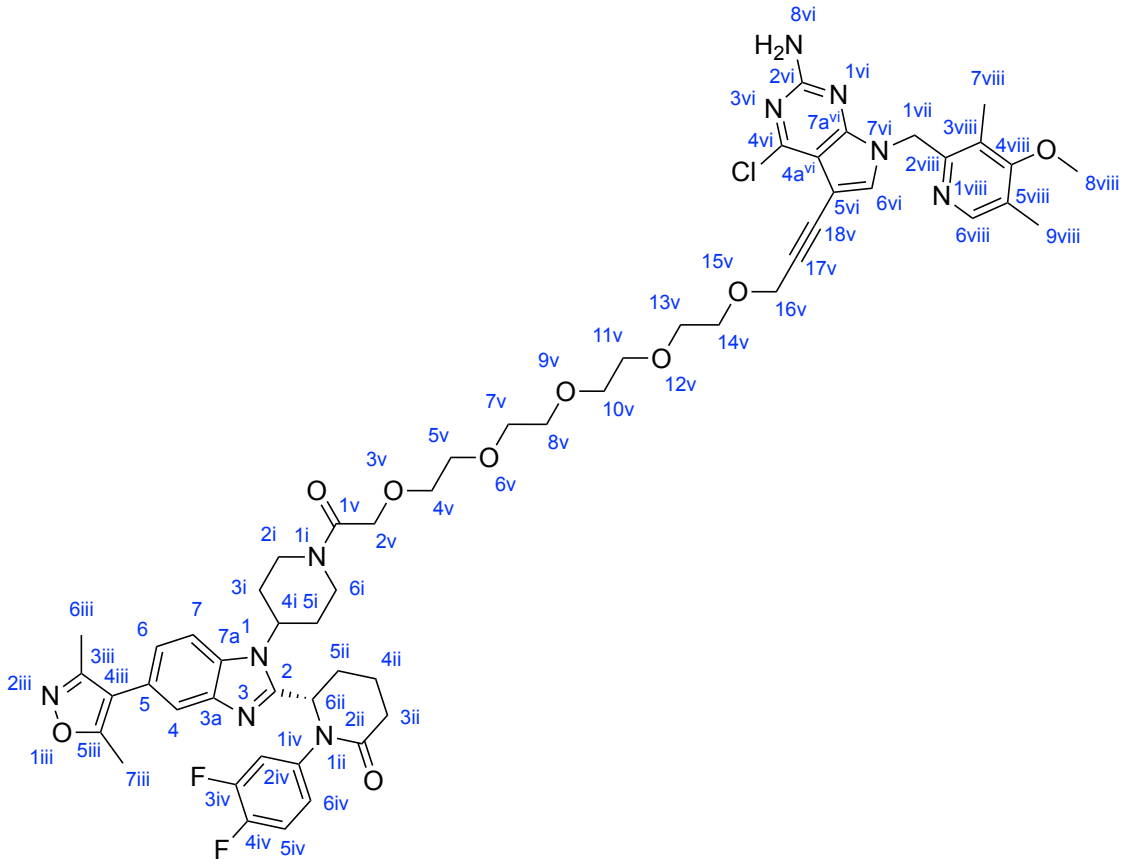


A microwave vial was charged with (6*S*)-1-(3,4-difluorophenyl)-6-(5-(3,5-dimethyl-1,2-oxazol-4-yl)-1-(1-(3,6,9,12-tetraoxapentadec-14-ynoyl)piperidin-4-yl)benzimidazol-2-yl)piperidin-2-one (**42**) (50.0 mg, 68.1 µmol, 1.00 eq.), 4-chloro-5-iodo-7-((4-methoxy-3,5-dimethylpyridin-2-yl)methyl)-7*H*-pyrrolo[2,3-*d*]pyrimidin-2-amine (**Iodo-BIIB021**) (31.7 mg, 71.5 µmol, 1.05 eq.), $Pd(PPh_3)_2Cl_2$ (2.39 mg, 3.41 µmol, 0.05 eq.), and CuI (1.30 mg, 6.81 µmol, 0.10 eq.), and then suspended in MeCN (5 mL) followed by addition of NEt_3 (48 uL, 341 µmol, 5.00 eq.). The vial was sealed and sparged with argon for 20 min before heating with microwave irradiation to 70 ºC for 40 min, followed by heating to 80 ºC for 20 min, after which time LC-MS analysis showed complete consumption of the limiting starting material. The reaction mixture was diluted with water (25 mL) and extracted with

CH_2Cl_2 (3 × 25 mL) and then 10% $(CH_3)_2CHOH/CH_2Cl_2$ (3 × 25 mL). The combined organic components were washed with saturated aqueous $NaHCO_3$ solution (25 mL), brine (25 mL), dried (Na_2SO_4), filtered, and concentrated *in vacuo*. The crude residue was first purified using flash column chromatography on silica gel (1–8% $MeOH/CH_2Cl_2$) and then further purified by preparative HPLC before lyophilisation to afford the title compound as a yellow powder (15 mg, 14.3 μmol, 21%);

***R*$_f$** 0.35 (10% $MeOH/CH_2Cl_2$); **m.p.** 106–108 ºC (from $MeCH/H_2O$); $[\alpha]_D^{25}$ = −70.67 (c. 1.0 $CHCl_3$); **^{1}H NMR** (600 MHz, CDCl3) 8.18 (1H, s, H-6viii), 7.67 (1H, d, *J* 1.6, H-4), 7.42 (1H, d, *J* 8.5, H-7), 7.17 – 7.10 (2H, m, H-5iv,6vi), 7.09 (1H, dd, *J* 8.4, 1.7, H-6), 7.03 (1H, q, *J* 9.0, H-2iv), 6.97 (1H, s, H-6iv), 5.31 – 5.25 (3H, m, H-1vii,6ii), 5.01 (2H, s, H-8vi), 4.79 (1H, m, H-2i'/6i'), 4.37 (2H, s, H-13v), 4.34 – 4.15 (4H, m, H-2i'/6i',2v,4i), 3.74 (3H, s, H-8viii), 3.73 – 3.54 (12H, m, H-4v,5v,7v,8v,10v,11v), 3.21 – 3.03 (1H, m, H-2i''/6i''), 2.84 (1H, dt, *J* 18.0, 5.6, H-3ii'), 2.75 – 2.55 (2H, m, H-3ii'',6i''), 2.42 (3H, s, H-7viii), 2.49 – 2.14 (5H, m, H-3i',5i',4ii',5ii',5ii''), 2.29 (3H, s, H-6iii), 2.24 (3H, s, H-9viii), 2.21 (3H, s, H-7iii), 1.96–1.77 (2H, m, H-4ii'',3i''/5i''), 1.35 (1H, s, 3i''/5i''); **^{13}C NMR** (151 MHz, $CDCl_3$) 171.0 (2ii), 168.0 (1v), 165.3 (5iii), 164.6 (4viii), 159.0 (3iii), 153.3 (2viii), 153.2 (2vi), 153.1 (7a^{vi}), 152.4 (2), 150.1 (dd, *J* 249.8, 13.2, 3iv), 149.6 (6viii), 149.5 (dd, *J* 249.7, 12.1, 4iv), 143.4 (3a), 138.7 (1iv), 132.8 (7a), 130.8 (6vi), 126.5 (5viii), 125.4 (3viii), 124.9 (5), 124.4 (6iv), 124.1 (6), 121.2 (4), 118.0 (d, *J* 18.0, 5iv), 117.5 (d, *J* 18.0, 2iv), 116.7 (4iii), 112.4 (7), 109.6 (4a^{vi}), 96.3 (5vi), 87.6 (14v), 79.1 (15v), 71.2 (2v, α), 71.1 (2v, β), 70.7, 70.6, 70.6, 70.6, 70.5 (4v–10v), 69.1 (11v), 60.1 (8viii), 59.4 (13v), 57.8 (6ii), 54.4 (4i), 47.4 (1vii), 44.9 (2i/6i, α), 44.8 (2i/6i, β), 41.7 (6i), 32.5 (3ii), 31.2 (3i/5i, α), 31.1 (3i/5i, β), 30.4 (3i/5i, α), 30.4 (3i/5i, β), 29.8 (5ii), 18.2 (4ii), 13.5 (9viii), 11.8 (7iii), 11.1 (6iii), 11.0 (7viii), N.B. presence of conformers denoted by α/β notation; **^{19}F NMR**: (565 MHz, $CDCl_3$) -135.05 – -135.39 (m), -137.87 – -138.18 (m); **LRMS** *m/z* (ESI^+) 1049 ($[M+H]^+$, 100%) 525 ($[M+2H]^{2+}$, 72%); **HRMS** *m/z* (ESI^+) [found: $[M+H]^+$ 1049.4273, $C_{54}H_{60}ClF_2N_{10}O_8^+$ requires 1049.4247]; **RP-HPLC** (Method 1) Retention time: 8.663 min (100%).

(6*S*)-6-(1-(1-(18-(2-Amino-4-chloro-7-((4-methoxy-3,5-dimethylpyridin-2-yl)methyl)-7*H*-pyrrolo[2,3-*d*]pyrimidin-5-yl)-3,6,9,12,15-pentaoxaoctadec-17-ynoyl)piperidin-4-yl)-5-(3,5-dimethyl-1,2-oxazol-4-yl)-1*H*-1,3-benzodiazol-2-yl)-1-(3,4-difluorophenyl)piperidin-2-one (AcDC-4)

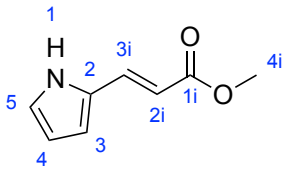


A microwave vial was charged with (6*S*)-1-(3,4-difluorophenyl)-6-(5-(3,5-dimethyl-1,2-oxazol-4-yl)-1-(1-(3,6,9,12,15-pentaoxaoctadec-17-ynoyl)piperidin-4-yl)benzimidazol-2-yl)piperidin-2-one (**43**) (50.0 mg, 64.3 µmol, 1.00 eq.), 4-chloro-5-iodo-7-((4-methoxy-3,5-dimethylpyridin-2-yl)methyl)-7*H*-pyrrolo[2,3-*d*]pyrimidin-2-amine (**Iodo-BIIB021**) (29.9 mg, 67.5 µmol, 1.05 eq.), $Pd(PPh_3)_2Cl_2$ (2.26 mg, 3.21 µmol, 0.05 eq.), and CuI (1.22 mg, 6.43 µmol, 0.10 eq.), and then suspended in MeCN (1 mL) followed by addition of NEt_3 (45 uL, 321 µmol, 5.00 eq.). The vial was sealed and sparged with argon for 20 min before heating 70 ºC for 4 h, after which time LC-MS analysis showed complete consumption of the limiting starting material. The reaction mixture was diluted with water (25 mL) and extracted with CH_2Cl_2 (3 × 25 mL). The combined organic components were

washed with aqueous EDTA solution (pH 8, 1 M, 25 mL), saturated aqueous $NaHCO_3$ solution (25 mL), brine (25 mL), dried (Na_2SO_4), filtered, and concentrated *in vacuo*. The crude residue was first purified using flash column chromatography on silica gel (1–7% MeOH/CH_2Cl_2) and then further purified by preparative HPLC before lyophilisation to afford the title compound as a yellow powder (37 mg, 33.7 μmol, 52%);

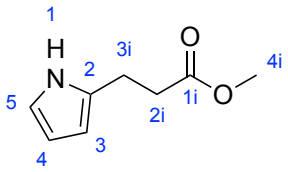
R_f 0.34 (10% MeOH/CH_2Cl_2); **m.p.** 96–99 ºC (from MeCH/H_2O); $[\alpha]_D^{25}$ = -67.72 (c. 0.5 MeCN); $\tilde{\nu}_{max}$ (thin film)/cm^{-1} 3433, 2928, 1649 (C=O), 1611 (C=O), 1451 (C-H) 1098 (C-O); **^{1}H NMR** (400 MHz, $CDCl_3$): 8.17 (1H, s, H-6viii), 7.67 (1H, d, *J* 1.6, H-4), 7.42 (1H, d, *J* 8.4, H-7), 7.16 – 7.10 (1H, m, H-5iv), 7.09 (1H, s, H-6vi), 7.08 (1H, dd, *J* 8.4, 1.7, H-6), 7.07–6.99 (1H, m, H-2iv), 7.00–6.92 (1H, m, H-6iv), 5.29–5.24 (3H, m, H-1vii',6ii), 5.07 (2H, s, H-8vi), 4.88–4.69 (1H, m, H-2i'/6i'), 4.39 (2H, s, H-16v), 4.33 – 4.11 (4H, m, H-2i/6i',2v,4i'), 3.73 (3H, s, H-8viii), 3.79 – 3.50 (16H, m, H-4v–14v), 3.11 (1H, dt, *J* 51.6, 13.2, H-2i''/6i''), 2.84 (1H, ddd, *J* 18.1, 5.3, 1.2, H-3ii'), 2.73–2.54 (2H, m, H-2i''/6i'',3ii''), 2.42 (3H, s, H-7viii), 2.50 – 2.14 (5H, m, H-3i',5i',4ii',5ii',5ii''), 2.29 (3H, s, H-6iii), 2.23 (3H, s, H-9viii), 2.19 (3H, s, H-7iii), 1.94 – 1.81 (2H, m, H-4ii'',3i''/5i''), 1.37–1.32 (1H, m, H-3i''/5i''); **^{13}C NMR** (131 MHz, $CDCl_3$): (151 MHz, CDCl3) 170.9 (2ii), 168.0 (1v), 165.3 (5iii), 164.4 (4viii), 158.9 (d, *J* 6.9, 3iii), 153.2 (2viii), 153.2 (2vi), 153.1 (7a^{vi}), 152.4 (2), 150.1 (dd, *J* 250.1, 13.4, 3iv), 149.7 (6viii), 149.5 (dd, *J* 249.5, 12.3, 4iv), 143.4 (3a), 138.6 (1iv), 132.7 (7a), 130.8 (6vi), 126.4 (5viii), 125.3 (3viii), 124.8 (5), 124.3 (d, *J* 16.8, 6iv), 124.1 (6), 121.1 (4), 117.9 (d, *J* 18.0, 5iv), 117.5 (d, *J* 17.9, 2iv), 116.7 (4iii), 112.4 (7), 109.6 (4a^{vi}), 96.3 (5vi), 87.6 (17v), 79.1 (18v), 71.1 (2v, α), 71.1 (2v, β), 70.7, 70.6, 70.6, 70.6, 70.6, 70.5, 70.5 (4v–13v), 69.1 (14v), 60.1 (8viii), 59.4 (16v), 57.8 (6ii), 54.4 (4i), 47.5 (1vii), 44.8 (2i/6i, α), 44.7 (2i/6i, β), 41.7 ((2i/6i), 32.4 (3ii), 31.2 (3i/5i, α), 31.1 (3i/5i, β), 30.4 (3i/5i, α), 30.3 (3i/5i, β), 29.8 (5ii), 18.1 (4ii), 13.4 (9viii), 11.7 (7iii), 11.0 (6iii), 11.0 (7viii), N.B. presence of conformers denoted by α/β notation; **^{19}F NMR**: (565 MHz, $CDCl_3$) -135.1 – -135.4 (m), -137.9 – -138.2 (m); **LRMS** *m/z* (ESI^+) 1093 ($[M+H]^+$, 100%), 547 ($[M+2H]^{2+}$, 81%) 547 ($[M+Na]^+$, 49%); **HRMS** *m/z* (ESI^+) [found: $[M+Na]^+$ 1115.4353, $C_{56}H_{63}ClF_2N_{10}O_9Na^+$ requires 1115.4328]; **RP-HPLC** (Method 1) Retention time: 8.533 min (99%).

Methyl (2*E*)-3-(1*H*-pyrrol-2-yl)prop-2-enoate (46)



To a solution of pyrrole-2-carboxaldehyde (951 mg, 10.0 mmol, 1.00 eq.) in anhydrous THF (20 mL) was added sodium hydride (60% *w/w*, 400 mg, 10.0 mmol, 1.00 eq.) at 0 ºC. The reaction solution was stirred for 30 min before dropwise addition of trimethyl phosphonoacetate (1.62 mL, 10.0 mmol, 1.00 eq.) at 0 ºC over 5 min. The reaction solution was allowed to warm to ambient temperature and stirred for 18 h before the reaction was judged to be complete by TLC analysis. The reaction mixture was diluted with EtOAc (100 mL) and partitioned with H_2O (100 mL). The aqueous component was further extracted with EtOAc (2 × 50 mL) and the combined organic components were washed with brine (50 mL), dried (Na_2SO_4), filtered, and concentrated *in vacuo* to afford the title compound as a colourless oil without further purification (1.55 g, 10.3 mmol, >99%) $\boldsymbol{R_f}$ 0.30 (20% EtOAc/petroleum ether); **^{1}H NMR** (400 MHz, $CDCl_3$): 8.74 (1H, br s, H-1), 7.49 (1H, d, *J* 15.9, H-3i), 6.85 (1H, ddd, *J* 2.8, 2.7, 1.4, H-5), 6.49 (1H, ddd, *J* 3.9, 2.4, 1.4, H-3), 6.21 (1H, ddd, *J* 3.7, 2.7, 2.3, H-4), 5.94 (1H, d, *J* 15.9, 2i), 3.70 (3H, s, H-4i); **LRMS** *m/z* (ESI^+) 627 ($[4M+Na]^+$, 100%); **HRMS** *m/z* (ESI^+) [found: $[M+H]^+$ 152.0707, $C_8H_{10}NO_2^+$ requires 152.0706]. These data agree with the literature values.[191]

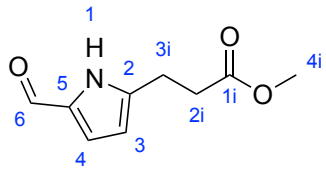
Methyl 3-(1*H*-pyrrol-2-yl)propanoate (47)



A solution of methyl (2*E*)-3-(1*H*-pyrrol-2-yl)prop-2-enoate (**46**) (1.37 g, 10.0 mmol, 1.00 eq.) in MeOH (50 mL) was sparged with nitrogen gas at ambient temperature for 10 min before addition of palladium on carbon (10 wt.%, 106 mg, 0.100 mmol, 0.01 eq.). The reaction mixture was further sparged with nitrogen for 10 min before it was sparged with hydrogen

gas for 20 min and left to stir vigorously under a hydrogen atmosphere overnight at ambient temperature. The reaction was judged to be complete by TLC analysis and sparged with nitrogen gas for 10 min before it was filtered over Celite® and the filtrate concentrated *in vacuo*. The crude residue was purified using flash column chromatography on normal phase silica gel (0 - 30% EtOAc/petroleum ether) to afford the title compound as a colourless oil (1.11 g, 7.98 mmol, 80%); R_f 0.33 (20% EtOAc/petroleum ether); **^{1}H NMR** (400 MHz, $CDCl_3$): 8.52 (1H, s, H-1), 6.68 (1H, td, *J* 2.6, 1.5, H-5), 6.11 (1H, q, *J* 2.9, H-4), 5.92 (1H, ddd, *J* 3.9, 2.4, 1.5, H-3), 3.70 (3H, s, H-4i), 2.92 (2H, t, *J* 6.7, H-3i), 2.65 (2H, t, *J* 6.7, H-2i).; **LRMS** *m/z* (ESI^+) 154 ($[M+H]^+$, 100%). These data agree with the literature values.[191]

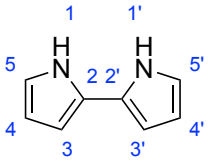
Methyl 3-(5-formyl-1*H*-pyrrol-2-yl)propanoate (48)



The Vilsmeier reagent was prepared by dropwise addition of $POCl_3$ (728 µL, 7.83 mmol, 1.20 eq.) over 10 min to a solution of DMF (607 µL, 7.83 mmol, 1.20 eq.) and DCE (4 mL) at 0 ºC and then allowed to warm to ambient temperature and stirred for 30 min. The reaction solution was cooled to 0 ºC and methyl 3-(1*H*-pyrrol-2-yl)propanoate (**47**) (1.00 g, 6.53 mmol, 1.00 eq.) was added in a solution of DCE (10 mL) at 0 ºC. The reaction solution was then heated to reflux at 85 ºC for 30 min before TLC analysis showed complete consumption of the starting material. The reaction solution was then cooled to ambient temperature before addition of an aqueous sodium acetate solution (0.98 M, 20 mL, 19.6 mmol, 3.00 eq.). The bi-phasic reaction mixture was then heated to reflux at 100 ºC for 45 min before the reaction was judged to be complete by TLC analysis. The reaction solution was cooled to ambient temperature and partitioned between CH_2Cl_2 and H_2O. The aqueous component was further extracted with CH_2Cl_2 and the combined organic components were washed with sat. aq. $NaHCO_3$ and brine, dried (Na_2SO_4), filtered and concentrated *in vacuo.*

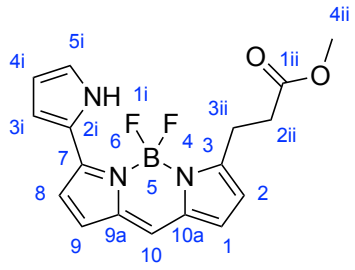
The crude material was purified using flash column chromatography on silica gel (20% EtOAc/petroleum ether) to afford the title compound as a colourless solid (1.02g, 5.63 mmol, 86%); ***R*$_f$** 0.18 (20% EtOAc/petroleum ether); **m.p.** 51 ºC (EtOAc); **^{1}H NMR** (400 MHz, $CDCl_3$): 10.54 (1H, s, H-1), 9.36 (1H, s, H-6), 6.88 (1H, dd, *J* 3.9, 2.5, H-4), 6.08 (1H, dd, *J* 3.9, 2.3, H-3), 3.69 (3H, s, H-4i), 3.02 (2H, t, *J* 7.3, H-3i), 2.70 (2H, t, *J* 7.3, H2i); **LRMS** *m/z* (ESI^+) 182 ($[M+H]^+$, 100%); **HRMS** *m/z* (ESI^+) [found: $[M+H]^+$ 182.0819, $C_9H_{12}NO_3^+$ requires 182.0812]. These data agree with the literature values.[191]

1*H*,1'*H*-2,2'-Bipyrrole (50)



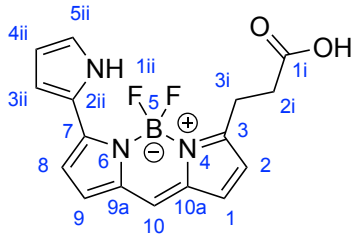
To a solution of 1*H*-pyrrole (3.11 mL, 45.0 mmol, 3.00 eq.) in anhydrous CH_2Cl_2 (250 mL) at −78 ºC was added TMSBr (3.92 mL, 30 mmol, 2 eq.) and PIFA (6.45 g, 15 mmol, 1.00 eq.). The reaction solution was stirred at −78 ºC under a nitrogen atmosphere for 1 h before the reaction was judged to be complete by TLC analysis. The reaction solution was then quenched by addition of a sat. aq. $NaHCO_3$ solution (100 mL) and partitioned. The aqueous component was further extracted with CH_2Cl_2 (2 × 50 mL) and the combined organic components were washed with brine (50 mL), dried (Na_2SO_4), filtered and concentrated *in vacuo*. The crude residue was purified using flash column chromatography on silica gel (10 – 40% EtOAc/petroleum ether) to afford the title compound as off-white solid (1.39 g, 10.5 mmol, 70%) which was stored under argon at 4 ºC; ***R*$_f$** 0.40 (20% EtOAc/petroleum ether); **^{1}H NMR** (400 MHz, $CDCl_3$): 8.23 (2H, s, H-1,1'), 6.78 (2H, ddd, *J* 2.8, 2.5, 1.4, H-5,5'), 6.25 (2H, ddd, *J* 3.6, 2.6, 2.6, H-3, 3'), 6.21 (2H, ddd, *J* 3.6, 2.6, 1.5, H-4,4').; **LRMS** *m/z* (ESI^+) 133 ($[M+H]^+$, 100%). These data agree with the literature values.[240]

Methyl 3-(5,5-difluoro-7-(1*H*-pyrrol-2-yl)-5*H*-5λ^4,6λ^4-dipyrrolo[1,2-c:2',1'-*f*][1,3,2]diazaborinin-3-yl)propanoate (51)



To a solution of methyl 3-(5-formyl-1*H*-pyrrol-2-yl)propanoate (**48**) (500 mg, 2.76 mmol, 1.00 eq.) and 1*H*,1'*H*-2,2'-bipyrrole (**50**) (365 mg, 2.76 mmol, 1.00 eq.) in anhydrous CH_2Cl_2 (20 mL) at 0 ºC was added $POCl_3$ (256 µL, 2.71 mmol, 1.00 eq.) over a period of 5 min. The reaction solution was stirred at 0 ºC for 3 h, before the reaction solution was concentrated *in vacuo* and the flask backed with argon. The residue was resuspended in anhydrous DIPEA (1.92 mL, 11.0 mmol, 4 eq.) and anhydrous CH_2Cl_2 (5 mL) before dropwise addition of $BF_3.OEt_2$ (2.05 mL, 13.8 mmol, 5 eq.) at 0 ºC over a period of 5 min. The reaction solution was stirred for 30 min before it was quenched by addition of saturated aqueous $NaHCO_3$ solution (50 mL) and extracted with CH_2Cl_2 (3 × 50 mL). The combined organics were washed with brine (50 mL), dried (Na_2SO_4), filtered, and concentrated *in vacuo*. The crude residue was purified using flash column chromatography on silica gel (50–100% CH_2Cl_2/pentane) to afford the title compound as an amorphous blue solid (198 mg, 0.577 mmol, 21%); R_f 0.51 (CH_2Cl_2); $\tilde{\nu}_{max}$ (thin film)/cm^{-1} 3418 (N-H) 2920 (C-H), 1733 (C=O), 1603 (C=C) 1574 (C=C), 1103 (B-F), 1042 (B-F); **^{1}H NMR** (400 MHz, $CDCl_3$): (400 MHz, $CDCl_3$) 10.42 (1H, s, H-1i), 7.15 (1H, td, *J* 2.7, 1.4, H-5i), 6.96 (1H, ddd, *J* 3.9, 2.5, 1.4, H-3i), 6.94 (1H, d, *J* 4.6, H-9), 6.90 (1H, s, H-10), 6.80 (1H, d, *J* 4.6, H-8), 6.77 (1H, d, *J* 4.0, H-1), 6.36 (1H, dt, *J* 3.9, 2.4, H-4i), 6.25 (1H, d, *J* 3.9, H-2), 3.72 (3H, s, H-4ii), 3.36 (2H, t, *J* 8.7, H-3ii), 2.81 (2H, t, *J* 7.5, H-2ii); **^{19}F NMR** (377 MHz, $CDCl_3$): -140.3 (2F, qd $^1J_{F,B}$ 36.0, $^5J_{F,C\text{-}3i}$ 9.1); **LRMS** *m/z* (ESI$^+$) 344 ([M+H]$^+$, 100%), 324 ([M-F]$^+$, 68%); **HRMS** *m/z* (ESI$^+$) [found: [M+H]$^+$ 344.1387, $C_{17}H_{17}BF_2N_3O_2^+$ requires 344.1376]. These data agree with the literature values.[191]

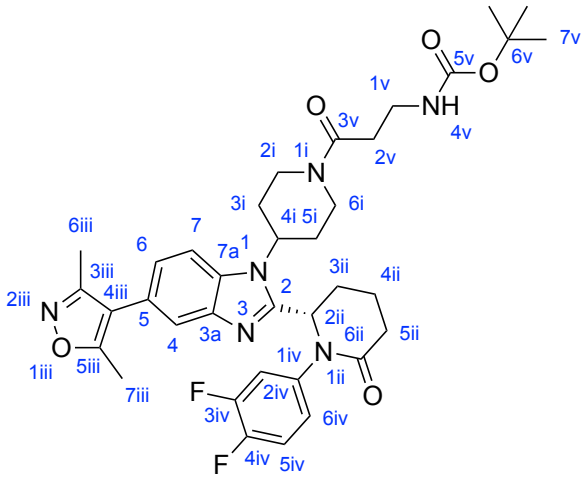
3-(2,2-Difluoro-12-(1*H*-pyrrol-2-yl)-3-aza-1-azonia-2-boranuidatricyclo[7.3.0.0^{3,7}]dodeca-1(12),4,6,8,10-pentaen-4-yl)propanoic acid (52)



Amano Lipase PS (240 mg) was reconstituted in Dulbecco's phosphate buffered saline solution (48 mL) at 40 ºC and methyl 3-(5,5-difluoro-7-(1*H*-pyrrol-2-yl)-5*H*-5λ^4,6λ^4-dipyrrolo[1,2-c:2',1'-*f*][1,3,2]diazaborinin-3-yl)propanoate (**51**) (170 mg, 350 µmol, 1.00 eq.) was added as a suspension in MeOH (1.2 mL) and hexane (10.8 mL). The biphasic reaction mixture was stirred rapidly overnight at 40 ºC before the reaction was diluted with Et_2O (50 mL) and partitioned. The organic component was further extracted with sat. aq. $NaHCO_3$ solution (3 × 50 mL) before it was washed with brine (20 mL), dried (Na_2SO_4), filtered, and concentrated *in vacuo* to recover the unconsumed starting material (88 mg, 256 µmol, 52%). The combined aqueous extracts were acidified with aq. hydrochloric acid solution to pH 4–5 and extracted with CH_2Cl_2 (3 × 50 mL). The combined organic extracts were washed with brine (50 mL), dried (Na_2SO_4), filtered, and concentrated *in vacuo*. The crude residue was purified using flash column chromatography on silica gel (0–2% MeOH/CH_2Cl_2) to afford the title compound as a blue solid (64.6 mg, 196 µmol, 40%); ***R*$_f$** 0.20 (5% MeOH/CH_2Cl_2); **m.p.** 160–163 (CH_2Cl_2) [lit.[241] 158–160 ºC]; **^{1}H NMR** (400 MHz, $CDCl_3$): 10.42 (1H, s, H-1ii), 7.19 (1H, ddd, *J* 3.1, 2.5, 1.3, H-5ii), 7.04 (1H, d, *J* 4.6, H-9), 6.99 (1H, ddd, J 2.8, 2.6, 1.4, H-3ii), 6.98 (1H, s, H-10), 6.87 (1H, d, *J* 4.6, H-8), 6.83 (1H, d, *J* 3.9, H-1), 6.38 (1H, ddd, *J* 3.9, 2.5, 2.2, H-4ii), 6.30 (1H, d, *J* 3.9, H-2), 3.35 (2H, t, *J* 7.7, H-3i), 2.86 (2H, t, *J* 7.4, H-2i); **^{19}F NMR** (376 MHz, $CDCl_3$) -140.6 (2F, qd, $^1J_{F,B}$ 35.8, $^5J_{F,C\text{-}3ii}$ 8.9); **^{13}C NMR** (131 MHz, $CDCl_3$): 178.2 (C-1i), 154.3 (C-3), 150.9 (C-7), 137.7 (C-9a), 133.6 (C-10a), 131.9 (C-9), 126.2 (C-3ii), 126.1 (C-1), 123.8 (C-2ii), 123.5 (C-10), 120.7 (C-8), 118.1 (C-5ii), 116.2 (C-2), 111.7 (C-4ii), 33.2 (C-2i), 23.8 (C-

3i); **LRMS** *m/z* (ESI$^+$) 330 ([M+H]$^+$, 100%); **HRMS** *m/z* (ESI$^+$) [found: [M+H]$^+$ 330.1218, $C_{16}H_{15}BF_2N_3O_2^+$ requires 330.1220]. These data agree with the literature values.[241]

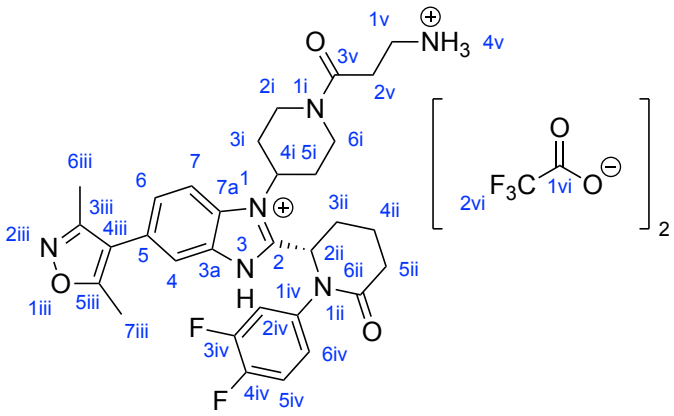
***tert*-Butyl *N*-(3-(4-(2-((2*S*)-1-(3,4-difluorophenyl)-6-oxopiperidin-2-yl)-5-(3,5-dimethyl-1,2-oxazol-4-yl)-1*H*-1,3-benzodiazol-1-yl)piperidin-1-yl)-3-oxopropyl)carbamate (53)**



To a solution of 3-((2-methylpropan-2-yl)oxycarbonylamino)propanoic acid (14.2 mg, 75.0 µmol, 1.10 eq.) in anhydrous CH_2Cl_2 (5 mL) was added NEt_3 (28.6 µL, 205 µmol, 3.00 eq.) and isobutyl chloroformate (8.9 µL, 68.2 µmol, 1.00 eq.) at 0 ºC. The reaction solution was stirred at 0 ºC for 10 min to form the mixed anhydride intermediate which was confirmed by TLC analysis. (6*S*)-1-(3,4-difluorophenyl)-6-(5-(3,5-dimethyl-1,2-oxazol-4-yl)-1-(piperidin-4-yl)-1*H*-1,3-benzodiazol-2-yl)piperidin-2-one (**Pip-obrodib**) (50.0 mg, 68.2 µmol, 1.00 eq.) was added to the reaction solution at 0 ºC and stirred for 15 min before it was allowed to warm to ambient temperature for a further 15 min, after which time the reaction was judged to be complete by TLC analysis. The reaction was quenched by addition of sat. aq. $NaHCO_3$ solution (25 mL) before the mixture was partitioned and the aqueous component further extracted with CH_2Cl_2 (3 × 25 mL). The combined organic components were washed with brine (20 mL) and concentrated *in vacuo* onto silica gel and purified using flash column chromatography on silica gel (0–10% MeOH/CH_2Cl_2) to afford the title compound as a solid (39.1 mg, 57.8 µmol, 85%). R_f 0.53 (10% MeOH/CH_2Cl_2); $[\alpha]_D^{25}$ = −94.65 (c. 1.0 MeCN); **m.p.** 140–144 ºC (CH_2Cl_2); $\tilde{\nu}_{max}$ (thin film)/cm^{-1} 1706 (C=O), 1645 (C=O), 1517 (C-F), 1453, 1288; **^{1}H NMR** (600 MHz, $CDCl_3$) 7.68 (1H, d, *J* 1.6, H-4),

7.47 (1H, d, *J* 8.5, H-7 α), 7.46 (1H, d, *J* 8.5 H-7 β), 7.16 – 7.07 (2H, m, H-2iv, H-6), 7.09 – 6.99 (1H, m H-5iv), 7.01 – 6.94 (1H, m, H-6iv), 5.30 – 5.22 (2H, m, H-2ii, H-4v), 4.91 (1H, ddd, *J* 11.9, 2.2, 2.1, H-2i'' or 6i'' α), 4.83 (1H, ddd, *J* 11.9, 2.2, 2.1 H-2i'' or 6i'' β), 4.28 – 4.18 (1H, m, H-4i), 4.07 (1H, d, *J* 17.1 H-6i'' or 2i'' α), 3.99 (1H, d, *J* 14.3 H-6i'' or 2i'' β), 3.46 (2H, m, H-1v), 3.17 (1H, dd, *J* 14.1, 12.2 H-2i' or 6i' α), 3.07 (1H, ddd, *J* 14.0, 12.2, 2.8 H-2i' or 6i' β), 2.86 (1H, ddd, *J* 18.0, 5.7, 5.7, H-5ii''), 2.70 – 2.51 (4H, m, H-6i' or 2i', H-2v, H-5ii'), 2.43 (3H, s, H-7iii), 2.48 – 2.14 (5H, m, H-3i'', H-3ii, H-4ii'', H-5i''), 2.29 (3H, s, H-6iii), 1.95 – 1.81 (2H, m, H-4ii', H-5i' or 3i'), 1.43 (9H, s, H-7v), 1.39 – 1.26 (1H, m, H-3i' or 5i') N.B. presence of conformers denoted by α/β notation; **^{13}C NMR** (151 MHz, $CDCl_3$) 170.9 (C-6ii), 170.2 (C-3v α), 170.1 (C-3v β), 165.3 (C-5iii), 158.9 (C-3iii), 156.2 (C-5v), 152.3 (C-2), 150.1 (dd, *J* 250.2, 13.3, C-3iv), 149.5 (dd, *J* 249.9, 12.3, C-4iv), 143.2 (C-3a), 138.6 (C-1iv), 132.7 (C-7a α), 132.6 (C-7a β), 125.0 (C-5), 124.4 (C-6iv), 124.2 (C-6), 121.1 (C-4), 117.9 (d, *J* 18.0, C-2iv), 117.6 (d, *J* 17.7, C-5iv), 116.7 (C-4iii), 112.4 (C-7 α), 112.3 (C-7 β), 79.5 (C-6v), 57.9 (C-2ii), (C-2ii α) 57.7 (C-2ii β), 54.5 (C-4i), 44.9 (C-2i,6i α), 44.8 (C-2i,6i β), 41.2 (C-2i,6i αβ), 36.5 (C-1v), 33.8 (C-2v α), 33.8 (C-2v β), 32.4 (C-5ii), 31.1 (C-3i,5i α), 30.9 (C-3i,5i β), 30.3 (C-3i,5i, αβ), 29.8 (C-3ii), 28.5 (C-7v), 18.2 (C-4ii), 11.7 (C-7iii), 11.0 (C-6iii) N.B. presence of conformers denoted by α/β notation; **^{19}F NMR** (565 MHz, $CDCl_3$) -135.01 – -135.25 (m), -137.79 – -137.99 (m): **LRMS** *m/z* (ESI^+) 677 ($[M+H]^+$, 100%), 699 ($[M+Na]^+$, 27%); **HRMS** *m/z* (ESI^+) [found: $[M+Na]^+$ 699.3082, $C_{36}H_{42}F_2N_6O_5Na^+$ requires 699.3077].

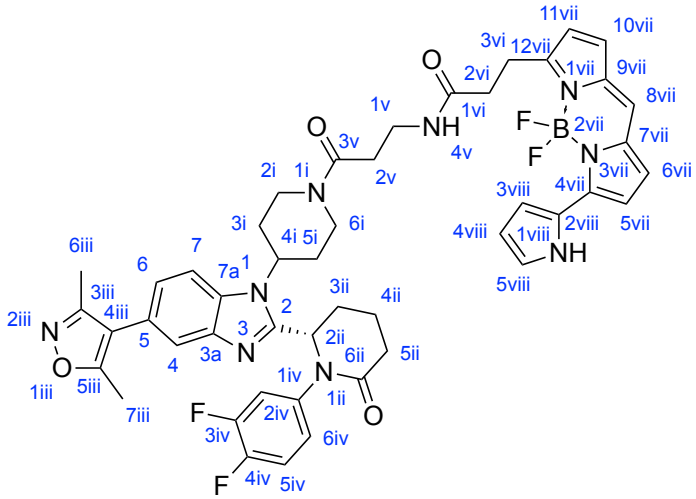
1-[1-(3-Azaniumylpropanoyl)piperidin-4-yl]-2-[(2*S*)-1-(3,4-difluorophenyl)-6-oxopiperidin-2-yl]-5-(3,5-dimethyl-1,2-oxazol-4-yl)-3*H*-1λ5,3-benzodiazol-1-ylium bis(trifluoroacetate) (54)



To a solution of *tert*-butyl *N*-(3-(4-(2-((2*S*)-1-(3,4-difluorophenyl)-6-oxopiperidin-2-yl)-5-(3,5-dimethyl-1,2-oxazol-4-yl)-1*H*-1,3-benzodiazol-1-yl)piperidin-1-yl)-3-oxopropyl)carbamate (**53**) (20.0 mg, 30.0 µmol, 1.00 eq.) in CH_2Cl_2 (0.5 mL) was added trifluoroacetic acid (0.5 mL) dropwise at ambient temperature. The reaction solution was stirred at ambient temperature for 30 min before the reaction was judged to be complete by TLC analysis. The reaction solution was concentrated *in vacuo* and the residue was triturated with Et_2O (5 mL) and then resuspended in H_2O (10 mL) before it was lyophilised to afford a colourless powder (18.3 mg, 22.7 µmol, 77%); $\mathbf{R_f}$ 0.00 (10% MeOH/CH_2Cl_2); $[\alpha]_D^{25}$ = -87.58 (c. 0.5, MeCN); $\tilde{\nu}_{max}$ (thin film)/cm^{-1} 1678 (C=O), 1643 (C=O), 1516 (C-F), 1459, 1201, 1134; **^{1}H NMR** (600 MHz, CD_3CN) 7.82–7.76 (1H, m, H-7), 7.75 (1H, s, H-4), 7.32 (3H, br s, H-4v), 7.31–7.25 (1H, m, H-2iv), 7.25–7.22 (1H, m, H-6), 7.20–7.13 (1H, m, H-6iv), 7.13–7.07 (1H, m, H-5iv), 5.65–5.60 (1H, m, H-2ii), 5.05 (1H, br s, H-3), 4.76–4.62 (1H, m, H-6i'/2i'), 4.59–4.50 (1H, m, H-4i), 4.01–3.87 (1H, m, H-2i'/6i'), 3.29–3.15 (3H, m, 1v, H-6i''/2i''), 2.96–2.83 (1H, m, H-2v'), 2.82 – 2.60 (3H, m, H-2i'',5ii',2v''), 2.39 (3H, s, H-7iii), 2.60–2.02 (6H, m, H-3i'',3ii'',3ii',4ii'',5i',5ii''), 2.23 (3H, s, H-6iii), 1.93–1.81 (2H, m, H-4ii',5i''), 1.45–1.37 (1H, m, H-3i'), N.B. presence of conformers; **^{13}C NMR** (151 MHz, CD_3CN) 171.4 (C-6iii), 170.5 (C-3v), 166.5 (C-5ii), 161.0 (q, J 34.5, C-2vi), 159.6 (C-3ii), 154.4 (C-2), 150.6 (dd, *J* 246.6, 13.4, C-3iv), 149.9 (dd, *J* 246.5, 12.2, C-4iv), 140.9 (C-3a),

140.0 (C-1iv), 132.9 (C-7a), 126.8 (C-5), 126.1 – 125.5 (m, C-5iv, C-6), 119.8 (C-4), 118.7 (dd, *J* 18.4, 4.0, C-2iv), 118.1 (C-6iv), 117.1 (C-4ii), 114.7 (C-7), 58.0 (C-2iii), 55.2 (C-4i), 45.3 (C-6i/2i α), 45.1 (C-6i/2i β), 41.6 (C-2i/6i α), 41.4 (C-2i/6i β), 37.7 (C-1v), 33.1 (C-5iii), 31.1 (C-3i/5i α), 30.8 (2C, 3i/5i β,5i/3i α), 30.5 (C-5i/3i β), 29.7 (C-3iii), 29.4 (C-2v), 18.8 (C-4iii), 11.8 (C-7ii), 11.0 (C-6ii), N.B. presence of conformers denoted by α/β notation; **^{19}F NMR** (565 MHz, CD_3CN): -138.3 (1F, m, F-3iv), -140.9 (1F, m, F-4iv), -76.3 (6F, m, F-2vi); **LRMS** *m/z* (ESI^+) 577 ($[M+H]^+$, 100%); **HRMS** *m/z* (ESI^+) [found: $[M+H]^+$ 577.2728, $C_{31}H_{35}F_2N_6O_3^+$ requires 577.2733]. **RP-HPLC** Retention time: 6.298 min (95%).

12-(2-((3-(4-(2-((2*S*)-1-(3,4-Difluorophenyl)-6-oxopiperidin-2-yl)-5-(3,5-dimethyl-1,2-oxazol-4-yl)-1*H*-1,3-benzodiazol-1-yl)piperidin-1-yl)-3-oxopropyl)carbamoyl)ethyl)-2,2-difluoro-4-(1*H*-pyrrol-2-yl)-1λ5,3-diaza-2-boratricyclo[7.3.0.0^{3,7}]dodeca-1(12),4,6,8,10-pentaen-1-ylium-2-uide (Inobrodib-BODIPY)



A vial was charged with 1-[1-(3-azaniumylpropanoyl)piperidin-4-yl]-2-[(2*S*)-1-(3,4-difluorophenyl)-6-oxopiperidin-2-yl]-5-(3,5-dimethyl-1,2-oxazol-4-yl)-3*H*-1λ5,3-benzodiazol-1-ylium bis(trifluoroacetate) (**54**) (10 mg, 17 µmol, 1.0 eq.), 3-(2,2-difluoro-12-(1*H*-pyrrol-2-yl)-3-aza-1-azonia-2-boranuidatricyclo[7.3.0.0^{3,7}]dodeca-1(12),4,6,8,10-pentaen-4-yl)propanoic acid (**52**) (6.0 mg, 18 µmol, 1.1 eq.), and HATU (7.0 mg, 18 µmol, 1.1 eq.), and then dissolved in DMF (1 mL) followed by addition of DIPEA (5 uL, 26 µmol, 1.5 eq.). The reaction mixture was stirred at ambient temperature 5˙ h, after which time LC-

MS analysis showed complete consumption of the limiting starting material. The reaction mixture was diluted with water (10 mL) and extracted with CH_2Cl_2 (3 × 10 mL). The combined organic components were dried (Na_2SO_4), filtered, and concentrated *in vacuo*. The crude residue was first purified using flash column chromatography on silica gel (4% MeOH/CH_2Cl_2) and then further purified by preparative HPLC before lyophilisation to afford the title compound as a blue powder (4.6 mg, 5.2 μmol, 30%). R_f 0.16 (4% MeOH/CH_2Cl_2); $\tilde{\nu}_{max}$ (thin film)/cm^{-1} 2925 (C-H),1713 (C=O), 1646 (C=O), 1605 (C=O), 1460, 1108; **^{1}H NMR** (600 MHz, $CDCl_3$): 10.56 (1H, s, H-1viii), 7.66 (1H, d, *J* 1.7, H-4), 7.42–7.37 (1H, m, H-7), 7.16–7.10 (1H, m, H-6), 7.28–7.24 (1H, m, H-5iv), 7.06 – 6.91 (6H, m, H-2iv,6iv,6vii,8vii,3viii,5viii), 6.88 (1H, d, *J* 4.5, H-5vii), 6.81 (1H, d, *J* 3.9, H-10vii), 6.50 (1H, t, *J* 6.3, H-4v), 6.52–6.47 (1H, m, H-4v), 6.29 (1H, d, *J* 3.9, H-11vii), 5.30–5.26 (1H, m, H-2ii), 4.93–4.79 (1H, m, H-6i'' or 2i''), 4.27–4.16 (1H, m, H-4i), 4.09–3.95 (1H, m, H-2i'' or 6i''), 3.71–3.52 (2H, m, H-1v), 3.34 – 3.28 (2H, m, H-3vi), 3.19–3.01 (1H, m, H-2i' or 6i'), 2.88–2.81 (1H, m, H-5ii'), 2.73–2.53 (6H, m, H-2v,2vi,5ii'',6i' or 2i'), 2.38 (3H, s, H-7iii), 2.48 – 2.10 (5H, m, H-3i'',5i'',3ii,4ii''), 2.25 (3H, s, H-6iii), 1.95–1.74 (2H, m, H-4ii',5i' or 3i'), 1.40–1.31 (1H, m, H-3i' or 5i'). N.B. presence of conformers gives significant broadening. **^{13}C NMR** (151 MHz, $CDCl_3$) 172.5 (1vi α), 172.4 (1vi β), 170.8 (6ii), 170.1 (3v α), 170.0 (3v β), 165.3 (5iii), 158.9 (3iii), 154.4 (12vii α), 154.3 (12vii β), 152.2 (2), 151.0 (4vii), 150.2 (dd, *J* 254.4, 13.3, 3iv), 149.5 (dd, *J* 249.5, 11.9, 4iv), 142.7 (7a), 138.5 (1iv), 137.7 (7vii), 133.6 (2viii), 132.5 (3a), 132.0 (6vii), 126.9 (3viii), 126.0 (10vii α), 126.0 (10vii β), 124.4 (5), 124.2 (6iv), 123.6 (8vii), 123.2 (6), 123.2 (5viii), 120.9 (5vii), 120.8 (4), 118.7 (9vii α), 118.6 (9vii β), 117.9 (d, *J* 18.1, 5iv), 117.6 (d, *J* 17.7, 2iv), 116.6 (4iii), 116.4 (11vii α), 116.3 (11vii β), 112.4 (7), 111.6 (4viii), 57.8 (2ii), 54.6 (4i), 44.9 (2i α), 44.9 (2i β) 41.4 (6i), 36.7 (2vi), 35.3 (1v), 33.2 (2v α), 33.1 (2v β), 32.5 (3ii), 31.2 (3i/5i α), 31.1 (3i/5i β), 30.2 (5i/3i α), 30.1 (5i/3i β), 29.8 (5ii α), 29.8 (5ii β), 25.7 (3vi), 18.3 (4ii), 11.7 (7iii), 11.0 (6iii) N.B. presence of conformers denoted by α/β notation; **^{19}F NMR** (565 MHz, $CDCl_3$) -135.10 (1F, s), -137.87 (1F, s), -139.88 – -140.52 (2F, m); **^{11}B NMR** (193 MHz, $CDCl_3$): 1.60 (t, *J* 36.7); **LRMS** *m/z* (ESI$^+$) 888 ([M+H]$^+$, 100%), 910 ([M+Na]$^+$, 97%); **HRMS** *m/z* (ESI$^+$) [found:

[M+H]$^+$ 888.3797, $C_{47}H_{47}BF_4N_9O_4^+$ requires 888.3775]. **RP-HPLC** Retention time: 9.452 min (>99%).

References

1. M. Mann and O. N. Jensen, *Nat Biotechnol*, 2003, **21**, 255-261.
2. R. Harmel and D. Fiedler, *Nat Chem Biol*, 2018, **14**, 244-252.
3. G. A. Khoury, R. C. Baliban and C. A. Floudas, *Sci Rep*, 2011, **1**, 90.
4. D. Virag, B. Dalmadi-Kiss, K. Vekey, L. Drahos, I. Klebovich, I. Antal and K. Ludanyi, *Chromatographia*, 2020, **83**, 1-10.
5. C. Choudhary, C. Kumar, F. Gnad, M. L. Nielsen, M. Rehman, T. C. Walther, J. V. Olsen and M. Mann, *Science*, 2009, **325**, 834-840.
6. K. T. Nguyen, S. H. Mun, C. S. Lee and C. S. Hwang, *Exp Mol Med*, 2018, **50**, 1-8.
7. T. Arnesen, P. Van Damme, B. Polevoda, K. Helsens, R. Evjenth, N. Colaert, J. E. Varhaug, J. Vandekerckhove, J. R. Lillehaug, F. Sherman and K. Gevaert, *Proc Natl Acad Sci U S A*, 2009, **106**, 8157-8162.
8. A. Drazic, L. M. Myklebust, R. Ree and T. Arnesen, *Biochimica Et Biophysica Acta-Proteins and Proteomics*, 2016, **1864**, 1372-1401.
9. A. J. Bannister and T. Kouzarides, *Cell Res*, 2011, **21**, 381-395.
10. T. Jenuwein and C. D. Allis, *Science*, 2001, **293**, 1074-1080.
11. C. Choudhary, B. T. Weinert, Y. Nishida, E. Verdin and M. Mann, *Nat Rev Mol Cell Biol*, 2014, **15**, 536-550.
12. E. Verdin and M. Ott, *Nat Rev Mol Cell Biol*, 2015, **16**, 258-264.
13. W. Gu and R. G. Roeder, *Cell*, 1997, **90**, 595-606.
14. R. E. Kiernan, C. Vanhulle, L. Schiltz, E. Adam, H. Xiao, F. Maudoux, C. Calomme, A. Burny, Y. Nakatani, K. T. Jeang, M. Benkirane and C. Van Lint, *EMBO J*, 1999, **18**, 6106-6118.
15. M. Ott, M. Schnolzer, J. Garnica, W. Fischle, S. Emiliani, H. R. Rackwitz and E. Verdin, *Curr Biol*, 1999, **9**, 1489-1492.
16. T. Narita, B. T. Weinert and C. Choudhary, *Nat Rev Mol Cell Biol*, 2019, **20**, 156-174.
17. F. Mateo, M. Vidal-Laliena, N. Canela, A. Zecchin, M. Martinez-Balbas, N. Agell, M. Giacca, M. J. Pujol and O. Bachs, *Nucleic Acids Res*, 2009, **37**, 7072-7084.
18. P. R. Thompson, D. Wang, L. Wang, M. Fulco, N. Pediconi, D. Zhang, W. An, Q. Ge, R. G. Roeder, J. Wong, M. Levrero, V. Sartorelli, R. J. Cotter and P. A. Cole, *Nat Struct Mol Biol*, 2004, **11**, 308-315.
19. C. E. McCullough and R. Marmorstein, *ACS Chem Biol*, 2016, **11**, 632-642.
20. E. Gronroos, U. Hellman, C. H. Heldin and J. Ericsson, *Mol Cell*, 2002, **10**, 483-493.
21. M. A. Najar, J. N. Beyer, C. E. W. Crawford and G. M. Burslem, *bioRxiv*, 2024, DOI: 10.1101/2024.06.18.599616, 2024.2006.2018.599616.
22. I. Ali, R. J. Conrad, E. Verdin and M. Ott, *Chem Rev*, 2018, **118**, 1216-1252.
23. S. D. Whedon and P. A. Cole, *Curr Opin Chem Biol*, 2023, **72**, 102255.
24. J. D. Gaddameedi, T. Chou, B. S. Geller, A. Rangarajan, T. A. Swaminathan, D. Dixon, K. Long, C. J. Golder, V. A. Vuong, S. Banuelos, R. Greenhouse, M. P. Snyder, A. M. Lipchik and J. J. Gruber, *J Med Chem*, 2023, **66**, 5774-5801.
25. M. Moustakim, P. G. Clark, L. Trulli, A. L. Fuentes de Arriba, M. T. Ehebauer, A. Chaikuad, E. J. Murphy, J. Mendez-Johnson, D. Daniels, C. D. Hou, Y. H. Lin, J. R. Walker, R. Hui, H. Yang, L. Dorrell, C. M. Rogers, O. P. Monteiro, O. Fedorov, K. V. Huber, S. Knapp, J. Heer, D. J. Dixon and P. E. Brennan, *Angew Chem Int Ed Engl*, 2017, **56**, 827-831.
26. M. C. Crawford, D. R. Tripu, S. A. Barritt, Y. Jing, D. Gallimore, S. C. Kales, N. V. Bhanu, Y. Xiong, Y. Fang, K. A. T. Butler, C. A. LeClair, N. P. Coussens, A. Simeonov, B. A. Garcia, C. C. Dibble and J. L. Meier, *ACS Chem Biol*, 2023, **18**, 2249-2258.
27. D. A. Hay, O. Fedorov, S. Martin, D. C. Singleton, C. Tallant, C. Wells, S. Picaud, M. Philpott, O. P. Monteiro, C. M. Rogers, S. J. Conway, T. P. Rooney, A. Tumber, C. Yapp, P. Filippakopoulos, M. E. Bunnage, S. Muller, S. Knapp, C. J. Schofield and P. E. Brennan, *J Am Chem Soc*, 2014, **136**, 9308-9319.
28. C. Gao, E. Bourke, M. Scobie, M. A. Famme, T. Koolmeister, T. Helleday, L. A. Eriksson, N. F. Lowndes and J. A. Brown, *Sci Rep*, 2014, **4**, 5372.
29. J. B. Baell, D. J. Leaver, S. J. Hermans, G. L. Kelly, M. S. Brennan, N. L. Downer, N. Nguyen, J. Wichmann, H. M. McRae, Y. Yang, B. Cleary, H. R. Lagiakos, S. Mieruszynski, G. Pacini, H. K. Vanyai, M. I. Bergamasco, R. E. May, B. K. Davey, K. J. Morgan, A. J. Sealey, B. Wang, N. Zamudio, S. Wilcox, A. L. Garnham, B. N. Sheikh, B. J. Aubrey, K. Doggett, M. C. Chung, M. de Silva, J. Bentley, P. Pilling, M. Hattarki, O. Dolezal, M. L. Dennis, H. Falk, B. Ren, S. A. Charman, K. L. White, J. Rautela, A. Newbold, E. D. Hawkins, R. W. Johnstone, N. D.

Huntington, T. S. Peat, J. K. Heath, A. Strasser, M. W. Parker, G. K. Smyth, I. P. Street, B. J. Monahan, A. K. Voss and T. Thomas, *Nature*, 2018, **560**, 253-257.
30. S. Sharma, C. Y. Chung, S. Uryu, J. Petrovic, J. Cao, A. Rickard, N. Nady, S. Greasley, E. Johnson, O. Brodsky, S. Khan, H. Wang, Z. Wang, Y. Zhang, K. Tsaparikos, L. Chen, A. Mazurek, J. Lapek, P. P. Kung, S. Sutton, P. F. Richardson, E. C. Greenwald, S. Yamazaki, R. Jones, K. A. Maegley, P. Bingham, H. Lam, A. E. Stupple, A. Kamal, A. Chueh, A. Cuzzupe, B. J. Morrow, B. Ren, C. Carrasco-Pozo, C. W. Tan, D. D. Bhuva, E. Allan, E. Surgenor, F. Vaillant, H. Pehlivanoglu, H. Falk, J. R. Whittle, J. Newman, J. Cursons, J. P. Doherty, K. L. White, L. MacPherson, M. Devlin, M. L. Dennis, M. K. Hattarki, M. De Silva, M. A. Camerino, M. S. Butler, O. Dolezal, P. Pilling, R. Foitzik, P. A. Stupple, H. R. Lagiakos, S. R. Walker, S. Hediyeh-Zadeh, S. Nuttall, S. K. Spall, S. A. Charman, T. Connor, T. S. Peat, V. M. Avery, Y. E. Bozikis, Y. Yang, M. Zhang, B. J. Monahan, A. K. Voss, T. Thomas, I. P. Street, S. J. Dawson, M. A. Dawson, G. J. Lindeman, M. J. Davis, J. E. Visvader and T. A. Paul, *Cell Chem Biol*, 2023, **30**, 1191-1210 e1120.
31. L. MacPherson, J. Anokye, M. M. Yeung, E. Y. N. Lam, Y. C. Chan, C. F. Weng, P. Yeh, K. Knezevic, M. S. Butler, A. Hoegl, K. L. Chan, M. L. Burr, L. J. Gearing, T. Willson, J. Liu, J. Choi, Y. Yang, R. A. Bilardi, H. Falk, N. Nguyen, P. A. Stupple, T. S. Peat, M. Zhang, M. de Silva, C. Carrasco-Pozo, V. M. Avery, P. S. Khoo, O. Dolezal, M. L. Dennis, S. Nuttall, R. Surjadi, J. Newman, B. Ren, D. J. Leaver, Y. Sun, J. B. Baell, O. Dovey, G. S. Vassiliou, F. Grebien, S. J. Dawson, I. P. Street, B. J. Monahan, C. J. Burns, C. Choudhary, M. E. Blewitt, A. K. Voss, T. Thomas and M. A. Dawson, *Nature*, 2020, **577**, 266-270.
32. F. Fiorentino, S. Sementilli, M. Menna, F. Turrisi, S. Tomassi, F. R. Pellegrini, A. Iuzzolino, F. D'Acunzo, A. Feoli, H. Wapenaar, S. Taraglio, C. Fraschetti, D. Del Bufalo, G. Sbardella, F. J. Dekker, A. Paiardini, D. Trisciuoglio, A. Mai and D. Rotili, *J Med Chem*, 2023, **66**, 6591-6616.
33. S. Wang, V. Tsui, T. D. Crawford, J. E. Audia, D. J. Burdick, M. H. Beresini, A. Cote, R. Cummings, M. Duplessis, E. M. Flynn, M. C. Hewitt, H. R. Huang, H. Jayaram, Y. Jiang, S. Joshi, J. Murray, C. G. Nasveschuk, E. Pardo, F. Poy, F. A. Romero, Y. Tang, A. M. Taylor, J. Wang, Z. Xu, L. E. Zawadzke, X. Zhu, B. K. Albrecht, S. R. Magnuson, S. Bellon and A. G. Cochran, *J Med Chem*, 2018, **61**, 9301-9315.
34. L. Bouche, C. D. Christ, S. Siegel, A. E. Fernandez-Montalvan, S. J. Holton, O. Fedorov, A. Ter Laak, T. Sugawara, D. Stockigt, C. Tallant, J. Bennett, O. Monteiro, L. Diaz-Saez, P. Siejka, J. Meier, V. Putter, J. Weiske, S. Muller, K. V. M. Huber, I. V. Hartung and B. Haendler, *J Med Chem*, 2017, **60**, 4002-4022.
35. C. E. Berndsen and J. M. Denu, *Curr Opin Struct Biol*, 2008, **18**, 682-689.
36. K. Sadoul, J. Wang, B. Diagouraga and S. Khochbin, *J Biomed Biotechnol*, 2011, **2011**, 970382.
37. T. Paysan-Lafosse, M. Blum, S. Chuguransky, T. Grego, B. L. Pinto, Gustavo A. Salazar, Maxwell L. Bileschi, P. Bork, A. Bridge, L. Colwell, J. Gough, Daniel H. Haft, I. Letunić, A. Marchler-Bauer, H. Mi, Darren A. Natale, Christine A. Orengo, Arun P. Pandurangan, C. Rivoire, C. J. A. Sigrist, I. Sillitoe, N. Thanki, P. D. Thomas, S. C. E. Tosatto, Cathy H. Wu and A. Bateman, *Nucleic Acids Research*, 2023, **51**, D418-D427.
38. X. Liu, L. Wang, K. Zhao, P. R. Thompson, Y. Hwang, R. Marmorstein and P. A. Cole, *Nature*, 2008, **451**, 846-850.
39. B. M. Dancy and P. A. Cole, *Chem Rev*, 2015, **115**, 2419-2452.
40. B. T. Weinert, V. Iesmantavicius, T. Moustafa, C. Scholz, S. A. Wagner, C. Magnes, R. Zechner and C. Choudhary, *Mol Syst Biol*, 2014, **10**, 716.
41. J. Baeza, M. J. Smallegan and J. M. Denu, *ACS Chem Biol*, 2015, **10**, 122-128.
42. G. R. Wagner and R. M. Payne, *J Biol Chem*, 2013, **288**, 29036-29045.
43. O. Pougovkina, H. te Brinke, R. Ofman, A. G. van Cruchten, W. Kulik, R. J. Wanders, S. M. Houten and V. C. de Boer, *Hum Mol Genet*, 2014, **23**, 3513-3522.
44. A. M. James, K. Hoogewijs, A. Logan, A. R. Hall, S. Ding, I. M. Fearnley and M. P. Murphy, *Cell Rep*, 2017, **18**, 2105-2112.
45. C. Hubbert, A. Guardiola, R. Shao, Y. Kawaguchi, A. Ito, A. Nixon, M. Yoshida, X. F. Wang and T. P. Yao, *Nature*, 2002, **417**, 455-458.
46. X. Zhang, Z. Yuan, Y. Zhang, S. Yong, A. Salas-Burgos, J. Koomen, N. Olashaw, J. T. Parsons, X. J. Yang, S. R. Dent, T. P. Yao, W. S. Lane and E. Seto, *Mol Cell*, 2007, **27**, 197-213.
47. P. Bali, M. Pranpat, J. Bradner, M. Balasis, W. Fiskus, F. Guo, K. Rocha, S. Kumaraswamy, S. Boyapalle, P. Atadja, E. Seto and K. Bhalla, *J Biol Chem*, 2005, **280**, 26729-26734.

48. Y. Li, X. Zhang, R. D. Polakiewicz, T. P. Yao and M. J. Comb, *J Biol Chem*, 2008, **283**, 12686-12690.
49. R. B. Parmigiani, W. S. Xu, G. Venta-Perez, H. Erdjument-Bromage, M. Yaneva, P. Tempst and P. A. Marks, *Proc Natl Acad Sci U S A*, 2008, **105**, 9633-9638.
50. E. Seto and M. Yoshida, *Cold Spring Harb Perspect Biol*, 2014, **6**, a018713.
51. A. J. de Ruijter, A. H. van Gennip, H. N. Caron, S. Kemp and A. B. van Kuilenburg, *Biochem J*, 2003, **370**, 737-749.
52. T. Eckschlager, J. Plch, M. Stiborova and J. Hrabeta, *International Journal of Molecular Sciences*, 2017, **18**, 1414.
53. M. Schiedel, M. Moroglu, D. M. H. Ascough, A. E. R. Chamberlain, J. Kamps, A. R. Sekirnik and S. J. Conway, *Angew Chem Int Ed Engl*, 2019, **58**, 17930-17952.
54. P. Filippakopoulos, S. Picaud, M. Mangos, T. Keates, J. P. Lambert, D. Barsyte-Lovejoy, I. Felletar, R. Volkmer, S. Muller, T. Pawson, A. C. Gingras, C. H. Arrowsmith and S. Knapp, *Cell*, 2012, **149**, 214-231.
55. S. G. Smith and M. M. Zhou, *ACS Chem Biol*, 2016, **11**, 598-608.
56. F. Madeira, N. Madhusoodanan, J. Lee, A. Eusebi, A. Niewielska, A. R. N. Tivey, R. Lopez and S. Butcher, *Nucleic Acids Res*, 2024, **52**, W521-W525.
57. J. C. Black, A. Mosley, T. Kitada, M. Washburn and M. Carey, *Mol Cell*, 2008, **32**, 449-455.
58. M. Delvecchio, J. Gaucher, C. Aguilar-Gurrieri, E. Ortega and D. Panne, *Nat Struct Mol Biol*, 2013, **20**, 1040-1046.
59. A. E. Ringel and C. Wolberger, *Structure*, 2013, **21**, 1479-1481.
60. J. G. M. Rack, T. Lutter, G. E. Kjaereng Bjerga, C. Guder, C. Ehrhardt, S. Varv, M. Ziegler and R. Aasland, *J Mol Biol*, 2014, **426**, 3960-3972.
61. C. Dhalluin, J. E. Carlson, L. Zeng, C. He, A. K. Aggarwal and M. M. Zhou, *Nature*, 1999, **399**, 491-496.
62. E. T. Manning, T. Ikehara, T. Ito, J. T. Kadonaga and W. L. Kraus, *Mol Cell Biol*, 2001, **21**, 3876-3887.
63. S. Mujtaba, Y. He, L. Zeng, S. Yan, O. Plotnikova, Sachchidanand, R. Sanchez, N. J. Zeleznik-Le, Z. Ronai and M. M. Zhou, *Mol Cell*, 2004, **13**, 251-263.
64. R. Raisner, S. Kharbanda, L. Jin, E. Jeng, E. Chan, M. Merchant, P. M. Haverty, R. Bainer, T. Cheung, D. Arnott, E. M. Flynn, F. A. Romero, S. Magnuson and K. E. Gascoigne, *Cell Rep*, 2018, **24**, 1722-1729.
65. Y. Zhang, Y. Xue, J. Shi, J. Ahn, W. Mi, M. Ali, X. Wang, B. J. Klein, H. Wen, W. Li, X. Shi and T. G. Kutateladze, *Nat Struct Mol Biol*, 2018, **25**, 841-849.
66. H. J. Dyson and P. E. Wright, *J Biol Chem*, 2016, **291**, 6714-6722.
67. Y. Zhang, K. Brown, Y. Yu, Z. Ibrahim, M. Zandian, H. Xuan, S. Ingersoll, T. Lee, C. C. Ebmeier, J. Liu, D. Panne, X. Shi, X. Ren and T. G. Kutateladze, *Nat Commun*, 2021, **12**, 4618.
68. Z. Ibrahim, T. Wang, O. Destaing, N. Salvi, N. Hoghoughi, C. Chabert, A. Rusu, J. Gao, L. Feletto, N. Reynoird, T. Schalch, Y. Zhao, M. Blackledge, S. Khochbin and D. Panne, *Nat Commun*, 2022, **13**, 7759.
69. L. Ma, Z. Gao, J. Wu, B. Zhong, Y. Xie, W. Huang and Y. Lin, *Mol Cell*, 2021, **81**, 1682-1697 e1687.
70. J. J. Ferrie, J. P. Karr, T. G. W. Graham, G. M. Dailey, G. Zhang, R. Tjian and X. Darzacq, *Mol Cell*, 2024, **84**, 234-243 e234.
71. M. Kikuchi, S. Morita, M. Wakamori, S. Sato, T. Uchikubo-Kamo, T. Suzuki, N. Dohmae, M. Shirouzu and T. Umehara, *Nat Commun*, 2023, **14**, 4103.
72. S. Hatazawa, J. Liu, Y. Takizawa, M. Zandian, L. Negishi, T. G. Kutateladze and H. Kurumizaka, *iScience*, 2022, **25**, 104563.
73. D. P. Teufel, M. Bycroft and A. R. Fersht, *Oncogene*, 2009, **28**, 2112-2118.
74. R. B. Berlow, H. J. Dyson and P. E. Wright, *Nature*, 2017, **543**, 447-451.
75. Y. Xu and W. Wan, *J Cell Sci*, 2023, **136**.
76. X. Guo, Y. Bai, M. Zhao, M. Zhou, Q. Shen, C. H. Yun, H. Zhang, W. G. Zhu and J. Wang, *Nucleic Acids Res*, 2018, **46**, 689-703.
77. M. Krosel, M. Gabathuler, L. Moser, M. Maciukiewicz, T. Zullig, T. Seifritz, M. Tomsic, O. Distler, C. Ospelt and K. Klein, *Sci Rep*, 2023, **13**, 17112.
78. T. P. Yao, S. P. Oh, M. Fuchs, N. D. Zhou, L. E. Ch'ng, D. Newsome, R. T. Bronson, E. Li, D. M. Livingston and R. Eckner, *Cell*, 1998, **93**, 361-372.
79. Y. Tanaka, I. Naruse, T. Hongo, M. Xu, T. Nakahata, T. Maekawa and S. Ishii, *Mech Dev*, 2000, **95**, 133-145.

80. E. Kalkhoven, *Biochem Pharmacol*, 2004, **68**, 1145-1155.
81. D. R. Warner, M. M. Pisano and R. M. Greene, *In Vitro Cell Dev Biol Anim*, 2002, **38**, 48-53.
82. A. Partanen, J. Motoyama and C. C. Hui, *Int J Dev Biol*, 1999, **43**, 487-494.
83. Y. Wang, K. Tu, D. Liu, L. Guo, Y. Chen, Q. Li, J. L. Maiers, Z. Liu, V. H. Shah, C. Dou, D. Tschumperlin, L. Voneschen, R. Yang and N. Kang, *Hepatology*, 2019, **70**, 1409-1423.
84. S. M. Son, S. J. Park, S. Y. Breusegem, D. Larrieu and D. C. Rubinsztein, *Nat Cell Biol*, 2024, **26**, 235-249.
85. E. Ortega, S. Rengachari, Z. Ibrahim, N. Hoghoughi, J. Gaucher, A. S. Holehouse, S. Khochbin and D. Panne, *Nature*, 2018, **562**, 538-544.
86. M. E. Breen and A. K. Mapp, *Curr Opin Chem Biol*, 2018, **45**, 195-203.
87. T. P. Rooney, P. Filippakopoulos, O. Fedorov, S. Picaud, W. A. Cortopassi, D. A. Hay, S. Martin, A. Tumber, C. M. Rogers, M. Philpott, M. Wang, A. L. Thompson, T. D. Heightman, D. C. Pryde, A. Cook, R. S. Paton, S. Muller, S. Knapp, P. E. Brennan and S. J. Conway, *Angew Chem Int Ed Engl*, 2014, **53**, 6126-6130.
88. M. Brand, J. Clayton, M. Moroglu, M. Schiedel, S. Picaud, J. P. Bluck, A. Skwarska, H. Bolland, A. K. N. Chan, C. M. C. Laurin, A. R. Scorah, L. See, T. P. C. Rooney, K. H. Andrews, O. Fedorov, G. Perell, P. Kalra, K. B. Vinh, W. A. Cortopassi, P. Heitel, K. E. Christensen, R. I. Cooper, R. S. Paton, W. C. K. Pomerantz, P. C. Biggin, E. M. Hammond, P. Filippakopoulos and S. J. Conway, *J Med Chem*, 2021, **64**, 10102-10123.
89. T. D. Crawford, F. A. Romero, K. W. Lai, V. Tsui, A. M. Taylor, G. de Leon Boenig, C. L. Noland, J. Murray, J. Ly, E. F. Choo, T. L. Hunsaker, E. W. Chan, M. Merchant, S. Kharbanda, K. E. Gascoigne, S. Kaufman, M. H. Beresini, J. Liao, W. Liu, K. X. Chen, Z. Chen, A. R. Conery, A. Cote, H. Jayaram, Y. Jiang, J. R. Kiefer, T. Kleinheinz, Y. Li, J. Maher, E. Pardo, F. Poy, K. L. Spillane, F. Wang, J. Wang, X. Wei, Z. Xu, Z. Xu, I. Yen, L. Zawadzke, X. Zhu, S. Bellon, R. Cummings, A. G. Cochran, B. K. Albrecht and S. Magnuson, *J Med Chem*, 2016, **59**, 10549-10563.
90. K. W. Lai, F. A. Romero, V. Tsui, M. H. Beresini, G. de Leon Boenig, S. M. Bronner, K. Chen, Z. Chen, E. F. Choo, T. D. Crawford, P. Cyr, S. Kaufman, Y. Li, J. Liao, W. Liu, J. Ly, J. Murray, W. Shen, J. Wai, F. Wang, C. Zhu, X. Zhu and S. Magnuson, *Bioorg Med Chem Lett*, 2018, **28**, 15-23.
91. F. A. Romero, J. Murray, K. W. Lai, V. Tsui, B. K. Albrecht, L. An, M. H. Beresini, G. de Leon Boenig, S. M. Bronner, E. W. Chan, K. X. Chen, Z. Chen, E. F. Choo, K. Clagg, K. Clark, T. D. Crawford, P. Cyr, D. de Almeida Nagata, K. E. Gascoigne, J. L. Grogan, G. Hatzivassiliou, W. Huang, T. L. Hunsaker, S. Kaufman, S. G. Koenig, R. Li, Y. Li, X. Liang, J. Liao, W. Liu, J. Ly, J. Maher, C. Masui, M. Merchant, Y. Ran, A. M. Taylor, J. Wai, F. Wang, X. Wei, D. Yu, B. Y. Zhu, X. Zhu and S. Magnuson, *J Med Chem*, 2017, **60**, 9162-9183.
92. A. M. Taylor, A. Cote, M. C. Hewitt, R. Pastor, Y. Leblanc, C. G. Nasveschuk, F. A. Romero, T. D. Crawford, N. Cantone, H. Jayaram, J. Setser, J. Murray, M. H. Beresini, G. de Leon Boenig, Z. Chen, A. R. Conery, R. T. Cummings, L. A. Dakin, E. M. Flynn, O. W. Huang, S. Kaufman, P. J. Keller, J. R. Kiefer, T. Lai, Y. Li, J. Liao, W. Liu, H. Lu, E. Pardo, V. Tsui, J. Wang, Y. Wang, Z. Xu, F. Yan, D. Yu, L. Zawadzke, X. Zhu, X. Zhu, R. J. Sims, 3rd, A. G. Cochran, S. Bellon, J. E. Audia, S. Magnuson and B. K. Albrecht, *ACS Med Chem Lett*, 2016, **7**, 531-536.
93. J. Welti, A. Sharp, N. Brooks, W. Yuan, C. McNair, S. N. Chand, A. Pal, I. Figueiredo, R. Riisnaes, B. Gurel, J. Rekowski, D. Bogdan, W. West, B. Young, M. Raja, A. Prosser, J. Lane, S. Thomson, J. Worthington, S. Onions, J. Shannon, S. Paoletta, R. Brown, D. Smyth, G. W. Harbottle, V. S. Gil, S. Miranda, M. Crespo, A. Ferreira, R. Pereira, N. Tunariu, S. Carreira, A. J. Neeb, J. Ning, A. Swain, D. Taddei, S. C. P. I. P. C. D. Team, M. J. Schiewer, K. E. Knudsen, N. Pegg and J. S. de Bono, *Cancer Discov*, 2021, **11**, 1118-1137.
94. F. Ritossa, *Experientia*, 1962, **18**, 571-573.
95. F. Ritossa, *Cell Stress Chaperones*, 1996, **1**, 97-98.
96. J. Wu, T. Liu, Z. Rios, Q. Mei, X. Lin and S. Cao, *Trends Pharmacol Sci*, 2017, **38**, 226-256.
97. F. H. Schopf, M. M. Biebl and J. Buchner, *Nat Rev Mol Cell Biol*, 2017, **18**, 345-360.
98. J. L. Johnson, *Biochim Biophys Acta*, 2012, **1823**, 607-613.
99. B. T. Lai, N. W. Chin, A. E. Stanek, W. Keh and K. W. Lanks, *Mol Cell Biol*, 1984, **4**, 2802-2810.
100. L. Whitesell and S. L. Lindquist, *Nat Rev Cancer*, 2005, **5**, 761-772.
101. G. Chiosis, C. S. Digwal, J. B. Trepel and L. Neckers, *Nat Rev Mol Cell Biol*, 2023, **24**, 797-815.

102. S. Tsutsumi, M. Mollapour, C. Prodromou, C. T. Lee, B. Panaretou, S. Yoshida, M. P. Mayer and L. M. Neckers, *Proc Natl Acad Sci U S A*, 2012, **109**, 2937-2942.
103. R. Dutta and M. Inouye, *Trends Biochem Sci*, 2000, **25**, 24-28.
104. S. Maiti and D. Picard, *Biomolecules*, 2022, **12**.
105. P. C. Echeverria, A. Bernthaler, P. Dupuis, B. Mayer and D. Picard, *PLoS One*, 2011, **6**, e26044.
106. L. Li, L. Wang, Q. D. You and X. L. Xu, *J Med Chem*, 2020, **63**, 1798-1822.
107. M. A. Biamonte, R. Van de Water, J. W. Arndt, R. H. Scannevin, D. Perret and W. C. Lee, *J Med Chem*, 2010, **53**, 3-17.
108. T. Shimamura, S. A. Perera, K. P. Foley, J. Sang, S. J. Rodig, T. Inoue, L. Chen, D. Li, J. Carretero, Y. C. Li, P. Sinha, C. D. Carey, C. L. Borgman, J. P. Jimenez, M. Meyerson, W. Ying, J. Barsoum, K. K. Wong and G. I. Shapiro, *Clin Cancer Res*, 2012, **18**, 4973-4985.
109. S. A. Eccles, A. Massey, F. I. Raynaud, S. Y. Sharp, G. Box, M. Valenti, L. Patterson, A. de Haven Brandon, S. Gowan, F. Boxall, W. Aherne, M. Rowlands, A. Hayes, V. Martins, F. Urban, K. Boxall, C. Prodromou, L. Pearl, K. James, T. P. Matthews, K. M. Cheung, A. Kalusa, K. Jones, E. McDonald, X. Barril, P. A. Brough, J. E. Cansfield, B. Dymock, M. J. Drysdale, H. Finch, R. Howes, R. E. Hubbard, A. Surgenor, P. Webb, M. Wood, L. Wright and P. Workman, *Cancer Res*, 2008, **68**, 2850-2860.
110. K. Lundgren, H. Zhang, J. Brekken, N. Huser, R. E. Powell, N. Timple, D. J. Busch, L. Neely, J. L. Sensintaffar, Y. C. Yang, A. McKenzie, J. Friedman, R. Scannevin, A. Kamal, K. Hong, S. R. Kasibhatla, M. F. Boehm and F. J. Burrows, *Mol Cancer Ther*, 2009, **8**, 921-929.
111. G. Speranza, L. Anderson, A. P. Chen, K. Do, M. Eugeni, M. Weil, L. Rubinstein, E. Majerova, J. Collins, Y. Horneffer, L. Juwara, J. Zlott, R. Bishop, B. A. Conley, H. Streicher, J. Tomaszewski, J. H. Doroshow and S. Kummar, *Invest New Drugs*, 2018, **36**, 230-239.
112. S. Mahajan, M. Grkovski, K. D. Staton, S. Ravassa, K. Domfe, H. W. Strauss, J. L. Humm, P. B. Zanzonico, B. J. Beattie, I. Cho, E. M. Burnazi, J. J. Fox, H. Schöder, J. R. Osborne, T. Youn, K. Jhaveri, G. Chiosis and M. P. Dunphy, *Clinical and Translational Imaging*, 2024, DOI: 10.1007/s40336-024-00658-9.
113. K. H. Huang, J. M. Veal, R. P. Fadden, J. W. Rice, J. Eaves, J. P. Strachan, A. F. Barabasz, B. E. Foley, T. E. Barta, W. Ma, M. A. Silinski, M. Hu, J. M. Partridge, A. Scott, L. G. DuBois, T. Freed, P. M. Steed, A. J. Ommen, E. D. Smith, P. F. Hughes, A. R. Woodward, G. J. Hanson, W. S. McCall, C. J. Markworth, L. Hinkley, M. Jenks, L. Geng, M. Lewis, J. Otto, B. Pronk, K. Verleysen and S. E. Hall, *J Med Chem*, 2009, **52**, 4288-4305.
114. J. Sanchez, T. R. Carter, M. S. Cohen and B. S. J. Blagg, *Curr Cancer Drug Targets*, 2020, **20**, 253-270.
115. S. Ohkubo, Y. Kodama, H. Muraoka, H. Hitotsumachi, C. Yoshimura, M. Kitade, A. Hashimoto, K. Ito, A. Gomori, K. Takahashi, Y. Shibata, A. Kanoh and K. Yonekura, *Mol Cancer Ther*, 2015, **14**, 14-22.
116. J. Dernovsek and T. Tomasic, *Pharmacol Ther*, 2023, **245**, 108396.
117. Y. Kurokawa, Y. Honma, A. Sawaki, Y. Naito, S. Iwagami, Y. Komatsu, T. Takahashi, T. Nishida and T. Doi, *Ann Oncol*, 2022, **33**, 959-967.
118. M. Mollapour and L. Neckers, *Biochim Biophys Acta*, 2012, **1823**, 648-655.
119. X. Yu, Z. S. Guo, M. G. Marcu, L. Neckers, D. M. Nguyen, G. A. Chen and D. S. Schrump, *J Natl Cancer Inst*, 2002, **94**, 504-513.
120. H. Hasegawa, Y. Yamada, K. Tsukasaki, N. Mori, K. Tsuruda, D. Sasaki, T. Usui, A. Osaka, S. Atogami, C. Ishikawa, Y. Machijima, S. Sawada, T. Hayashi, Y. Miyazaki and S. Kamihira, *Leukemia*, 2011, **25**, 575-587.
121. J. J. Kovacs, P. J. Murphy, S. Gaillard, X. Zhao, J. T. Wu, C. V. Nicchitta, M. Yoshida, D. O. Toft, W. B. Pratt and T. P. Yao, *Mol Cell*, 2005, **18**, 601-607.
122. P. J. Murphy, Y. Morishima, J. J. Kovacs, T. P. Yao and W. B. Pratt, *J Biol Chem*, 2005, **280**, 33792-33799.
123. K. Reynald, M. Rowlands, L. Stimson, A. Bannister, P. Workman and W. Aherne, *Cancer Research*, 2007, **67**, 2480-2480.
124. Y. Yang, R. Rao, J. Shen, Y. Tang, W. Fiskus, J. Nechtman, P. Atadja and K. Bhalla, *Cancer Res*, 2008, **68**, 4833-4842.
125. X. Zhang, Y. Yang, D. Y. Li, Z. Wu, H. Y. Liu, Z. Y. Zhao, H. Y. Zhu, F. Xie and X. Z. Li, *Frontiers in Oncology*, 2022, **12**, 868866.
126. Q. Zhou, A. T. Agoston, P. Atadja, W. G. Nelson and N. E. Davidson, *Mol Cancer Res*, 2008, **6**, 873-883.

127. J. H. Park, S. H. Kim, M. C. Choi, J. Lee, D. Y. Oh, S. A. Im, Y. J. Bang and T. Y. Kim, *Biochem Biophys Res Commun*, 2008, **368**, 318-322.
128. S. J. Backe, R. A. Sager, M. R. Woodford, A. M. Makedon and M. Mollapour, *J Biol Chem*, 2020, **295**, 11099-11117.
129. B. T. Scroggins, K. Robzyk, D. Wang, M. G. Marcu, S. Tsutsumi, K. Beebe, R. J. Cotter, S. Felts, D. Toft, L. Karnitz, N. Rosen and L. Neckers, *Mol Cell*, 2007, **25**, 151-159.
130. P. V. Hornbeck, B. Zhang, B. Murray, J. M. Kornhauser, V. Latham and E. Skrzypek, *Nucleic Acids Res*, 2015, **43**, D512-520.
131. J. Liu, J. D. Farmer, Jr., W. S. Lane, J. Friedman, I. Weissman and S. L. Schreiber, *Cell*, 1991, **66**, 807-815.
132. D. M. Sabatini, H. Erdjument-Bromage, M. Lui, P. Tempst and S. H. Snyder, *Cell*, 1994, **78**, 35-43.
133. E. J. Brown, M. W. Albers, T. B. Shin, K. Ichikawa, C. T. Keith, W. S. Lane and S. L. Schreiber, *Nature*, 1994, **369**, 756-758.
134. S. L. Schreiber, *Cell Chemical Biology*, 2024, **31**, 1050-1063.
135. S. L. Schreiber, *Cell Chem Biol*, 2024, **31**, 1050-1063.
136. T. Ito, H. Ando, T. Suzuki, T. Ogura, K. Hotta, Y. Imamura, Y. Yamaguchi and H. Handa, *Science*, 2010, **327**, 1345-1350.
137. E. S. Fischer, K. Bohm, J. R. Lydeard, H. Yang, M. B. Stadler, S. Cavadini, J. Nagel, F. Serluca, V. Acker, G. M. Lingaraju, R. B. Tichkule, M. Schebesta, W. C. Forrester, M. Schirle, U. Hassiepen, J. Ottl, M. Hild, R. E. Beckwith, J. W. Harper, J. L. Jenkins and N. H. Thoma, *Nature*, 2014, **512**, 49-53.
138. W. Rehman, L. M. Arfons and H. M. Lazarus, *Ther Adv Hematol*, 2011, **2**, 291-308.
139. P. Y. Ting, S. Borikar, J. R. Kerrigan, N. M. Thomsen, E. Aghania, A. E. Hinman, A. Reyes, N. Pizzato, B. D. Fodor, F. Wu, M. S. Belew, X. Mao, J. Wang, S. Chitnis, W. Niu, A. Hachey, J. S. Cobb, N. A. Savage, A. Burke, J. Paulk, D. Dovala, J. Lin, M. C. Clifton, E. Ornelas, X. Ma, N. F. Ware, C. C. Sanchez, J. Taraszka, R. Terranova, J. Knehr, M. Altorfer, S. W. Barnes, R. E. J. Beckwith, J. M. Solomon, N. A. Dales, A. W. Patterson, J. Wagner, T. Bouwmeester, G. Dranoff, S. C. Stevenson and J. E. Bradner, *Science*, 2024, **385**, 91-99.
140. D. M. Spencer, T. J. Wandless, S. L. Schreiber and G. R. Crabtree, *Science*, 1993, **262**, 1019-1024.
141. Z. Liu, M. Hu, Y. Yang, C. Du, H. Zhou, C. Liu, Y. Chen, L. Fan, H. Ma, Y. Gong and Y. Xie, *Mol Biomed*, 2022, **3**, 46.
142. X. Liu and A. Ciulli, *ACS Cent Sci*, 2023, **9**, 1269-1284.
143. S. L. Paiva and C. M. Crews, *Curr Opin Chem Biol*, 2019, **50**, 111-119.
144. D. P. Bondeson, B. E. Smith, G. M. Burslem, A. D. Buhimschi, J. Hines, S. Jaime-Figueroa, J. Wang, B. D. Hamman, A. Ishchenko and C. M. Crews, *Cell Chem Biol*, 2018, **25**, 78-87 e75.
145. B. E. Smith, S. L. Wang, S. Jaime-Figueroa, A. Harbin, J. Wang, B. D. Hamman and C. M. Crews, *Nat Commun*, 2019, **10**, 131.
146. X. Chen, M. C. Crawford, Y. Xiong, A. B. Shaik, K. F. Suazo, L. G. Bauer, M. S. Penikalapati, J. H. Williams, K. V. M. Huber, T. Andressen, R. E. Swenson and J. L. Meier, *JACS Au*, 2024, **4**, 3094-3103.
147. S. M. Banik, K. Pedram, S. Wisnovsky, G. Ahn, N. M. Riley and C. R. Bertozzi, *Nature*, 2020, **584**, 291-297.
148. D. Takahashi, J. Moriyama, T. Nakamura, E. Miki, E. Takahashi, A. Sato, T. Akaike, K. Itto-Nakama and H. Arimoto, *Mol Cell*, 2019, **76**, 797-810 e710.
149. Y. Fu, N. Chen, Z. Wang, S. Luo, Y. Ding and B. Lu, *Cell Res*, 2021, **31**, 965-979.
150. R. Sarott, S. Gourisankar, B. Karim, S. Nettles, H. Yang, B. G. Dwyer, J. M. Simanauskaite, J. Tse, H. Abuzaid, A. Krokhotin, T. Zhang, S. M. Hinshaw, M. R. Green, G. R. Crabtree and N. S. Gray, *bioRxiv*, 2023, DOI: 10.1101/2023.10.23.563687, 2023.2010.2023.563687.
151. S. Gourisankar, A. Krokhotin, W. Ji, X. Liu, C. Y. Chang, S. H. Kim, Z. Li, W. Wenderski, J. M. Simanauskaite, H. Yang, H. Vogel, T. Zhang, M. R. Green, N. S. Gray and G. R. Crabtree, *Nature*, 2023, **620**, 417-425.
152. N. J. Henning, L. Boike, J. N. Spradlin, C. C. Ward, G. Liu, E. Zhang, B. P. Belcher, S. M. Brittain, M. J. Hesse, D. Dovala, L. M. McGregor, R. Valdez Misiolek, L. W. Plasschaert, D. J. Rowlands, F. Wang, A. O. Frank, D. Fuller, A. R. Estes, K. L. Randal, A. Panidapu, J. M. McKenna, J. A. Tallarico, M. Schirle and D. K. Nomura, *Nat Chem Biol*, 2022, **18**, 412-421.
153. S. Yamazoe, J. Tom, Y. Fu, W. Wu, L. Zeng, C. Sun, Q. Liu, J. Lin, K. Lin, W. J. Fairbrother and S. T. Staben, *J Med Chem*, 2020, **63**, 2807-2813.

154. P. H. Chen, Z. Hu, E. An, I. Okeke, S. Zheng, X. Luo, A. Gong, S. Jaime-Figueroa and C. M. Crews, *ACS Chem Biol*, 2021, **16**, 2808-2815.
155. W. W. Wang, L. Y. Chen, J. M. Wozniak, A. M. Jadhav, H. Anderson, T. E. Malone and C. G. Parker, *J Am Chem Soc*, 2021, **143**, 16700-16708.
156. M. Kabir, N. Sun, X. Hu, T. C. Martin, J. Yi, Y. Zhong, Y. Xiong, H. U. Kaniskan, W. Gu, R. Parsons and J. Jin, *J Am Chem Soc*, 2023, **145**, 14932-14944.
157. B. Ma, K. S. Khan, T. Xu, J. Xeque Amada, Z. Guo, Y. Huang, Y. Yan, H. Lam, A. S. Cheng and B. W. Ng, *J Am Chem Soc*, 2024, **146**, 9779-9789.
158. S. U. Siriwardena, D. N. P. Munkanatta Godage, V. M. Shoba, S. Lai, M. Shi, P. Wu, S. K. Chaudhary, S. L. Schreiber and A. Choudhary, *J Am Chem Soc*, 2020, **142**, 14052-14057.
159. C. Bashore, S. Prakash, M. C. Johnson, R. J. Conrad, I. A. Kekessie, S. J. Scales, N. Ishisoko, T. Kleinheinz, P. S. Liu, N. Popovych, A. T. Wecksler, L. Zhou, C. Tam, I. Zilberleyb, R. Srinivasan, R. A. Blake, A. Song, S. T. Staben, Y. Zhang, D. Arnott, W. J. Fairbrother, S. A. Foster, I. E. Wertz, C. Ciferri and E. C. Dueber, *Nat Chem Biol*, 2023, **19**, 55-63.
160. T. K. Neklesa, H. S. Tae, A. R. Schneekloth, M. J. Stulberg, T. W. Corson, T. B. Sundberg, K. Raina, S. A. Holley and C. M. Crews, *Nat Chem Biol*, 2011, **7**, 538-543.
161. M. G. Costales, Y. Matsumoto, S. P. Velagapudi and M. D. Disney, *J Am Chem Soc*, 2018, **140**, 6741-6744.
162. W. J. Gibson, A. Sadagopan, V. M. Shoba, A. Choudhary, M. Meyerson and S. L. Schreiber, *J Am Chem Soc*, 2023, **145**, 26028-26037.
163. C. S. C. Ng, A. Liu, B. Cui and S. M. Banik, *Nature*, 2024, **633**, 941-951.
164. P. K. Parua and R. P. Fisher, *Nat Chem Biol*, 2020, **16**, 716-724.
165. J. Liu, X. Hu, K. Luo, Y. Xiong, L. Chen, Z. Wang, H. Inuzuka, C. Qian, X. Yu, L. Xie, A. Muneer, D. Zhang, J. A. Paulo, X. Chen, J. Jin and W. Wei, *J Am Chem Soc*, 2024, **146**, 11507-11514.
166. P. B. Dervan, *Bioorg Med Chem*, 2001, **9**, 2215-2235.
167. J. Taniguchi, Y. H. Feng, G. N. Pandian, F. Hashiya, T. Hidaka, K. Hashiya, S. Park, T. Bando, S. Ito and H. Sugiyama, *Journal of the American Chemical Society*, 2018, **140**, 7108-7115.
168. A. M. Chiarella, K. V. Butler, B. E. Gryder, D. Lu, T. A. Wang, X. Yu, S. Pomella, J. Khan, J. Jin and N. A. Hathaway, *Nat Biotechnol*, 2020, **38**, 50-55.
169. B. Nabet, J. M. Roberts, D. L. Buckley, J. Paulk, S. Dastjerdi, A. Yang, A. L. Leggett, M. A. Erb, M. A. Lawlor, A. Souza, T. G. Scott, S. Vittori, J. A. Perry, J. Qi, G. E. Winter, K. K. Wong, N. S. Gray and J. E. Bradner, *Nat Chem Biol*, 2018, **14**, 431-441.
170. T. Clackson, W. Yang, L. W. Rozamus, M. Hatada, J. F. Amara, C. T. Rollins, L. F. Stevenson, S. R. Magari, S. A. Wood, N. L. Courage, X. Lu, F. Cerasoli, Jr., M. Gilman and D. A. Holt, *Proc Natl Acad Sci U S A*, 1998, **95**, 10437-10442.
171. Q. Jin, L. R. Yu, L. Wang, Z. Zhang, L. H. Kasper, J. E. Lee, C. Wang, P. K. Brindle, S. Y. Dent and K. Ge, *EMBO J*, 2011, **30**, 249-262.
172. B. T. Weinert, T. Narita, S. Satpathy, B. Srinivasan, B. K. Hansen, C. Scholz, W. B. Hamilton, B. E. Zucconi, W. W. Wang, W. R. Liu, J. M. Brickman, E. A. Kesicki, A. Lai, K. D. Bromberg, P. A. Cole and C. Choudhary, *Cell*, 2018, **174**, 231-244 e212.
173. M. R. Bauer, A. Kramer, G. Settanni, R. N. Jones, X. Ni, R. Khan Tareque, A. R. Fersht, J. Spencer and A. C. Joerger, *ACS Chem Biol*, 2020, **15**, 657-668.
174. L. Y. Chen, S. J. Singha Roy, A. M. Jadhav, W. W. Wang, P. H. Chen, T. Bishop, M. A. Erb and C. G. Parker, *ACS Chem Biol*, 2024, **19**, 1918-1929.
175. N. Brooks, M. Raja, B. W. Young, G. J. Spencer, T. C. P. Somervaille and N. A. Pegg, *Blood*, 2019, **134**, 2.
176. H. Xu, G. Luo, T. Wu, J. Hu, C. Wang, X. Wu, Y. Zhang, Y. Xu and Q. Xiang, *Biochem Biophys Res Commun*, 2022, **623**, 17-22.
177. Q. Chang, J. Li, Y. Deng, R. Zhou, B. Wang, Y. Wang, M. Zhang, X. Huang and Y. Li, *J Med Chem*, 2024, **67**, 2466-2486.
178. J. Hu, H. Xu, T. Wu, C. Zhang, H. Shen, R. Dong, Q. Hu, Q. Xiang, S. Chai, G. Luo, X. Chen, Y. Huang, X. Zhao, C. Peng, X. Wu, B. Lin, Y. Zhang and Y. Xu, *J Med Chem*, 2024, **67**, 6952-6986.
179. A. Hammitzsch, C. Tallant, O. Fedorov, A. O'Mahony, P. E. Brennan, D. A. Hay, F. O. Martinez, M. H. Al-Mossawi, J. de Wit, M. Vecellio, C. Wells, P. Wordsworth, S. Muller, S. Knapp and P. Bowness, *Proc Natl Acad Sci U S A*, 2015, **112**, 10768-10773.
180. J. Shi, R. Van de Water, K. Hong, R. B. Lamer, K. W. Weichert, C. M. Sandoval, S. R. Kasibhatla, M. F. Boehm, J. Chao, K. Lundgren, N. Timple, R. Lough, G. Ibanez, C. Boykin, F. J. Burrows, M. R. Kehry, T. J. Yun, E. K. Harning, C. Ambrose, J. Thompson, S. A. Bixler,

A. Dunah, P. Snodgrass-Belt, J. Arndt, I. J. Enyedy, P. Li, V. S. Hong, A. McKenzie and M. A. Biamonte, *J Med Chem*, 2012, **55**, 7786-7795.
181. Q. Liu, G. Tu, Y. Hu, Q. Jiang, J. Liu, S. Lin, Z. Yu, G. Li, X. Wu, Y. Tang, X. Huang, J. Xu, Y. Liu and L. Wu, *Eur J Med Chem*, 2022, **228**, 114013.
182. Z. Li, S. Ma, L. Zhang, S. Zhang, Z. Ma, L. Du and M. Li, *Journal of Medicinal Chemistry*, 2023, **66**, 733-751.
183. S. R. Kasibhatla, K. Hong, M. A. Biamonte, D. J. Busch, P. L. Karjian, J. L. Sensintaffar, A. Kamal, R. E. Lough, J. Brekken, K. Lundgren, R. Grecko, G. A. Timony, Y. Ran, R. Mansfield, L. C. Fritz, E. Ulm, F. J. Burrows and M. F. Boehm, *J Med Chem*, 2007, **50**, 2767-2778.
184. *WO Pat.,* WO 2018/073586 A1, 2018.
185. WO2019202332, 2019.
186. G. L. Beutner, I. S. Young, M. L. Davies, M. R. Hickey, H. Park, J. M. Stevens and Q. M. Ye, *Organic Letters*, 2018, **20**, 4218-4222.
187. A. J. J. Lennox and G. C. Lloyd-Jones, *Isr J Chem*, 2010, **50**, 664-674.
188. J. P. Collman and M. Zhong, *Org Lett*, 2000, **2**, 1233-1236.
189. K. Nishiura, Y. Urawa and S. Soda, *Advanced Synthesis & Catalysis*, 2004, **346**, 1679-1684.
190. A. Alberola, C. Andres, A. G. Ortega and R. Pedrosa, *J Heterocyclic Chem*, 1984, **21**, 1575-1576.
191. H. Kim, K. Kim, S. H. Son, J. Y. Choi, K. H. Lee, B. T. Kim, Y. Byun and Y. S. Choe, *ACS Chem Neurosci*, 2019, **10**, 1445-1451.
192. P. Filippakopoulos, J. Qi, S. Picaud, Y. Shen, W. B. Smith, O. Fedorov, E. M. Morse, T. Keates, T. T. Hickman, I. Felletar, M. Philpott, S. Munro, M. R. McKeown, Y. Wang, A. L. Christie, N. West, M. J. Cameron, B. Schwartz, T. D. Heightman, N. La Thangue, C. A. French, O. Wiest, A. L. Kung, S. Knapp and J. E. Bradner, *Nature*, 2010, **468**, 1067-1073.
193. Y. S. Day, C. L. Baird, R. L. Rich and D. G. Myszka, *Protein Sci*, 2002, **11**, 1017-1025.
194. G. E. Winter, D. L. Buckley, J. Paulk, J. M. Roberts, A. Souza, S. Dhe-Paganon and J. E. Bradner, *Science*, 2015, **348**, 1376-1381.
195. V. Zoppi, S. J. Hughes, C. Maniaci, A. Testa, T. Gmaschitz, C. Wieshofer, M. Koegl, K. M. Riching, D. L. Daniels, A. Spallarossa and A. Ciulli, *J Med Chem*, 2019, **62**, 699-726.
196. M. S. Gadd, A. Testa, X. Lucas, K. H. Chan, W. Chen, D. J. Lamont, M. Zengerle and A. Ciulli, *Nat Chem Biol*, 2017, **13**, 514-521.
197. B. E. Smith, S. L. Wang, S. Jaime-Figueroa, A. Harbin, J. Wang, B. D. Hamman and C. M. Crews, *Nat Commun*, 2019, **10**.
198. X. G. Liu, X. Zhang, D. W. Lv, Y. X. Yuan, G. R. Zheng and D. H. Zhou, *Future Med Chem*, 2020, **12**, 1155-1179.
199. S. Imaide, K. M. Riching, N. Makukhin, V. Vetma, C. Whitworth, S. J. Hughes, N. Trainor, S. D. Mahan, N. Murphy, A. D. Cowan, K. H. Chan, C. Craigon, A. Testa, C. Maniaci, M. Urh, D. L. Daniels and A. Ciulli, *Nat Chem Biol*, 2021, **17**, 1157-1167.
200. R. P. Wurz, H. Rui, K. Dellamaggiore, S. Ghimire-Rijal, K. Choi, K. Smither, A. Amegadzie, N. Chen, X. Li, A. Banerjee, Q. Chen, D. Mohl and A. Vaish, *Nat Commun*, 2023, **14**, 4177.
201. K. M. Riching, S. Mahan, C. R. Corona, M. McDougall, J. D. Vasta, M. B. Robers, M. Urh and D. L. Daniels, *ACS Chem Biol*, 2018, **13**, 2758-2770.
202. T. Machleidt, C. C. Woodroofe, M. K. Schwinn, J. Mendez, M. B. Robers, K. Zimmerman, P. Otto, D. L. Daniels, T. A. Kirkland and K. V. Wood, *ACS Chem Biol*, 2015, **10**, 1797-1804.
203. M. B. Robers, M. L. Dart, C. C. Woodroofe, C. A. Zimprich, T. A. Kirkland, T. Machleidt, K. R. Kupcho, S. Levin, J. R. Hartnett, K. Zimmerman, A. L. Niles, R. F. Ohana, D. L. Daniels, M. Slater, M. G. Wood, M. Cong, Y. Q. Cheng and K. V. Wood, *Nat Commun*, 2015, **6**, 10091.
204. T. Geiger, A. Wehner, C. Schaab, J. Cox and M. Mann, *Mol Cell Proteomics*, 2012, **11**, M111 014050.
205. Z. Li, S. Ma, L. Zhang, S. Zhang, Z. Ma, L. Du and M. Li, *J Med Chem*, 2023, **66**, 733-751.
206. E. S. Ehrlich, T. Wang, K. Luo, Z. Xiao, A. M. Niewiadomska, T. Martinez, W. Xu, L. Neckers and X. F. Yu, *Proc Natl Acad Sci U S A*, 2009, **106**, 20330-20335.
207. H. McDonough and C. Patterson, *Cell Stress Chaperones*, 2003, **8**, 303-308.
208. L. Stepanova, X. Leng, S. B. Parker and J. W. Harper, *Genes Dev*, 1996, **10**, 1491-1502.
209. L. Nicosia, G. J. Spencer, N. Brooks, F. M. R. Amaral, N. J. Basma, J. A. Chadwick, B. Revell, B. Wingelhofer, A. Maiques-Diaz, O. Sinclair, F. Camera, F. Ciceri, D. H. Wiseman, N. Pegg, W. West, T. Knurowski, K. Frese, K. Clegg, V. L. Campbell, J. Cavet, M. Copland, E. Searle and T. C. P. Somervaille, *Cancer Cell*, 2023, **41**, 2136-2153 e2113.

210. A. R. Conery, R. C. Centore, A. Neiss, P. J. Keller, S. Joshi, K. L. Spillane, P. Sandy, C. Hatton, E. Pardo, L. Zawadzke, A. Bommi-Reddy, K. E. Gascoigne, B. M. Bryant, J. A. Mertz and R. J. Sims, *Elife*, 2016, **5**, e10483.
211. J. Lee, L. L. Zhang, W. Wu, H. Guo, Y. Li, M. Sukhanova, G. Venkataraman, S. Huang, H. Zhang, M. Alikhan, P. Lu, A. Guo, N. Galanina, J. Andrade, M. L. Wang and Y. L. Wang, *Blood Adv*, 2018, **2**, 2039-2051.
212. P. Liu, J. Xiao, Y. Wang, X. Song, L. Huang, Z. Ren, K. Kitazato and Y. Wang, *Mol Med*, 2021, **27**, 110.
213. L. M. Lasko, C. G. Jakob, R. P. Edalji, W. Qiu, D. Montgomery, E. L. Digiammarino, T. M. Hansen, R. M. Risi, R. Frey, V. Manaves, B. Shaw, M. Algire, P. Hessler, L. T. Lam, T. Uziel, E. Faivre, D. Ferguson, F. G. Buchanan, R. L. Martin, M. Torrent, G. G. Chiang, K. Karukurichi, J. W. Langston, B. T. Weinert, C. Choudhary, P. de Vries, J. H. Van Drie, D. McElligott, E. Kesicki, R. Marmorstein, C. Sun, P. A. Cole, S. H. Rosenberg, M. R. Michaelides, A. Lai and K. D. Bromberg, *Nature*, 2017, **550**, 128-132.
214. T. Y. Lin, J. Fenger, S. Murahari, M. D. Bear, S. K. Kulp, D. Wang, C. S. Chen, W. C. Kisseberth and C. A. London, *Blood*, 2010, **115**, 4217-4225.
215. O. H. Kramer, S. Mahboobi and A. Sellmer, *Trends Pharmacol Sci*, 2014, **35**, 501-509.
216. J. Trepel, M. Mollapour, G. Giaccone and L. Neckers, *Nat Rev Cancer*, 2010, **10**, 537-549.
217. S. Burma, B. P. Chen, M. Murphy, A. Kurimasa and D. J. Chen, *J Biol Chem*, 2001, **276**, 42462-42467.
218. Y. Ziv, D. Bielopolski, Y. Galanty, C. Lukas, Y. Taya, D. C. Schultz, J. Lukas, S. Bekker-Jensen, J. Bartek and Y. Shiloh, *Nat Cell Biol*, 2006, **8**, 870-876.
219. M. Wang, S. Wey, Y. Zhang, R. Ye and A. S. Lee, *Antioxid Redox Signal*, 2009, **11**, 2307-2316.
220. W. B. Pratt, A. M. Silverstein and M. D. Galigniana, *Cell Signal*, 1999, **11**, 839-851.
221. T. Svinkina, H. Gu, J. C. Silva, P. Mertins, J. Qiao, S. Fereshetian, J. D. Jaffe, E. Kuhn, N. D. Udeshi and S. A. Carr, *Mol Cell Proteomics*, 2015, **14**, 2429-2440.
222. J. Gil and S. Encarnación-Guevara, in *Clinical Proteomics: Methods and Protocols*, eds. F. J. Corrales, A. Paradela and M. Marcilla, Springer US, New York, NY, 2022, DOI: 10.1007/978-1-0716-1936-0_7, pp. 73-86.
223. M. L. Drummond and C. I. Williams, *J Chem Inf Model*, 2019, **59**, 1634-1644.
224. E. Amatya and B. S. J. Blagg, *Bioorg Med Chem Lett*, 2023, **80**, 129111.
225. E. Gasteiger, A. Gattiker, C. Hoogland, I. Ivanyi, R. D. Appel and A. Bairoch, *Nucleic Acids Res*, 2003, **31**, 3784-3788.
226. H. E. Gottlieb, V. Kotlyar and A. Nudelman, *J Org Chem*, 1997, **62**, 7512-7515.
227. J. T. Seal, S. J. Atkinson, P. Bamborough, A. Bassil, C. W. Chung, J. Foley, L. Gordon, P. Grandi, J. R. J. Gray, L. A. Harrison, R. G. Kruger, J. J. Matteo, M. T. McCabe, C. Messenger, D. Mitchell, A. Phillipou, A. Preston, R. K. Prinjha, F. Rianjongdee, I. Rioja, S. Taylor, I. D. Wall, R. J. Watson, J. M. Woolven, A. Wyce, X. P. Zhang and E. H. Demont, *J Med Chem*, 2021, **64**, 10772-10805.
228. *WO Pat.,* WO 2019/202332 A1, 2019.
229. T. Szirtes, L. Kisfaludy, E. Palosi and L. Szporny, *Journal of Medicinal Chemistry*, 2002, **29**, 1654-1658.
230. A. Gangjee, J. Yu, R. L. Kisliuk, W. H. Haile, G. Sobrero and J. J. McGuire, *J Med Chem*, 2003, **46**, 591-600.
231. F. Seela and X. Peng, *Synthesis*, 2004, **2004**, 1203-1210.
232. S. Kapic, H. Cipcic Paljetak, S. Alihodzic, R. Antolovic, V. Erakovic Haber, R. L. Jarvest, D. J. Holmes, J. P. Broskey and E. Hunt, *Bioorg Med Chem*, 2010, **18**, 6569-6577.
233. R. C. B. Nicolescu, Z. R. Maylin, F. J. Perez-Areales, J. Iegre, H. S. Pandha, M. Asim and D. R. Spring, *ChemMedChem*, 2023, **18**, e202200548.
234. D. Hwang, N. Nilchan, A. R. Nanna, X. Li, M. D. Cameron, W. R. Roush, H. Park and C. Rader, *Cell Chem Biol*, 2019, **26**, 1229-1239 e1229.
235. *WO Pat.,* WO 2022/169780 A1, 2022.
236. *WO Pat.,* WO 2020/014489 A2, 2020.
237. P. T. Lowe, S. Dall'Angelo, I. N. Fleming, M. Piras, M. Zanda and D. O'Hagan, *Org Biomol Chem*, 2019, **17**, 1480-1486.
238. M. Assali, N. Kittana, S. A. Qasem, R. Adas, D. Saleh, A. Arar and O. Zohud, *Rsc Adv*, 2019, **9**, 1055-1061.
239. J. Vaclavik, R. Zschoche, I. Klimankova, V. Matousek, P. Beier, D. Hilvert and A. Togni, *Chemistry*, 2017, **23**, 6490-6494.

240. T. Dohi, K. Morimoto, A. Maruyama and Y. Kita, *Org Lett*, 2006, **8**, 2007-2010.
241. *United States Pat.,* US5274113A, 1993.
242. S. Sun, J. Y. Zhou, W. Yang and H. Zhang, *Anal Biochem*, 2014, **446**, 76-81.

Appendices

Appendix A Supplementary notes and figures to chapters

A.i Figures

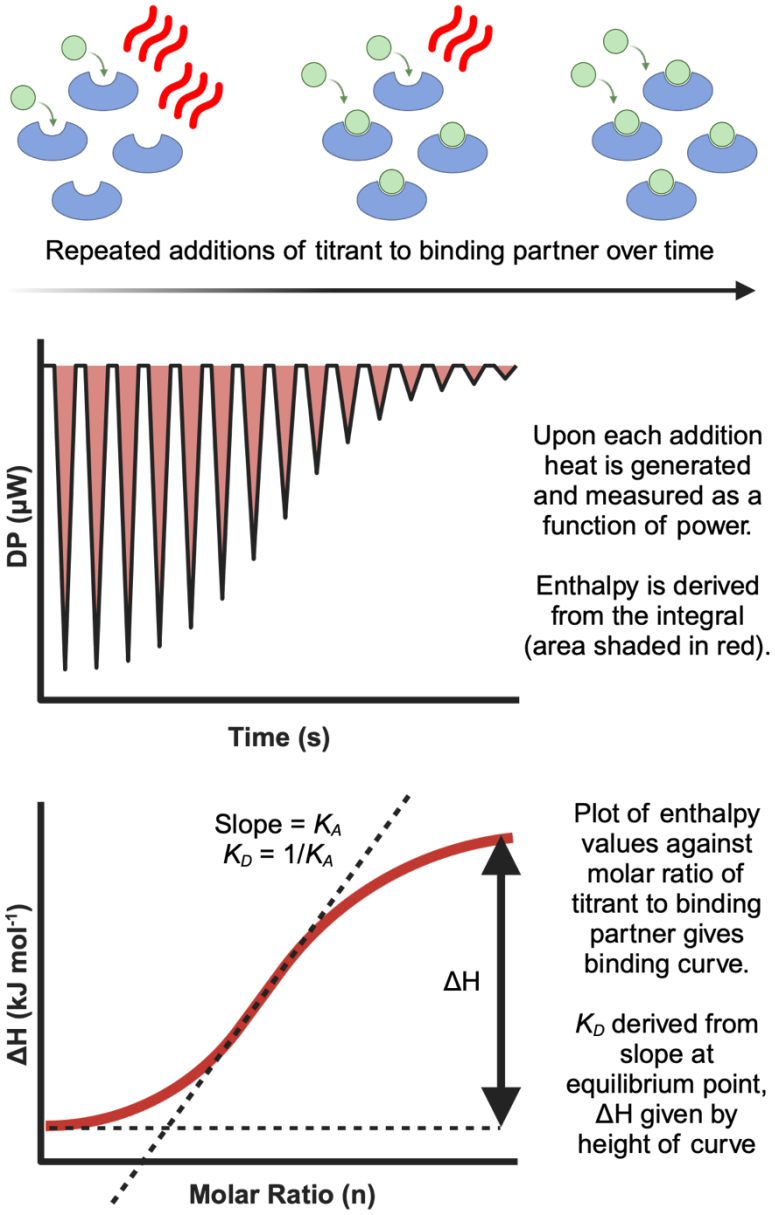


Figure A.1: Principle of ITC for measuring compound-protein dissociation constant (K_D). A fixed amount of titrant (green sphere) at fixed concentration (either compound or protein) is repeatedly added to its binding partner (blue crescent) at fixed concentration. The binding interaction generates heat (red waves) and it measured as a function of power. Enthalpy of binding for each addition is derived from the integral the measured power over time (red shaded region) and plotted against the molar ratio of titrant to binding partner to obtain a binding curve (red line). The K_d is determined as the inverse of the slope at the equivalence point.

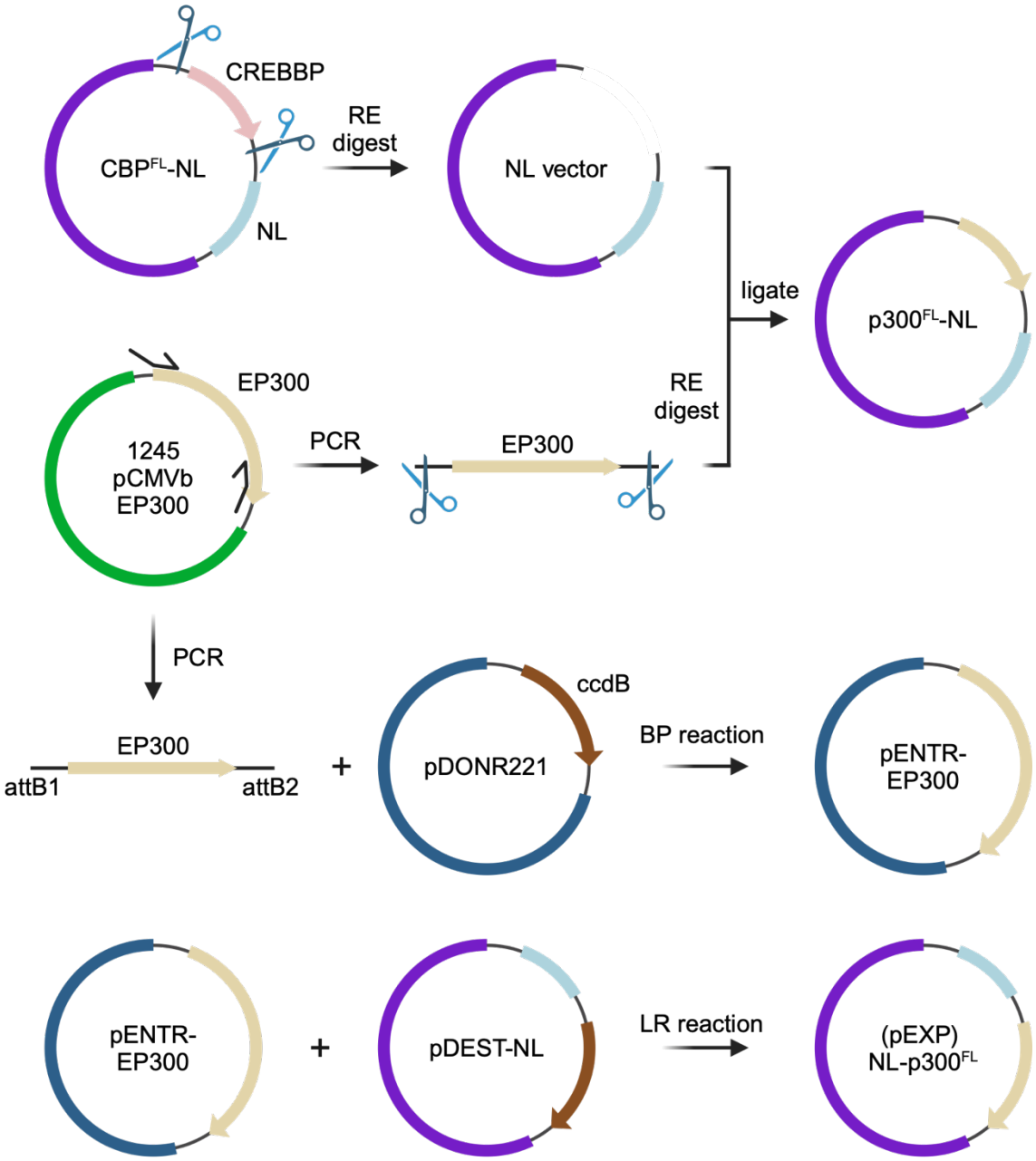


Figure A.2: Summary of molecular cloning methods used in this thesis. The p300^{FL}-NL plasmid construct was generated by restriction endonuclease (RE) PCR cloning. The NL (light blue) containing vector (purple) was prepared by RE digest of the CBP^{FL}-NL plasmid construct, to excise the CREBBP gene. The EP300 gene (yellow) was amplified by PCR with primers designed to append complimentary RE sites and remove the stop codon. The gene fragment was digested and ligated with the vector (purple) to afford the p300^{FL}-NL plasmid construct. The NL-p300^{FL} plasmid construct was generated by Gateway® cloning. The EP300 gene was amplified by PCR with primers designed to append attB sites and then subjected to a BP recombination reaction with pDONR221 to obtain the pENTR-EP300 construct. The ccdB gene (brown) present in the pDONR221 and pDEST-NL constructs is toxic to the *E. coli* strain used for amplification and serves as a second selection pressure against transformants not carrying the desired recombination reaction product. The pENTR-EP300 construct can be used to insert the EP300 gene into pDEST vectors and obtain plasmid constructs for *N*-terminal fusion products. The pDEST-NL vector was previously generated by the laboratory of Dr Kilian Huber and was kindly gifted to be used in this work. A LR recombination reaction with pENTR-EP300 and pDEST-NL obtain pEXP NL-p300^{FL}.

A.ii Comparison of 6×His-CBP^{BRD} and 6×His-p300^{BRD} sequences

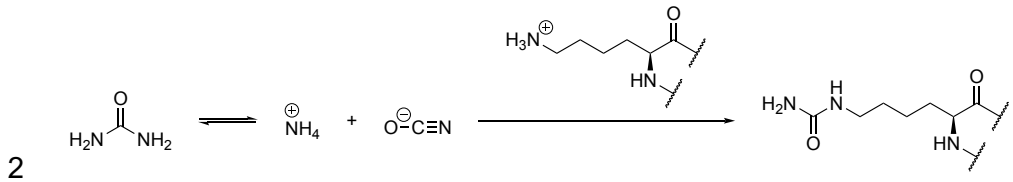
MHHHHHHSSGVDLGTENLYFQSMAPGQSKKKIFKPEELRQALMPTLEALYRQDPESLPFRQPVDPQLLGIPDYFDIVKSPMDLSTIKRKLDTGQYQEPWQYVDDIWLMFNNAWLYNRKTSRVYKYCSKLSCEVFEQEIDPVMQSLG 6×His-TEV-p300^{BRD}

MHHHHHHSSGVDLGTENLYFQSMRKKIFKPEELRQALMPTLEALYRQDPESLPFRQPVDPQLLGIPDYFDIVKNPMDLSTIKRKLDTGQYQEPWQYVDDVWLMFNNAWLYNRKTSRVYKFCSKLACEVFEQEIDPVMQSLG 6×His-TEV-CBP^{BRD}

Figure A.3: Comparison of the aligned sequences of 6×His-TEV-p300^{BRD} and 6×His-TEV-CBP^{BRD}. Differences in sequences are shown by larger letters and the 6×His-TEV sequence is shown in grey.

A.iii Controls to ensure measured K294Ac levels are genuine

In **Figure 4.21**, it is worth noting that the signal from Hsp90α(K294Ac) was weaker than expected, compared to previous experiments immunoblotting experiments. We considered the effect of a different buffer composition used in the subcellular fractionation procedure compared to the chaotropic denaturing urea buffer employed in previous immunoblotting experiments. Sun *et al.* have previously reported on the decomposition of urea containing lysis buffers to form isocyanic acid, and this in turn can react with lysine residues to generate carbamates (**Figure A.4**). In their work, they suggest addition of ammonium bicarbonate to buffers to prevent this process, by Le Chatelier's principle.[242]



2

Figure A.4 Formation of carbamates at lysine residues on proteins in urea containing buffers by decomposition of urea into isocyanate and ammonia.

This formation of carbamates is a well characterised artefact in proteomics studies employing urea containing buffers. Given the chemical similarity between the carbamyl-lysine and acetyl-lysine residues, in terms of size and charge in physiological conditions, a possibility arose that the previously measured Hsp90α(K294Ac) from samples prepared in urea containing buffers was an artefact of post-lysis carbamylation. To address this concern, we lysed untreated cells from the same population in a range of different buffers and present the results in **Figure A.5**. We observed the signal for Hsp90α(K294Ac) was consistent in all the buffers tested, except for where ammonium bicarbonate had been added ($NH_4.HCO_3$). The origin of this was attributed to the higher pH of the final buffer composition (measured at pH 8.5, all other buffers were adjusted to pH 7.6) which would have increased the reactivity of lysine residues to non-enzymatic acetylation with Ac-CoA

post-lysis. However, despite this artefact, the experiment confirmed that the UTB buffer employed in previous western blot experiments did not give a significantly different signal for Hsp90α(K294Ac) than non-urea containing buffers.

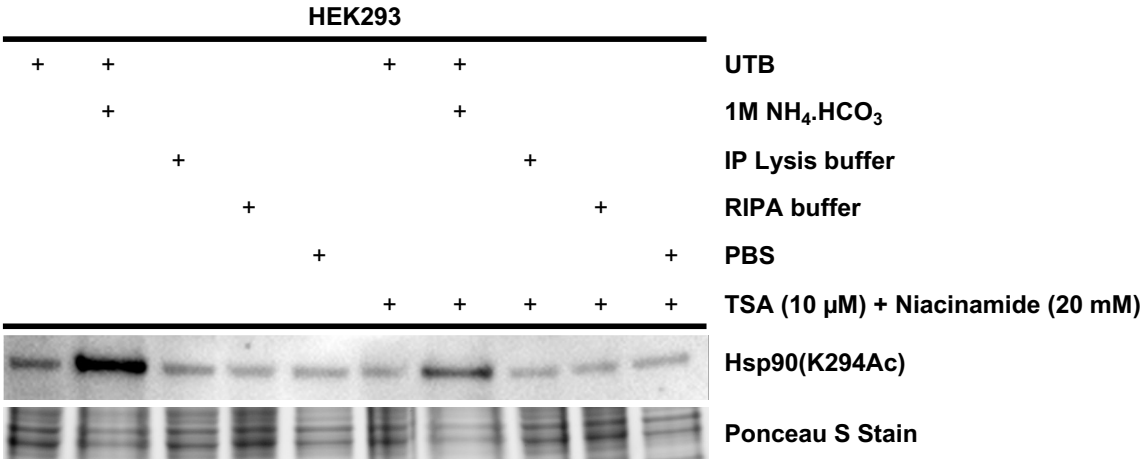
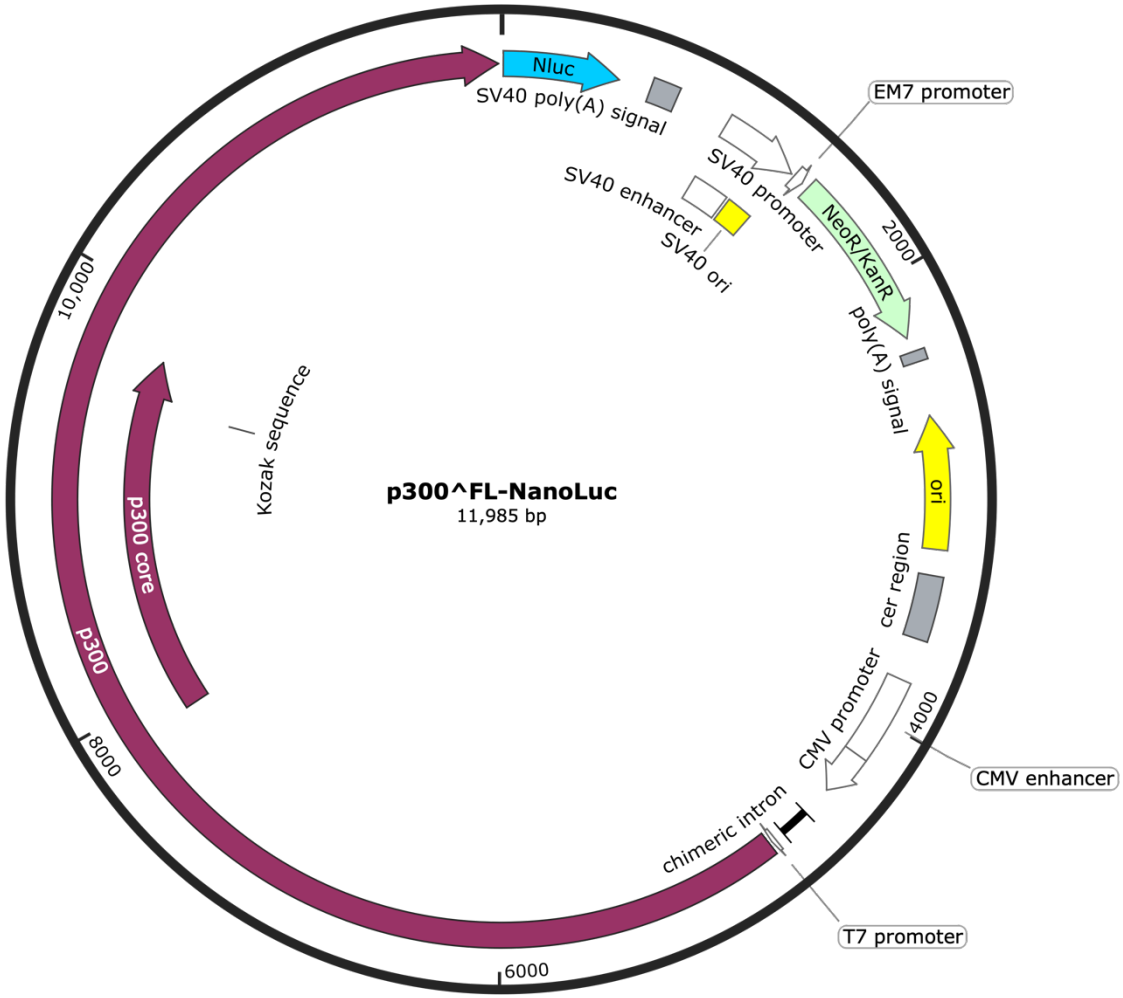
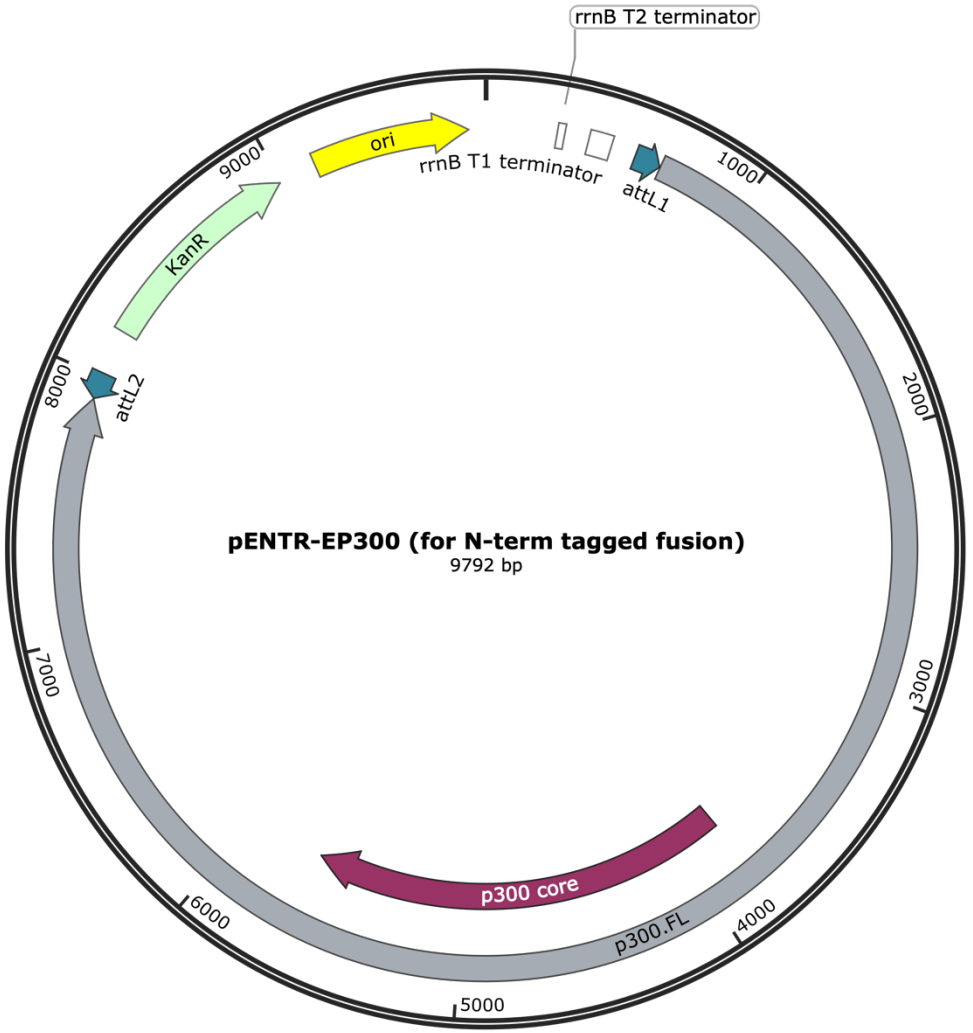
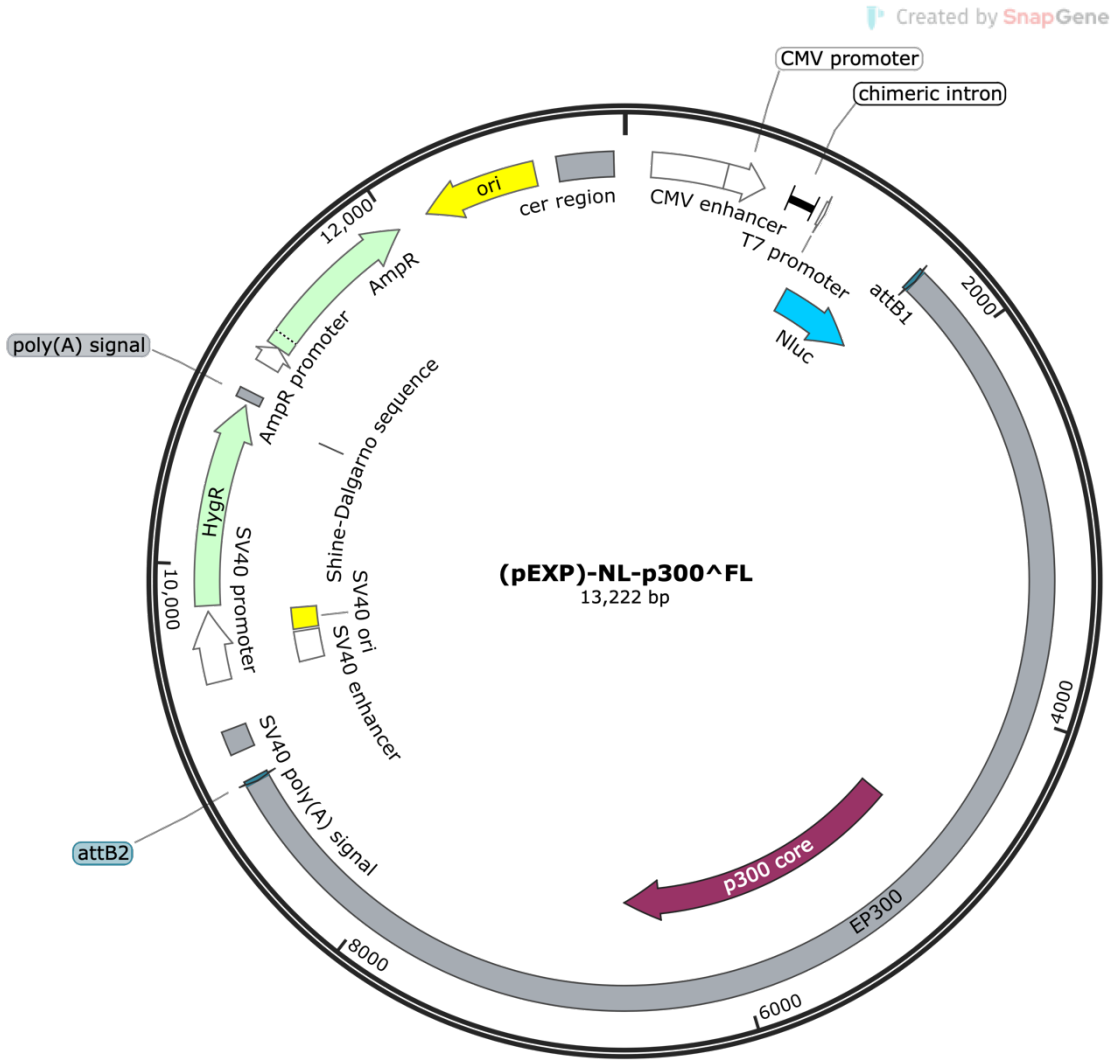


Figure A.5: Immunoblot analysis of HEK293 whole cell lysate prepared in a range of different lysis buffers shows consistent Hsp90α(K294Ac) signal levels in urea containing buffer (UTB) and non-urea containing buffers. An anomalously high signal was observed for buffers supplemented with ammonium bicarbonate ($NH_4.HCO_3$) rationalised due a higher final pH value of 8.5 (compared to 7.6 for other buffer compositions) which may have contributed to non-enzymatic lysine acetylation post-lysis.

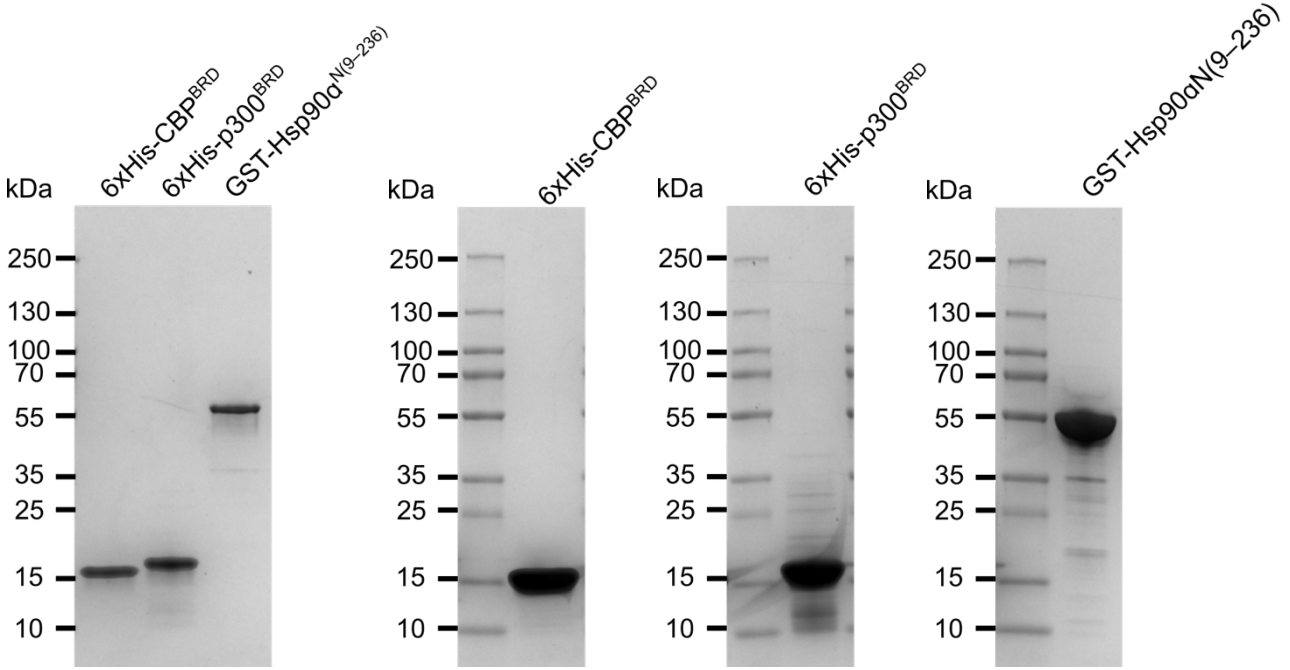
Appendix B Annotated maps of plasmid clones created in this thesis



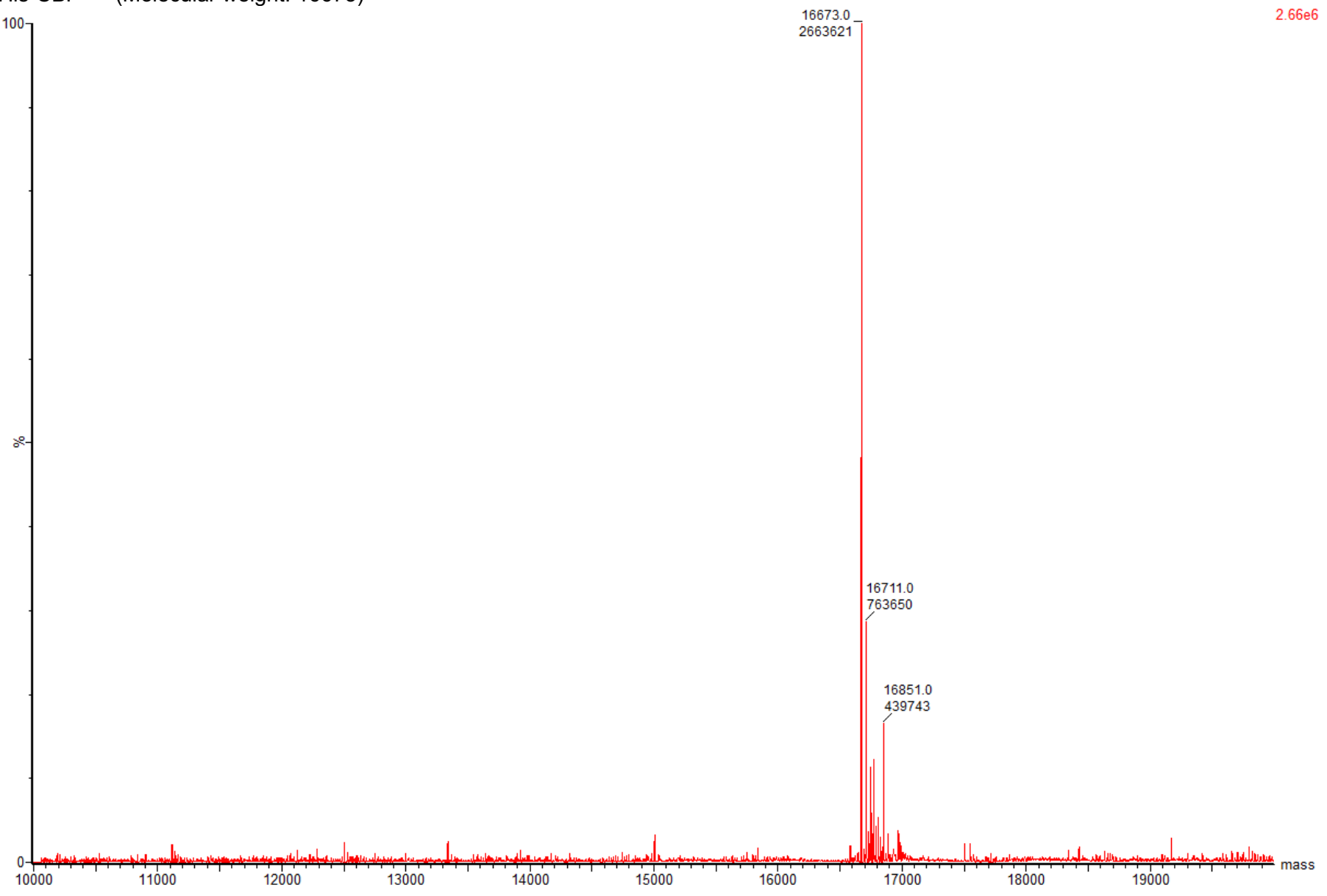

rrnB T2 terminator
ori
rrnB T1 terminator
attL1
KanR
attL2
pENTR-EP300 (for N-term tagged fusion)
9792 bp
p300 core
p300.FL
1000
2000
3000
4000
5000
6000
7000
8000
9000


Created by SnapGene
CMV promoter
chimeric intron
ori
cer region
CMV enhancer
T7 promoter
attB1
Nluc
2000
4000
6000
8000
10,000
12,000
AmpR
AmpR promoter
poly(A) signal
Shine-Dalgarno sequence
HygR
SV40 promoter
SV40 ori
SV40 enhancer
SV40 poly(A) signal
attB2
p300 core
EP300
(pEXP)-NL-p300^FL
13,222 bp

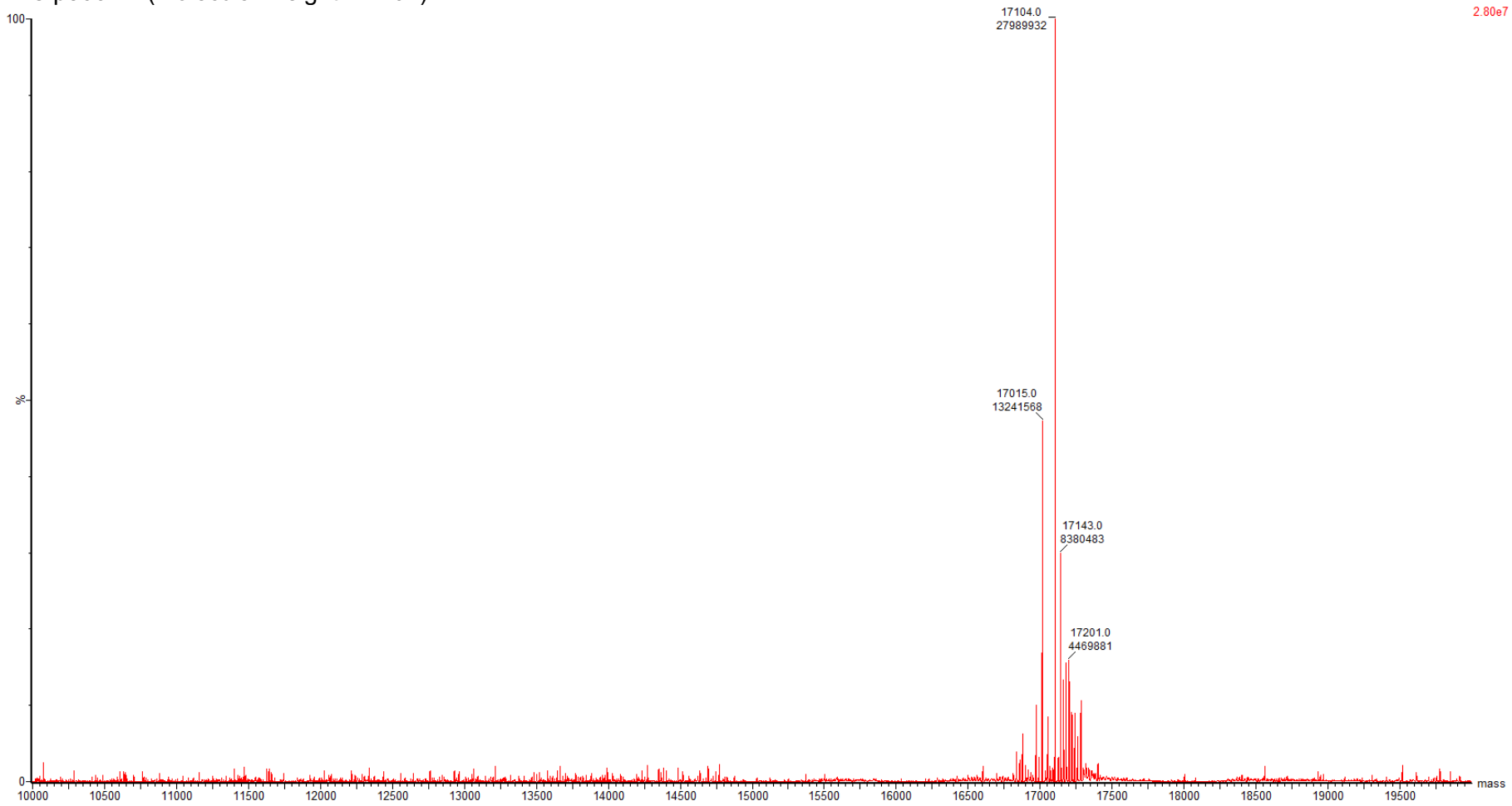
Appendix C SDS-PAGE and LC-MS of purified recombinant proteins



6xHis-CBP^{BRD} (Molecular weight: 16673)

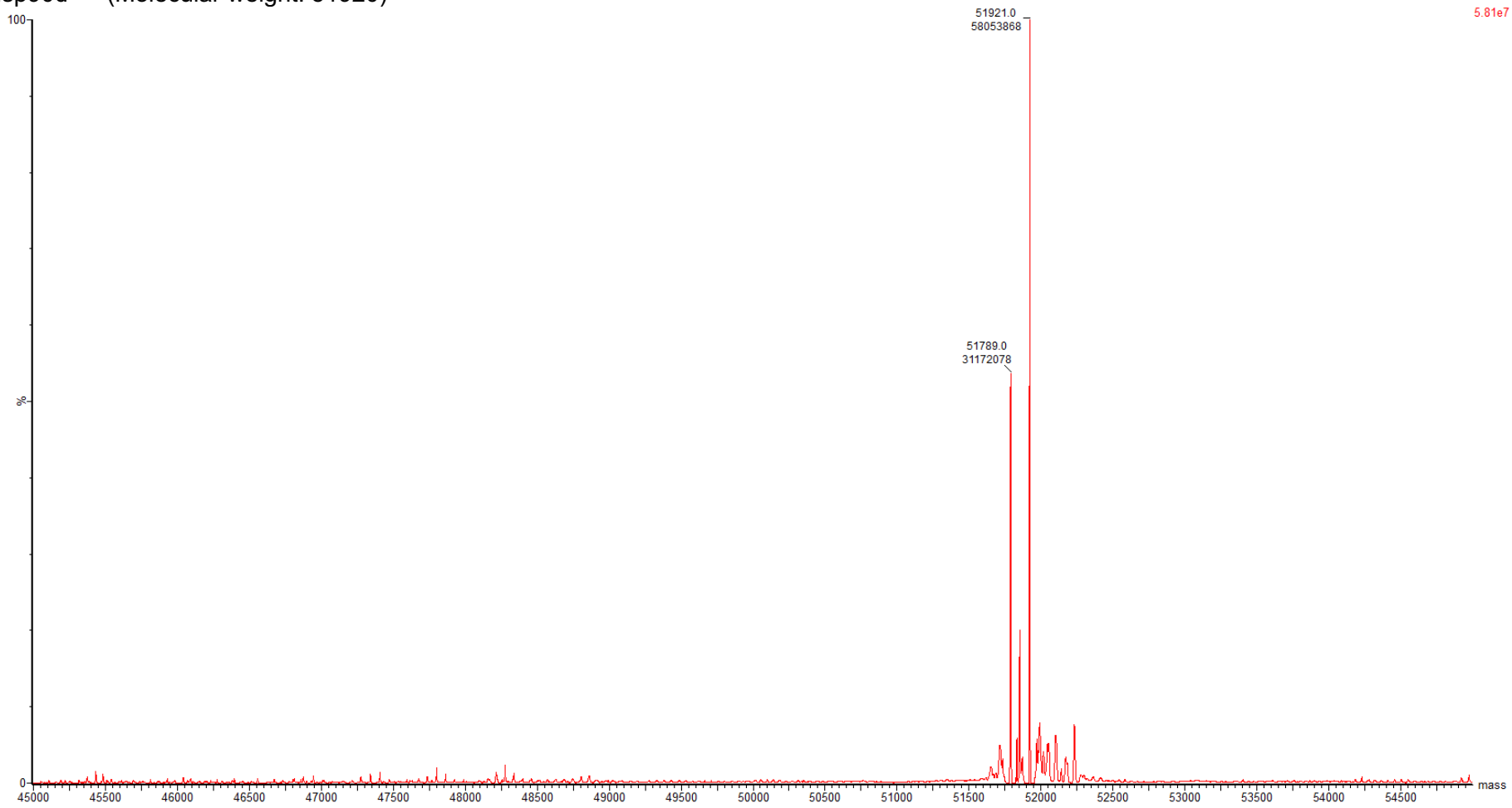


6xHis-p300^{BRD} (Molecular weight: 17104)



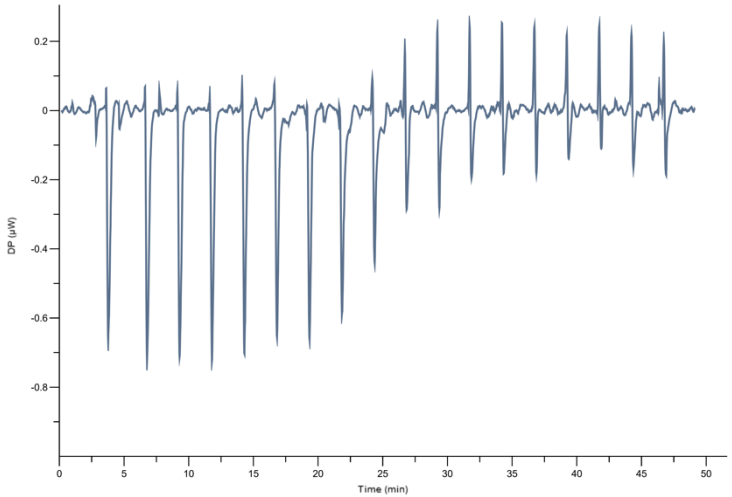
x

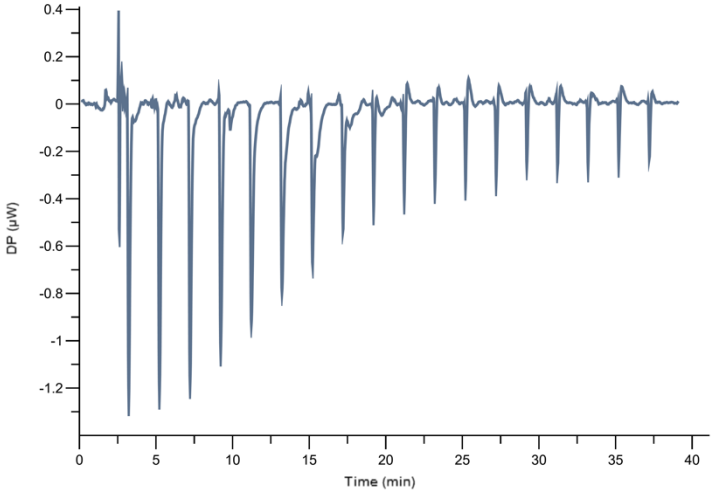
Hsp90α^{NTD} (Molecular weight: 51920)

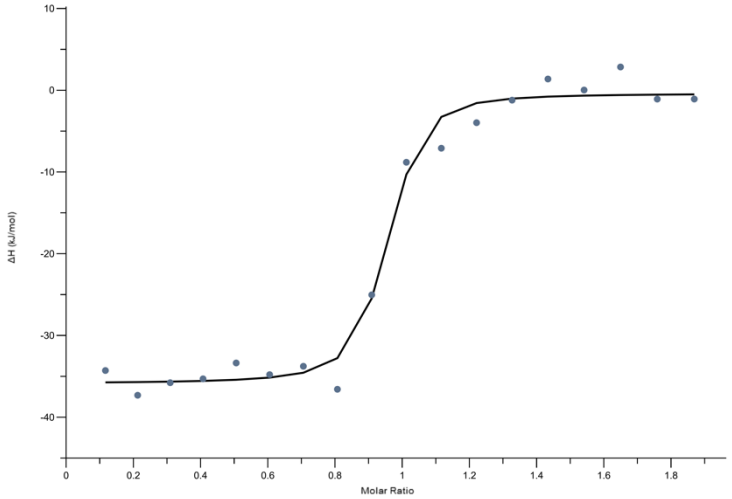


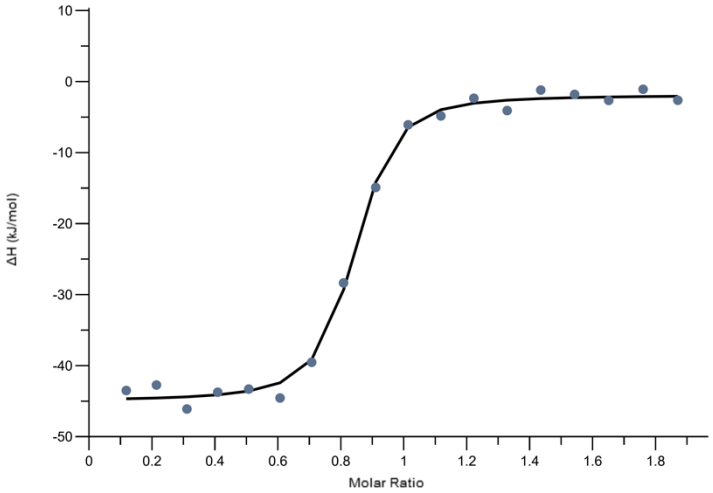
Appendix D ITC Traces

Syringe: 6×His-p300^{BRD}, Cell: Inobrodib

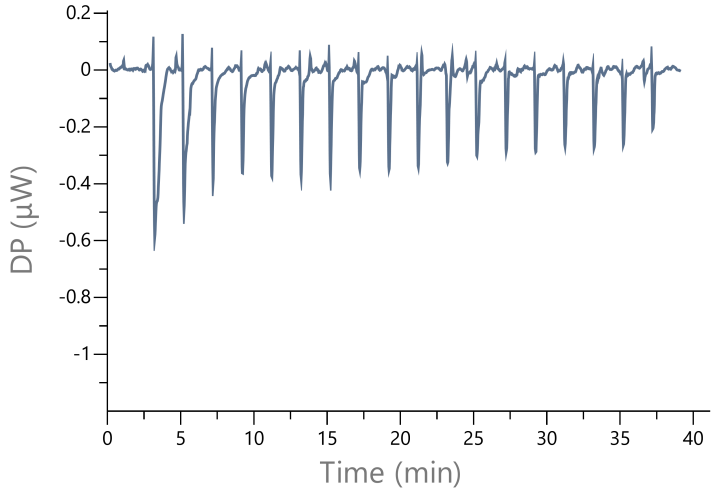


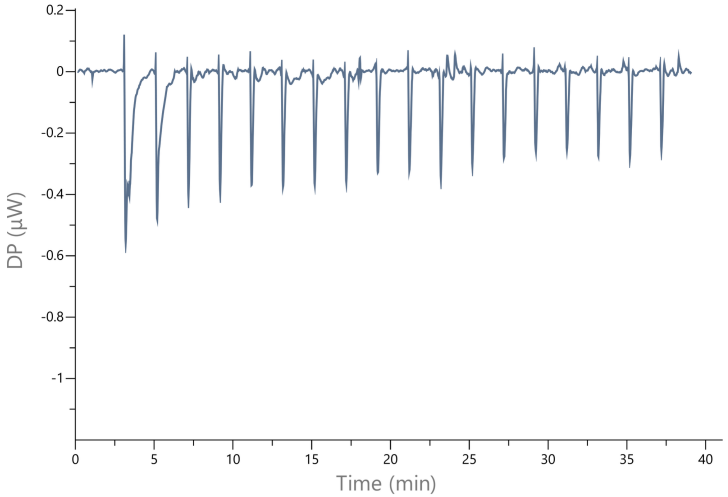


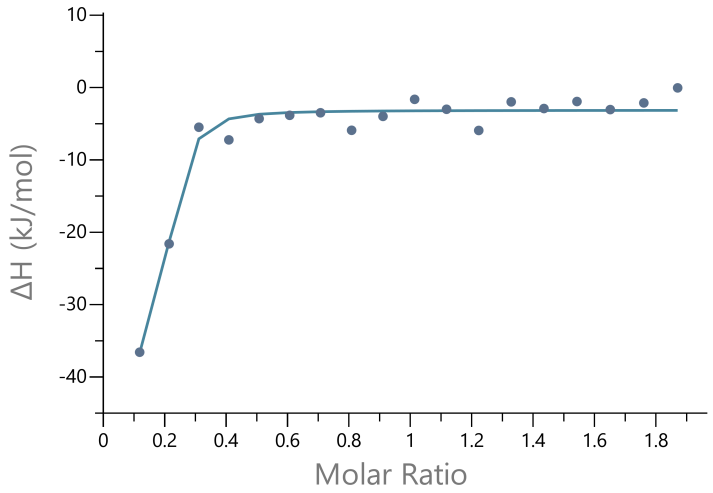


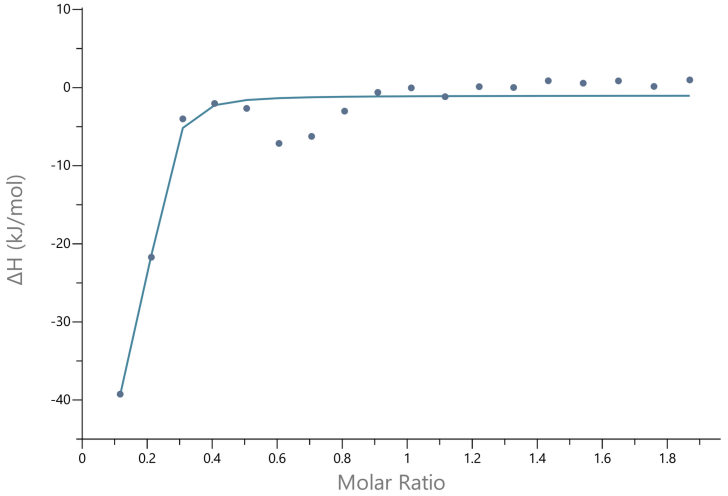


Syringe: 6×His-p300^{BRD}, Cell: AcDC-1

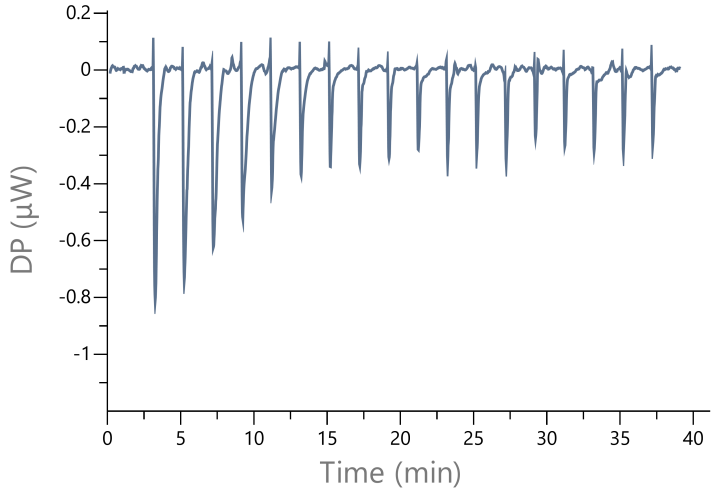


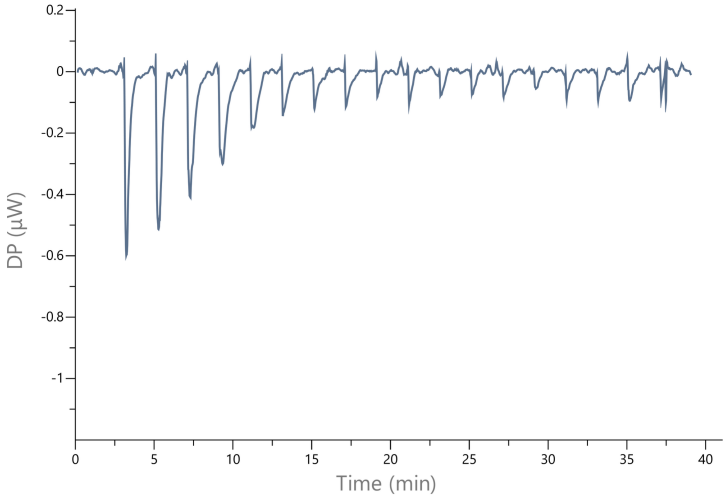


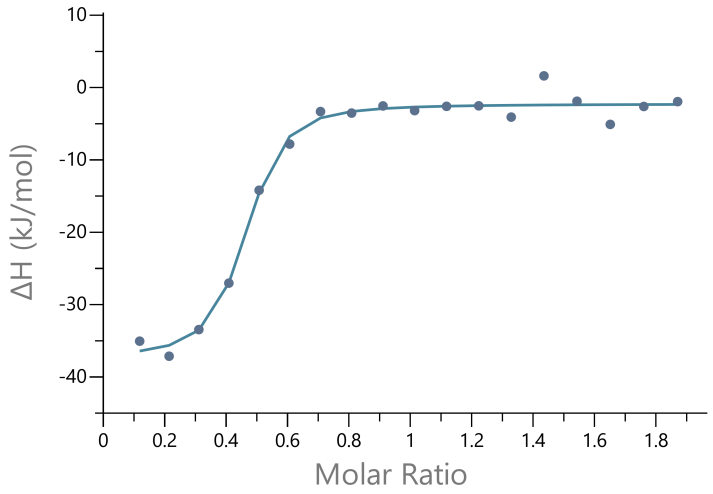


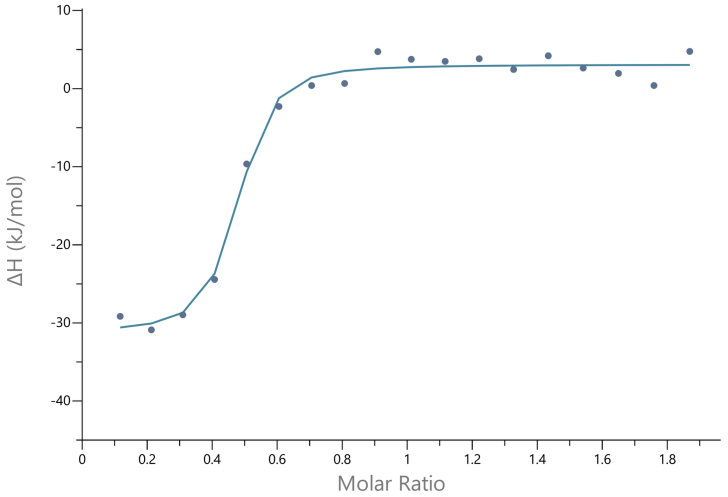


Syringe: 6×His-p300^{BRD}, Cell: AcDC-2

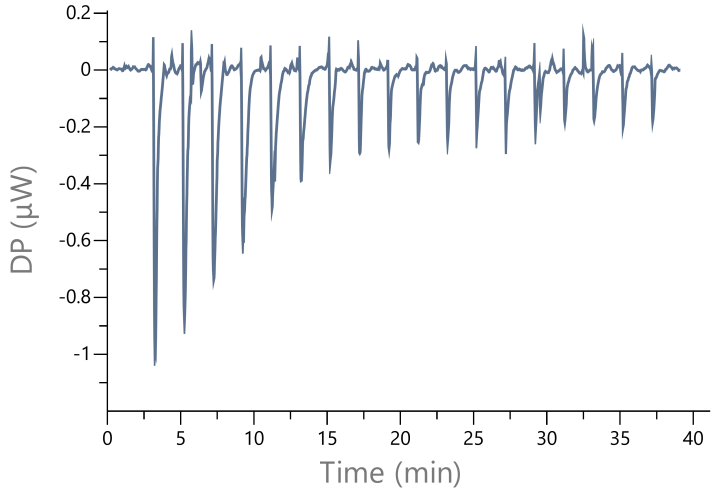


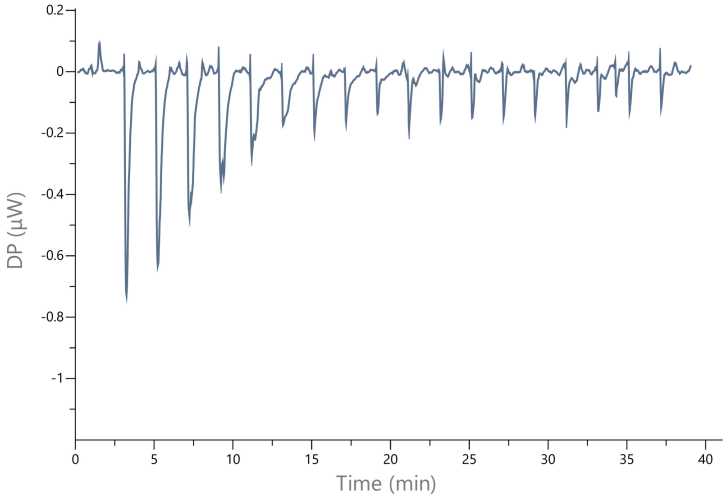


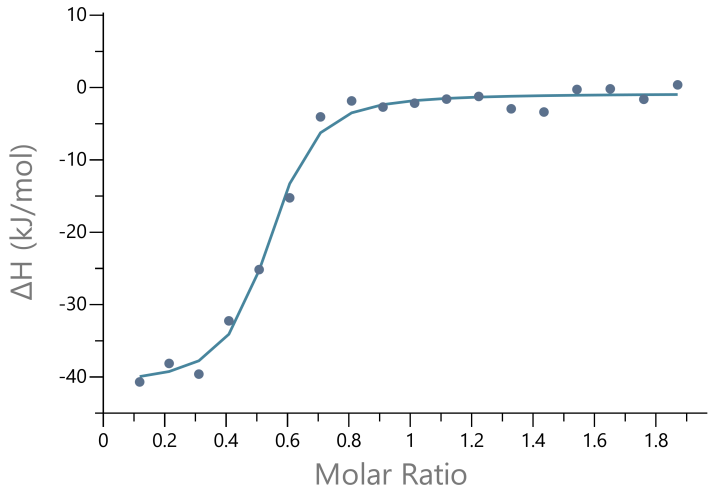


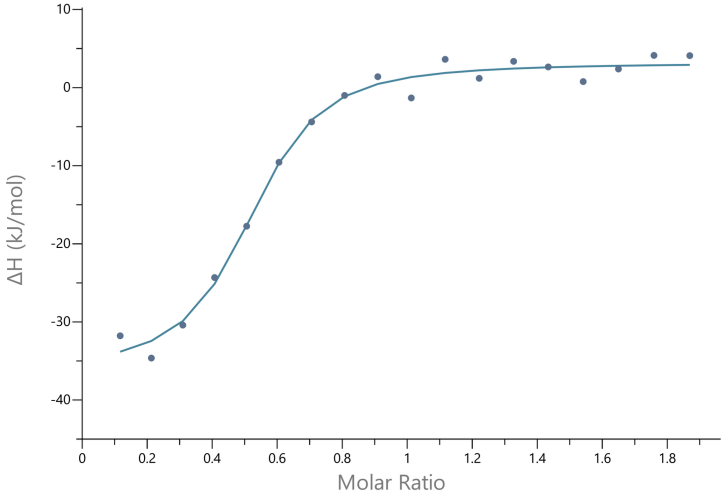


Syringe: 6×His-p300^{BRD}, Cell: AcDC-3

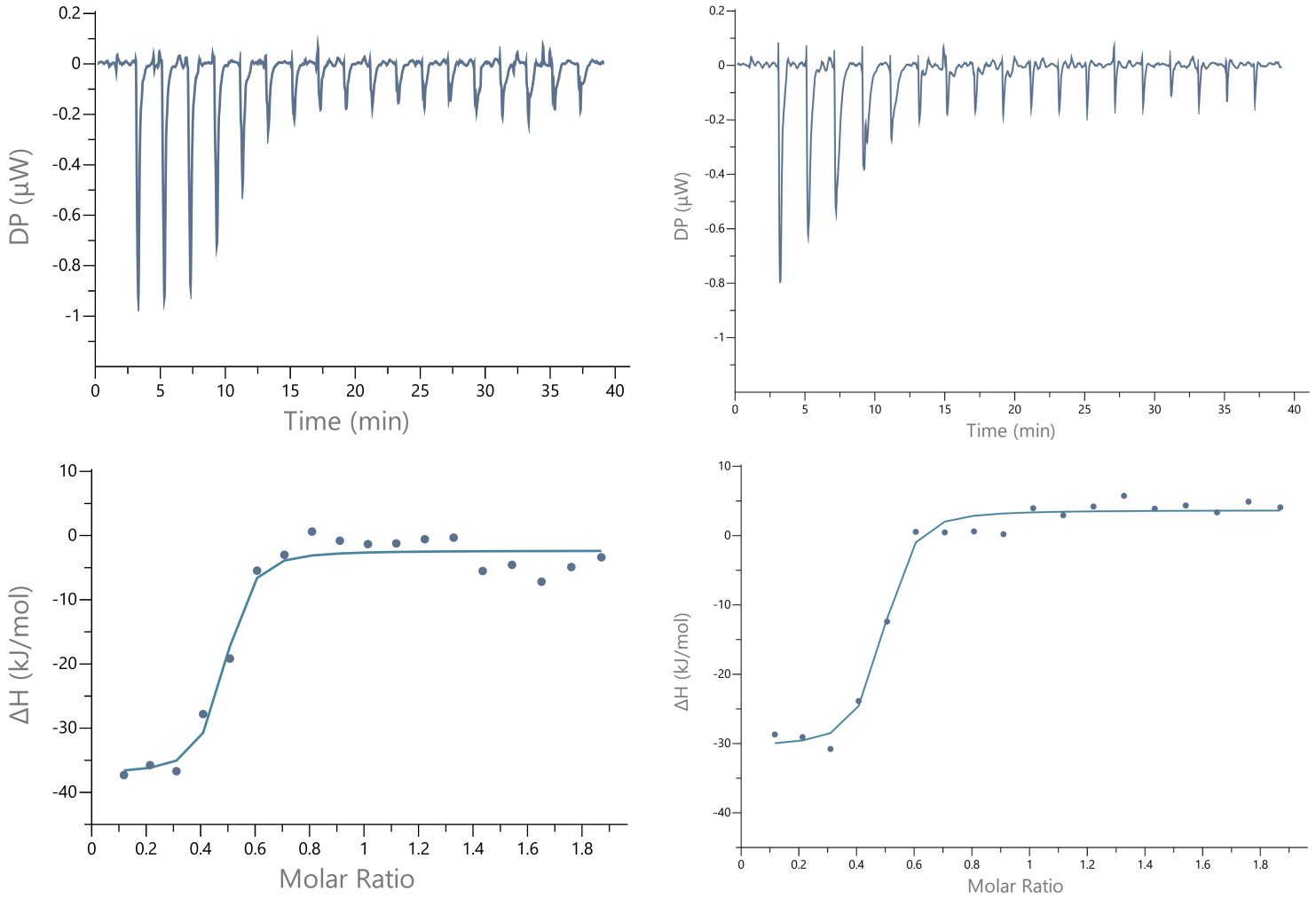




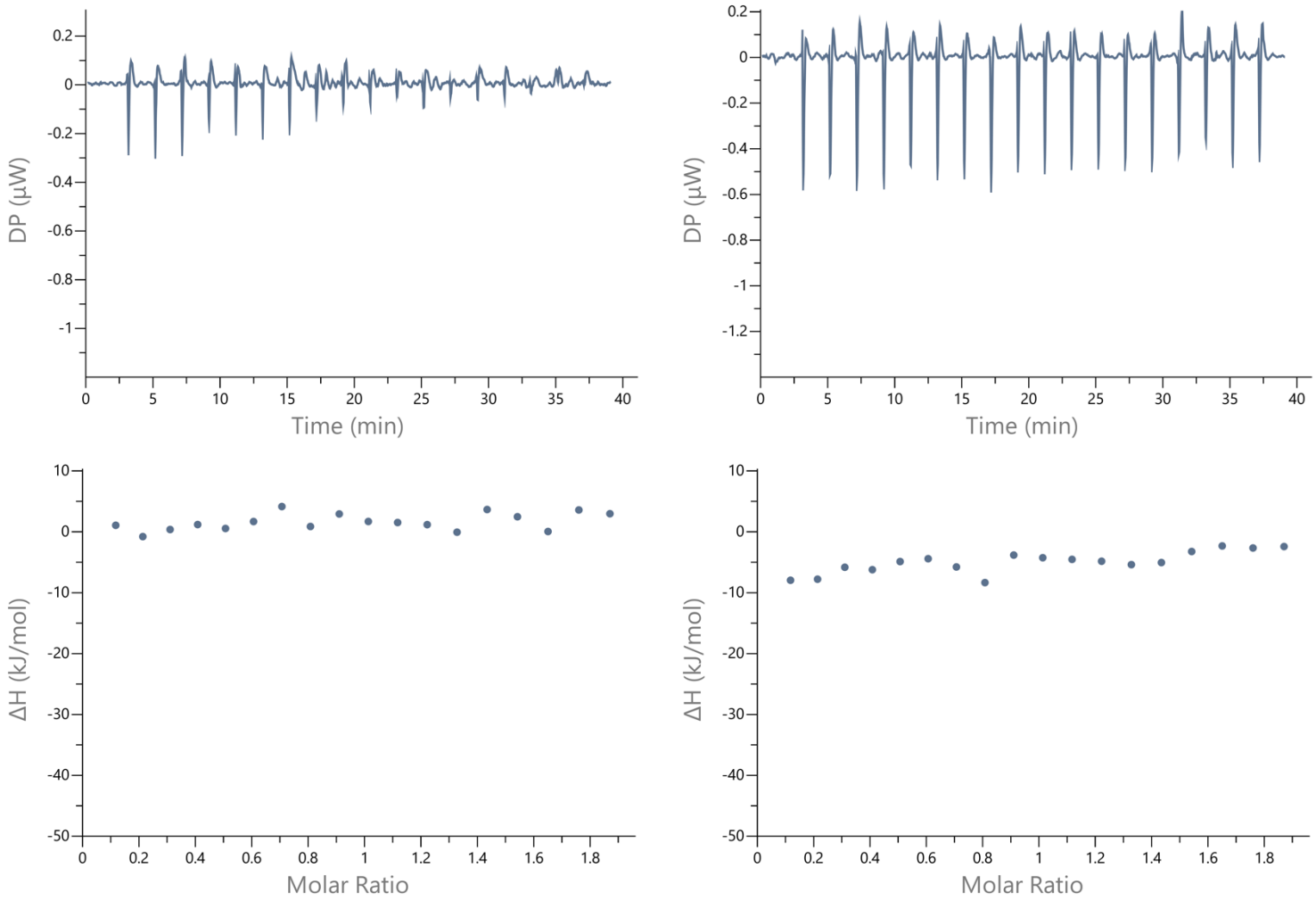




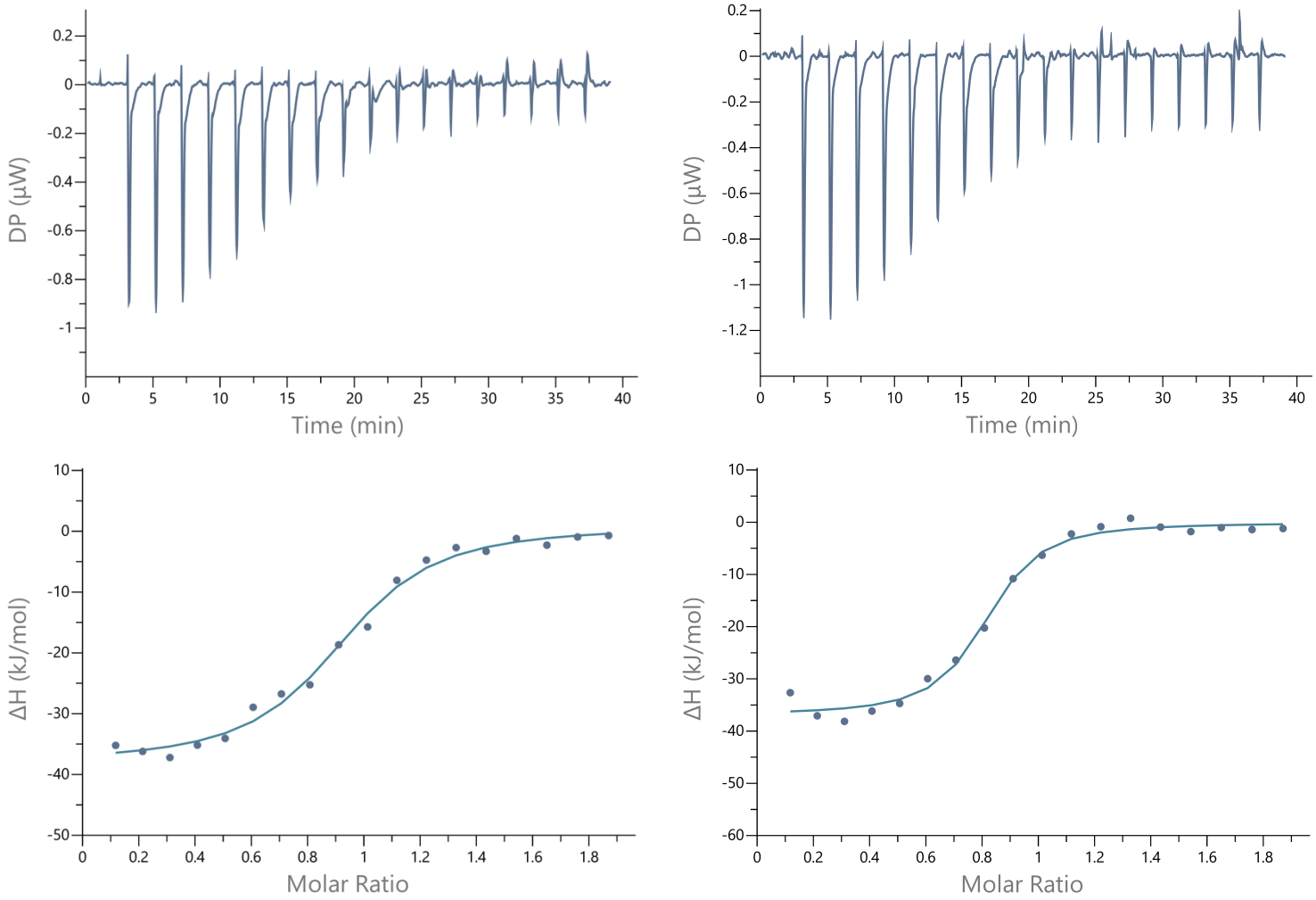
Syringe: 6×His-p300^{BRD}, Cell: AcDC-4



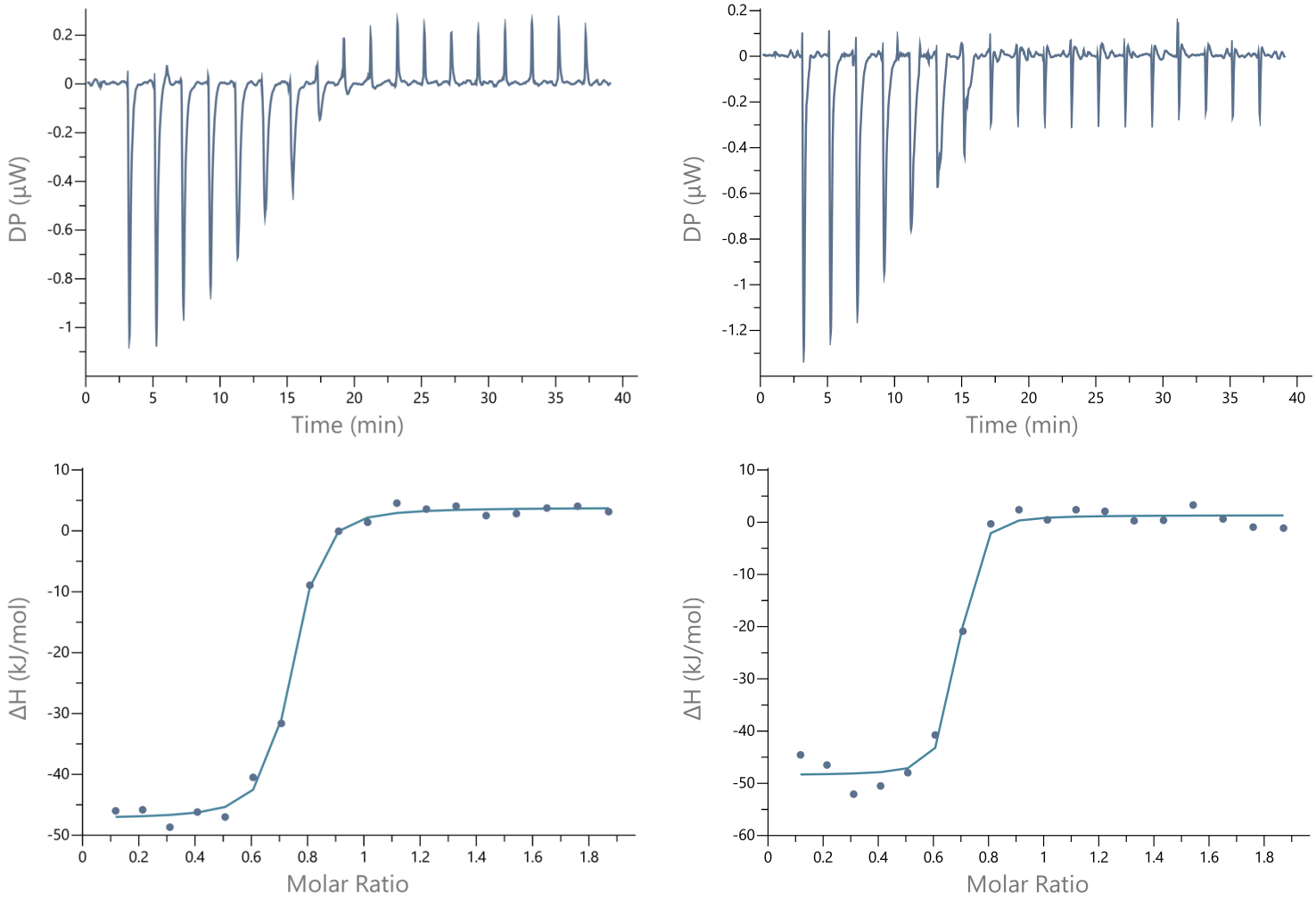
Syringe: 6×His-p300^{BRD}, Cell: DMSO + GST-Hsp90^{NTD}



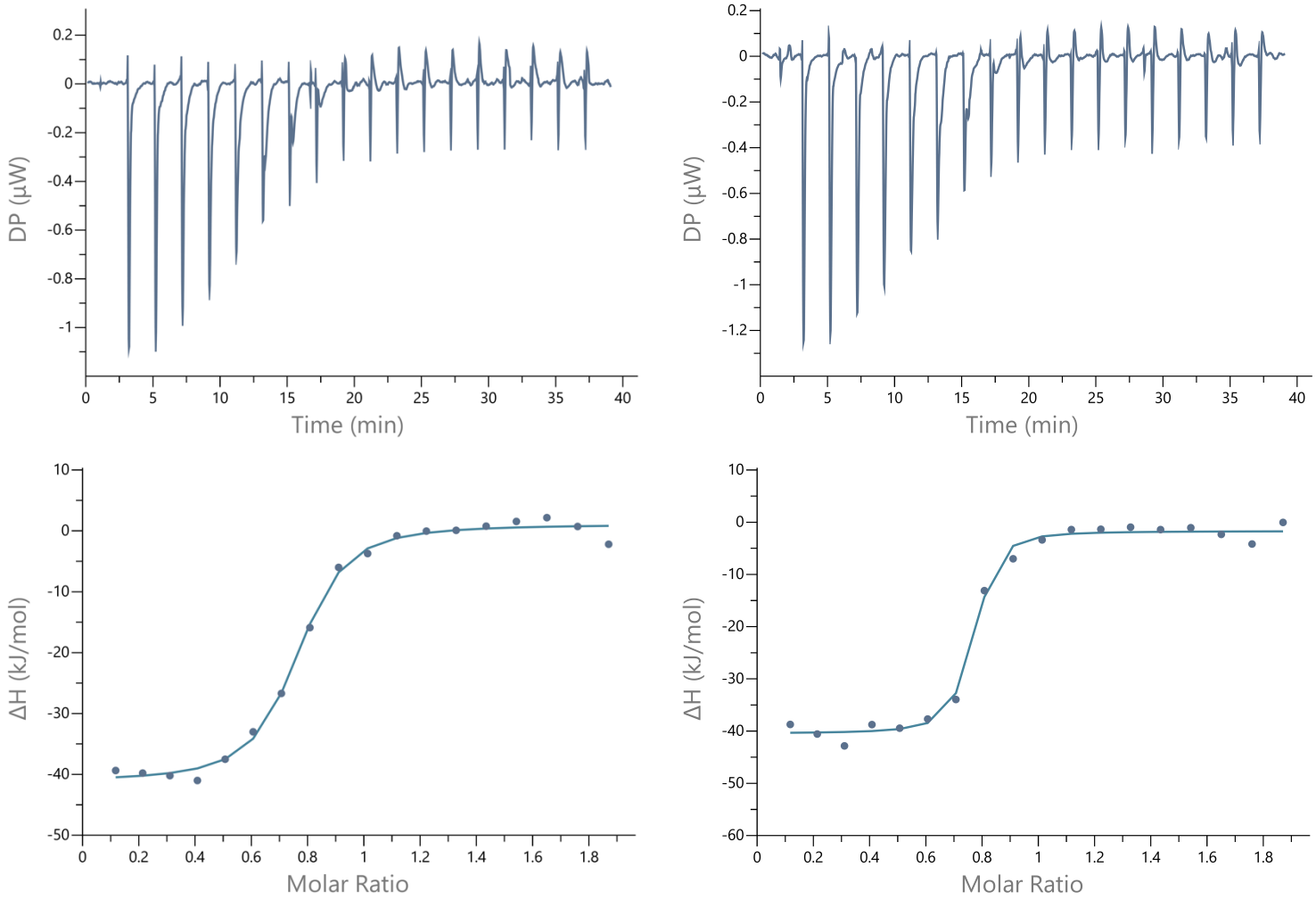
Syringe: 6×His-p300^{BRD}, Cell: AcDC-1 + GST-Hsp90^{NTD}



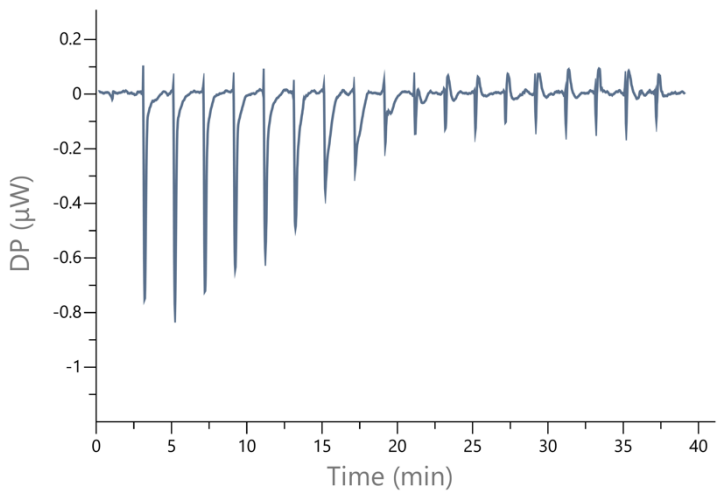
Syringe: 6×His-p300^{BRD}, Cell: AcDC-2 + GST-Hsp90^{NTD}

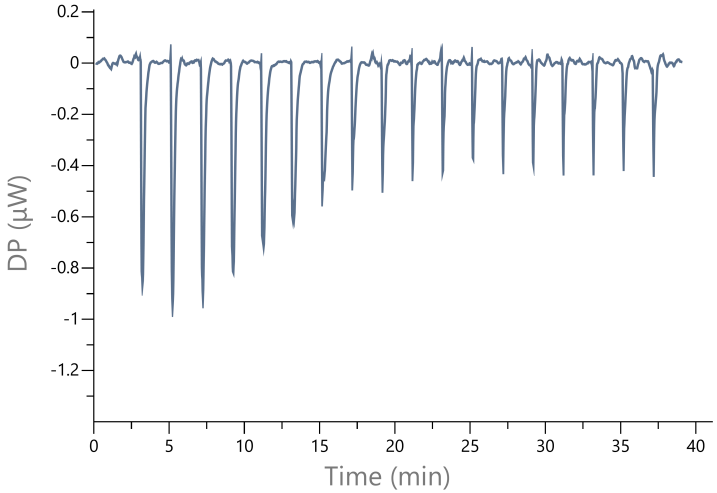


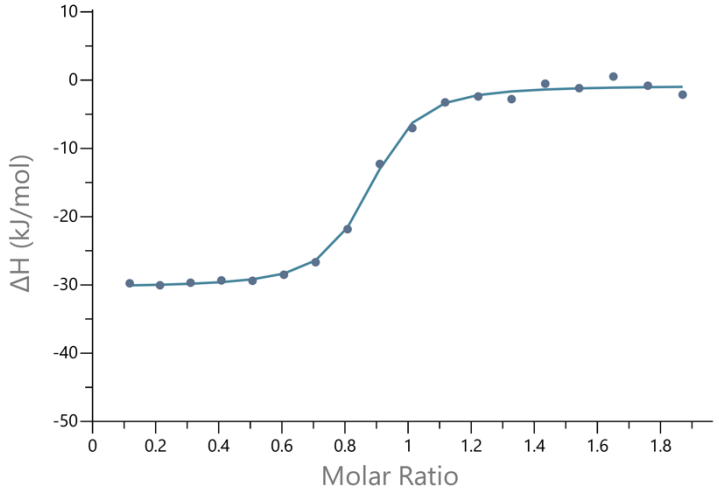
Syringe: 6×His-p300^{BRD}, Cell: AcDC-3 + GST-Hsp90^{NTD}

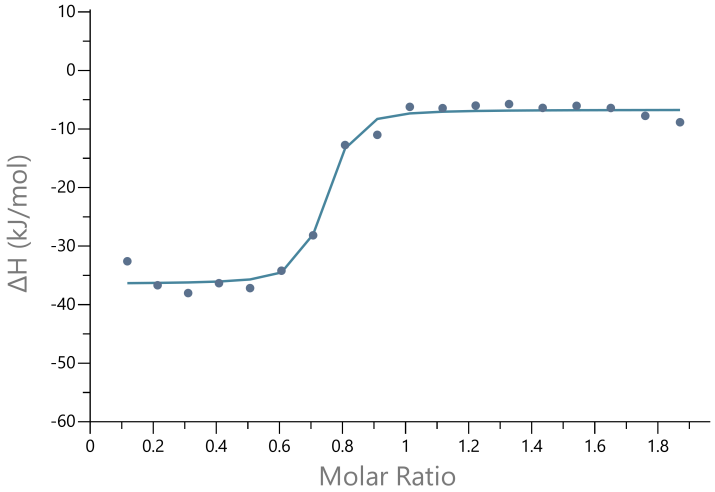


Syringe: 6×His-p300^{BRD}, Cell: AcDC-4 + GST-Hsp90^{NTD}

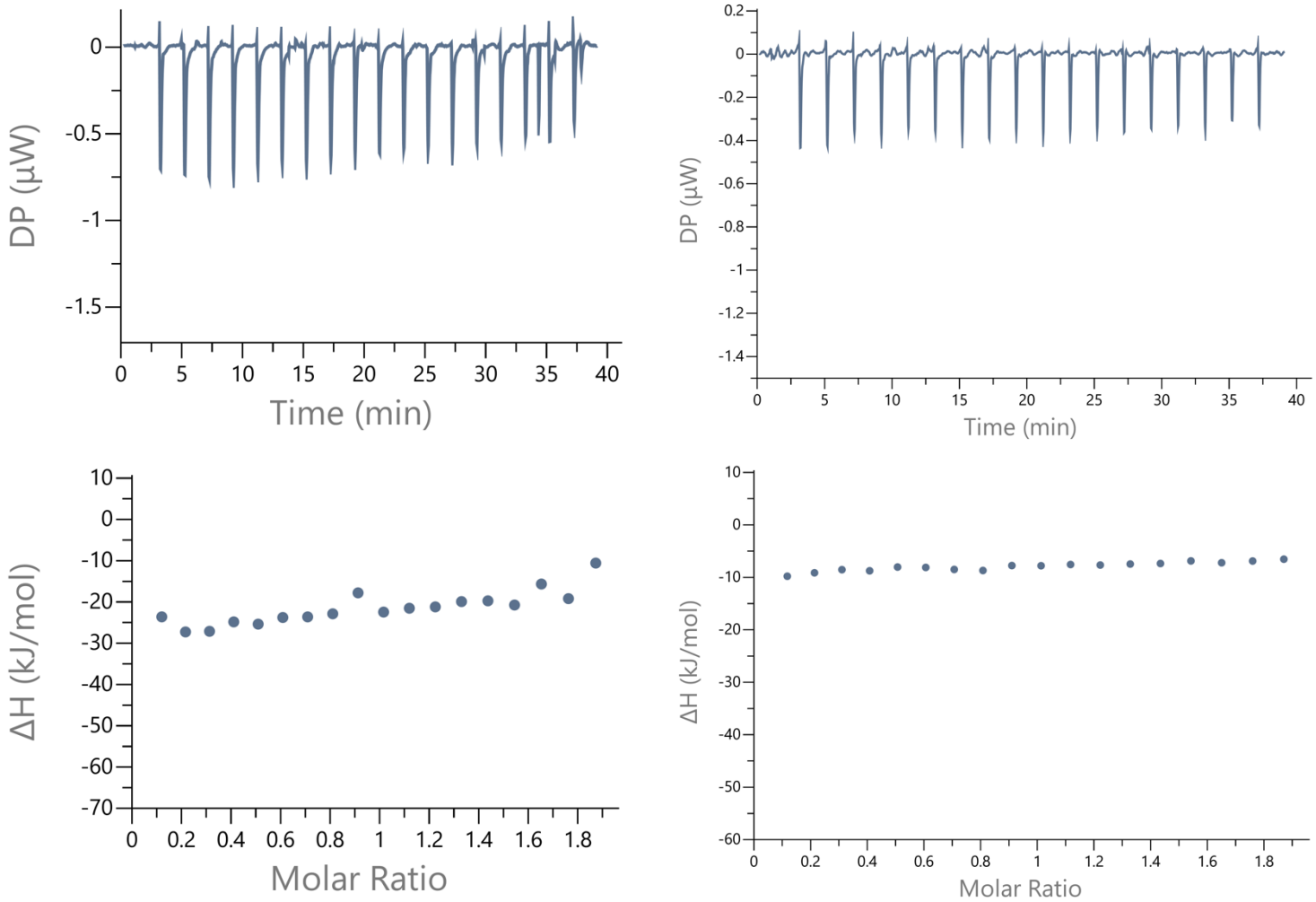




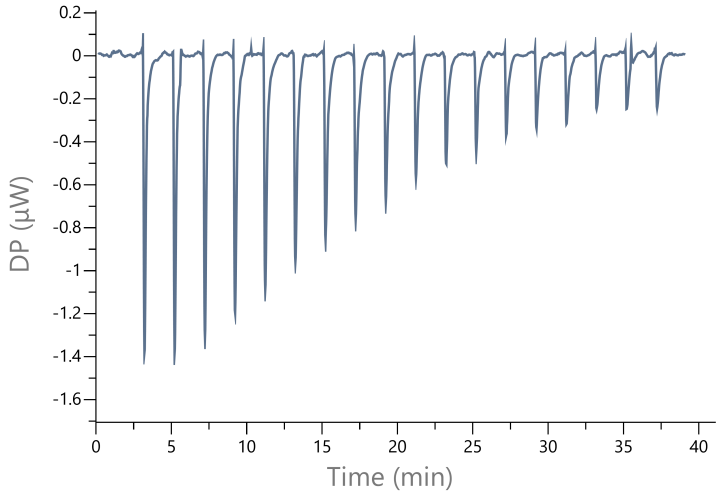


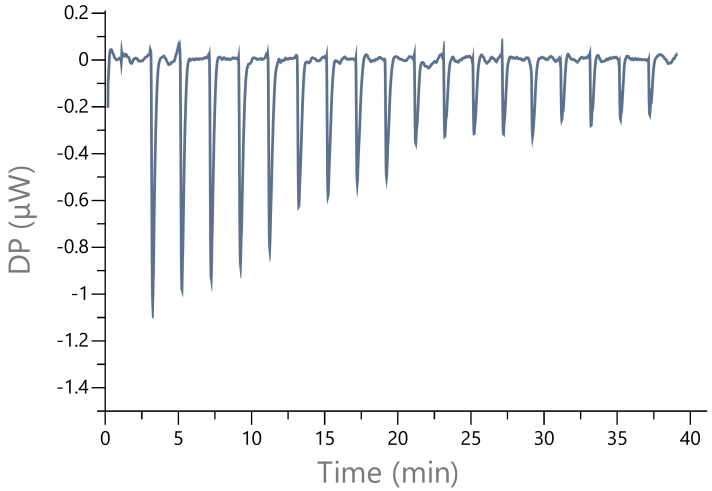


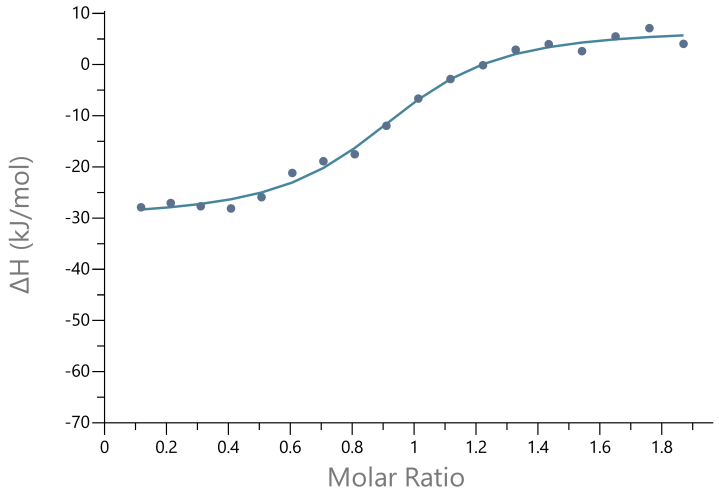
Syringe: 6×His-CBP^{BRD}, Cell: DMSO + GST-Hsp90^{NTD}

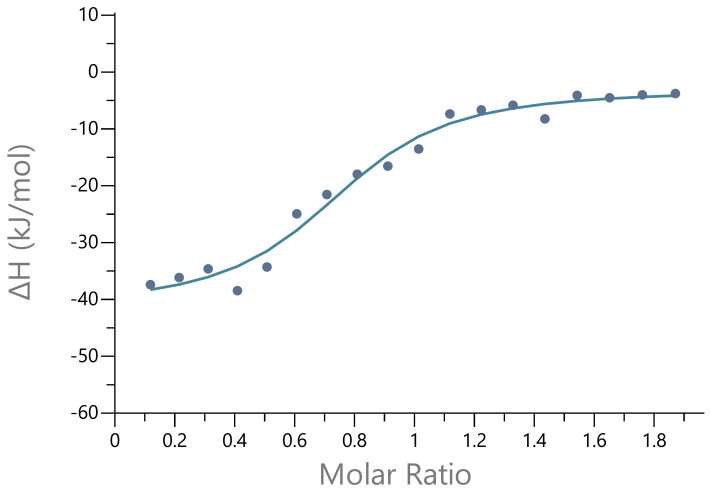


Syringe: 6×His-CBP^{BRD}, Cell: AcDC-1 + GST-Hsp90^{NTD}

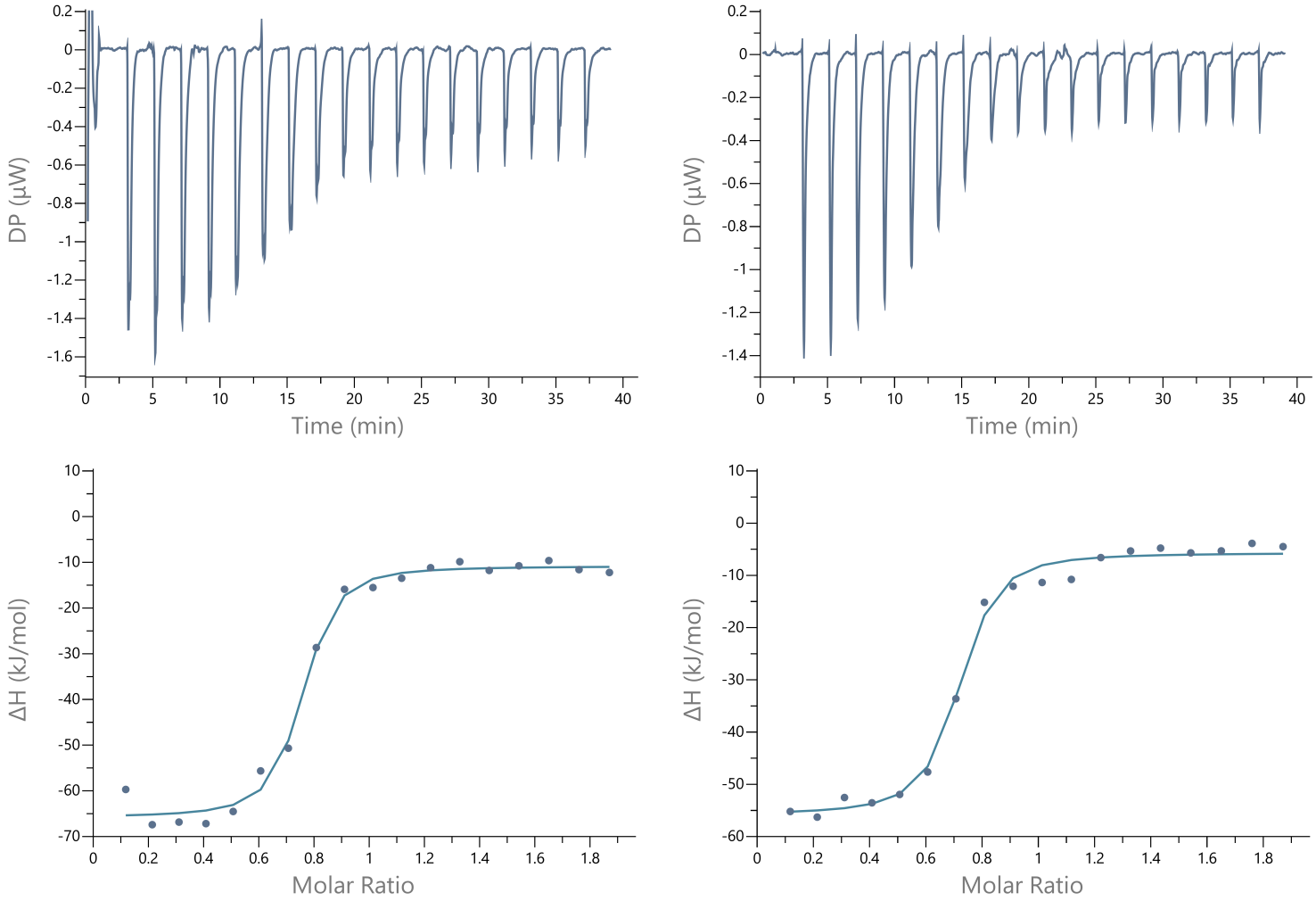




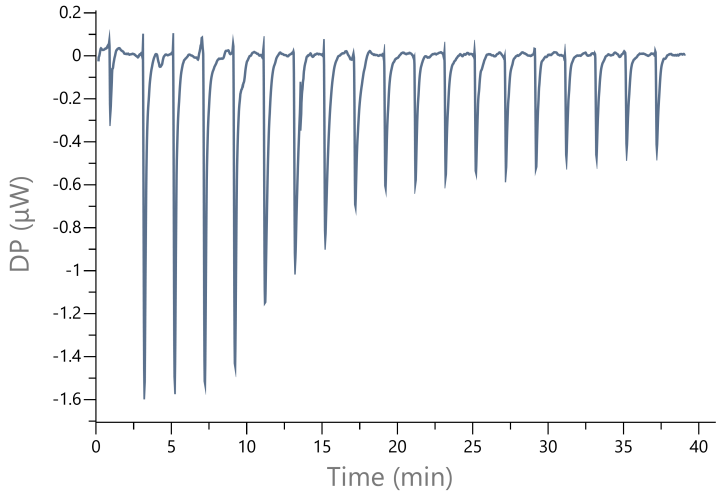


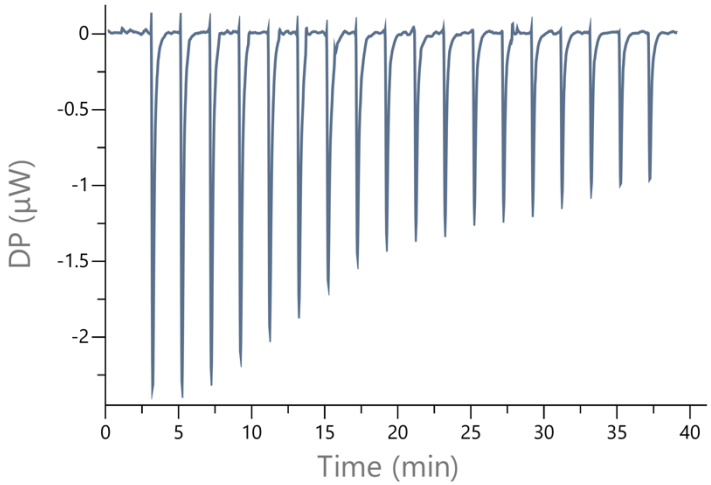


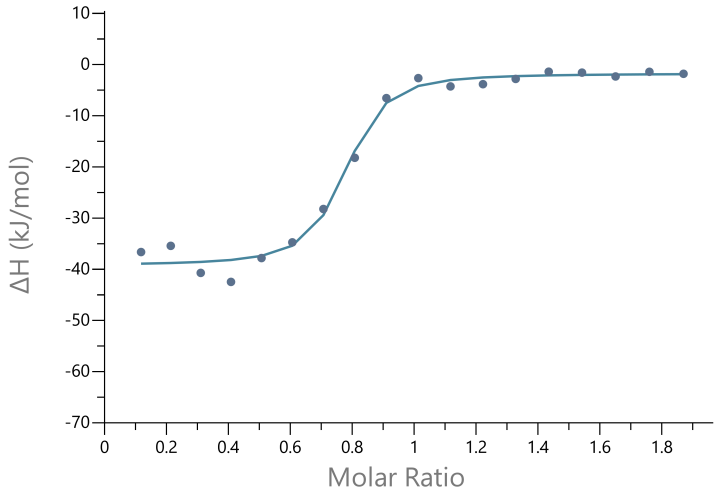
Syringe: 6×His-CBP^{BRD}, Cell: AcDC-2 + GST-Hsp90^{NTD}

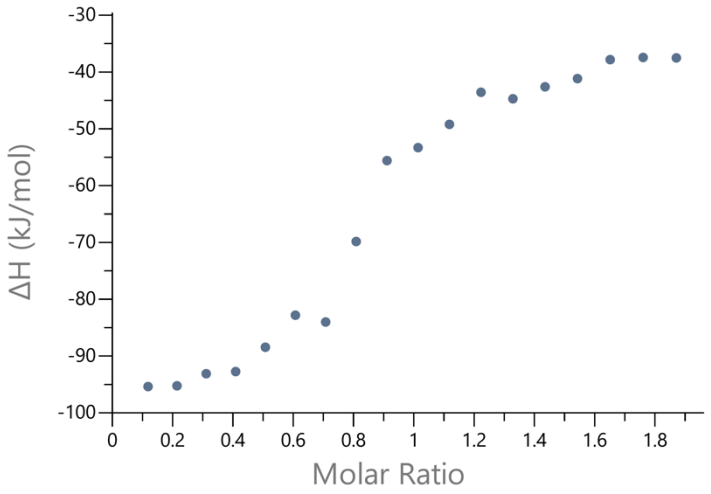


Syringe: 6×His-CBP^{BRD}, Cell: AcDC-3 + GST-Hsp90^{NTD}

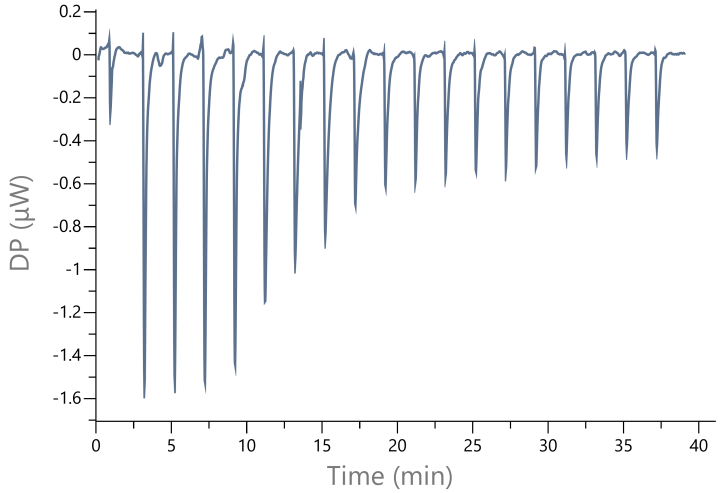


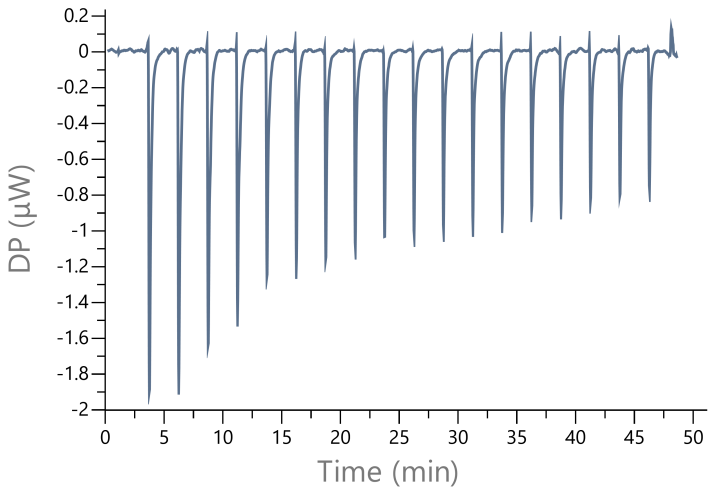


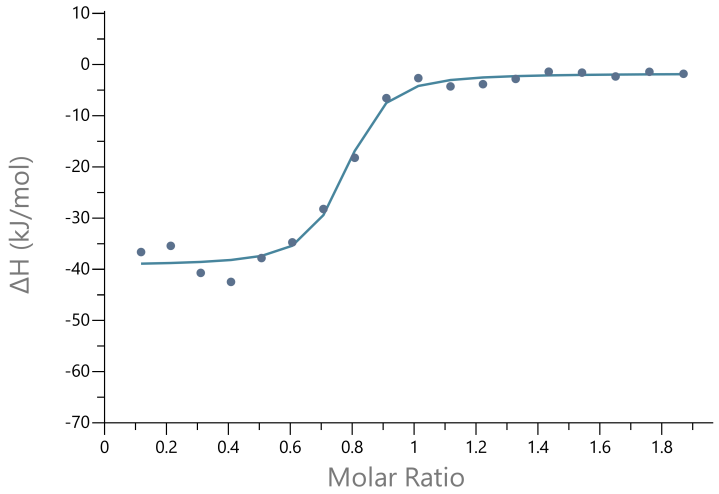


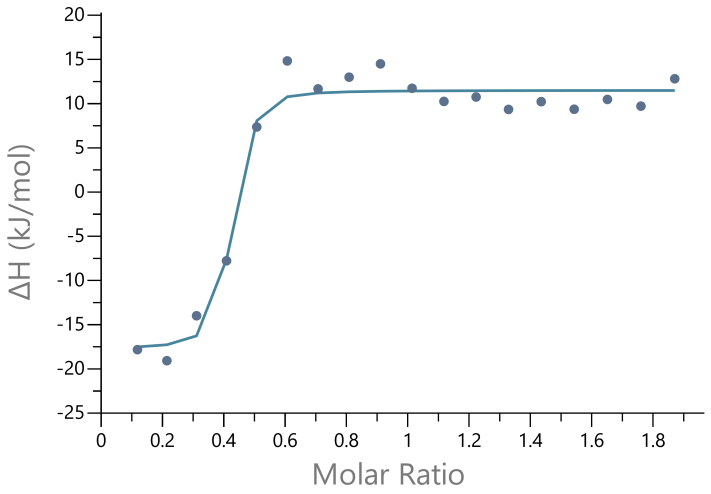


Syringe: 6×His-CBP^{BRD}, Cell: AcDC-4 + GST-Hsp90^{NTD}



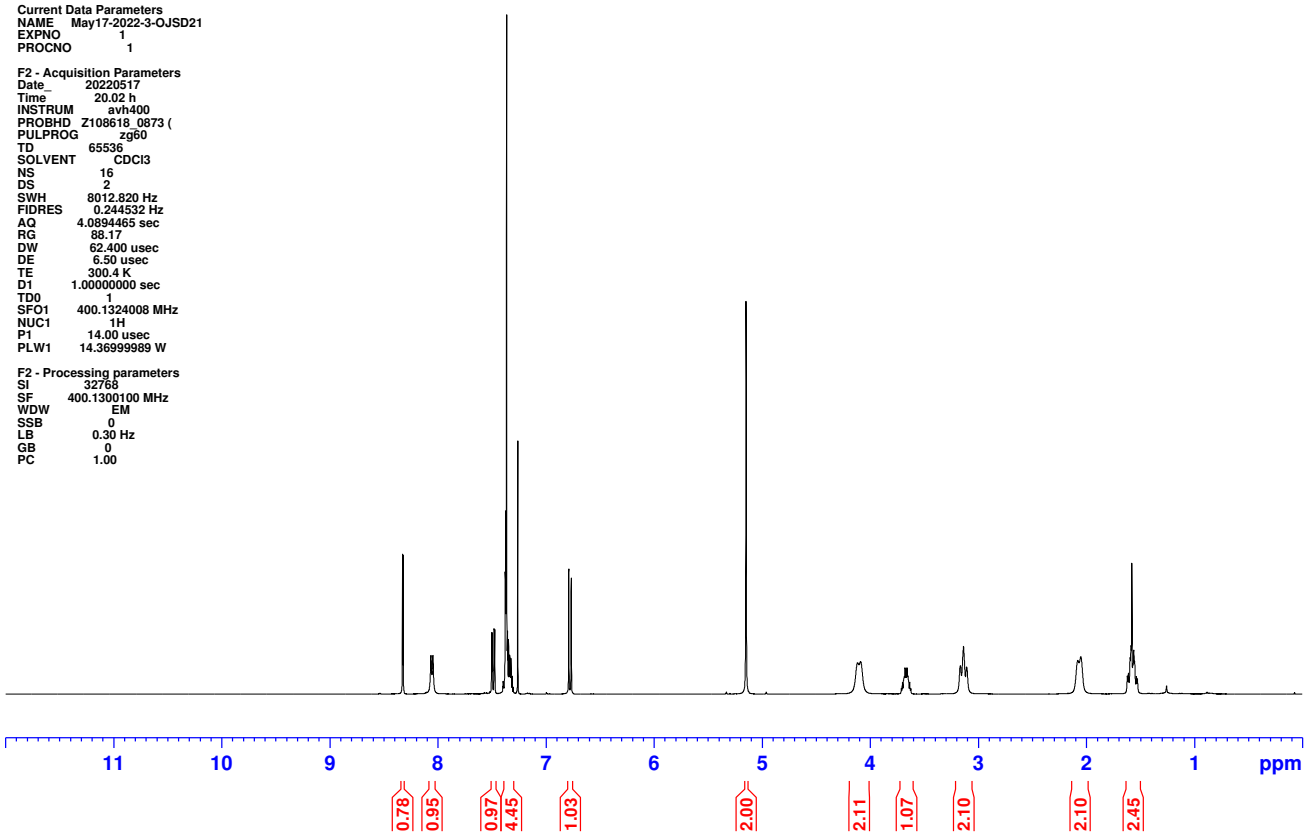


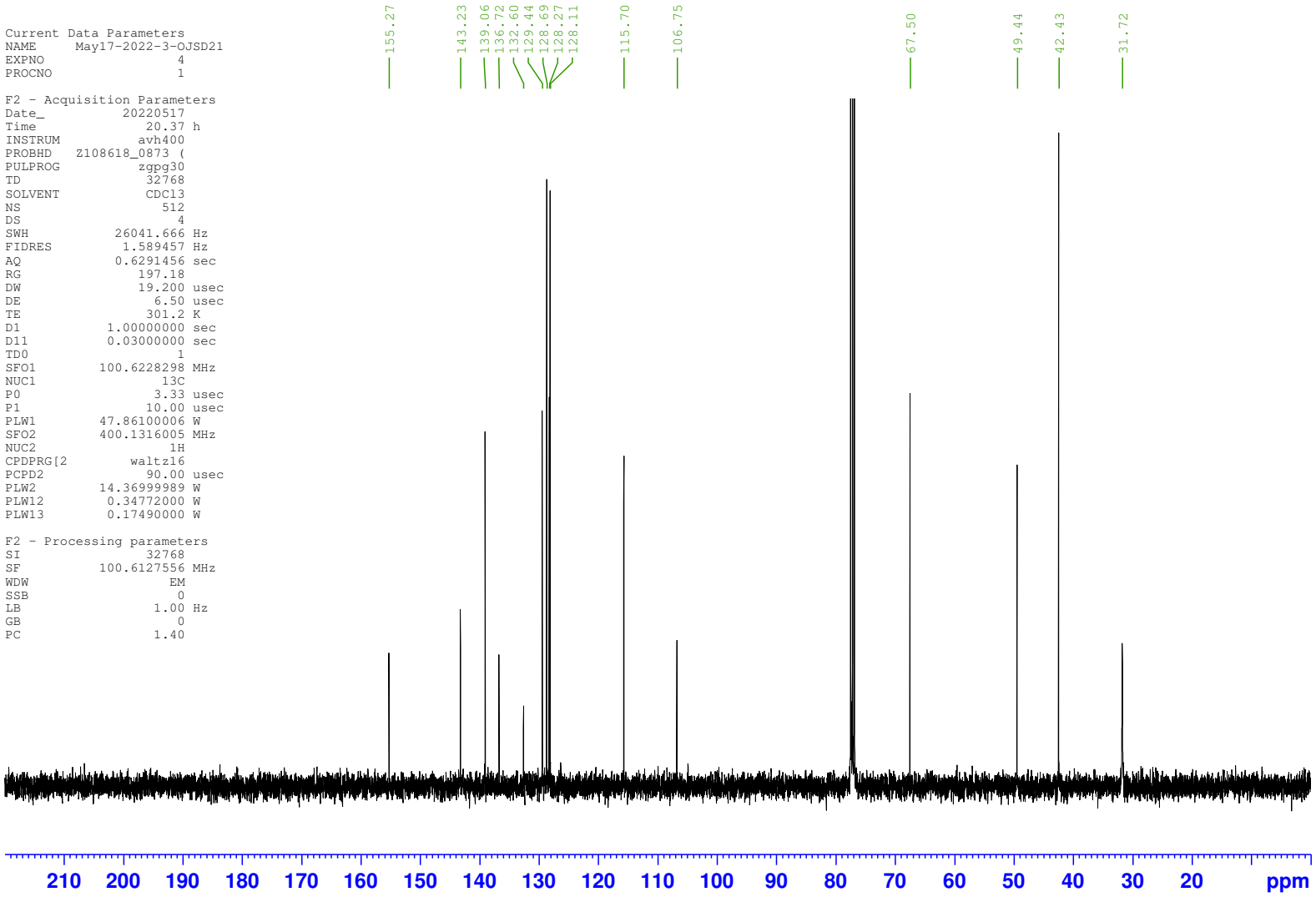




Appendix E NMR spectra of novel compounds

Benzyl 4-((4-bromo-2-nitrophenyl)amino)piperidine-1-carboxylate (10)



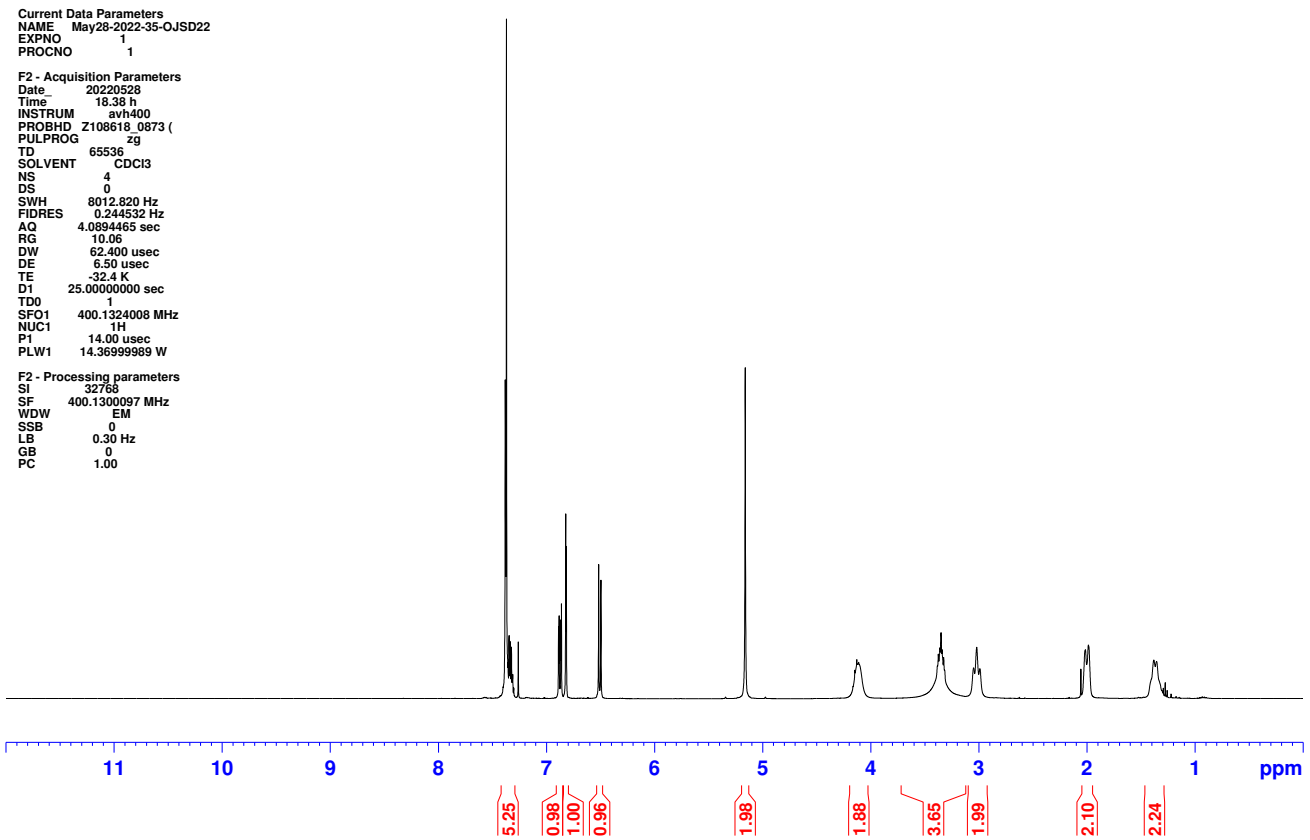


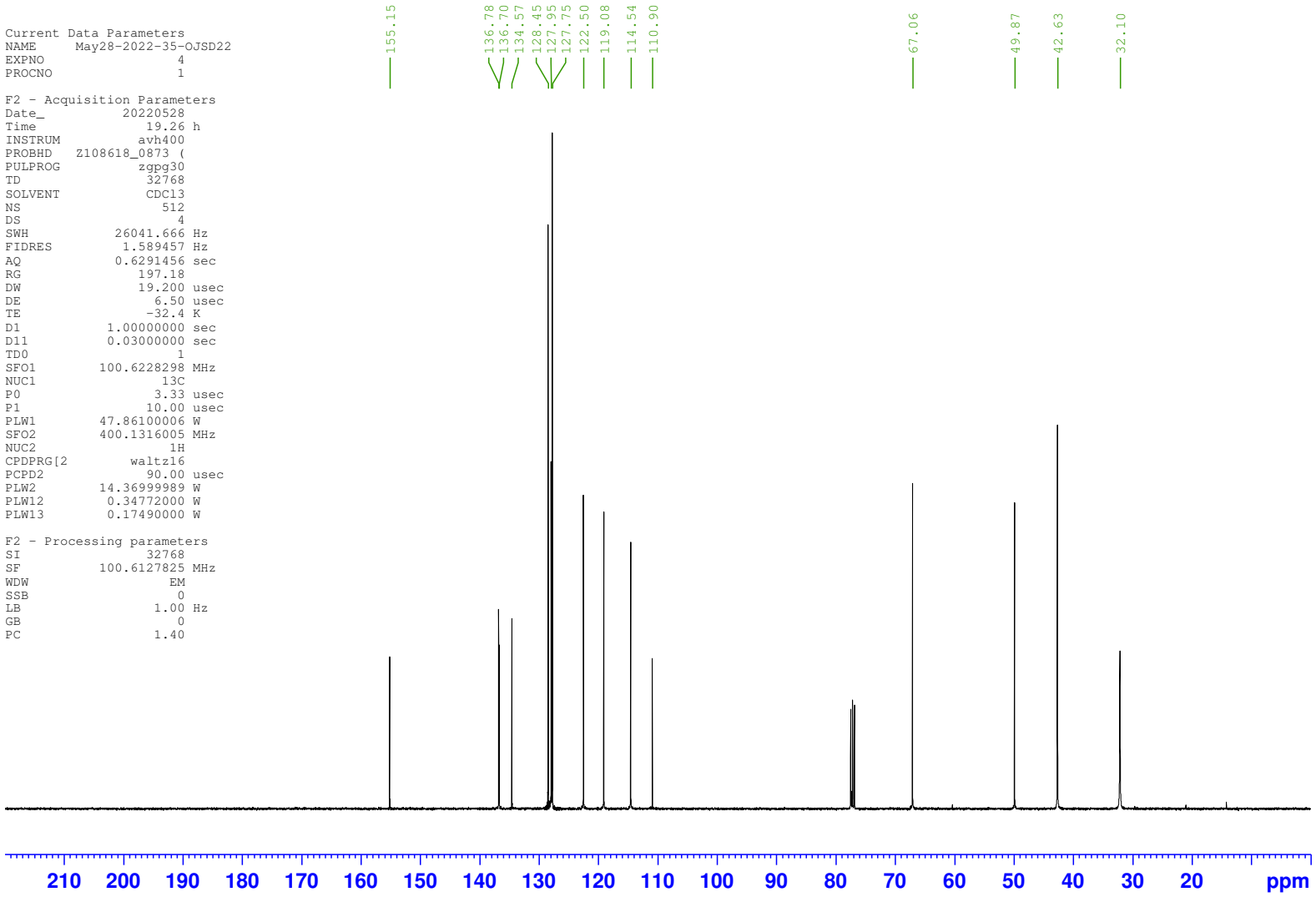

```
Current Data Parameters
NAME      May17-2022-3-OJSD21
EXPNO                       4
PROCNO                      1

F2 - Acquisition Parameters
Date_           20220517
Time              20.37 h
INSTRUM           avh400
PROBHD   Z108618_0873 (
PULPROG           zgpg30
TD                32768
SOLVENT           CDCl3
NS                  512
DS                    4
SWH           26041.666 Hz
FIDRES         1.589457 Hz
AQ            0.6291456 sec
RG               197.18
DW                19.200 usec
DE                 6.50 usec
TE                301.2 K
D1           1.00000000 sec
D11          0.03000000 sec
TD0                  1
SFO1        100.6228298 MHz
NUC1               13C
P0                3.33 usec
P1               10.00 usec
PLW1        47.86100006 W
SFO2        400.1316005 MHz
NUC2               1H
CPDPRG[2        waltz16
PCPD2             90.00 usec
PLW2        14.36999989 W
PLW12        0.34772000 W
PLW13        0.17490000 W

F2 - Processing parameters
SI                32768
SF          100.6127556 MHz
WDW                 EM
SSB                  0
LB                1.00 Hz
GB                   0
PC                1.40
```

Benzyl 4-((2-amino-4-bromophenyl)amino)piperidine-1-carboxylate (11)





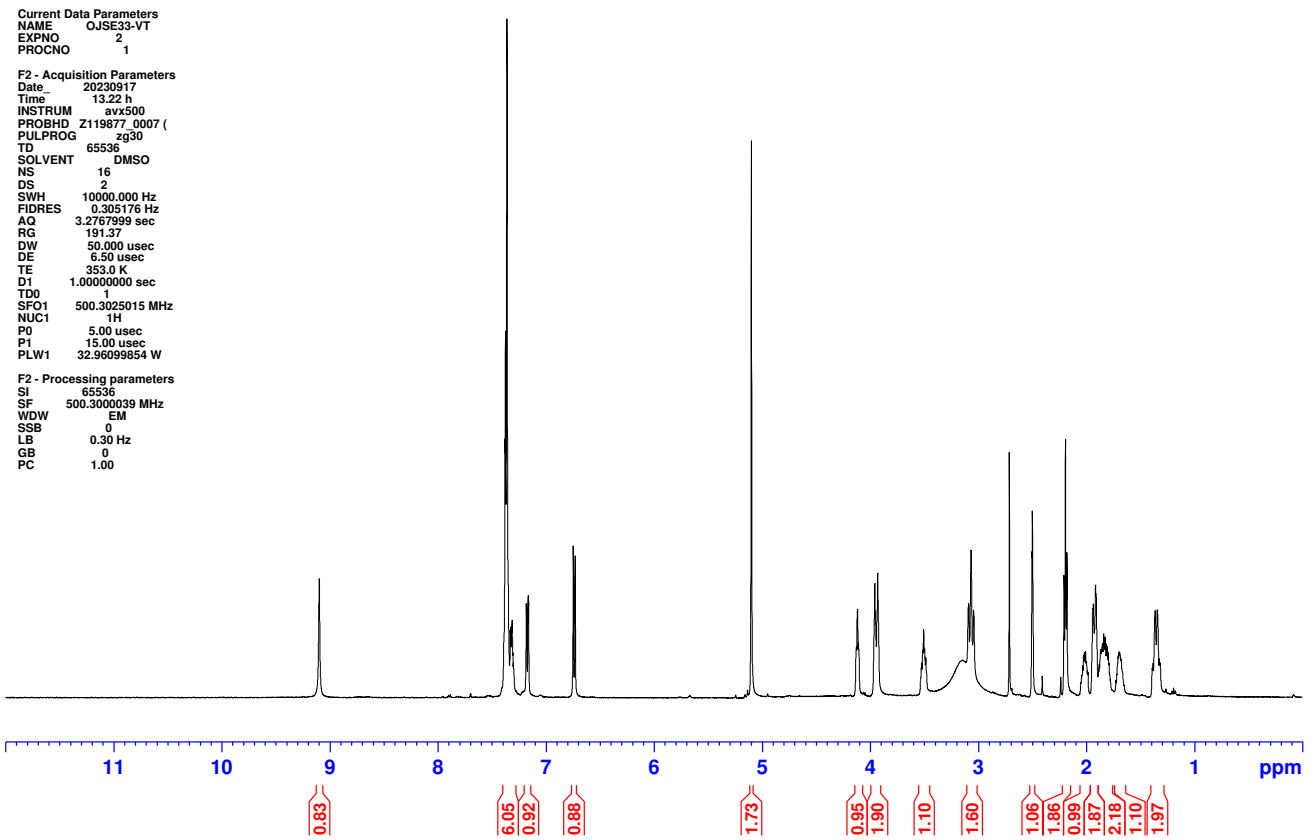

```
Current Data Parameters
NAME      May28-2022-35-OJSD22
EXPNO                      4
PROCNO                     1

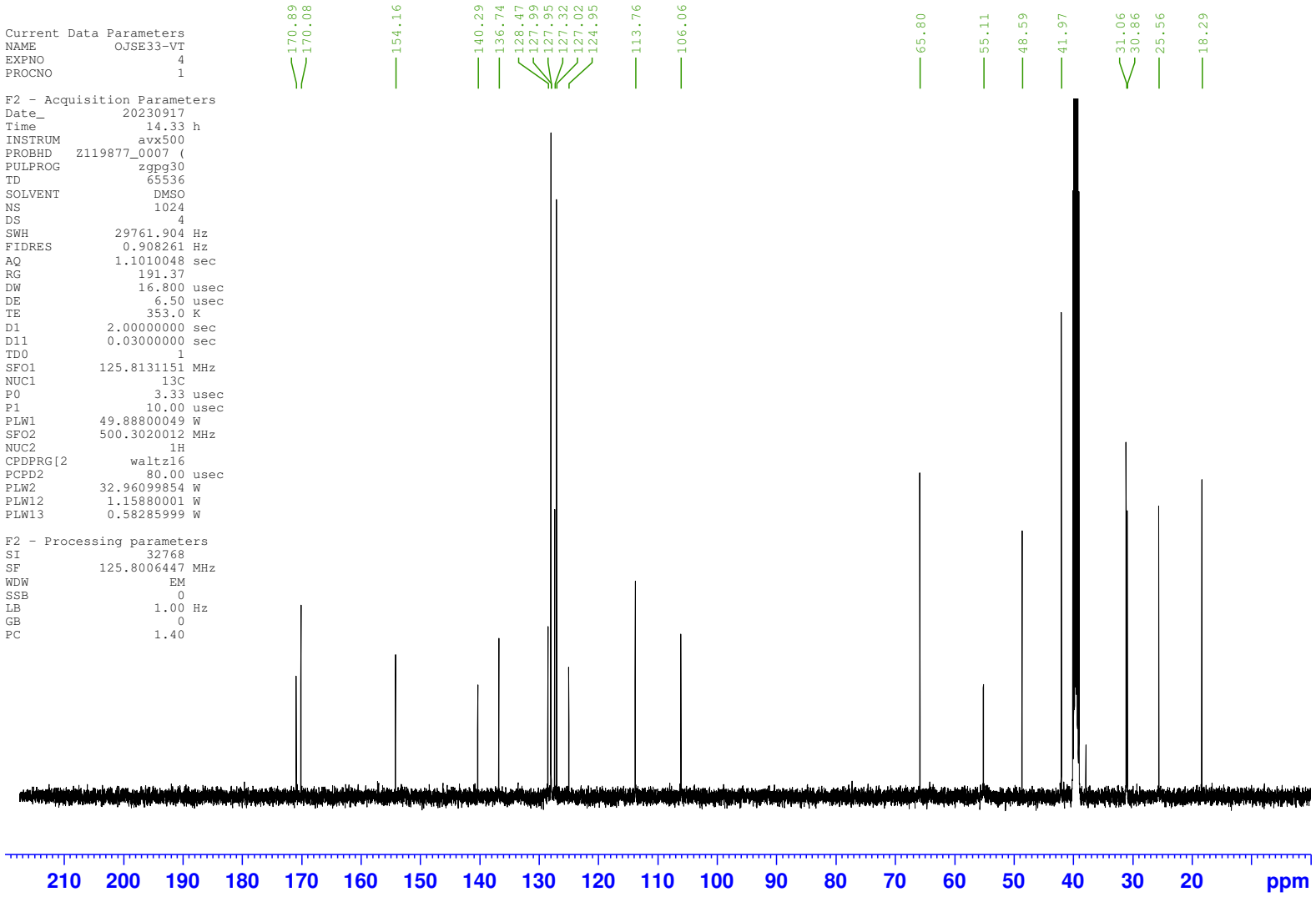
F2 - Acquisition Parameters
Date_           20220528
Time              19.26 h
INSTRUM          avh400
PROBHD   Z108618_0873 (
PULPROG          zgpg30
TD                32768
SOLVENT           CDCl3
NS                  512
DS                    4
SWH           26041.666 Hz
FIDRES         1.589457 Hz
AQ            0.6291456 sec
RG               197.18
DW               19.200 usec
DE                6.50 usec
TE               -32.4 K
D1           1.00000000 sec
D11          0.03000000 sec
TD0                   1
SFO1        100.6228298 MHz
NUC1                13C
P0                 3.33 usec
P1                10.00 usec
PLW1        47.86100006 W
SFO2        400.1316005 MHz
NUC2                 1H
CPDPRG[2         waltz16
PCPD2             90.00 usec
PLW2        14.36999989 W
PLW12        0.34772000 W
PLW13        0.17490000 W

F2 - Processing parameters
SI                32768
SF          100.6127825 MHz
WDW                  EM
SSB                   0
LB                 1.00 Hz
GB                    0
PC                 1.40
```

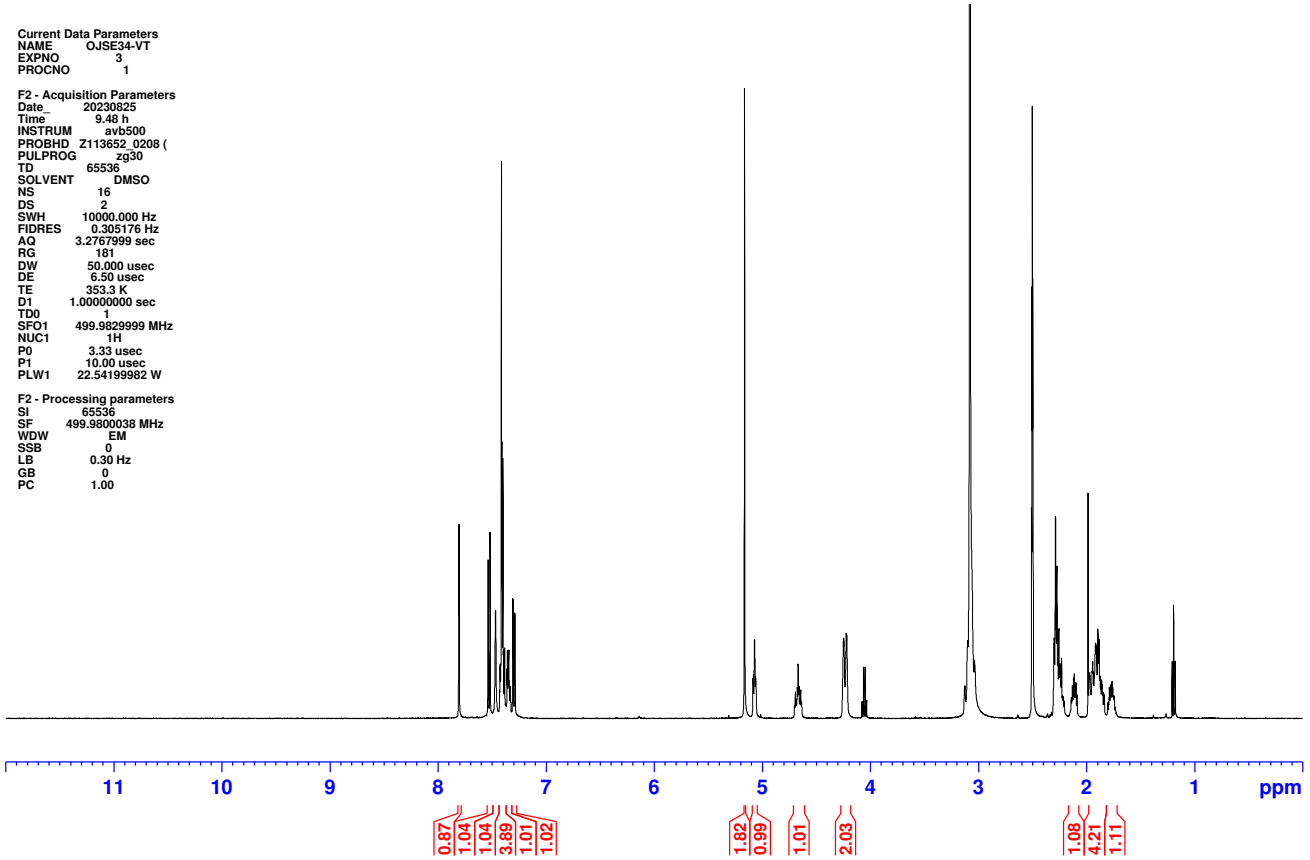
XXX

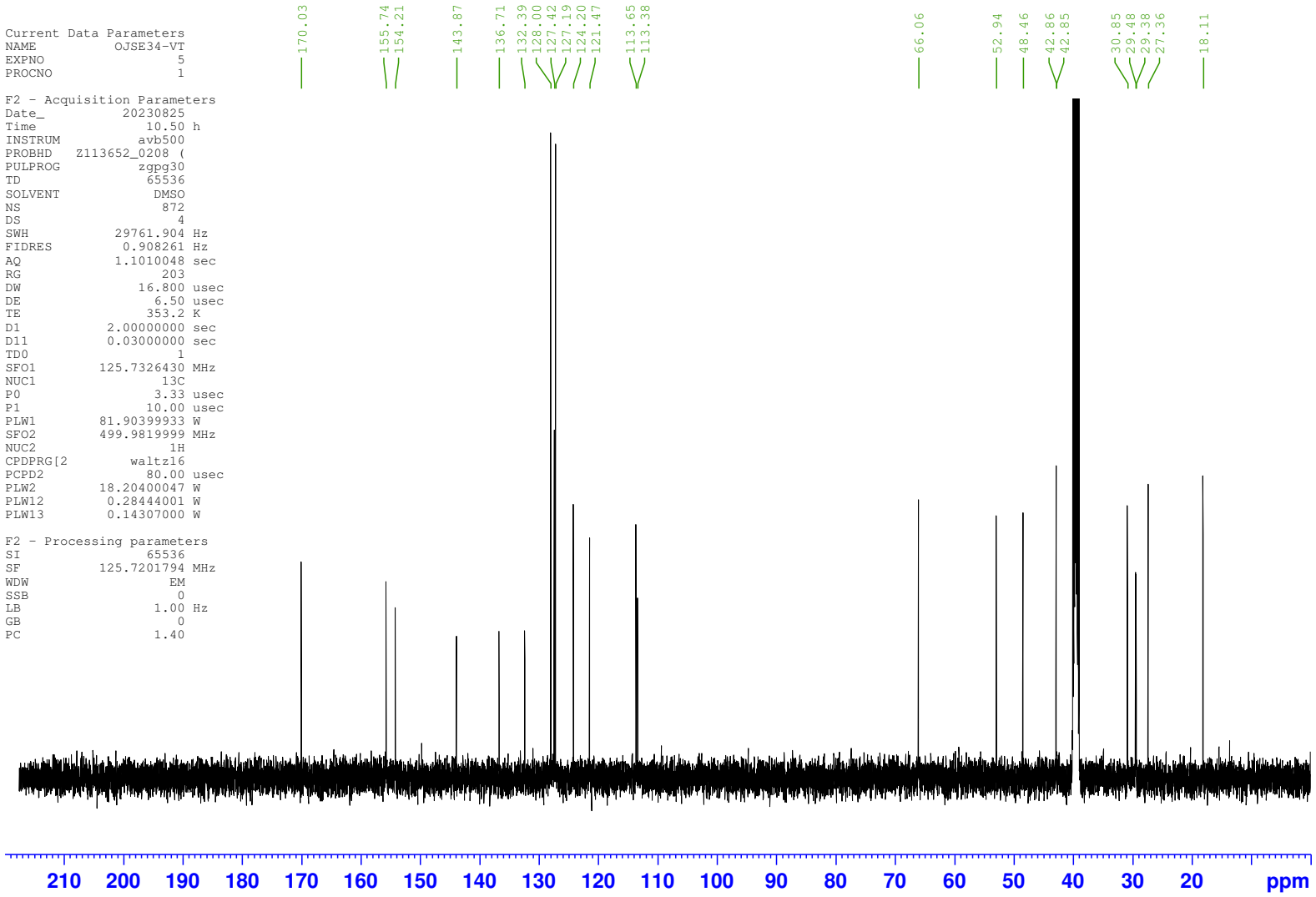
Benzyl 4-((4-bromo-2-((2*S*)-6-oxopiperidine-2-amido)phenyl)amino)piperidine-1-carboxylate (12)



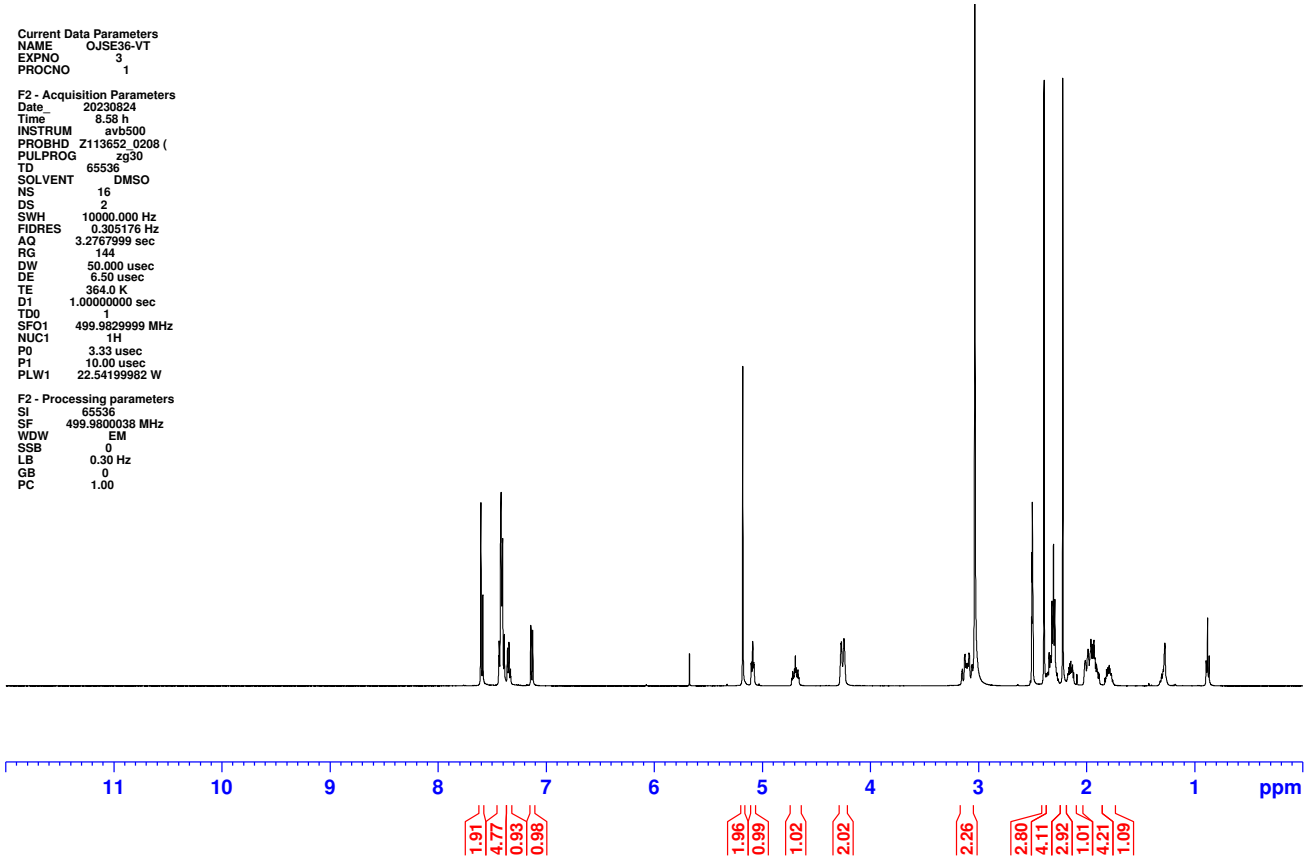

Current Data Parameters
NAME OJSE33-VT
EXPNO 4
PROCNO 1
F2 - Acquisition Parameters
Date_ 20230917
Time 14.33 h
INSTRUM avx500
PROBHD Z119877_0007 (
PULPROG zgpg30
TD 65536
SOLVENT DMSO
NS 1024
DS 4
SWH 29761.904 Hz
FIDRES 0.908261 Hz
AQ 1.1010048 sec
RG 191.37
DW 16.800 usec
DE 6.50 usec
TE 353.0 K
D1 2.00000000 sec
D11 0.03000000 sec
TD0 1
SFO1 125.8131151 MHz
NUC1 13C
P0 3.33 usec
P1 10.00 usec
PLW1 49.88800049 W
SFO2 500.3020012 MHz
NUC2 1H
CPDPRG[2 waltz16
PCPD2 80.00 usec
PLW2 32.96099854 W
PLW12 1.15880001 W
PLW13 0.58285999 W
F2 - Processing parameters
SI 32768
SF 125.8006447 MHz
WDW EM
SSB 0
LB 1.00 Hz
GB 0
PC 1.40
170.89
170.08
154.16
140.29
136.74
128.47
127.99
127.95
127.32
127.02
124.95
113.76
106.06
65.80
55.11
48.59
41.97
31.06
30.86
25.56
18.29
210 200 190 180 170 160 150 140 130 120 110 100 90 80 70 60 50 40 30 20 ppm

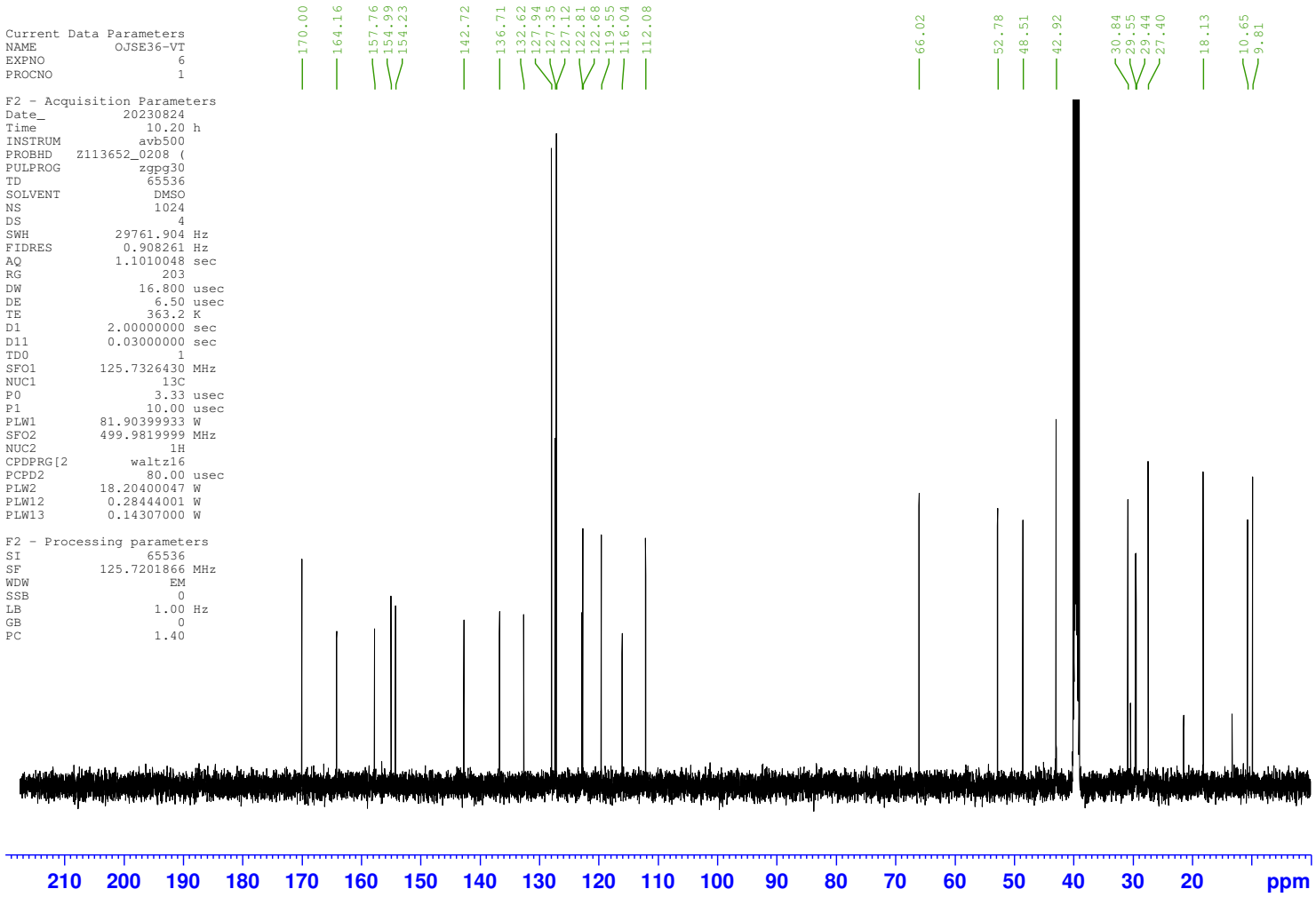
Benzyl 4-(5-bromo-2-[(2*S*)-6-oxopiperidin-2-yl]-1*H*-1,3-benzodiazol-1-yl)piperidine-1-carboxylate (13)



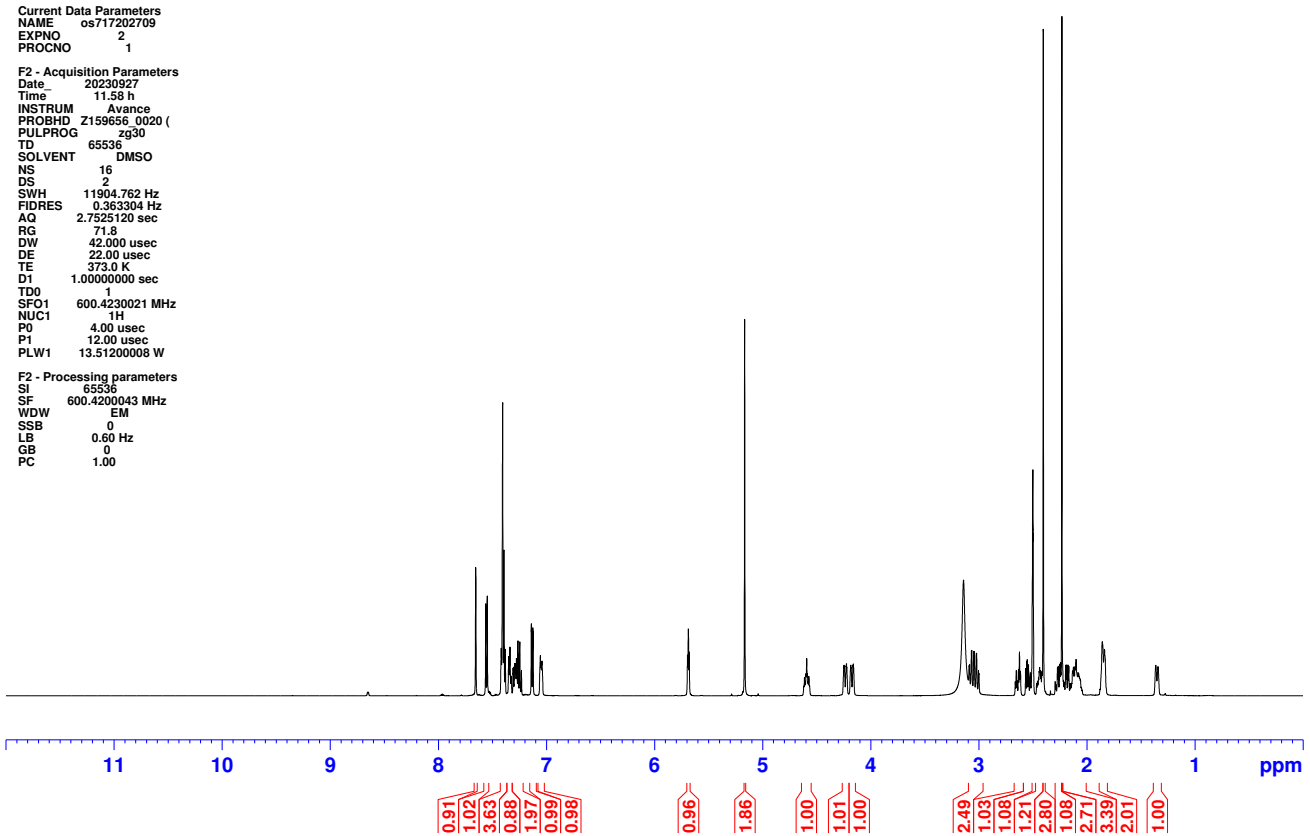

Current Data Parameters
NAME OJSE34-VT
EXPNO 5
PROCNO 1
F2 - Acquisition Parameters
Date_ 20230825
Time 10.50 h
INSTRUM avb500
PROBHD Z113652_0208 (
PULPROG zgpg30
TD 65536
SOLVENT DMSO
NS 872
DS 4
SWH 29761.904 Hz
FIDRES 0.908261 Hz
AQ 1.1010048 sec
RG 203
DW 16.800 usec
DE 6.50 usec
TE 353.2 K
D1 2.00000000 sec
D11 0.03000000 sec
TD0 1
SFO1 125.7326430 MHz
NUC1 13C
P0 3.33 usec
P1 10.00 usec
PLW1 81.90399933 W
SFO2 499.9819999 MHz
NUC2 1H
CPDPRG[2 waltz16
PCPD2 80.00 usec
PLW2 18.20400047 W
PLW12 0.28444001 W
PLW13 0.14307000 W
F2 - Processing parameters
SI 65536
SF 125.7201794 MHz
WDW EM
SSB 0
LB 1.00 Hz
GB 0
PC 1.40
170.03
155.74
154.21
143.87
136.71
132.39
128.00
127.42
127.19
124.20
121.47
113.65
113.38
66.06
52.94
48.46
42.86
42.85
30.85
29.48
29.38
27.36
18.11
210 200 190 180 170 160 150 140 130 120 110 100 90 80 70 60 50 40 30 20 ppm

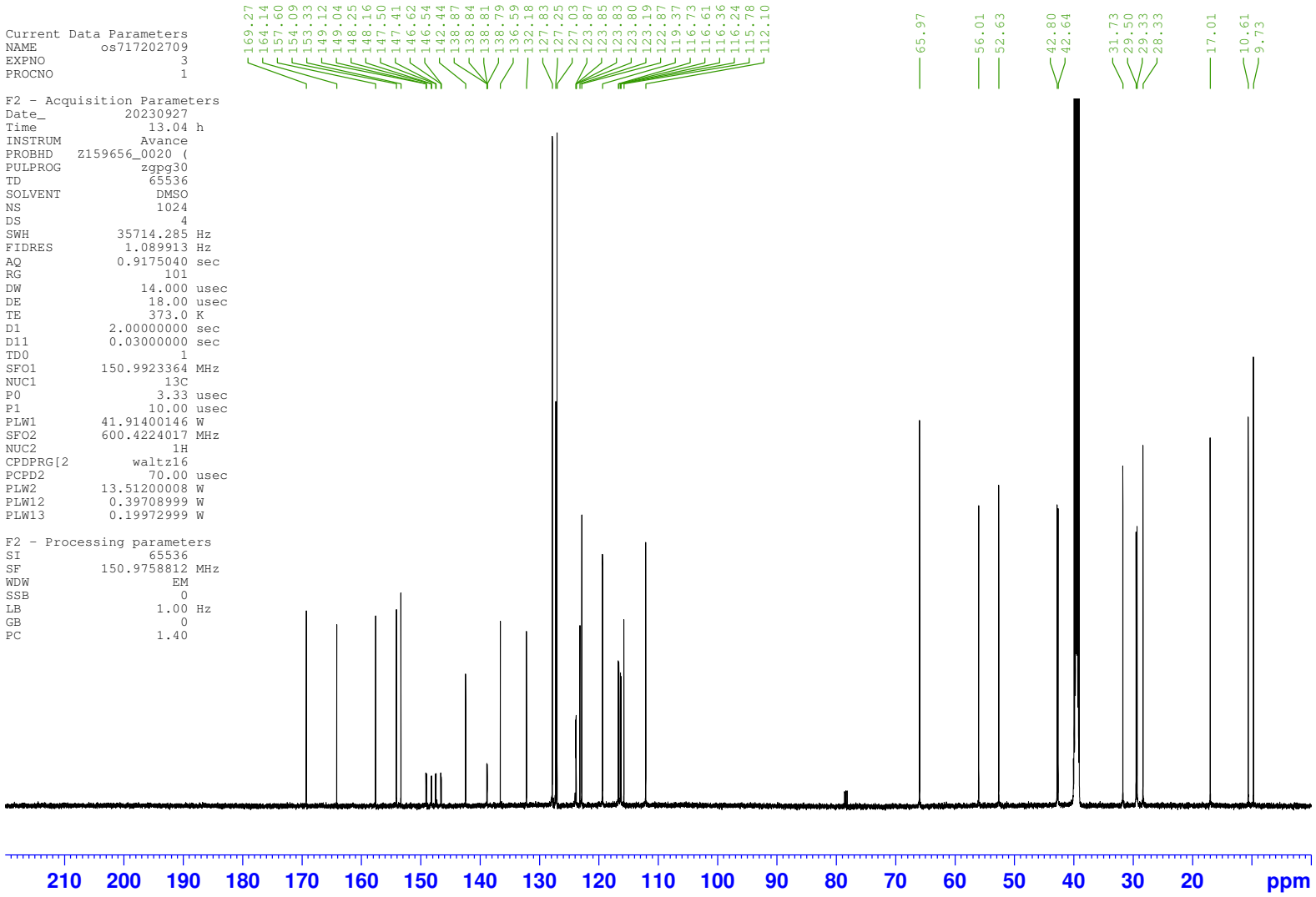
Benzyl 4-[5-(3,5-dimethyl-1,2-oxazol-4-yl)-2-[(2*S*)-6-oxopiperidin-2-yl]-1*H*-1,3-benzodiazol-1-yl]piperidine-1-carboxylate (14)




Current Data Parameters
NAME OJSE36-VT
EXPNO 6
PROCNO 1
F2 - Acquisition Parameters
Date_ 20230824
Time 10.20 h
INSTRUM avb500
PROBHD Z113652_0208 (
PULPROG zgpg30
TD 65536
SOLVENT DMSO
NS 1024
DS 4
SWH 29761.904 Hz
FIDRES 0.908261 Hz
AQ 1.1010048 sec
RG 203
DW 16.800 usec
DE 6.50 usec
TE 363.2 K
D1 2.00000000 sec
D11 0.03000000 sec
TD0 1
SFO1 125.7326430 MHz
NUC1 13C
P0 3.33 usec
P1 10.00 usec
PLW1 81.90399933 W
SFO2 499.9819999 MHz
NUC2 1H
CPDPRG[2 waltz16
PCPD2 80.00 usec
PLW2 18.20400047 W
PLW12 0.28444001 W
PLW13 0.14307000 W
F2 - Processing parameters
SI 65536
SF 125.7201866 MHz
WDW EM
SSB 0
LB 1.00 Hz
GB 0
PC 1.40
170.00
164.16
157.76
154.99
154.23
142.72
136.71
132.62
127.94
127.35
127.12
122.81
122.68
119.55
116.04
112.08
66.02
52.78
48.51
42.92
30.84
29.55
29.44
27.40
18.13
10.65
9.81
210 200 190 180 170 160 150 140 130 120 110 100 90 80 70 60 50 40 30 20 ppm

Benzyl 4-(2-((2*S*)-1-(3,4-difluorophenyl)-6-oxopiperidin-2-yl)-5-(3,5-dimethyl-1,2-oxazol-4-yl)-1*H*-1,3-benzodiazol-1-yl)piperidine-1-carboxylate (15)

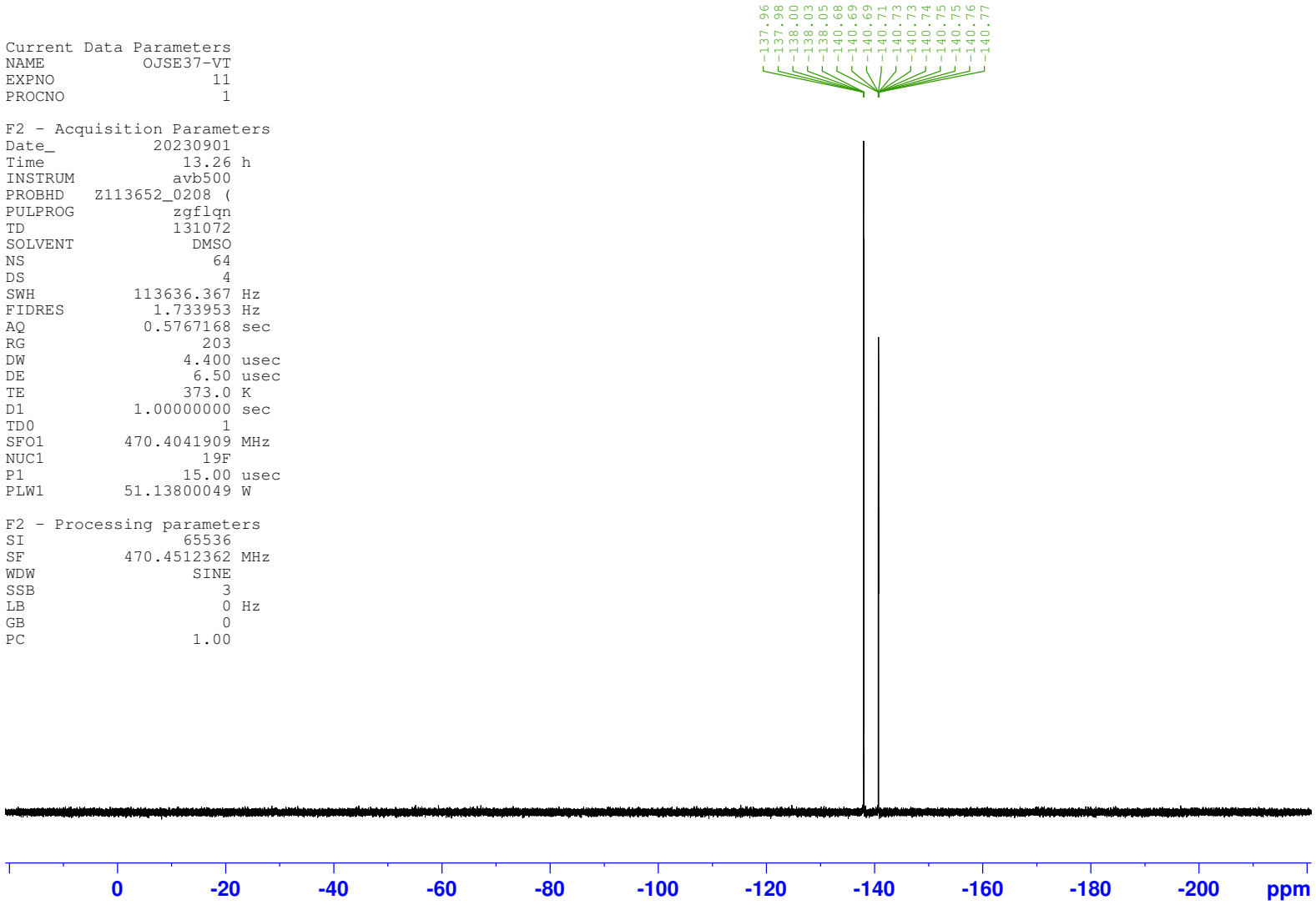



Current Data Parameters
NAME os717202709
EXPNO 3
PROCNO 1
F2 - Acquisition Parameters
Date_ 20230927
Time 13.04 h
INSTRUM Avance
PROBHD Z159656_0020 (
PULPROG zgpg30
TD 65536
SOLVENT DMSO
NS 1024
DS 4
SWH 35714.285 Hz
FIDRES 1.089913 Hz
AQ 0.9175040 sec
RG 101
DW 14.000 usec
DE 18.00 usec
TE 373.0 K
D1 2.00000000 sec
D11 0.03000000 sec
TD0 1
SFO1 150.9923364 MHz
NUC1 13C
P0 3.33 usec
P1 10.00 usec
PLW1 41.91400146 W
SFO2 600.4224017 MHz
NUC2 1H
CPDPRG[2 waltz16
PCPD2 70.00 usec
PLW2 13.51200008 W
PLW12 0.39708999 W
PLW13 0.19972999 W
F2 - Processing parameters
SI 65536
SF 150.9758812 MHz
WDW EM
SSB 0
LB 1.00 Hz
GB 0
PC 1.40
169.27
164.14
157.60
154.09
153.33
149.12
149.04
148.25
148.16
147.50
147.41
146.62
146.54
142.44
138.87
138.84
138.81
138.79
136.59
132.18
127.83
127.25
127.03
123.87
123.85
123.83
123.80
123.19
122.87
119.37
116.73
116.61
116.36
116.24
115.78
112.10
65.97
56.01
52.63
42.80
42.64
31.73
29.50
29.33
28.33
17.01
10.61
9.73
210 200 190 180 170 160 150 140 130 120 110 100 90 80 70 60 50 40 30 20 ppm

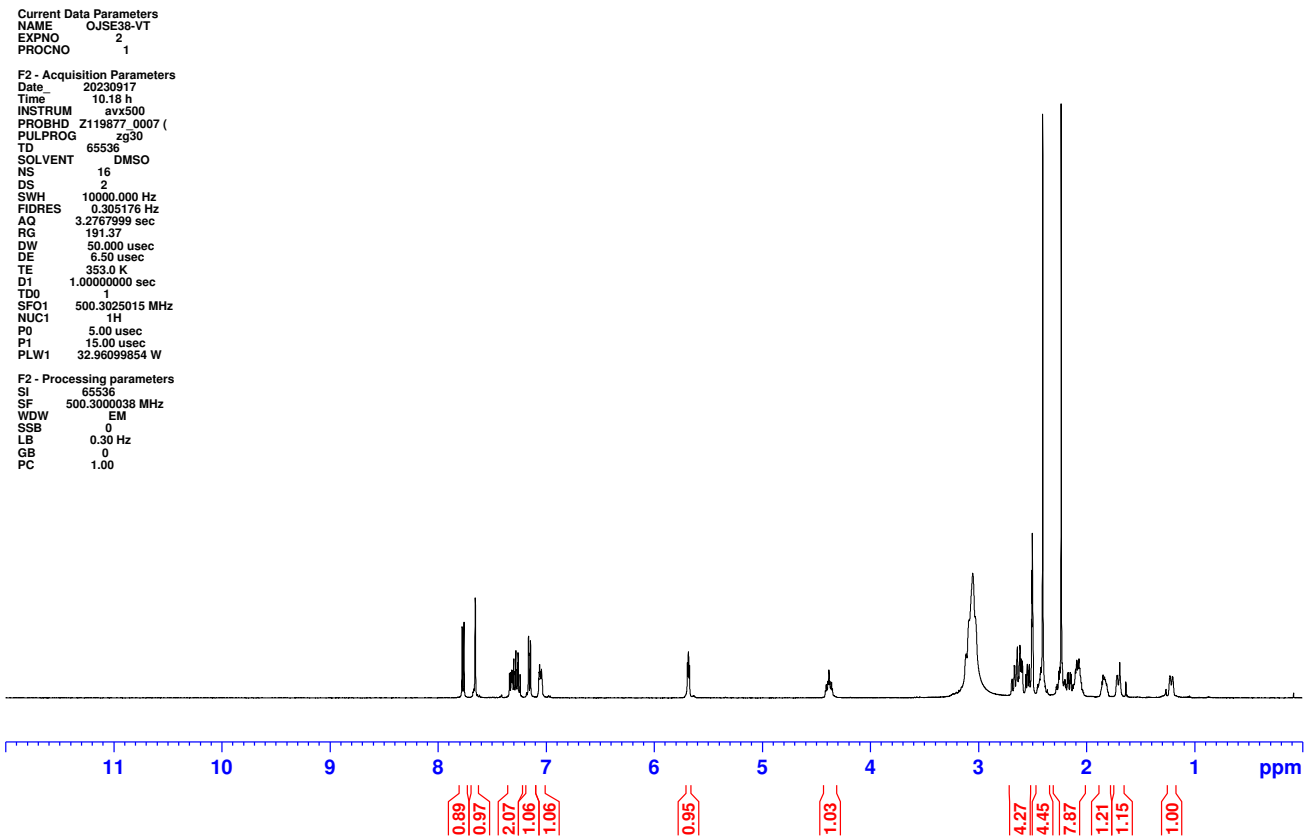
```
Current Data Parameters
NAME          OJSE37-VT
EXPNO                11
PROCNO                1

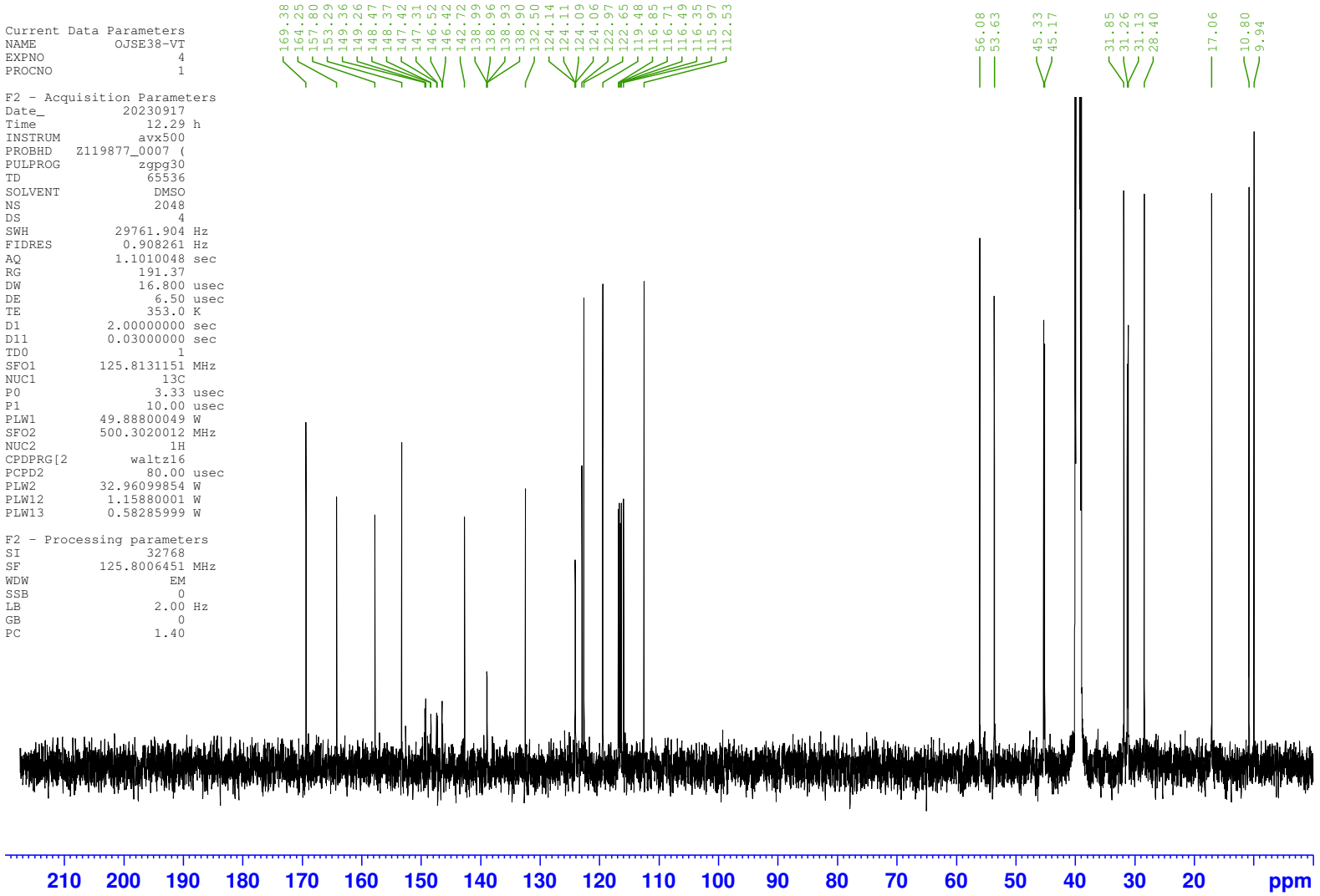
F2 - Acquisition Parameters
Date_          20230901
Time              13.26 h
INSTRUM          avb500
PROBHD   Z113652_0208 (
PULPROG          zgflqn
TD               131072
SOLVENT            DMSO
NS                    64
DS                     4
SWH           113636.367 Hz
FIDRES          1.733953 Hz
AQ             0.5767168 sec
RG                   203
DW                4.400 usec
DE                 6.50 usec
TE                373.0 K
D1            1.00000000 sec
TD0                   1
SFO1         470.4041909 MHz
NUC1                 19F
P1                15.00 usec
PLW1         51.13800049 W

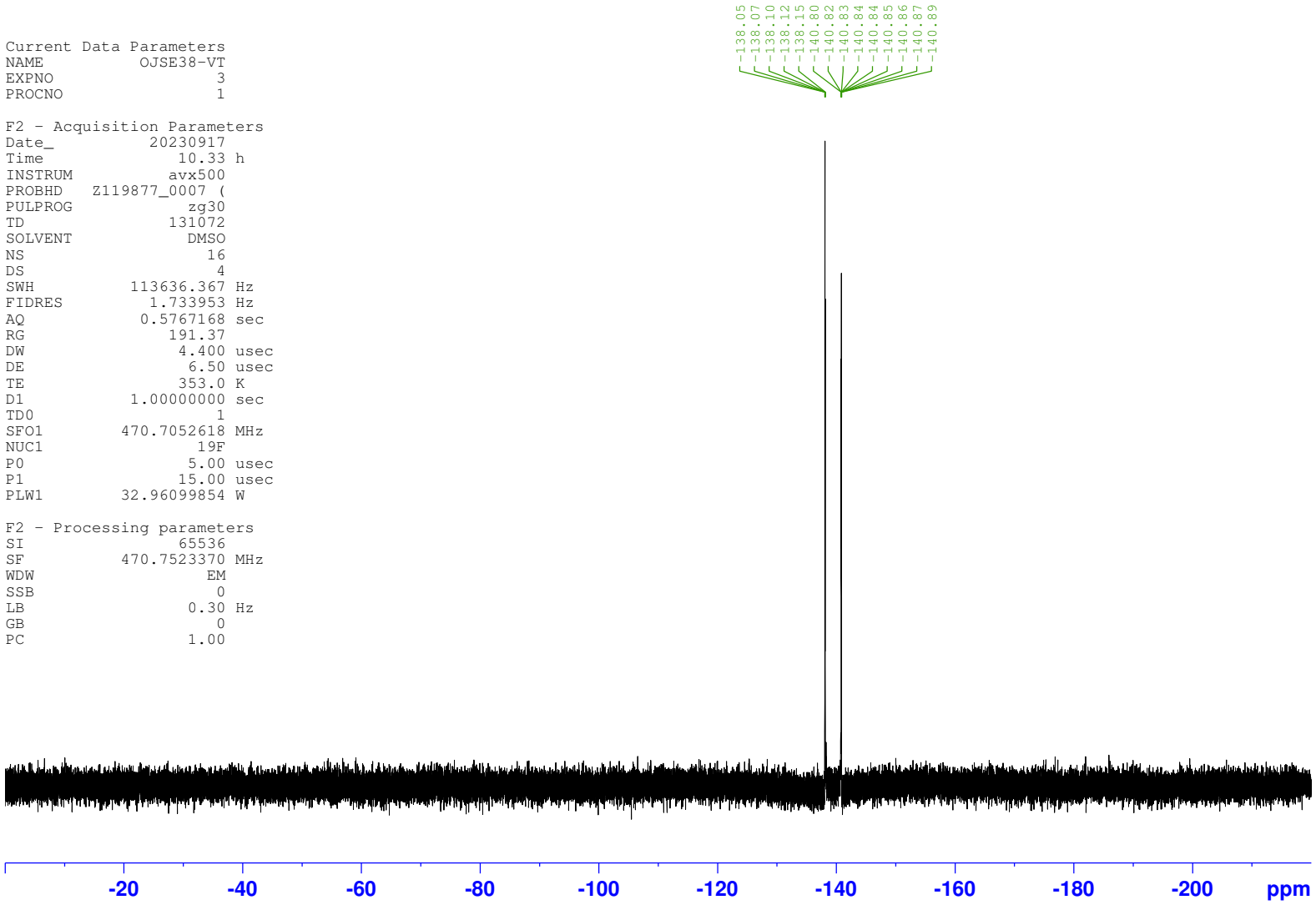
F2 - Processing parameters
SI                65536
SF           470.4512362 MHz
WDW                SINE
SSB                   3
LB                    0 Hz
GB                    0
PC                 1.00
```



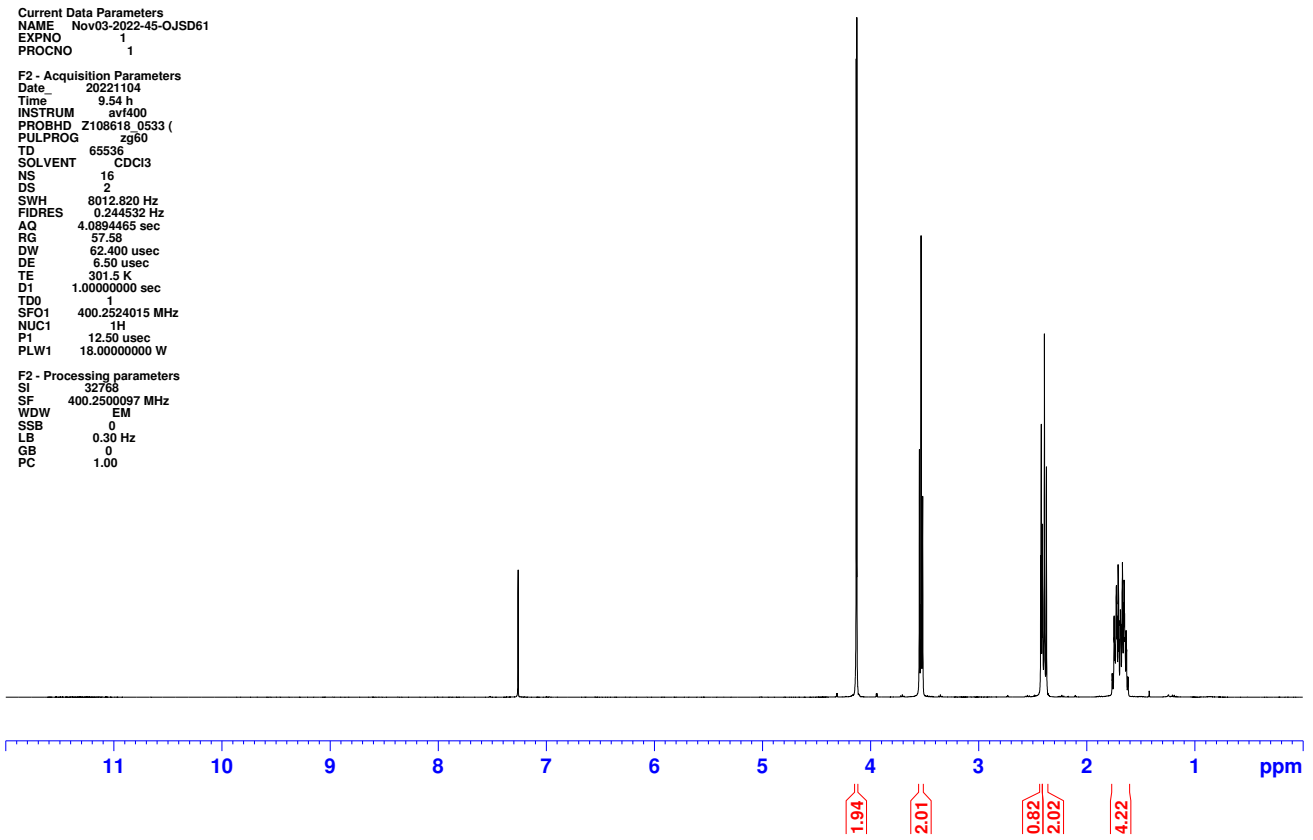
(6*S*)-1-(3,4-Difluorophenyl)-6-(5-(3,5-dimethyl-1,2-oxazol-4-yl)-1-(piperidin-4-yl)-1*H*-1,3-benzodiazol-2-yl)piperidin-2-one (Pip-obrodib)

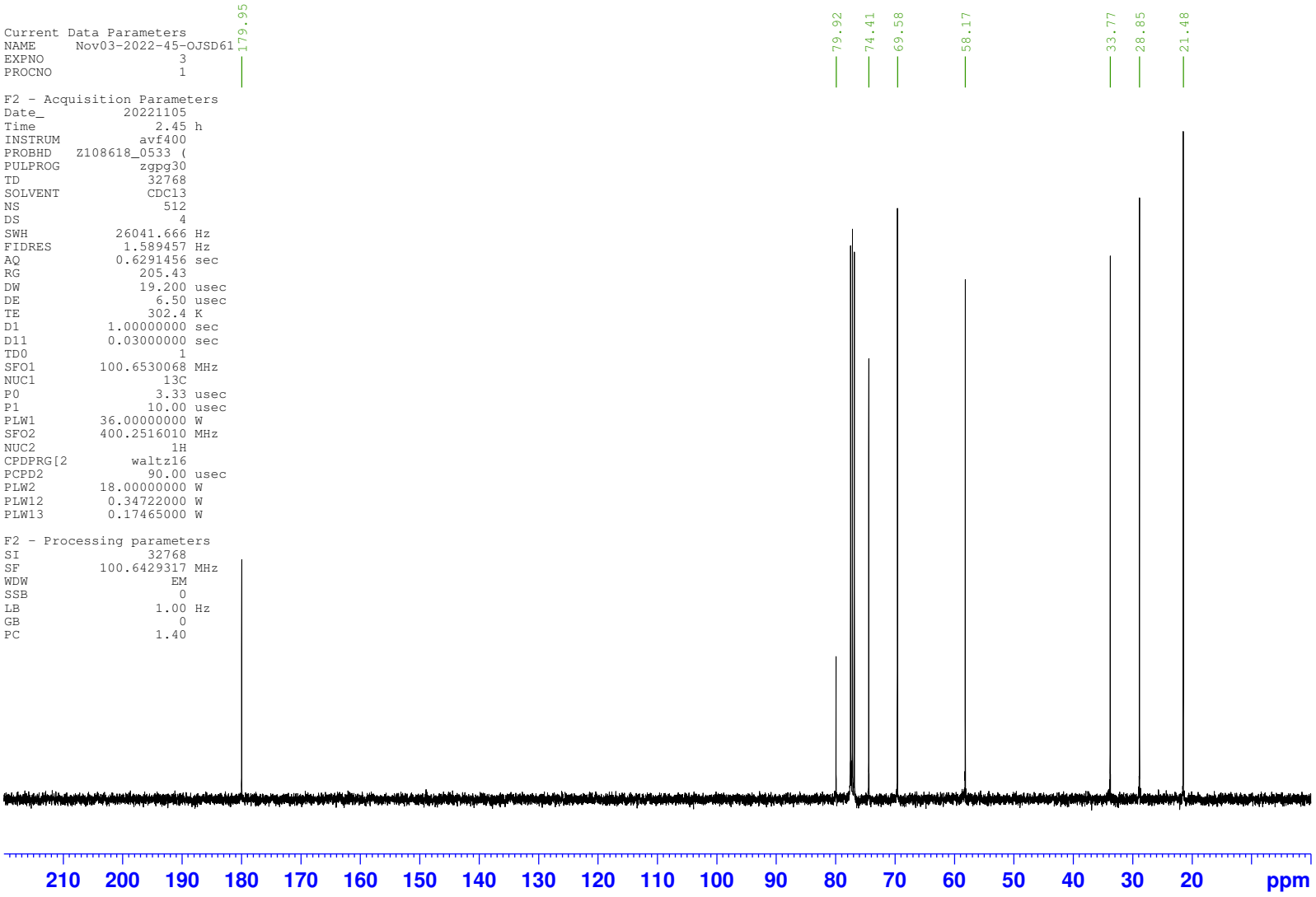



Current Data Parameters
NAME OJSE38-VT
EXPNO 4
PROCNO 1
F2 - Acquisition Parameters
Date_ 20230917
Time 12.29 h
INSTRUM avx500
PROBHD Z119877_0007 (
PULPROG zgpg30
TD 65536
SOLVENT DMSO
NS 2048
DS 4
SWH 29761.904 Hz
FIDRES 0.908261 Hz
AQ 1.1010048 sec
RG 191.37
DW 16.800 usec
DE 6.50 usec
TE 353.0 K
D1 2.00000000 sec
D11 0.03000000 sec
TD0 1
SFO1 125.8131151 MHz
NUC1 13C
P0 3.33 usec
P1 10.00 usec
PLW1 49.88800049 W
SFO2 500.3020012 MHz
NUC2 1H
CPDPRG[2 waltz16
PCPD2 80.00 usec
PLW2 32.96099854 W
PLW12 1.15880001 W
PLW13 0.58285999 W
F2 - Processing parameters
SI 32768
SF 125.8006451 MHz
WDW EM
SSB 0
LB 2.00 Hz
GB 0
PC 1.40
169.38
164.25
157.80
153.29
149.36
149.26
148.47
148.37
147.42
147.31
146.52
146.42
142.72
138.99
138.96
138.93
138.90
132.50
124.14
124.11
124.09
124.06
122.97
122.65
119.48
116.85
116.71
116.49
116.35
115.97
112.53
56.08
53.63
45.33
45.17
31.85
31.26
31.13
28.40
17.06
10.80
9.94
210
200
190
180
170
160
150
140
130
120
110
100
90
80
70
60
50
40
30
20
ppm

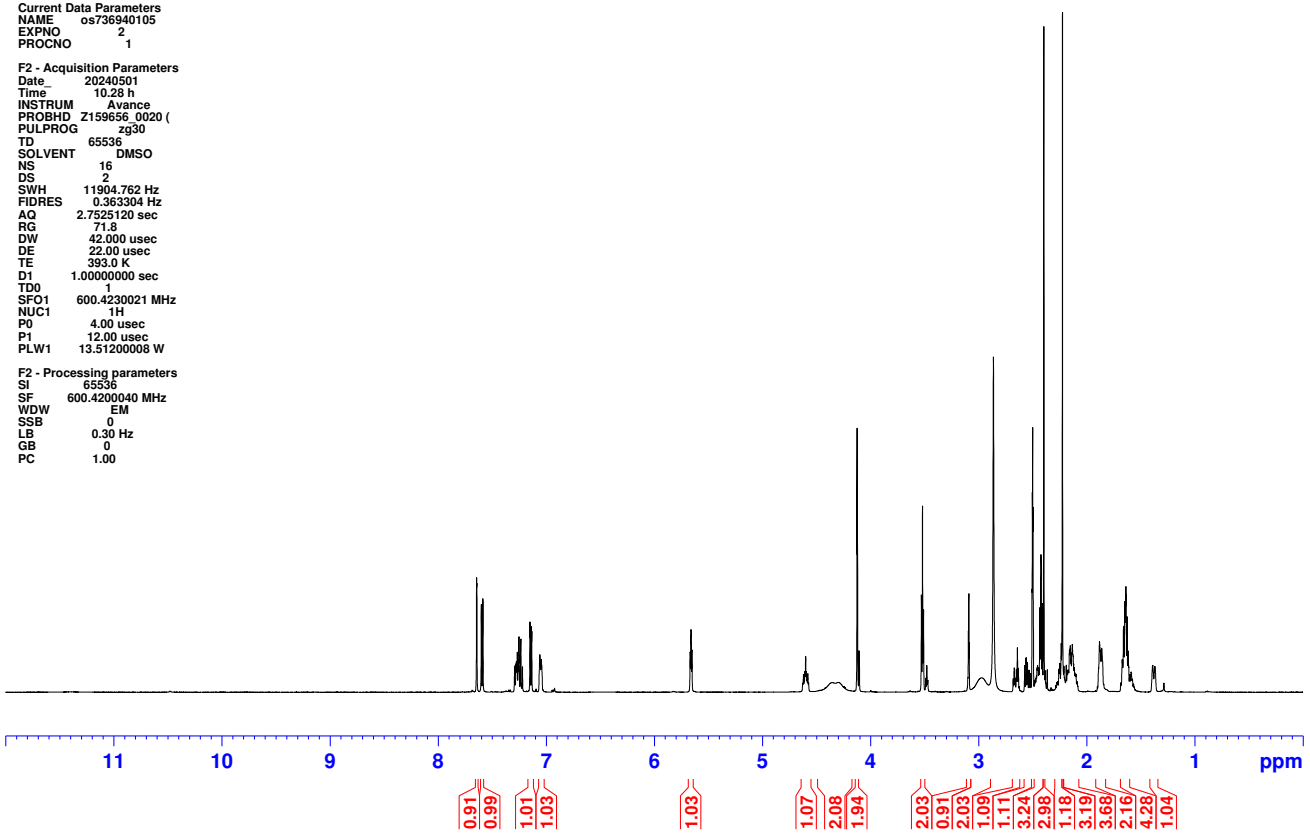

Current Data Parameters
NAME OJSE38-VT
EXPNO 3
PROCNO 1
F2 - Acquisition Parameters
Date_ 20230917
Time 10.33 h
INSTRUM avx500
PROBHD Z119877_0007 (
PULPROG zg30
TD 131072
SOLVENT DMSO
NS 16
DS 4
SWH 113636.367 Hz
FIDRES 1.733953 Hz
AQ 0.5767168 sec
RG 191.37
DW 4.400 usec
DE 6.50 usec
TE 353.0 K
D1 1.00000000 sec
TD0 1
SFO1 470.7052618 MHz
NUC1 19F
P0 5.00 usec
P1 15.00 usec
PLW1 32.96099854 W
F2 - Processing parameters
SI 65536
SF 470.7523370 MHz
WDW EM
SSB 0
LB 0.30 Hz
GB 0
PC 1.00
138.05
138.07
138.10
138.12
138.15
140.80
140.82
140.83
140.84
140.84
140.85
140.86
140.87
140.89
-20
-40
-60
-80
-100
-120
-140
-160
-180
-200
ppm

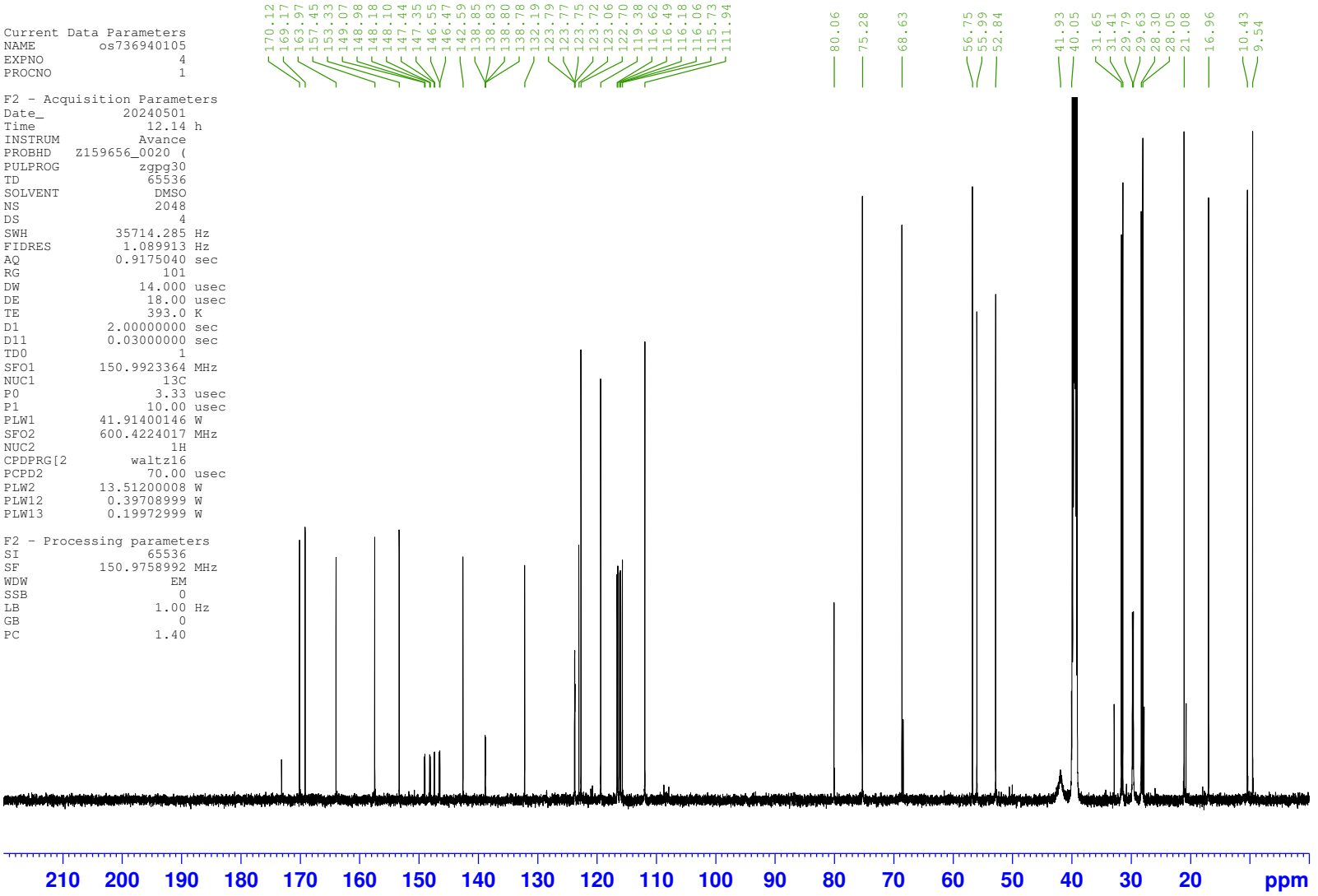
5-(Prop-2-yn-1-yloxy)pentanoic acid (39)

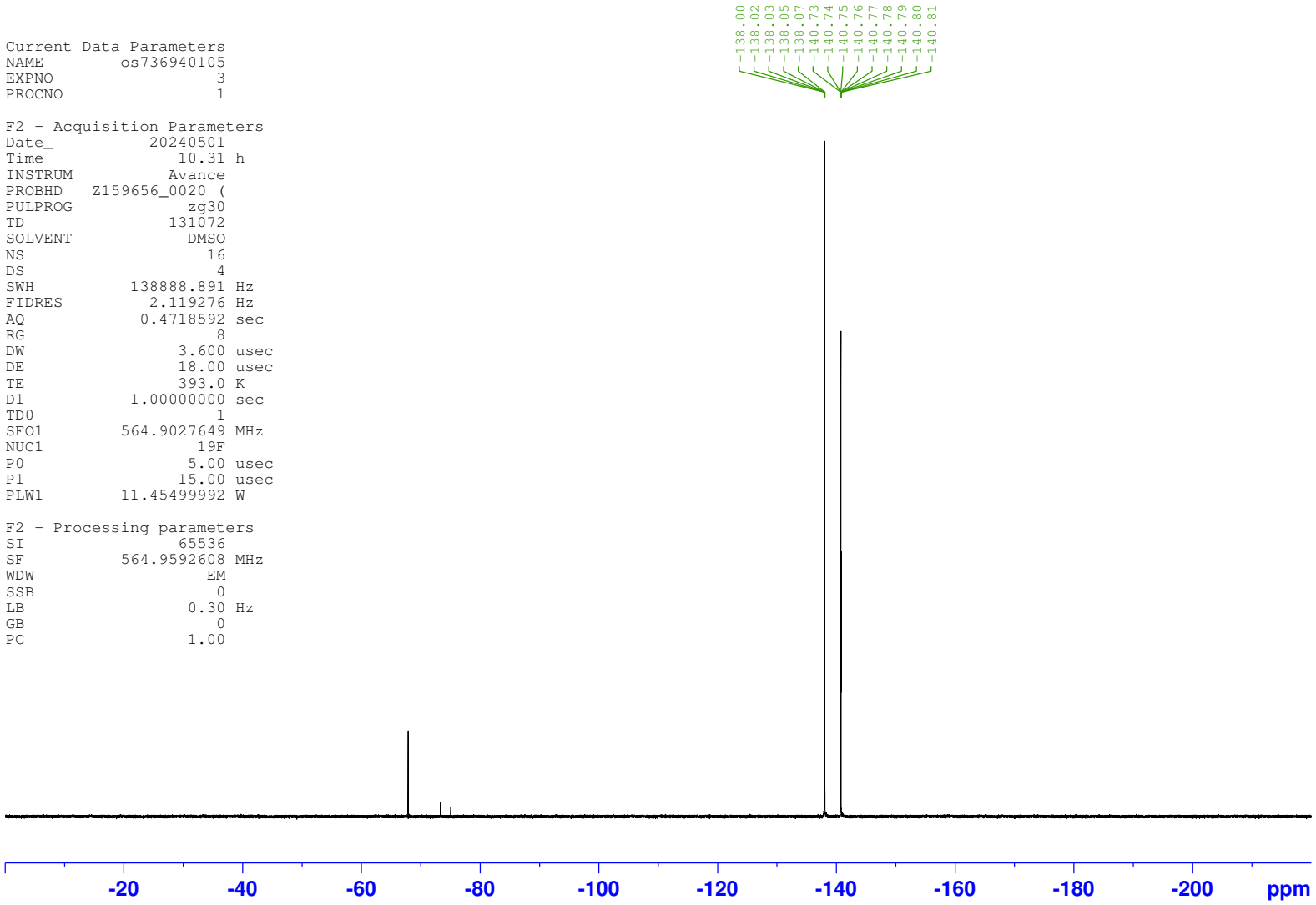



Current Data Parameters
NAME Nov03-2022-45-OJSD61
EXPNO 3
PROCNO 1
F2 - Acquisition Parameters
Date_ 20221105
Time 2.45 h
INSTRUM avf400
PROBHD Z108618_0533 (
PULPROG zgpg30
TD 32768
SOLVENT CDCl3
NS 512
DS 4
SWH 26041.666 Hz
FIDRES 1.589457 Hz
AQ 0.6291456 sec
RG 205.43
DW 19.200 usec
DE 6.50 usec
TE 302.4 K
D1 1.00000000 sec
D11 0.03000000 sec
TD0 1
SFO1 100.6530068 MHz
NUC1 13C
P0 3.33 usec
P1 10.00 usec
PLW1 36.00000000 W
SFO2 400.2516010 MHz
NUC2 1H
CPDPRG[2 waltz16
PCPD2 90.00 usec
PLW2 18.00000000 W
PLW12 0.34722000 W
PLW13 0.17465000 W
F2 - Processing parameters
SI 32768
SF 100.6429317 MHz
WDW EM
SSB 0
LB 1.00 Hz
GB 0
PC 1.40
179.95
79.92
74.41
69.58
58.17
33.77
28.85
21.48
210 200 190 180 170 160 150 140 130 120 110 100 90 80 70 60 50 40 30 20 ppm

(6S)-1-(3,4-Difluorophenyl)-6-(5-(3,5-dimethyl-1,2-oxazol-4-yl)-1-(1-(5-(prop-2-yn-1-yloxy)pentanoyl)piperidin-4-yl)-1H-1,3-benzimidazol-2-yl]piperidin-2-one (40)




Current Data Parameters
NAME os736940105
EXPNO 4
PROCNO 1
F2 - Acquisition Parameters
Date_ 20240501
Time 12.14 h
INSTRUM Avance
PROBHD Z159656_0020 (
PULPROG zgpg30
TD 65536
SOLVENT DMSO
NS 2048
DS 4
SWH 35714.285 Hz
FIDRES 1.089913 Hz
AQ 0.9175040 sec
RG 101
DW 14.000 usec
DE 18.00 usec
TE 393.0 K
D1 2.00000000 sec
D11 0.03000000 sec
TD0 1
SFO1 150.9923364 MHz
NUC1 13C
P0 3.33 usec
P1 10.00 usec
PLW1 41.91400146 W
SFO2 600.4224017 MHz
NUC2 1H
CPDPRG[2 waltz16
PCPD2 70.00 usec
PLW2 13.51200008 W
PLW12 0.39708999 W
PLW13 0.19972999 W
F2 - Processing parameters
SI 65536
SF 150.9758992 MHz
WDW EM
SSB 0
LB 1.00 Hz
GB 0
PC 1.40
170.12
169.17
163.97
157.45
153.33
149.07
148.98
148.18
148.10
147.44
147.35
146.55
146.47
142.59
138.85
138.83
138.80
138.78
132.19
123.79
123.77
123.75
123.72
123.06
122.70
119.38
116.62
116.49
116.18
116.06
115.73
111.94
80.06
75.28
68.63
56.75
55.99
52.84
41.93
40.05
31.65
31.41
29.79
29.63
28.30
28.05
21.08
16.96
10.43
9.54
210 200 190 180 170 160 150 140 130 120 110 100 90 80 70 60 50 40 30 20 ppm

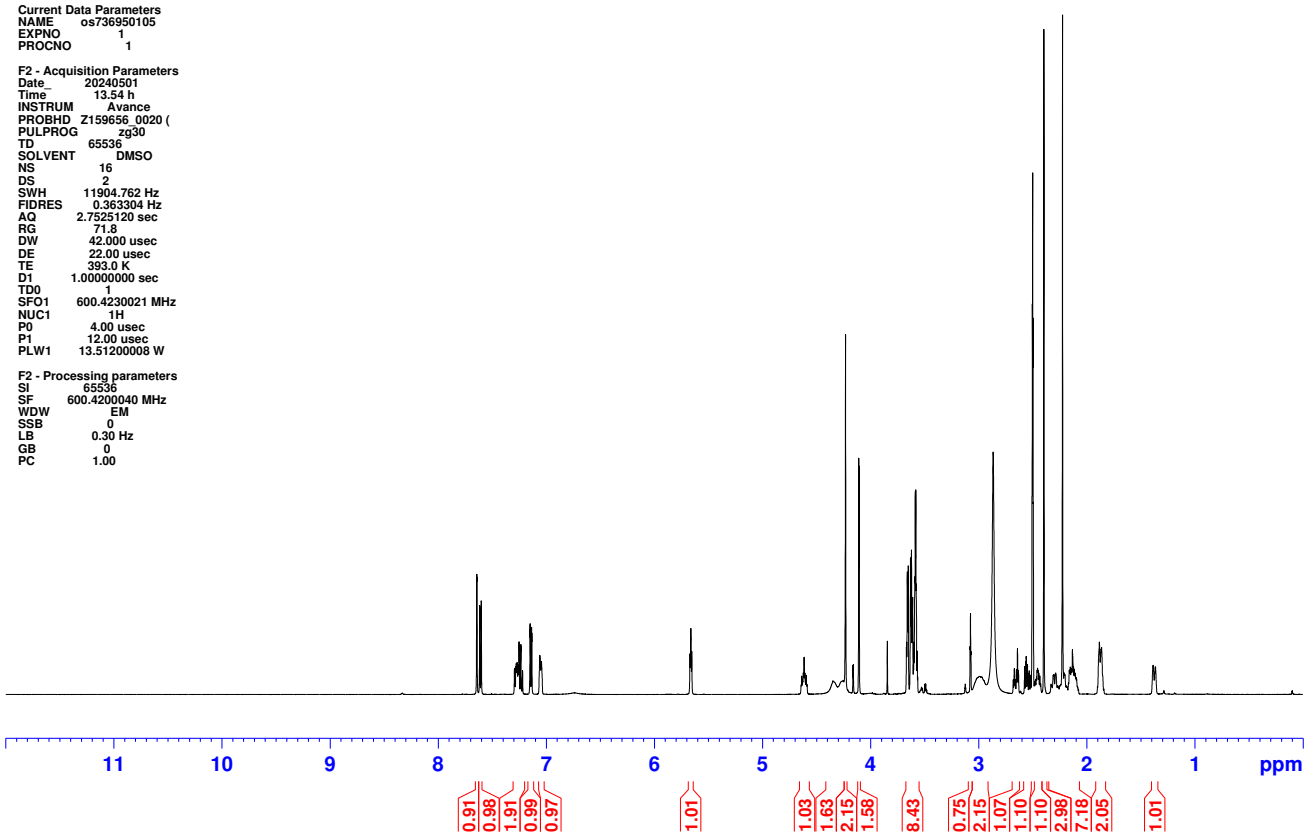


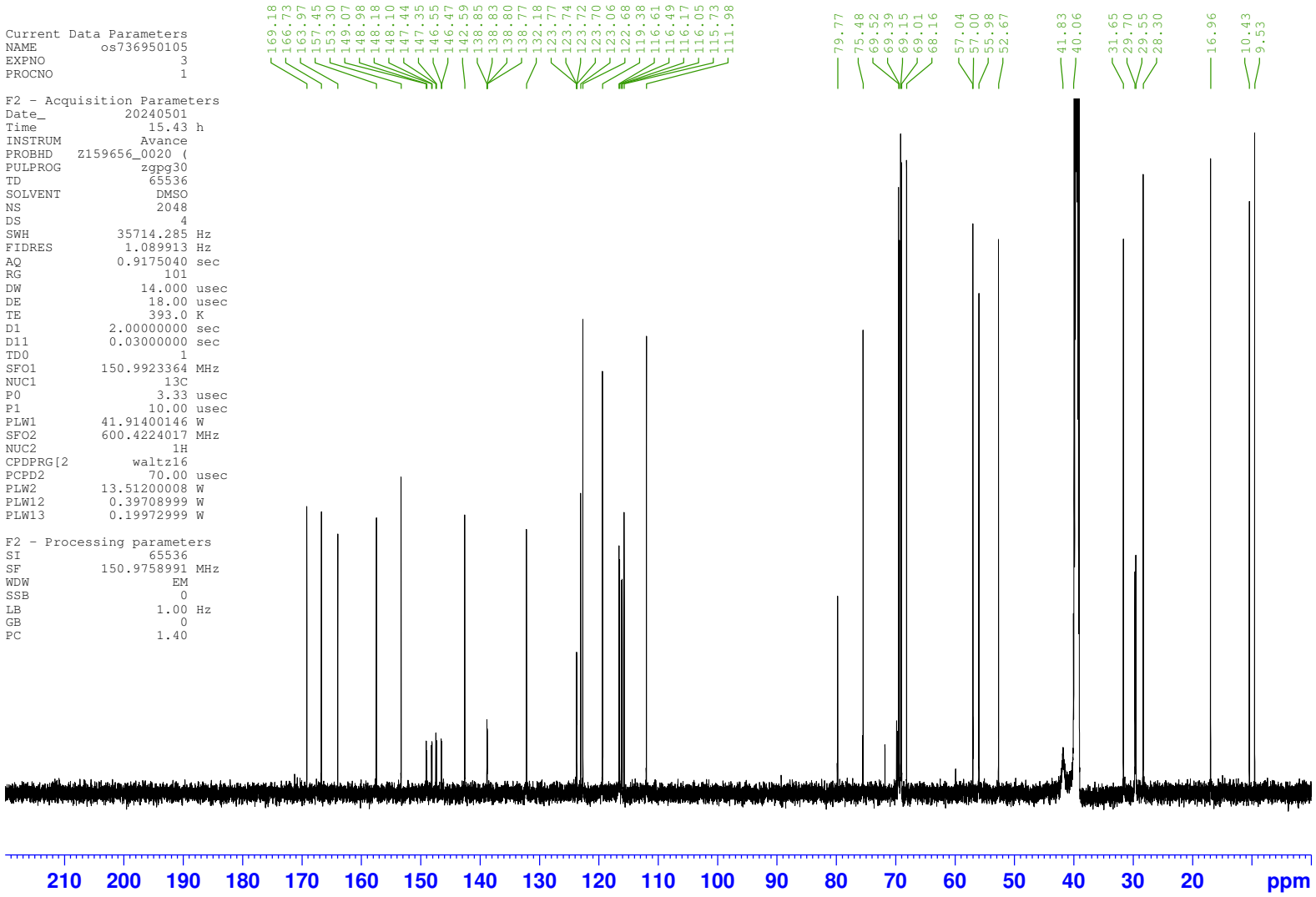

```
Current Data Parameters
NAME         os736940105
EXPNO                  3
PROCNO                 1

F2 - Acquisition Parameters
Date_           20240501
Time              10.31 h
INSTRUM           Avance
PROBHD   Z159656_0020 (
PULPROG             zg30
TD                131072
SOLVENT             DMSO
NS                    16
DS                     4
SWH           138888.891 Hz
FIDRES          2.119276 Hz
AQ             0.4718592 sec
RG                     8
DW                 3.600 usec
DE                18.00 usec
TE                393.0 K
D1            1.00000000 sec
TD0                    1
SFO1         564.9027649 MHz
NUC1                19F
P0                 5.00 usec
P1                15.00 usec
PLW1         11.45499992 W

F2 - Processing parameters
SI                 65536
SF           564.9592608 MHz
WDW                   EM
SSB                    0
LB                  0.30 Hz
GB                     0
PC                  1.00
```

(6*S*)-1-(3,4-Difluorophenyl)-6-(5-(3,5-dimethyl-1,2-oxazol-4-yl)-1-(1-(2-(2-(2-prop-2-ynoxyethoxy)ethoxy)acetyl)piperidin-4-yl)benzimidazol-2-yl)piperidin-2-one (41)

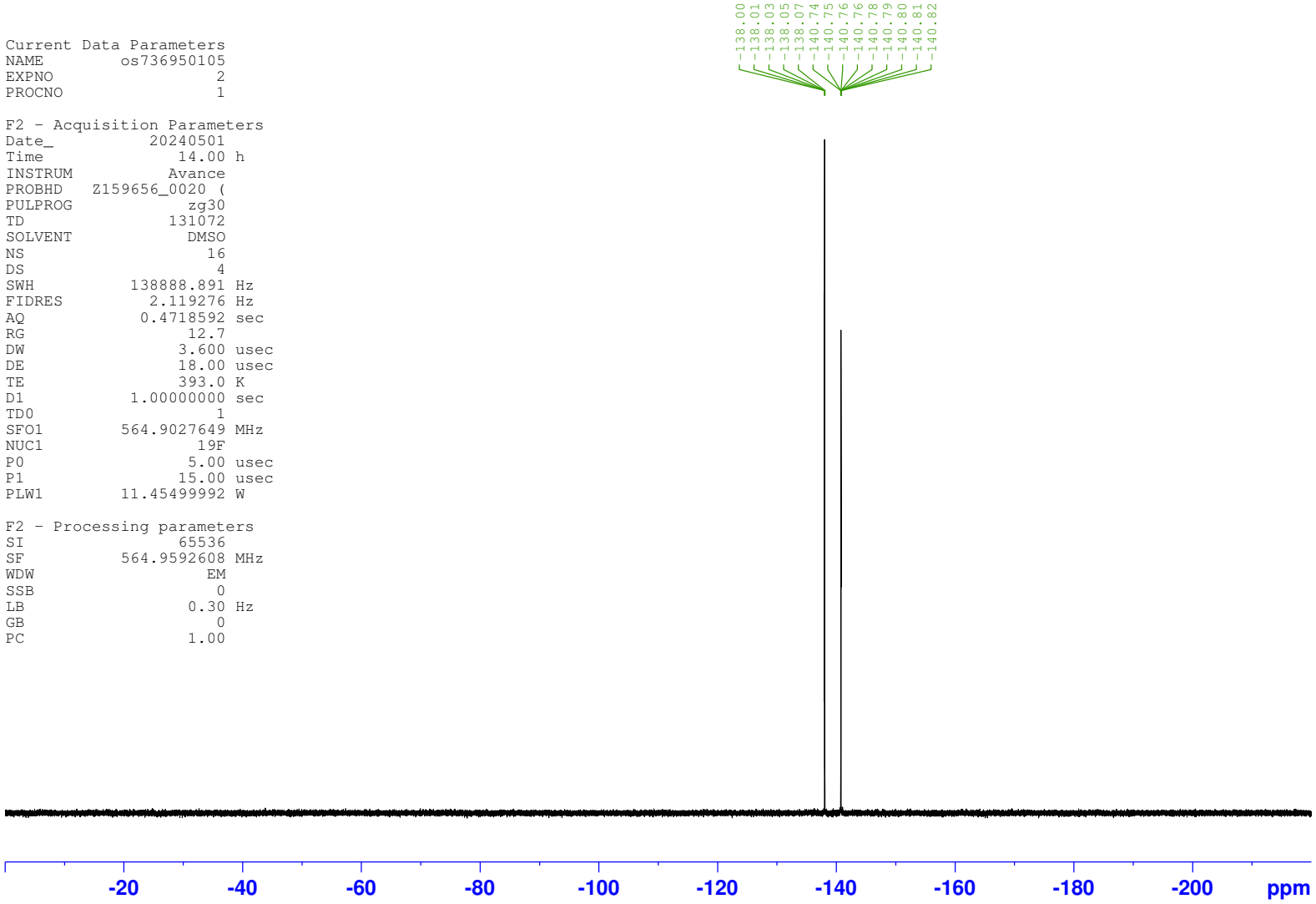



Current Data Parameters
NAME os736950105
EXPNO 3
PROCNO 1
F2 - Acquisition Parameters
Date_ 20240501
Time 15.43 h
INSTRUM Avance
PROBHD Z159656_0020 (
PULPROG zgpg30
TD 65536
SOLVENT DMSO
NS 2048
DS 4
SWH 35714.285 Hz
FIDRES 1.089913 Hz
AQ 0.9175040 sec
RG 101
DW 14.000 usec
DE 18.00 usec
TE 393.0 K
D1 2.00000000 sec
D11 0.03000000 sec
TD0 1
SFO1 150.9923364 MHz
NUC1 13C
P0 3.33 usec
P1 10.00 usec
PLW1 41.91400146 W
SFO2 600.4224017 MHz
NUC2 1H
CPDPRG[2 waltz16
PCPD2 70.00 usec
PLW2 13.51200008 W
PLW12 0.39708999 W
PLW13 0.19972999 W
F2 - Processing parameters
SI 65536
SF 150.9758991 MHz
WDW EM
SSB 0
LB 1.00 Hz
GB 0
PC 1.40
169.18
166.73
163.97
157.45
153.30
149.07
148.98
148.18
148.10
147.44
147.35
146.55
146.47
142.59
138.85
138.83
138.80
138.77
132.18
123.77
123.74
123.72
123.70
123.06
122.68
119.38
116.61
116.49
116.17
116.05
115.73
111.98
79.77
75.48
69.52
69.39
69.15
69.01
68.16
57.04
57.00
55.98
52.67
41.83
40.06
31.65
29.70
29.55
28.30
16.96
10.43
9.53
210
200
190
180
170
160
150
140
130
120
110
100
90
80
70
60
50
40
30
20
ppm

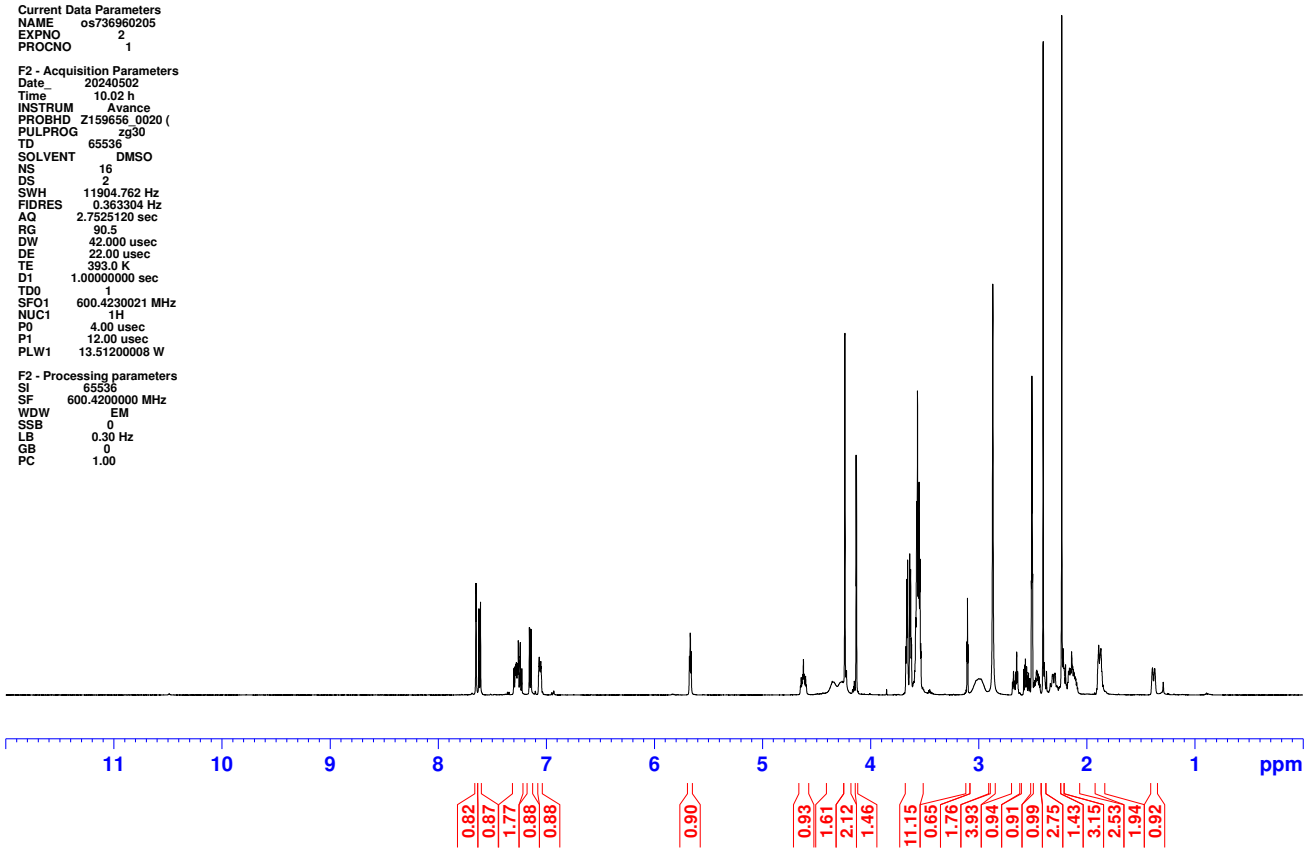
```
Current Data Parameters
NAME         os736950105
EXPNO                  2
PROCNO                 1

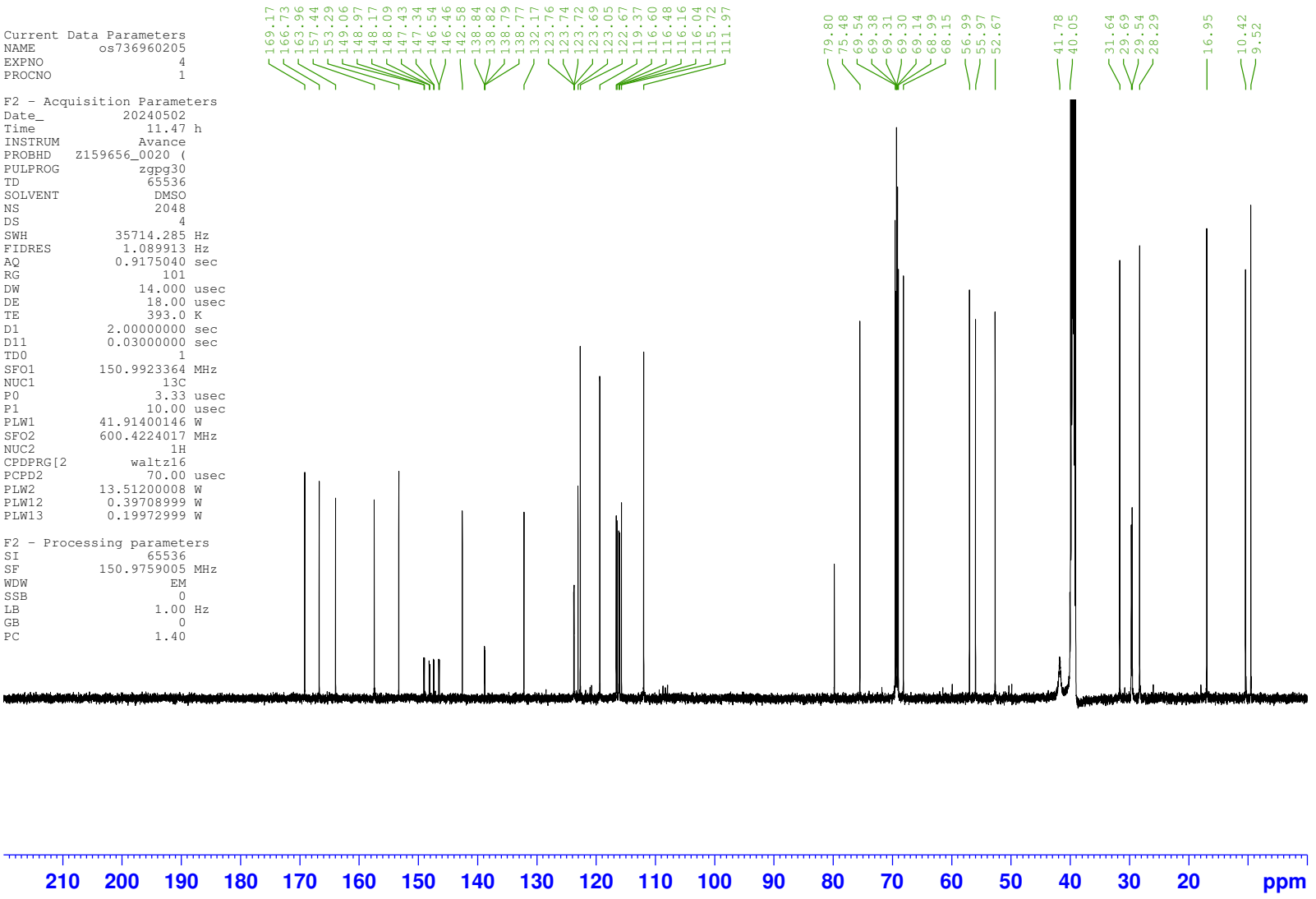
F2 - Acquisition Parameters
Date_           20240501
Time              14.00 h
INSTRUM           Avance
PROBHD   Z159656_0020 (
PULPROG             zg30
TD                131072
SOLVENT              DMSO
NS                     16
DS                      4
SWH           138888.891 Hz
FIDRES          2.119276 Hz
AQ             0.4718592 sec
RG                  12.7
DW                 3.600 usec
DE                18.00 usec
TE                393.0 K
D1            1.00000000 sec
TD0                    1
SFO1         564.9027649 MHz
NUC1                19F
P0                 5.00 usec
P1                15.00 usec
PLW1         11.45499992 W

F2 - Processing parameters
SI                 65536
SF           564.9592608 MHz
WDW                   EM
SSB                    0
LB                  0.30 Hz
GB                     0
PC                  1.00
```



(6S)-1-(3,4-Difluorophenyl)-6-(5-(3,5-dimethyl-1,2-oxazol-4-yl)-1-(1-(3,6,9,12-tetraoxapentadec-14-ynoyl)piperidin-4-yl)benzimidazol-2-yl)piperidin-2-one(6*S*)-1-(3,4-Difluorophenyl)-6-(5-(3,5-dimethyl-1,2-oxazol-4-yl)-1-(1-(3,6,9,12-tetraoxapentadec-14-ynoyl)piperidin-4-yl)benzimidazol-2-yl)piperidin-2-one (42)

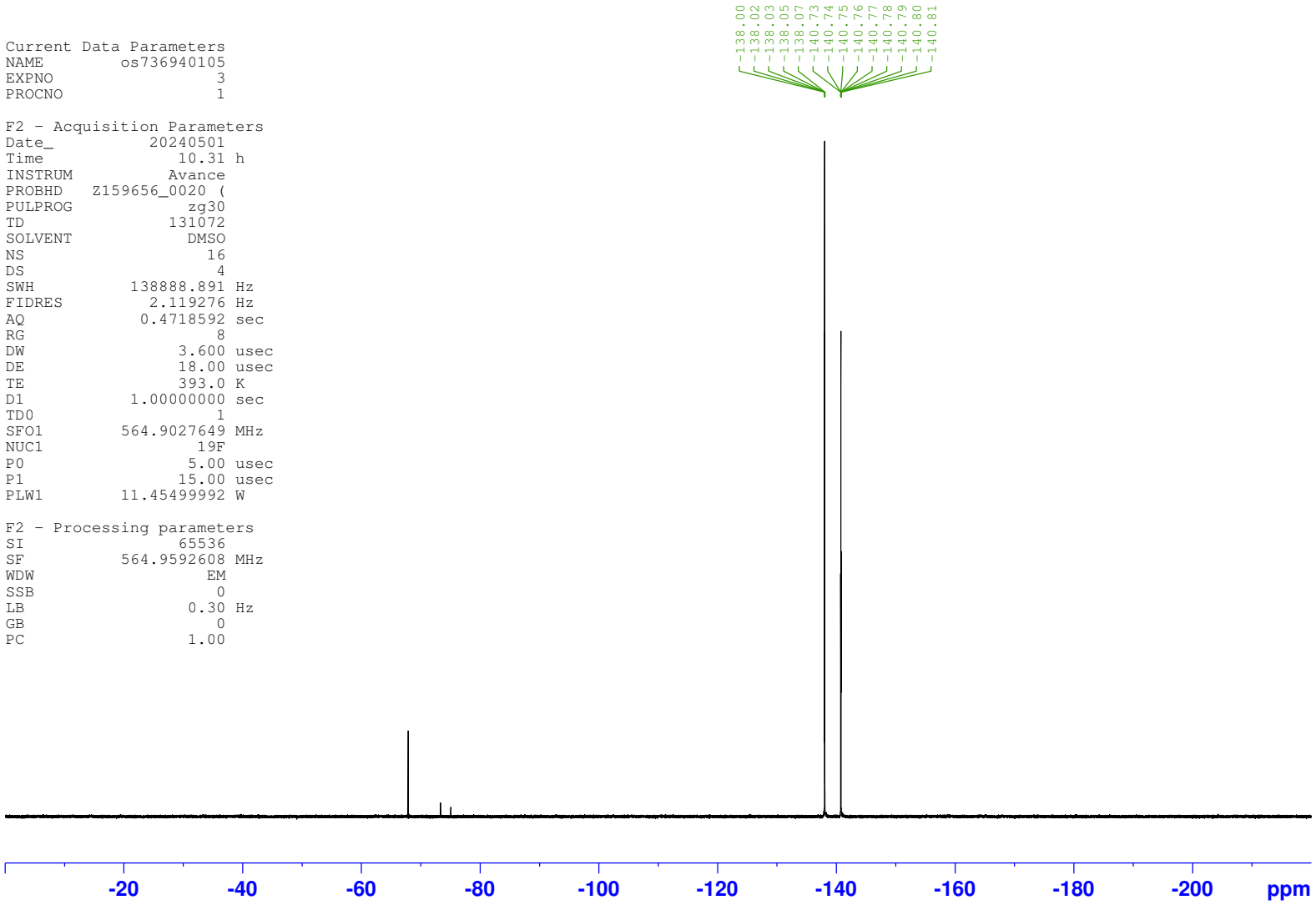



Current Data Parameters
NAME os736960205
EXPNO 4
PROCNO 1
F2 - Acquisition Parameters
Date_ 20240502
Time 11.47 h
INSTRUM Avance
PROBHD Z159656_0020 (
PULPROG zgpg30
TD 65536
SOLVENT DMSO
NS 2048
DS 4
SWH 35714.285 Hz
FIDRES 1.089913 Hz
AQ 0.9175040 sec
RG 101
DW 14.000 usec
DE 18.00 usec
TE 393.0 K
D1 2.00000000 sec
D11 0.03000000 sec
TD0 1
SFO1 150.9923364 MHz
NUC1 13C
P0 3.33 usec
P1 10.00 usec
PLW1 41.91400146 W
SFO2 600.4224017 MHz
NUC2 1H
CPDPRG[2 waltz16
PCPD2 70.00 usec
PLW2 13.51200008 W
PLW12 0.39708999 W
PLW13 0.19972999 W
F2 - Processing parameters
SI 65536
SF 150.9759005 MHz
WDW EM
SSB 0
LB 1.00 Hz
GB 0
PC 1.40
169.17
166.73
163.96
157.44
153.29
149.06
148.97
148.17
148.09
147.43
147.34
146.54
146.46
142.58
138.84
138.82
138.79
138.77
132.17
123.76
123.74
123.72
123.69
123.05
122.67
119.37
116.60
116.48
116.16
116.04
115.72
111.97
79.80
75.48
69.54
69.38
69.31
69.30
69.14
68.99
68.15
56.99
55.97
52.67
41.78
40.05
31.64
29.69
29.54
28.29
16.95
10.42
9.52
210
200
190
180
170
160
150
140
130
120
110
100
90
80
70
60
50
40
30
20
ppm

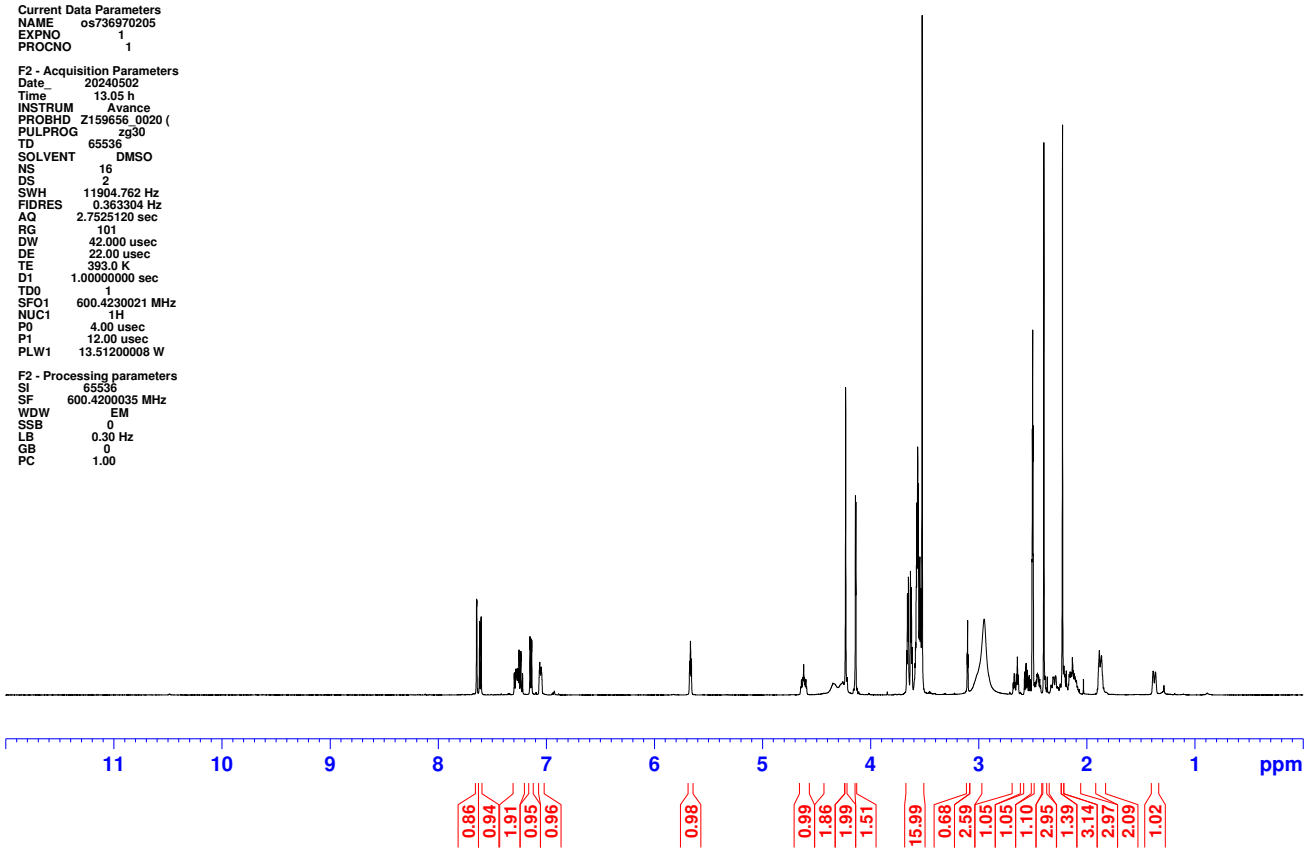
```
Current Data Parameters
NAME         os736940105
EXPNO                  3
PROCNO                 1

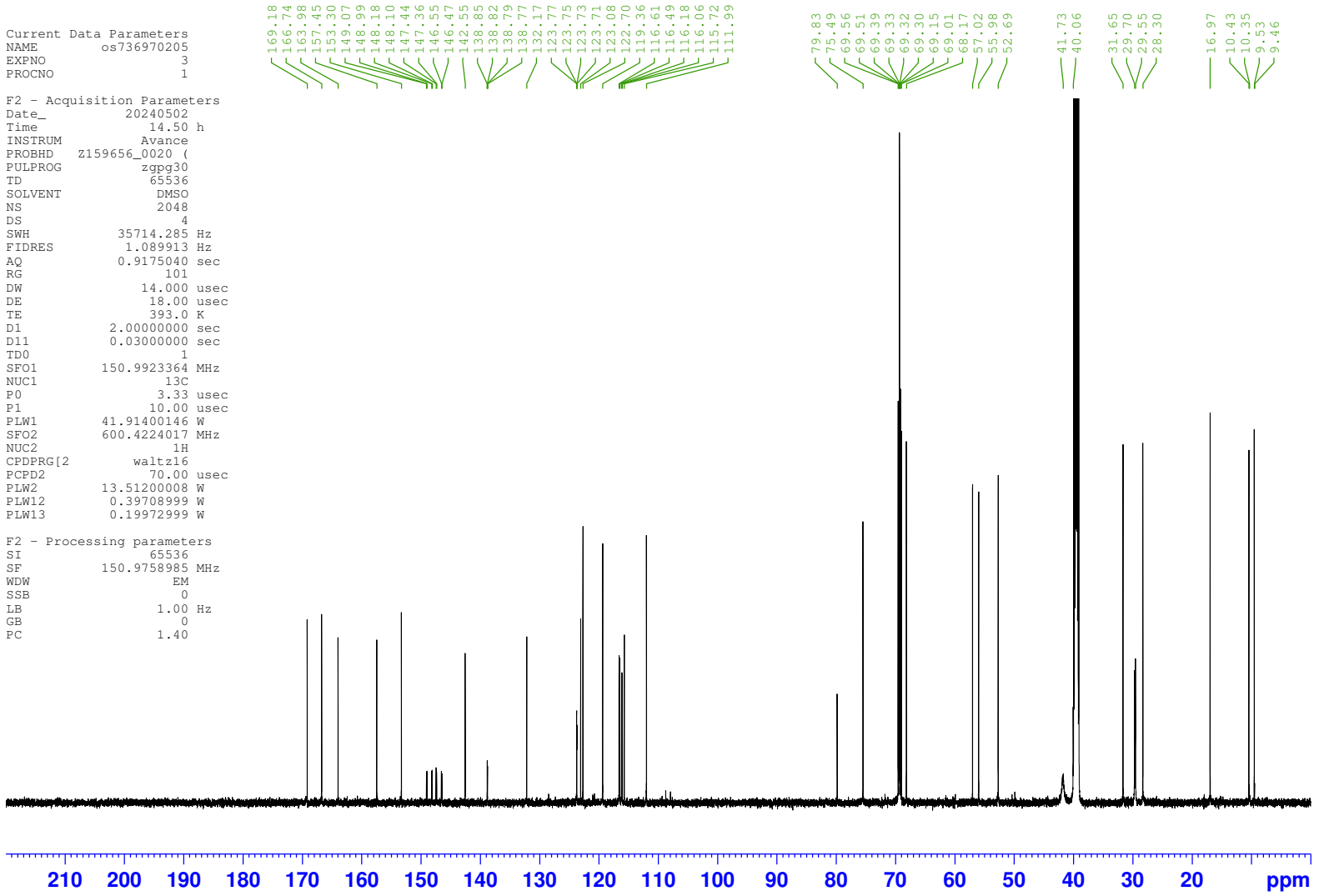
F2 - Acquisition Parameters
Date_           20240501
Time              10.31 h
INSTRUM           Avance
PROBHD   Z159656_0020 (
PULPROG             zg30
TD                131072
SOLVENT              DMSO
NS                     16
DS                      4
SWH           138888.891 Hz
FIDRES          2.119276 Hz
AQ             0.4718592 sec
RG                     8
DW                 3.600 usec
DE                18.00 usec
TE                393.0 K
D1            1.00000000 sec
TD0                    1
SFO1         564.9027649 MHz
NUC1                19F
P0                 5.00 usec
P1                15.00 usec
PLW1         11.45499992 W

F2 - Processing parameters
SI                 65536
SF           564.9592608 MHz
WDW                   EM
SSB                    0
LB                  0.30 Hz
GB                     0
PC                  1.00
```



(6S)-1-(3,4-Difluorophenyl)-6-(5-(3,5-dimethyl-1,2-oxazol-4-yl)-1-(1-(3,6,9,12,15-pentaoxaoctadec-17-ynoyl)piperidin-4-yl)benzimidazol-2-yl)piperidin-2-one(6*S*)-1-(3,4-Difluorophenyl)-6-(5-(3,5-dimethyl-1,2-oxazol-4-yl)-1-(1-(3,6,9,12,15-pentaoxaoctadec-17-ynoyl)piperidin-4-yl)benzimidazol-2-yl)piperidin-2-one (43)



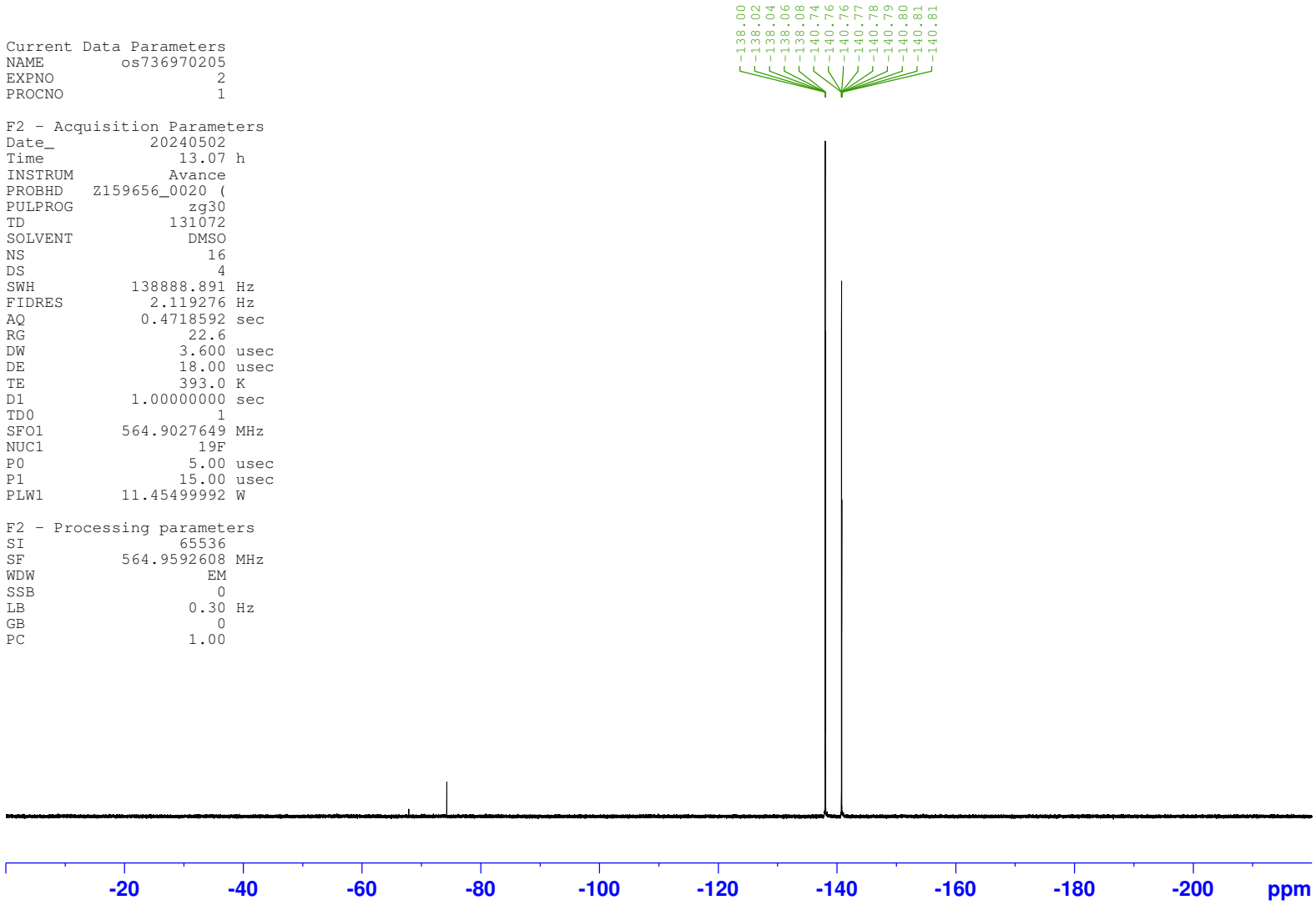



```
Current Data Parameters
NAME         os736970205
EXPNO                  3
PROCNO                 1

F2 - Acquisition Parameters
Date_           20240502
Time               14.50 h
INSTRUM           Avance
PROBHD   Z159656_0020 (
PULPROG          zgpg30
TD                65536
SOLVENT            DMSO
NS                 2048
DS                    4
SWH           35714.285 Hz
FIDRES         1.089913 Hz
AQ            0.9175040 sec
RG                  101
DW               14.000 usec
DE               18.00 usec
TE                393.0 K
D1           2.00000000 sec
D11          0.03000000 sec
TD0                   1
SFO1        150.9923364 MHz
NUC1               13C
P0                3.33 usec
P1               10.00 usec
PLW1        41.91400146 W
SFO2        600.4224017 MHz
NUC2                1H
CPDPRG[2        waltz16
PCPD2            70.00 usec
PLW2        13.51200008 W
PLW12        0.39708999 W
PLW13        0.19972999 W

F2 - Processing parameters
SI                65536
SF          150.9758985 MHz
WDW                  EM
SSB                   0
LB                 1.00 Hz
GB                    0
PC                 1.40
```

lv

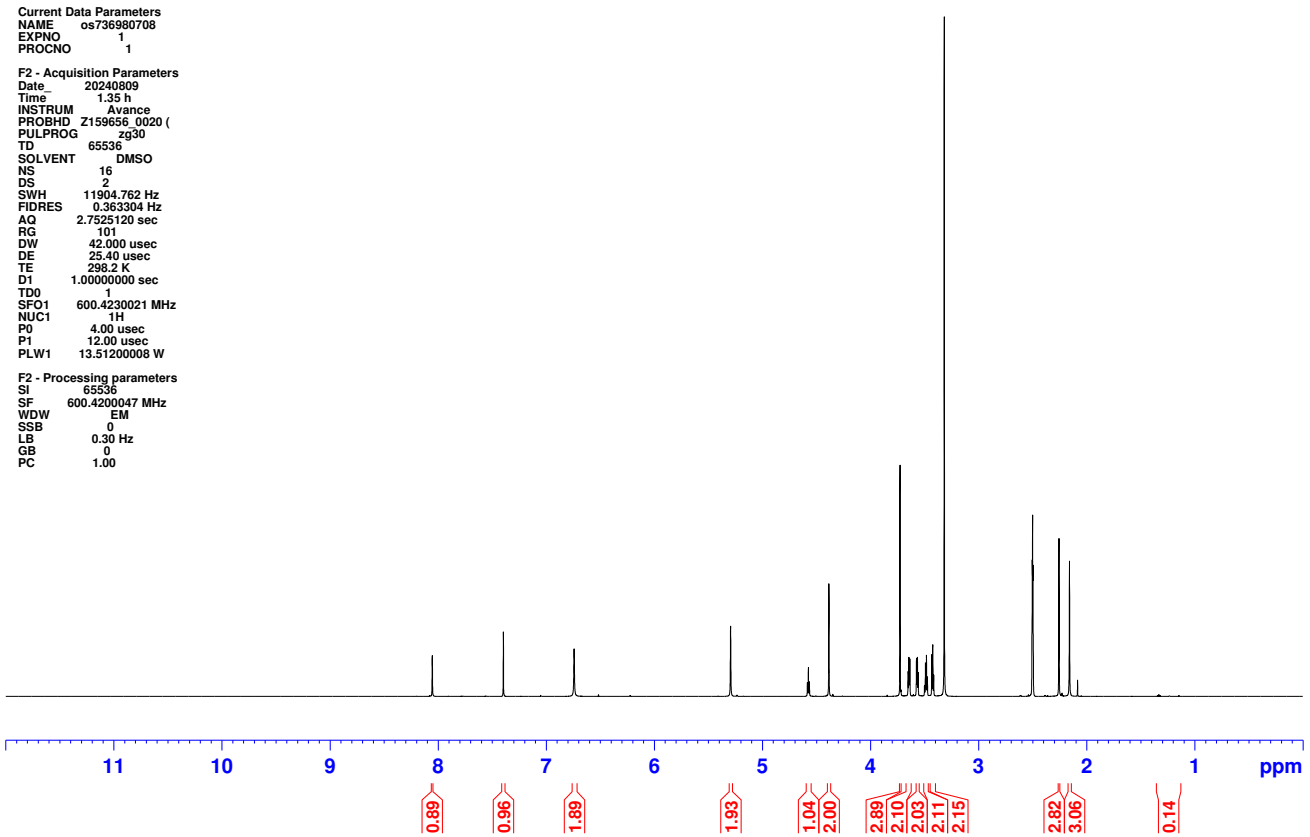


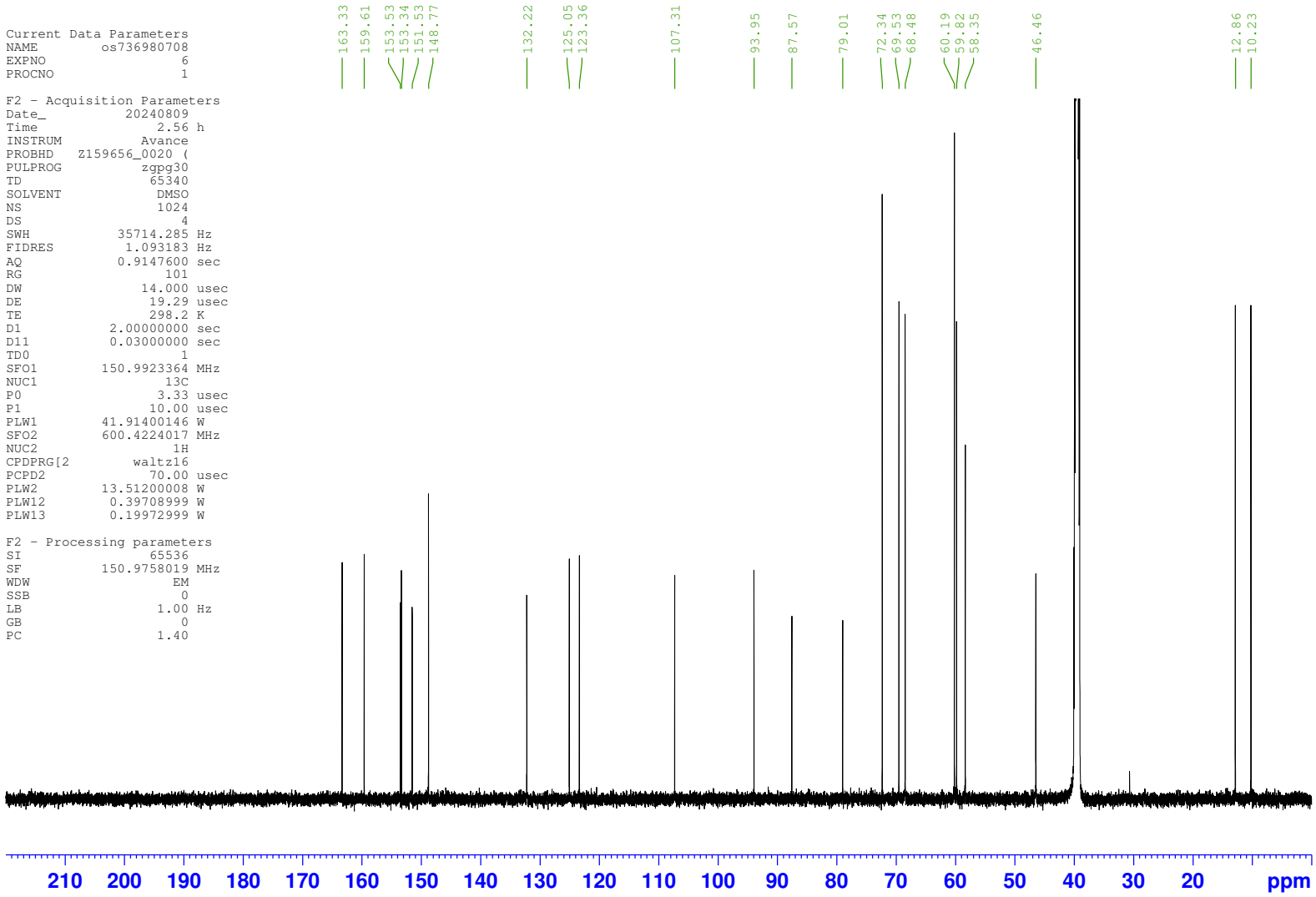

```
Current Data Parameters
NAME         os736970205
EXPNO                  2
PROCNO                 1

F2 - Acquisition Parameters
Date_           20240502
Time              13.07 h
INSTRUM          Avance
PROBHD   Z159656_0020 (
PULPROG             zg30
TD                131072
SOLVENT             DMSO
NS                    16
DS                     4
SWH           138888.891 Hz
FIDRES          2.119276 Hz
AQ             0.4718592 sec
RG                  22.6
DW                3.600 usec
DE               18.00 usec
TE                393.0 K
D1           1.00000000 sec
TD0                    1
SFO1         564.9027649 MHz
NUC1                19F
P0                 5.00 usec
P1                15.00 usec
PLW1         11.45499992 W

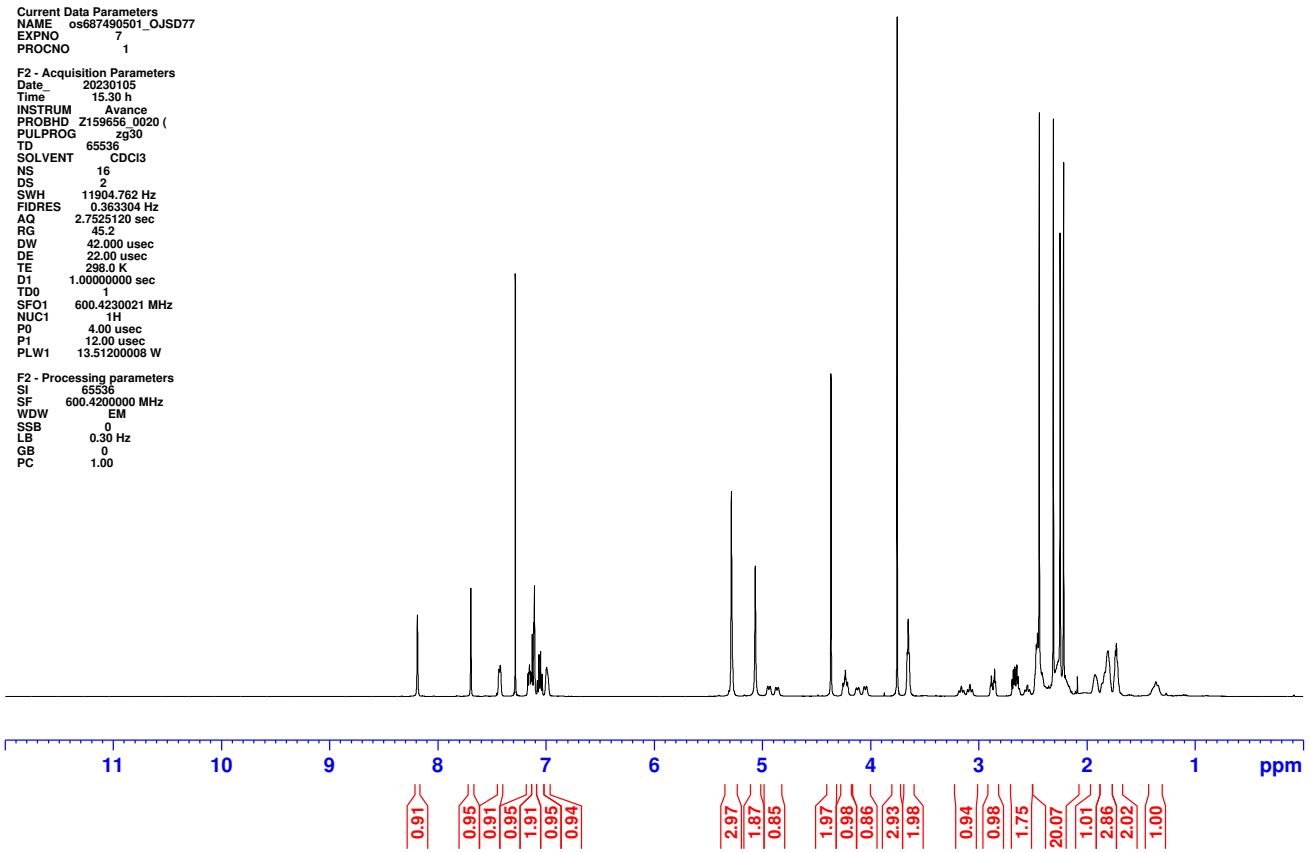
F2 - Processing parameters
SI                 65536
SF           564.9592608 MHz
WDW                   EM
SSB                    0
LB                  0.30 Hz
GB                     0
PC                  1.00
```

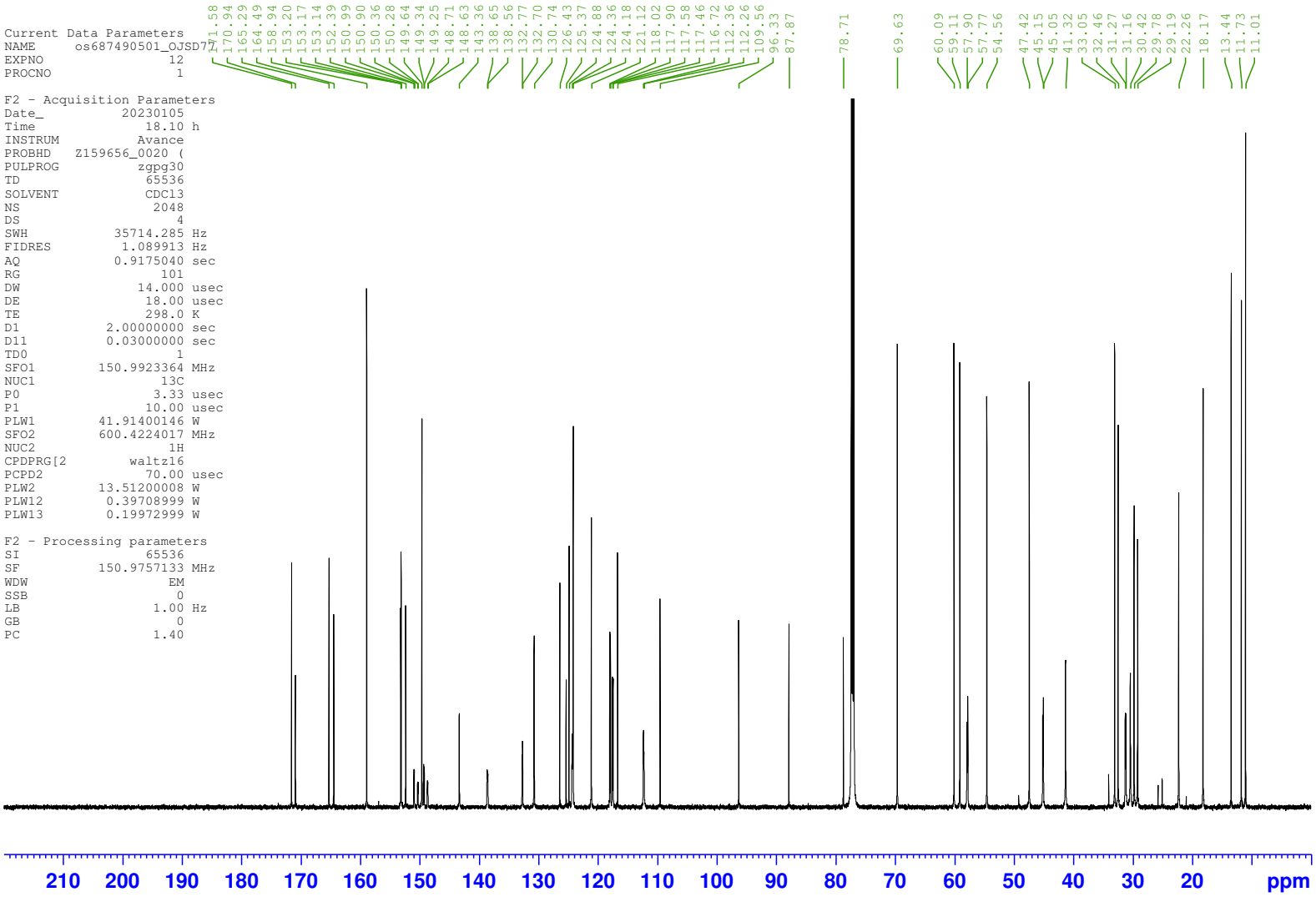
2-(2-(3-(2-Amino-4-chloro-7-((4-methoxy-3,5-dimethylpyridin-2-yl)methyl)pyrrolo[2,3-*d*]pyrimidin-5-yl)prop-2-ynoxy)ethoxy)ethanol (44)




Current Data Parameters
NAME os736980708
EXPNO 6
PROCNO 1
F2 - Acquisition Parameters
Date_ 20240809
Time 2.56 h
INSTRUM Avance
PROBHD Z159656_0020 (
PULPROG zgpg30
TD 65340
SOLVENT DMSO
NS 1024
DS 4
SWH 35714.285 Hz
FIDRES 1.093183 Hz
AQ 0.9147600 sec
RG 101
DW 14.000 usec
DE 19.29 usec
TE 298.2 K
D1 2.00000000 sec
D11 0.03000000 sec
TD0 1
SFO1 150.9923364 MHz
NUC1 13C
P0 3.33 usec
P1 10.00 usec
PLW1 41.91400146 W
SFO2 600.4224017 MHz
NUC2 1H
CPDPRG[2 waltz16
PCPD2 70.00 usec
PLW2 13.51200008 W
PLW12 0.39708999 W
PLW13 0.19972999 W
F2 - Processing parameters
SI 65536
SF 150.9758019 MHz
WDW EM
SSB 0
LB 1.00 Hz
GB 0
PC 1.40
163.33
159.61
153.53
153.34
151.53
148.77
132.22
125.05
123.36
107.31
93.95
87.57
79.01
72.34
69.53
68.48
60.19
59.82
58.35
46.46
12.86
10.23
210 200 190 180 170 160 150 140 130 120 110 100 90 80 70 60 50 40 30 20 ppm

(6*S*)-6-(1-(1-(5-((3-(2-Amino-4-chloro-7-((4-methoxy-3,5-dimethylpyridin-2-yl)methyl)-7*H*-pyrrolo[2,3-*d*]pyrimidin-5-yl)prop-2-yn-1-yl)oxy)pentanoyl)piperidin-4-yl)-5-(3,5-dimethyl-1,2-oxazol-4-yl)-1*H*-1,3-benzimidazol-2-yl)-1-(3,4-difluorophenyl)piperidin-2-one (AcDC-1)

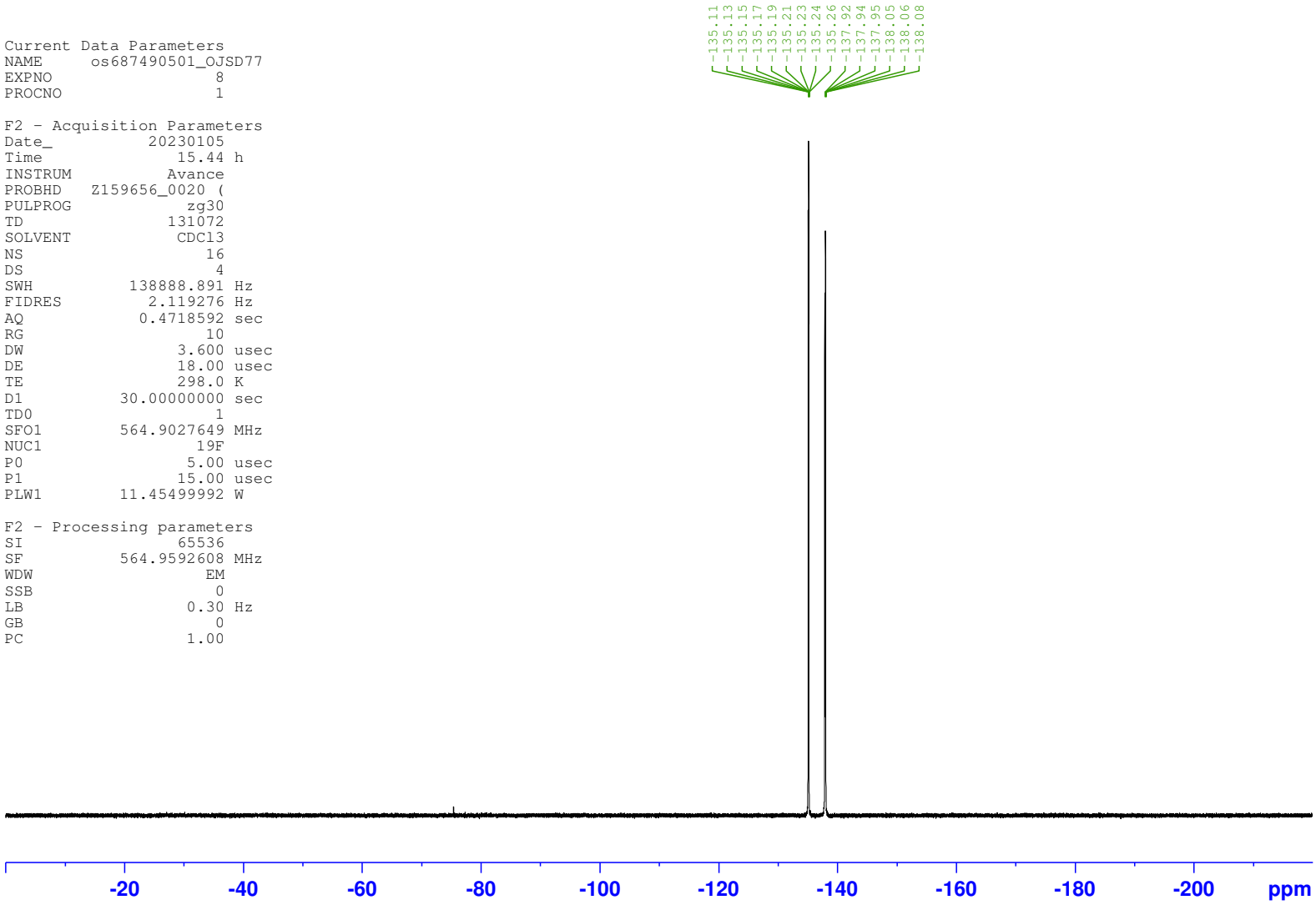



Current Data Parameters
NAME os687490501_OJSD71
EXPNO 12
PROCNO 1
F2 - Acquisition Parameters
Date_ 20230105
Time 18.10 h
INSTRUM Avance
PROBHD Z159656_0020 (
PULPROG zgpg30
TD 65536
SOLVENT CDCl3
NS 2048
DS 4
SWH 35714.285 Hz
FIDRES 1.089913 Hz
AQ 0.9175040 sec
RG 101
DW 14.000 usec
DE 18.00 usec
TE 298.0 K
D1 2.00000000 sec
D11 0.03000000 sec
TD0 1
SFO1 150.9923364 MHz
NUC1 13C
P0 3.33 usec
P1 10.00 usec
PLW1 41.91400146 W
SFO2 600.4224017 MHz
NUC2 1H
CPDPRG[2 waltz16
PCPD2 70.00 usec
PLW2 13.51200008 W
PLW12 0.39708999 W
PLW13 0.19972999 W
F2 - Processing parameters
SI 65536
SF 150.9757133 MHz
WDW EM
SSB 0
LB 1.00 Hz
GB 0
PC 1.40
171.58
170.94
165.29
164.49
158.94
153.20
153.17
153.14
152.39
150.99
150.90
150.36
150.28
149.64
149.34
149.25
148.71
148.63
143.36
138.65
138.56
132.77
132.70
130.74
126.43
125.37
124.88
124.36
124.18
121.12
118.02
117.90
117.58
117.46
116.72
112.36
112.26
109.56
96.33
87.87
78.71
69.63
60.09
59.11
57.90
57.77
54.56
47.42
45.15
45.05
41.32
33.05
32.46
31.27
31.16
30.42
29.78
29.19
22.26
18.17
13.44
11.73
11.01
210
200
190
180
170
160
150
140
130
120
110
100
90
80
70
60
50
40
30
20
ppm

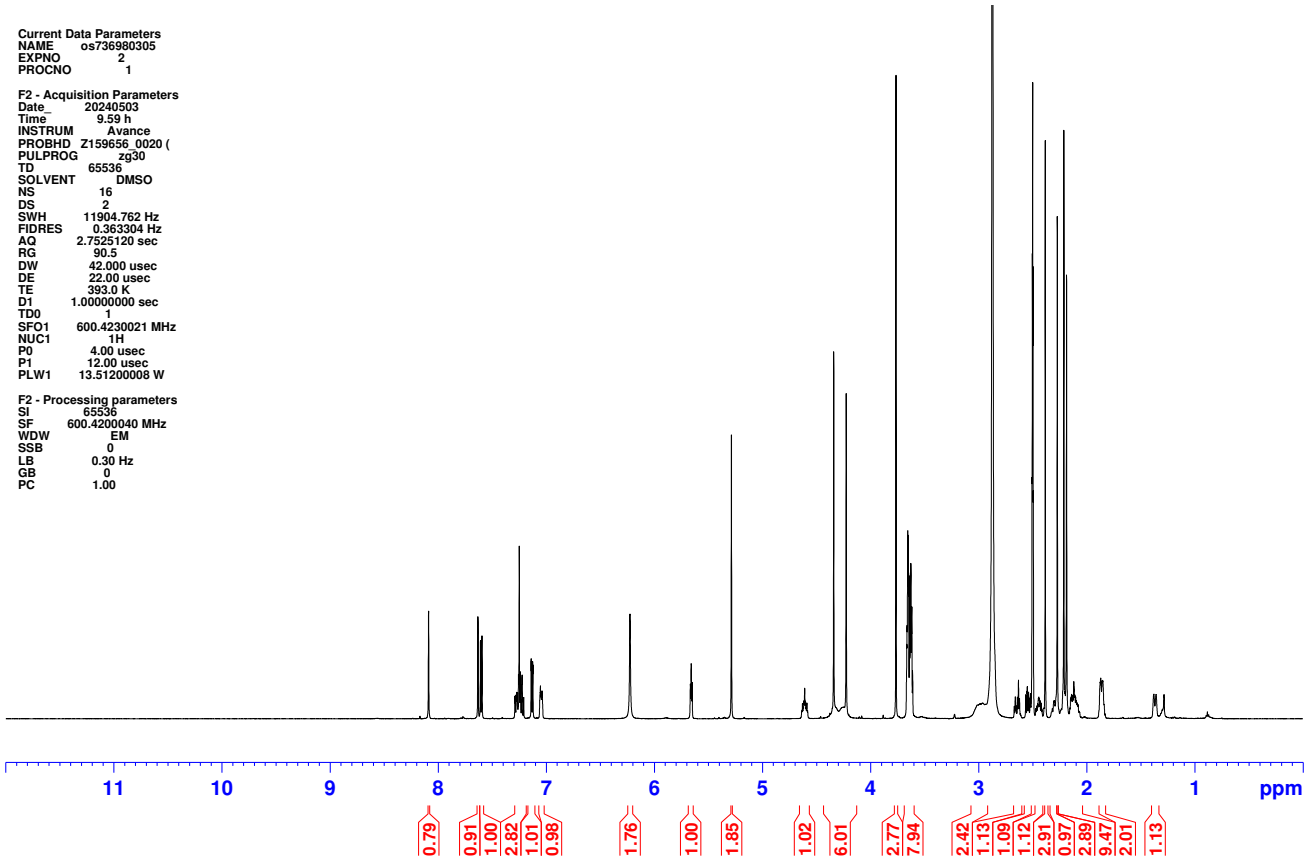
```
Current Data Parameters
NAME      os687490501_OJSD77
EXPNO                    8
PROCNO                   1

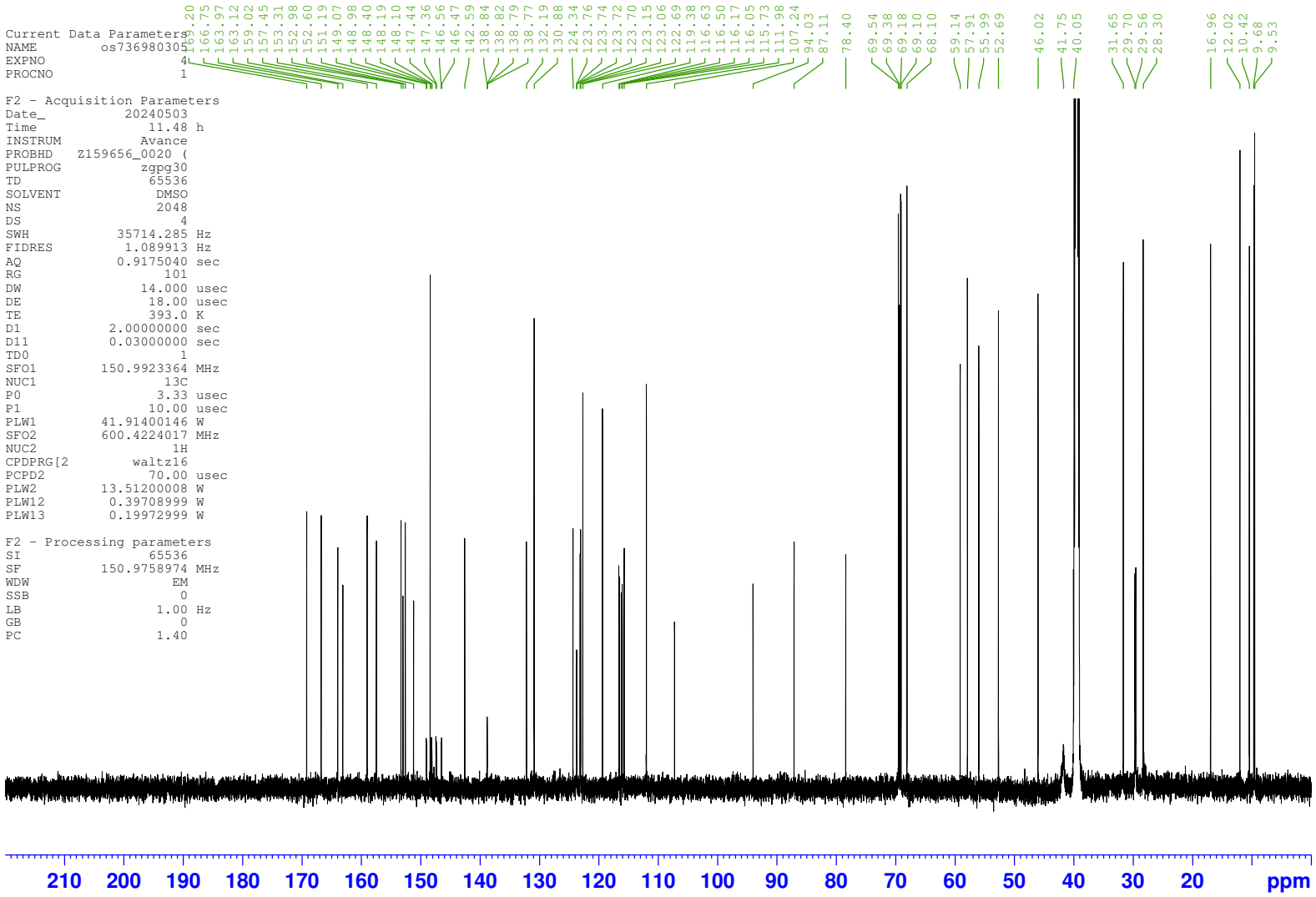
F2 - Acquisition Parameters
Date_             20230105
Time                15.44 h
INSTRUM            Avance
PROBHD    Z159656_0020 (
PULPROG              zg30
TD                 131072
SOLVENT             CDCl3
NS                     16
DS                      4
SWH            138888.891 Hz
FIDRES           2.119276 Hz
AQ              0.4718592 sec
RG                     10
DW                  3.600 usec
DE                 18.00 usec
TE                 298.0 K
D1            30.00000000 sec
TD0                     1
SFO1          564.9027649 MHz
NUC1                  19F
P0                  5.00 usec
P1                 15.00 usec
PLW1          11.45499992 W

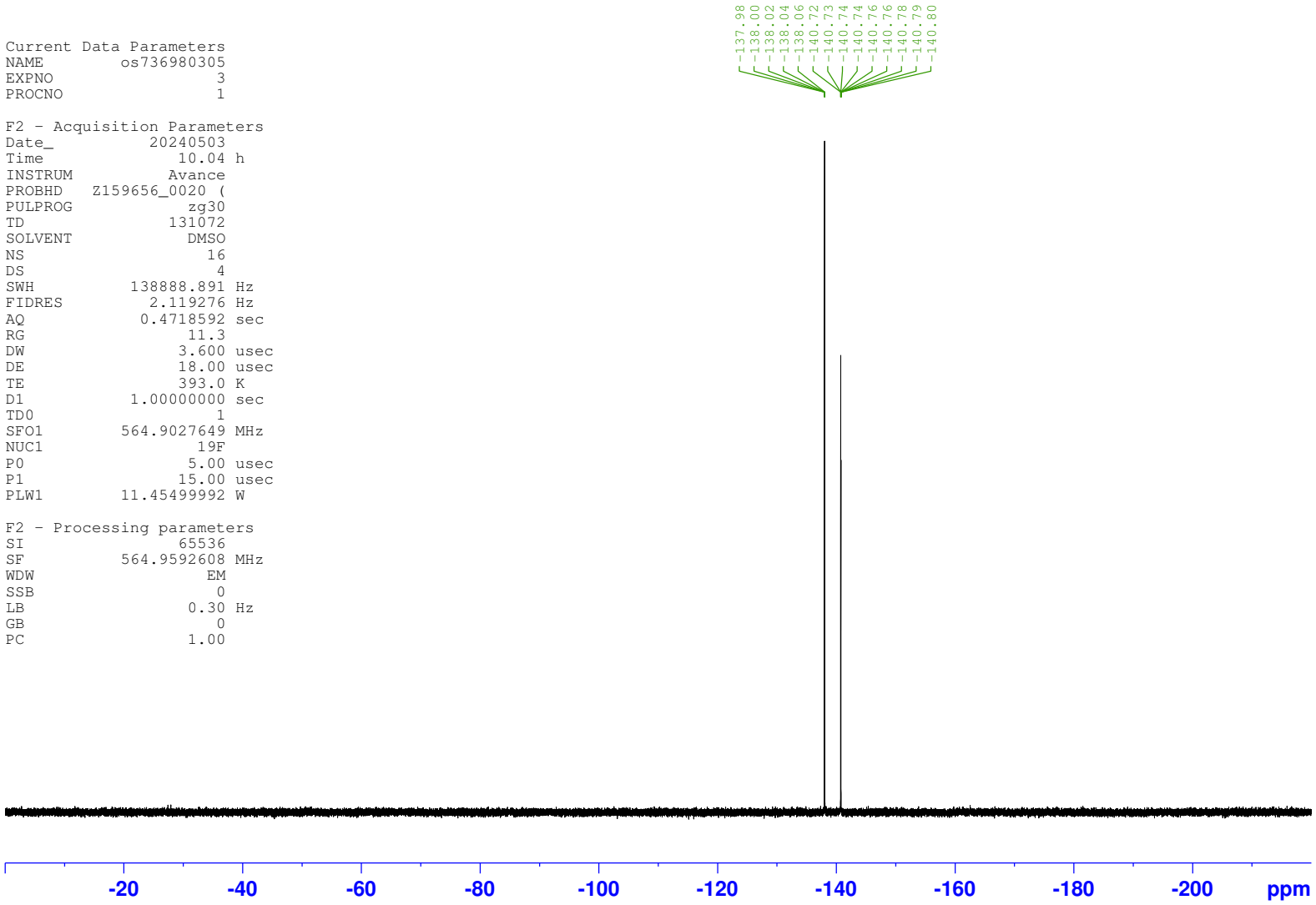
F2 - Processing parameters
SI                  65536
SF            564.9592608 MHz
WDW                    EM
SSB                     0
LB                   0.30 Hz
GB                      0
PC                   1.00
```



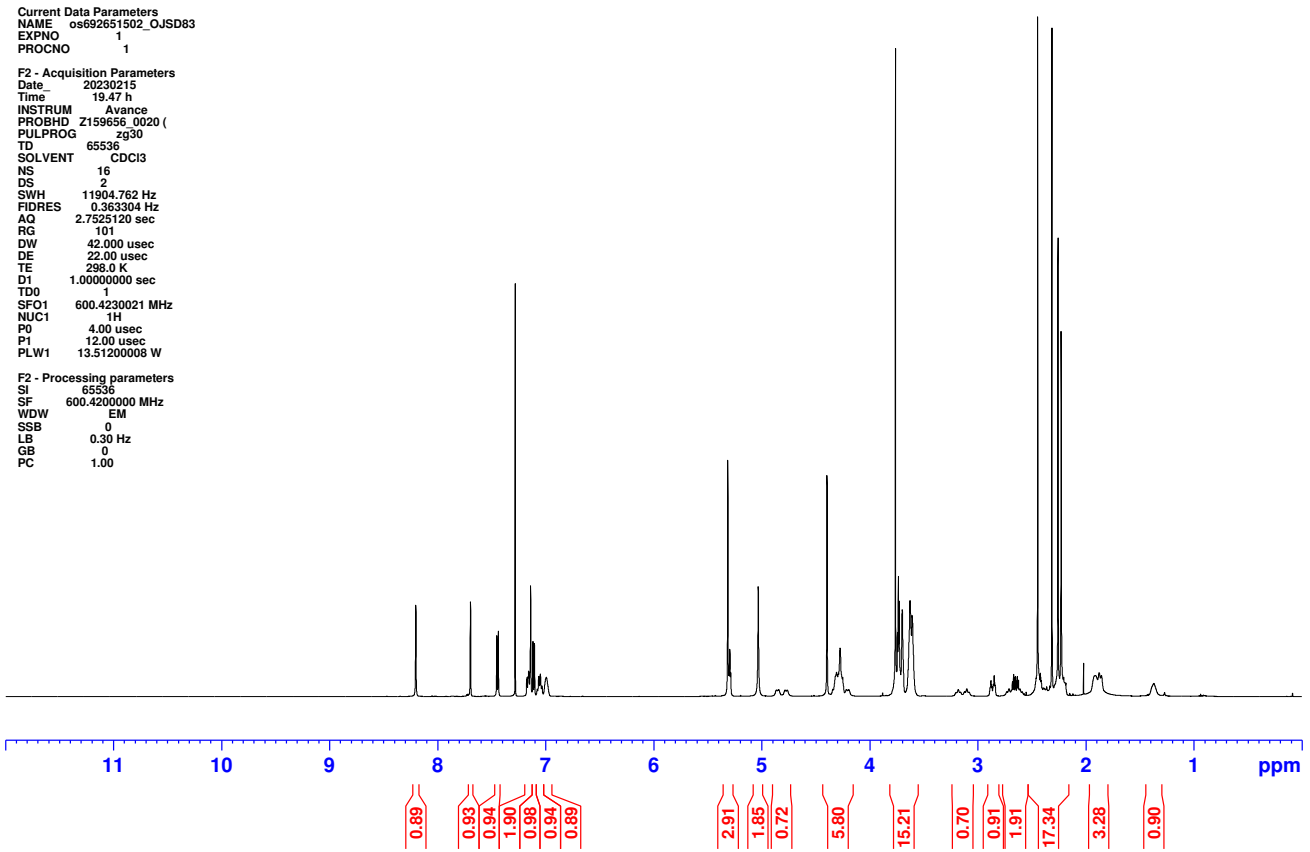
(6*S*)-6-(1-(1-(2-(2-(2-((3-(2-Amino-4-chloro-7-((4-methoxy-3,5-dimethylpyridin-2-yl)methyl)-7*H*-pyrrolo[2,3-*d*]pyrimidin-5-yl)prop-2-yn-1-yl)oxy)ethoxy)ethoxy)acetyl)piperidin-4-yl)-5-(3,5-dimethyl-1,2-oxazol-4-yl)-1*H*-1,3-benzimidazol-2-yl)-1-(3,4-difluorophenyl)piperidin-2-one (AcDC-2)

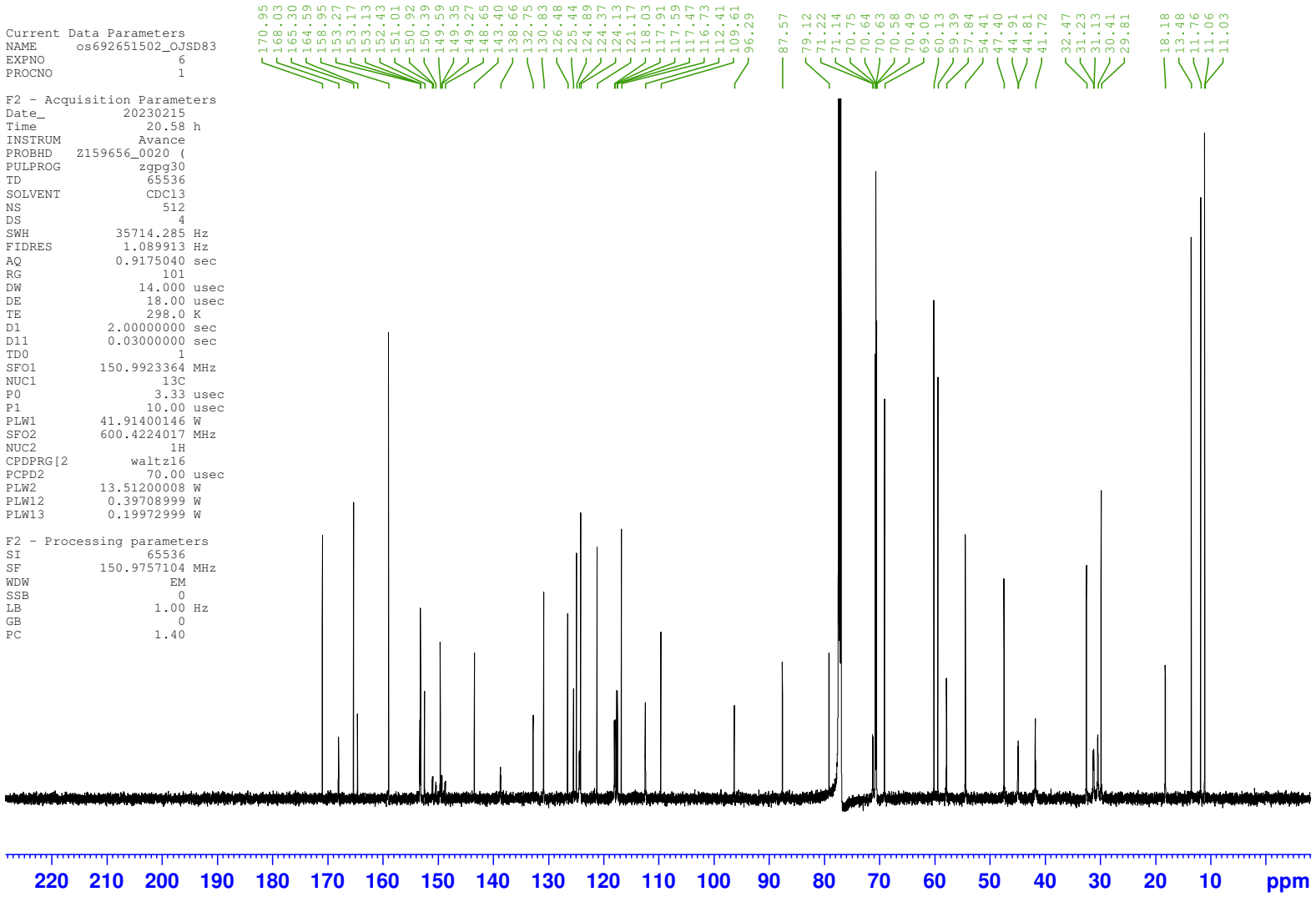


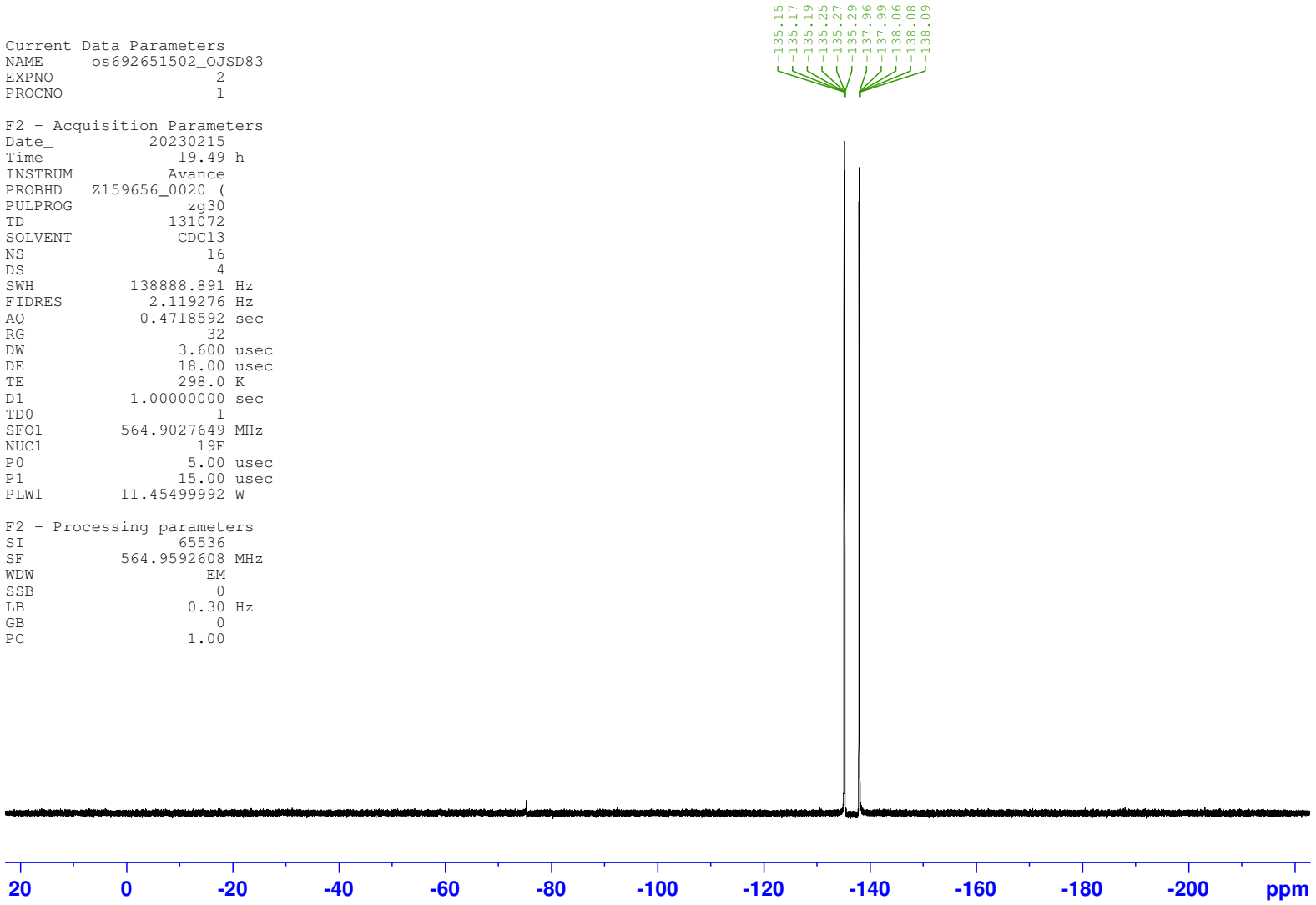

Current Data Parameters
NAME os736980305
EXPNO 4
PROCNO 1
F2 - Acquisition Parameters
Date_ 20240503
Time 11.48 h
INSTRUM Avance
PROBHD Z159656_0020 (
PULPROG zgpg30
TD 65536
SOLVENT DMSO
NS 2048
DS 4
SWH 35714.285 Hz
FIDRES 1.089913 Hz
AQ 0.9175040 sec
RG 101
DW 14.000 usec
DE 18.00 usec
TE 393.0 K
D1 2.00000000 sec
D11 0.03000000 sec
TD0 1
SFO1 150.9923364 MHz
NUC1 13C
P0 3.33 usec
P1 10.00 usec
PLW1 41.91400146 W
SFO2 600.4224017 MHz
NUC2 1H
CPDPRG[2 waltz16
PCPD2 70.00 usec
PLW2 13.51200008 W
PLW12 0.39708999 W
PLW13 0.19972999 W
F2 - Processing parameters
SI 65536
SF 150.9758974 MHz
WDW EM
SSB 0
LB 1.00 Hz
GB 0
PC 1.40
169.20
166.75
163.97
163.12
159.02
157.45
153.31
152.98
152.60
151.19
149.07
148.98
148.40
148.19
148.10
147.44
147.36
146.56
146.47
142.59
138.84
138.82
138.79
138.77
132.19
130.88
124.34
123.76
123.74
123.72
123.70
123.15
123.06
122.69
119.38
116.63
116.50
116.17
116.05
115.73
111.98
107.24
94.03
87.11
78.40
69.54
69.38
69.18
69.10
68.10
59.14
57.91
55.99
52.69
46.02
41.75
40.05
31.65
29.70
29.56
28.30
16.96
12.02
10.42
9.68
9.53
210 200 190 180 170 160 150 140 130 120 110 100 90 80 70 60 50 40 30 20 ppm


Current Data Parameters
NAME os736980305
EXPNO 3
PROCNO 1
F2 - Acquisition Parameters
Date_ 20240503
Time 10.04 h
INSTRUM Avance
PROBHD Z159656_0020 (
PULPROG zg30
TD 131072
SOLVENT DMSO
NS 16
DS 4
SWH 138888.891 Hz
FIDRES 2.119276 Hz
AQ 0.4718592 sec
RG 11.3
DW 3.600 usec
DE 18.00 usec
TE 393.0 K
D1 1.00000000 sec
TD0 1
SFO1 564.9027649 MHz
NUC1 19F
P0 5.00 usec
P1 15.00 usec
PLW1 11.45499992 W
F2 - Processing parameters
SI 65536
SF 564.9592608 MHz
WDW EM
SSB 0
LB 0.30 Hz
GB 0
PC 1.00
137.98
138.00
138.02
138.04
138.06
140.72
140.73
140.74
140.74
140.76
140.76
140.78
140.79
140.80
-20
-40
-60
-80
-100
-120
-140
-160
-180
-200
ppm

(6*S*)-6-(1-(1-(15-(2-Amino-4-chloro-7-((4-methoxy-3,5-dimethylpyridin-2-yl)methyl)-7*H*-pyrrolo[2,3-*d*]pyrimidin-5-yl)-3,6,9,12-tetraoxapentadec-14-ynoyl)piperidin-4-yl)-5-(3,5-dimethyl-1,2-oxazol-4-yl)-1*H*-1,3-benzodiazol-2-yl)-1-(3,4-difluorophenyl)piperidin-2-one (AcDC-3)




Current Data Parameters
NAME os692651502_OJSD83
EXPNO 6
PROCNO 1
F2 - Acquisition Parameters
Date_ 20230215
Time 20.58 h
INSTRUM Avance
PROBHD Z159656_0020 (
PULPROG zgpg30
TD 65536
SOLVENT CDCl3
NS 512
DS 4
SWH 35714.285 Hz
FIDRES 1.089913 Hz
AQ 0.9175040 sec
RG 101
DW 14.000 usec
DE 18.00 usec
TE 298.0 K
D1 2.00000000 sec
D11 0.03000000 sec
TD0 1
SFO1 150.9923364 MHz
NUC1 13C
P0 3.33 usec
P1 10.00 usec
PLW1 41.91400146 W
SFO2 600.4224017 MHz
NUC2 1H
CPDPRG[2 waltz16
PCPD2 70.00 usec
PLW2 13.51200008 W
PLW12 0.39708999 W
PLW13 0.19972999 W
F2 - Processing parameters
SI 65536
SF 150.9757104 MHz
WDW EM
SSB 0
LB 1.00 Hz
GB 0
PC 1.40
170.95
168.03
165.30
164.59
158.95
153.27
153.17
153.13
152.43
151.01
150.92
150.39
149.59
149.35
149.27
148.65
143.40
138.66
132.75
130.83
126.48
125.44
124.89
124.37
124.13
121.17
118.03
117.91
117.59
117.47
116.73
112.41
109.61
96.29
87.57
79.12
71.22
71.14
70.75
70.64
70.63
70.58
70.49
69.06
60.13
59.39
57.84
54.41
47.40
44.91
44.81
41.72
32.47
31.23
31.13
30.41
29.81
18.18
13.48
11.76
11.06
11.03
220 210 200 190 180 170 160 150 140 130 120 110 100 90 80 70 60 50 40 30 20 10 ppm

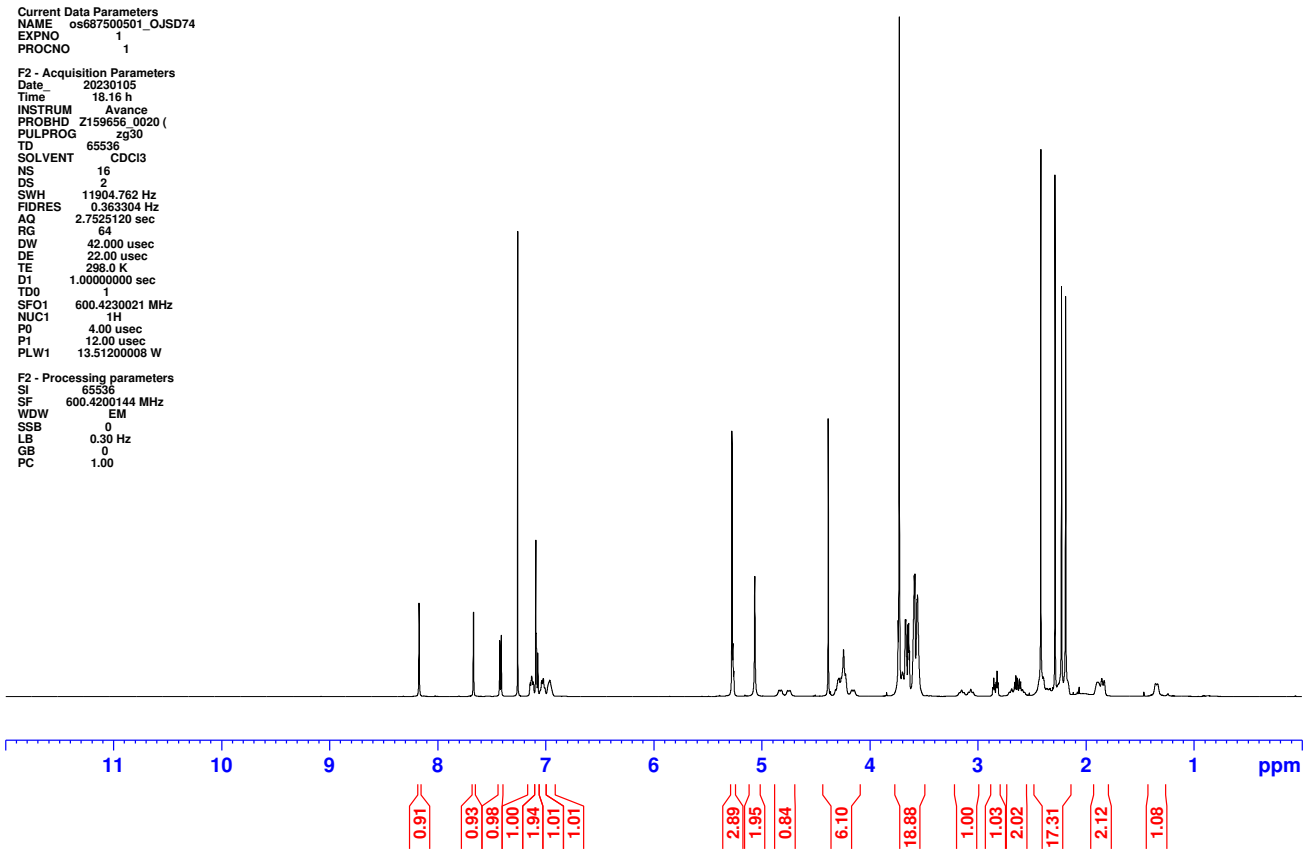


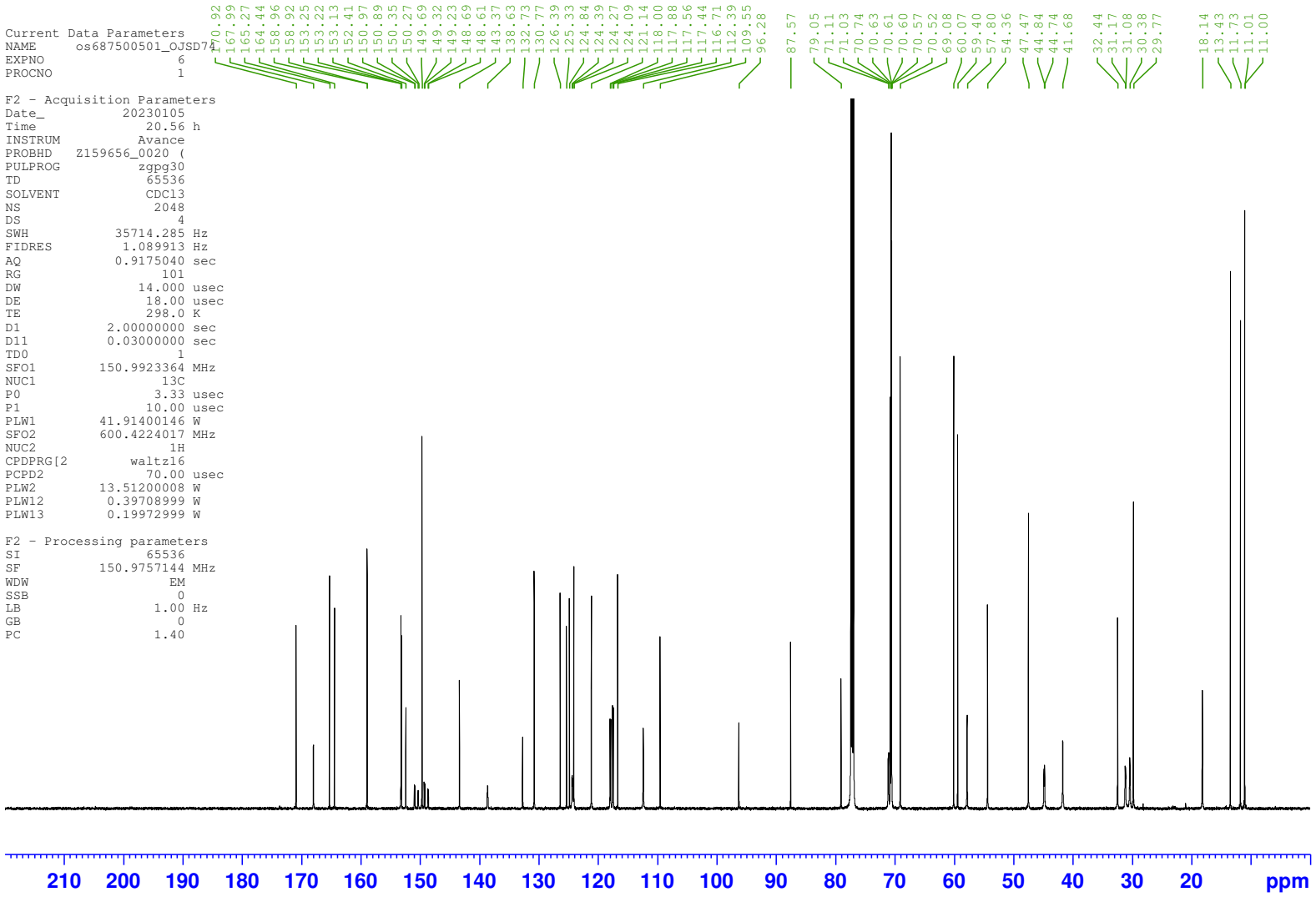

```
Current Data Parameters
NAME      os692651502_OJSD83
EXPNO                    2
PROCNO                   1

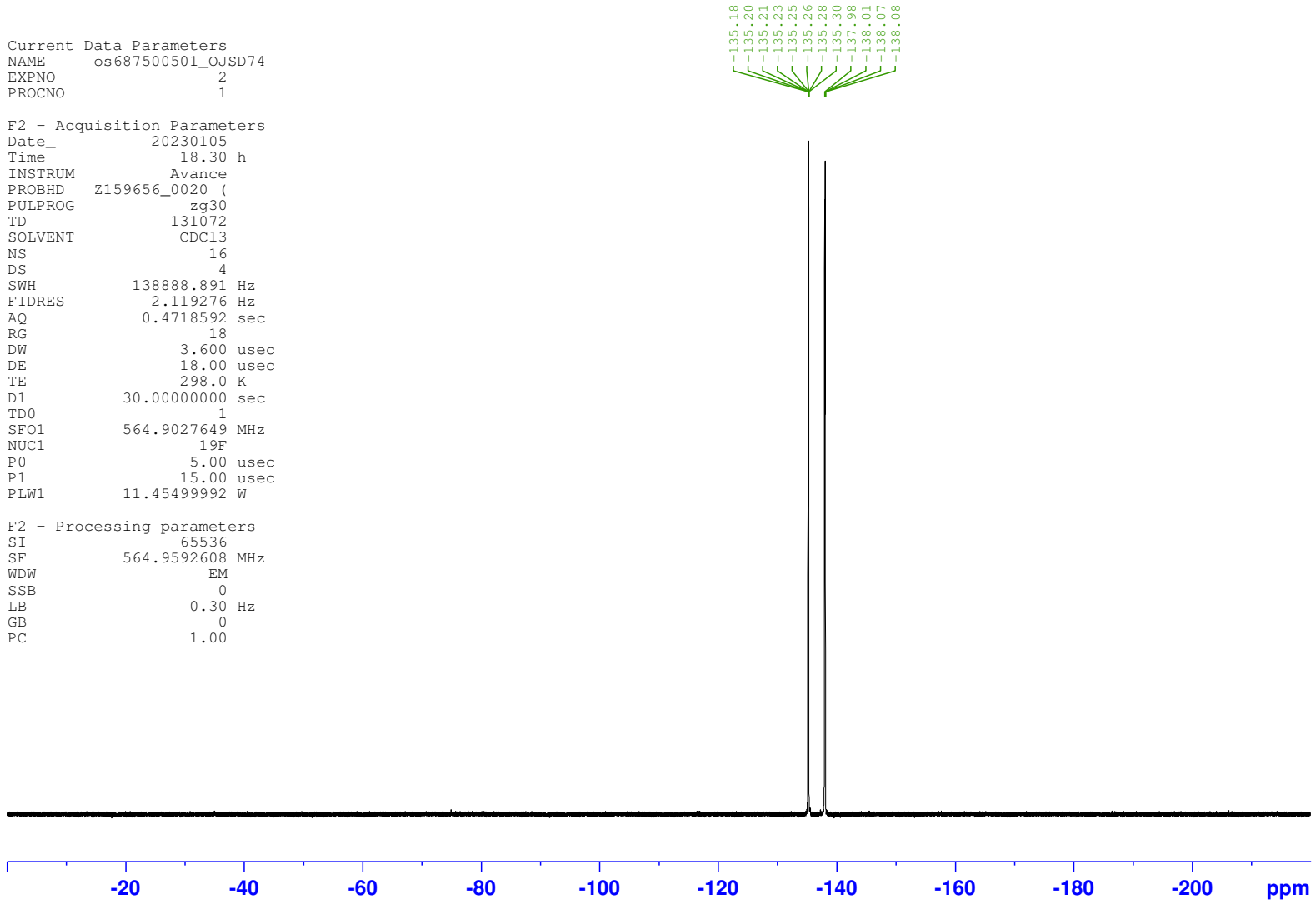
F2 - Acquisition Parameters
Date_             20230215
Time                19.49 h
INSTRUM            Avance
PROBHD    Z159656_0020 (
PULPROG              zg30
TD                 131072
SOLVENT             CDCl3
NS                     16
DS                      4
SWH            138888.891 Hz
FIDRES           2.119276 Hz
AQ              0.4718592 sec
RG                     32
DW                  3.600 usec
DE                 18.00 usec
TE                 298.0 K
D1             1.00000000 sec
TD0                     1
SFO1           564.9027649 MHz
NUC1                  19F
P0                  5.00 usec
P1                 15.00 usec
PLW1          11.45499992 W

F2 - Processing parameters
SI                  65536
SF            564.9592608 MHz
WDW                    EM
SSB                     0
LB                   0.30 Hz
GB                      0
PC                   1.00
```

(6S)-6-(1-(1-(18-(2-Amino-4-chloro-7-((4-methoxy-3,5-dimethylpyridin-2-yl)methyl)-7H-pyrrolo[2,3-*d*]pyrimidin-5-yl)-3,6,9,12,15-pentaoxaoctadec-17-ynoyl)piperidin-4-yl)-5-(3,5-dimethyl-1,2-oxazol-4-yl)-1H-1,3-benzodiazol-2-yl)-1-(3,4-difluorophenyl)piperidin-2-one (AcDC-4)




170.92
167.99
165.27
164.44
158.96
158.92
153.25
153.22
153.13
152.41
150.97
150.89
150.35
150.27
149.69
149.32
149.23
148.69
148.61
143.37
138.63
132.73
130.77
126.39
125.33
124.84
124.39
124.27
124.09
121.14
118.00
117.88
117.56
117.44
116.71
112.39
109.55
96.28
87.57
79.05
71.11
71.03
70.74
70.63
70.61
70.60
70.57
70.52
69.08
60.07
59.40
57.80
54.36
47.47
44.84
44.74
41.68
32.44
31.17
31.08
30.38
29.77
18.14
13.43
11.73
11.01
11.00
Current Data Parameters
NAME os687500501_OJSD74
EXPNO 6
PROCNO 1
F2 - Acquisition Parameters
Date_ 20230105
Time 20.56 h
INSTRUM Avance
PROBHD Z159656_0020 (
PULPROG zgpg30
TD 65536
SOLVENT CDC13
NS 2048
DS 4
SWH 35714.285 Hz
FIDRES 1.089913 Hz
AQ 0.9175040 sec
RG 101
DW 14.000 usec
DE 18.00 usec
TE 298.0 K
D1 2.00000000 sec
D11 0.03000000 sec
TD0 1
SFO1 150.9923364 MHz
NUC1 13C
P0 3.33 usec
P1 10.00 usec
PLW1 41.91400146 W
SFO2 600.4224017 MHz
NUC2 1H
CPDPRG[2 waltz16
PCPD2 70.00 usec
PLW2 13.51200008 W
PLW12 0.39708999 W
PLW13 0.19972999 W
F2 - Processing parameters
SI 65536
SF 150.9757144 MHz
WDW EM
SSB 0
LB 1.00 Hz
GB 0
PC 1.40
210
200
190
180
170
160
150
140
130
120
110
100
90
80
70
60
50
40
30
20
ppm

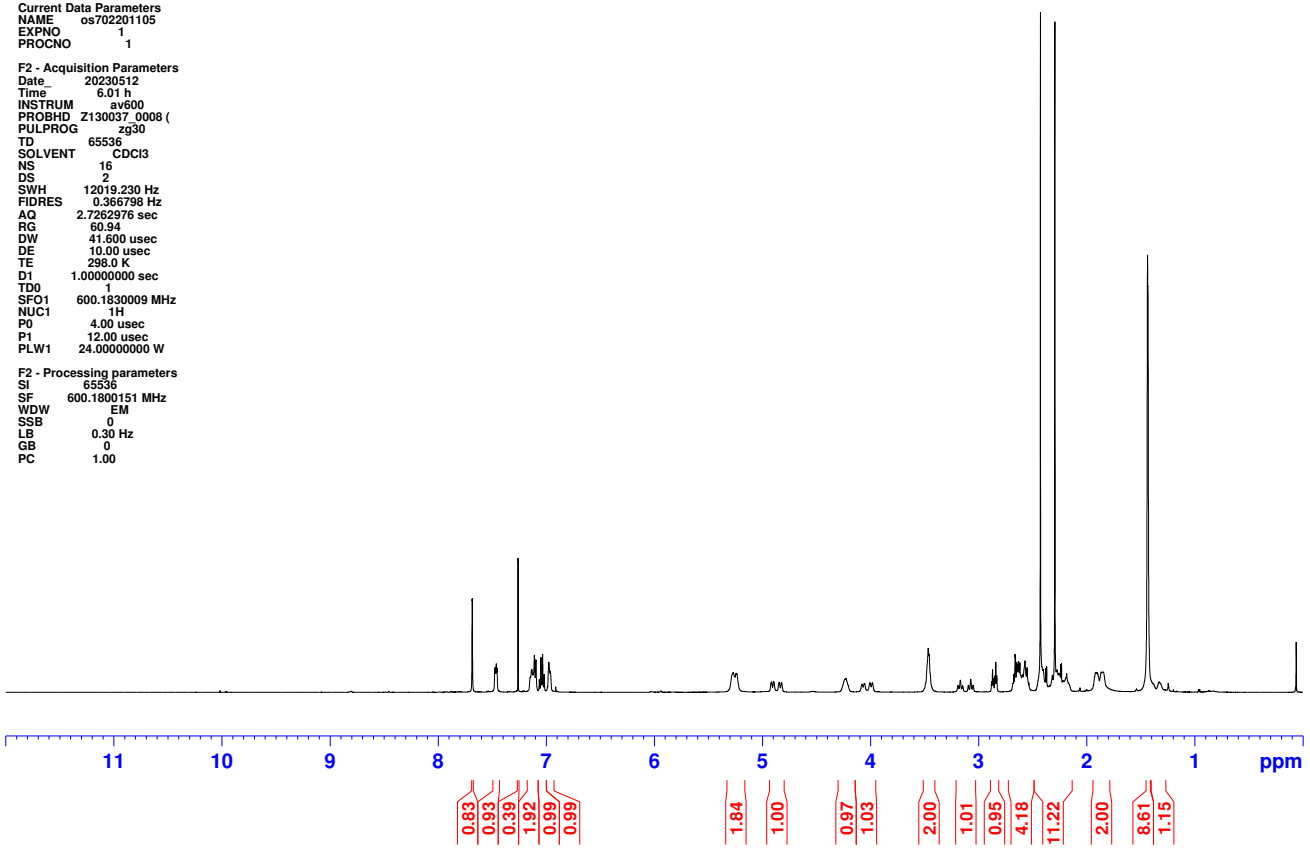


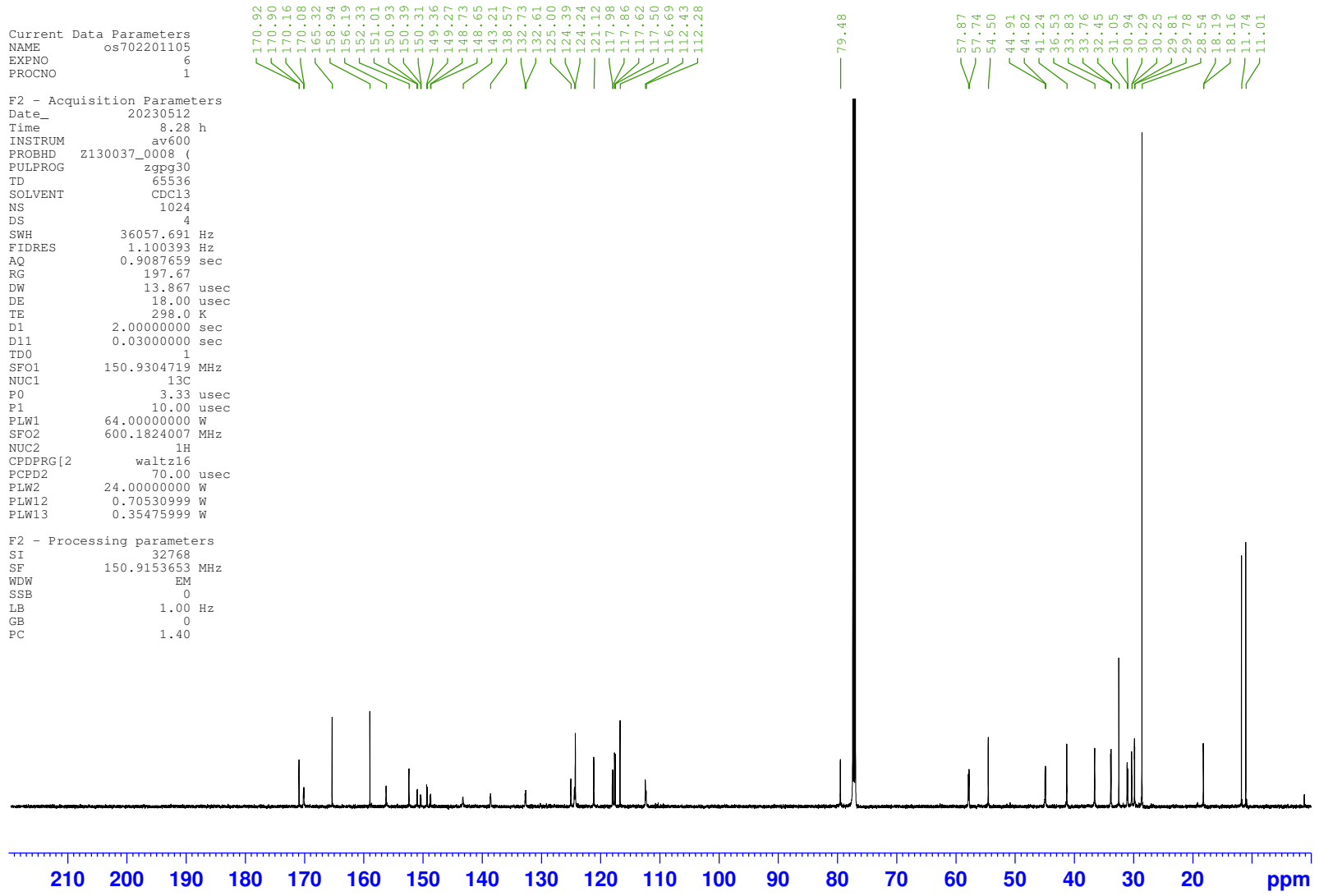

```
Current Data Parameters
NAME      os687500501_OJSD74
EXPNO                    2
PROCNO                   1

F2 - Acquisition Parameters
Date_            20230105
Time                18.30 h
INSTRUM            Avance
PROBHD    Z159656_0020 (
PULPROG              zg30
TD                 131072
SOLVENT             CDCl3
NS                     16
DS                      4
SWH           138888.891 Hz
FIDRES          2.119276 Hz
AQ             0.4718592 sec
RG                     18
DW                 3.600 usec
DE                18.00 usec
TE                298.0 K
D1           30.00000000 sec
TD0                    1
SFO1         564.9027649 MHz
NUC1                 19F
P0                 5.00 usec
P1                15.00 usec
PLW1         11.45499992 W

F2 - Processing parameters
SI                 65536
SF           564.9592608 MHz
WDW                   EM
SSB                    0
LB                  0.30 Hz
GB                     0
PC                  1.00
```

tert-Butyl _N_-(3-(4-(2-((2_S_)-1-(3,4-difluorophenyl)-6-oxopiperidin-2-yl)-5-(3,5-dimethyl-1,2-oxazol-4-yl)-1_H_-1,3-benzodiazol-1-yl)piperidin-1-yl)-3-oxopropyl)carbamate (53)






```
Current Data Parameters
NAME         os702201105
EXPNO                  6
PROCNO                 1

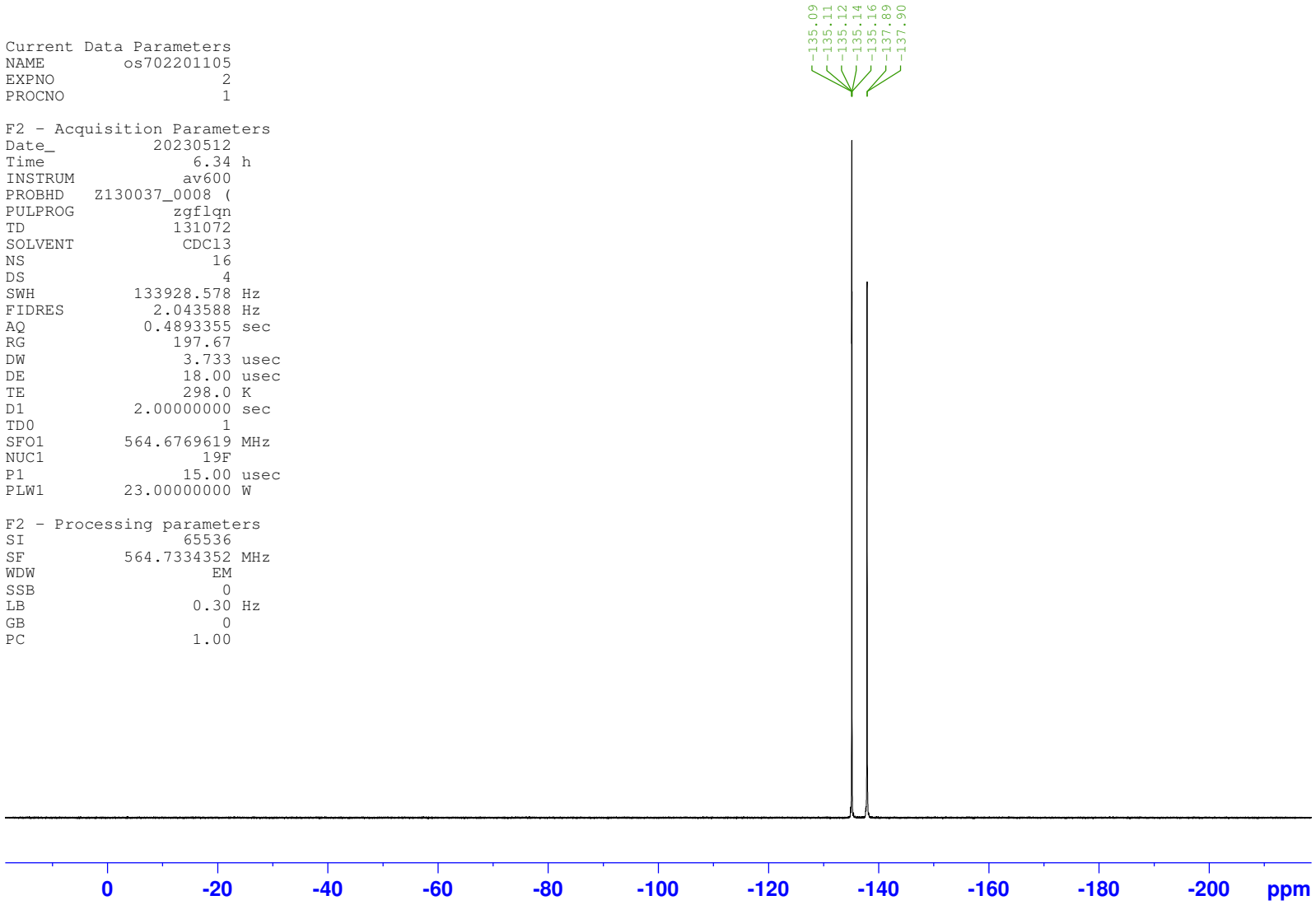
F2 - Acquisition Parameters
Date_           20230512
Time                8.28 h
INSTRUM            av600
PROBHD   Z130037_0008 (
PULPROG           zgpg30
TD                 65536
SOLVENT            CDCl3
NS                  1024
DS                     4
SWH            36057.691 Hz
FIDRES          1.100393 Hz
AQ             0.9087659 sec
RG                197.67
DW                13.867 usec
DE                18.00 usec
TE                298.0 K
D1            2.00000000 sec
D11           0.03000000 sec
TD0                    1
SFO1         150.9304719 MHz
NUC1                13C
P0                 3.33 usec
P1                10.00 usec
PLW1         64.00000000 W
SFO2         600.1824007 MHz
NUC2                1H
CPDPRG[2         waltz16
PCPD2             70.00 usec
PLW2         24.00000000 W
PLW12         0.70530999 W
PLW13         0.35475999 W

F2 - Processing parameters
SI                 32768
SF           150.9153653 MHz
WDW                   EM
SSB                    0
LB                  1.00 Hz
GB                     0
PC                  1.40
```

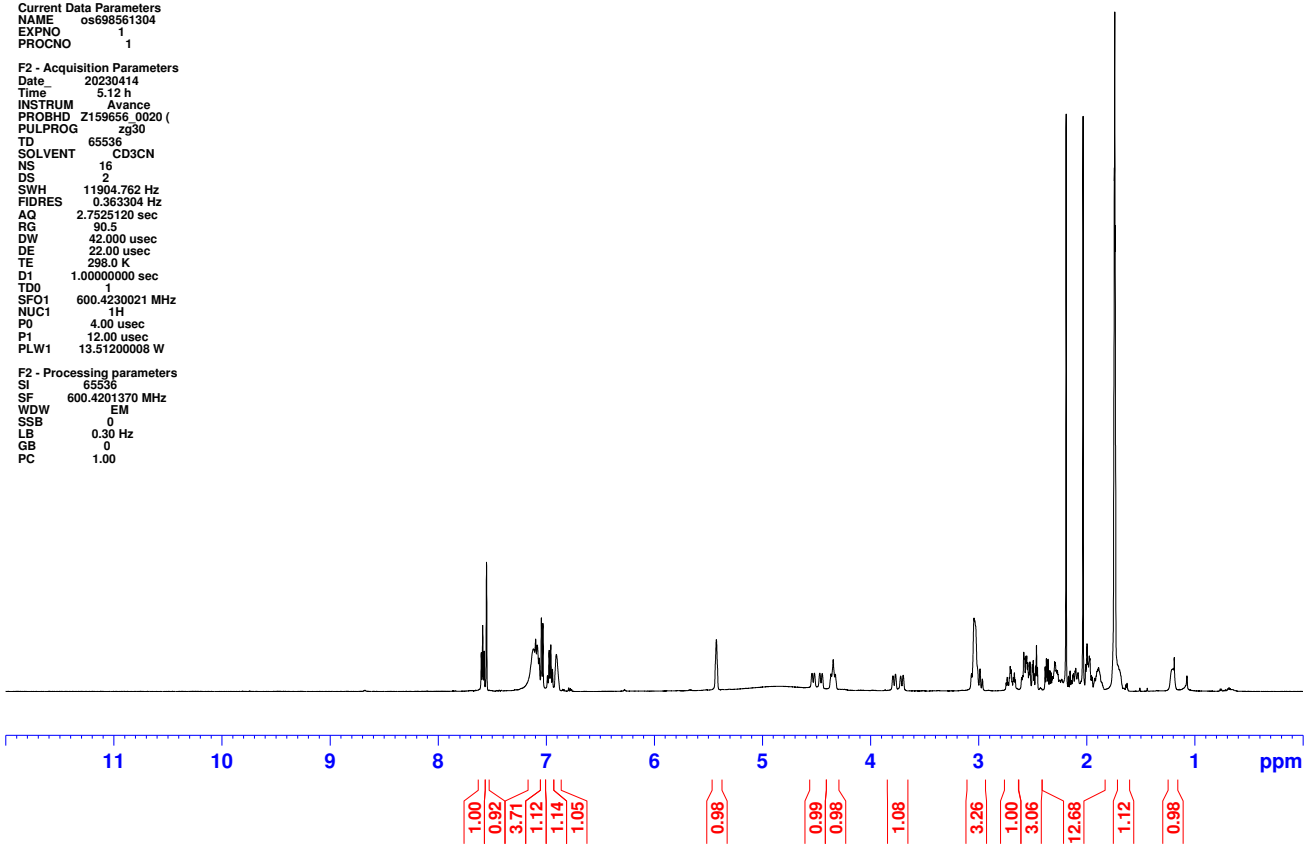
```
Current Data Parameters
NAME         os702201105
EXPNO                  2
PROCNO                 1

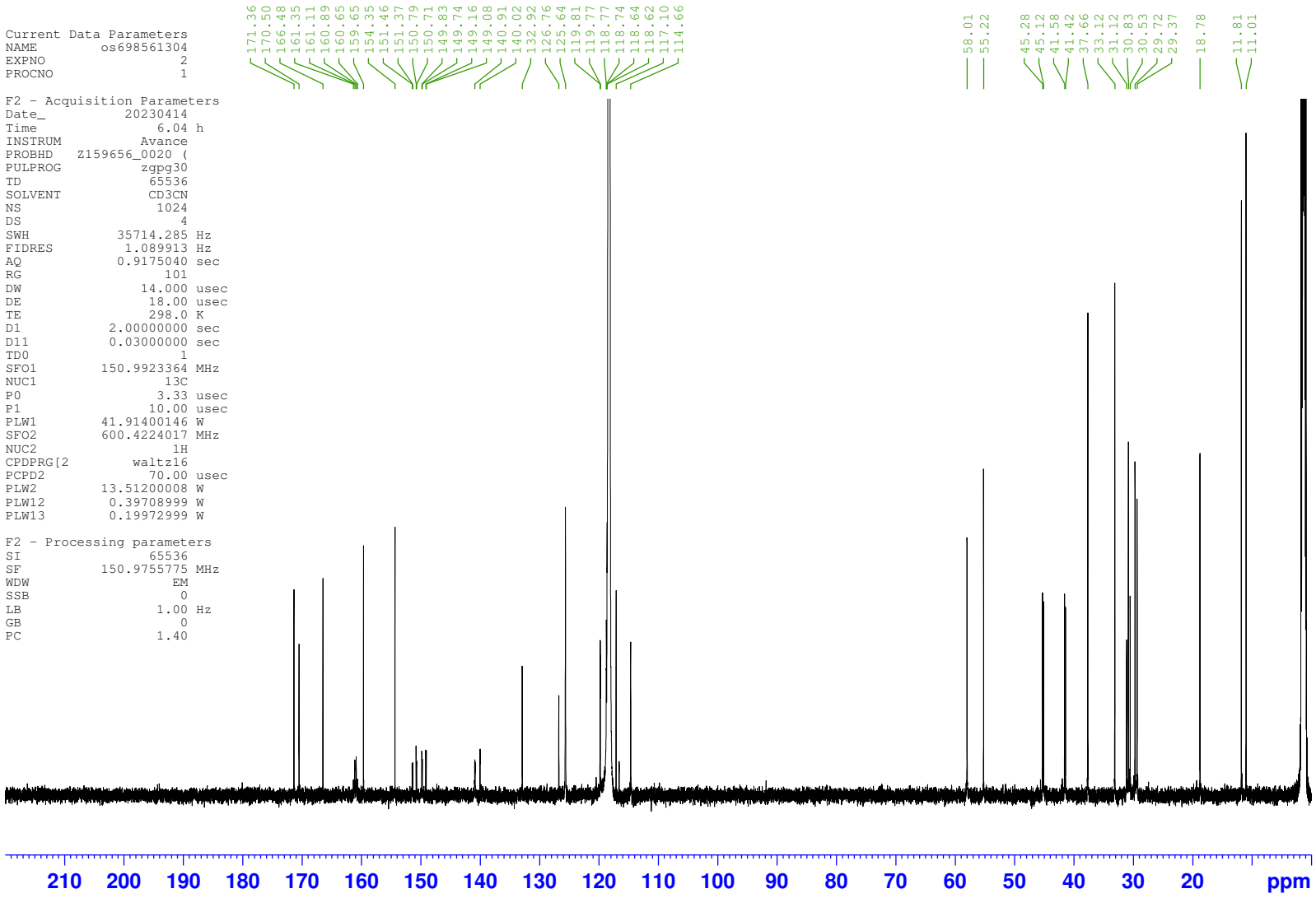
F2 - Acquisition Parameters
Date_           20230512
Time                6.34 h
INSTRUM            av600
PROBHD   Z130037_0008 (
PULPROG           zgflqn
TD                131072
SOLVENT            CDCl3
NS                    16
DS                     4
SWH           133928.578 Hz
FIDRES          2.043588 Hz
AQ             0.4893355 sec
RG                197.67
DW                 3.733 usec
DE                18.00 usec
TE                298.0 K
D1            2.00000000 sec
TD0                    1
SFO1         564.6769619 MHz
NUC1                 19F
P1                15.00 usec
PLW1         23.00000000 W

F2 - Processing parameters
SI                 65536
SF           564.7334352 MHz
WDW                   EM
SSB                    0
LB                  0.30 Hz
GB                     0
PC                  1.00
```



1-[1-(3-Azaniumylpropanoyl)piperidin-4-yl]-2-[(2*S*)-1-(3,4-difluorophenyl)-6-oxopiperidin-2-yl]-5-(3,5-dimethyl-1,2-oxazol-4-yl)-3*H*-1λ5,3-benzodiazol-1-ylium bis(trifluoroacetate) (54)

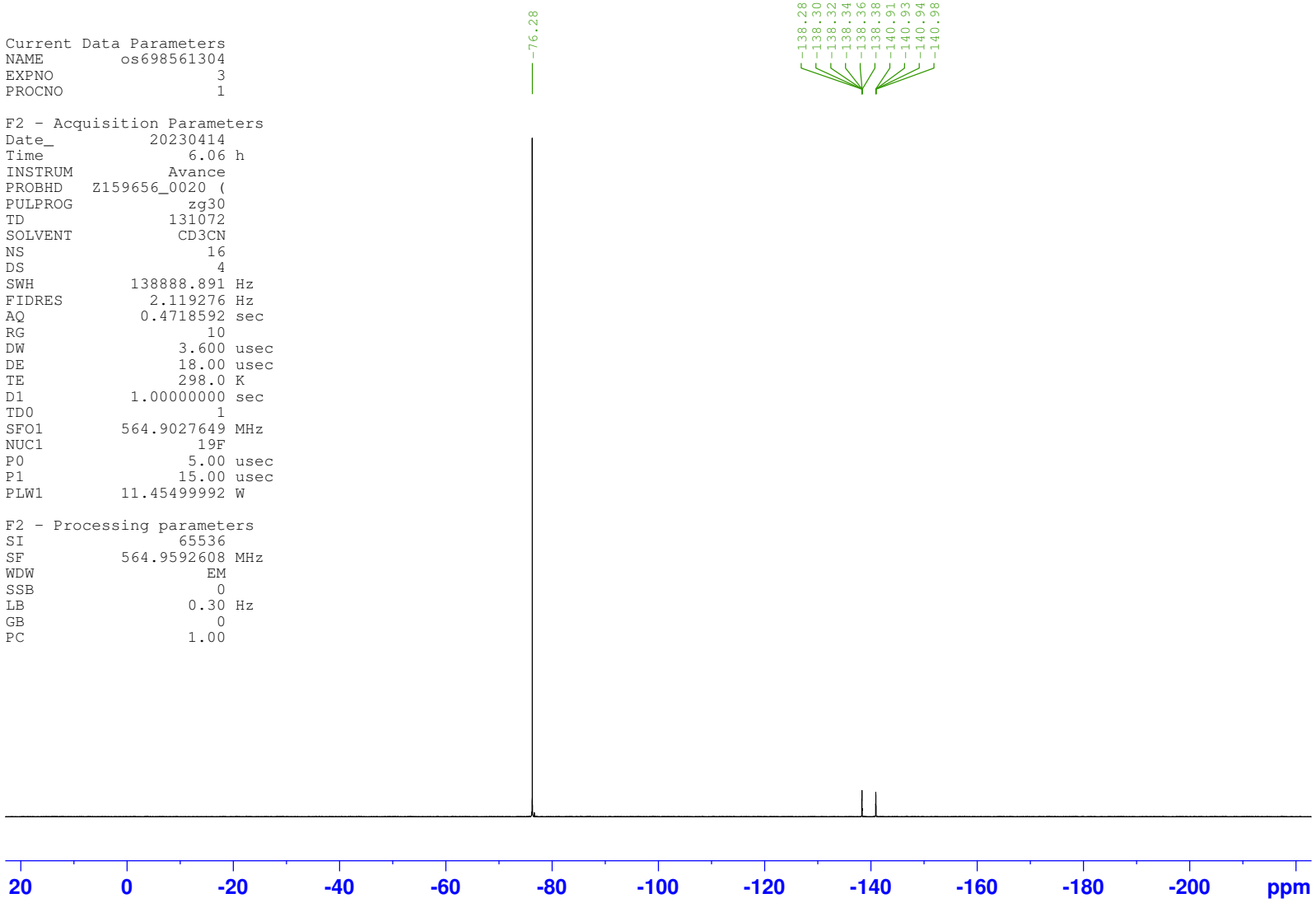



Current Data Parameters
NAME os698561304
EXPNO 2
PROCNO 1
F2 - Acquisition Parameters
Date_ 20230414
Time 6.04 h
INSTRUM Avance
PROBHD Z159656_0020 (
PULPROG zgpg30
TD 65536
SOLVENT CD3CN
NS 1024
DS 4
SWH 35714.285 Hz
FIDRES 1.089913 Hz
AQ 0.9175040 sec
RG 101
DW 14.000 usec
DE 18.00 usec
TE 298.0 K
D1 2.00000000 sec
D11 0.03000000 sec
TD0 1
SFO1 150.9923364 MHz
NUC1 13C
P0 3.33 usec
P1 10.00 usec
PLW1 41.91400146 W
SFO2 600.4224017 MHz
NUC2 1H
CPDPRG[2 waltz16
PCPD2 70.00 usec
PLW2 13.51200008 W
PLW12 0.39708999 W
PLW13 0.19972999 W
F2 - Processing parameters
SI 65536
SF 150.9755775 MHz
WDW EM
SSB 0
LB 1.00 Hz
GB 0
PC 1.40
171.36
170.50
166.48
161.35
161.11
160.89
160.65
159.65
154.35
151.46
151.37
150.79
150.71
149.83
149.74
149.16
149.08
140.91
140.02
132.92
126.76
125.64
119.81
119.77
118.77
118.74
118.64
118.62
117.10
114.66
58.01
55.22
45.28
45.12
41.58
41.42
37.66
33.12
31.12
30.83
30.53
29.72
29.37
18.78
11.81
11.01
210
200
190
180
170
160
150
140
130
120
110
100
90
80
70
60
50
40
30
20
ppm

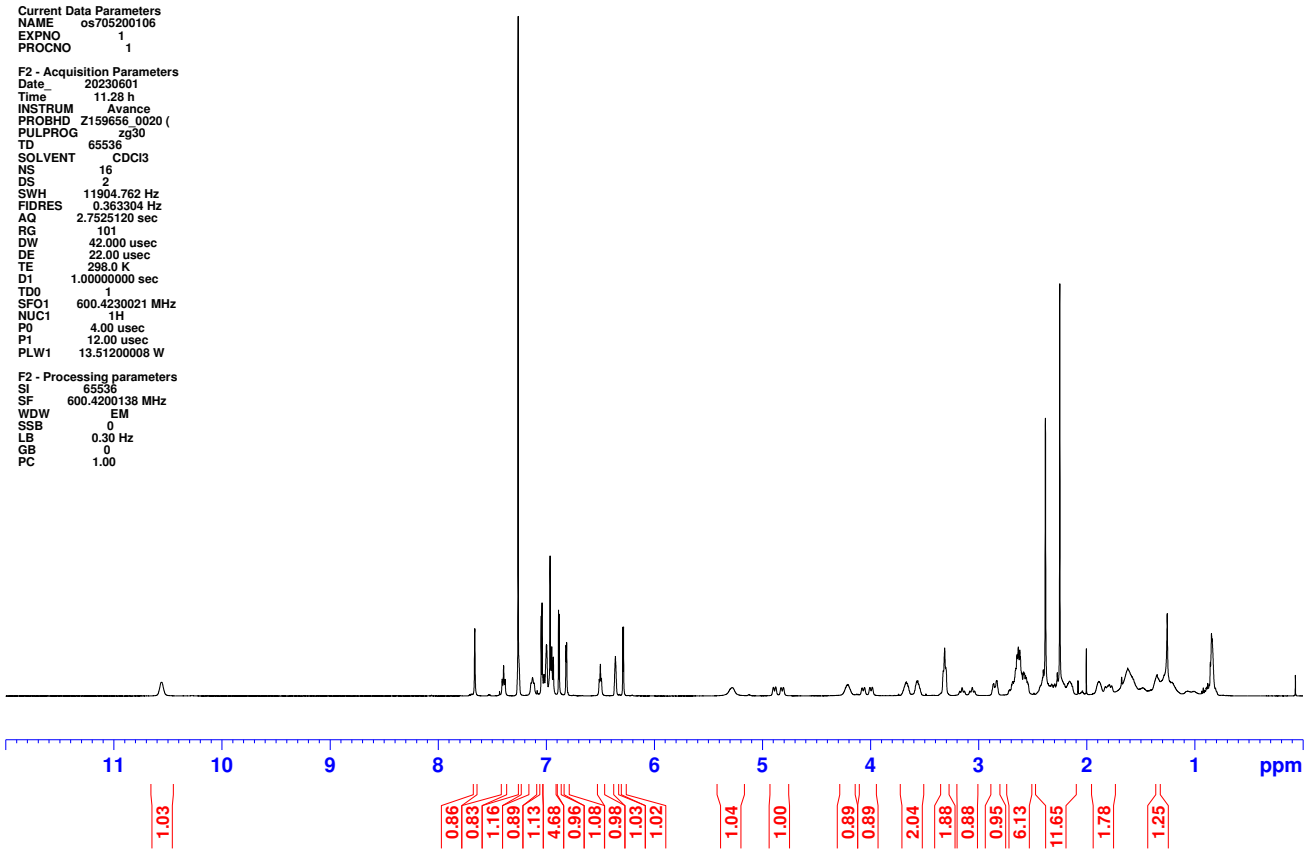
```
Current Data Parameters
NAME         os698561304
EXPNO                  3
PROCNO                 1

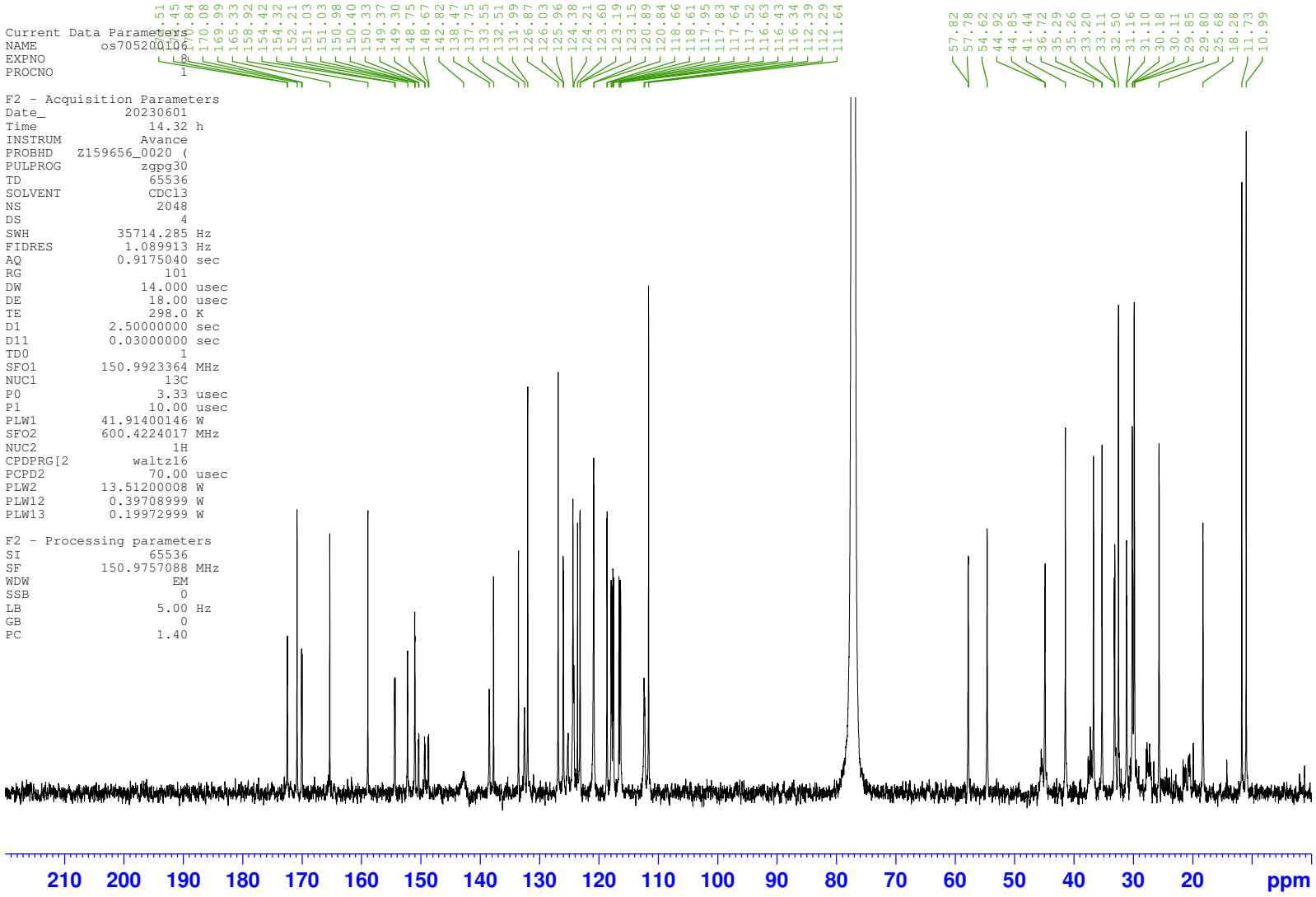
F2 - Acquisition Parameters
Date_           20230414
Time                6.06 h
INSTRUM           Avance
PROBHD   Z159656_0020 (
PULPROG             zg30
TD                131072
SOLVENT            CD3CN
NS                    16
DS                     4
SWH           138888.891 Hz
FIDRES          2.119276 Hz
AQ             0.4718592 sec
RG                    10
DW                3.600 usec
DE                18.00 usec
TE                298.0 K
D1            1.00000000 sec
TD0                    1
SFO1         564.9027649 MHz
NUC1                19F
P0                 5.00 usec
P1                15.00 usec
PLW1         11.45499992 W

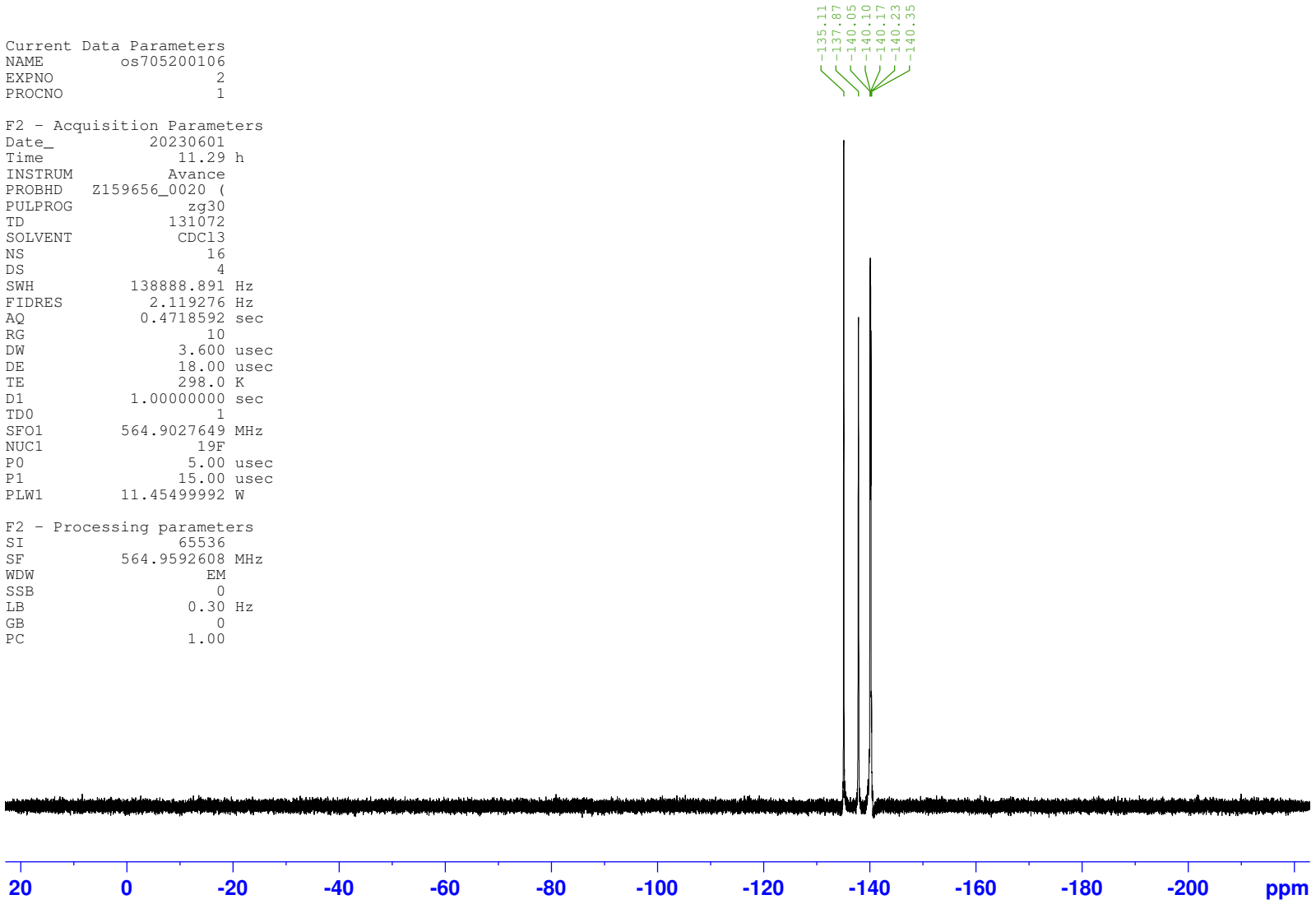
F2 - Processing parameters
SI                 65536
SF           564.9592608 MHz
WDW                   EM
SSB                    0
LB                  0.30 Hz
GB                     0
PC                  1.00
```



12-(2-((3-(4-(2-((2*S*)-1-(3,4-Difluorophenyl)-6-oxopiperidin-2-yl)-5-(3,5-dimethyl-1,2-oxazol-4-yl)-1*H*-1,3-benzodiazol-1-yl)piperidin-1-yl)-3-oxopropyl)carbamoyl)ethyl)-2,2-difluoro-4-(1*H*-pyrrol-2-yl)-1λ5,3-diaza-2-boratricyclo[7.3.0.0^{3,7}]dodeca-1(12),4,6,8,10-pentaen-1-ylium-2-uide (Inobrodib-BODIPY)




Current Data Parameters
NAME os705200106
EXPNO 8
PROCNO 1
F2 - Acquisition Parameters
Date_ 20230601
Time 14.32 h
INSTRUM Avance
PROBHD Z159656_0020 (
PULPROG zgpg30
TD 65536
SOLVENT CDC13
NS 2048
DS 4
SWH 35714.285 Hz
FIDRES 1.089913 Hz
AQ 0.9175040 sec
RG 101
DW 14.000 usec
DE 18.00 usec
TE 298.0 K
D1 2.50000000 sec
D11 0.03000000 sec
TD0 1
SFO1 150.9923364 MHz
NUC1 13C
P0 3.33 usec
P1 10.00 usec
PLW1 41.91400146 W
SFO2 600.4224017 MHz
NUC2 1H
CPDPRG[2 waltz16
PCPD2 70.00 usec
PLW2 13.51200008 W
PLW12 0.39708999 W
PLW13 0.19972999 W
F2 - Processing parameters
SI 65536
SF 150.9757088 MHz
WDW EM
SSB 0
LB 5.00 Hz
GB 0
PC 1.40
170.51
170.45
170.84
170.08
169.99
165.33
158.92
154.42
154.32
152.21
151.03
151.03
150.98
150.40
150.33
149.37
149.30
148.75
148.67
142.82
138.47
137.75
133.55
132.51
131.99
126.87
126.03
125.96
124.38
124.21
123.60
123.19
123.15
120.89
120.84
118.66
118.61
117.95
117.83
117.64
117.52
116.63
116.43
116.34
112.39
112.29
111.64
57.82
57.78
54.62
44.92
44.85
41.44
36.72
35.29
35.26
33.20
33.11
32.50
31.16
31.10
30.18
30.11
29.85
29.80
25.68
18.28
11.73
10.99
210
200
190
180
170
160
150
140
130
120
110
100
90
80
70
60
50
40
30
20
ppm




```
Current Data Parameters
NAME         os705200106
EXPNO                  2
PROCNO                 1

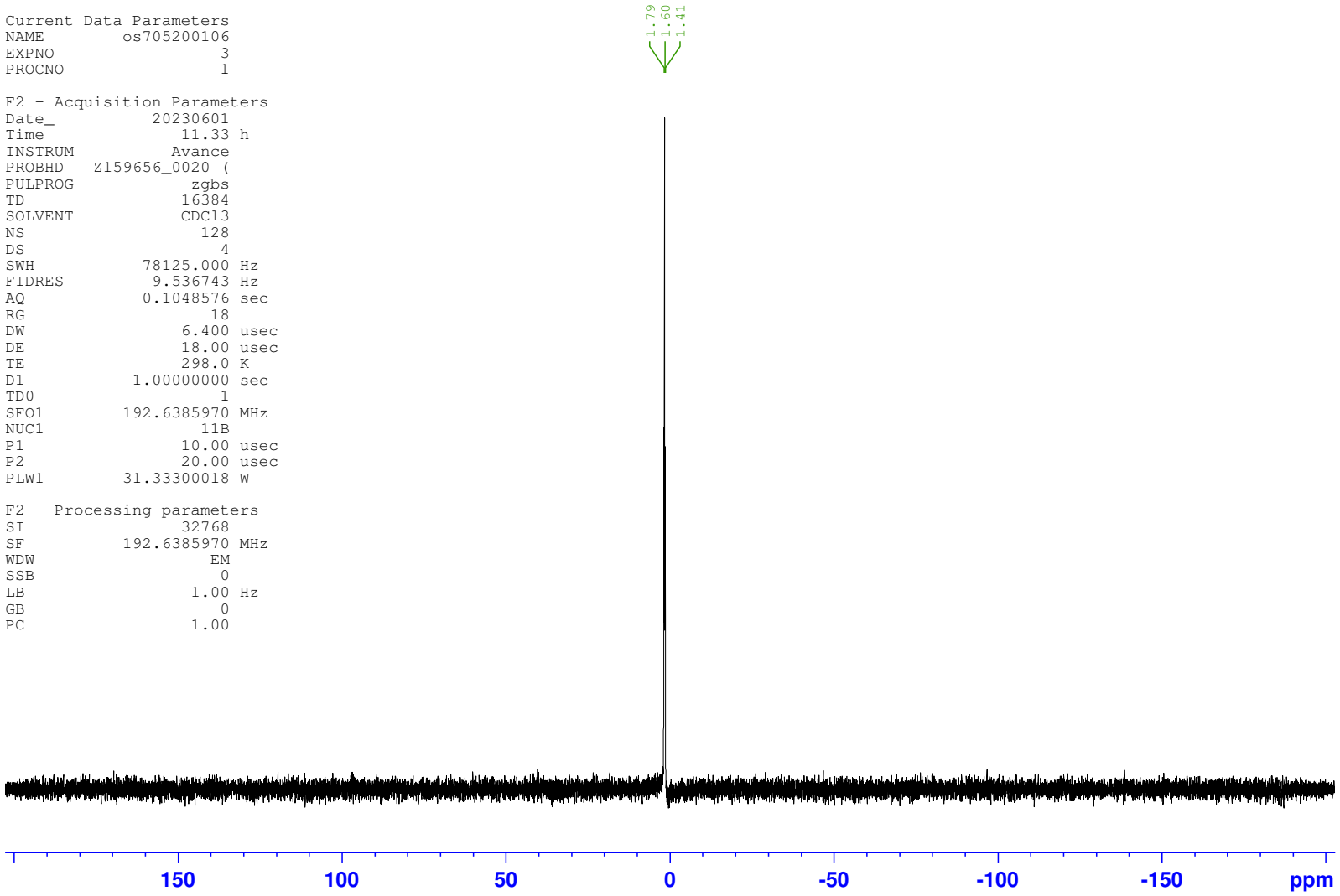
F2 - Acquisition Parameters
Date_           20230601
Time               11.29 h
INSTRUM           Avance
PROBHD   Z159656_0020 (
PULPROG             zg30
TD                131072
SOLVENT            CDCl3
NS                    16
DS                     4
SWH           138888.891 Hz
FIDRES          2.119276 Hz
AQ             0.4718592 sec
RG                    10
DW                 3.600 usec
DE                18.00 usec
TE                298.0 K
D1             1.00000000 sec
TD0                    1
SFO1         564.9027649 MHz
NUC1                19F
P0                 5.00 usec
P1                15.00 usec
PLW1         11.45499992 W

F2 - Processing parameters
SI                 65536
SF           564.9592608 MHz
WDW                   EM
SSB                    0
LB                  0.30 Hz
GB                     0
PC                  1.00
```

```
Current Data Parameters
NAME        os705200106
EXPNO                 3
PROCNO                1

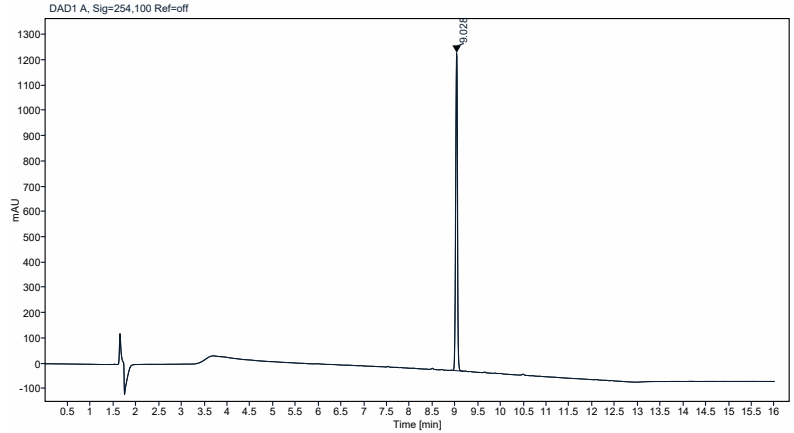
F2 - Acquisition Parameters
Date_          20230601
Time              11.33 h
INSTRUM          Avance
PROBHD   Z159656_0020 (
PULPROG             zgbs
TD                 16384
SOLVENT            CDCl3
NS                   128
DS                     4
SWH            78125.000 Hz
FIDRES          9.536743 Hz
AQ             0.1048576 sec
RG                    18
DW                 6.400 usec
DE                18.00 usec
TE                298.0 K
D1            1.00000000 sec
TD0                    1
SFO1        192.6385970 MHz
NUC1                11B
P1                10.00 usec
P2                20.00 usec
PLW1        31.33300018 W

F2 - Processing parameters
SI                 32768
SF          192.6385970 MHz
WDW                   EM
SSB                    0
LB                  1.00 Hz
GB                     0
PC                  1.00
```

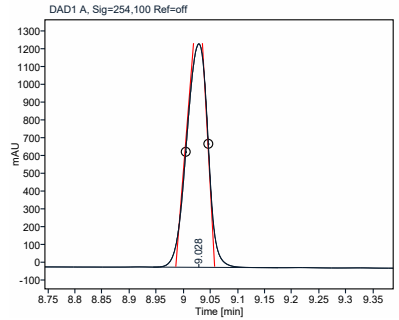


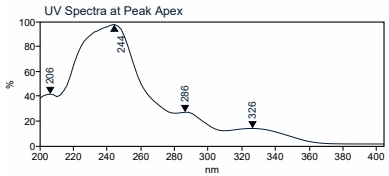
Appendix F HPLC chromatograms of novel compounds used in biology

(6S)-6-(1-(1-(5-((3-(2-Amino-4-chloro-7-((4-methoxy-3,5-dimethylpyridin-2-yl)methyl)-7H-pyrrolo[2,3-*d*]pyrimidin-5-yl)prop-2-yn-1-yl)oxy)pentanoyl)piperidin-4-yl)-5-(3,5-dimethyl-1,2-oxazol-4-yl)-1H-1,3-benzimidazol-2-yl)-1-(3,4-difluorophenyl)piperidin-2-one

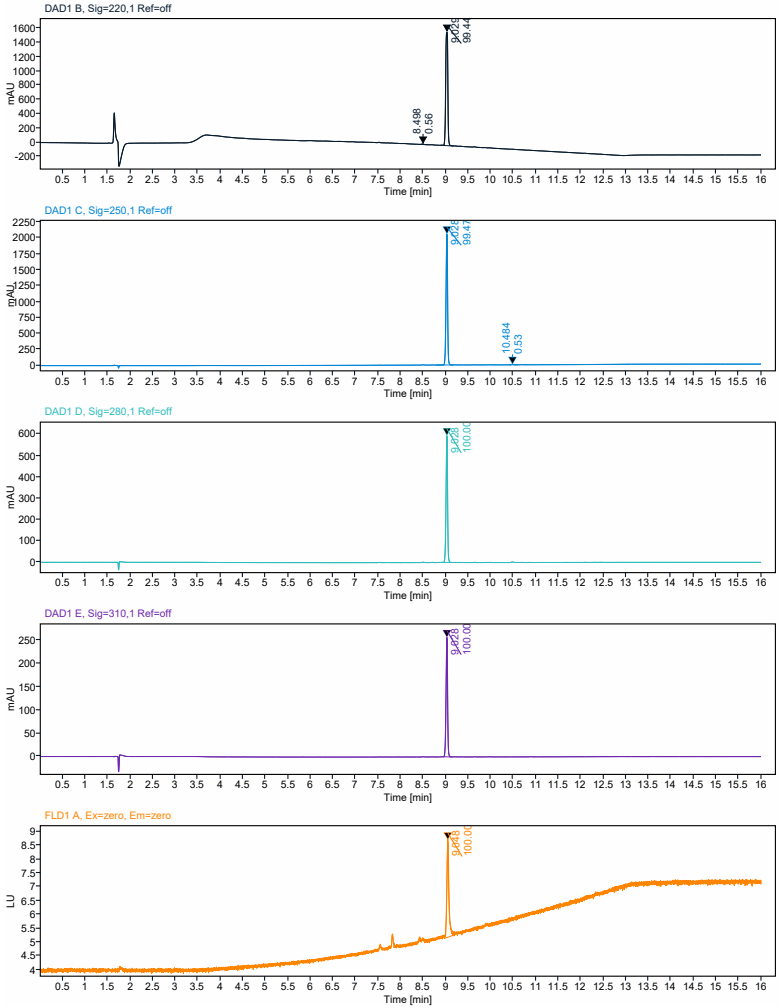


Major Peak Analysis

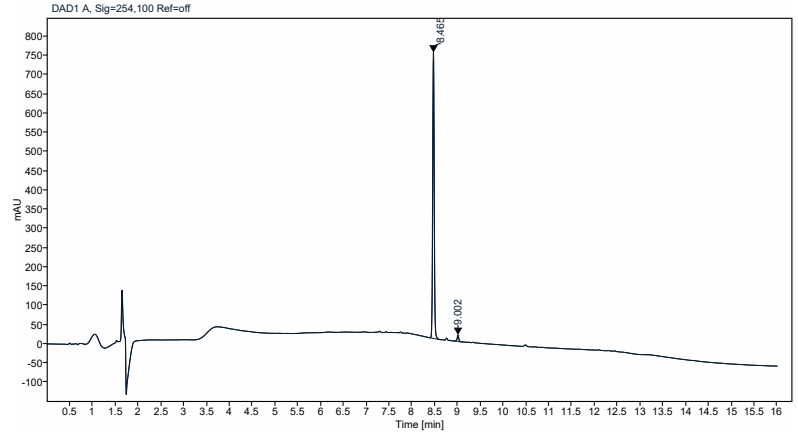




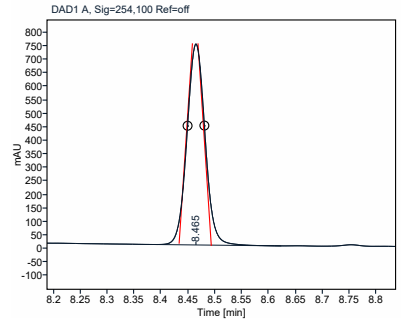
Retention Time	9.028
Peak Width at Base	0.045
Height	1256.581
Area	3449.530
Area Percent	100.00

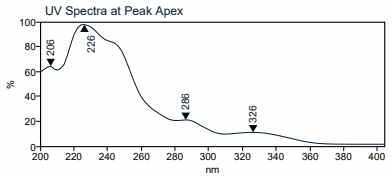


(6S)-6-(1-(1-(2-(2-(2-((3-(2-Amino-4-chloro-7-((4-methoxy-3,5-dimethylpyridin-2-yl)methyl)-7H-pyrrolo[2,3-*d*]pyrimidin-5-yl)prop-2-yn-1-yl)oxy)ethoxy)ethoxy)acetyl)piperidin-4-yl)-5-(3,5-dimethyl-1,2-oxazol-4-yl)-1H-1,3-benzimidazol-2-yl)-1-(3,4-difluorophenyl)piperidin-2-one

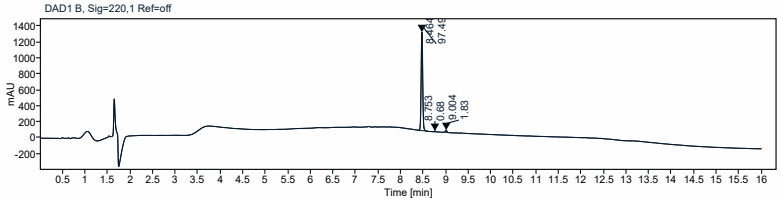


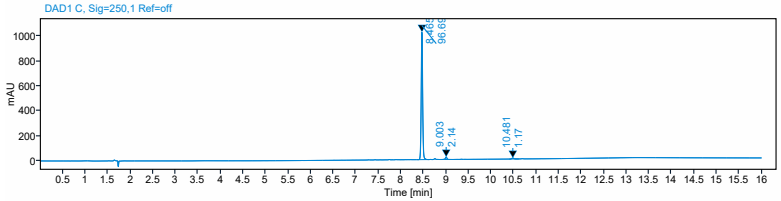
Major Peak Analysis

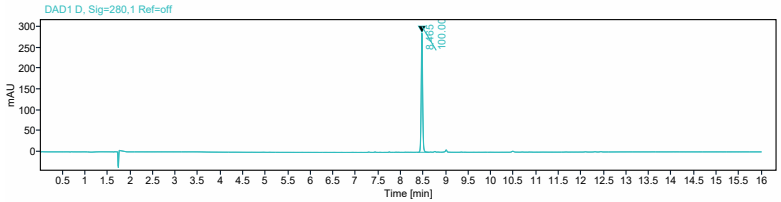


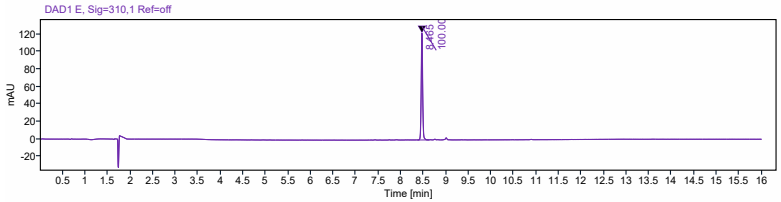


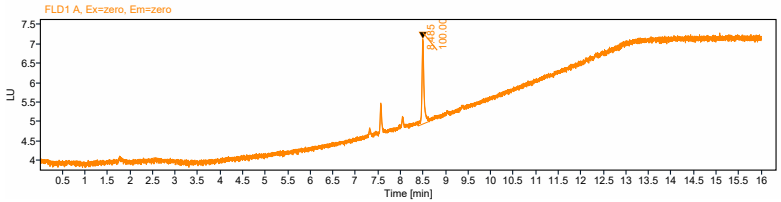
Retention Time	8.465
Peak Width at Base	0.037
Height	743.457
Area	1746.230
Area Percent	97.73



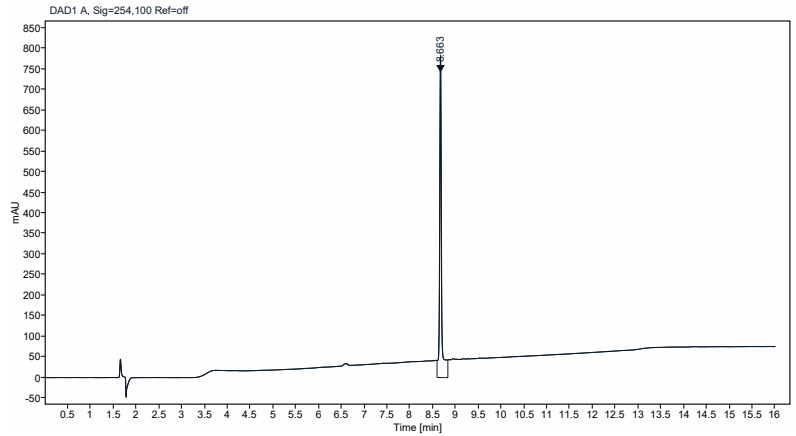




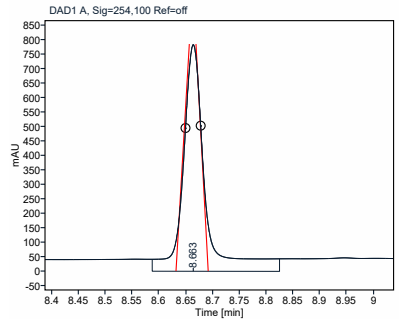


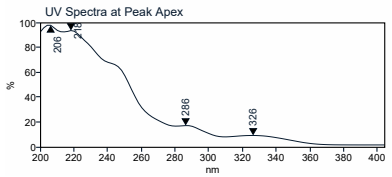


(6S)-6-(1-(1-(15-(2-Amino-4-chloro-7-((4-methoxy-3,5-dimethylpyridin-2-yl)methyl)-7H-pyrrolo[2,3-*d*]pyrimidin-5-yl)-3,6,9,12-tetraoxapentadec-14-ynoyl)piperidin-4-yl)-5-(3,5-dimethyl-1,2-oxazol-4-yl)-1H-1,3-benzodiazol-2-yl)-1-(3,4-difluorophenyl)piperidin-2-one

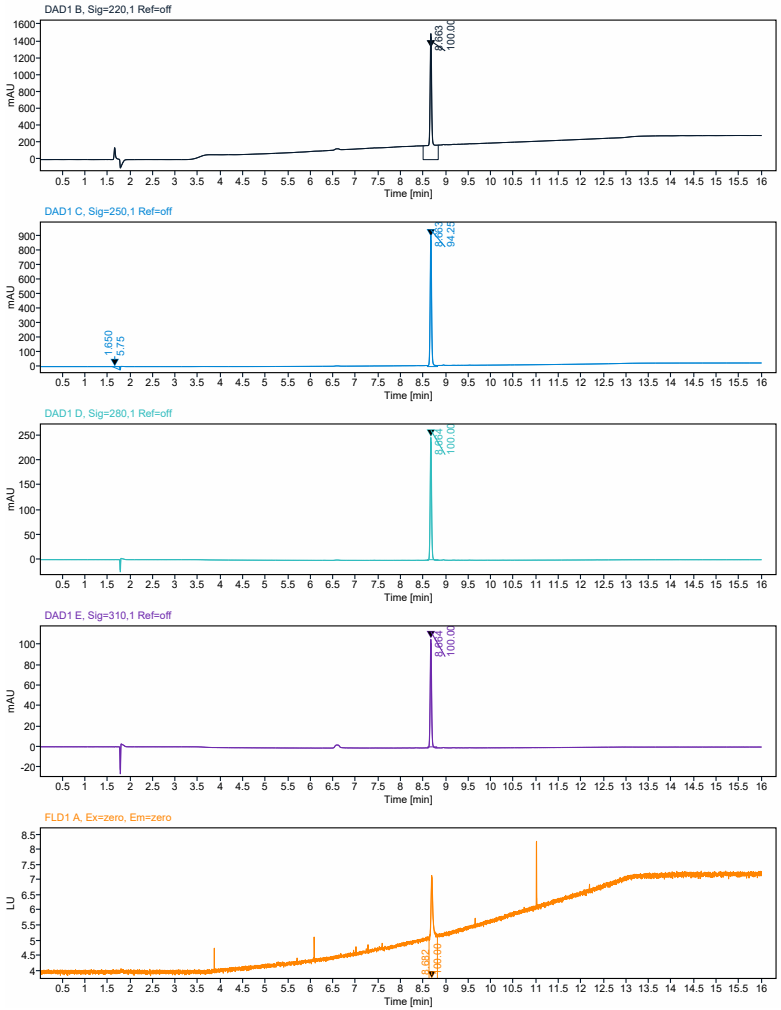


Major Peak Analysis

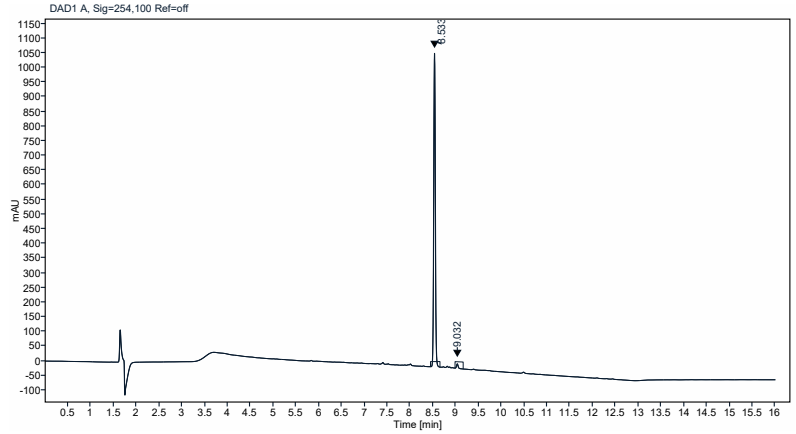




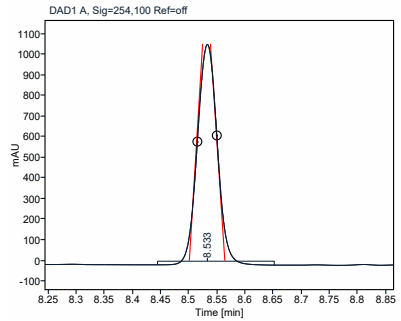
Retention Time	8.663
Peak Width at Base	0.034
Height	742.092
Area	1641.772
Area Percent	100.00

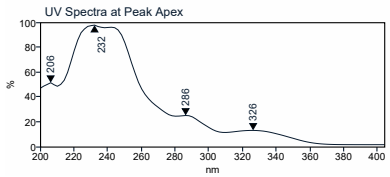


(6S)-6-(1-(1-(18-(2-Amino-4-chloro-7-((4-methoxy-3,5-dimethylpyridin-2-yl)methyl)-7H-pyrrolo[2,3-*d*]pyrimidin-5-yl)-3,6,9,12,15-pentaoxaoctadec-17-ynoyl)piperidin-4-yl)-5-(3,5-dimethyl-1,2-oxazol-4-yl)-1H-1,3-benzodiazol-2-yl)-1-(3,4-difluorophenyl)piperidin-2-one



Major Peak Analysis





Retention Time	8.533
Peak Width at Base	0.039
Height	1068.721
Area	2639.728
Area Percent	98.58

